

The
University
Of
Sheffield.

Department
Of
Mechanical
Engineering.

PhD Mechanical Engineering

**Antimicrobial efficacy of laser sintered polyamide 12 / silver
microcomposites**

James R. Wingham¹

July, 2022

Supervisors: Dr Candice Majewski¹ and Dr Joanna Shepherd²

1. Department of Mechanical Engineering, Faculty of Engineering,
The University of Sheffield.
2. School of Clinical Dentistry, Faculty of Medicine, Dentistry & Health,
The University of Sheffield.

Thesis submitted to the University of Sheffield in partial fulfilment
of the requirements for the degree of Doctor of Philosophy

“Useless research, move on. Most bacteria are beneficial or harmless.” — Zworm

“Seems like a pointless, tax payer funded, exercise by the university.” — Tim Eforerevolt

“Selling more rubbish on the could and maybe then blasting our ears with climate change and footprints.” — Flash Gorgon

“That won’t help much at controlling the bugs that spread in hospitals.” — Galahad

“or they just make a copper phone case...that would stop slugs as well.” — Dickie Sorge

*The secret within is a filler,
Oh so tiny and stuffed full of silver.
3D printed with flair,
Nasty bugs best beware,
'cause for you this material's a killer!*

Abstract

The spread of infectious disease is at the centre of global attention, with the demand for novel methods to control this spread higher than ever before. Antimicrobial materials, such as the ones presented here, can prove an effective tool for this, even against those with Antimicrobial Resistance. This research sought to exploit the nuances of the Laser Sintering process to introduce antimicrobial properties into Additively Manufactured parts.

Commercial and bespoke silver-containing additives, chosen to determine the effects of particle size and degradation rates, were successfully used to create intrinsically antimicrobial materials for use in Laser Sintering. These were mixed into a polyamide 12 powder feedstock, with the resulting printed microcomposite parts analysed for their engineering properties and antimicrobial functionality.

The composite powder feedstock was processed effectively and showed no significant effect on the mechanical properties, crystallinity, or microstructure of the printed parts. The additive was found to be well-dispersed throughout the printed parts, and antimicrobial silver ions were seen to be released in water as expected.

The microcomposite parts showed both bactericidal and antibiofouling effects (planktonic and biofilm) against both Gram-positive and Gram-negative bacteria (*Staphylococcus aureus* and *Pseudomonas aeruginosa*) in nutrient-poor conditions, even when the parts had no direct contact with the bacteria. No antimicrobial effect was measured in nutrient-rich conditions, with thiols present identified as preventing the silver from affecting the bacteria; and parts shown to have no cytotoxic effect against human cells. The custom-made additives were found to be more effective against *Staphylococcus aureus* than *Pseudomonas aeruginosa*, with the efficacy found to be more sensitive to the silver content of the additive than the degradation rate.

This research has demonstrated the potential for this approach to be adopted more broadly, and has provided crucial insights into significant factors influencing its effectiveness. Further work should focus on testing the efficacy against a wider range of microbes, the effect of additive loading, and the use of different base polymers.

Acknowledgements

I would like to thank everyone who has supported me throughout this project. To thank friends and family, who have put up with me in these strange times of lockdowns and piano-playing flying rabbits, and to specifically thank the following:

Candice Majewski – Dinosaurs. That’s all you need to know about Candice. A genuine inspiration, without whom I would never have even considered taking this on!

Joey Shepherd – A sword-wielding, axe-throwing supervisor. What more could I ask for?

Bob Turner – Whose expertise in bacteria and beyond have helped advance this project to new heights, and for providing additional bacterial testing data for the project.

Thomas Paterson – For introducing me to the world of Microbiology and training me up in its ways.

Ifty Ahmed – For his support and expertise in phosphate-based glasses and supervising the manufacturing of the tailored glass additives.

Md Towhidul Islam – For manufacturing the tailored glass additives.

Wendy Birtwistle and **Kurt Bonser** – For their technical assistance, but mainly for the random conversations in the polymer sintering lab.

All the technical staff and academics across the University who have welcomed me into their labs. Specifically **Jason Heath** and **Robert Moorehead** in the Microbiology labs, **Caroline Fry** for training me on Micro-CT, **Oday Hussein** for training me on particle size analysis, **Chris Hill** for his training and help with SEM and EDX, and **FaraPack Polymers** for the ICP-ESMS.

Alec Shackelford – For giving me an excuse to work in a world-renowned Physics lab at 3am.

Ryan Brown – Mainly for the office table tennis matches.

Rhys Williams – For his seemingly limitless Chemistry knowledge.

Luke Fox – For showing me how to get the most out of trade shows (and training me in tensile testing).

Ste Knox – For his help in the Chemistry lab, and his very specific random knowledge.

Sourabh Paul – “If you search amongst shit, you will find vegetables.”

Oliver Leete – “Glass is a fickle bitch.”

This work was funded by The University of Sheffield Department of Mechanical Engineering Centenary Scholarship and the EPSRC Doctoral Training Partnership (1949272), and is aligned with the EPSRC Future Manufacturing Hub in Manufacture using Advanced Powder Processes (EP/P006566/1).

Contents

| | | |
|----------|--|-----------|
| 1 | Introduction to Additive Manufacturing | 1 |
| 1.1 | Definition | 1 |
| 1.2 | Background | 1 |
| 1.2.1 | History | 1 |
| 1.2.2 | Generic Additive Manufacturing Process | 3 |
| 1.2.3 | Advantages of Additive Manufacturing | 4 |
| 1.2.4 | Limitations of Additive Manufacturing | 5 |
| 1.2.5 | Applications | 7 |
| 1.3 | Categories of Additive Manufacturing Processes | 11 |
| 1.3.1 | Vat Photopolymerisation | 11 |
| 1.3.2 | Material Extrusion | 11 |
| 1.3.3 | Material Jetting | 12 |
| 1.3.4 | Binder Jetting | 13 |
| 1.3.5 | Sheet Lamination | 13 |
| 1.3.6 | Directed Energy Deposition | 14 |
| 1.3.7 | Powder Bed Fusion | 15 |
| 1.4 | Polymer Powder Bed Fusion Processes | 15 |
| 1.4.1 | Selective Inhibition Sintering | 15 |
| 1.4.2 | Selective Mask Sintering | 16 |
| 1.4.3 | Selective Heat Sintering | 17 |
| 1.4.4 | High Speed Sintering | 17 |
| 1.4.5 | Multi-Jet Fusion | 18 |
| 1.4.6 | Laser Sintering | 19 |
| 2 | Introduction to Laser Sintering | 21 |
| 2.1 | Laser Sintering Process | 21 |
| 2.1.1 | Detailed Process Steps | 22 |
| 2.1.2 | Benefits | 23 |
| 2.1.3 | Limitations | 24 |
| 2.1.4 | Applications | 25 |
| 2.2 | Materials and Build Set-up (Pre-Processing) | 29 |
| 2.2.1 | Materials | 29 |
| 2.2.2 | Powder Characteristics | 32 |
| 2.2.3 | Design for Laser Sintering | 34 |
| 2.2.4 | Build Set-up | 34 |
| 2.3 | Build Considerations (In-Processing) | 35 |
| 2.3.1 | Powder Heating | 35 |
| 2.3.2 | Build Parameters | 36 |
| 2.3.3 | Microstructure | 38 |
| 2.3.4 | Cooldown | 41 |
| 2.4 | Post-Processing | 41 |
| 2.4.1 | Powder Removal | 41 |
| 2.4.2 | Aesthetic and Surface Finish Processes | 42 |
| 2.4.3 | Functional Processes | 43 |
| 2.5 | Quality Control and Long-term Effects | 44 |
| 2.5.1 | Geometry and Porosity | 44 |
| 2.5.2 | Long-term Effects | 44 |
| 2.6 | Composite Materials | 47 |

| | | |
|----------|--|-----------|
| 2.6.1 | Composite Material Feedstock Types | 47 |
| 2.6.2 | Production Methods | 49 |
| 2.6.3 | Quality Control | 51 |
| 2.6.4 | Commercially Available Materials | 52 |
| 2.6.5 | Academic Research | 53 |
| 2.7 | Key Points | 56 |
| 2.7.1 | Relation to the Fundamental Objectives | 56 |
| 2.7.2 | Fundamental Objectives to be Addressed | 56 |
| 3 | Introduction to Antimicrobial Materials | 57 |
| 3.1 | What are Bacteria? | 57 |
| 3.1.1 | Categorising Types of Bacteria | 57 |
| 3.1.2 | Biofilms | 58 |
| 3.1.3 | Antimicrobial Resistance | 59 |
| 3.2 | Detecting Bacteria – How to Quantify the Bacterial Load | 60 |
| 3.2.1 | Testing Conditions – Media Choice | 60 |
| 3.2.2 | Determining the Number of Bacteria | 60 |
| 3.3 | Controlling the Spread of Microbes on Surfaces | 62 |
| 3.3.1 | Definitions | 62 |
| 3.3.2 | Methods of Sterilisation and Disinfection | 63 |
| 3.4 | Antimicrobial Materials | 65 |
| 3.4.1 | Concept | 65 |
| 3.4.2 | Definitions | 65 |
| 3.4.3 | Strategies of Antimicrobial Materials | 66 |
| 3.4.4 | Antimicrobial Materials in Additive Manufacturing | 68 |
| 3.5 | Silver as an Antimicrobial | 69 |
| 3.5.1 | Metals as Antimicrobials | 69 |
| 3.5.2 | History and Uses of Silver | 69 |
| 3.5.3 | Silver Antibacterial Method of Action | 70 |
| 3.6 | Polyamide / Silver Micro- and Nano-Composites | 72 |
| 3.6.1 | Method of Action | 72 |
| 3.6.2 | Differences in Properties due to the Incorporated Silver Additives | 72 |
| 3.6.3 | Effect of Base Polymer Properties | 74 |
| 3.6.4 | Effect of Additive Properties | 74 |
| 3.6.5 | Silver Phosphate Glasses | 75 |
| 3.7 | Project Definition | 75 |
| 3.7.1 | Gaps in the Knowledge | 75 |
| 3.7.2 | Aim | 75 |
| 3.7.3 | Research Questions | 75 |
| 3.7.4 | Objectives | 76 |
| 3.7.5 | Contribution to Knowledge | 77 |
| 3.7.6 | Hypothesis | 77 |
| 4 | Commercially Available Silver Phosphate Additives | 79 |
| 4.1 | Powder Characterisation and Part Printing | 80 |
| 4.1.1 | Powder Morphology | 80 |
| 4.1.2 | Particle Size | 81 |
| 4.1.3 | Thermal Properties | 83 |
| 4.1.4 | Laser Sintering | 85 |
| 4.2 | Microcomposite Properties | 89 |
| 4.2.1 | Tensile Properties | 89 |
| 4.2.2 | Part Thermal Properties | 92 |
| 4.2.3 | Surface Composition | 93 |
| 4.2.4 | Microstructure | 95 |
| 4.2.5 | Additive Dispersion | 101 |
| 4.2.6 | Silver Content | 104 |
| 4.3 | Part Use and Functionality | 106 |
| 4.3.1 | Effect of Sterilisation | 106 |
| 4.3.2 | Water Uptake – Spherical Samples | 110 |
| 4.3.3 | Water Uptake – Effect of Geometry | 115 |
| 4.3.4 | Silver Release | 119 |

| | | |
|----------|---|------------|
| 4.4 | Antibacterial Testing | 121 |
| 4.4.1 | Bacterial Strains | 121 |
| 4.4.2 | Preliminary Testing – Powder Efficacy | 121 |
| 4.4.3 | Preliminary Testing – Static Peg Assay | 123 |
| 4.4.4 | Contact Efficacy (Planktonic) | 130 |
| 4.4.5 | Additional Microbial Testing (carried out by R. Turner) | 133 |
| 4.5 | Chapter Summary | 137 |
| 5 | Custom-Made Silver Phosphate Additives | 139 |
| 5.1 | Powder Characterisation and Part Printing | 140 |
| 5.1.1 | Additive Production | 140 |
| 5.1.2 | Additive Composition | 141 |
| 5.1.3 | Morphology | 143 |
| 5.1.4 | Particle Size | 144 |
| 5.1.5 | Laser Sintering | 145 |
| 5.2 | Micro-Composite Properties | 147 |
| 5.2.1 | Colour Measurements | 147 |
| 5.2.2 | Tensile Properties | 148 |
| 5.2.3 | Surface Composition | 150 |
| 5.3 | Part Use and Functionality | 152 |
| 5.3.1 | Water Uptake | 152 |
| 5.4 | Antibacterial Testing | 155 |
| 5.4.1 | Powder Efficacy | 155 |
| 5.4.2 | Contact Efficacy | 158 |
| 5.4.3 | Non-Contact Efficacy | 163 |
| 5.5 | Chapter Summary | 166 |
| 6 | Conclusions | 167 |
| 6.1 | Achievement of the Overall Aims | 167 |
| 6.2 | Summary of Work and Contributions to Knowledge | 167 |
| 6.3 | Obstacles to Completion | 173 |
| 6.4 | Significance and Potential for Impact | 173 |
| 6.5 | Further Work | 174 |
| | References | 176 |
| A | Laser Sintering Builds and Detailed Protocols | 201 |
| A.1 | Laser Sintering Build Details | 201 |
| A.2 | Part Dimensions | 204 |
| A.3 | Tensile Testing Protocol | 205 |
| A.4 | Water Uptake Protocol | 206 |
| A.5 | Serial Dilution (Miles and Misra) Protocol | 207 |
| A.6 | Static Peg Assay Protocol | 208 |
| B | Additional Results | 209 |
| B.1 | Particle Size Analysis | 209 |
| B.2 | Silver Additive Content | 214 |
| B.3 | Effect of Autoclaving | 214 |
| B.3.1 | Water Content | 214 |
| B.3.2 | Additional Results | 215 |
| B.4 | Water Uptake | 219 |
| B.5 | Silver Ion Release | 219 |
| B.6 | Additional Microbial Testing (Carried out by R. Turner) | 220 |
| B.6.1 | Nutrient-Poor Media | 220 |
| B.6.2 | Nutrient-Rich Media | 221 |
| B.6.3 | Nutrient-Poor Media with Glutathione | 223 |
| B.6.4 | Non-Contact Efficacy | 224 |
| B.6.5 | Cytotoxicity | 224 |
| B.7 | Colour Measurements | 225 |
| C | Additional and Preliminary Experiments | 227 |
| C.1 | Additional Tensile Testing | 227 |

| | | |
|----------|---|------------|
| C.1.1 | Effect of Powder Recycling | 227 |
| C.1.2 | Effect of Additive Loading | 229 |
| C.1.3 | Effect of Autoclaving – Preliminary Experiment | 230 |
| C.1.4 | Comparison with High Speed Sintering | 231 |
| C.2 | Preliminary Antimicrobial Testing | 232 |
| C.2.1 | Sterilisation Testing | 232 |
| C.2.2 | Contact Efficacy (Planktonic only) | 235 |
| C.3 | Other Commercially Available Silver Phosphate Glasses | 236 |
| C.3.1 | Particle Size Analysis | 236 |
| C.3.2 | Laser Sintering | 237 |
| D | Publications | 241 |
| D.1 | Overview | 241 |
| | Use of silver-based additives for the development of antibacterial functionality in Laser Sintered polyamide 12 parts | 243 |
| | Tailored Additives for Incorporation of Antibacterial Functionality Into Laser Sintered Parts | 255 |

Nomenclature

Acronyms

| | |
|----------|---|
| 3D CAD | Three-Dimensional Computer-Aided Design |
| AM | Additive Manufacturing |
| AMR | Antimicrobial Resistance |
| BHI | Brain Heart Infusion |
| CFU | Colony Forming Units |
| CM | Conventional (Subtractive) Manufacturing |
| CNC | Computer Numerically Controlled |
| DfAM | Design for Additive Manufacture |
| DfM | Design for Manufacture |
| DSC | Differential Scanning Calorimetry |
| EDX | Energy-dispersive X-ray Spectroscopy |
| EPS | Extracellular Polysaccharide |
| EtO | Ethylene Oxide |
| FEA | Finite Element Analysis |
| ICP-ESMS | Inductively Coupled Plasma Electrospray Mass Spectrometry |
| LEFM | Linear Elastic Fracture Mechanics |
| Micro-CT | X-ray Computed Micro Tomography |
| NC | No Contours |
| PBS | Phosphate Buffered Saline |
| QACs | Quaternary Ammonium Compounds |
| QC | Quality Control |
| RAM | Radiation Absorbing Material |
| RM | Rapid Manufacturing |
| ROI | Region of Interest |
| ROS | Reactive Oxygen Species |
| RP | Rapid Prototyping |
| RT | Rapid Tooling |
| SEM | Scanning Electron Microscopy |
| STL | (Derived from) STereoLithography |
| TGA | Thermogravimetric Analysis |
| WIP | Work In Progress |

Materials

| | |
|---------------|---|
| β -TCP | β -Tricalcium Phosphate |
| ABS | Acrylonitrile Butadiene Styrene |
| CB | Carbon Black |
| CF | Carbon Fibre |
| CHA | Carbonated Hydroxyapatite |
| CNTs | Carbon Nanotubes |
| co-PES | co-Polyethersulfone |
| HA | Hydroxyapatite |
| HDPE | High-density Polyethylene |
| MWCNT | Multi-Walled Carbon Nanotube |
| P40, P45, P50 | Custom-Made Glasses |
| PA | Polyamide (e.g. PA12, Nylon) |
| PBG | Phosphate-Based Glass |
| PBT | Polybutylene Terephthalate |
| PC | Polycarbonate |
| PCL | Polycaprolactone / Poly- ϵ -caprolactone |
| PEEK | Polyether Ether Ketone |
| PEK | Polyaryletherketone |
| PEKK | Polyetherketoneketone |
| PET | Polyethylene Terephthalate |
| PHBV | Poly(Hydroxybutyrate-co-Hydroxyvalerate) |
| PI | Polyimide |
| PLA | Polylactic Acid |
| PLGA | Poly(L-lactide-co-glycolide) |
| PLLA | Poly-L-lactic Acid |
| PMMA | Polymethylmethacrylate |
| POM | Polyoxymethylene |
| PP | Polypropylene |
| PS | Polystyrene |
| PTWs | Potassium Titanium Whiskers |
| PVA | Polyvinyl Alcohol |
| PVDF | Poly(vinylidene fluoride) |
| SAN | Styrene-acrylonitrile |
| SMMA | Styrene methyl methacrylate |
| TPE | Thermoplastic Elastomer |
| TPU | Thermoplastic Polyurethane |
| UHMWPE | Ultra-high-molecular-weight Polyethylene |


AM Processes

| | |
|-----|-------------|
| 3DP | 3D Printing |
|-----|-------------|

| | |
|------|-------------------------------------|
| cDLP | Continuous Digital Light Processing |
| CMB | Controlled Metal Buildup |
| DED | Directed Energy Deposition |
| DLP | Digital Light Processing |
| DMD | Direct Metal Deposition |
| DSPC | Direct Shell Production Casting |
| EBM | Electron Beam Melting |
| FDM | Fused Deposition Modelling |
| FFF | Fused Filament Fabrication |
| HSS | High Speed Sintering |
| LAM | Laser Additive Manufacturing |
| LENS | Laser Engineered Net Shaping |
| LOM | Laminated Object Manufacturing |
| LS | Laser Sintering |
| MJF | Multi-Jet Fusion |
| MLS | MicroLightSwitch |
| PBF | Powder Bed Fusion |
| PBJ | Powder Binder Jetting |
| SAF | Selective Absorption Fusion |
| SDL | Selective Deposition Lamination |
| SGC | Solid Ground Curing |
| SHS | Selective Heat Sintering |
| SIS | Selective Inhibition Sintering |
| SLA | Stereolithography (Apparatus) |
| SLS | Selected Laser Sintering |
| SMS | Selective Mask Sintering |
| UAM | Ultrasonic Additive Manufacturing |
| VLM | Variable Lamination Machines |

Symbols

| | | |
|---------------------|---------------------------|----------------------------|
| ψ | Sphericity | (-) |
| ρ | Density | (g/cc, or – for ρ_l) |
| σ_f | Stress at Fracture | (MPa) |
| σ_{uts} | Ultimate Tensile Strength | (MPa) |
| OD ₆₀₀ | Optical Density at 600 nm | (-) |
| θ_{wca} | Water contact angle | (°) |
| ε_{max} | Elongation at Break | (%) |
| A | Surface Area | (mm ²) |
| a | Crack Size | (mm) |
| c_p | Specific Heat Capacity | (J/kg/K) |
| D | Diffusion Constant | (mm/s ²) |

| | | |
|---|---|----------------------|
| d | Diameter | (mm) |
| E | Young's Modulus | (MPa) |
| h_f | Heat of Fusion | (kJ/kg) |
| K_{1c} | Critical Stress Intensity Factor (plane strain) | (MPa \sqrt{m}) |
| l | Voxel Size | (μm) |
| m | Mass | (g) |
| M_∞ | Mass uptake at saturation | (g) |
| M_t | Mass uptake at time t | (g) |
| P | Laser Power | (W) |
| T | Temperature | ($^\circ\text{C}$) |
| t | Thickness | (mm) |
| V | Volume | (mm 3) |
| v | Speed | (mm/s) |
| w | Water Content | (%) |
| Y | Calibration Function (for crack geometry) | (-) |
|  | Figure created by the author | |

Subscripts

| | |
|-----|-------------------|
| int | Initial |
| maj | Major |
| min | Minimum |
| vol | Volume Equivalent |
| b | Powder Bed |
| c | Critical |
| D | Disc |
| l | Powder Layer |
| P | Peg |
| S | Sphere |
| s | Laser Scan |

List of Figures

| | | |
|------|---|----|
| 1.1 | Timeline of Novel Commercial AM Technologies | 2 |
| 1.2 | Generic Additive Manufacturing Process | 3 |
| 1.3 | Applications of Additive Manufacturing | 7 |
| 1.4 | Examples of AM Models | 8 |
| 1.5 | Examples of Rapid Tooling | 9 |
| 1.6 | Examples of AM Functional Parts | 10 |
| 1.7 | Vat Photopolymerisation Schematic | 11 |
| 1.8 | Material Extrusion Schematic | 12 |
| 1.9 | Material Jetting Schematic | 12 |
| 1.10 | Binder Jetting Schematic | 13 |
| 1.11 | Sheet Lamination Schematic | 14 |
| 1.12 | Directed Energy Deposition Schematic | 14 |
| 1.13 | Powder Bed Fusion Schematic | 15 |
| 1.14 | Selective Inhibition Sintering Schematic | 16 |
| 1.15 | Selective Mask Sintering Schematic | 16 |
| 1.16 | Selective Heat Sintering Schematic | 17 |
| 1.17 | High Speed Sintering Schematic | 17 |
| 1.18 | Multi-Jet Fusion Schematic | 18 |
| 1.19 | Laser Sintering Schematic | 19 |
| 2.1 | Laser Sintering Chapter Structure | 21 |
| 2.2 | Schematic of Laser Sintering | 22 |
| 2.3 | Benefits of Unsintered Powder Acting as Supports | 23 |
| 2.4 | Example Material Hinges and Flexible Materials Printed Using Laser Sintering | 23 |
| 2.5 | Surface Roughness of Laser Sintered Parts | 24 |
| 2.6 | Example Model and Prototype Applications of Laser Sintering | 25 |
| 2.7 | Example Functional Applications of Laser Sintering | 26 |
| 2.8 | Example End-use Medical Applications of Laser Sintering | 27 |
| 2.9 | Example Surgical and Potential Future Medical Applications of Laser Sintering | 28 |
| 2.10 | Example Rapid Tooling Applications of Laser Sintering | 29 |
| 2.11 | Example Applications of Laser Sintering in Fashion | 29 |
| 2.12 | Additive Manufacturing Materials Growth | 30 |
| 2.13 | Pyramid of Polymers Processed with Laser Sintering | 30 |
| 2.14 | Structure of Amorphous and Semi Crystalline Polymers | 31 |
| 2.15 | Transition Temperatures of Amorphous and Crystalline Polymers | 31 |
| 2.16 | Skeletal Diagram of PA12 | 32 |
| 2.17 | Effect of Particle Size on Packing Density | 32 |
| 2.18 | Example Functional Applications of Laser Sintering | 33 |
| 2.19 | Orange Peel Effect in Used Powder Parts | 33 |
| 2.20 | Example Design Guide for Laser Sintering | 34 |
| 2.21 | Stable Sintering Region | 36 |
| 2.22 | Temperature Variations in Laser Sintering | 36 |
| 2.23 | Scan Strategy and Contours | 37 |
| 2.24 | Cross-section of a Laser Sintered Part Observed using Optical Microscopy | 39 |
| 2.25 | Effect of Increasing Energy Input on Powder Particles in LS | 39 |
| 2.26 | Effect of Particle Size with Equal Energy Input | 39 |
| 2.27 | Effect of Particle Size Distribution on Porosity | 40 |
| 2.28 | Effect of Energy Density and Degree of Particle Melt on the Mechanical Properties | 40 |

| | | |
|------|--|-----|
| 2.29 | Example Powder Removal | 42 |
| 2.30 | Example Aesthetic and Surface Finish Post-Processing Steps | 42 |
| 2.31 | Example Functional Post-Processing Methods | 43 |
| 2.32 | Uses of Micro-CT to Analyse Laser Sintered Parts | 44 |
| 2.33 | Long Term Mechanical Properties of PA12 Laser Sintered Parts | 45 |
| 2.34 | Mechanical Properties and Colour Change of PA12 Laser Sintered Parts with Exposure to Ultraviolet Light | 46 |
| 2.35 | Types of Feedstock used to Create Composite Parts | 47 |
| 2.36 | Additive Dispersion in the Printed Parts for Different Feedstock Types | 48 |
| 2.37 | Methods of Composite Polymer Powder Production | 50 |
| 2.38 | Micro-CT Scans in Polymer AM to Detect Inclusions and Additives | 51 |
| | | |
| 3.1 | Structure of a Prokaryotic Cell | 57 |
| 3.2 | Differences in Cell Wall Structure in Gram-Positive and Gram-Negative Bacteria | 58 |
| 3.3 | Stages of Biofilm Formation | 58 |
| 3.4 | Schematic of Antimicrobial Resistance | 59 |
| 3.5 | Miles and Misra Serial Dilution | 60 |
| 3.6 | Methods of Estimating Bacterial Load | 61 |
| 3.7 | Resistance of Microorganisms to Sterilisation and Disinfection Levels | 62 |
| 3.8 | Schematic of Hospital Acquired Infections | 65 |
| 3.9 | Approaches to Anti-Adhesive Surfaces | 66 |
| 3.10 | Approaches to Contact-Active Surfaces | 67 |
| 3.11 | Approach Against Quorum Sensing in Biocide-Releasing Surfaces | 67 |
| 3.12 | Timeline of Medicinal Silver Use | 69 |
| 3.13 | Failure Methods for Antimicrobial Surface Coatings | 70 |
| 3.14 | Silver Ion Method of Action | 71 |
| 3.15 | Silver Micro- and Nano-Composite Release Method | 72 |
| 3.16 | Mechanical Properties of Compression Moulded PA6/66 / Silver Micro-Composites | 73 |
| 3.17 | Relationship of Water Uptake and Silver Ion Release Rate in a Compression Moulded PA6/Silver Nano-Composite | 73 |
| 3.18 | Silver Ion Release from Compression Moulded PA12/Silver Nano-Composites | 74 |
| 3.19 | Proposed Method of Silver Ion Release in Water from a Laser Sintered Part with Silver-Containing Phosphate Glass Additives | 78 |
| | | |
| 4.1 | Commercially Available Silver Phosphate Additives Chapter Structure | 79 |
| 4.2 | Powder Morphology from SEM | 80 |
| 4.3 | Commercial Powder Particle Size Analysis | 82 |
| 4.4 | Differential Scanning Calorimetry Schematic | 83 |
| 4.5 | Example Processed DSC Curve – Powder | 84 |
| 4.6 | Powder Analysis from DSC | 84 |
| 4.7 | Laser Sintering Equipment | 85 |
| 4.8 | Photos of a Failed LS Build | 87 |
| 4.9 | Build Layout for Builds 10–12 | 88 |
| 4.10 | Photo of Printed Parts | 88 |
| 4.11 | Tensile Testing Apparatus | 89 |
| 4.12 | Tensile Test Specimen Dimensions | 90 |
| 4.13 | Tensile Testing Results | 91 |
| 4.14 | Example Processed DSC Curve – Part | 92 |
| 4.15 | DSC of Printed Parts | 92 |
| 4.16 | SEM of Part Surfaces | 94 |
| 4.17 | Map of Elements from EDX | 95 |
| 4.18 | Schematic Diagram of Micro-CT | 96 |
| 4.19 | Micro-CT Specimen Photos | 96 |
| 4.20 | Example Slices from Micro-CT – Reconstruction, Region of Interest, Pores | 97 |
| 4.21 | Pore Size Analysis | 98 |
| 4.22 | Relationship of Sphericity and Major Pore Diameter | 99 |
| 4.23 | Example Slices from Micro-CT – Additive | 101 |
| 4.24 | 3D View from Micro-CT of Additive Dispersion | 102 |
| 4.25 | Views of a “Clump” of Additive | 102 |
| 4.26 | Additive Volume Equivalent Diameters | 103 |
| 4.27 | Complete Spatial Randomness Results | 104 |

| | | |
|------|---|-----|
| 4.28 | Part Chemical Composition from ICP-ESMS | 105 |
| 4.29 | View of a Fractured Tensile Test Specimen | 107 |
| 4.30 | Protocol for Conditioning and Mass Measurements | 109 |
| 4.31 | Stress-Strain Data from Sterilisation Experiments | 110 |
| 4.32 | Tensile Properties from Sterilisation Experiments | 111 |
| 4.33 | Effect of Water Content on the Mechanical Properties | 112 |
| 4.34 | Water Uptake Results | 114 |
| 4.35 | Ellipsoid Specifications | 116 |
| 4.36 | Printed Ellipsoids | 116 |
| 4.37 | Water Uptake Racks | 117 |
| 4.38 | Water Uptake Setup | 117 |
| 4.39 | Effect of Geometry Water Uptake Results | 118 |
| 4.40 | Ag ⁺ Release Results | 120 |
| 4.41 | Powder Efficacy Protocol with Timepoints | 122 |
| 4.42 | Preliminary Powder Efficacy Results | 123 |
| 4.43 | Static Peg Assay Lid Design | 123 |
| 4.44 | Completed Peg Board | 124 |
| 4.45 | Static Peg Assay Layout | 124 |
| 4.46 | Static Peg Assay Protocol | 126 |
| 4.47 | Static Peg Assay Results (<i>S. aureus</i> S235) | 127 |
| 4.48 | Static Peg Assay Results (<i>P. aeruginosa</i> SOM1) | 128 |
| 4.49 | Bacterial Growth After Incubation | 129 |
| 4.50 | Crystal Violet Staining of Pegs | 129 |
| 4.51 | Part Contact Efficacy Protocol with Timepoints | 131 |
| 4.52 | Part Effectiveness Against <i>S. aureus</i> S235 in PBS | 132 |
| 4.53 | Additional Antimicrobial Testing in Nutrient-Poor Media | 134 |
| 4.54 | Additional Antimicrobial Testing in Nutrient-Rich Media | 136 |
| 4.55 | Cytotoxicity Test Results | 137 |
| | | |
| 5.1 | Custom-Made Silver Phosphate Additives Chapter Structure | 139 |
| 5.2 | Photos of the Three Custom Silver Phosphate Glass Additives | 141 |
| 5.3 | SEM Images of the Custom Additives | 143 |
| 5.4 | Particle Size Analysis | 145 |
| 5.5 | Photos During Laser Sintering | 146 |
| 5.6 | Photo of Printed Parts | 146 |
| 5.7 | Setup Used for Colour Measurements | 147 |
| 5.8 | Tensile Testing Results | 149 |
| 5.9 | SEM of Part Surfaces Containing the Custom Additives | 150 |
| 5.10 | P50 Part EDX | 151 |
| 5.11 | Custom Glasses Water Uptake Results | 153 |
| 5.12 | Custom Glasses Water Uptake Percent Increase | 154 |
| 5.13 | Shaking Incubator Rack Design | 155 |
| 5.14 | Powder Efficacy Protocol | 156 |
| 5.15 | Powder PBS Tests | 157 |
| 5.16 | Powder PBS Test Photos | 158 |
| 5.17 | Contact protocol | 159 |
| 5.18 | <i>S. aureus</i> S235 Contact PBS Tests | 160 |
| 5.19 | <i>P. aeruginosa</i> SOM1 Contact PBS Tests | 161 |
| 5.20 | Part PBS Test Photos | 162 |
| 5.21 | Non-contact protocol | 164 |
| 5.22 | Non-Contact PBS Tests | 165 |

List of Tables

| | | |
|------|--|-----|
| 2.1 | Key Parameters in Laser Sintering | 37 |
| 2.2 | Commercially Available LS Composite Powders | 52 |
| 2.3 | Composite Polymers Researched in Laser Sintering | 54 |
| 2.4 | Additives for PA12 | 55 |
| 3.1 | Dry Sterilisation Times | 63 |
| 4.1 | Particle Size Analysis Results | 81 |
| 4.2 | DSC Powder Results | 85 |
| 4.3 | Standard PA2200 Parameters | 86 |
| 4.4 | Tensile Testing Statistical Comparison | 91 |
| 4.5 | DSC Part Results | 93 |
| 4.6 | Elemental Compositions from EDX | 94 |
| 4.7 | Combinations of Conditioning and Drying for Each Sample Set | 107 |
| 5.1 | Custom Additive Oxide Compositions | 140 |
| 5.2 | Precursors used for the Custom Glasses | 140 |
| 5.3 | Elemental Compositions (Weight Percentage) Measured Using EDX | 141 |
| 5.4 | Elemental Compositions (Atomic Percentage) Calculated from EDX | 141 |
| 5.5 | Oxide Compositions of Each Additive Obtained from EDX | 142 |
| 5.6 | Particle Size | 144 |
| 5.7 | Colour Values Measured for the Four Materials | 148 |
| 5.8 | Tensile Testing Statistical Comparison | 148 |
| 5.9 | Powder Tests Statistical Comparison | 157 |
| 5.10 | <i>S. aureus</i> S235 Contact Tests Statistical Comparison | 160 |
| 5.11 | <i>P. aeruginosa</i> SOM1 Contact Tests Statistical Comparison | 161 |
| 5.12 | Non-Contact Tests Statistical Comparison | 165 |

Thesis Foreword

Motivations for Research

As a Mechanical Engineer with a fascination for Additive Manufacturing (AM), this project provided the perfect opportunity to explore the cutting edge of research and contribute to the rapidly growing body of knowledge surrounding it. With some previous experience with desktop polymer AM machines, I was keen to explore the possibilities with more sophisticated industrial AM technologies, namely using polymer powder-based approaches. To this end, the “Advanced Polymer Sintering Laboratory” at The University of Sheffield was the perfect base for this; established as a world-leading centre focused on polymer powder bed fusion, and specialising in Laser Sintering (LS) and High Speed Sintering (HSS).

Background and Scope

The project (and its associated funding) was initially defined with a very broad scope, based around exploring new materials for either LS or HSS, with the exact direction of the research able to adapt throughout the project. Around the same time as the beginning of this research, conversations between Dr Candice Majewski, Dr Joey Shepherd (project supervisors) and an external company (BioCote) had led to the idea of incorporating silver-containing additives into AM parts made using powder-based techniques; with the ultimate aim of imbuing them with antibacterial properties.

It was around that idea this project was based, initially working in parallel with Dr Bob Turner who was working on the more Microbiology-focused research associate project “When the drugs don’t work... Manufacturing our pathogen defenses” (EP/R036748/1); allowing for a far more in-depth analysis of the antibacterial properties and cytotoxicity of the parts than would otherwise have been possible.

Later in the project, after having analysed the commercial additives and following a guest lecture from Dr Ifty Ahmed on manufacturing phosphate-based glass powders, I sought out a collaboration to pursue the possibility of creating tailored additives. This allowed a more rigorous exploration of the effect of certain properties (namely silver content and degradation rate) on the antimicrobial efficacy of the printed parts.

Approach to Research

At its core this project was inherently multidisciplinary, spanning the fields of Mechanical Engineering, Microbiology, Materials Science, and Chemistry. Coming from a background in Mechanical Engineering, it was from this viewpoint that the research was approached. The intention with this thesis is that enough information and literature is included so that anyone from an Engineering background with no prior knowledge in AM, could understand the steps taken and the reasoning behind them.

The experiments presented here which are primarily based in other disciplines all started from discussions with experts in that particular field. Following this and with additional training, the methodologies were devised in consultation with said experts. Wherever possible (accounting for machine access, time required, and restrictions due to COVID-19), I undertook sufficient training to carry out the experiments myself, constituting the vast majority of this research.

Broad Aims

From the outset, the broad aims of this research were to expand the range of materials available for polymer powder-based AM processes. This was quickly narrowed down to the aforementioned aim of incorporating antibacterial properties into AM parts through the use of silver-containing additives, initially focusing on Laser Sintering.

Fundamental Objectives

Based on the broad aims, some fundamental objectives were identified at the start of the project. Each of these represented a potential barrier to successfully creating an antibacterial material with Laser Sintering. These were to:

- Determine whether the material could be processed by the Laser Sintering machine.
- Measure any effect on the mechanical properties to see if the inclusion of the additive significantly affected the Engineering properties of the printed parts.
- Assess whether the additive (specifically the silver) had been successfully incorporated into the parts in a homogeneous manner.
- Identify and quantify the method of silver release from the parts (including any limitations on the use cases).
- Test the antimicrobial properties of the printed parts against disease-causing bacteria.

Following the successful completion of these initial objectives, the focus could then turn to carrying out more rigorous testing to determine the limits of this method, and identify key factors in the design and implementation of this approach.

Chapter 1

Introduction to Additive Manufacturing

1.1 Definition

Additive Manufacturing (AM) has been defined as the “process of joining materials to make parts from 3D model data, usually layer upon layer, as opposed to subtractive manufacturing and formative manufacturing methodologies” [1]. This term is commonly used in industry, however is seldom used by the general public; with the term “3D Printing” now often used synonymously with AM due to its intuitiveness and the greater levels of media coverage it has received.

The term Additive Manufacturing encompasses a family of processes; the fundamental principle of which is that parts can be made from three-dimensional Computer-Aided Design (3D CAD) models, without the need for process planning to take place for individual features [2,3]. The simplicity of designing a part without having to consider how it could be manufactured conventionally, combined with the geometric freedom possible with AM, is leading to more and more industries using AM to manufacture end-use products.

1.2 Background

1.2.1 History

The number of AM technologies developed by researchers and in industry is vast, with hundreds of very similar machines marketed throughout AM’s history; most of which use different acronyms for similar processes. A selection of commercially released processes deemed significantly novel by the author, are shown in Figure 1.1; note that processes based on existing technologies (potentially with differing acronyms) have been excluded.

Stereolithography (SLA) was the first recognisable AM technology to be patented in 1986 [8], representing a radical shift in how manufacturing was approached and opening up the market for other AM processes to follow. At this stage, the technology was only suitable for prototyping due to the limited range of materials available and the poor mechanical properties. With industry, and even the inventor of SLA (C. Hull), viewing the process as nothing more than a prototyping technique [9], the term Rapid Prototyping (RP) was adopted as the first widely used term for AM.

The use of AM for prototyping established the technology despite its relatively slow uptake. It would not be until a much later date, when the accuracy and mechanical properties of parts improved sufficiently, that AM would could be used to test the form, fit and function of components [10]. In this application, the AM parts are merely representations of the final parts and would be swapped out at a later stage for conventionally manufactured parts.

The first instance of AM used to manufacture end-use parts commercially, was the QuickCast process; this used SLA models as the “wax” patterns in investment casting [11]. While the AM part itself was not used as the final part, the use of AM in the creation of tooling, known as Rapid Tooling (RT), still constitutes a large market in AM [12].

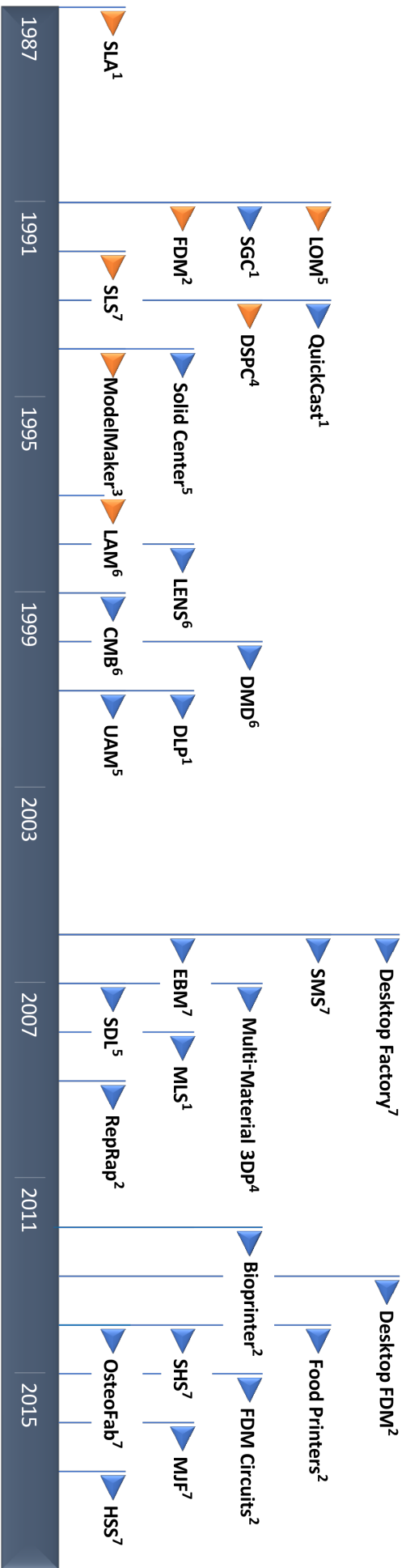


Figure 1.1: Timeline of novel commercial AM technologies, including which category they are part of (first instances shown in orange). **AM Categories:** 1. Vat Photopolymerisation, 2. Material Extrusion, 3. Binder Jetting, 4. Directed Energy Deposition, 5. Powder Bed Fusion (see Section 1.3 for details on these). **Acronyms:** SLA (Stereolithography), FDM (Fused Deposition Modelling), SGC (Solid Ground Curing), LOM (Laminated Object Manufacturing), SLS (Selective Laser Sintering), DSPC (Direct Shell Production Casting), LAM (Laser Additive Manufacturing), LENS (Laser Engineered Net Shaping), CMB (Controlled Metal Buildup), DMD (Direct Metal Deposition), UAM (Ultrasonic Additive Manufacturing), DLP (Digital Light Processing), VLM (Variable Lamination Machines), SMS (Selective Mask Sintering), EBM (Electron Beam Melting), 3DP (3D Printing), SDL (Selective Deposition Lamination), MLS (Micro-Lightswitch), SHS (Selective Heat Sintering), MJF (Multi Jet Fusion), HSS (High Speed Sintering) [4–7]. 🇧🇪

Recently, there has been a major increase in the use of AM to directly create end-use products. This has historically been referred to as Rapid Manufacturing (RM) and Direct Digital Manufacture (DDM); however, the term AM has now replaced these. This is now the largest application for AM parts and is seeing AM recognised as a major manufacturing method [13].

1.2.2 Generic Additive Manufacturing Process

While there are many different AM processes, each with their own distinct operating procedure and build method, all of these processes follow the same generic process [14]. This generalised process is shown in Figure 1.2 and examined in more detail in this section. All of these steps are present in some form for every AM process, however the complexity of each step will vary considerably depending on the exact technique used.

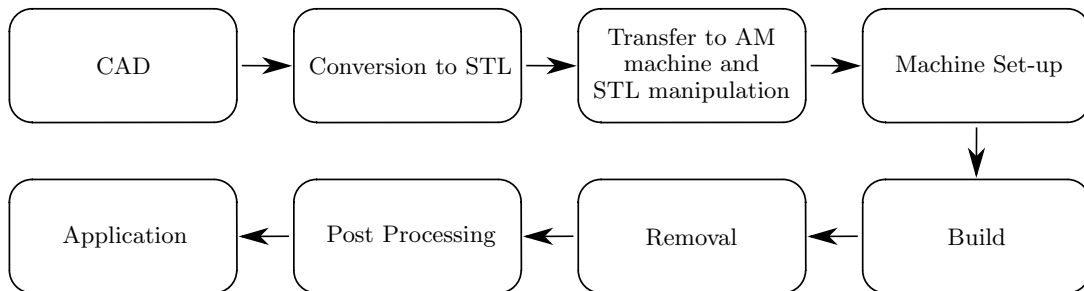


Figure 1.2: Generic additive manufacturing process flow diagram [15]. 🌐

Computer Aided Design (CAD)

Unlike most conventional manufacturing methods, AM necessitates the part be fully defined in a 3D CAD model prior to production. While at first this difference could appear very subtle, this represents a fundamental shift in the skill set required by designers. Whereas before, a craftsman could sculpt the shape of a product by hand to achieve the perfect design, this is no longer feasible; with the use of advanced (often expensive) scanning systems required to translate the physical model into 3D CAD.

The limiting factor in many applications has now become the skill designers have in CAD, with an advanced knowledge of multiple CAD packages often required to fully exploit the capabilities of AM. This presents a particular problem when trying to introduce AM to the wider population (such as AM at home or for children [16]), with current projects aiming to create more intuitive and easy to use CAD systems to enable this.

Conversion to STL

The diversity of the methods available to create 3D CAD models mean that there are many different file types these models could have. The challenge arises when AM machines are required to read these files and produce parts; it is simply not feasible to create a machine capable of reading (and successfully interpreting) every file type.

The files therefore need to be converted into a standard type that AM machines can read; however there is much debate on the “best” file type for AM machines to operate, with multiple options now available. The default for the vast majority of AM machines is `.stl` (derived from STereoLithography), which approximates the surface of a part as a series of tessellated triangles [17]. While this overcomes the obstacle of readability, these files are not easily altered and exclude much of the information about the part (such as material, colour or exact geometry).

Among the file types proposed to replace `.stl`, the two current front-runners are the `.amf` (Additive Manufacturing File Format) developed by ASTM [18], and `.3mf` (3D Manufacturing Format) developed by Microsoft and the 3MF Consortium [19, 20]. Both of these have similar benefits, with the ability to support curved surfaces, colour, texture, functionally graded materials and both being open-source. While these new file types have been suggested, it is likely that most simple AM machines will retain `.stl` as their default for the foreseeable future.

Transfer to AM Machine and STL Manipulation

Once the file has been converted into a suitable format, this then needs to be transferred to the AM machine; this is a trivial task for some systems, but for others this can be a more involved process. This step generally involves positioning the part within the build area (with options including changing the position, orientation and size), and the option to print multiple parts within the same build in most AM processes [14].

Machine Set-up

These operations differ significantly between machines, with different options available in each system. A common build parameter available to change is the layer height, with other parameters such as scan speed, bed temperature, laser power / nozzle temperature, and many more often available.

The physical set-up of the machine is also included in this step, with users required to check there is enough material for the build, the machine has a sufficient power source, and any additional pre processing steps (such as preheating for powder bed processes) have been carried out.

Build

The method by which the AM machine builds the part varies depending on the AM process and the exact machine; although all of these methods will construct parts layer by layer. This is an automated process with little need for human interaction beyond occasionally checking the build for fatal errors. The external conditions (such as room temperature) may need to be controlled during this step, depending on the sensitivity of the process.

A detailed description of how the main categories of AM machines operate can be found in Section 1.3.

Removal from Machine

Although some attempts at automation have been made, removal of the printed part(s) from the machine is usually done manually. This can be a very delicate process depending on the AM technique and the material used; for example parts requiring post-sintering or infiltration in binder jetting (see Section 1.3.4) can be very fragile at this stage, with a high possibility to damage the parts through human error. Part removal can therefore be a highly skilled process, depending on the material and geometry used.

Post-Processing

Often referred to as additive manufacturing's "dirty secret" by the media, post-processing is the name given to anything that needs to be done to the parts in between removal from the machine and their eventual use. The complexity of this step varies greatly depending on the AM process used and the application that the part will be used for. The potential for this to be the lengthiest step in the process is the cause of the negative publicity. The emphasis in marketing was instead on the "print times", with any post-processing steps required either shown in minimal detail or excluded completely.

Key tasks in this step include the removal of powder and/or support structures from the parts after they have been removed from the build area. Other, more complex, processes can be carried out as required; these can include sintering, infiltration, surface modifications and painting.

Application

Following the post-processing, the finished part can be used for its intended application. More details on common applications for AM parts can be found in Section 1.2.5.

1.2.3 Advantages of Additive Manufacturing

Reduction in Tooling

The main benefit of AM is the increased geometric complexity it provides, without the increase in cost this would traditionally entail [21]. This is only possible due to the tool-less manufacturing method that AM utilises, moving away from the traditional Design for Manufacture (DfM) mantra, instead using the much less restricting Design for Additive Manufacture (DfAM) approach. In practice, this can simply mean not requiring draft angles or parting lines, all the way to including complex lattice structures for lightweight components.

The elimination of tooling also has major cost benefits, especially for shorter production runs. For example in injection moulding, the cost of manufacturing the dies can be thousands of pounds and take many weeks. With AM, since this tooling is not required, the lead times can be reduced dramatically and the associated cost can be eliminated. This makes AM well suited to the production of unique parts [22], allowing for greater levels of customisation and personalisation to become possible.

Agile Manufacturing

Agility has been defined as “using market knowledge and a virtual corporation to exploit profitable opportunities in a volatile market place” [23]; the responsiveness of AM makes it ideal for implementing this approach. It is the flexibility of individual machines which makes this possible, each capable of switching between designs instantly, without delays caused by tooling changeovers. These systems can adapt their products and production rates quickly, with the only delays occurring from the heating up of machines and post-processing of parts [24].

Even when not used for the creation of end-use products, where AM is used solely as a prototyping tool, the agile nature of the machines has significant benefits. The potential to increase the quality of a product during the design stage stems mostly from the reduction in time needed to manufacture prototypes [17]. This enables designers to make and test a greater number of prototypes, explore more alternative designs, finalise the designs at a later stage, and receive feedback on designs more quickly.

Inventory Reduction

With conventional products, there is often a need for multiple processes to create the desired product. For this to happen, there is generally a large amount of Work In Progress (WIP); this takes the form of large bins / warehouses of components in varying states of manufacture. With AM, any stock held is either raw material, the finished product or in post-processing, effectively eliminating the WIP and reducing the capital investment required [22]. The geometric complexity possible with AM enables this, as the entire part can often be manufactured in one step (and post-processing).

The size of the factory required is also reduced as a result of the tool-less nature of AM. Conventional factories have the need to store large amounts of different tools, dies (at least one for each design) and machines for differing processes. With AM, a “digital inventory” is employed, with all of the different designs stored electronically. This, combined with the lower number of machines required, can have significant space (and cost) savings associated with it.

Sustainability and Environmental Impact

The environmental benefits of using AM can be significant, due to both the reduced material wastage and the potential to improve the design. Aerospace applications are a prime example of where these benefits can be realised; with buy-to-fly ratios of 10:1 common with Conventional Manufacturing (CM) [25] and high fuel costs and environmental impact during flight.

The choice of whether to use AM for these high performance applications is more complex, since the part properties (such as surface finish) or the materials available are often not suitable. Methods to determine whether the use of CM, AM, or a combination of AM and CM as a finishing process, are now being put forward based on their environmental impact; these methods consider both the primary energy consumption and the CO₂ produced [25–27]. The complexity and hardness of the material is a deciding factor in these processes, since the energy consumption of the AM process can be very similar to CM, with the differences arising in the powder production and chip recycling.

Over the lifetime of a component, the light-weighting possible with AM can also have significant environmental benefits. Many aerospace companies are now using AM in their aircraft due to the potential fuel savings, with some studies suggesting that this could be as high as 6.4% [28]. For example, Airbus and Autodesk redesigned an A320 partition with a weight saving of 45% (30 kg), estimated to save 3,000 kg of fuel per partition, per aircraft; a potential saving of 465,000 tonnes of CO₂ if applied to all A320s [24].

1.2.4 Limitations of Additive Manufacturing

Cost

The capital investment required for an AM machine can be large, with companies currently still trying to recoup their development costs by inflating the machine prices [24]; this can deter businesses from investing in the technology and slows the adoption of AM in general. With the exception of a few

components (such as lasers and galvanic mirrors), most of the components in AM machines are relatively inexpensive. It is expected that the price of machines will drop as more companies enter the market and competition increases; this has already been seen in simple desktop material extrusion machines [12].

There is an alternative to this, with multiple AM service providers (such as Shapeways [29]) now operational, smaller businesses can focus on creating and selling the 3D CAD designs; instead outsourcing the part production. However, the material costs constitute a large part of the production cost in AM and still need to be accounted for. It is widely known that the material costs for AM are greatly inflated compared to their bulk price [30]; this is especially true for thermoplastic filaments, the materials for which are commonly used in injection moulding. Again, this cost is likely to decrease as more companies enter the market.

The cost justification is therefore of greater importance with AM, since the cost of producing the part is often more expensive than using conventional methods. In order to justify its use, a redesign to optimise the part for AM (which could include adding functionality, part consolidation or lightweighting) could be required, including analysing the cost saving over the lifetime of the component [21, 24].

Speed and Throughput

The cost of producing individual AM parts does not vary significantly depending on the number of parts made. While this is beneficial for individual parts or small batches, it presents a challenge when considering large batch or mass production. Studies have been carried out to find the crossover point at which CM becomes more cost effective than AM [31]; while the capacity and efficiency of AM machines is ever increasing, this point is still at best in the 10,000s rather than the scales seen in mass production.

An obvious way to decrease the cost of components is to make more at once; however the scalability of most AM technologies presents a major challenge. While machines capable of creating very large components (or many small components) exist, the only way to feasibly achieve this in a realistic time-frame is to increase the layer height, thus compromising on the accuracy.

Although the lead times for AM parts are much shorter than in CM, the time needed to actually manufacture the parts is generally much longer. This is therefore another hurdle to overcome, as the benefits of its use have to outweigh this longer production time [21].

Part Properties and Quality Assurance

The mechanical properties of AM parts tend to be inherently anisotropic due to their layer by layer construction [32]. This provides additional complexity to designers, as the orientation of parts in the build area will influence the performance of the parts; this orientation can affect a variety of properties, such as strength, stiffness and surface finish.

The repeatability and reliability of AM parts is an issue, as variations within the same machine make it difficult to guarantee the properties of parts over a long production run. The number of processes and materials now available mean that creating standard Quality Assurance checks for AM parts is challenging, an obstacle which needs to be overcome for mass production. Committees such as ASTM F42 and ISO/TC 261 are endeavouring to make these standards, which are starting to be created and implemented in industry [33].

Intellectual Property

The issue of Intellectual Property (IP) is complex both with the production of AM machines, and the parts they produce. Much of the AM technology developed has been open source, with designs such as the RepRap project [34] used in multiple machines. While this is not an issue, the added functionalities of cheaper desktop systems are starting to stray dangerously close to the patented industrial machines.

While conflicts such as patent infringements are relatively clear-cut, this is not the case when it comes to the AM parts themselves. There are multiple issues here, ranging from the ownership of 3D CAD models and who should be permitted to profit from or distribute these, to who should be responsible for the failure of a product when so many people are involved in different stages of the design and manufacture. There is no defined answer to these as of yet; however, the use of AM for immoral and potentially dangerous applications, is often a talking point in the media.

Traditional Attitudes and Expertise

“This ‘baggage’ of Rapid Prototyping is probably a larger hurdle to the uptake of [Additive Manufacturing] than any of the technical issues we face” — Hopkinson et al. [35]

The legacy left by the name “Rapid Prototyping” has caused problems with the adoption of AM, companies who have used the same processes without issue up until now are often deterred by the misnomer that AM is only suitable for prototyping. While these attitudes are starting to change with more end-use parts being produced, this is one of the hardest aspects to change since it is not always based on reliable evidence.

The training and expertise required to operate the AM machines also poses an issue for the adoption of AM. For example if AM were to be used in a hospital environment, the expertise to run the machines and make the models is not something that is currently easily found [36]. For this, either additional training or staff would be required; both of these would increase the overall cost and could prevent the installation of the system.

1.2.5 Applications

The applications of AM are increasing rapidly every day, with more designers, companies and researchers developing new processes and uses than ever before. A snapshot of the AM market can be seen in Figure 1.3 for 2021, where it can be seen that the production of functional parts is the largest application.

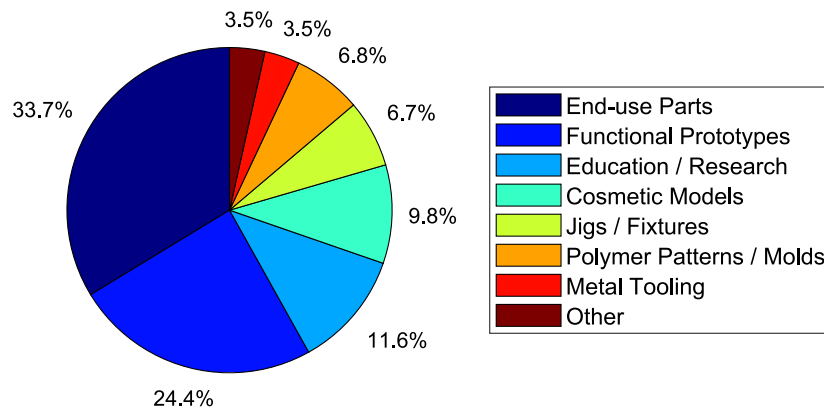


Figure 1.3: AM applications in 2021, with functional parts the largest sector, comprising 58.1% [37]. 🚫

Listing every instance that AM has been used for is not feasible (or interesting to read); however, all of the applications of AM fit into three categories: Prototypes and Models, Rapid Tooling and Functional Parts. In this Section these categories are briefly described, with examples of real-life applications to convey the advantages that using AM provides.

Prototypes and Models

The first widespread use of AM was to create cosmetic models and prototypes, this still forms a large part of the market; with approximately 10% of parts used for this purpose [37]. One of the main industries using AM purely for visual modelling (so far) is architectural, capitalising on the photo-realistic full colour models possible with AM to create sales models (see Figure 1.4a).

While architectural models do not require specific mechanical properties, the ability of AM to create functionally graded materials has been used in the medical industry to enhance training [38]; models such as the one shown in Figure 1.4b can be created to accurately simulate bone, grey matter, blood and much more. The use of models is also used to aid in the planning of complex surgeries, decreasing the likelihood of mistakes by the surgeons or the need for repeat procedures [39].

An example of a more specialised application of AM is creating models for photoelastic stress analysis [42–45]. This simple, yet powerful, technique is used to experimentally determine stress distributions in components, and to verify Finite Element Analysis (FEA) models (as shown in Figure 1.4c). Traditionally machined from transparent blocks of resin, the use of AM to create these models presents a significant cost saving.

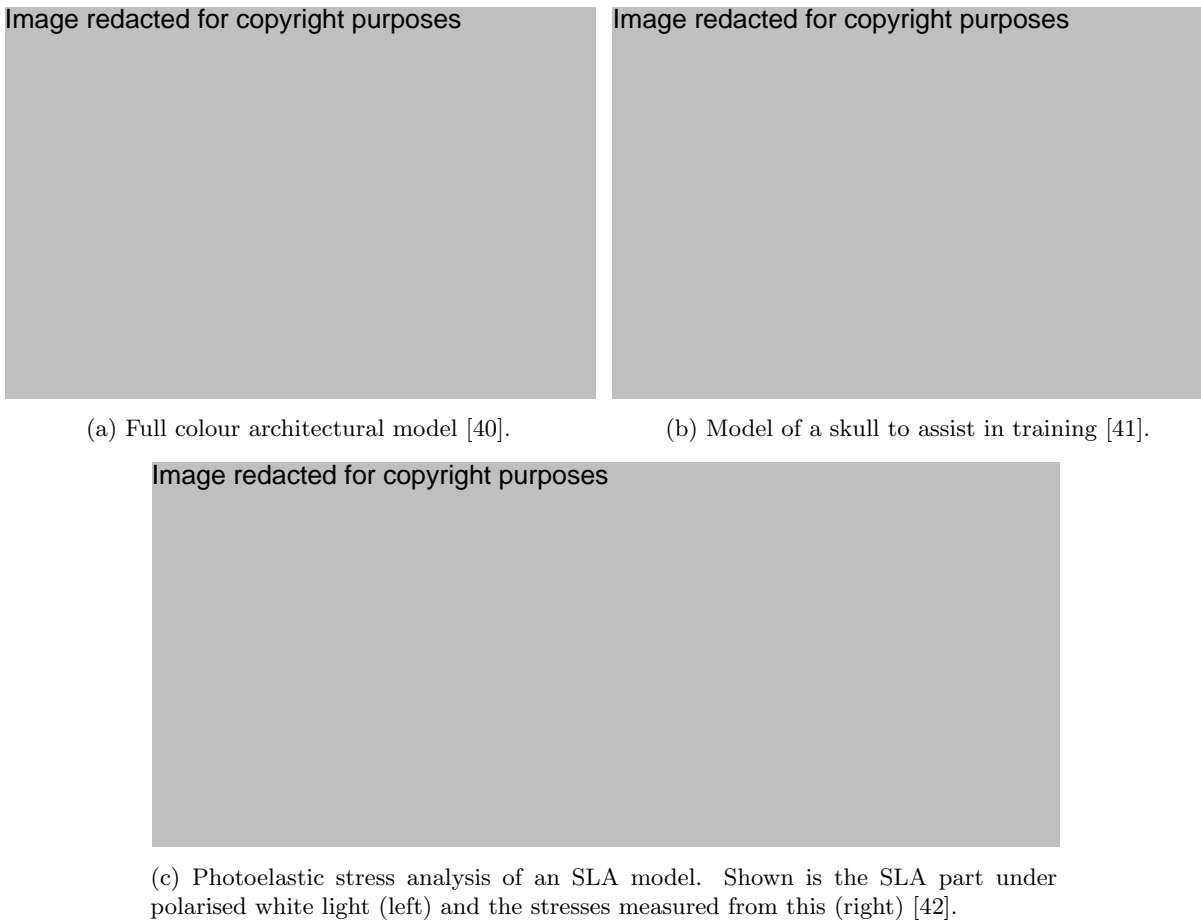


Figure 1.4: Examples of models made using AM.

Rapid Tooling


In Rapid Tooling (RT), AM parts are used to create tooling for more conventional manufacturing processes, rather than being used as prototypes or as end-use parts. There are two ways in which this can be achieved, with either indirect or direct RT. With indirect RT, AM parts are used in the production of tooling; whereas with direct RT, the AM part itself is the tooling.

A common example of indirect RT is investment casting, where AM is used to create the “wax” patterns which are subsequently burnt out of the ceramic moulds [46]. Applications for this include the production of unique, customised jewellery and complex metallic parts; companies such as Shapeways offer these services for precious metals (see Figure 1.5a) [29, 47].

For direct tooling, AM is used to manufacture the tooling directly; this method is able to utilise the benefits of AM fully, to create previously unachievable designs. For example, the geometric freedom possible with AM allows the construction of conformal cooling channels, able to improve the production and properties of the finished parts (see Figure 1.5b) [49].

The use of AM for manufacturing jigs and fixtures (for example dunnage design for securing cargo) can also be considered to be indirect tooling [46]. Whereas these do not directly impact the production or properties of the parts, these do aid in its production and protection; with cheaper technologies such as material extrusion ideally suited to these.

Both indirect and direct RT are well suited to medical applications, the use of AM to create patient-specific biomodels can have multiple uses. For example, in surgery these can be used indirectly as guides (e.g. guide holes for drilling); or they can be used directly to shape conventional implants (e.g. maxillofacial implants), which both improves the end result and reduces surgery time [39, 50, 51]. The ability to digitally mirror scanned features can also be used here to help with symmetry.

Image redacted for copyright purposesImage redacted for copyright purposes

(a) Octopus ring produced in silver using AM and investment casting [29].

(b) Conformal cooling channels in a steel SLM injection mould insert [48].

Figure 1.5: Examples of rapid tooling made using AM.

Functional Parts

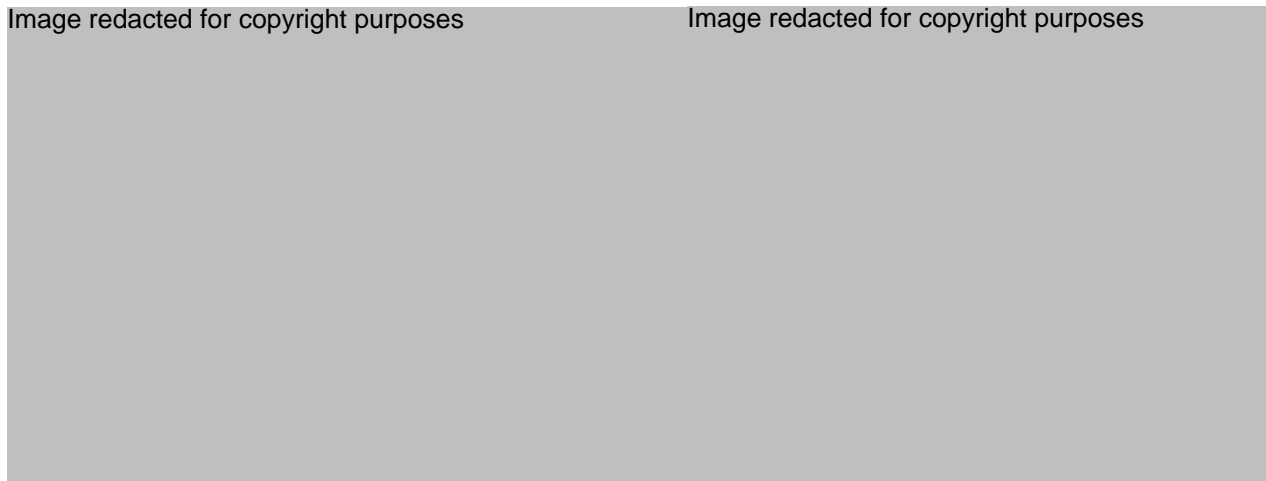
The production of functional, end-use products has become the largest application in AM due to the geometric complexity possible, the flexibility of the machines, and part properties which are now achievable. In addition to the shortened lead times and increased ability to respond to market demand, there are three main ways in which these advantages are being used; these being lightweighting of components, part consolidation, and part customisation / personalisation.

The lightweighting of parts using AM exploits the geometric complexity available and the functionality of 3D CAD and FEA packages. This is generally achieved using two methods, these being topology optimisation and the inclusion of lattice structures. An example of topology optimisation can be seen in Figure 1.6a, where a node undertaking a complex loading was redesigned for used with AM [52]; this redesign reduced the node weight by 75% and the overall weight of the structure by 40%.

The use of lattice structures within a part is a relatively simple way of reducing the weight, without compromising on the structural integrity. This is commonly used in AM parts, with more CAD packages creating specific tools to create these intricate patterns. An example of where this has been taken to the extreme is the “ultralight metallic microlattice” (see Figure 1.6b), which uses a lattice structure which is completely hollow; this 99.9% air construction has been dubbed “the world’s lightest metal” [56].

Part consolidation is also possible with AM, this involves combining previously separate components to reduce the number of assembly operations required. This reduces the amount of WIP (decreasing the size of factory required), reduces the number of part inspections needed (fewer parts), and can also improve the performance (e.g. potential leaking at joins) [24]. An example of this is GE Aviation’s “Advanced Turboprop” engine (see Figure 1.6c), which has been reduced from 855 parts to 12 parts using AM, while improving its power and efficiency [57].

The flexibility of AM and the ability to create parts based on 3D scans makes it ideal for medical applications, where geometries are patient specific. These parts can include internal implants, external prostheses or custom devices such as hearing aids. All of these can be created to the patient’s exact measurements, with properties tailored for the specific purpose. An example of a cranial implant created to encourage cell growth can be see in Figure 1.6d, other common examples of AM implants include joint replacements [58].



(a) A topology optimised structural steel node redesigned by Arup (right), which is 75% lighter than the original (left) [52].

(b) "Ultralight metallic microlattice" developed at HRL Laboratories [53].

Image redacted for copyright purposes

Image redacted for copyright purposes

(c) GE Aviation's advanced turboprop engine, which consolidates 855 parts into 12 using AM [54].

(d) Patient specific cranial implant, made by Oxford Performance Materials [55].

Figure 1.6: Examples of functional parts made using AM

1.3 Categories of Additive Manufacturing Processes

The nature of many AM machines, coupled with the rate at which new processes are being developed, mean that it is impossible to definitively categorise AM into distinct groups. However, attempts to do so have been made, with the ASTM categories commonly used. The categories are based on the method of joining the material, and have been defined as: binder jetting, directed energy deposition, material extrusion, material jetting, powder bed fusion, sheet lamination and vat photopolymerisation [1].

While these categories are a useful method of sorting AM machines, they provide no indication as to which materials can be processed with each technique. As useful as a system based on materials would be, the ability of some AM machines to print multiple materials (with some methods able to print polymers, metals and ceramics) means that this is not feasible.

A brief introduction to the ASTM categories is shown in this section, all of the definitions (shown in quotation marks) are as defined in ASTM/ISO 59200-15 [1].

1.3.1 Vat Photopolymerisation

Vat Photopolymerisation is the “process in which liquid photopolymer in a vat is selectively cured by light-activated polymerisation”. This process is exclusively used for photopolymers, with very high accuracy and surface finish often achieved.

This category includes two main processes, these being Stereolithography (SLA) and Digital Light Processing / Continuous Digital Light Processing (DLP / cDLP); a schematic of which can be found in Figure 1.7. Both of these techniques use an ultraviolet (UV) light source to cure a resin, with SLA using a scanning laser point and DLP projecting a 2D image onto the resin.



Figure 1.7: Vat photopolymerisation schematic, cDLP (left), and SLA (right) [59].

These processes are generally limited to one material per build, however the ability of DLP to build an entire layer at once can provide a considerable speed advantage when optimised. Support structures are often needed with these processes, although small overhangs can be built without.

1.3.2 Material Extrusion

Material Extrusion is defined as the “process in which material is selectively dispensed through a nozzle or orifice”, this has become the most widely used 3D printing method due to its relative simplicity and low cost.

Machines in this category all operate in a similar manner, which can be seen in Figure 1.8; this process is referred to as Fused Deposition Modelling (FDM) or Fused Filament Fabrication (FFF). The process normally uses amorphous thermoplastic filaments, which are heated in the nozzle and re-solidify immediately after extrusion [60].



Figure 1.8: Material extrusion schematic [61].

The ease with which filaments can be handled and processed, means that it is now commonplace for machines to print with multiple materials in each build [62]. This can be used simply to create different colours within parts, or for support structures, with properties such as chemical or water solubility optimised for ease of removal [15, 63, 64].

1.3.3 Material Jetting

Material Jetting is defined as a “process in which droplets of build material are selectively deposited”, this is normally achieved using an inkjet printhead to deposit the liquid material. While this step does not vary extensively between systems, there are two distinct processes by which material is solidified; divided into UV cured resins (Figure 1.9), and temperature induced phase changes.



Figure 1.9: Material jetting (photopolymers) schematic [65].

For photopolymers, the liquid material is cured using a UV lamp after deposition, as shown in Figure 1.9. Other materials processed in this way are deposited in a molten form, with the colder substrate initiating the phase change and creating the part.

As with material extrusion, multiple materials can be processed within the same build; however, the range of materials which can be processed is much larger, with much greater control over the part properties.

1.3.4 Binder Jetting

Binder Jetting is the “process in which a liquid bonding agent is selectively deposited to join powder materials”, and is one of the most versatile AM processes in terms of material choice as it can process virtually any powder. Also known as Powder Binder Jetting (PBJ) and Three-Dimensional Printing (3DP), it uses an inkjet printhead to dispense adhesive on a powder bed to build parts (as shown in Figure 1.10); this method is commonly used for polymers, metals and ceramics [66].



Figure 1.10: Binder jetting schematic [67].

This process does not use heat to join the material, instead relying solely on the binder. Advantages of this include: a virtually unlimited range of processable materials, the ability of loose powder to act as support material, and the use of coloured binders to achieve full colour prints; all of these benefits are in a process that is one of the most scalable in AM. Factors such as these have led to PBJ becoming widely used to print moulds for sand casting in industry [68].

The parts produced directly by binder jetting are relatively weak, since most of the strength comes from the adhesive [69]; the parts produced directly by PBJ are therefore only suitable for non-load bearing applications, such as architectural models. For most applications, additional post-processing steps are required to strengthen the “green” parts; these can include sintering, infiltration and hot isostatic pressing [70].

1.3.5 Sheet Lamination

Sheet Lamination is the “process in which sheets of material are bonded to form a part”; this broad description includes multiple processes, such as Laminated Object Manufacturing (LOM), Selective Deposition Lamination (SDL) and Ultrasonic Additive Manufacturing (UAM). All of which use sheets of materials as feedstock, which are then bonded together and the profiles cut.

For LOM, sheets are pre-coated in adhesive, bonded using thermal energy, and cut using a laser (Figure 1.11) [71–73]. However, this process is expensive due to the laser costs, has a high material wastage, poor transverse strength, and the unwanted material can be difficult to remove [74]. SDL uses a paper feedstock onto which an adhesive is selectively applied, and the profile cut using a carbide blade; this process improves on LOM, while making small, colour printers possible [75].

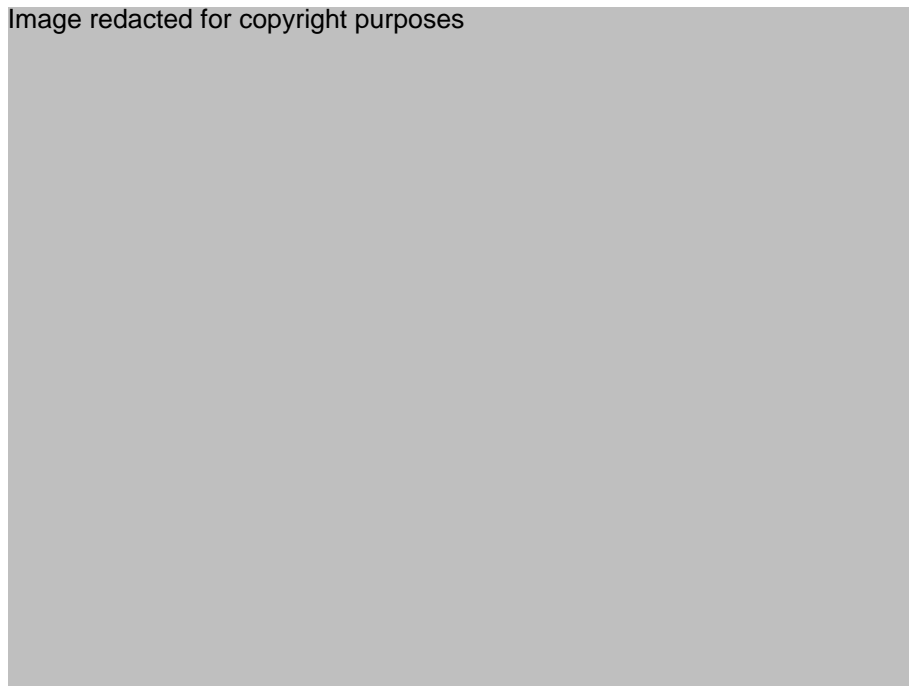


Figure 1.11: Sheet lamination schematic, shown is Laminated Object Manufacturing (LOM) [76].

For metal parts, UAM bonds foils using ultrasonic consolidation, before the profiles are machined with conventional Computer Numerically Controlled (CNC) processes; this finishing process means that the parts have excellent dimensional accuracy [77]. Since no heat is used during the build, this process is also well suited to embedding electronics and optical/functional fibres [78].

1.3.6 Directed Energy Deposition

Directed Energy Deposition (DED) is the “process in which focused thermal energy is used to fuse materials by melting as they are being deposited”, this process is only used for metals. DED uses a powder or wire feed, which is melted by either a laser beam or an electron beam during deposition so that it contacts the substrate in its molten form [79, 80]. Shown in Figure 1.12, this process allows for different materials to be used in the same build.



Figure 1.12: Directed energy deposition schematic [81].

While DED does not have the accuracy of many other AM processes, there are distinct advantages to using this method. Since the set-up is relatively manoeuvrable, the nozzle can be fitted to conventional CNC arms, making the build areas much larger than in other processes. This also enables the process to be used on existing parts to perform repairs; with the molten material even allowing the same crystalline structure as the substrate to form in the printed sections [82, 83].

1.3.7 Powder Bed Fusion

Powder Bed Fusion (PBF) is the “process in which thermal energy selectively fuses regions of a powder bed”. There are many ways in which this is achieved, with the different methods generally divided into metal and polymer processes. All of these processes are similar to the one shown in Figure 1.13, with a powder bed either sintered or melted using a laser, electron beam (metals only) or infra-red heat source.



Figure 1.13: Powder bed fusion schematic, shown is Laser Sintering [84].

Most of these systems use a scanning point to sinter or melt the powder, however this process is relatively slow, with the time taken per layer dependant on the packing of the build area. Some processes have attempted to speed up the print time by sintering larger areas; however these are relatively new, with the more well established scanning methods still dominating the market.

Polymer powder AM processes have been consistently identified as the most profitable in AM for several years, with the revenue from polymer powder material sales overtaking all other AM materials in 2021 [85, 86]. With companies using AM seeking to invest further in these processes [85], research into this area has a strong link with current industry practice, increasing the potential impact.

Interest in these is in part due to the technical capabilities of the processes, with polymer PBF able to print without support structures, making it more suitable for larger production volumes as parts can be nested in the build area. The mechanical properties of the printed polymers are also generally higher and more consistent than in other AM processes. For these reasons and their popularity in industry, the focus of this research is on polymer PBF; these processes are discussed in more detail in Section 1.4.

1.4 Polymer Powder Bed Fusion Processes

1.4.1 Selective Inhibition Sintering

Selective Inhibition Sintering (SIS) was one of the first methods to attempt to speed up the printing process by sintering larger areas at a time. The process (shown in Figure 1.14), involves printing an inhibiting agent onto the powder bed using an inkjet printhead to create a boundary in the parts. Plates are then placed over some of the powder to reduce the sintering area, before the entire layer is heated using an infra-red lamp [87–89]. This final heating stage can sinter the powder, or consolidate it sufficiently to be bulk sintered in a conventional sintering oven at a later stage [90].

Unlike other AM powder processes, the entire build area is sintered in SIS, with the exception of the boundaries created by the inhibiting agent. This means that material not used to create the part is extracted after the print as solid, sintered blocks; since this is no longer usable powder, there is more material wastage with this process.



Figure 1.14: Selective inhibition sintering schematic. Steps: 1) Laying thin powder layer 2) Deposition of sintering inhibitor 3) Minimising radiation frame 4) Sintering by thermal radiation [87].

This method has potential for both metals and polymers, with the benefits of not requiring a binder material for metals, and the potential to print full colour polymer parts using coloured inhibition agents [90,91]. However, this method has not yet been commercialised on a large scale.

1.4.2 Selective Mask Sintering

Selective Mask Sintering (SMS) was originally developed in 1996 by Speedpart (Sweden), now Sintermask Technologies (Germany), with the process commercialised in 2006 [4, 92]. The process uses an infra-red lamp to selectively sinter an entire layer at once, with a Radiation Absorbing Material (RAM) used to mask areas of the powder bed and create the part. This infra-red-absorbing toner is printed onto a glass plate, which is cleaned and re-printed for successive layers [93, 94]; this is shown in Figure 1.15.



Figure 1.15: Selective mask sintering schematic, modified from [95].

To lower the power needed to sinter the powder, the polymer powder is mixed with a RAM (usually carbon black) to aid the sintering. While these fillers do affect the mechanical properties, this allows for optimisation of other properties such as thermal conductivity [95].

The use of support structures is not needed with SMS, since the unsintered powder can act as supports. The benefits that SMS has over more established PBF techniques are; the ability to operate without an inert environment, the capital and running costs of the machine, and the ability to remove parts from the build area as soon as the print is completed [93].

1.4.3 Selective Heat Sintering

Selective Heat Sintering (SHS) was created by A. Hartmann and F. Tjellesen for their Master's project in 2008 [96]. SHS was created with the main focus of making 3D printing more affordable to businesses, as such this process uses relatively inexpensive thermal printheads to selectively sinter a powder bed; a schematic of a SHS machine is shown in Figure 1.16.



Figure 1.16: Selective heat sintering schematic [97]. a) powder deposition mechanisms b,c) layer heaters d) build volume e) build platform f) powder feed g) thermally conductive sheet.

This technology was commercialised as the “Blueprinter” with relative success; however, the price was still sufficiently high to prevent SHS from being widely adopted [5,98]. This ultimately led to the collapse of the company, with few users now still running SHS machines [99].

1.4.4 High Speed Sintering

High Speed Sintering (HSS), also commercialised as Selective Absorption Fusion (SAF), was developed as a technique specifically to reduce the part printing time and cost of the AM machine. This was achieved by depositing RAM onto a powder bed using an inkjet printhead, before exposing the entire layer to an infra-red heat source [100,101]. The increased absorbance of the RAM leads to only the printed area sintering, the time taken for which is independent of the number of parts in the build; a schematic of this is shown in Figure 1.17.



Figure 1.17: High speed sintering schematic [102].

The exposure of the entire layer to the heat source, means that the thermal stresses in the parts will be lower (compared to laser based systems), leading to increased mechanical properties for some materials

compared to Laser Sintering [103, 104]. The trade-off for these increased properties, is the increase in unwanted sintering around the parts and shrinkage during printing. The increased hardening of the powder cake lengthens the post-processing, while the shrinkage can have a significant effect on the geometric accuracy, depending on the orientation [102, 105–107].

The inclusion of the RAM in the printed part is unavoidable, the effects of which have to be considered in addition to the base material; this also adds complexity to the printing process as there are more parameters to optimise [108–111].

1.4.5 Multi-Jet Fusion

A technology of note is HP’s Multi-Jet Fusion (MJF), which uses a combination of the RAM (from the HSS process) and a “detailing agent” (similar to the inhibiting agent in SIS) to prevent sintering and create parts [6]. This is the most recent major release of a polymer powder bed AM process, only commercialised during the course of this research and being quickly adopted by industry worldwide [85].

In the MJF process (shown in Figure 1.18), the RAM aids in the absorption of energy from an infrared lamp, performing the same function as in HSS. However, the detailing agent applied around the edges of the parts differs to that used in SIS, as it aids in preventing large areas of the surrounding powder from sintering. Additional inks can also be included in the detailing agent, allowing for the printing of full-colour parts.

Image redacted for copyright purposes

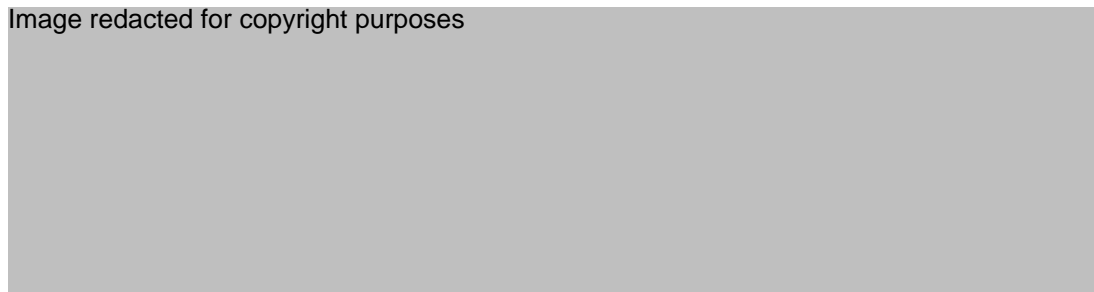


Figure 1.18: Multi-Jet Fusion schematic, showing (a) the deposition of powder, (b–c) the application of fusing and detailing agents, (d) energy input from an infrared lamp, (e) the fused part supported by unfused powder [112].

Initially limited to PA12 and PA11, the portfolio of materials now include PP, some flexible polymers, and glass-filled PA11 and PA12 [113]. Parts made in this way have good dimensional accuracy, with powder reuse up to 80% possible. However, a higher degree of anisotropy has been observed for these, with the strongest parts made in the z-direction and a large differences in elongation at break between the x and y directions (27% and 16–19% for PA12) [114, 115].

1.4.6 Laser Sintering

Laser Sintering (LS), first commercialised as Selective Laser Sintering (SLS), is the most established PBF process and has been identified consistently as the most profitable AM process by industry in recent years [85]. Its versatility, accuracy, reliability, and part mechanical properties, have made it the “one to beat” in polymer PBF. It is commonly used in industry due to its ability to reliably create complex geometries from a wide range of materials compared to other AM processes, without the need for support structures. The general process can be seen in Figure 1.19, where a laser is used to selectively sinter a powder bed.



Figure 1.19: Laser sintering schematic [116].

In particular, polymer LS machines manufactured by EOS have been singled out as the most profitable by industry [85], with the potential for impact of research carried out on these machines greatly increased as a result. This is especially true when focusing on polyamide (PA) materials, with 48.9% of companies using AM identifying it as their most profitable polymer. This is further reflected in the availability of materials, with 61% of currently available polymer powder feedstocks being polyamide-based, of which 46% contain additional additives (or fillers) to create a composite feedstock [117]. These composite materials are also of great interest in academia [118,119], with much of the materials development research focused on these.

It was for these reasons (and those mentioned in the Thesis Foreword) that LS was chosen as the focus for this research, and in particular the use of composite materials in LS. A more in depth introduction to Laser Sintering is presented in Chapter 2.

Chapter 2

Introduction to Laser Sintering

This chapter introduces the Laser Sintering (LS) process in more detail, with the basic structure shown in Figure 2.1. It covers aspects from common applications, through to the effect of individual process parameters, before exploring materials for LS in greater detail, with the main focus on composite materials in Section 2.6.

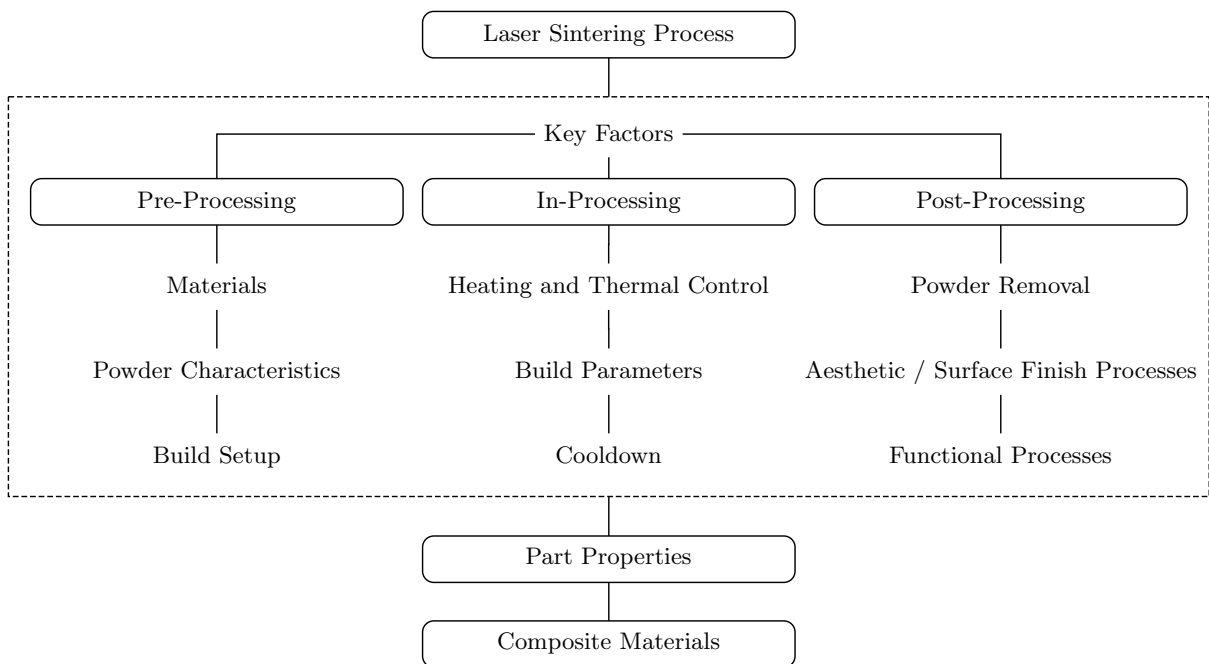


Figure 2.1: Laser Sintering chapter structure. With key factors divided into pre-, in- and post-processing sections. 🚫

Key factors affecting the process and the printed parts (expanded in Figure 2.1) have been split into three sections, based on when they occur or where they are most relevant. However, it is important to note that these are all interconnected and must all be considered in the creation of printed parts.

2.1 Laser Sintering Process

First developed by Carl Deckard for his Masters thesis at the University of Texas in the 1980s [120,121], Laser Sintering (LS) has now been widely adopted in industry as a method of creating functional, end-use products. A schematic of a typical Laser Sintering machine is shown in Figure 2.2, with the individual steps detailed in Section 2.1.1.

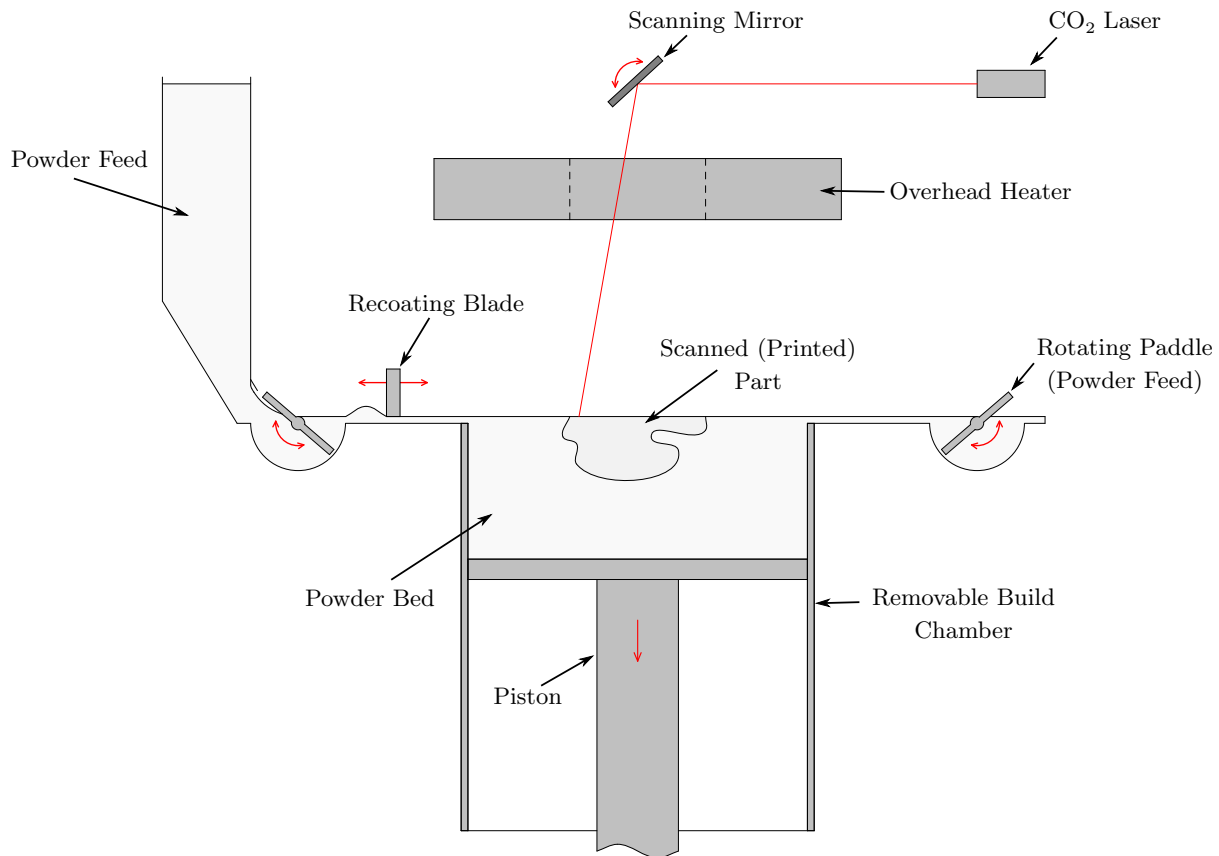


Figure 2.2: Schematic diagram of Laser Sintering (based on an EOS P100). 

2.1.1 Detailed Process Steps

The required steps for LS can be split into three main categories; the materials and build set-up (pre-processing), printing (in-processing), and post-processing. An overview of the key processes in each of these categories is shown here.

Pre-Processing:

1. Create the desired part geometries (using 3D CAD or similar). Export the geometries as `.stl` files and position / orient them in the build area.
2. Slice `.stl` files to generate the individual layers, then transfer this to the LS machine.
3. Fill the powder feed with the desired material.

Printing (In-Processing) – these processes are controlled by the LS machine, with no human intervention necessary:

4. The build chamber (and in some instances the powder feed) is preheated and purged with nitrogen (or other inert gas) throughout the build to reduce the possibility of powder oxidation.
5. The recoating blade spreads a thin layer of powder over the build chamber.
6. A CO_2 laser selectively melts (or sinters) the powder to form the cross section of the part.
7. The piston lowers the powder bed.
8. Steps 5–7 are repeated until the part is complete.
9. The build must be left to cool down, usually for the same length of time as the build process, before any post-processing can take place.

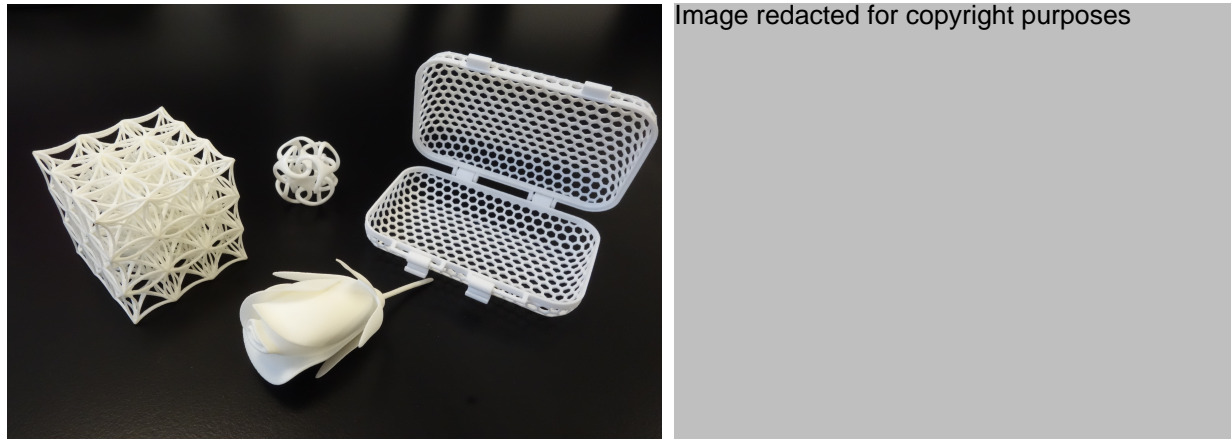
Post-processing:

10. Remove the parts from the powder “cake” (the unsintered powder surrounding the parts) and remove loose powder using an appropriate method.
11. Apply any additional post-processing for the specific application (see Section 2.4).

2.1.2 Benefits

Geometric Complexity and Part Nesting

One of the main advantages of polymer PBF over FDM and heat-based metal PBF, is that the unsintered powder can act as a support material for the parts during printing. This not only means that more complex geometries can be made without the need for support structures (as shown in Figure 2.3a), it enables the creation of parts throughout the build volume.



(a) Selection of parts printed with LS. 🚫

(b) Example of nesting in the build chamber [122].

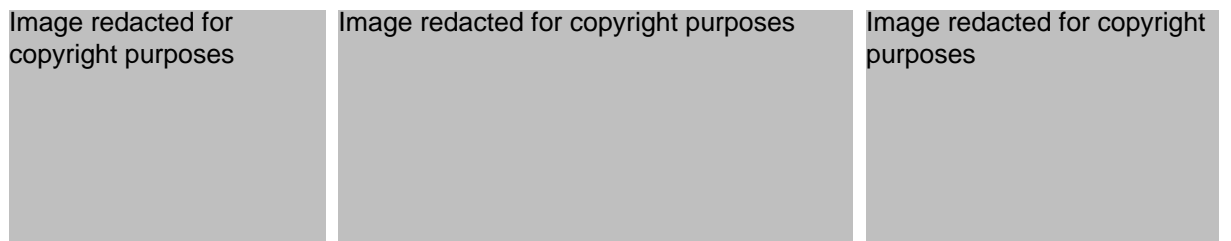
Figure 2.3: Benefits due to the unsintered powder acting as a support material during the build.

By positioning (or nesting) multiple parts in the same build, both horizontally and throughout the height of the build (as shown in Figure 2.3b), the cost per part can be greatly reduced [123]. This is especially true for the height of the build, as the material used and time of the build are most affected by this. Added to this, steps such as pre-heating (see Section 2.3.1) take the same amount of time regardless of the number of parts. The combination of these mean that the most efficient packing method maximises the number of parts per layer, throughout the entirety of the build.

This nesting of parts means that it is also possible to print fully assembled parts, with multiple components. These can be as simple as two hinged components (Figure 2.3a), to printed textiles (see Fashion in Section 2.1.4 for more details).

Mechanical Properties and Material Choice

The mechanical properties and materials available for LS are the other big advantage that LS has over other AM processes. Generally, LS is more commonly used for the processing of engineering polymers (see Section 2.2.1) which are suitable for the production of functional products (see Figure 2.4), rather than just for models. The mechanical properties of LS parts are also seen to be more isotropic than other polymer AM processes such as FDM [32].



(a) Clip [124].

(b) Spring [125].

(c) Shoe sole [126].

Figure 2.4: Examples of material (or “living”) hinges and flexible materials printed using LS.

The combination of these, means that LS can be used to create functional products with features such as material hinges (Figure 2.4a,b). Since the processing of elastomeric materials is also possible, the production of perhaps unexpected items such as shoe soles (Figure 2.4c) becomes viable. These is only possible due to the mechanical properties achievable with LS.

2.1.3 Limitations

Surface Roughness and Post-Processing

One of the characteristic features of LS parts, is their “powdery” surface finish. This is due to the partial sintering of particles at the surface (as shown in Figure 2.5a), which despite being firmly attached to the part, give the appearance and feel of the powder particles. This can be advantageous in some applications, particularly where a larger surface area is desirable (for the uptake of liquids or release of medicaments); however this roughness has also been linked to a perceived reduction in quality compared to other manufacturing processes [127]. The vast majority of post-processing techniques for LS are therefore targeted at smoothing out this surface. These processes can be time consuming and expensive and must be considered when designing for LS (see Section 2.4 for more details).



(a) LS surface [128].

(b) “Stair-stepping” effect. 🇧🇪

Figure 2.5: Surface roughness of LS parts.

The “stair-stepping” effect is also present in LS parts, although to a lesser degree than in some other AM processes. This is due to the layer height (commonly 100–150 μm) and is most noticeable on objects with shallow gradients, such as the ones shown in Figure 2.5b.

Powder Handling and Environmental Controls

For any process which uses a powder material, the infrastructure and personal protective equipment required for the its safe handling must be considered. During the LS process, there are multiple instances in which the operator could need to handle the powder; including the preparation of the feedstock, loading of the feedstock into the machine, removing the build from the machine, removing the loose powder from the build, any additional post-processing (such as bead blasting), and sieving of unsintered powder for reuse.

In terms of infrastructure, specialised clean-up stations designed for individual AM machines are available [129], which are essential to some extent for the processing and re-processing of powders. Additional environmental controls such as temperature and extraction are also required for some machines and materials, to ensure consistent processing and protect against the purge gasses and any emissions from the powder as it melts. All of these add to the initial setup costs associated with LS, which could be prohibitive in its uptake.

Size Limitations and Cost

Compared to other AM processes, LS is fairly competitive in terms of the size of components it can produce. However, the thermal stability required across the build chamber makes it both challenging and expensive to create larger build volumes. Whereas it is now common for basic FDM machines to have large build volumes (sometimes in excess of 1 m^3), the largest LS printers only have a fraction of this, with 3D Systems’ sPro 230 currently one of the largest at $0.55 \times 0.55 \times 0.75\text{ m}$ [130].

Not only can these printers be expensive to buy (with the sPro 230 retailing at over \$250,000), the running costs of materials, floorspace (including the powder handling and environmental controls), and labour (particularly for post-processing) mean that the benefits of adopting this technology must be significant to consider the investment. Due to these costs, a common route into the use of LS is through service bureaus, which produce parts for multiple consumers thereby reducing the costs for the individual customers.

Smaller “desktop” LS machines are starting to come onto the market [131, 132], at a much lower cost (around \$5,000–\$15,000). However, these smaller machines are much less capable than the larger industrial machines, both in terms of the build volumes and in the materials they can process.

2.1.4 Applications

Models and Prototypes

For over 30 years, the main application of AM processes was for making prototypes and models. Although the production of end-use parts has now eclipsed this, AM still remains one of the preferred methods of rapid prototyping for a large number of products. The awareness and availability of different AM processes now mean that a more informed choice can be made regarding the process used, maximising the benefits each process can bring.

For LS, the mechanical properties achievable mean that it is more commonly used for the production of functional prototypes (Figure 2.6a,b), used to test the form, fit and function of products, rather than purely visual representations of the final products. These also enable the production of models which undergo loading, such as wind tunnel models (Figure 2.6c), where the strength and toughness of the material is essential.

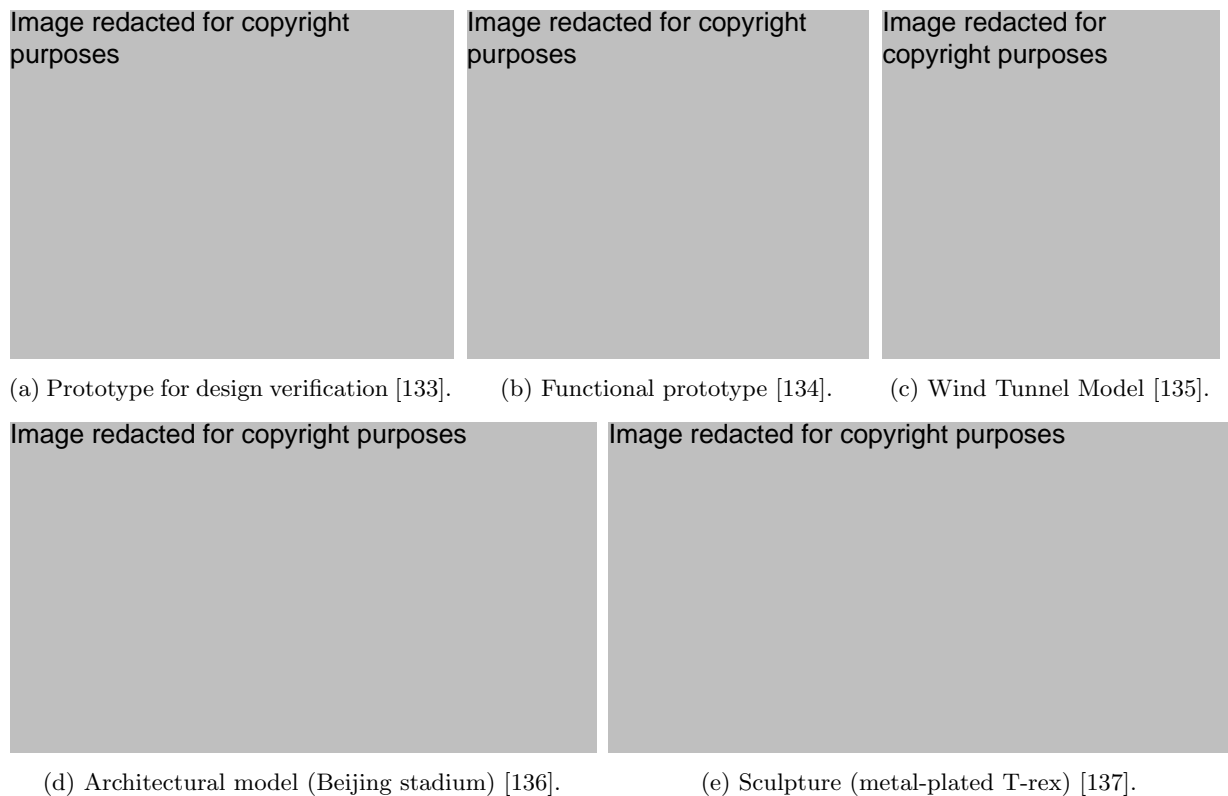


Figure 2.6: Example model and prototype applications of Laser Sintering.

The use of LS solely for the creation of visual models is diminishing, however the geometric complexity achievable makes it well suited to certain applications, such as architectural models (Figure 2.6d). It is also increasing in popularity with artists for the creation of sculptures, such as the one shown in Figure 2.6e, which makes use of metal-plating in post-processing to maximise the impact.

Functional End-use Parts

The primary use for LS is for the manufacture of functional components, either for final part production, or during initial design development [138], examples of which are shown in Figure 2.7. The use of LS for batch or medium-mass production is becoming increasingly popular due to the geometric complexity available, paired with higher mechanical properties than are generally available in other polymer AM processes. However, the key benefit LS has over other AM processes is the ability of the unsintered powder to act as support material for the rest of the build. This allows multiple parts to be nested in the same build, with potentially hundreds or even thousands of components being manufactured at a time.

The size of parts is the most important factor here, with larger items (such as the cooling duct in Figure 2.7a) taking up a significant proportion of the build, making it less viable to mass produce with LS, whereas for smaller items (such as the ones shown in Figures 2.7b,c), a large number of these can be built at the same time, allowing them to be produced in larger volumes. This aspect of “filling the

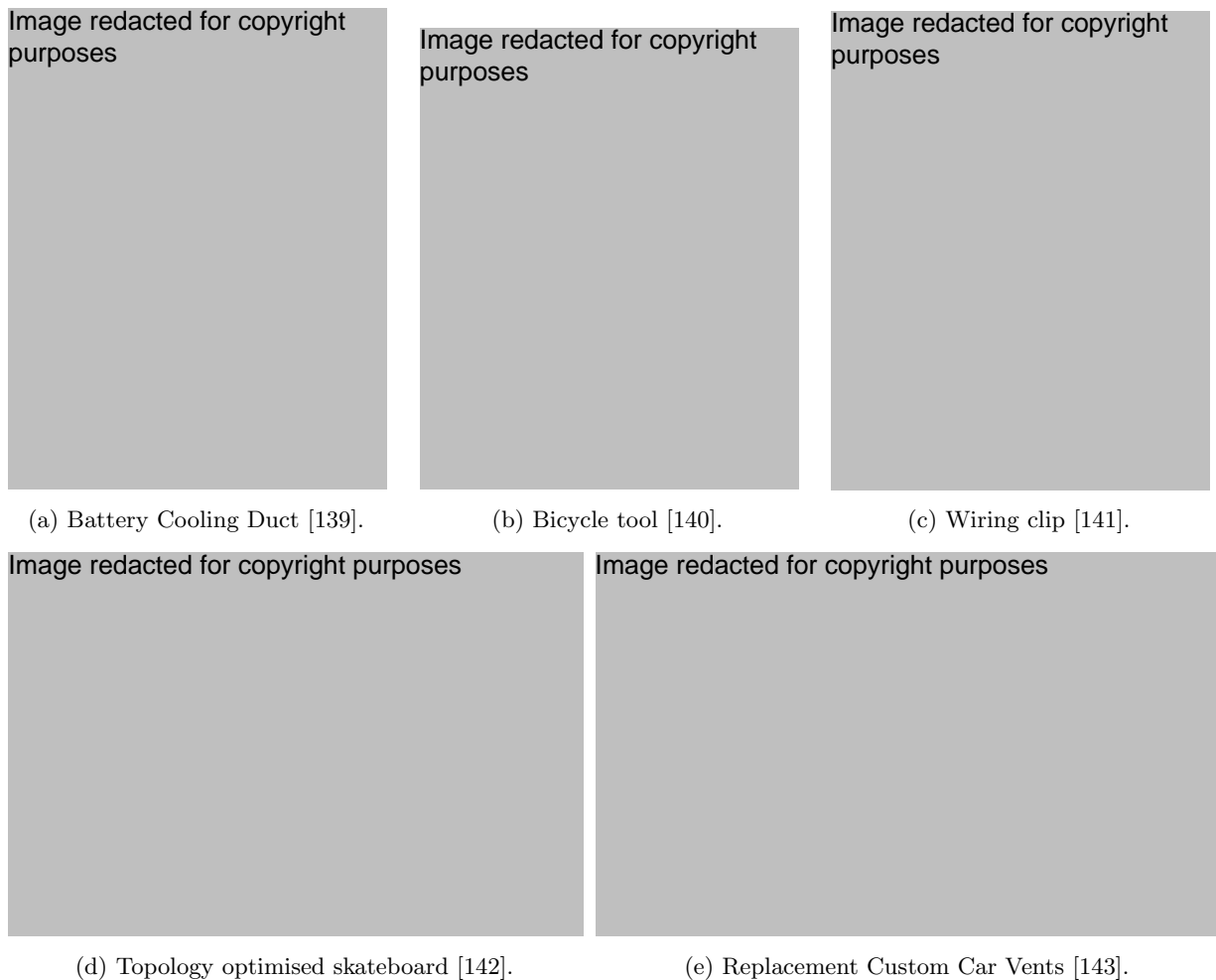


Figure 2.7: Example end-use applications of LS. With examples of low volume production (a), medium-mass production (400 units/month) in design development [144] (b), higher-mass production (20,000 units) (c), and one-off custom production (d, e).

build” is now commonly presented by service bureaus for cost estimates on printed parts, enabling the customer to easily calculate the cut-off point between LS and conventional methods such as IM [145].

LS is also widely used to manufacture of one-off production parts, generally where the mechanical properties of the printed parts are important. This is commonly for complex geometries which would be difficult to manufacture conventionally (Figure 2.7d), and is also used to create replacement parts which are no longer in production (Figure 2.7e). The size of parts which can be produced with LS is also a positive here, as it can produce larger components than the majority of AM processes (typically in the range of $0.3 \times 0.3 \times 0.3$ mm, up to $0.55 \times 0.55 \times 0.75$ m in the sPro 230 [130]) while maintaining accuracy and complexity.

Medical End-use Applications

The geometric freedom LS provides, coupled with the mechanical properties and size of parts that can be produced, makes it ideal for producing patient specific medical devices such as braces and prostheses.

The most widely publicised example of this, is for wrist casts (Figure 2.8a), which are less bulky than the traditional plaster casts, provide better air-flow and can be used in water. This idea can be further extended to supports such as crutches (or even bionic suits – Figure 2.8c), which can also be made from 3D scan data to better fit the user.

One example of LS bracing which could show a significant advantage over traditional casts, is for the treatment of scoliosis, a curvature of the spine. Although it can affect people of all ages, progressive curves are most prevalent in 10-15 year old girls [151,152]. Bracing is sometimes used with children to prevent this progression, but has to be worn for long periods of time (up to 16-24 hours a day) to be effective [152], potentially for many years. These rigid braces can be hot and unsightly, leading to many

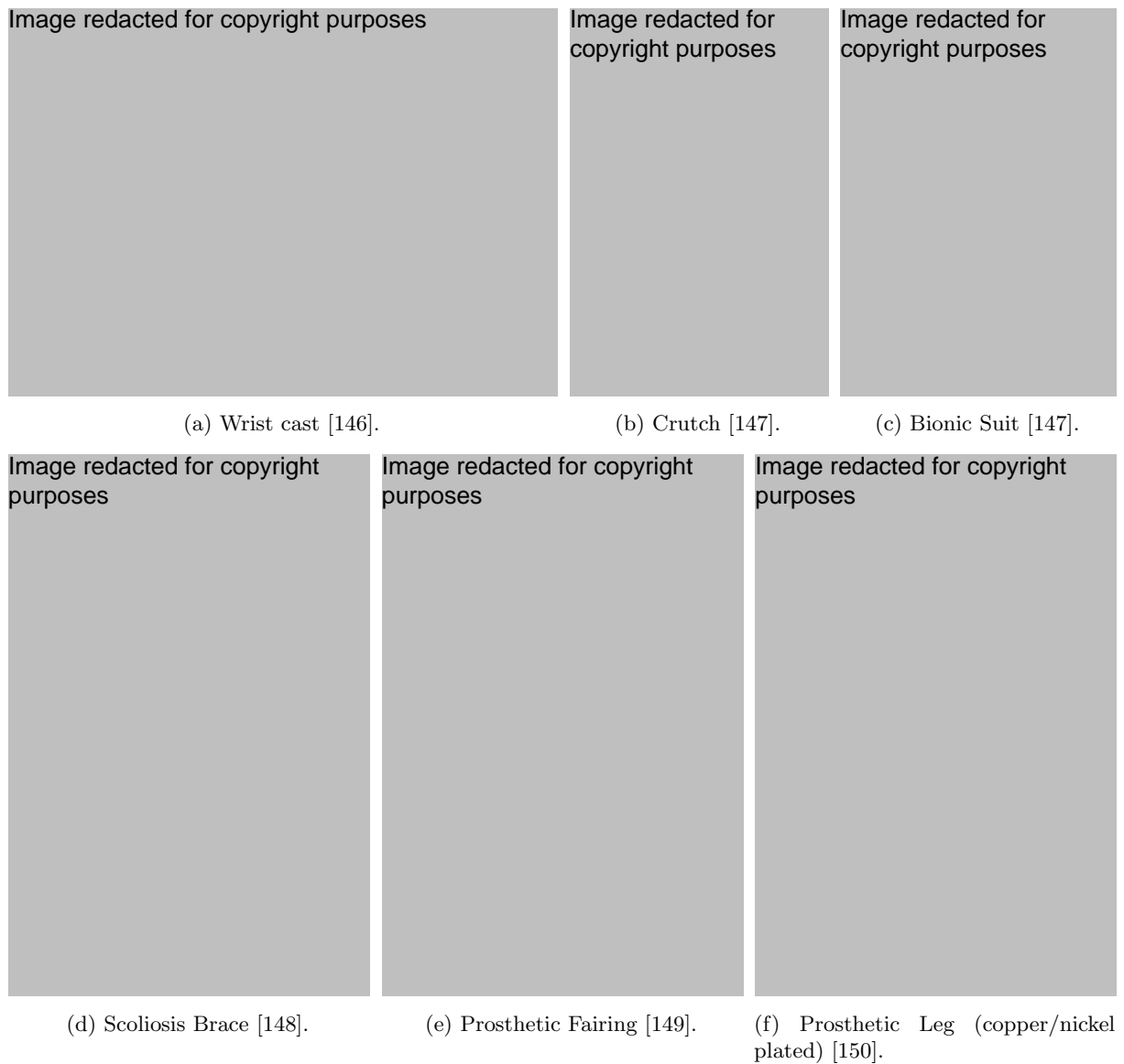


Figure 2.8: Example end-use medical applications of Laser Sintering.

patients wearing them for less than the recommended time.

By using LS, scoliosis braces (as shown in Figure 2.8d) can be made allow more air flow, making them more comfortable to wear, while also allowing them to be customised to the patients preferences. By turning this into a fashion piece, not just a medical device, it is more likely to be worn and patients are less likely to feel embarrassed or socially awkward wearing them [148].

Similarly, prostheses are another area in which personalisation is greatly desired. Although these are obviously made to the needs of the individual, the aesthetics are usually secondary to the function. One of the simplest ways to improve this is through the use of fairings (Figure 2.8e), which are fitted to a conventional prosthesis. With LS, this fairing can be both personal and functional, allowing for a more natural feel in areas such as sports [153]. In the future, there is even the potential to print the prosthesis itself, such as the metal-plated one shown in Figure 2.8f.

Surgical and Future Medical Applications

There are a number of ways in which LS can be used in the planning and preparation for surgeries, as well as during procedures. For the planning of complex surgeries, models can be printed out to better visualise the particular challenges (Figure 2.9a). Functional models can also be created to aid in training (Figure 2.9b), allowing students to get more “hands-on” experience, reducing the need for volunteer patients and cadavers [154, 155].

The ability of LS to process various biocompatible and bioactive materials [158, 160–166], combined with

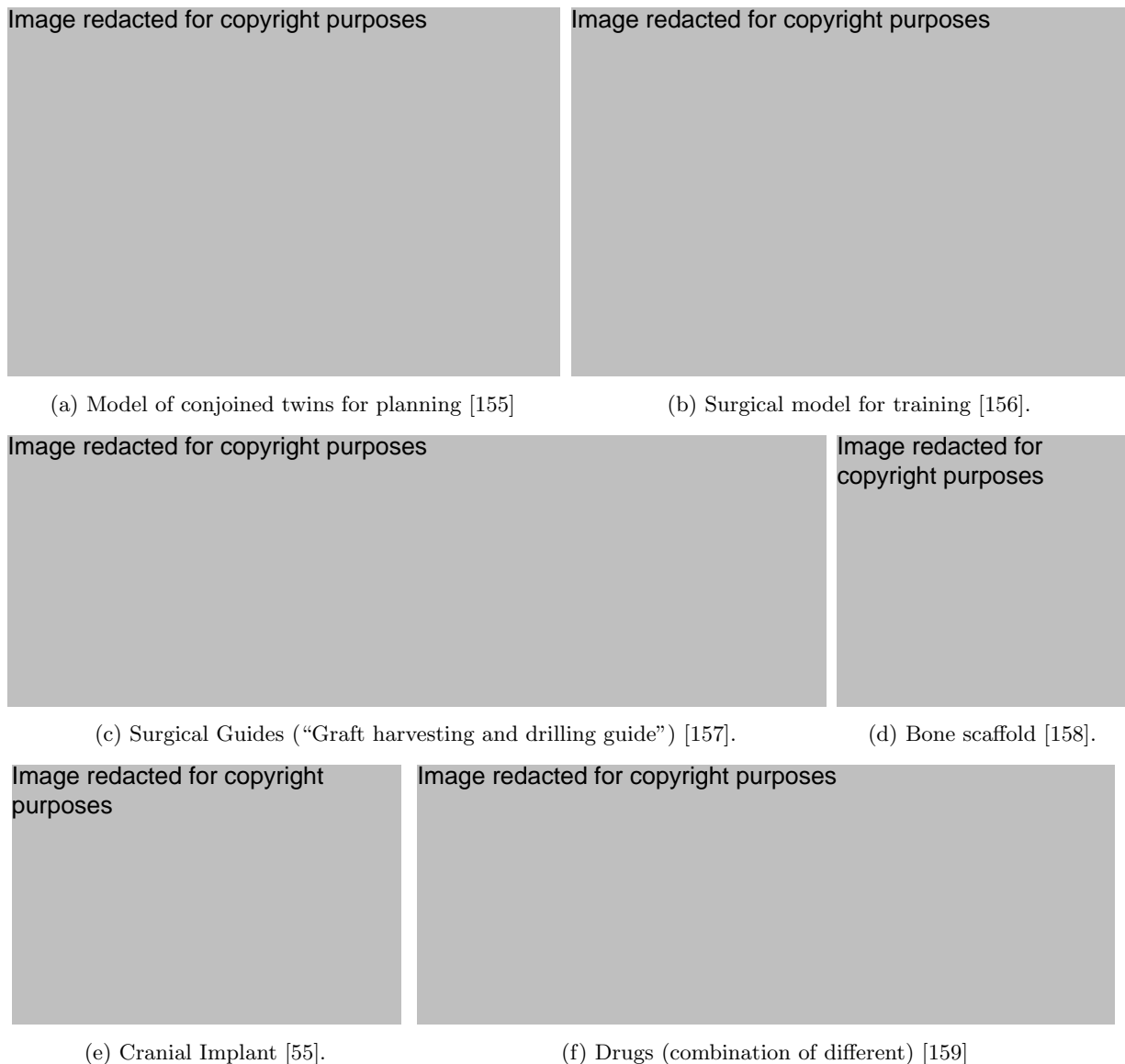


Figure 2.9: Example surgical and potential future medical applications of Laser Sintering.

the geometric complexity and mechanical properties achievable with LS, make it particularly well suited to use inside the body itself. This can be in the form of surgical guides [167] (Figure 2.9c), or even in the form of implants [168] (Figure 2.9d,e). For the latter of these, the geometry and material properties can be optimised to increase factors such as bone regrowth, leading to a shorter recovery times and reducing the need for repeat surgeries.

The increase in popularity of smaller, desktop FDM systems [169], has seen an increased demand for equivalent setups for other AM technologies. For LS, these systems are starting to emerge [131], which are capable of processing a limited range of materials. While they may not be suited to high performance engineering applications, they are perfectly suited to smaller build volumes (for example $110 \times 110 \times 110$ mm in the Sintratec Kit [131]) of lower temperature materials; potentially leading to more specialised uses such as creating drugs with custom release rates [170], or those combining multiple drugs into one [159] (Figure 2.9f).

Rapid Tooling

The strength and durability of parts produced with LS makes it suitable to produce jigs and fixtures for conventional manufacturing processes. Items (such as the ones shown in Figure 2.10a,b) can be designed to perfectly fit both the workpiece, and any machinery used in production. The use of these jigs and fixtures can increase the speed of production, while improving the consistency of parts produced.

The range of materials which can be used in LS, specifically lower melting point materials, allow the

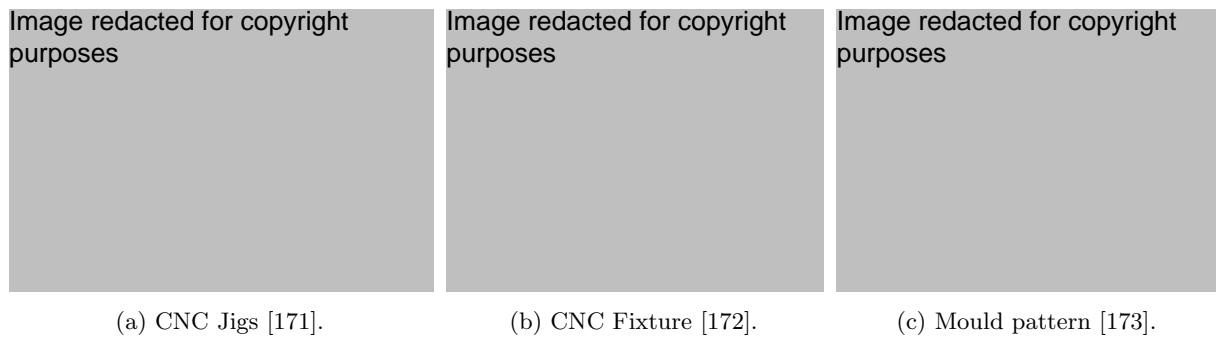


Figure 2.10: Example rapid tooling applications of Laser Sintering.

creation of mould patterns for use in investment (or “lost wax”) casting [174]. Parts (such as the one shown in Figure 2.10c) can be created in materials like polystyrene (PS), which can be burnt out to create a mould.

Fashion

One of the more unusual applications of LS has been its use in fashion. With pieces such as the kinematic dress (Figure 2.11a), the ability to create complex assemblies is key, with thousands of interlocking components making a wearable “fabric”. This is only possible due to the (usually) easily removable loose unsintered powder acting as supports, allowing for large overhangs and closely nested parts without the need for the additional support structures seen with other AM processes. Other instances have chosen to make use of the more solid nature of printed parts (Figure 2.11b), combining them with other technologies to make a more striking design.

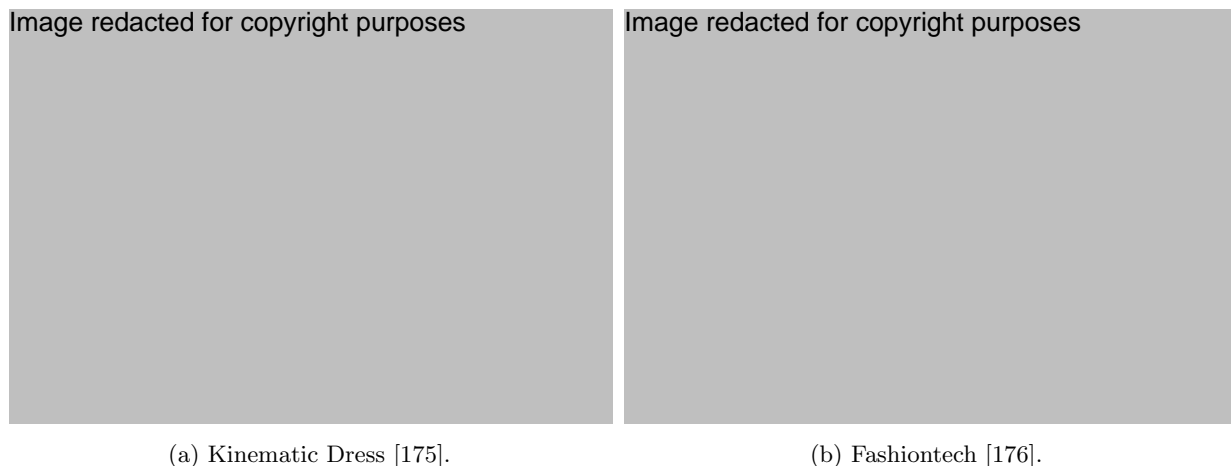


Figure 2.11: Examples of Laser Sintering used in fashion.

2.2 Materials and Build Set-up (Pre-Processing)

2.2.1 Materials

The number of materials available for AM processes in general is expanding rapidly, with over 220 different powder feedstocks now commercially available for polymer PBF processes [117]. This range is reflected in the revenue from global material sales, with polymer powders now the largest sector, accounting for 34.7% of all AM material sales in 2021 [85] (see Figure 2.12). A range of polymers have been shown to be suitable for LS; but despite this, the market is dominated by polyamides (PA), with a 95% share of the market [118]. Further to this, over 90% of all LS parts are currently produced using PA12 [138].

A summary of the materials processed to date with LS is shown in Figure 2.13, where they are sorted by performance and by their polymer chain structure (amorphous or semi crystalline). In some instances, these materials can also be processed in combination, resulting in parts made of polymer blends [180,181].

The majority of the materials shown in Figure 2.13 are thermoplastics, capable of being melted by the

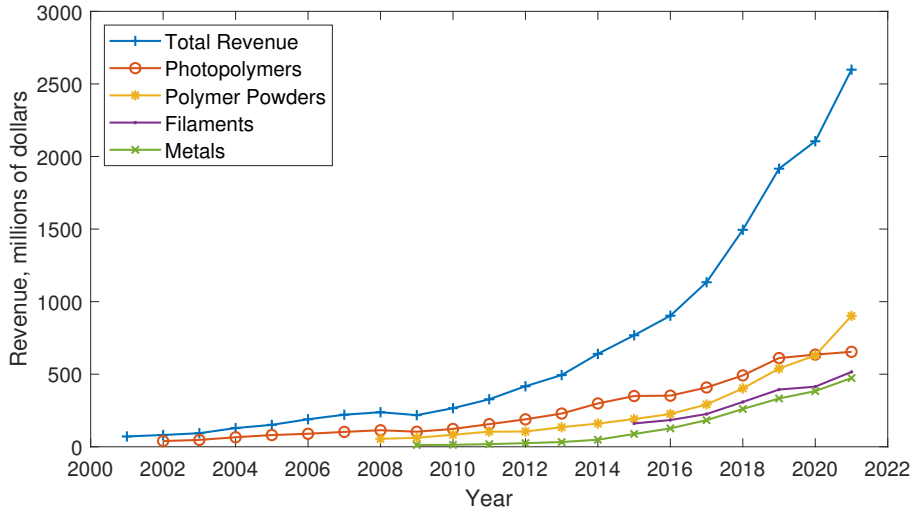


Figure 2.12: AM materials growth for photopolymers, polymer powders, filaments and metals. Polymer powders can be seen to overtake photopolymers as the largest market share in 2021 [85,177–179].

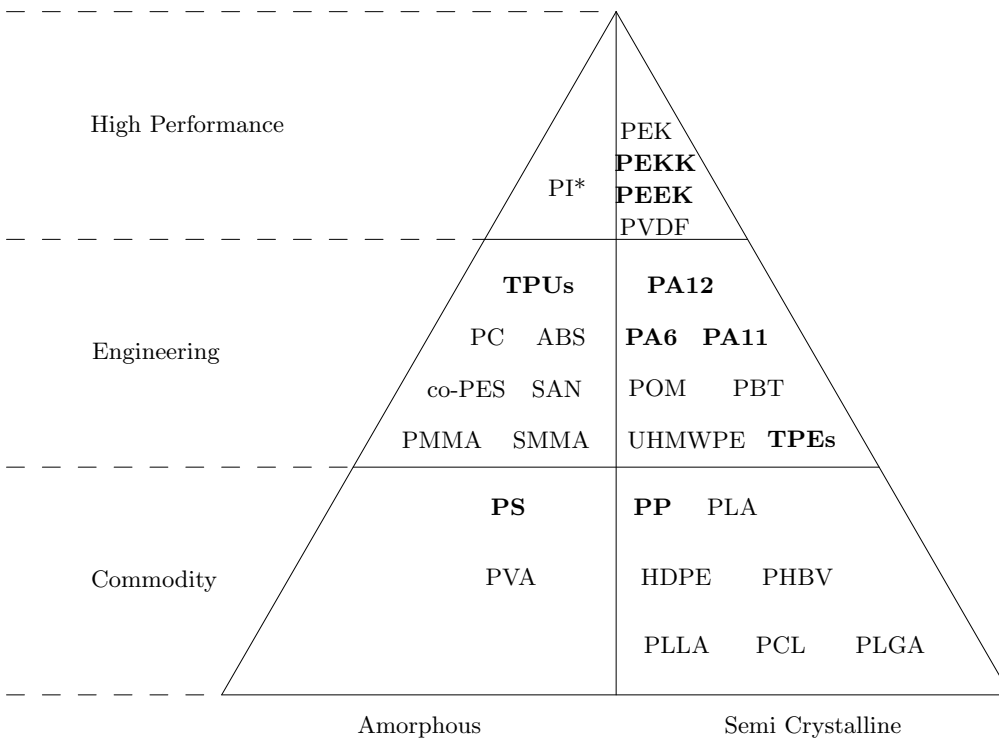


Figure 2.13: Polymers processed with LS (most common shown in bold), sorted by amorphous and semi crystalline, and by performance [138, 182, 183]. **Abbreviations:** ABS (Acrylonitrile Butadiene Styrene) [120], PC (Polycarbonate) [184, 185], SAN (Styrene–acrylonitrile) [186], PP (Polypropylene), PLA (Polylactic Acid), HDPE (High-density Polyethylene) [187], UHMWPE (Ultra-high-molecular-weight Polyethylene) [188, 189], SMMA (Styrene methyl methacrylate) [190], PMMA (Polymethylmethacrylate), POM (Polyoxymethylene), PS (Polystyrene) [174, 191], PEKK (Polyetherketoneketone) [192], PEEK (Polyether Ether Ketone) [193], PEK (Polyaryletherketone) [194], PVDF (Poly(vinylidene fluoride)) [195], co-PES (co-Polyethersulfone) [196], PVA (Polyvinyl Alcohol) [163], PCL (Polycaprolactone) [197], PLGA Poly(L-lactide-co-glycolide) [198,199], PLLA (Poly-L-lactic Acid), PHBV (Poly(Hydroxybutyrate-co-Hydroxyvalerate)) [165], PBT (Polybutylene Terephthalate) [200], PI (Polyimide) [201], TPUs (Thermoplastic Polyurethanes) and TPEs (Thermoplastic Elastomers) [192,202,203]. *PI is the only thermoset polymer to be processed.

laser and constituting the primary use of LS. Some preliminary research has been done on the processing of thermosets, where the laser is used to cure the polymer; however, PI [201] is the only instance of LS being used for a thermoset material.

Semi-Crystalline and Amorphous Polymers

Polymers can be classified as either amorphous or semi crystalline, depending on the organisation of the polymer chains (as shown in Figure 2.14) [204]. For amorphous polymers, the polymer chains show no alignment with one another; whereas in semi crystalline materials, the chains align in crystalline regions, which are in turn surrounded by amorphous regions.

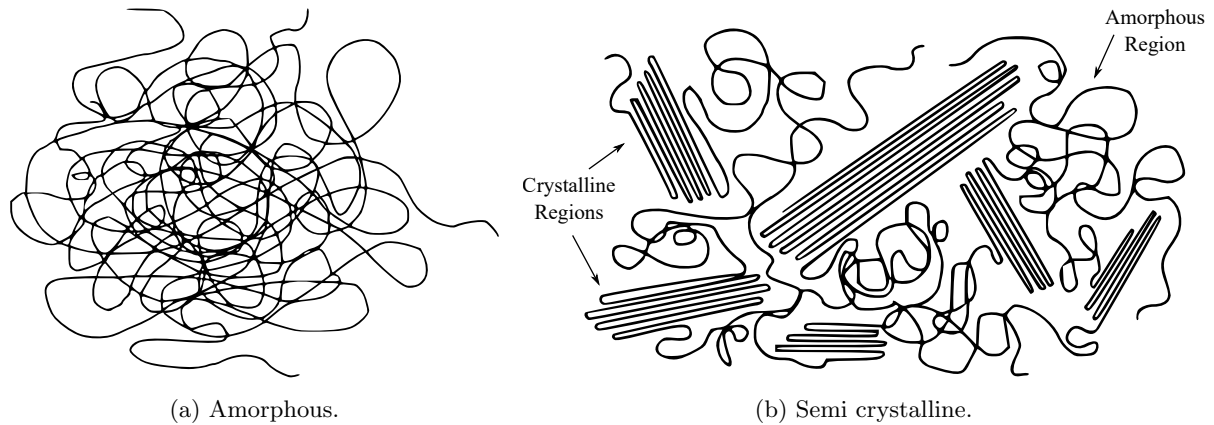


Figure 2.14: Structure of amorphous and semi crystalline polymer chains. Modified from [205].

There are many differences caused by this, for example the crystalline regions cause materials to be more opaque and also cause greater shrinkage than amorphous materials [206]. A less tangible property, the feel of the material, has also been described as superior in amorphous polymers, leading to their preferential use in applications where they are directly handled [183]. However, the mechanical properties of semi crystalline polymers often far exceed those of amorphous materials.

The main difference between the two classifications in terms of their LS processability, is behaviour of the material as it is heated. For semi crystalline polymers, there is a distinct melt temperature (T_m) after which the solid material melts into a liquid. However, for amorphous polymers there is only a glass transition temperature (T_g), above which the material softens and becomes more pliable. The behaviour of a selection of crystalline (or semi-crystalline) and amorphous polymers is shown in Figure 2.15.

Image redacted for copyright purposes



Figure 2.15: Phases and transition temperatures of selected amorphous and crystalline polymers [182].

Generally, in LS machines the energy input from the laser is minimised, with pre-heating often used as a means to achieve this (see Section 2.3.1). For amorphous polymers, which start to flow at temperatures above their T_g , this preheating could cause unwanted sintering of the entire bed at relatively low temperatures. In order to heat the polymer to a temperature where it can flow more freely (broadly shown as T_f); this needs to be mostly achieved with the laser, and leads to more challenges such as powder degradation of small particles (see Section 2.3.3).

Polyamides

Polyamides (PA) are a class of semi-crystalline polymers whose properties have made them the material of choice for LS. These all have the same basic structure (shown in Figure 2.16), differing only in the number of carbon atoms in the polymer chain. PA12 (12 \times carbon atoms) contains the longest polymer chain of all the polyamides, and is widely used with conventional methods due to its mechanical properties and low water absorption compared to other polyamides.

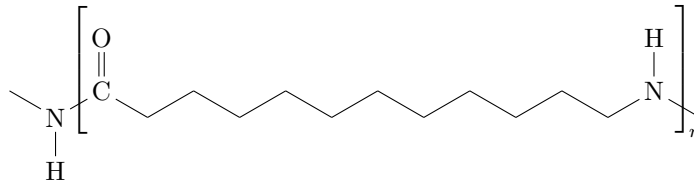


Figure 2.16: Skeletal diagram of polyamide 12 (PA12) [207]. 🚫

The melt characteristics of PA12 are the reason why it is so popular with LS, the reasoning behind which is explored in detail in Section 2.3.1. Briefly, these beneficial melt characteristics include a large processing window, narrow melt peak, low initial zero-shear viscosity, and relatively low shrinkage [208]. This combination means that it is relatively simple to select an appropriate bed temperature (T_b), and the sharp melt peak means that it can be quickly melted with relatively little additional energy input from the laser.

The temperature at which PA12 is processed is the lowest of the polyamides used in LS. It is primarily for this reason that it is more widely used than PA11 and PA6, as the increased T_b required for these requires high temperature LS machines [208]. These materials are also regarded to be more difficult to process, with a smaller range of parameters able to produce parts.

2.2.2 Powder Characteristics

Size

The size of the powders used in LS can have a major impact not only on the printed parts, but on its processability. In terms of the detail achievable in the finished product, it might seem logical that having the smallest particle size possible would be the most beneficial. However, the practicalities of working with and processing very small particles prevents this from being the case.

Inside the LS process, smaller particles are more affected by static electricity, tending to agglomerate or stick to the recoating blade / roller and preventing an even layer of powder from being deposited. In addition to this, the health and safety requirements for working with small powders are considerably higher, increasing the difficulty and cost.

A trade-off therefore needs to be made between the feature resolution and what is practical to print. With larger particles, the packing density (ρ_l – the proportion of a layer that can be filled with material) becomes more of an issue. The way to counter this is by using a broader size distribution of particles (typically 10–90 μm for commercial LS powders, as demonstrated in Figure 2.17), where a higher ρ_l can be achieved (typically around 0.5 for commercial LS powders [209]).

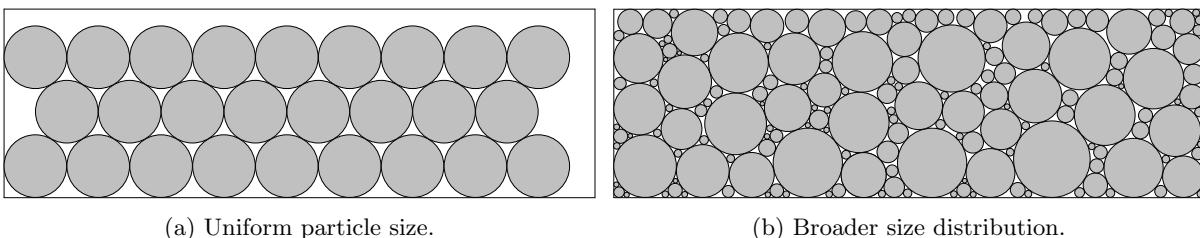


Figure 2.17: 2D visualisation of differences in packing density (ρ_l) due to particle size distribution, with a higher ρ_l achievable with a broader distribution. 🚫

Morphology

The morphology of the powdered material has a large effect on its processability inside the LS machine. The main reasons for this are the effect on the achievable ρ_l , and the flowability of the material (how easy it is to feed into and spread over the powder bed).

With commercial methods of creating powders for LS (such as those shown in Figure 2.18a–c), it is possible to create roughly spherical particles [210], commonly referred to as “potato-, cauliflower-, or tomato-shaped”. These are generally free flowing enough to obtain an even spread of powder over the powder bed [211].

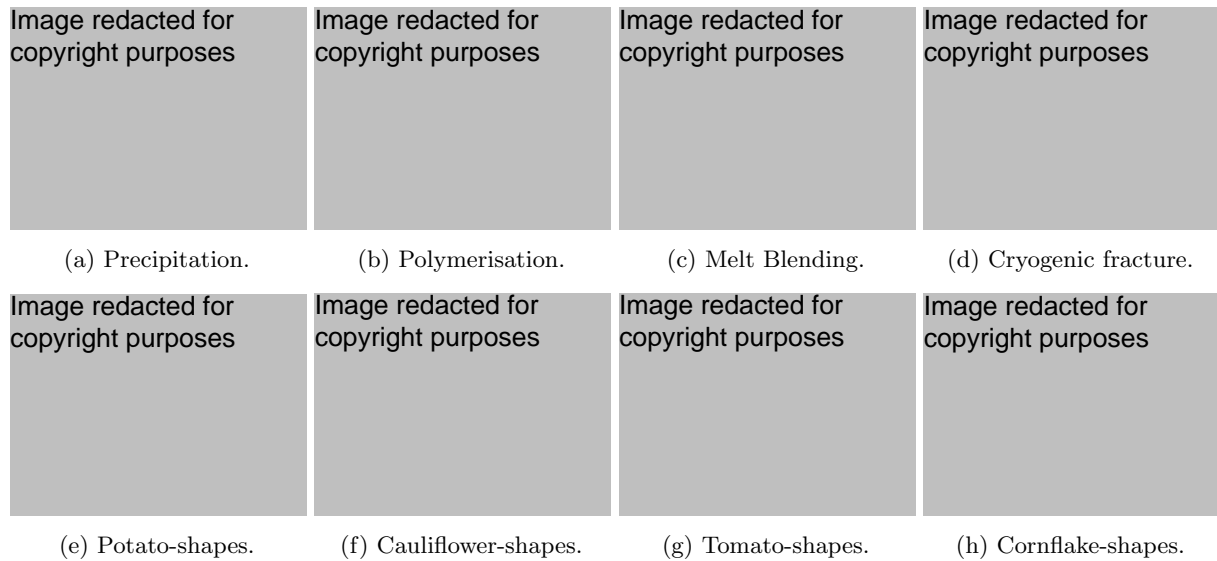


Figure 2.18: Polymer powder morphologies for LS and the foodstuffs they resemble [212–216].

For many materials, especially in a research setting, it is impractical to carry out these commercial methods on the experimental polymers. A popular method of creating fine powders in this case, is through cryogenic fracture (see Figure 2.18d). This process freezes and subsequently ball mills the material until the required size distribution is achieved. The particles created with this method tend to be flatter, more jagged and generally more “cornflake-shaped”, leading to poor flowability [217]. This can lead to uneven powder coverage on the bed and a reduced ρ_l , ultimately leading to more porous and inconsistent parts.

Thermal History

The unsintered powder from a LS build (referred to as “used” powder), can be reused to an extent, but is not infinitely recyclable. During printing, the powdered material is held at elevated temperatures for extended periods of time, leading to changes in material properties which alter its behaviour if used in subsequent builds [218–220].

The molecular weight is one such property which is affected by this, with the spherulites in the polymer growing throughout the build [218, 221, 222]. These longer molecular chains lead to differences in thermal properties, such as a higher T_m and lower crystallisation onset ($T_{c,onset}$); as well as other factors which greatly affect the sintering behaviour, including the zero-shear viscosity and the surface tension [223, 224]. This change is most noticeable in the surface finish of printed parts, which exhibit rougher surface known as the “orange peel” effect [225], an example of which is shown in Figure 2.19.

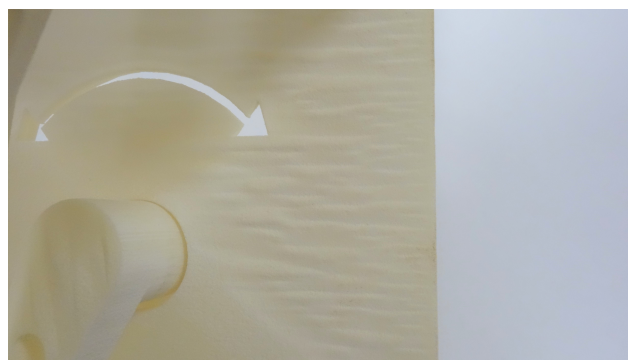


Figure 2.19: Photo of a part printed in used PA2200 powder, showing the characteristic surface waviness of the orange peel effect. 🚫

Despite these apparent downsides of powder reuse, parts made in this aged powder display lower shrinkage, porosity [224], and a higher elongation at break (ε_{\max}). Combined with the high cost and material wastage associated with only using virgin (unused) powder, there is a clear incentive to reuse some of this material. Generally, parts produced commercially use a mix of used and virgin powder (typically 20–50% used powder [86]), both to reduce costs and improve the mechanical properties and processability beyond those otherwise achievable¹.

Eventually, the powder will deteriorate beyond a state where it can be reused in LS, even in combination with virgin powder, and has to be disposed. This waste can be reduced (or even eliminated) by controlling the packing of the build, or by utilising the powder for other purposes, such as filaments for FDM [226].

2.2.3 Design for Laser Sintering

With all design processes, there are limitations in the manufacturing methods which affect the design of final part. While LS has fewer restrictions than most conventional methods, for example accounting for draft angles, there are still limitations of the process which have to be accounted for. As LS becomes more widely used in industry, an increasing number of design guides (such as the one shown in Figure 2.20) are being produced to aid in the design.

Image redacted for copyright purposes




Figure 2.20: Example of a design guide for Laser Sintering. Modified from [227].

Guides such as [227, 228] are particularly useful if the designer is planning to use AM, but is unsure of which method is most appropriate. Crucially, the numbers stated in these guides are not true for every machine, with aspects such as the material, exact parameters and orientation (to name a few), potentially affecting the printability of the part. Consultation with machine technicians, or experienced users, is therefore still needed in order to ensure the part is suitable for the process.

Lightweighting

The lightweighting of parts is often desirable for sectors such as aerospace and automotive, where a reduction in mass can relate to a cost saving in fuel or an increase in speed. The use of lattices or hollow sections is relatively straightforward in LS, however care should be taken to ensure the removal of unsintered powder is still possible. The addition of escape holes (see Figure 2.20), as well as planning access for powder removal in post-processing must be considered for these types of features.

Even if not used for these critical applications, the lightweighting of parts is still advised. This not only reduces the amount of material used, but also decreases the time required for the build, as the laser-point has to scan each feature in the layer.

2.2.4 Build Set-up

Part Nesting

As previously mentioned, multiple components are usually nested in each build in order to reduce costs (see Section 2.1.2). Although the cost per part is much more uniform than for processes such as IM, fixed costs such as the warm-up and cooldown times mean that maximising the use of the build volume

¹A simple experiment exploring how powder reuse affects the mechanical properties of LS PA12 is shown in Appendix C.1.1.

is desirable. This can either be done manually or using specialised software [122], with the spacing in between components (as specified in Figure 2.20) critical to ensure the parts do not fuse together during printing.

Part Positioning and Orientation

While financially, maximising the number of parts in a build is the most sensible option, this is normally not the only consideration when planning a build. For most LS machines, the position of parts in the build will have some effect on their mechanical properties due to the temperature distribution (see Section 2.3.1). This restricts the areas in which parts can be made, often rendering the edges of the build chamber unusable. The number of parts in a layer (or more specifically the proportion of a layer which is filled) can also affect these properties [229].

Further to this, the orientation can have a large effect on the mechanical properties of parts [230–232], with the z direction (normal to the layers) slightly weaker than within the layers. The feature resolution will also be affected by this, with the “stair-stepping” effect affecting the surface finish, and limiting the accuracy of features in the z direction.

In most instances, the orientation will have a negligible affect on the performance of the final product. However, in situations where the focus is on obtaining specific mechanical properties or geometric tolerances, this cannot be ignored. Potential solutions for increasing the isotropy could lie in altering the scan strategy [233], an option which is not yet available on most commercial systems.

Shrinkage Compensation

With most materials used in LS, especially with semi-crystalline polymers, the shrinkage of the material as it re-solidifies must be accounted for. Although this can be quite a large amount (depending on the material), this is highly predictable and is usually accounted for in the slicing software used to create the build file. By applying scaling factors in the xy and z directions, usually as specified by the manufacturer, parts can be produced with the desired dimensions without changing the `.stl` file.

2.3 Build Considerations (In-Processing)

2.3.1 Powder Heating

Bed Temperature

For LS, there is an opportunity with semi crystalline polymers to exploit the difference between the T_m and the recrystallisation temperature (T_c), which is the temperature at which the molten material re-solidifies. By choosing a bed temperature (T_b) in between the two values, the material scanned with the laser can be kept molten throughout the build, while the unscanned powder remains solid (see Figure 2.21).

The stable sintering region is defined as the temperature range where sintering will occur, and is bounded by the end of the melt peak and the degradation temperature of the material ($T_{\text{degradation}}$) [234, 235]. The value of $T_{\text{degradation}}$ cannot be obtained with DSC and is most commonly determined using Thermogravimetric Analysis (TGA).

Throughout the build process, the build chamber is pre-heated and held at this elevated T_b temperature just below the melting point of the powder. This minimises the energy required from the laser, enabling faster scan speeds and reducing the power laser required. For semi-crystalline polymers, this also means the parts can be kept in a molten state until the end of the build by using a bed temperature in between the T_m and T_c [210]. This prevents thermal stresses arising during building and minimises and subsequent warping.

Thermal Control

In practice, maintaining a uniform temperature across the powder bed is rarely possible, with variations inside the chamber leading to differences in properties of the printed parts. Restrictions on space available for heaters, often result in complex and often unpredictable convection currents which unevenly heat the powder (as shown in Figure 2.22).

In most cases, these variations are consistent between builds, enabling the operator to account for these differences during the build setup. But even if a perfectly uniform pre-heat temperature was achievable,

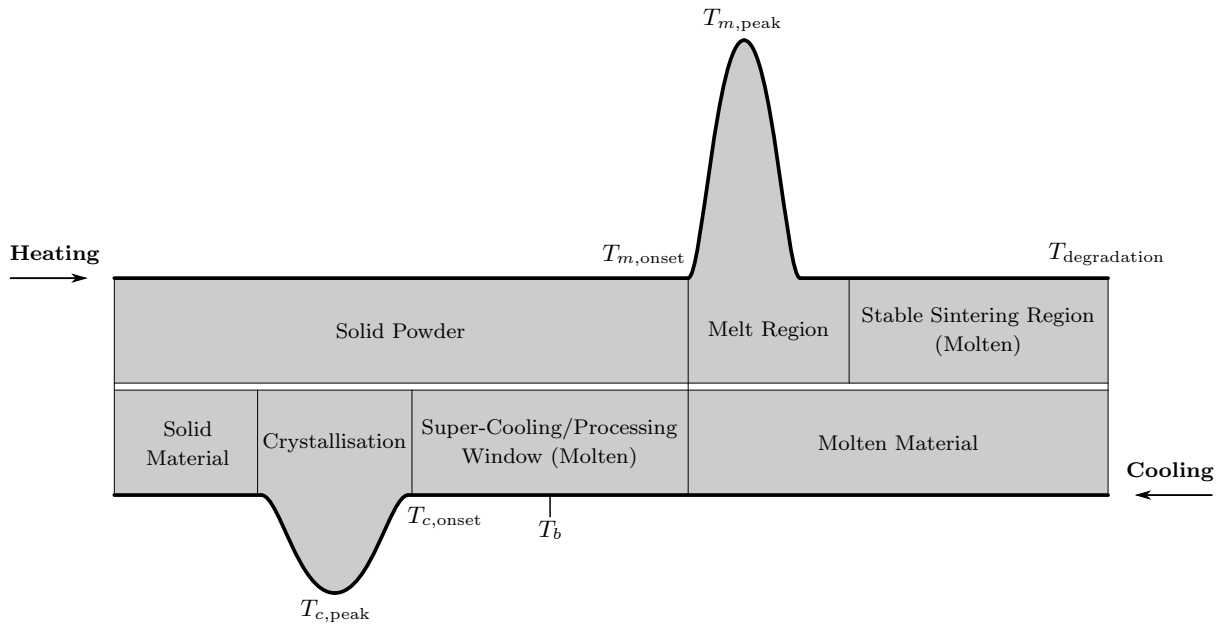



Figure 2.21: A typical Differential Scanning Calorimetry (DSC) trace (heat flow measurement) for a semi-crystalline polymer, showing the phase changes undergone by the material, and the stable sintering region and bed temperature (T_b) identifiable from the curve. Also shown are the melt onset ($T_{m,onset}$) and peak ($T_{m,peak}$), degradation temperature ($T_{degradation}$), and the recrystallisation temperature onset ($T_{c,onset}$) and peak ($T_{c,peak}$). 



Figure 2.22: Successive thermal images of a powder bed in LS, showing an uneven temperature distribution and evidence of unstable convection currents (bottom left of the images). The left image was taken 7 seconds before the right. [219]

this could still lead to uneven melting of the particles due to the size distribution in the powder (see Section 2.3.3).

2.3.2 Build Parameters

Definitions

As one might expect, there are a multitude of parameters available to change inside a Laser Sintering machine. A brief summary of some of the key parameters are shown in Table 2.1, although more options are available depending on the exact machine used.

Additional settings such as contours and scan strategies are also important, as they can influence both the mechanical properties and the surface finish. These are normally locked in the software, with an orthogonal scan strategy used (see Figure 2.23). In addition to the main scanning of the parts, a contour is commonly used to create a smoother surface and increase the dimensional accuracy of printed parts. Since contours often have different parameters to the main sections, these are generally excluded when processing experimental materials.

| | Symbol | Definition | Unit |
|---------------------------|----------|------------------------|-------------|
| Machine Parameter | P | Laser Power | W |
| | v_s | Scan Speed | mm/s |
| | d_s | Scan Spacing | mm |
| | t_l | Layer Thickness | mm |
| | T_b | Bed Temperature | °C |
| | r_s | Laser Beam Radius | mm |
| Material Properties [209] | T_m | Melt Temperature | 186°C |
| | c_p | Specific Heat Capacity | 4040 J/kg/K |
| | h_f | Heat of Fusion | 108 kJ/kg |
| | ρ | Density | 0.97 g/cc |
| | ρ_l | Layer Packing Density | 0.5 |

Table 2.1: Key build parameters and material properties for polyamide 12.

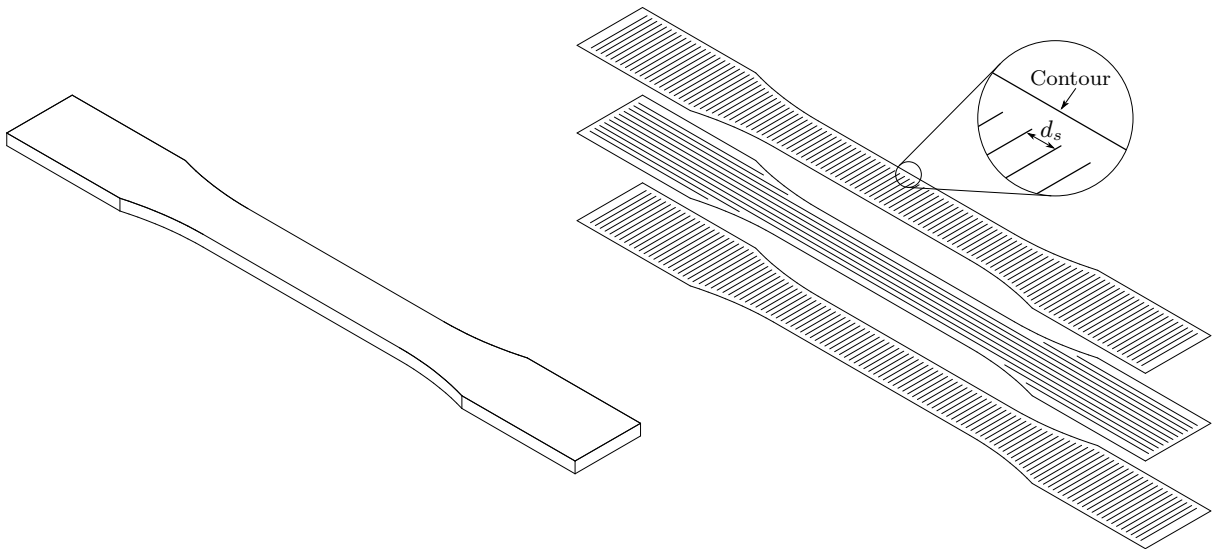


Figure 2.23: Example of an orthogonal scan strategy in LS, with an additional contour. 🚫

Optimising Parameters – Where to Start

When trialling a new material for LS, there are different methods which can be used to reduce the number of parameters to optimise, rather than attempting every combination of key parameters. For some parameters (such as r_s), these are inherent to the machine used and are not usually changed for different materials. Other parameters, such as d_s , although easily changed in the slicing software, are not generally varied in initial trials.

The powder characteristics can be used to provide a starting estimate for some of these parameters, an example of which is the heating profile which can be used to find an appropriate T_b (as described in Section 2.3.1). The powder size and morphology can also be used to determine a suitable t_l , although this will also be dependent on the machine capabilities and the accuracy required from the printed parts.

The two remaining key parameters (P and v_s), form the basis of most material trials in LS, with the laser power often considered in isolation during the initial stages. From a printability viewpoint the effects of this can be clear to see, with too low a power not providing enough energy to melt the powder, and too high a power causing degradation (or “smoking”) of the powder during printing.

In terms of the effect of P on the printed part properties, a significant difference can be seen in the mechanical properties; with the ultimate tensile strength (σ_{uts}), elongation at break (ε_{max}) and Young’s modulus (E) all increasing with increasing P , up to the point where the polymer starts to degrade [209, 230, 236]. This is due to the higher levels of melting and lower porosity in the printed parts [236–238]. Since the mechanical properties can reveal such a large amount of information about the effectiveness of the print settings, relatively simple tests (such as tensile testing) can be used to optimise the process.

Energy Density

With so many different settings available to change, and with differences in the setups of individual LS machines, there have been multiple attempts to combine key parameters into a single metric representative of the build. The concept of the Energy Density (ED), is that it estimates the energy delivered to any point on the powder bed which has been scanned by the laser.

The initial estimates for the ED were simplified into 2D metrics, as shown in Equation 2.1. The ED shown in Equation 2.1a [230] is known as the Andrew number, and is the most commonly used form of the ED equations; this simply relates the laser power, scan spacing, and scan speed. A less used version of the ED in 2D (shown in Equation 2.1b [239]), uses the additional information of the laser beam radius in the calculation. This represents the laser intensity \times the approximate time a circle radius r_s is exposed to the laser \times the approximate number of exposures.

$$\text{Energy Density (J/mm}^2\text{)} = \frac{P}{d_s v_s} \quad (2.1a)$$

$$\text{Energy Density (J/mm}^2\text{)} = \frac{P}{\pi r_s^2} \frac{2r_s}{v_s} \frac{2r_s}{d_s} \quad (2.1b)$$

A simple modification to the Andrew number (Equation 2.1a), can be made to convert this 2D approximation into a 3D metric by using the layer thickness. In this way, the energy input per volume can be found, rather than by area. This volumetric ED, is shown in Equation 2.2.

$$\text{Volumetric Energy Density (J/mm}^3\text{)} = \frac{P}{d_s v_s t_l} \quad (2.2)$$

By combining this information with the material properties of the powder used, an expression can be determined for the theoretical combination of parameters which result in complete melting of the powder particles. The Energy Melt Ratio (EMR) describes the ratio of energy supplied to the powder (the volumetric ED) to the theoretical energy required to melt the powder (as shown in Equation 2.3 [209]).

$$\begin{aligned} \text{EMR} &= \frac{\text{Volumetric Energy Density}}{\text{Energy required to melt the powder}} = \frac{\frac{P}{d_s v_s t_l}}{\frac{[c_p (T_m - T_b) + h_f] \rho \rho_l}{\text{Laser Power}}} \\ &= \frac{\text{Scan Spacing} \times \text{Laser Speed} \times \text{Layer Thickness}}{[\text{Specific Heat Capacity} \times (\text{Melt Temp} - \text{Bed Temp}) + \text{Heat of Fusion}] \times \text{Density} \times \text{Packing Density}} \end{aligned} \quad (2.3)$$

For many studies processing new materials using LS, the parameters chosen to optimise are almost always found in these equations. In most instances, the Andrew number is seen as the first step, with the laser power and scan speed often used exclusively for optimisation. Where the layer thickness and material are kept constant, all these terms are proportional to one another and any trends observed will be true for all versions of ED (or EMR).

The EMR provides a theoretical measure of the Degree of Particle Melt (DPM), being the proportion of each powder particle that is melted during the LS process. The experimental method to derive this, along with the implications of this (including the effect on the mechanical properties) are considered in Section 2.3.3.

2.3.3 Microstructure

Degree of Particle Melt

The entire concept of LS revolves around either partially or fully melting powder particles to form solid objects. With this in mind, it is useful to know the extent to which the chosen parameters (or chosen ED) melt the powder.

The Degree of Particle Melt (DPM) is a term used for semi-crystalline polymers processed using LS to quantify the proportion of the powder particle that has been melted. This can be observed using optical microscopy (Figure 2.24) or by using DSC [240,241], where the different crystalline regions make it possible to distinguish between the melted and unmelted phases. In addition to larger scale measurements of the

printed parts (such as mechanical properties), the microstructure and DPM can provide quantitative information on the effectiveness of chosen process parameters. They can also aid in understanding why certain trends in part properties occur at a more fundamental level.



Figure 2.24: Cross-section of an LS part observed using optical microscopy [242].

There are two ways in which the DPM can be affected, namely by changing the energy input to the powder (changing the ED), or by changing the powder size. As mentioned previously, the most common method used to optimise the LS process is by changing the ED [243]; a representation of how this affects a uniformly sized powder is shown in Figure 2.25. The DPM can be seen to be increasing until the particle is fully melted, with any further energy input leading to degradation of the powder.

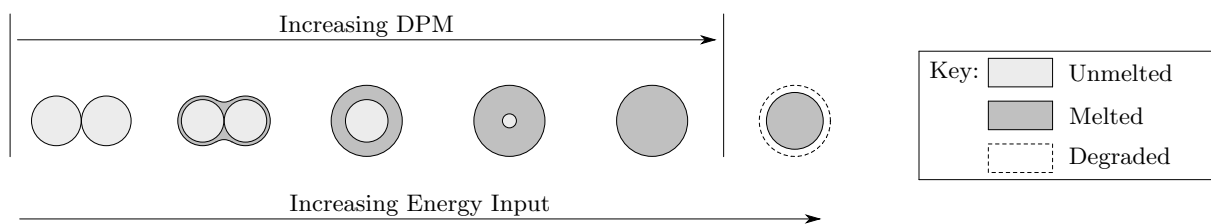


Figure 2.25: Effect of increasing energy input on the powder particles during Laser Sintering. This shows (left to right) too little energy resulting in unmelted particles, just enough energy for adjacent particles to start joining, $2 \times$ double phase particles (with both a melted and unmelted regions), enough energy to obtain a fully melted particle, and finally a particle which is starting to degrade due to excess energy. 🚫

The size of the particle will also change the effect that the energy input has, as shown in Figure 2.26. For a given energy, a small particle could fully degrade, whereas larger particles could only be partially melted. Practically, the degradation of material during the LS process is something which is best avoided. This is both due to the potentially harmful substances released, and because these could “fog up” the laser window and absorb some of the laser energy, ultimately leading to inconsistent printing [187].

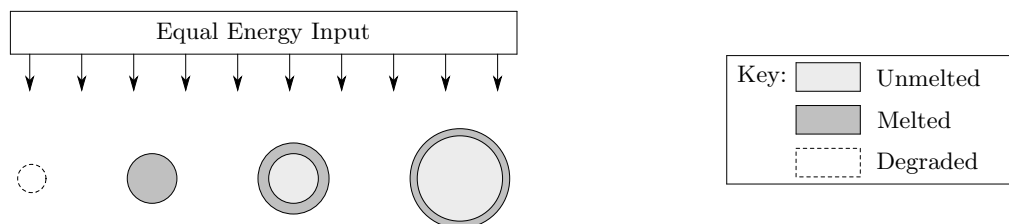


Figure 2.26: Representation of differently sized powder particles exposed to the same amount of energy. Showing degradation of small particles, full melting for one specific particle size, and partial melting for larger sizes. 🚫

Porosity

A less obvious benefit of a broader size distribution is shown in Figure 2.27, where the effects of both high and low ED on non-uniform and uniform particle sizes are shown [236]. The only way to achieve full melting of all particles, is by starting with uniform particle sizes (Figure 2.27a). In theory, this means that if exactly the right ED was found, all of the particles would react in the same manner and full melting would occur. The downside of this, is that for any slight deviation from this optimum ED, entire layers could be unattached or all of the powder would start degrading, constituting a failure in the build.

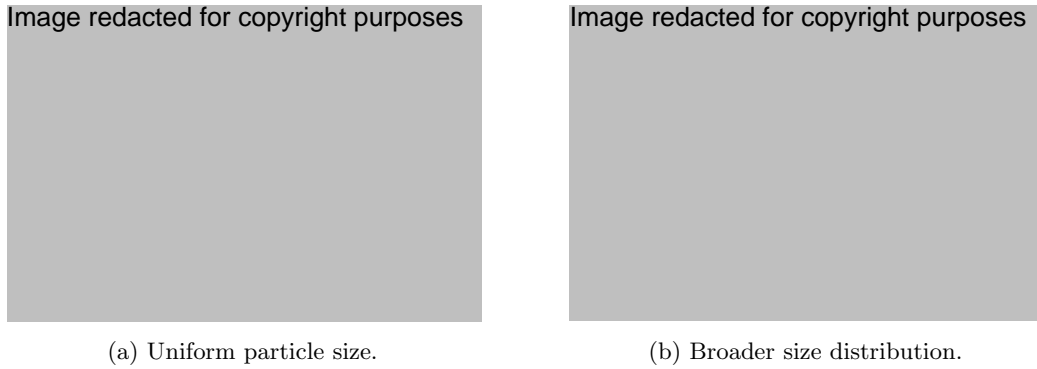


Figure 2.27: Effect of particle size distribution on porosity for varying ED. Modified from [236].

For a broader size distribution (Figure 2.27b), the differently sized particles mean that there will be varying levels of melting, due to the effects shown in Figure 2.26. Because of this, the powder is far more tolerant to sub-optimal process parameters, with both of the examples shown producing parts. This scenario is more representative of real LS powders, and the effect of varying ED is well documented for widely used materials such as PA12. As one might expect, the overall porosity has been found to decrease with increasing ED, although at a higher ED a greater number of small pores have been observed [236–238].

Effect of EMR and DPM on mechanical properties

With the changes in ED making such a large difference to the part microstructure, a corresponding change in the mechanical properties can be observed. The exact effect of changing the EMR (and subsequently the DPM) of the parts, will depend on the material, powder morphology, and on which parameters have been changed in order to increase the EMR. However, for PA12 this is fairly well established, with the effect on tensile strength shown in Figure 2.28.

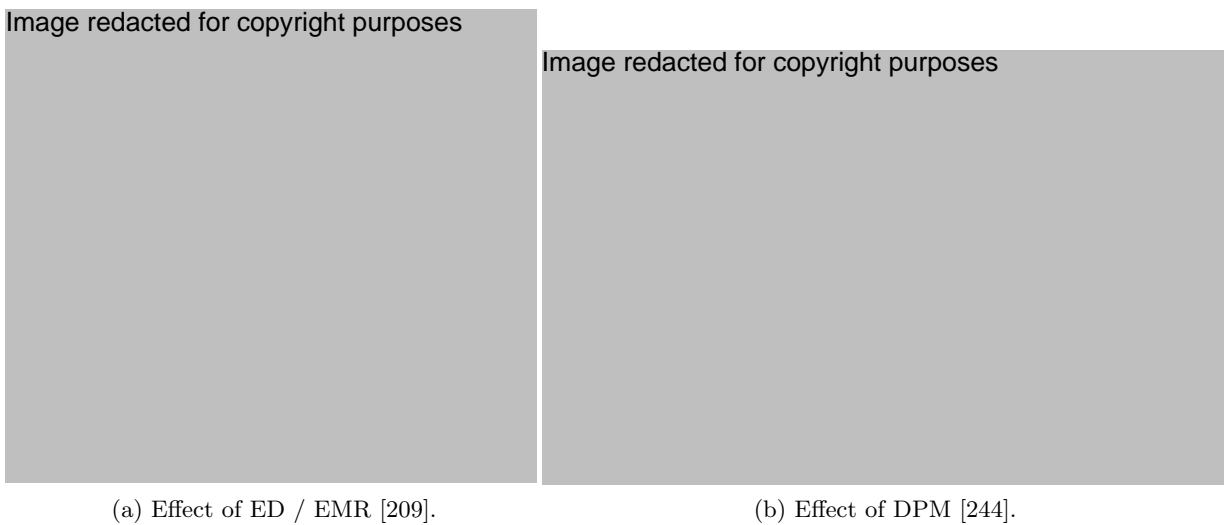


Figure 2.28: Effect of EMR and DPM on the mechanical properties of LS PA12 parts.

In Figure 2.28a, the EMR was varied by changing P and v_s , with the results showing an initial increase in yield strength (σ_y) before plateauing at a value just over 1 [209]. This trend in mechanical properties for increasing values of ED has been found in multiple studies, with values of Young's modulus (E), ultimate

tensile strength (σ_{uts}) and elongation at break (ε_{max}) all shown to increase with increasing ED before plateauing or decreasing [230, 236].

A physical explanation for this difference can be found when looking more closely at the microstructure, both in terms of the porosity and DPM in the printed part. The trend between σ_{uts} and DPM shown in Figure 2.28b appears very similar to that in Figure 2.28a for EMR, with the values peaking at or just before full melting occurs [241, 243–245].

This similarity is perhaps unsurprising given that the EMR is a theoretical predictor of DPM. However, the two differ in the position of the peak values, with the EMR peaking slightly after full melting, and the DPM peaking just before. This can be explained by the approximations made in the calculation of the EMR (Equation 2.3), and the additional energy losses which cannot easily be accounted for. These include losses due to the variation in thermal control, the absorbance of the laser energy by the powder, and the cleanliness of the LS machine (for example the laser window, which when dirty can reduce the laser power transmitted).

The relationship between these theoretical and experimental measures, once again shows how simply measuring the mechanical properties can provide a large insight into the microstructure of the parts and the suitability of the parameters used. While there are more parameters, machine configurations and powder characteristics which can affect the printed parts, the factors used in the EMR calculation (Equation 2.3) encompass the factors which have the highest impact on the part properties.

2.3.4 Cooldown

An often overlooked and underestimated step of the printing process is the cooldown time required after a build has completed. The time required to reach a set temperature will depend on the volume of powder in the machine; as a general rule of thumb, the LS builds should be allowed to cool for the same length of time as the build process, before powder removal [246].

This is especially important for semi crystalline polymers, as it is during this time that the material which has been held in a super-cooled molten state, cools to a low enough temperature to recrystallise (see Figure 2.21). Although it should be noted that some re-crystallisation is still possible throughout the build [187, 247].

The rate of cooling can have a direct impact on the microstructure of printed parts, most notably on the crystallinity. In general, a slower cooling rate has been linked with increased crystallinity, as the polymer chains have more time to form crystalline regions [247]. For LS PA12 the effects of varying the rate of cooling have also been observed, with a faster cooldown leading to a lower crystallinity, marginally higher E , marginally lower σ_{uts} , and a higher (and more varied) ε_{max} [244].

The relationship between crystallinity and the mechanical properties of polymers is well documented, with the effects almost entirely limited to temperatures between the T_g and T_m , below which the effect of crystallinity is small [247]. The largest differences can be seen in E , which is directly proportional to the crystallinity. Other properties, including the fatigue response and the yield strength, have also been shown to increase with an increased crystallinity [247, 248].

2.4 Post-Processing

Post-processing of parts can be a costly and time consuming, and is often overlooked when planning the use of AM. For manufacturing polymer parts in an industrial setting, post-processing can take up to a quarter of the total manufacturing time [179]; meaning that careful consideration should be made in choosing the appropriate steps and reducing the complexity, and therefore time, for these processes.

2.4.1 Powder Removal

The only compulsory post-processing step for all LS parts, is the removal of loose, unsintered powder from the build (see Figure 2.29). This is usually accomplished manually using compressed air jets, and can be a complex process for fragile or detailed parts; however in some cases automated systems (typically using a combination of water and air jets [249]) are becoming more popular as they can drastically reduce the costs associated post-processing.

Following the powder removal, there are various optional processes which can be used to enhance the aesthetics, surface finish, and functionality of the parts. Some of the more popular of these options are addressed in Sections 2.4.2 and 2.4.3.

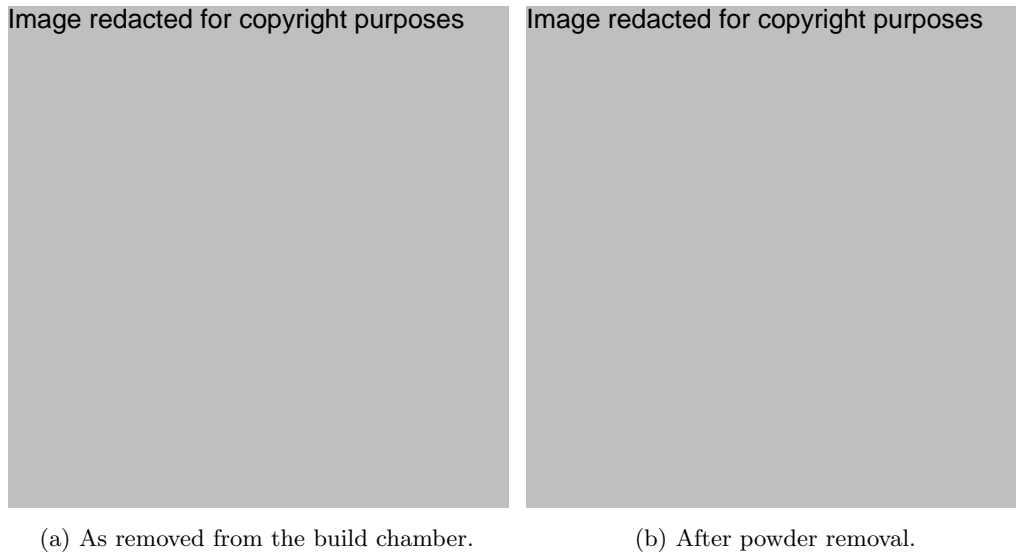


Figure 2.29: Example of powder removal for a LS part [250].

2.4.2 Aesthetic and Surface Finish Processes

One of the most common processes used to enhance the aesthetics of printed parts is dyeing (see Figure 2.30b). This process is simple to carry out, and the hygroscopic nature of polyamide 12 means that it is an effective method to colour areas on or near the surface. Most importantly, this method does not alter the surface finish or geometry of the printed part.

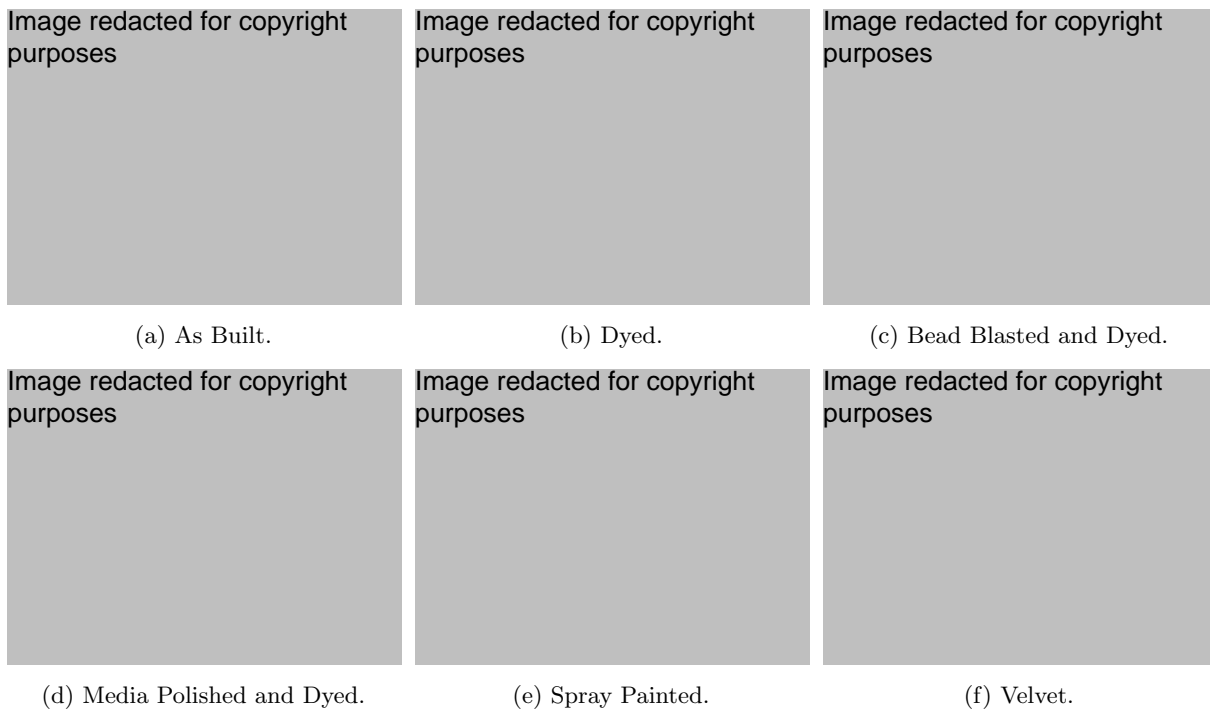


Figure 2.30: Example post-processing options to change the aesthetic and surface finish of LS parts [251].

For some applications, it is desirable to alter the “grainy” surface finish associated with as built LS parts; the most widely used of these processes are based around smoothing or polishing the surface. Bead blasting (Figure 2.30c), fires small glass beads at the parts and is often used in conjunction with compressed air jets in the removal of loose powder.

On the other hand, media polishing (Figure 2.30d) is an additional step after powder removal, in which the part is submerged in ceramic chips and subjected to ultrasonic vibrations. This can result in a smoother finish; however, this is a slightly more aggressive automated process which could compromise or damage small features.

Vapour smoothing, is also an additional step which uses solvents to dissolve and re-solidify the surface of the parts [252, 253]. As this does not rely on mechanical force to finish the parts, this can also be used for flexible materials, or intricate geometries, which would be challenging to polish by other methods.

Other methods used for aesthetic purposes include painting (Figure 2.30e) and more specialised processes such as flocking to obtain a velvet surface (Figure 2.30f). These techniques are most prevalent where the parts do not have a functional purpose, however there are finishes available which enhance the properties and functionality of the printed parts.

2.4.3 Functional Processes

Some post-processing are purely focused on enhancing the functionality of the printed components, rather than the aesthetics. These can be methods such as applying a waterproof coating (Figure 2.31a), or heat treating parts to increase the level of sintering and alter the mechanical properties [254].

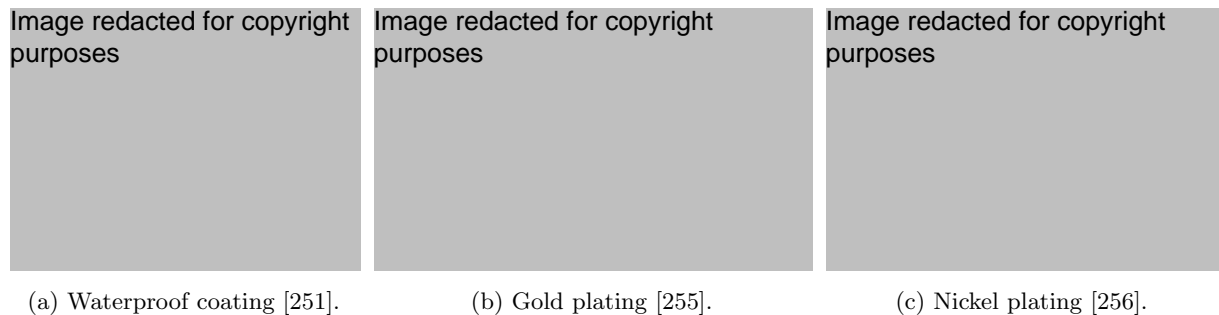


Figure 2.31: Example commercially available functional post-processing methods for LS parts.

Other less common commercially available methods, include metal plating of parts through electroless (sometimes followed by electro-) plating, as shown in Figures 2.31b,c [255, 257]. As well as enhancing the mechanical properties, this can also be used solely to alter the aesthetics of the parts, further diversifying the applications which LS could be used for (see Figures 2.6e and 2.8f for examples of metal plated products).

In academic research various infiltrants have been investigated, including “superglue”, brick sealant, and MDF sealant [254]; all of which were primarily chosen to attempt to alter the surface finish, rather than alter the mechanical properties. However, there are numerous instances of epoxy infiltrants being used to increase the mechanical properties, especially in lesser-used materials such as PC [184], PS [191] (also infiltrated with wax [174]), and SAN [186], which otherwise would have properties too low for practical use.

This method has also been applied to composite materials (namely PA12 and carbon fibre) for the same reason, both decreasing the porosity and increasing its strength [258]. Further research into epoxy-polymer composites have focused on other properties of printed parts, with the epoxy infiltrant used to increase the transparency of previously opaque SMMA [190] and PS [259] parts.

2.5 Quality Control and Long-term Effects

With LS parts used in a variety of end-use applications, identifying appropriate quality control (QC) techniques and prior knowledge of how the printed parts might perform in certain situations are of increasing interest in industry. This section briefly covers the use of micro-CT as a QC method, and some of the long-term properties of LS PA12 parts.

2.5.1 Geometry and Porosity²

X-Ray Computed Micro-Tomography (Micro-CT) is a non-destructive 3D imaging technique capable of analysing the internal and external geometry of complex components. This is now widely used as a method to examine the porosity of AM parts (as shown in Figure 2.32) and has been described as the only technique capable of industrial QC of internal features created with AM [261,262].

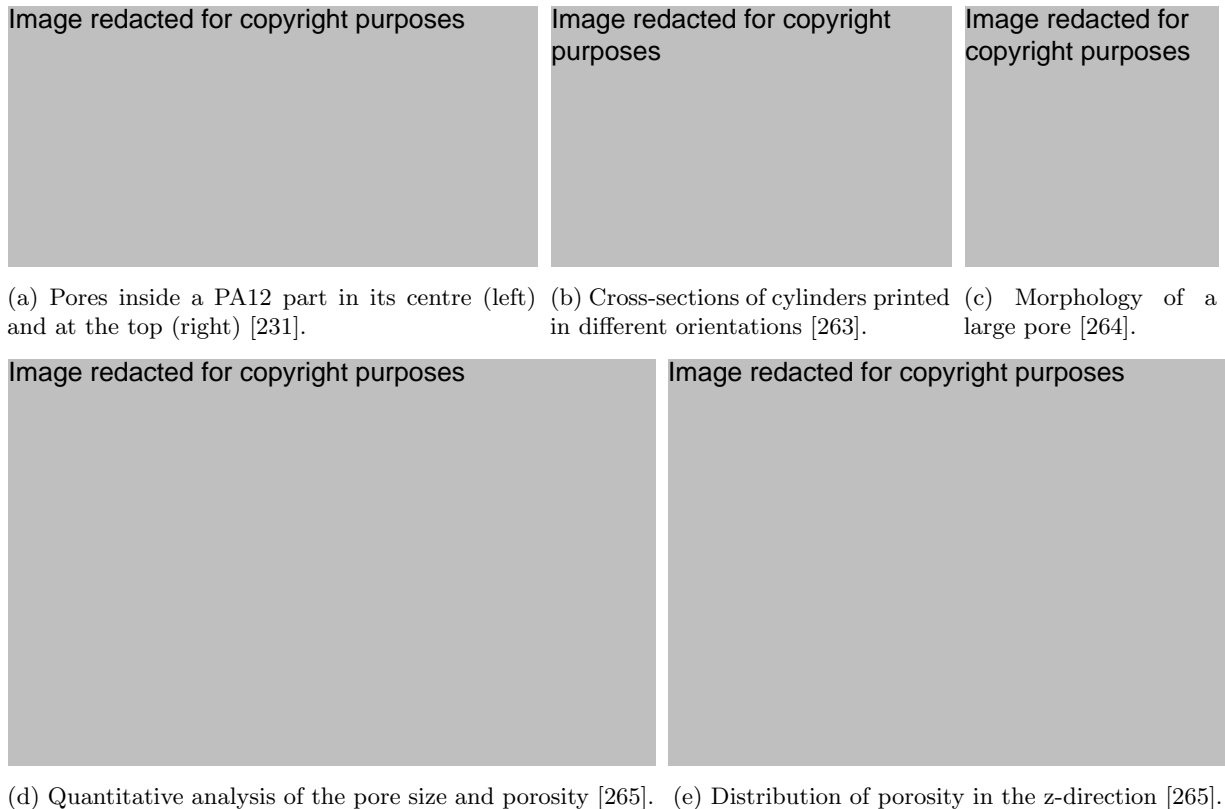


Figure 2.32: Uses of Micro-CT to analyse Laser Sintered parts.

The majority of recent literature on micro-CT in AM has focused around metals [261]; however, studies using polymer LS have also utilised this approach to measure porosity and geometry. Polyamide 12 (PA12) is the most widely used material for LS and is the most well documented for use with micro-CT. Other polymeric materials have also been analysed using this process, such as PEK [194] and PEEK [193].

For PA12, the use of micro-CT has evolved from a qualitative technique for viewing pores (Figure 2.32a–c) [231,236,266], into a more quantitative method (see Figure 2.32d,e) of determining the porosity [267], pore size [237,238,268,269] and pore distribution within the parts [229,263,265]. This method is also used to measure the geometry of external features, varying from a simple analysis of a cross-section (Figure 2.32b), to more involved methods which compare the scan data to the original CAD models.

2.5.2 Long-term Effects

Water Absorption³

It has previously been shown that the mechanical properties of polyamides are affected by their water content, as the absorbed water molecules break hydrogen bonds in the material, lowering the glass

²A version of this introduction to micro-CT has been published in [260].

³A version of this introduction to water absorption has been published in [270]

transition temperature and potentially degrading the polymer [271–276]. While some papers have alluded to this affecting the properties of LS polyamide parts [206,277–279], few have explicitly measured this [280,281] and conflicting effects on the mechanical properties have often been found.

Focusing on the tensile properties of PA12, it is generally agreed that the ultimate tensile strength and the Young’s modulus decrease with an increase in water content [206,277,278,280–282], however the effect on the elongation at break has been reported to both increase [277,278] and decrease [280,281] as a result. It is worth noting that the majority of these studies did not measure the water content directly, often only hypothesising that observed changes in properties were due to increased water content.

In [277], changes were found both due to water content and time (shown in Figure 2.33); further differentiated between water absorption (from liquid water) and moisture absorption (water vapour). Trends of decreasing σ_{uts} , E , and increasing ε_{max} can be seen for the “wet” samples, as observed in injection moulded PA12. However short term increases can be seen, likely from mechanisms other than water content. Crucially, since the water content was not measured, a direct causation could not be established.

Image redacted for copyright purposes

(a) Ultimate tensile strength.

(b) Young’s modulus.

(c) Elongation at break.

Figure 2.33: Long term mechanical properties of LS PA12 parts stored in dry, controlled (50% relative humidity), and wet (immersed in water) conditions. Modified from [277].

The studies which have measured water content only considered the extremes of “dry” and “wet”, saturating samples under accelerated conditions (submerged at 90°C for 80+ days). This introduces more potential causes of differences (such as physical ageing or higher temperatures) and with only two data points, cannot be used to observe trends. Another key point not yet investigated, is whether after exposure to these adverse conditions, the properties of the parts can be recovered through methods such as drying, or whether they represent a permanent degradation of the polymer.

Fatigue

Multiple studies have focused on the repeated loading of parts, primarily based on PA12 and often comparing to an equivalent injection moulded part. LS parts have been found to be more resistant to cracking than those made with IM [283]; which has been shown irrespective of the orientation of the print [266] but with cracks tending to form along the layer lines for LS parts. Comparing between LS samples with printed and machined notches, the reduced numbers of pores at the surface (see Figure 2.32a) found in printed notches, has been linked to an increased resistance to cracking [266]. Despite this, grinding of the surface in post-processing shows no significant change in the fatigue properties [283].

The loading and environmental conditions also play a part in this, with more energy damped when the parts are above the T_g , despite a lower stiffness (E) [266,284]. Perhaps obvious factors (such as the DPM) have also been linked to crack propagation, with crack initiation found to occur around unfused or partially fused powder particles [187,284]. Exposure to water has also been shown to decrease the fatigue properties of both PA12 and PA11 printed parts [281].

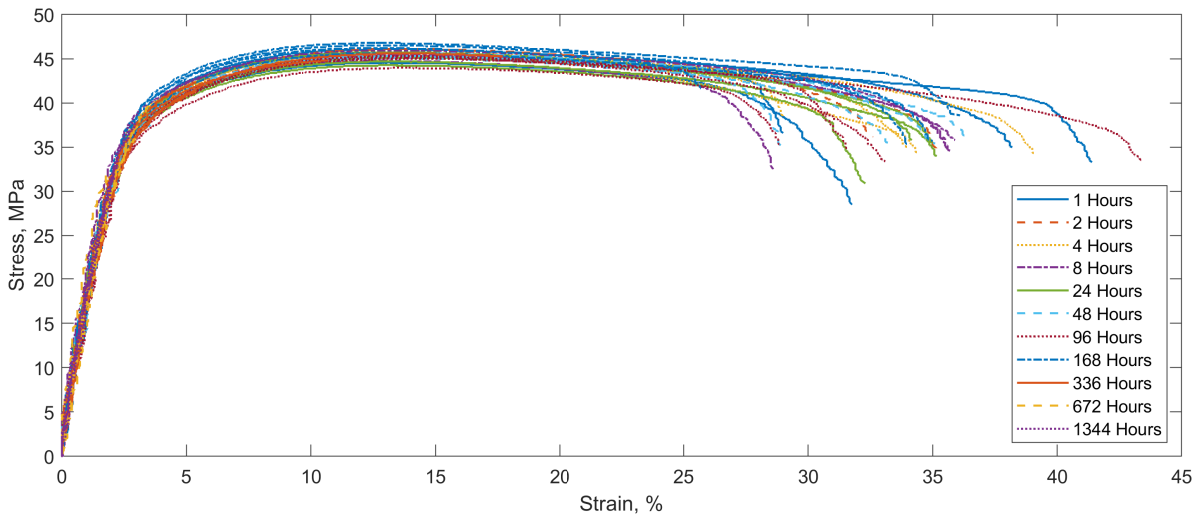
The material choice can have a large impact on the fatigue properties, with PA11 printed parts shown to have much higher properties than those printed in PA12. However, other options including composite materials can also be used to alter the mechanical properties. Focusing on PA12 composites, the addition of multi-walled carbon nanotubes (MWCNT) has been found to slightly increase the fatigue strength [285].

Whereas the effect of incorporating short glass fibres has been found to vary based on the temperature, with benefits only observed at lower (-50°C) temperatures [286].

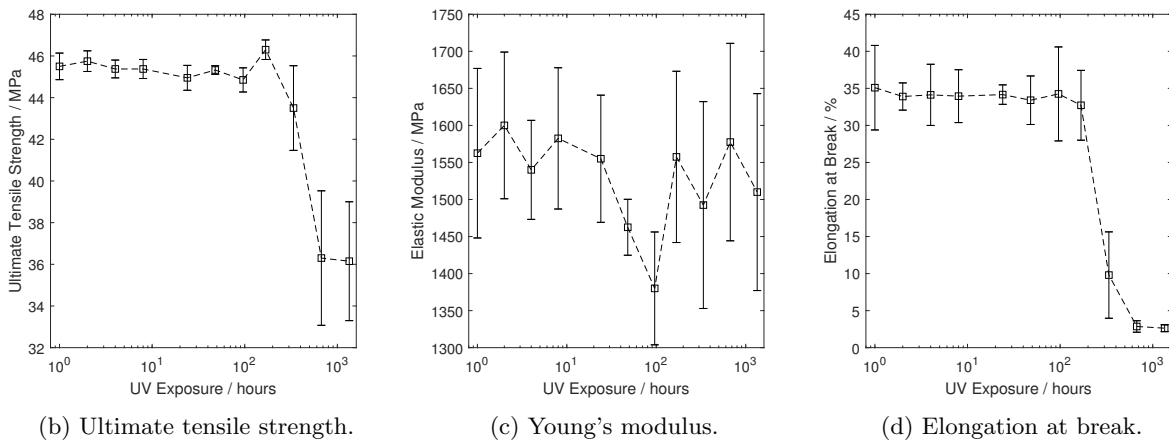
Ultraviolet Light Exposure⁴

As Laser Sintered PA12 parts age, a slight difference in colour can be observed. This “yellowing” of parts can be seen to a small degree in Figure 2.3a, where all parts shown started off the same colour and only developed differences in colour, due to the differences in age. This change has been anecdotally linked to exposure to ultraviolet (UV) light, although this has not been rigorously investigated.

Previously thought to be primarily an aesthetic change, the results in Figure 2.34 show for the first time the effects of UV light on the mechanical properties on LS PA12 parts [287]. This also tracks the colour change for the timescale shown (Figure 2.34e), with a gradual change seen over the prolonged exposure.



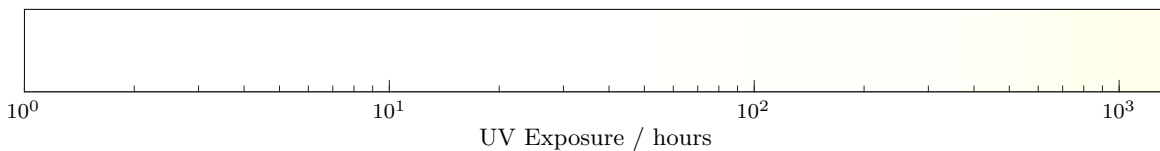
(a) Stress–Strain graph of LS parts exposed to varying amount of UV light.



(b) Ultimate tensile strength.

(c) Young’s modulus.

(d) Elongation at break.



(e) Colour change of LS parts after exposure to UV light.

Figure 2.34: Mechanical properties and colour change of LS PA12 parts when exposed to UV light. 🚫

In Figure 2.34d, the most notable change can be seen in ϵ_{\max} , significantly decreasing with UV exposure. However, the stress–strain curves (Figure 2.34a) show that all of the tests follow broadly the same profile, with higher exposure times merely breaking earlier in the curve. This suggests that the exposure to UV is not affecting the bulk properties of the parts before fracture, but they are significantly more brittle.

⁴The research in this section was carried out in part by the author, and is published in [287].

2.6 Composite Materials

A common method to alter the properties of polymers with conventional manufacturing methods is by incorporating additives (or fillers) into the material [288]. By doing this the parts are made of a composite material, with capabilities which could exceed those of the base polymer. In LS, these composite materials are also rapidly gaining popularity for the same reason. The difficulty in processing new materials with LS has added to this, as different properties can be achieved in already established materials.

2.6.1 Composite Material Feedstock Types

Conventionally, in order to manufacture an additive-containing part, the polymer feedstock must first have the desired additive dispersed throughout its volume. The resulting composite polymer material can then be processed in the same manner as a pure polymer (for example by injection moulding) to form the geometry.

In LS, the nature of a powder feedstock means that there are more options available when it comes to incorporating additives in the printed parts. This is shown visually in Figure 2.35, where distinctly different scenarios for incorporating these additives can be obtained. Although each of the powders may appear different, the method by which the additive is included in the final part is the same. In each case, the additive is held in place by the melting of the polymer around it, rather than by a direct sintering of the additive itself [182].

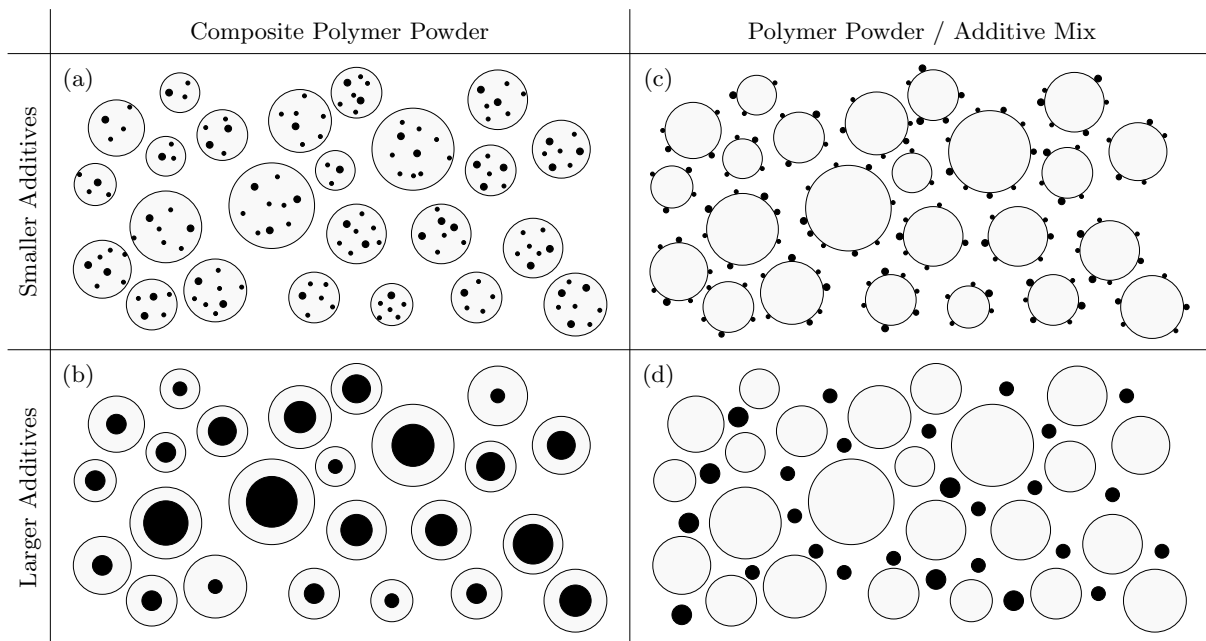


Figure 2.35: Types of feedstock used with LS to create composite parts, showing the different ways additives (black) can be combined with the polymer. Composite polymer powders (a,b) represent each powder particle as a composite material, whereas with a polymer powder / additive mix (c,d) the polymer and additive remain separate until printing. 🚫

The methods to create these vary in complexity, scale and cost, with the size and purpose of the additive often dictating which method should be used. The fundamental choice is between creating a composite polymer powder, or using a polymer powder / additive mix (see Figure 2.35), the methods by which these are produced differ starkly and could constitute a large financial investment. These options are summarised in this section, with individual methods of production explored in more detail in Section 2.6.2.

Composite Polymer Powder vs. Polymer Powder / Additive Mix

Summary of powder feedstock types (as defined in Figure 2.35):

- (a) *Composite Polymer Powder – Smaller Additives.* Creating these powders is a very involved process, as any material produced must not only contain the additive, but be in a powder form suitable for LS (see Section 2.2.2). This method more closely resembles conventional methods of incorporating additives, as it creates a homogeneous composite polymer before forming it into the final product.

- (b) *Composite Polymer Powder – Larger Additives*. Similarly to (a), these powders must also be made specifically for use in LS. With these larger additives, rather than introducing the additive to the polymer, a coating is formed around the additive. This is commonly used to create “green” parts (known as indirect LS), where the binder is burnt out to make parts solely made of the additive, usually creating parts in metal or ceramic material.
- (c) *Polymer Powder / Additive Mix – Smaller Additives*. Mixing a purpose-made LS polymer powder with an additive is the simplest way of creating a composite feedstock. However, the additive size will determine how effective this mixing can be. For smaller ($<1\ \mu\text{m}$, generally nano-sized) additives, factors such as static forces and moisture can have a major effect, meaning that additive agglomeration is much more likely. Coating methods can be used to overcome this, although achieving an even coating is not guaranteed. For these mixes, as the nano-sized additives are still in a powder form, higher levels of health and safety are generally required to work with these more hazardous materials.
- (d) *Polymer Powder / Additive Mix – Larger Additives*. For these larger additives ($1\text{--}100+\ \mu\text{m}$), the composite feedstock can often simply be made by mixing with a polymer powder. Although much simpler and cheaper than (a) and (b), the limitation of this is often the homogeneity of the mix. As the particles are still separate, there is the possibility of agglomeration, or of the powders separating out over time (especially with materials of different densities).

Printed Part Additive Dispersion

Putting the practicalities of creating the powder feedstock aside, one of the most important aspects of using any composite material, is how its components are distributed within the part. For the four cases specified in Figure 2.35, the dispersion and homogeneity of the printed part can differ greatly. This can be seen in Figure 2.36, where example microstructures for each case are shown.

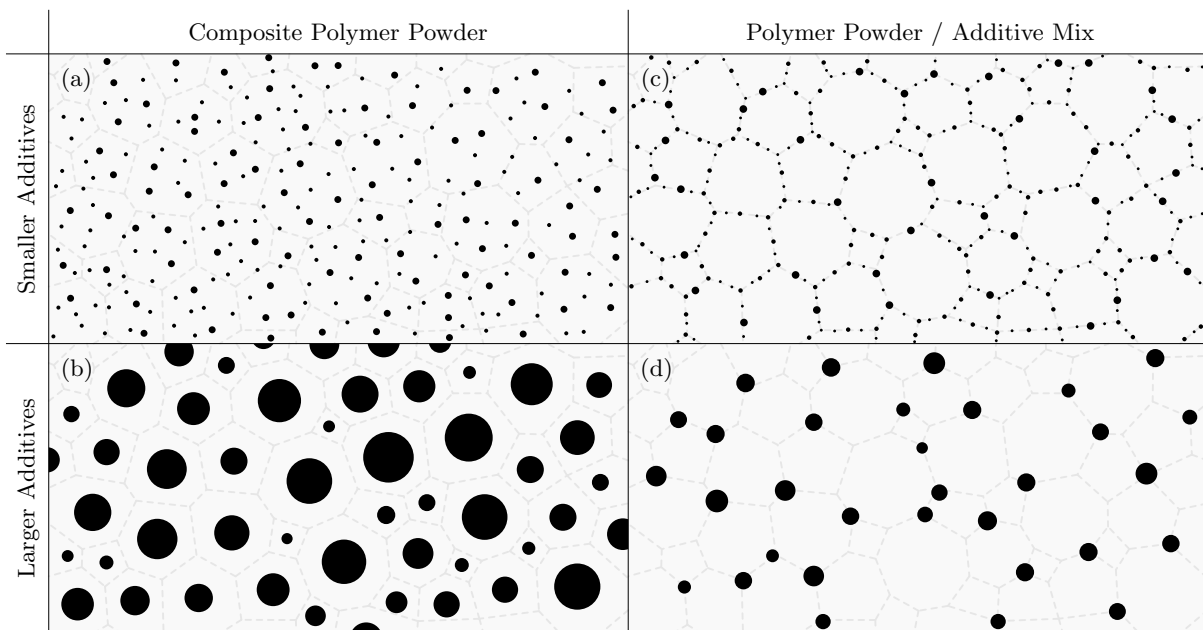


Figure 2.36: Additive dispersion for different types of composite feedstock (as specified in Figure 2.35) in a printed part. Shown is the additive (black) and the boundaries between individual polymer powder particles (dashed) after melting. 🚫

In Figure 2.36, the composite polymer powders (a, b) can be seen to create more homogeneous parts than the polymer powder mixes. For the smaller additives (a), the microstructure is nominally the same as the starting powder, whereas in (b) the additives remain in the centre of the now melted particles to create a uniform distribution. Due to this uniformity, these methods are often preferred when incorporating additives to enhance the mechanical properties.

Conversely for the polymer powder mixes (c, d), the additives are trapped at the edges of the polymer grains, as adjacent particles melt into one another. With proper feedstock preparation and mixing, these can form homogeneous parts. However, this is more difficult to achieve than with the composite powders, and greater quality control is needed. Since these methods can lead to additive agglomeration, or to

connected lines of additives (both of which are potential stress concentrations), these are generally used for additives such as flow enhancers which are not designed to improve the mechanical properties.

2.6.2 Production Methods

There are a multitude of different methods for creating a composite feedstock for LS, depending on both the materials to be combined and the desired feedstock type (see Figure 2.35, 2.36). Generally, the choice is solely between creating a composite polymer powder or a polymer powder mix. However, it is also sometimes desirable to use both of these approaches in succession, introducing even more additives into the parts by coating or mixing them with a composite polymer powder.

These methods are summarised in Figure 2.37, and each of the processes shown are briefly explained in this section. These are divided into three categories; solid-state shear pulverisation includes processes which apply a high shear force to fuse and fragment the polymer, solution-based methods include any processes which dissolve (or melt) the polymer in a solvent, and physical mixing includes processes which keep the polymer powder and additive separate [118].

Solid-state shear pulverisation

Cryogenic Milling – In this process, bulk materials are cooled (usually to below -50°C) alongside larger metal or ceramic balls. The entire chamber is then rotated, with the resulting high energy collisions leading to fragmentation and fusing of the polymer bulk material. With this, it is possible to mix and mechanically alloy [289] polymers and additives and create the composite powder in one step [290]. Another popular option, is to create a bulk composite polymer using twin screw extrusion, before subsequently using cryogenic milling solely as a means of turning this into a powder [160].

Wet grinding – This process is similar to cryogenic milling in its method of powder creation; however in this, the high energy collisions take place in a mechanically stirred solvent [291]. Often followed by the rounding of particles in a downer reactor (where particles pass through a heated cylinder to melt and smooth their outer layer), it is only through a subsequent coating step that wet-grinding has been used in the production of composite materials.

Solution-based Methods

Dissolution-precipitation (also known as thermally induced phase separation TIPS) – In this widely used method, the bulk polymer is added to a solvent in which when heated, it completely dissolves; upon cooling, the polymer precipitates out in a highly controlled fashion, allowing the mass production of near-spherical powders [210]. For the creation of composite powders, the additive can be dispersed in the solvent, mixed using either ultrasonic oscillations or mechanical stirring and when the solution cools, the additive can be incorporated into the powder precipitates [292]. The resulting powder suspension is then decanted, washed and dried before use. This method is also suitable for coating larger additives [163], including applications for indirect LS [293].

Solution-intercalation – This is very similar to dissolution-precipitation; however in this, the polymer is dissolved in the solution without the addition of heat. In the same manner, the additive can be dispersed in the solvent, allowing the creation of a composite powder when the polymer precipitates out of the solution [294].

Spray Drying – In this, the polymer is dissolved in a solvent, before being forced through an atomiser nozzle, instantly evaporating the solvent to precipitate the polymer [295]. Due to the speed of this process, the resulting powders have been found to have high porosity and low mechanical properties [296]. Although not yet used for the production of composite powders for LS, the dispersion of additives in the solvent could achieve this.

Melt-emulsion with rotation shearing – This methods melts the polymer in a solvent / emulsifier mix, and then uses rotation shearing to break up the molten polymer into smaller droplets; when cooled, the droplets solidify to form the powder [297]. This is also not currently used to create LS composites, but could be by dispersing additives in the solvent / emulsifier mix.

Emulsion-polymerization (also called *in-situ* polymerization or intercalation polymerization) – To create composites with this method, monomers are added to a nano-additive containing emulsifier [298]. During polymerization, the additive is trapped (or intercalated) by cross-linking of newly formed polymer chains [165, 299].

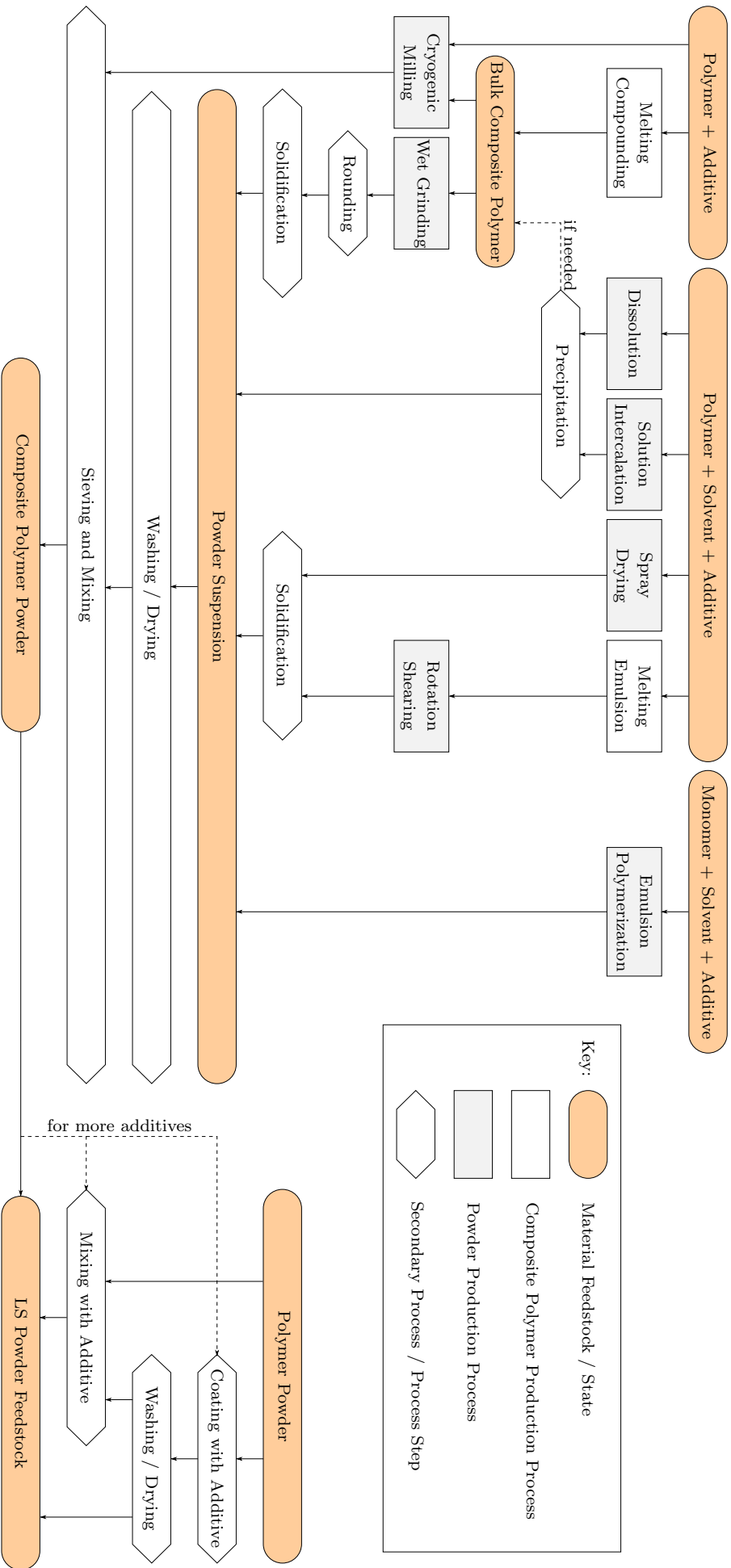


Figure 2.37: Methods of Composite Polymer Powder Production.

Physical Mixing

Coating (or wet-coating) – This process coats a polymer powder in the additive, without creating a individual composite powder particles. With wet-coating, the (generally nano-sized) additives are dispersed in a solvent before the powder is added to the resultant slurry. This is then filtered, potentially washed, and dried to remove the solvent and obtain the coating [300].

Mixing (or dry-coating) – This is the simplest of all the methods for creating a LS composite powder feedstock. This simply mixes the polymer powder and the additive in a rotary tumbler to combine the two (or more) materials [162, 200, 301, 302]. For small additives, this has the effect of coating the polymer powder, whereas for larger additives, this simply attempts to create a homogeneous mix of the the polymer and additive particles. This method is often used in research due to its simplicity and ability to process small volumes of powders.

2.6.3 Quality Control

One of the potential downsides of physical mixing techniques, is the dispersion achieved both in the feedstock and in the printed parts. For larger additives, or those with significantly different densities to the polymer, there is the possibility for segregation either during or after tumbling; whereas for smaller (especially nano-sized) additives, agglomeration of the additive is a major issue.

Despite these known challenges, relatively little research has been carried out exploring this, with surprisingly few techniques used to determine the dispersion of additives within the printed parts. The most commonly used methods revolve around taking a slice of a part and analysing the 2D dispersion on the slice using optical microscopy. One potential candidate for non-destructive QC of micro-composite parts is micro-CT, which is already used in the analysis of AM parts to analyse internal features (see Section 2.5.1).

The ability of micro-CT to distinguish between multiple materials with sufficiently different densities or chemical compositions means that as well as detecting pores inside printed parts, detection of inclusions (or contaminants) is also possible both in the printed part and in the material feedstock [303]. So far, this detection of contaminants has been mainly in metallic parts [304, 305], however there are some examples where polymers processed with FDM have been investigated [303, 306] (as shown in Figure 2.38a).



(a) Inclusions (white) in an FDM part [303]. (b) Pores (coloured), polymer matrix (grey) and CF (white) in an LS part [258].

Figure 2.38: Micro-CT scans in polymer AM used to detect inclusions or additives in printed parts.

In the majority of these cases, these scans are used to detect unwanted contaminants which could show more thorough cleaning of a machine is required when switching materials. For the FDM scan in Figure 2.38a this is not the case, as the inclusions shown were intentionally included in the filament to achieve the desired colour, essentially creating a micro-composite part.

This method has occasionally been used to analyse micro-composite parts [264]; however these analyses have still focused on the geometry and porosity, very rarely analysing the additive inside the part. In metal AM, micro-CT has been used to qualitatively identify different metal powders in titanium alloys [307, 308]. However, the quantitative analysis of additives in polymer PBF parts is only just starting to be investigated, with an example showing the distribution of pores and CF shown in Figure 2.38b. The focus of this was primarily on determining the pore dispersion, but it also highlights the position of the carbon fibres (CF) which were incorporated in this LS part.

2.6.4 Commercially Available Materials

While it is possible for consumers to combine additives with polymer powders themselves, there is already a range of commercially available composite powders being sold specifically for LS (as shown in Table 2.2). The focus of the vast majority of these additives is on increasing the strength and stiffness of the printed parts, with additional benefits such as slightly increased thermal and electrical conduction sometimes seen. The exceptions to these, are the flame resistant composites, which focus on adding functionality rather than improving mechanical properties.

| Additive / Filler | Material | |
|----------------------------|--|---|
| | PA12 | Other |
| Glass Beads | PA3200 GF [309] | PA11: Adsint PA11 GB30 [310] |
| | PA 415-GS, PA 616-GS, PA 615-GS, PA 614-GS [311] | PA11: PA11-GF 3450 [312] |
| | DuraForm GF, DuraForm ProX GF [313] | PA6: EP-PA6GF [314] |
| | EP-PA12GF [314] | PP: Laser PP CP 75 [315] |
| | FS 3401 GB [316] | |
| Mineral / Glass Fibre | PA 620-MF [311] | PA: Windform LX 3.0 [317] |
| | DuraForm HST, DuraForm ProX HST [313] | PA: Windform GT [317] |
| | FS 3250 MF [316] | |
| Mineral (unknown) | | PA6: Ultrasint PA6 MF [310] PP: Laser PP CP 22 [315] |
| Aluminium | Alumide [309] | |
| | PA 605-A [311] | |
| | DuraForm ProX AF+ [313] | |
| Glass + Aluminium | PA12-GFX 2550 [312] | PA: Windform GF 2.0 |
| Carbon Fibre (CF) | CarbonMide [309] | PA11: HP 11-30, PA 802-CF [311] |
| | PA603-CF [311] | PA11: Adsint PA11 CF [310] |
| | FS 3400 CF [316] | PA: Windform XT 2.0 [317] |
| | | PA: Windform SP [317] PEKK: HT-23 [311] |
| Carbon Fibre + Glass Beads | PA 640-GSL [311] | PA 840 GSL [311] |
| Flame Resistant | PA2200 FR, PA2241 [309] | PA11: FR-106 [311] |
| | PA 606-FR [311] | PA6: Ultrasint PA6 FR [310] |
| | DuraForm FR 1200, DuraForm ProX FR 1200 [313] | |

Table 2.2: Commercially available composite powders for LS (comprehensive as of January 2020).

It is important to note that although the powders in Table 2.2 are specifically marketed as composite materials, almost all LS polymer powders contain additives of some type. These are generally flow enhancing additives (such as silicas [187, 208, 236]), additives to increase the energy absorbed from the laser (such as CB or Ti [318]), or additives which enhance the colour of the material (such as TiO₂ for whiteness). These are generally small (micron-sized) particles which are mixed with a polymer powder, however since they are often essential for processing with LS, they are not regarded as composite materials.

2.6.5 Academic Research

In terms of academic research, a wide range of additives and polymers have been investigated for diverse applications. These have generally been to alter the mechanical / physical properties of the printed parts, to create “green” parts for indirect LS, or to increase the biocompatibility / bioresorbability of parts printed for medical applications. A summary of these composites is shown in Table 2.3, it should be noted that PA12 composites are not shown here and are shown separately in Table 2.4.

It should also be noted that the quality of the printed parts was not investigated here, with a initial and more in-depth analyses presented side by side. For some of these (as evidenced by the overlap with the commercialised composite powders in Table 2.2), the studies yielded significant and repeatable results with a wide range of real-world applications. However in others, despite the apparent success in processing with a novel filler material, these often came at the expense of other factors such as the mechanical properties (with over a tenfold reduction in strength seen in some cases).

Due to the variety of intended purposes and potential applications for these materials, a reduction in mechanical properties does not necessarily constitute a failure. However, the specificity of some applications (such as some materials intended for creating implants) means that these are unlikely to be commercialised on a large scale in the near future, with specialists instead creating the powder feedstock themselves as required.

| Category | Filler / Additive | Polymer | Purpose |
|-----------|--------------------------------|---|---|
| Metals | Stainless Steel | PS | Indirect LS of “green” parts |
| | Cu | PC [319] | Composites for nano/micro-electromechanical systems |
| | | PMMA [320] | Indirect LS of “green” parts |
| | Ni | PC [319] | Composites for nano/micro-electromechanical systems |
| Ceramics | Al ₂ O ₃ | PEEK [318,321] | Increase biocompatibility |
| | | PMMA [322] | |
| | | PS | Indirect LS of “green” parts |
| | | PVA | |
| | ZrO ₂ | PEEK [321] | Increase biocompatibility |
| | | PP [323] | Indirect LS of “green” parts (stabilised with Y ₂ O ₃) |
| | | PA6 [324] | Alter mechanical properties, improve thermal resistance |
| | SiO ₂ | PA11 [302] | Alter mechanical properties |
| | BaTiO ₃ | PA11 | Improve dielectric and piezoelectric properties |
| | SiC | PMMA | Indirect LS of “green” parts |
| | Glass beads | PA11 [325] | Alter mechanical properties |
| | | PEK [326] | Alter mechanical and thermal properties |
| | Montmorillonite (nanoclay) | PA11 [327] | Improve thermal stability and flame resistance |
| | Hectorite (nanoclay) | PA6 [324] | Alter mechanical properties, improve flame resistance |
| | TiO ₂ | PEEK [318,321] | Increase biocompatibility (Ti added to increase laser energy absorbance) |
| PCL [318] | | | |
| CHA | PLLA [158,165] PHBV [165] | Increase biocompatibility to make bone scaffolds | |
| HA | PEEK [162,321] | | |
| | PLLA | | |
| | PCL | Increase biocompatibility to make bone / tissue scaffolds, either directly or by producing indirect “green” parts | |
| | PVA [163] | | |
| | PMMA [161] HDPE [164] | | |
| β-TCP | PCL PLGA [198] | Increase biocompatibility and bioresorbability of tissue scaffolds | |

Table 2.3 *continued overleaf*

Table 2.3 *continued*

| Category | Filler / Additive | Polymer | Purpose |
|--------------|------------------------|---------------------------|---|
| Carbon-based | CNTs [327] | PA11 | Increase flame resistance, alter mechanical properties and increase laser energy absorbance |
| | CF | PA11 PEKK | Increase flame resistance, alter mechanical properties and increase laser energy absorbance |
| | Graphene | PA11 PEEK [328] | Increase electrical conductivity, thermal conductivity and alter mechanical properties |
| | Graphite | PC PEEK | Increase laser energy absorbance Increase laser energy absorbance, alter mechanical properties |
| Organic | Epoxy* | PC [184] | Alter mechanical properties |
| | | PS [191] | |
| | | SAN [186] | |
| | Wax* | SMMA [190] | Increase transparency |
| | | PS [174] | Alter mechanical properties for investment casting patterns |
| | Brominated hydrocarbon | PA11 [329] | Increase fire resistance |
| Wood | PES [196, 330] | – | |
| Progesterone | PCL [170] | Custom drug release rates | |

Table 2.3: Composite polymer materials researched in LS, references are from [118] unless specified. For researched composites of PA12 see Table 2.4. **Abbreviations:** CHA (Carbonated Hydroxyapatite), HA (Hydroxyapatite), β -TCP (β -Tricalcium Phosphate), CNTs (Carbon Nanotubes). *Epoxy and wax composites were infiltrated after printing.

Polyamide 12 Composites

The widespread use of PA12 in industry, both with and without additives, has made it an obvious choice for research into novel additives. This can be seen in Table 2.4, which shows the additives combined with PA12 to date for research, along with the main benefits (where applicable) observed in the printed parts.

| Category | Filler / Additive (from [118] unless specified) | Purpose |
|------------------------------|---|---|
| Metals | Cu [331] | Change thermal conductivity / specific heat capacity |
| | Al [332] | Alter mechanical properties |
| | Carbon Steel [333] | |
| | Stainless Steel | Indirect LS of “green” parts |
| | Mo | |
| Ceramics | Glass beads [278, 280, 334, 335] | Alter mechanical properties |
| | Glass fibres [286, 334] | |
| | Al ₂ O ₃ [293] | Indirect LS of “green” parts |
| | Al ₅₉ Cu _{25.5} Fe _{12.5} B ₃ [301] | Reduce friction and wear, reduce porosity |
| | SiO ₂ | |
| | SiC [336] | Alter mechanical properties, increase thermal stability |
| | Montmorillonite (nanoclay) [337] | |
| | TiO ₂ | Increase UV resistance and thermal stability, alter mechanical properties |
| | PTWs | |
| | Rectorite | Alter mechanical properties |
| | Unspecified ceramic fibres [280] | |
| Carbon-based | HA [160] | Increase bioactivity |
| | NaCl [338] | Increase porosity, where the NaCl is subsequently dissolved |
| | CNTs [285] | Alter mechanical properties, improve creep resistance |
| | CF [258, 269, 339, 340] | Alter mechanical properties, improve thermal stability |
| | CB [341–343] | Increase electrical conductivity, increase laser energy absorbance |
| Organic | Graphite [344, 345] | Alter mechanical properties, increase conductivity |
| | PA6 | |
| | PC | Alter mechanical properties, increase thermal stress resistance |
| | PEEK | |
| | PP [180] | |
| | HDPE [346] | – |
| | PS | |
| | Epoxy* [347] | Alter mechanical properties |
| | Epoxy* + CF [258] | |
| PBT [181] | Alter mechanical properties and fatigue resistance | |
| Brominated hydrocarbon [329] | Increase fire resistance | |

Table 2.4: Additives combined with PA12 to create LS composite parts. **Abbreviations:** PTWs (Potassium Titanium Whiskers), CB (Carbon Black). *Epoxy composites were infiltrated after printing.

Most of these studies focused the part mechanical properties, or processability during printing (adding flow enhancers or materials to increase laser energy absorption). The ability of PA12 to incorporate ceramics (such as glasses) into the material has been particularly successful, with glass-filled PA12 (in various forms) now constituting a major proportion of the commercial composite parts and powders sold.

With a range of fillers now identified and established for altering the mechanical properties of PA12, the focus of new additives is turning to adding functionality into parts. This both broadens the range of potential applications for LS parts, and strengthens the business case for adopting AM, with the increased benefits making a stronger case for switching from conventional manufacturing methods.

2.7 Key Points

Process and General Use

- Laser Sintering is a powder-based AM process, with the geometric complexity possible and ability to process Engineering-grade materials making it well suited for manufacturing end-use parts.
- Parts made with LS are used for a variety of applications, ranging from models and one-off custom components, to batch or medium-mass production of functional end-use parts.
- LS is increasingly being used for critical applications, such in the medical sector and during surgery.

Processing Considerations and Opportunities

- The lack of choice in material properties of LS parts has started to limit its uptake, with 95% of the market dominated by polyamides despite new materials being developed.
- Composite materials (using fillers / additives) can be used to alter the properties of LS parts, without needing to change the base polymer used.
- The majority of academic research and commercialised composite feedstocks, focuses on the use of PA12 as a base polymer, with particular success seen for glass-containing composites.
- While most of the currently available additives focus on altering the mechanical properties, there is a trend towards additives being used to add new functionality into printed parts with LS.

2.7.1 Relation to the Fundamental Objectives

The literature presented here gives some insight into the expected outcomes of the fundamental objectives for the project (see Thesis Foreword), specifically addressing the first three points.

Determine whether the material could be processed by the Laser Sintering machine

While it is not possible to say with any certainty that a feedstock will process successfully in LS for a given parameter set, the literature can give a good indication. The wide variety of PA12 / glass feedstocks produced, both released commercially (Section 2.6.4) and researched in academia (Section 2.6.5), suggest that this combination is likely able to produce parts. As the initial choice for this project is using phosphate-based glass additives, this does not highlight any causes for concern.

Measure any effect on the mechanical properties to see if the inclusion of the additive significantly affected the Engineering properties of the printed parts

With the majority of the commercial composite feedstocks and academic research focuses on using additives to alter the mechanical properties of the printed parts, this is an aspect that has to be addressed. The use of glass beads in the literature suggest that an increase in the stiffness of the parts could be observed, however the composition, size, and morphology of the glass used could affect this.

Assess whether the additive (specifically the silver) had been successfully incorporated into the parts in a homogeneous manner

Currently, there is no established method for analysing the additives inside microcomposite LS parts. However, the capabilities of micro-CT as a non-destructive 3D imaging technique (see Section 2.5.1) make it a prime candidate for this. Based on the literature, this method could not only be used to qualitatively analyse the inclusion of the additives, but quantitatively analyse the dispersion.

2.7.2 Fundamental Objectives to be Addressed

The literature presented so far relates to the objectives based on the processability of the material in Laser Sintering, and the likely effects on the printed parts. However, for the remaining two fundamental objectives, further research into Microbiological testing techniques and silver-containing materials has to be carried out. This forms the basis of Chapter 3, addressing the following objectives:

- Identify and quantify the method of silver release from the parts (including any limitations on the use cases).
- Test the antimicrobial properties of the printed parts against disease-causing bacteria.

Chapter 3

Introduction to Antimicrobial Materials

The term microbe covers any form of life which is on a microscopic scale; these are generally single-celled organisms, with the most common being bacteria, fungi and viruses. With fundamental differences between the different types of microbes, this report focuses solely on bacteria, however a similar approach is expected to be applicable against other microorganisms.

3.1 What are Bacteria?

Bacteria are single-celled organisms found in almost every habitat on Earth [348]. The sheer number of species and strains means there is significant variation in their structure, although certain features are common to all bacteria (see Figure 3.1).

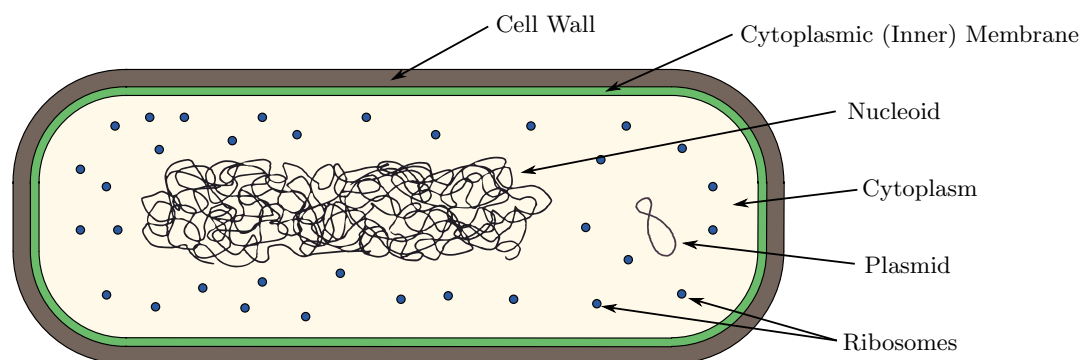


Figure 3.1: Structure of a prokaryotic cell (which includes bacteria), with common features identified. Typical sizes for cells such as these are in the region of $1\ \mu\text{m}$ in diameter. Diagram based on [349]. 🚫

In Figure 3.1, the inside of the cell (cytoplasm) houses the DNA-containing nucleoid, the protein-synthesising ribosomes, and in some cases an additional circle of DNA (called a plasmid) which contains genes encoding for additional properties such as antimicrobial resistance; all of which is contained by the cytoplasmic membrane, with the cell wall providing structure and strength to the cell [349]. Most bacteria also have features outside the cell wall to enable additional traits (for example flagella to make a cell motile – able to move) [350].

3.1.1 Categorising Types of Bacteria

Gram staining is a widely used method for identifying bacteria, categorising cells based on the structure of their cell wall [349, 351]. “Gram-positive” bacteria are characterised by their thick peptidoglycan layer, giving the cell structural strength and allowing it to resist the stain (see Figure 3.2). In contrast, “Gram-negative” bacteria have an outer membrane and a much thinner peptidoglycan layer; which the Gram stain is able to penetrate, colouring the cell in the process [350].

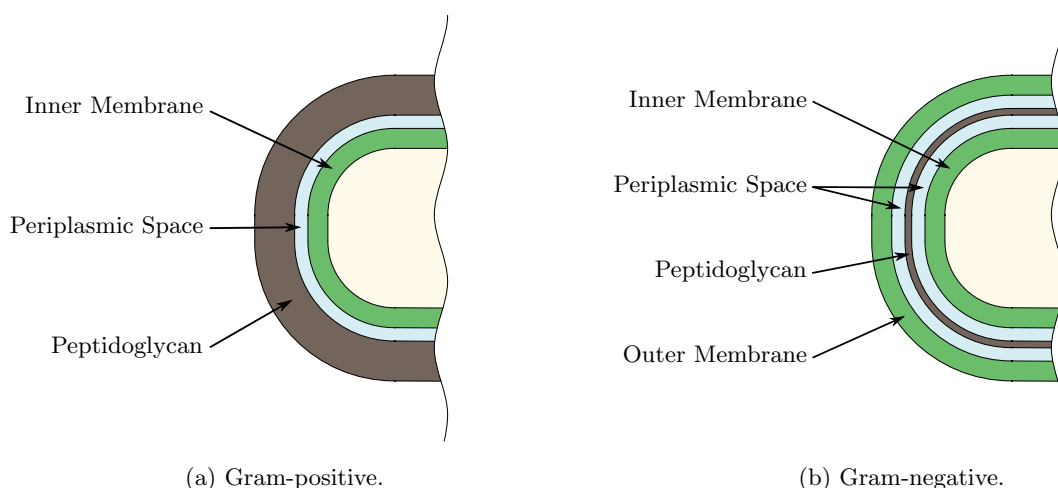


Figure 3.2: Differences in cell wall structure for Gram-positive and Gram-negative bacteria [349, 351]. 🚫

The different reactions to Gram staining are indicative of a broader response to external stimulus, with the cell wall structure suggesting, for example, how well the bacteria might survive in extreme environments. This also includes how they might react to antimicrobial agents, as the cell wall plays a major part in the defence of the bacteria. For this reason, any testing carried out should include both Gram-negative and Gram-positive bacteria to better represent the overall population.

3.1.2 Biofilms

Bacteria can change their individual makeup en masse, resulting in large scale events such as bioluminescence [352, 353]. The way in which bacteria communicate to achieve this is thought to be due to quorum (minimum threshold) sensing of signal molecules produced by individual cells, only triggering events when a high enough concentration of bacteria are present.

Biofilms are by far the most commonly observed and problematic of all these events, which sees cells produce an extracellular polysaccharide (EPS – slime) matrix to contain the planktonic (individual) bacteria. A mature biofilm (see Figure 3.3 for biofilm formation) not only creates a perfect microhabitat for the bacteria, but also makes it resistant to conditions that would kill planktonic cells, such as desiccation.

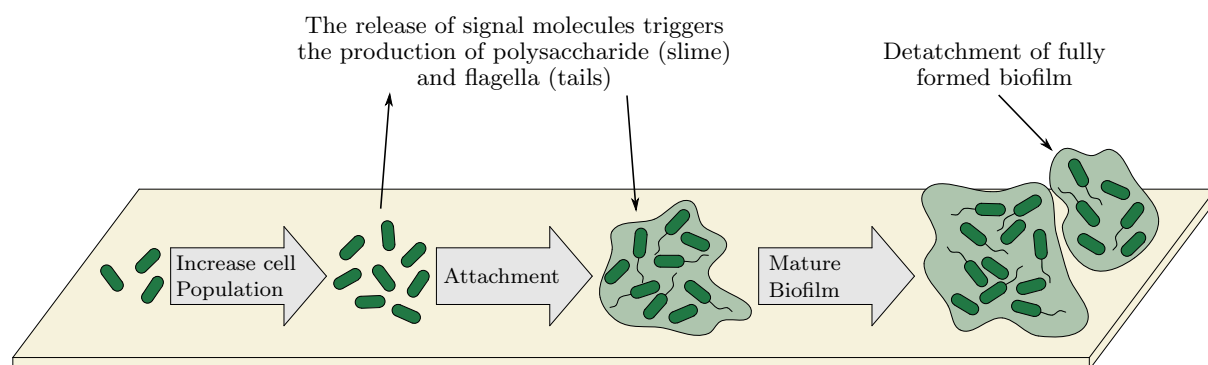


Figure 3.3: The four stages of biofilm formation (shown is the method of *Pseudomonas aeruginosa*). Generally following (1) the reversible attachment of planktonic bacteria; (2) irreversible attachment of the same cells; (3) production of extracellular polysaccharide (EPS) forming intercellular bridges, providing the biofilm a protective coat; and (4) mature biofilm with nutrient channels, detachment of some bacteria to form new biofilms. Diagram and stages based on [354]. 🚫

While in some cases the use of biofilms can be beneficial, this is not always the case, especially with infections where bacteria (such as *Pseudomonas aeruginosa*) establish inside the human body. Removing these “tenacious and nearly impenetrable” [349] biofilms is more complex than with planktonic cells, as their EPS matrix can slow or entirely prevent the penetration of antimicrobial agents (such as antibiotics), making them difficult to treat [354].

An example of a beneficial biofilm is in wastewater treatment, where bio-carriers are designed to en-

courage biofilm formation to aid in organic matter removal, nitrification, denitrification and phosphorus removal [355]. Conversely, for applications such as water filtration and purification, biofilm formation can cause major problems, blocking filters and introducing large inefficiencies into the process [356]. Interestingly, in both these cases, Laser Sintering of PA12 was investigated as a means to enhance the performance of the systems; with the surface roughness suggested to increase [355] and decrease [356] the bacterial attachment respectively on the surface of the printed components, potentially indicative of confirmation bias in the studies.

With both planktonic bacteria and biofilms widespread in nature, any antimicrobial testing should determine the effects on both of these.

3.1.3 Antimicrobial Resistance

One of the main ways that bacterial infections are treated is through the use of antibiotics, which specifically target bacteria. However, the increased use of antimicrobials has given rise to Antimicrobial Resistance (AMR), where random mutations in the cells allow the bacteria to thrive, even in the presence of antimicrobials which have been used before successfully (see Figure 3.4).

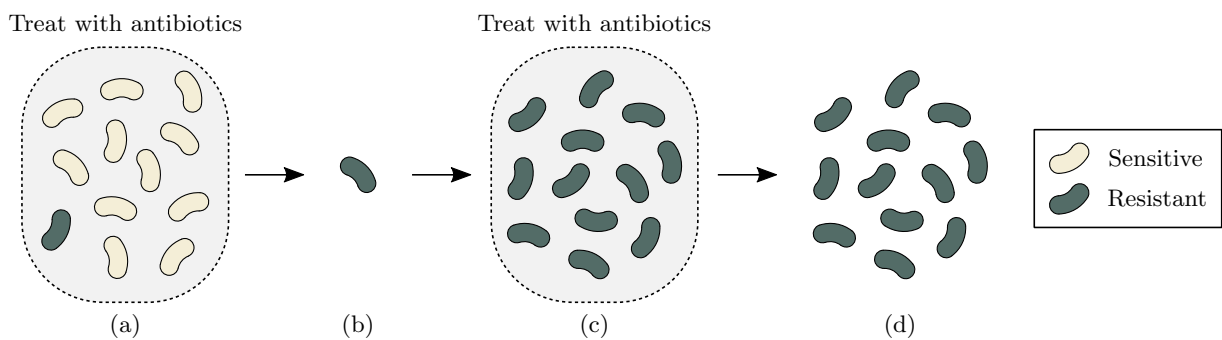


Figure 3.4: Schematic of Antimicrobial Resistance (AMR). (a) Antibiotics are used to kill a population of bacteria, one of which has developed resistance through a random mutation (b) all of the sensitive bacteria are killed, leaving the resistant strain to reproduce (c) the bacteria are again treated with the antibiotic but (d) the treatment has no effect. Diagram based on [357]. 🚫

These drug-resistant bacteria are already responsible for over 1.27 million deaths per year, and with the current trend is predicted to rise to 10 million deaths a year by 2050 [358–360]. The overuse and misuse of antibiotics is exacerbating the rise of AMR. In everyday use, more patients are demanding to be prescribed antibiotics even if they will not be effective, with doctors also more likely to prescribe them on the assumption that the patient expects it [361]. In hospitals, studies have found that antibiotics have often been given alongside treatments for COVID-19, even when no bacterial infection was detected [362].

To tackle this issue (and in addition to only using antibiotics where appropriate), the largest impact can be made by controlling the spread of disease, thus reducing the initial level of infection and the subsequent need for treatment [360]. This includes improving general levels of hygiene, for example washing hands more regularly, as well as general cleanliness for items and surfaces which could harbour bacteria and spread via touch. It is this aspect which most relevant to the research presented in this report, with the main focus (as initially specified in the Thesis Foreword) on antimicrobial materials. A more in depth analysis of how to control the spread of bacteria residing on surfaces covered in Section 3.3, with antimicrobial materials explored in more detail in Section 3.4.

3.2 Detecting Bacteria – How to Quantify the Bacterial Load

The microscopic nature of bacteria presents challenges in terms of quantifying the amount of bacteria in any given place (the bacterial load). This is further compounded by the range of information which can be used to indicate the health of a bacterial population; with factors such as the biomass (volume of cells), metabolic activity (how active the cells are – are they alive or dead?), and form (planktonic or biofilm) all contributing to quantifying the amount of bacteria present.

3.2.1 Testing Conditions – Media Choice

Before addressing method of quantifying bacteria, it is important to set the context for any given test. The choice of media (the liquid bacteria are exposed to) is often chosen to imitate real-world situations, for example to replicating the properties of blood inside the body. The media used can be generalised into nutrient-rich and nutrient-poor, based on the conditions required for the bacteria to grow.

In nutrient-rich conditions, as the name suggests the bacteria have all the nutrients they need to grow and multiply. This can include media such as blood plasma, or Brain Heart Infusion (BHI – based on boiled bovine or porcine heart and brain) which is commonly used to grow bacteria such as *Staphylococcus aureus* or *Pseudomonas aeruginosa*. These can also be combined with agar to create a gel, suitable for sustaining storing bacteria for short periods of time at low temperatures (typically 4 weeks at 4°C), or for growing bacteria on at higher temperatures.

In nutrient-poor conditions, the lack of nutrients required for growth and cell division means that the number of cells can be kept constant (or prevented from increasing) throughout the experiment. Without these sustaining nutrients the length of the experiment has to be more carefully considered, however for shorter time-scales (typically in the region of a few days) this is not generally an issue. The use of saline or Phosphate Buffered Saline (PBS) is generally used for this, with the added salts used to maintain the osmotic balance between the inside and outside of the cells.

3.2.2 Determining the Number of Bacteria¹

There are a multitude of different methods available to characterise and quantify bacteria and biofilms. This section introduces some of the methods used in this research, with their strengths and limitations. Further details can be found in the experimental testing chapters, Sections 4.4 and 5.4.

Counting Colony Forming Units

One of the most accurate methods of determining the number of healthy bacteria in a given sample is through serial dilutions, allowing the number of Colony Forming Units (CFUs – cells capable of growth and division) to be counted. Using the methods described by Miles and Misra [363] (see Figure 3.5), this involves taking the original sample (or inoculum) and serially diluting it by factors of 10.

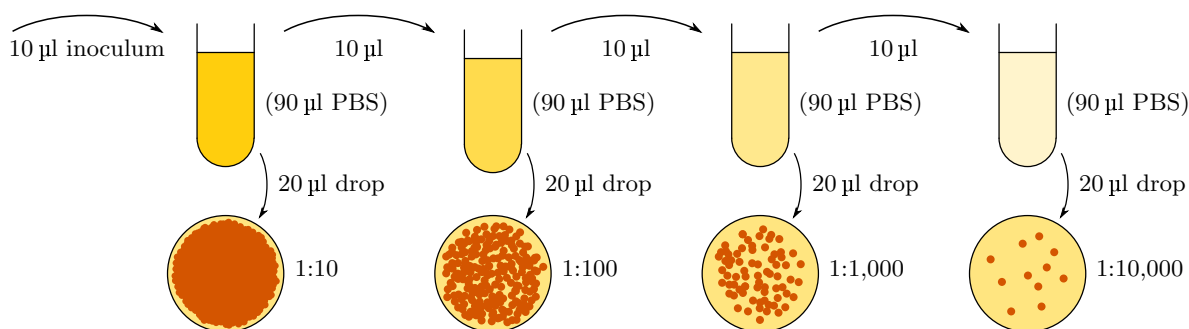


Figure 3.5: Schematic diagram of a serial dilution used to count the number of CFUs per ml. 🍷

For each of these dilutions, a small amount of this is dropped onto a nutrient-rich agar plate and incubated at a temperature suitable for growth. The incubation allows colonies to form from individual bacteria, with the colonies large enough to be counted by eye. The number of CFUs per ml in the inoculum can then be calculated by taking the dilution and drop size into account.

¹Throughout this research, the methodology was approached from an Engineering point of view, with no prior knowledge of bacterial testing. The microbiological tests specified here were suggested in consultations with Microbiologists as being the most relevant and meaningful, with other methods not considered.

While this is one of the most accurate methods for quantifying bacteria, the process is extremely labour intensive and takes a long time (typically 18–24 h) to yield results, making it less suitable for large numbers of samples or when results are needed quickly. This also requires a suspension of bacteria, meaning that it cannot be used to quantify biofilms without first removing them from the surface.

Optical Density

One of the simplest methods of estimating the number of bacteria in a suspension is by measuring the optical density. This revolves around the idea that as bacteria grow, the turbidity (or cloudiness – see Figure 3.6a) of the liquid increases. Despite its simplicity, this quick method (results in seconds) can be used as an estimate of the total number of cells. The Optical Density at 600 nm (OD_{600}) is generally used for this, and is especially useful when starting experiments since it does not harm or interfere with the bacteria. Typical dilutions for experiments are in the region of an OD_{600} of 0.1 or 0.01.

The limitation with this method, is that the OD_{600} does not give any indication of the current health of the cells, with dead cells contributing to the turbidity of the suspension as well as surviving bacteria. This should therefore be used alongside other methods to more fully define the bacteria.

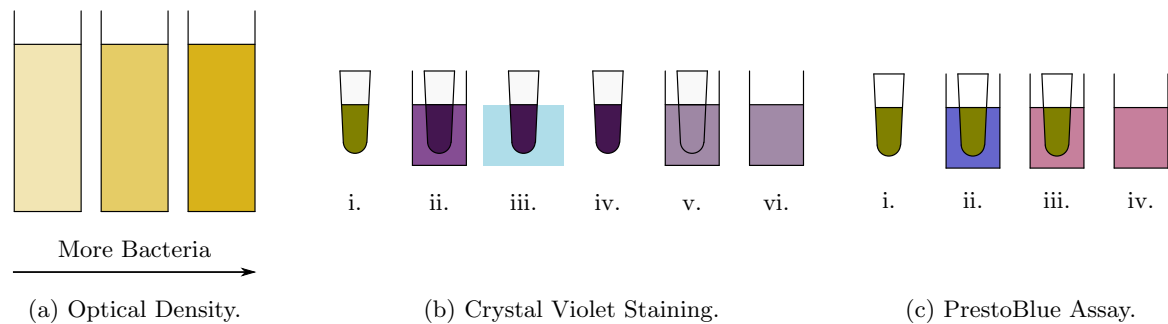


Figure 3.6: Methods of estimating bacterial load. Steps: (b) i. grow biofilm, ii. stain with crystal violet, iii. rinse away excess dye, iv. dry biofilm, v. dissolve biofilm in acid, vi. measure OD_{570} . (c) i. grow biofilm, ii–iii. incubate with PrestoBlue, iv. excite at 550 nm and read fluorescence at 590 nm. 🚫

Crystal Violet Staining

In terms of quantifying the biomass of bacteria, crystal violet staining can be particularly useful for characterising adhered biofilms. For this purpose (as shown in Figure 3.6b), the biofilm is immersed in dilute crystal violet, whereupon it stains the organic matter (including cells and extracellular material such as polysaccharides). The biofilm is then rinsed with water to remove the stain and any unattached bacteria from the biofilm, then dried to obtain the desiccated, stained biofilm. This is then dissolved in acid (such as dilute acetic acid), with the concentration of the stain in the dissolved solution measured optically (at a wavelength of 570 nm – OD_{590}) to obtain the quantitative measurement.

This technique provides a relatively simple and scalable method for measuring the biomass of biofilms attached to surfaces. However, care should be taken in the process to ensure repeatability in the results; notably involving the rising of the stained biofilms, where it is possible to dislodge sections of poorly secured biofilms which could be of interest. Crucially, this is a destructive technique, so must be the final stage of analysis if used in conjunction with other methods.

PrestoBlue Cell Viability Assay

In order to quantify the activity of a living biofilm, reagents such as PrestoBlue[®] can be used. For this method (as shown in Figure 3.6c), the reagent is added to the media and incubated with the biofilm (around 10 minutes). In this time, some of the reagent will be taken in by the cells, reduced, and released from the cell, changing from blue to red in the process. This colour change can then be measured using absorbance or fluorescence measurements (measured at 590 nm when excited at 550 nm).

This measurement gives an overall indication of the cell viability and metabolic activity. Since it does not disrupt the bacteria, this can also be used with other methods or as repeat measurements over time. The drawback of this, however, is that by their nature some cells will be more active than others, meaning that this method cannot differentiate between a small number of very active cells, and a large number of less active cells. Despite this, it provides a good indication of the health of a biofilm, especially combined with one of the other methods in this section.

3.3 Controlling the Spread of Microbes on Surfaces

Before exploring the different methods available for destroying bacteria, it is important to recognise the extent to which this is possible and whether this is even necessary. The approach to sterilisation is best defined in healthcare environments; where it is common practice to sterilise items before use, in order to prevent the spread of infection and disease. This section briefly covers the guidelines put in place for these environments, the rationale for which can be applied more generally to everyday applications.

3.3.1 Definitions

In general use and in much of the literature surrounding antimicrobials, the terminology is often confused or used incorrectly. For clarity, such terms are defined throughout this section, with the subtle but important distinction between sterilisation and disinfection a prime example.

Sterilisation is defined as “any process by means of which all forms of microbial life (bacteria, spores, fungi, and viruses), contained in liquids, on instruments and utensils, or within various substances, are completely destroyed” [364].

Disinfection is defined as “any process, chemical or physical, by means of which pathogenic agents or disease-producing microbes are destroyed” [364]. The distinction here is that spores, which could potentially cause infection in certain situations, are not destroyed.

Within these definitions, there are multiple levels depending on the nature of the microorganisms that need to be destroyed. While these levels can change depending on the items to be sterilised and the method of application, a guideline to these is shown in Figure 3.7.

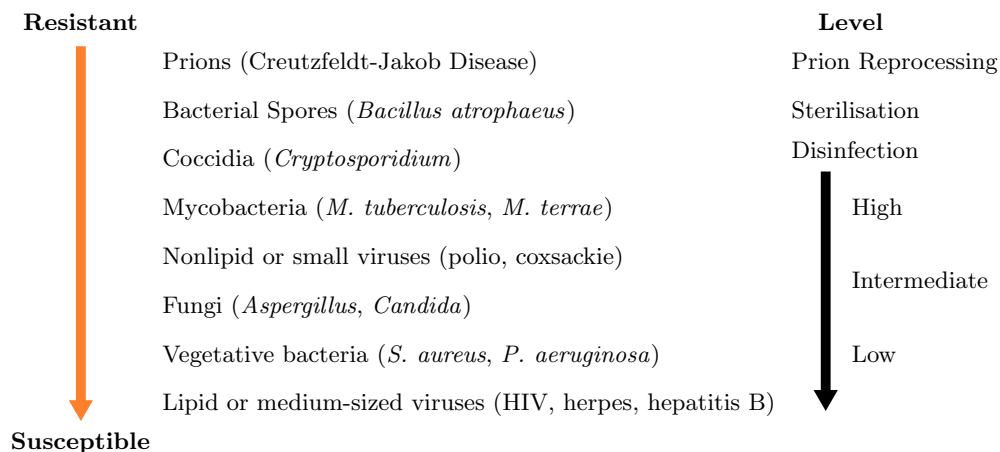


Figure 3.7: Resistance of microorganisms to sterilisation and disinfection levels. Modified from [365]. 🚫

A Rational Approach – Does it actually need to be sterile?

Whereas it could be assumed that for every potential disease-spreading situation, the highest level of sterilisation or disinfection available is preferable, this is neither necessary nor practical. With this in mind, Spaulding devised a rational approach to the levels of sterilisation required; defining critical items, semicritical items, and noncritical items [366]. Although these definitions are over 50 years old, they still form the basis of many standard practices today. These terms are defined below [365–367]:

Critical Items carry a high risk of infection if contaminated with any microorganisms. These include items such as surgical instruments, which come into direct contact with sterile tissue or the vascular system; these need to be sterilised before use.

Semicritical Items contact mucous membranes or nonintact skin, where the body still retains some level of protection against microorganisms. For these items, high-level disinfection is sufficient, where all of the microorganisms except a small number of spores are completely destroyed.

Noncritical Items are any other items that come into contact with skin, where the sterility of items is not essential. These items, such as hand railings and computer keyboards, only require low-level disinfection, as the skin provides sufficient protection from many microorganisms.

While Spaulding’s definitions can be criticised for being over-simplified, they are still used due to their irrefutable logic. There are many methods which can be used to sterilise or disinfect these items, the choice of which will depend on their classification and the conditions the items can withstand. A selection of these common methods are described in Section 3.3.2.

3.3.2 Methods of Sterilisation and Disinfection

Although the focus of this chapter (and indeed this report overall) is not on the cleaning of surfaces, this is nonetheless a vital aspect of controlling the spread of disease. In this research, for any bacterial testing to be carried out, any test specimens would first have to be sterilised in order to remove any contamination.

In the production of sterile medical devices, there are four main methods used to sterilise parts: steam, dry heat, ethylene oxide (gas), and ionising radiation [183,368]. These are briefly covered in this section, as well as the use of chemical disinfectants. As each of these had the potential to degrade or change the properties of the Laser Sintered parts, this also had to be considered alongside the practicality and level of sterilisation they provide.

Dry Heat

Perhaps the simplest method conceptually of sterilising an item is through the use of heat. While this is one of the most straightforward methods of sterilisation, the high temperatures (typically in the region of 150–190°C [368]) and long cycle times make it unsuitable for many materials; with other options preferred in healthcare settings. Guidelines for these temperatures and times are shown in Table 3.1, but it should be noted that for large or complex items with poor thermal conductivity, these times will have to increase to compensate.

| Temperature (°C) | Minimum time required (minutes) |
|---------------------|------------------------------------|
| 180 | 30 |
| 170 | 60 |
| 160 | 120 |
| 150 | 150 |
| 140 | 180 |
| 121 | 360 or overnight |

Table 3.1: Times required for dry sterilisation at varying temperatures [369].

In terms of Laser Sintering, some research has been carried out on the effect of dry heat sterilisation on PA11 parts, with no significant difference in part properties found after one cycle [370]. While no studies have specifically focused on this for PA12, there is an extensive body of literature on the effects of powder ageing and reuse due to exposure to high temperatures during the printing process [187,221,224]. These temperatures (typically 160–175°C) are comparable to those in dry heat sterilisation, with potentially similar consequences. Although these differences could be minimal, this is quickly approaching the melting onset of the polymer (around 175–185°C), and extreme care would therefore need to be taken to avoid drastically deforming the printed parts.

Steam

The most widely used method of sterilisation is through the use of steam (combined with temperature and pressure), typically achieved in an autoclave. This method is not only effective and reliable, the cycle times required are short, and there is no residual chemical contamination. These work on the same principle as dry heat, but here the steam provides a more effective way of transferring the heat [371].

Due to this increased effectiveness, the cycle times are considerably shorter than with dry heat, and the temperatures required are markedly lower. In gravity fed systems (where steam is introduced at the top, displacing the air below due to its higher density), this is typically at 121°C for 20-30 minutes; whereas in a pre-vacuum system (where the use of a pre-vacuum results in near instantaneous steam penetration of even porous items), cycles are generally held at 132°C for a much shorter time (typically 4 minutes) [365], but are less suitable for sterilising liquids due to the increased evaporation [371].

While LS polyamide 12 is often marketed by materials manufacturers as being able to withstand the conditions in steam sterilisation [372], there is a remarkable lack of literature supporting this, with

specific regards to the mechanical properties. With such parts now being used for critical applications, such as surgical guides [167, 373], there is a need for a deeper knowledge of how these parts are affected by the steam sterilisation process. Some research has been carried out in this area [282]; however, this only focused on the multiple re-use of items and used a combination of different methods to sterilise the parts, making it impossible to differentiate the effects of each process. As the largest use of these parts is likely to be custom made, single-use applications, the effects of a single sterilisation cycle need to be understood more deeply.

Ionising Radiation

Generally achieved through gamma irradiation or electron beams, ionising radiation can be a quick method of sterilising parts on a large scale [368]. This is increasingly being used for mass produced, single use medical devices, as the systems can be fitted into a production line and can penetrate packaging. However, this method is both harmful to humans and has an extremely high cost [374]; the cause of this cost is both due to the running costs of the beam, and the high capital costs of equipment (including additional equipment such as conveyors) and purpose-built buildings, which must contain sufficient radiation shielding to make the process safe to use. Due to this, these systems are not generally used in healthcare settings, where smaller systems such as steam sterilisation are preferred [183, 365].

This method is generally considered alongside ethylene oxide sterilisation (see next section) for products which are not able to withstand high temperatures or moisture. In the UK, this split is approximately 80:20 (ionising radiation : ethylene oxide), however this varies between countries, with the global split around 45:55 [368].

For polymers (including those produced with LS), this ionising radiation has the potential to change both the appearance (yellowing of parts) and their properties [183]. The resistance to these effects varies depending on the specific polymer; however for LS PA12, differences in the mechanical properties have been observed with exposure to gamma radiation [375]. This, combined with the high capital cost, means that further research into the effects on the printed parts (and the implications for the applications) would be needed before adopting this technique more widely.

Ethylene Oxide

Ethylene Oxide (EtO), or “gas” sterilisation, is a common method of sterilising medical devices which are particularly sensitive to heat or moisture. This is generally used for mass produced items, rather than in a healthcare setting, including both the devices and their packaging [368]. Although most items (including PA12) are suitable for EtO sterilisation, there are significant drawbacks to this method arising due to the extreme toxicity of the gas.

The cycle times for EtO sterilisation are in the region of days to weeks, with lengthy pre-conditioning steps (to reach the desired temperature and humidity) and de-gassing steps to ensure that no residual gas is left on the product. As an explosive, carcinogenic, mutagenic and teratogenic gas, the use of ethylene oxide requires large specialised installations for use [365, 368, 376]. In commercial large scale operations, this is achievable, however for research purposes this is not feasible.

Chemical Disinfectants

There are a myriad of different chemical disinfectants available for use, each with their own specific instructions and use cases. Among these, alcohol is a commonly used high level disinfectant, which fully evaporates after use and leaves no chemical residue [367]. The use of ethyl or isopropyl alcohol is generally preferred in healthcare settings, with the slightly less effective methyl alcohol rarely used [365].

Alcohols are fast acting bactericidal (able to kill bacteria) disinfectants, which are optimally effective when diluted to 60–90% [365]. While they cannot be used to remove spores from critical items, it is regularly used as an antiseptic (for disinfecting living tissue) or for disinfecting surfaces.

With any chemical disinfectant, some polymers can be susceptible to environmental stress cracking, even when no external stress is applied during use [183]. This only applies to amorphous polymers (so does not include PA12), and is generally due to internal stresses accumulated during casting. In LS, upon immediate removal from the machine, the printed parts are assumed to be sterile due to the high temperatures experienced during printing; with any subsequent contamination limited to the surface. For this reason, the use of a high level disinfectant such as alcohol could prove an effective method to kill any bacteria on the part surface before testing.

3.4 Antimicrobial Materials

3.4.1 Concept

Almost all surfaces can act as reservoirs for microbes, able to harbour and transmit them to whoever (or whatever) comes into contact with them. While the high microbial load on household items might be discomfoting to contemplate [377], the noncritical nature of the items means that in most cases the threat this poses is minimal. However, when these surround people with compromised immune systems, they pose more of a risk.

For example in a (simplified) hospital setting, the transfer of microbes can occur directly from person to person, or by touching a surface which then becomes contaminated (see Figure 3.8a) [378]. The concept behind antimicrobial surfaces, is that by creating an environment in which microbes cannot survive, the methods of transmitting infection are reduced (see Figure 3.8b). In practice, this would be accompanied by regular cleaning, but with an antimicrobial surface, the item itself also helps control the spread of microbes.

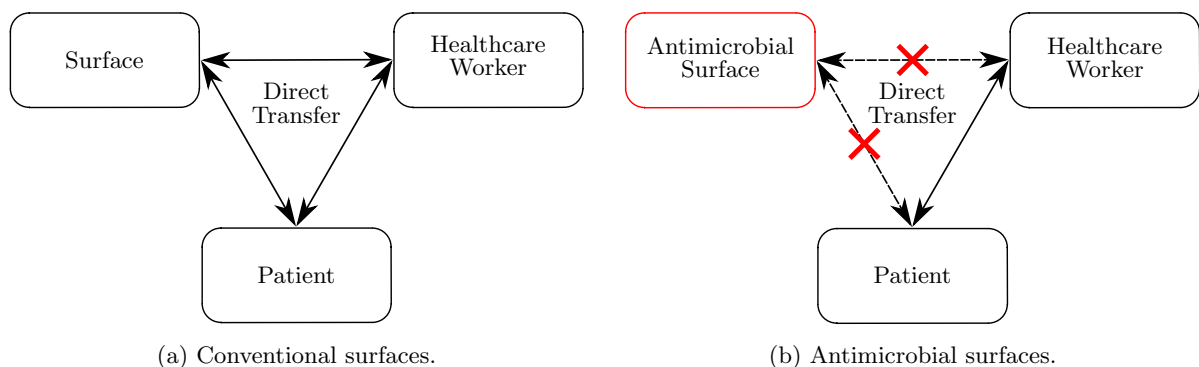


Figure 3.8: Schematic of how microbes spread in a hospital (nosocomial infection loop). Based on [378]. 🚫

There are many different strategies which are used to create these antimicrobial materials (see Section 3.4.3); but before exploring these, the definition of what classes as an antimicrobial surface needs to be further refined.

3.4.2 Definitions

The definition of “antimicrobial” can vary dramatically depending on the product or finishing process in question. The definitions here focus specifically on antibacterial surfaces, since this variation is especially noticeable with bacteria, with two fundamentally different approaches available.

A common definition is the prevention of bacterial growth on a surface; however, delaying growth, preventing the formation of biofilms, and delaying or preventing bacterial growth in the surrounding environment can also be defined as antimicrobial attributes. For clarity, the following definitions have been used in this report.

Antibacterial surfaces are “surfaces that are capable of reducing the extent of attachment and proliferation of bacteria” [379]. This broad definition essentially includes any materials which make it more challenging for bacteria to attach to the surface. This can be further split into antibiofouling surfaces, and bactericidal surfaces.

Antibiofouling surfaces generally function by “preventing bacterial cells from attaching to the material” [379]. Crucially, these surfaces do not harm or kill the bacteria in any way, they simply prevent (or reduce or delay) the formation of biofilms on the surface.

Bactericidal surfaces are those which “inactivate the bacterial cells (causing cell death)” [379]. As opposed to antibiofouling surfaces, these prevent the attachment of bacteria by killing the cells, and is perhaps the more intuitive definition of an antibacterial material. This approach acts to reduce the overall number of living bacteria in the system.

3.4.3 Strategies of Antimicrobial Materials

Anti-Adhesive Surfaces

The first approach to creating an antimicrobial material centres around preventing the initial adhesion of bacteria to the material (antibiofouling surfaces). Two approaches for achieving this are creating hydrophobic / superhydrophobic or very hydrophilic surfaces.

Superhydrophobic materials are defined as having a water contact angle of $\theta_{\text{wca}} > 150^\circ$ (in Figure 3.9a the marked angle therefore has to be below 30°) and a slide angle of less than 10° . For these surfaces, the method of reducing biofilm formation (or biofouling) is by reducing the bacteria adhesion, enabling easier cleaning of the surface [380]. However, there are conflicting reports as to whether the use of superhydrophobic surfaces actually decreases biofouling [381, 382].

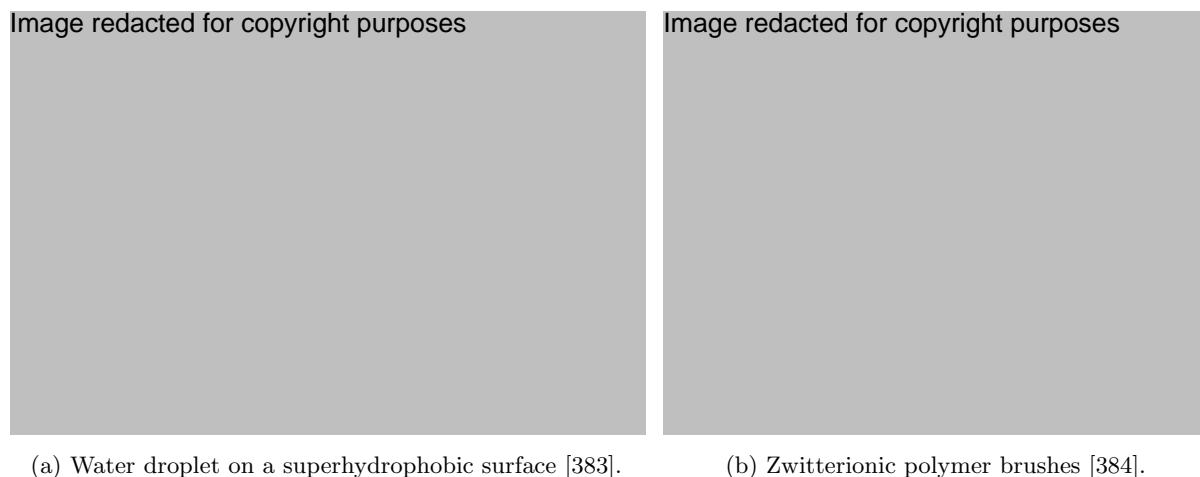


Figure 3.9: Approaches to anti-adhesive surfaces.

At the other end of the scale, zwitterionic polymer brushes have been used to create antimicrobial hydrophilic surfaces. Zwitterionic molecules contain both a positive and negative charge, leading to an overall charge of zero. When exposed to water, these have a strong attraction to the surrounding water molecules, creating a hydration shell which surrounds the material; this acts as a barrier to prevent the bacteria from contacting the surface (shown in Figure 3.9b) [384, 385].

Using a purely anti-adhesive (antibiofouling) method, the overall number of bacteria in the system cannot be reduced. To obtain a biocidal effect (that is, one having the ability to kill bacteria), this must be combined with another strategy. Both of the anti-adhesive methods in this section have been combined with biocide-releasing surfaces to successfully reduce biofouling on the materials [385, 386].

Contact-Active Surfaces

A contact-active antimicrobial surface is one which kills bacteria by direct contact with the surface (bactericidal and antibiofouling). This outcome can be achieved in a number of ways, although the complexity of achieving these means they are not often used in practice. A brief overview of three of these strategies is shown in Figure 3.10.

Similarly to the lotus leaf inspired superhydrophobic surfaces, nature again provided inspiration for the geometry-based method of action, this time from the cicada wing [387, 390]. The nano-scale patterned wing causes the bacterial cells to rupture when pressed against the surface, however this has only been shown to be effective for Gram-negative bacteria.

One of the greatest challenges with contact-active surfaces, is the restriction in motility of the antimicrobial, causing it to be less effective [388]. An example of a solution to this is shown in Figure 3.10b, where the biocide (in this case a Quaternary Ammonium Compound, QAC) has been anchored to the surface using long polymer chains [388, 391]. This method presents a non-leaching solution that retains enough motility in the QACs to create a biocidal surface. This can even grant more control over the biocide, with temperature dependent biocidal activity possible [392]. SLA has utilised this anchoring method to produce an antimicrobial AM material, with primary focus on dental applications [393, 394].

This challenge of restricted motility is most apparent in the third type of contact-active surface. Bacteriophages (commonly referred to as phages) are viruses that only affect bacterial cells [354]; although

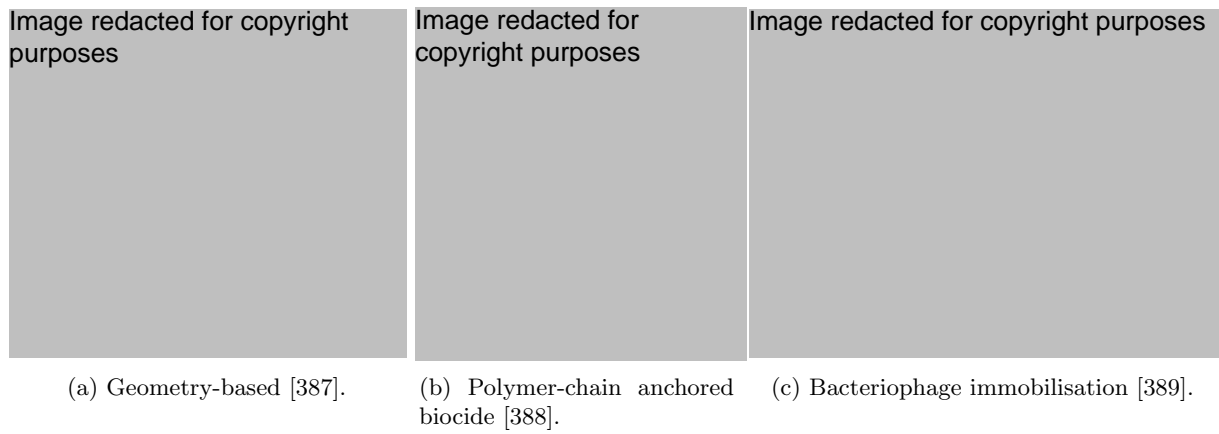


Figure 3.10: Approaches to contact-active surfaces.

very effective when unconstrained, these phages have to attach to the bacterial cells in very specific orientations to have any effect. The approach shown in Figure 3.10c works by immobilising phages on the surface; this also shows the main challenge of this approach, in that if the phage is immobilised in the wrong orientation, it can never have a biocidal effect [389,395]. Despite this, as the phages do not have any effect on humans or animals, this approach has fewer potential side-effects than other strategies.

Biocide-Releasing Surfaces

Grouped into this category are materials which release particles into their surroundings to have a bactericidal effect or otherwise disrupt bacteria. This category is dominated by metal-containing surfaces which release nanoparticles or metal ions [380,396]. These composite coatings act against bacteria in several different ways [397], making them broadly effective against a wide range of bacteria and more challenging for strains to develop AMR. The use of silver in these materials is covered in more detail in Section 3.5.

Generally, biocide-releasing surfaces are associated with depleting reserves over time. However, approaches based on photocatalytic oxidation (with materials such as titanium oxide, TiO_2), can be regenerated with exposure to certain wavelengths of light [380,396]. Rather than releasing material contained in the surface, these create highly reactive hydroxyl radicals (OH^{\bullet}) from water surrounding them, causing significant damage to bacterial cells.

More recent approaches have also focused on aspects such as triggered release, with surfaces reacting to (and subsequently disrupting) the quorum sensing signal molecules (see Section 3.1.2) through mechanisms shown in Figure 3.11 [353,398]. Other approaches have analysed carbon-containing surfaces, specifically with graphene, graphene oxide, reduced graphene oxide, and carbon nanotubes [399]; with trace amounts of these biocides released alongside potential contact-active means [380].

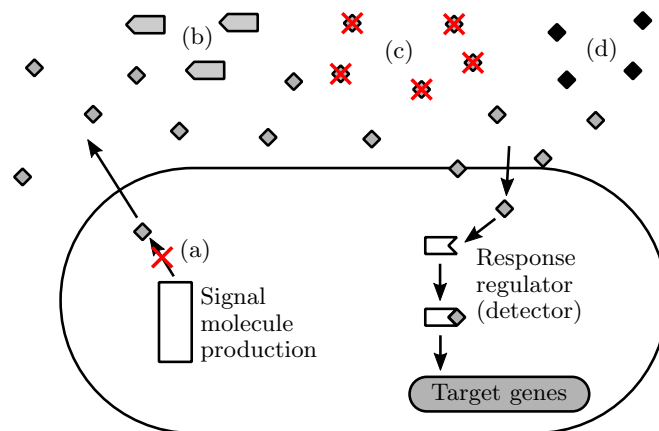


Figure 3.11: Methods of chemical disruption to quorum-sensing molecules. (a) signal molecules are prevented from being produced, (b) molecules designed to fit the response regulator without triggering a response are introduced, (c) signal molecules are destroyed, (d) bacteria are flooded with additional signal molecules, causing changes to happen too early to be effective. Diagram based on [353].

3.4.4 Antimicrobial Materials in Additive Manufacturing

Antimicrobial materials are becoming more popular in AM, with various materials developed for different processes and applications. The higher profile of these are filaments for FDM, with some companies focused on offering antimicrobial materials for AM commercially, and research into a wide range of processes being carried out.

Material Extrusion

Perhaps due to the sharp increase in the popularity of desktop FDM machines, the majority of the antimicrobial materials developed for AM have been focused on material extrusion. Companies such as Copper3D have based themselves entirely around this concept, marketing copper-filled filaments for their antimicrobial properties [400]. These materials have been suggested for a wide variety of applications, from creating low-cost prostheses [401], to enhancing the safety and long-term flexibility in space travel [402–404].

Most of these materials in material extrusion have centred on biocide-releasing strategies to create an antimicrobial effect. In addition to copper, other metals have been investigated in a similar manner, notably silver and zinc [405–407]. The incorporation of antimicrobial dyes [408] and drugs [409–411] is also being researched, with the focus on controlling the release rate of antibiotics, preventing biofilm formation on medical devices, and creating anti-fungal materials for dental applications. Contact-active strategies have also been investigated, with QACs anchored to the surface in an additional post-processing step [412].

Vat Photopolymerisation

For vat photopolymerisation systems such as SLA and DLP, heating of the resin is relatively minor, enabling the inclusion of more thermally sensitive drugs before printing to achieve a more controlled release rate of antibiotics [413]. With this method, contact-active surfaces have also been created, with the anchored QACs mixed into the resin before printing to print inherently antimicrobial parts [414].

The viscosity of the resin is often a limiting factor for including additives in SLA. However, this has been overcome with silver, by creating nano-particles in situ from silver salts in the resin, thus creating a biocide-releasing nano-composite material without sacrificing the viscosity of the resin [415].

Binder Jetting

In the powder-based binder jetting techniques, antibiotics have been incorporated into both polymer and ceramic powders for use as bone scaffolds. The techniques used to achieve this have either been through the including of the antibiotic in the binder (jetting it onto the powder to form the parts) [416, 417], or through the physical mixing of powdered antibiotics with the other feedstock material prior to printing [417].

Powder Bed Fusion

Metal powder bed fusion processes (in particular SLM) are increasingly being used to create patient-specific implants, with the research surrounding adding antimicrobial functionality centred on this application. To obtain biocide-releasing parts, approaches have been based on different post-processing techniques, rather than creating inherently antimicrobial parts. These have included using the porosity available with SLM to inject an antibiotic-containing Calcium Phosphate cement [418], and applying an antibiotic-containing coating to the printed parts [419].

The only current example of an antimicrobial material in polymer Laser Sintering, is the “OsteoFab technology” from Oxford Performance Materials [420]. This revolves around the use of a proprietary PEKK material, and is marketed primarily for use in surgery to create bone scaffolds [421–424]. The antibacterial properties this displays have been primarily attributed to the surface pattern, resulting in a hydrophobic (anti-adhesive) surface, with sharp profiles (contact-active) creating the antibacterial effect. These effects have been linked to the surface finish in LS, however ongoing research also suggests that there may be some intrinsic antimicrobial properties from the PEKK material itself.

3.5 Silver as an Antimicrobial

Prior to the start of this project, silver was identified as the starting antimicrobial agent in the creation of antimicrobial LS parts (see Thesis Foreword). This was, in part due to its widespread use in antimicrobial materials, and strong efficacy against a broad range of microbes; both of these aspects are expanded upon in this section.

3.5.1 Metals as Antimicrobials

Since the time of Persian kings (circa 550 BC), certain metals have been used as antimicrobials [425,426]. These include a range of essential (required for the normal function of organisms) and non-essential (no known biological function) metals, with varying effects and levels of toxicity to bacteria. Despite these differences, the antimicrobial effects arise almost entirely from the metal ions, rather than their solid metallic state.

Essential metals [and their ions] identified for their antimicrobial efficacy include; Chromium [Cr(VI)], Manganese [Mn(II)], Iron [Fe(II), Fe(III)], Cobalt [Co(II)], Nickel [Ni(II)], Copper [Cu(II)], Zinc [Zn(II)], Molybdenum [Mo(VI)], and Cadmium [Cd(II)] [397]. Although required for some cell functions, unfavourable concentrations of these ions can result in a number of different effects within the cells taking place, some of which cause harm to the organism and potentially result in cell death.

On the other hand, non-essential metals generally show a much higher toxicity towards bacteria, and much in lower concentrations [425] than essential metals. This is especially true for Silver [Ag(I)], Mercury [Hg(II)] and Tellurium [Te(IV)]; with other metals including Arsenic [As(III)], Lead [Pb(II)], Gallium [Ga(III)], and Antimony [Sb(III)] also identified as toxic to bacteria [397]. Among these, silver has consistently been favoured throughout history, due to its increased antimicrobial potency, abundance, and other useful (mechanical and aesthetic) properties. For these reasons, silver was chosen for this research, with its history as an antimicrobial, and methods of action briefly covered in this section.

3.5.2 History and Uses of Silver

In addition to its uses as a malleable and durable metal for creating jewellery and functional items, silver has been used throughout much of human history for its antimicrobial properties, whether knowingly or not [427]. This has evolved from simply using the base metal, to using silver salts, solutions and colloids in the direct and indirect treatment of infection (see Figure 3.12).

Image redacted for copyright purposes




Figure 3.12: A brief timeline of silver used for medicinal purposes. Modified from [427].

Recently, attention has turned to using small amounts of silver in the creation of antimicrobial materials using methods such as surface coatings, accompanying a vast body of literature focused on the creation and application of silver nano-particles. These nano-particles are thought to have additional methods of action against bacteria, attaching to and damaging the cell wall, and being mistakenly taken into the cell, where they release ions directly into the cell [426].

However, the production of these nanoparticles poses significant challenges relating to consistency; with the additional practical considerations needed to safely incorporate them into LS parts making them unsuitable for initial investigations such as this. In terms of this project, the lab in which the LS is based

did not have the capability to handle nanoparticles, with much stricter environmental controls such as fume hoods required to handle these safely. In order to successfully incorporate these smaller additives into the parts (without modifying the LS machine to handle nanoparticles, at a significant cost and potentially compromising on the performance), it is also likely that more involved and costly methods of creating the composite powder feedstocks would also be required (see Section 2.6.1). For these reasons, it was decided not to use nanoparticles in this project.

Surface Coatings

Most antimicrobial materials are made using a coating on the part surface. This can be done through simply soaking porous parts in the antimicrobial media, using a carrier material (such as PMMA or PLGA) [428], or direct application to the base material [429]. Silver is by far the most commonly used metal used in antimicrobial coatings, investigated for use in wound dressings for treating burns [430], coating catheters for preventing biofilm formation [429], and coating implants [379] to name a few.

While these coatings can have significant benefits, the methods used to create these are not perfect, and are not suitable for every application. These coatings are often non-uniform, mechanically weak and lack long-term stability [379]. For particularly complex part shapes (topology) and surface characteristics (such as porosity) possible with AM, it can be challenging to cover every surface and the parts can be susceptible to damage (as shown in Figure 3.13).

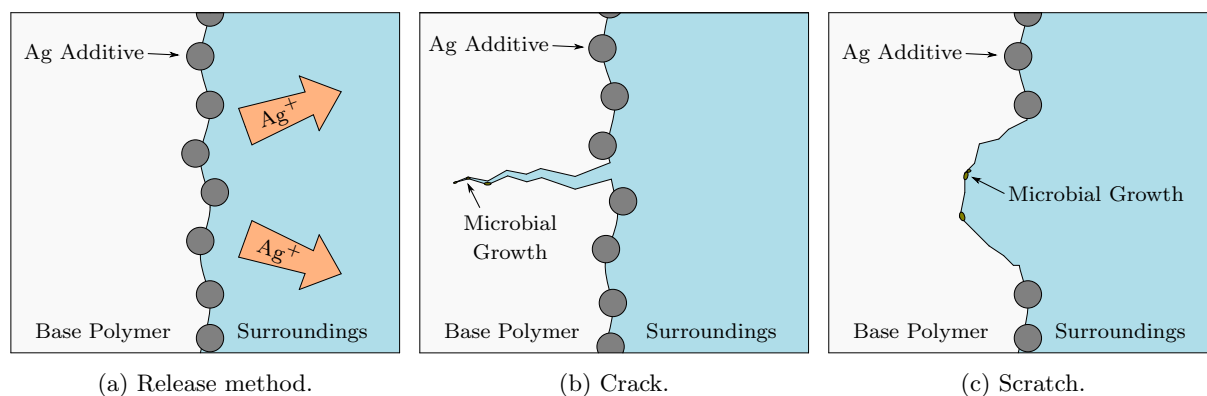


Figure 3.13: Surface coatings method of action and failure methods. 🚫

Micro- and Nano-Composites

An alternative to surface coatings, is to incorporate the antimicrobial into the bulk of the material. In this way, should the original surface be damaged, it simply exposes a new surface which is also antimicrobial. This approach, when used to create micro- or nano-composite parts with silver, generally relies on the reaction of the metallic additive with water to create and release the antimicrobial ions.

In order for this reaction to occur, the matrix material must allow water to diffuse through it and react with the incorporated silver additives. This significantly narrows the selection of suitable materials to create this, however some polymers known to absorb water (such as polyamides) are perfect candidates for such a task. These are explored in more detail in Section 3.6.

3.5.3 Silver Antibacterial Method of Action

Despite being used for its antimicrobial effect for thousands of years [425], the method of action by which silver disrupts bacteria is not yet fully known. Whilst in its metallic form silver is biologically inert [427], its notoriety stems from the multiple methods by which its ions attack cells, making it more challenging for any particular strain to develop resistance.

Some of the more well established methods by which silver acts are summarised in Figure 3.14, focusing on the effects of silver ions as opposed to metallic silver. These can be broadly categorised as direct effects from the ions, or indirect through the formation of reactive oxygen species (ROS).

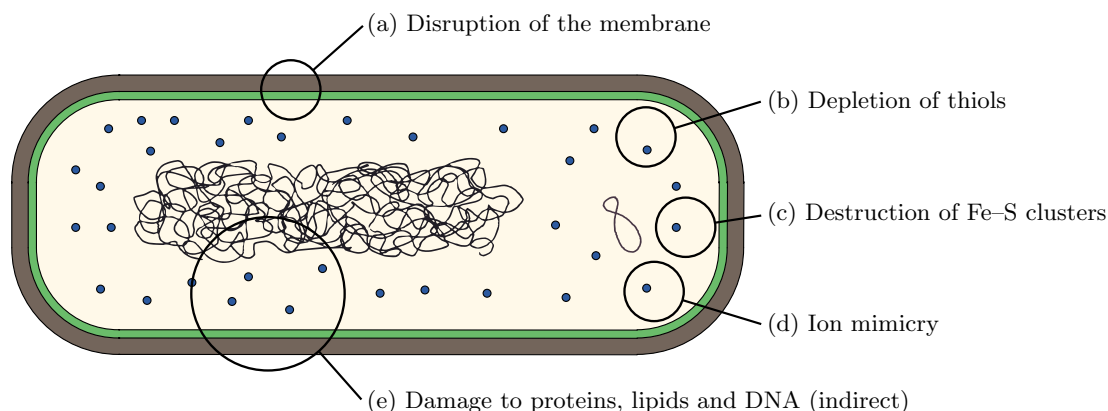


Figure 3.14: Method of action for silver ions. This includes (a) disruption of the cell membrane, (b) the depletion of cellular thiols, (c) the destruction of iron–sulphur clusters, releasing iron ions into the cell, and (d) ion mimicry, inactivating certain proteins. Through these mechanisms, this can (e) damage the proteins, lipids and DNA in the cell [397, 426, 431]. 🚫

Direct Effects

It is generally agreed that silver disrupts the cell membrane in some way, however the extent to which this occurs is disputed [426, 431]. This method focuses on the cell respiration, by affecting the bacterial electron transport chain through the inhibition of quinone [397]. Further disruption has also been suggested, including effects such as proton leakage through the membrane or damage to the membrane itself.

Inside the cells, thiols (such as glutathione) act as antioxidants to mitigate the effects of any reactive oxygen species (ROS) created during respiration or through other means. Silver has the ability to deplete the cellular thiols (although the exact method is not yet understood), making the cell more vulnerable to metal attacks or ROS, and could prevent the repair of oxidised protein thiols [397].

The destruction of iron–sulphur clusters, which contain proteins and some cellular redox enzymes, is a widely known method of action for silver [397, 426, 431]. In addition to disrupting the proteins inside these clusters, in some cases Ag^+ is incorporated into proteins targeting other ions, with this “mimicry” rendering the protein inactive.

Indirect Effects

In the process of destroying iron–sulphur clusters, additional Fe^{2+} is released into the cell, which accelerates the production of ROS through the Fenton reaction (shown in Equation 3.1) [397, 426]. In this, by-products from aerobic respiration (such as hydrogen peroxide, H_2O_2) oxidise Fe^{2+} to create hydroxide (OH^-) and the highly reactive hydroxyl radical (OH^\bullet).



These ROS then react inside the cell, damaging critical aspects such as the proteins, lipids and DNA.

Antimicrobial Resistance

The combination of different methods Ag^+ uses to attack the cells makes it uncommonly difficult for any particular strain of bacteria to develop a resistance (or tolerance) to silver. However, it would be remiss not to note that studies have started to identify bacteria developing such a resistance [432, 433].

Studies such as these show that (as is the case with antibiotics), it is unlikely that silver will be able to be used indefinitely to obtain the same results. Despite this, instances of bacteria showing resistant traits are currently rare, with silver remaining extremely potent against a wide range of microbes. The possibility of bacteria developing AMR to silver was therefore seen as something to be aware of, but did not impact the choice of silver as the focus of this research.

3.6 Polyamide / Silver Micro- and Nano-Composites

With such a small amount (typically <1 mg/l [425]) of silver ions needed in order to have an antimicrobial effect, these properties can be imparted into other materials through the incorporation of silver additives into the bulk material. These additives then act as a reservoir, slowly dispensing Ag^+ into (and then out of) the material to achieve long-term antimicrobial functionality.

In order to release Ag^+ from the incorporated additives, generally a reaction involving water has to occur. For this reason, the ability of the bulk material to absorb water (how hygroscopic it is) is key; with the speed of the water uptake (and its maximum water content) governing how quickly the Ag^+ is produced.

Polyamides are known to absorb water (see Section 2.5.2) and are widely used in LS, making them ideal candidates for creating silver-containing micro- or nano-composite materials. While this has not been researched using AM, some research has been carried out in this area using materials created with compression moulding. This research by Kumar et al. [434–437] and Damm et al. [438–440] predominantly focused on the use of PA6/66, key takeaways from which are covered in this section.

3.6.1 Method of Action

In a polyamide / metallic silver composite (schematically shown in Figure 3.15), the concept revolves around water diffusing into the parts, reacting with the metallic silver additives, then diffusing Ag^+ out into the surroundings [426].

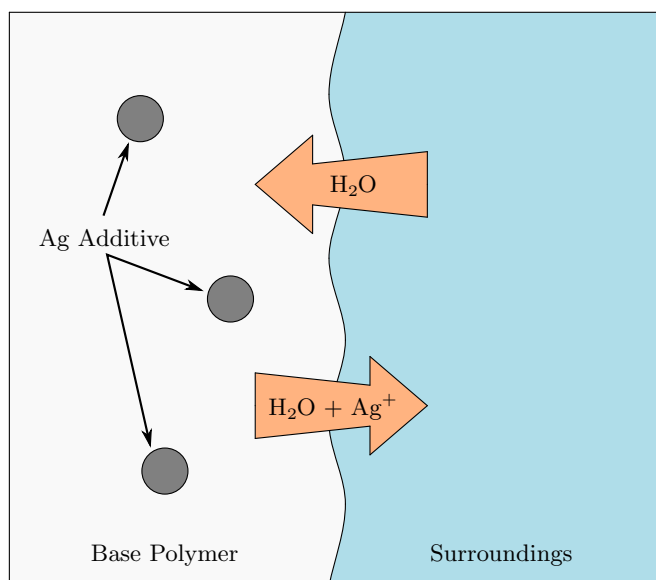
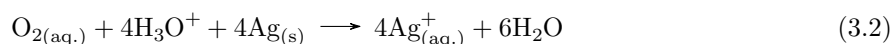


Figure 3.15: Release method of metallic silver containing micro- and nano-composite materials. 🚫

In this scenario, the reaction to create silver ions from the metallic silver, relies on the oxygen dissolved in the water ($\text{O}_{2(\text{aq.})}$), as shown in Equation 3.2 [438].



As the additives are distributed throughout the material, this reaction occurs firstly with any additives on the surface, and is then sometimes followed by a slight decrease in Ag^+ release while the water is absorbed into the polymer, before an eventual increase as the water reaches more embedded additive particles [434].

3.6.2 Differences in Properties due to the Incorporated Silver Additives

With the use of additives commonly used to affect the properties of polymer parts (see Section 2.6.5 for examples in LS), potential changes were investigated alongside the antimicrobial functionality. It is worth noting that although determining these properties (such as mechanical properties) is an essential part of the material characterisation, the results of obtained are almost inconsequential; with small differences usually able to be accommodated through design changes or uses in different applications.

Effect on Mechanical Properties

The effects on the mechanical properties of PA6/66 are shown in Figure 3.16a, where a decrease in σ_{uts} and ε_{max} can be seen for all the micro-composite parts. Interestingly, the differences for samples saturated in water are far smaller (Figure 3.16b), with both the pure polymer and microcomposites showing a marked decrease in σ_{uts} and a significant increase in ε_{max} .

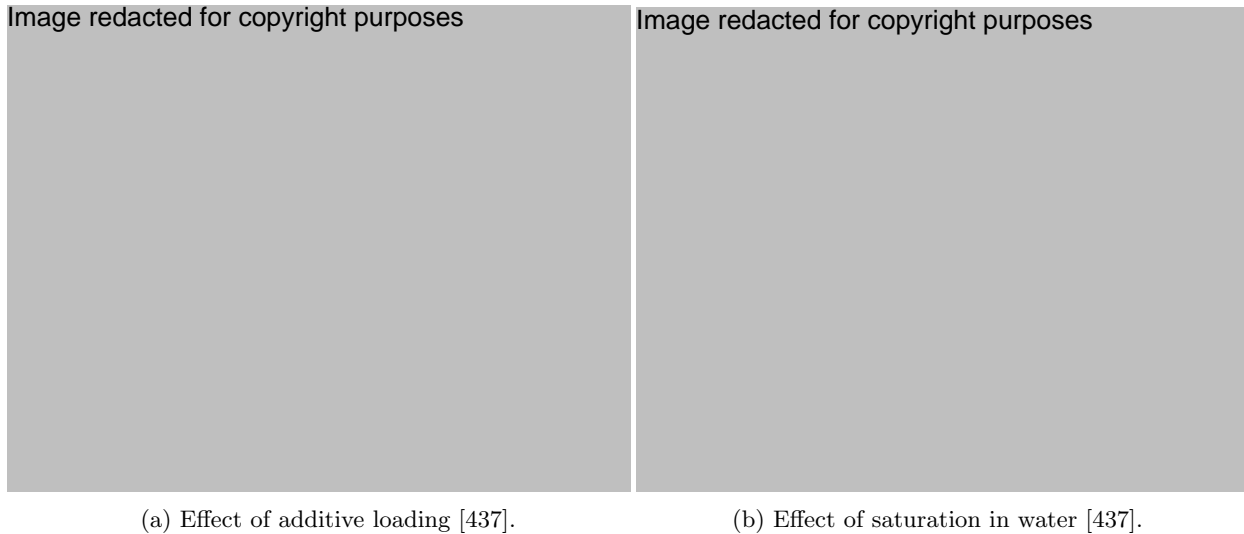


Figure 3.16: Mechanical properties (tensile) of compression moulded PA6/66 / silver microcomposites containing 0.8 μm diameter metallic silver additives.

Effect on Crystallinity and Effect of Water Diffusion Rate

In addition to the mechanical properties, the incorporation of silver was found to affect the crystallinity, with the additives acting as nucleation points within the material [435]. Generally, an increase in the additive loading led to a lower crystallinity in the PA6/66 parts, with silver-containing parts also showing a higher T_c and a narrower crystallisation peak (see Section 2.3.1).

While in Engineering applications the crystallinity of polymers is not necessarily prioritised, this could have a large effect on the antimicrobial efficacy. This is due to the decreased diffusion rate in polyamides due to an increase in crystallinity [441]; in this instance, the diffusion rate of water throughout the polyamide has been directly linked with the silver ion release rate (see Figure 3.17) [435, 438]. The position of the additives relative to the crystalline regions is also likely to affect this, with the diffusion rate at its highest in the amorphous regions of the polymer (see Section 2.2.1).



Figure 3.17: Relationship of water uptake and Ag^+ release rate in a compression moulded PA6/Silver nano-composite part containing 2 wt% silver [438].

3.6.3 Effect of Base Polymer Properties

The choice of base polymer for any micro- or nano-composite material will have a large effect on its performance. In terms of the antimicrobial functionality (through the release of Ag^+), this is most likely impacted by the rate of diffusion for water throughout the part, and the maximum water uptake of the material [438].

In polyamides, the difference in polymer chain length (see Section 2.2.1) is the key factor, with the shorter chains (such as PA6) able to absorb much more water at a faster rate than the longer chains (such as PA12, with maximum water uptake of 1.5–2.0%) [207, 442, 443]. The effect of this can be seen in Figure 3.18, with the Ag^+ released over 100 days seen to be significantly higher in the PA6 nano-composites compared to in PA12.

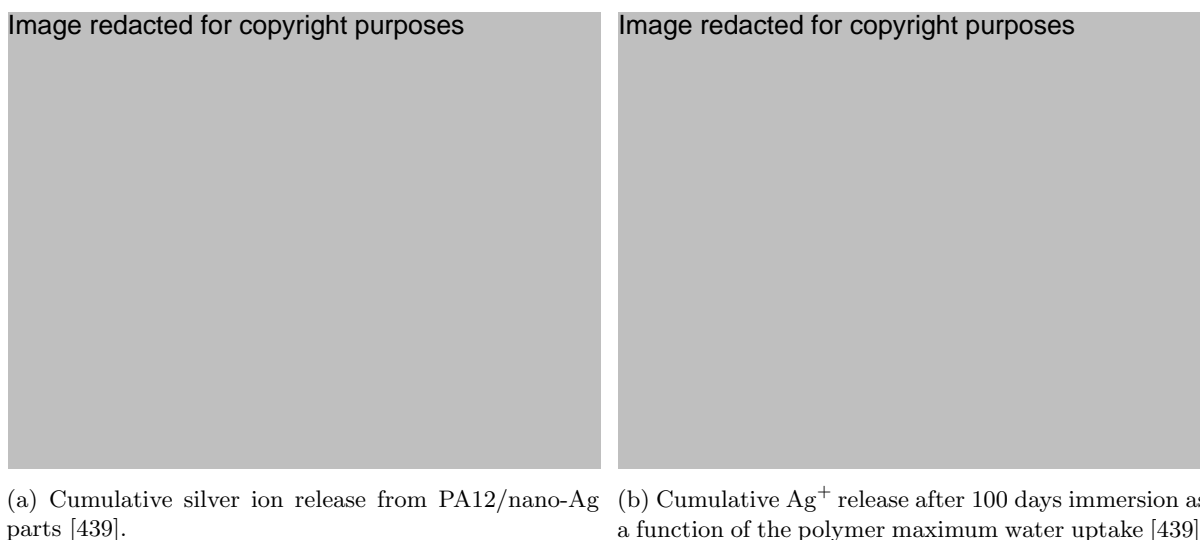


Figure 3.18: Ag^+ release from compression moulded PA12/Ag nano-composites.

Despite the comparatively low performance of PA12 among polyamides in terms of the water absorption and ion release (as shown in Figure 3.18), it remains a strong contender for creating composite parts with LS. This mainly arises due to its processability in LS (with a proven ability to incorporate additives), while still showing a not insignificant water uptake and Ag^+ release. By using PA12, it still enables a good understanding of the added functionality, while limiting the likelihood of additional complications during printing.

3.6.4 Effect of Additive Properties

Particle Size / Distribution

With solid silver additives, reactions to produce silver ions can only take place on the surface, meaning that the surface area of the incorporated particles has a large effect on the performance. To maximise the surface area to volume ratio, smaller particles (nano-scale) have been used in various applications to increase this release. However, with these smaller particles obtaining an even dispersion throughout the material can be difficult, with the agglomeration of smaller particles in some cases making them less effective than larger (micro-scale) additives [434].

Additive Composition

An alternative to using smaller metallic silver, is to use larger (micro-scale) additives containing silver nano-particles or silver ions. In these cases, it is the dissolution of the additive particle which releases the metallic silver or Ag^+ directly (see Section 3.6.5). Common commercial carriers include zeolites, and phosphate glasses (such as zirconium phosphate) [436, 444].

The use of these carriers allows for a much more tailored approach to the Ag^+ release, with the option to customise the dissolution rate and silver loading. In a composite material, these carriers can also provide an easier path for water to penetrate into the parts (where diffusion through the polymer could be much slower), with the increased porosity after dissolution also leading to faster diffusion. This means that if used correctly these carriers can be as effective as elemental silver additives, even at lower concentrations

and with a lower total silver content [436]. The lower total silver content could lead to a shorter lifespan, however this can be adjusted to the requirements of the application.

3.6.5 Silver Phosphate Glasses²

As seen in Section 3.5, the form of silver present can enhance or inhibit the antimicrobial effect, with Ag^+ being far more potent than metallic silver. By using carrier materials, Ag^+ can be directly released, meaning that equivalent efficacies can be achieved with far lower concentrations of silver [446]. This occurs through reactions such as Equation 3.3, in which silver oxide dissolves to create silver ions in neutral or acidic solutions [447].



To control this reaction, silver oxide is usually accompanied by other glasses such as phosphates. Silver-containing phosphate-based glasses show a fairly linear dissolution rate, with associated linear release of Ag^+ , over its lifetime [446, 448]. This can be controlled by the proportions phosphate (P_2O_5), with more phosphate leading to a faster dissolution rate. The amount of silver has also been linked to the dissolution rate, with more silver (and less sodium oxide, Na_2O) leading to changes in the structure, making it stronger and reducing the decomposition rate [448–450]

3.7 Project Definition

3.7.1 Gaps in the Knowledge

In the field of Laser Sintering, the limiting factor to its uptake more widely in industry is the restricted material choice, with the technology itself now relatively well understood. Current research is not only focusing on creating new base polymers, but on creating composite materials through the inclusion of additives, succeeding in altering the mechanical properties of the parts and adding new functionality.

The field of antimicrobial materials is rapidly expanding, with the need for novel methods of controlling the spread of microbes becoming more apparent with the rise in global fatalities due to antimicrobial resistance. Biocide-releasing surfaces are generally widely utilised, with antimicrobial metal-doped glasses often included as additives in these instances. Examples of these types of materials are now starting to emerge in Additive Manufacturing. However, no research to date has been carried out on creating an antimicrobial, biocide-releasing composite for Laser Sintering.

In the creation of a composite, antimicrobial material for Laser Sintering, there are additional unknowns. In terms of the incorporation of the additive, qualitative testing on the the additive dispersion has been carried out on LS composites (as a quality control check), but to the author's knowledge, no quantitative analysis of the dispersion has been carried out to date. For the chosen antimicrobial agent of silver, the functionality of the parts is strongly linked to the water uptake and release of silver ions. The water uptake characteristics of LS PA12 parts have not been measured, with conflicting reports on how this increased water content affects the mechanical properties.

3.7.2 Aim

The overall aim of this research was to investigate the effectiveness of incorporating silver-containing phosphate glass additives into printed polymers to create intrinsically antimicrobial parts using Laser Sintering.

3.7.3 Research Questions

In order to achieve the aim, key research questions were identified:

- RQ 1. Can powder feedstocks containing silver-doped phosphate-based additives be effectively processed in Laser Sintering?
- RQ 2. Does the addition of these additives affect the Engineering properties of the parts, and are these sufficiently dispersed throughout the part?

²A version of this introduction to silver-doped phosphate-based glasses is published in [445]

- RQ 3. Do the printed parts absorb water and release silver ions, and how does this compare to similar materials manufactured with other processes?
- RQ 4. Do the printed parts show display significant antibacterial functionality, against representative and problematic strains of bacteria?
- RQ 5. Can the customisability of phosphate-based glasses be exploited to tailor the effectiveness of the additives, and the printed microcomposite parts?

3.7.4 Objectives

For each research question, task-level objectives were created. These form the basis of the experimental work presented in Chapters 4 and 5.

RQ 1 Processability in Laser Sintering

1. Identify a suitable base polymer and commercially available silver-containing phosphate based glass additive to use in Laser Sintering.
 - (a) Characterise the properties of the powders known to affect processability in Laser Sintering.
2. Identify a suitable method of creating a composite powder feedstock.
3. Attempt to print microcomposite parts using Laser Sintering.

RQ 2 Engineering Properties

4. Characterise the properties of successfully printed microcomposites and compare to standard LS parts.
 - (a) Test the tensile properties.
 - (b) Test the thermal properties (including crystallinity).
 - (c) Identify a suitable method of measuring microstructure and additive distribution to validate the feedstock preparation method used in objective 2.
 - (d) Measure the silver content of the printed parts.

RQ 3 Situational Properties

5. Characterise the situational properties of the printed parts relevant to the part functionality in end-use applications.
 - (a) Determine the effects and reversibility of any sterilisation processes used on the mechanical properties of the printed parts.
 - (b) Measure the water absorption of the parts.
 - (c) Measure the silver release from the microcomposites to ensure silver has not been lost during the printing process.

RQ 4 Antimicrobial Properties

6. Test the antimicrobial functionality of the parts against representative strains of bacteria and against benchmark polymer parts.
 - (a) Test the efficacy of the powder feedstock.
 - (b) Test the effect of the parts on biofilm formation and on planktonic bacteria.
 - (c) Test the efficacy of the parts in different media.
7. Evaluate the effectiveness of using silver-based additives to create an antimicrobial material using Laser Sintering.

RQ 5 Tailored Additives

8. Design and manufacture custom silver-doped phosphate-based additives, based on the key characteristics of the commercial additives.
9. Characterise the additives, processability in Laser Sintering, Engineering properties, situational properties, and antimicrobial properties, using the the same methods as in Objectives 2–7 (RQ 1–RQ 4) for the commercial additives.

3.7.5 Contribution to Knowledge

Upon completion, this project will represent the first research into creating an intrinsically antimicrobial material for use in Laser Sintering. This will initially focus on the use of commercially available silver-doped phosphate-based additives to maximise the potential immediate impact in industry; then focusing on the design, manufacture and testing of custom silver-doped phosphate-based additives. This is the first research into the production of silver-containing additives for Laser Sintering, and the first research into the effects of the additive composition on the antimicrobial properties of the printed parts.

This work will also contribute more broadly to the field of Laser Sintering. In the production of the composite materials, Micro-CT will be explored for the first time as a means to quantitatively analyse the additive dispersion and part microstructure throughout the volume of the part. In this manner, the method of additive incorporation can be validated non-destructively, using a method suitable for quality control of production parts.

Further to this, the water uptake characteristics and the effects these have on the mechanical properties of LS PA12 parts will be explored. This both deepens the understanding of how the silver-releasing microcomposite here might act, as well as adding to existing knowledge of how the water content affects the mechanical properties of LS PA12 parts. The effect of steam sterilisation will be investigated as part of this, again for the first time in Laser Sintering. The reversibility of any changes will also be investigated to determine whether the effects can be mitigated.

3.7.6 Hypothesis

Based on all the literature presented, a proposed method action for an antimicrobial material containing silver-doped phosphate-based glass additives, created using Laser Sintering is shown in Figure 3.19.

In this, the silver-containing phosphate glass additive is incorporated into the PA12 base polymer to create a microcomposite part. By absorbing water from the surroundings, these additives react to form silver ions, which then diffuse through the part and into the surroundings. This means that the strongest antimicrobial effect is likely to occur when parts have direct contact with water, although reactions with humidity in the air could also take place.

This approach forms the basis of all the following research. This includes the creation and characterisation of microcomposite parts, with the focus on determining whether the additives alter any of the part properties, and measuring any antimicrobial efficacy.

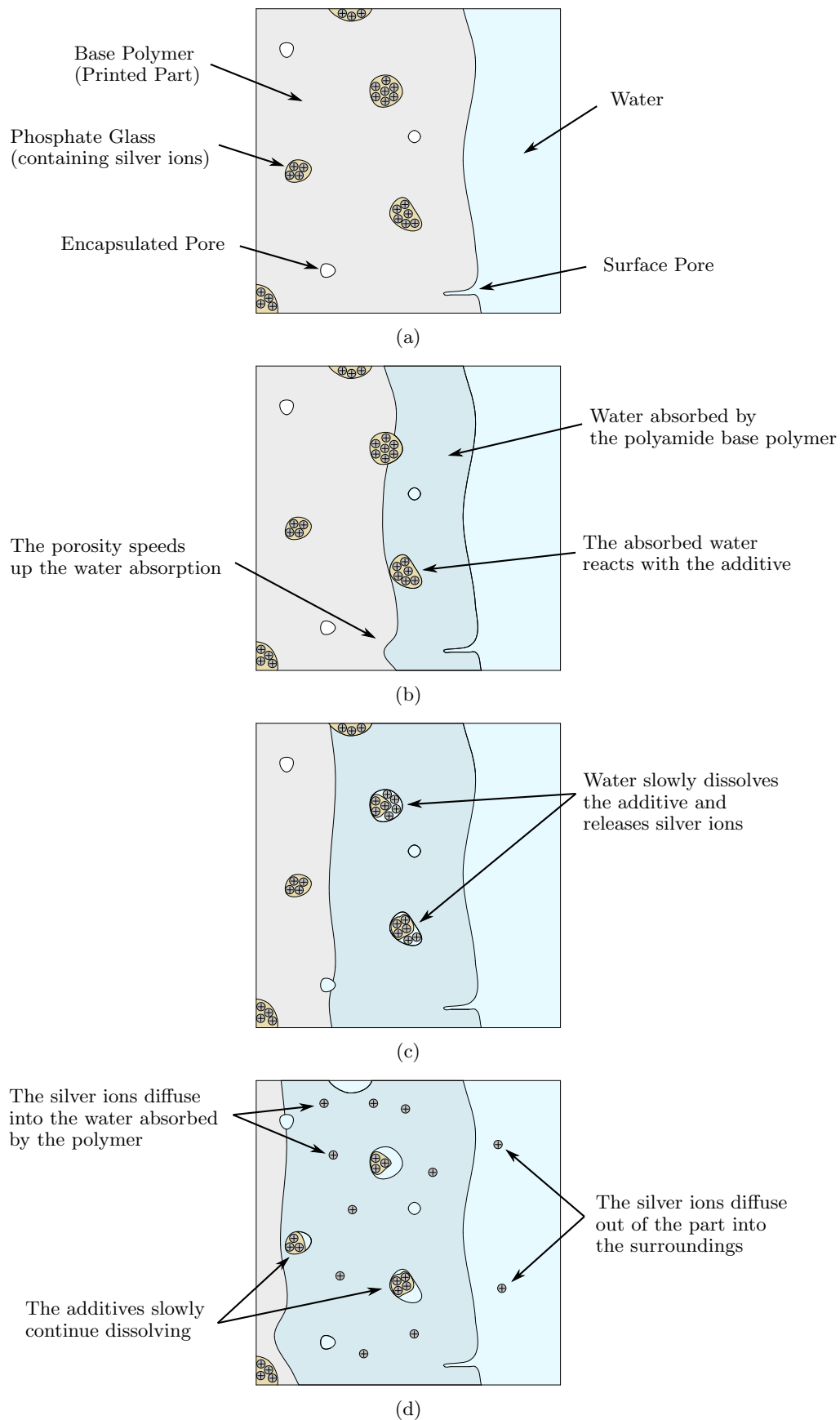


Figure 3.19: Schematic diagram for silver ion release into water from an LS polyamide part incorporating silver-containing phosphate glass additives (see Section 2.6). Showing (a) an example cross-section at the part surface, with features common in LS (see Section 2.5.1); (b) the hygroscopic nature of the polyamide absorbing water from the surroundings, aided by the part porosity and low crystallinity (see Section 2.3.3); (c) the additives dissolving, releasing silver ions (see Equation 3.3) and creating an easier route for water to travel through the part; and (d) the silver ions diffusing into the polymer, before diffusing out into the surroundings where they can have an antimicrobial effect. 🍷

Chapter 4

Commercially Available Silver Phosphate Additives

The focus of this chapter is on the creation, characterisation, and application of an antimicrobial micro-composite material for use in Laser Sintering (see Figure 4.1 for the chapter structure). The feedstock powders and printing process are first addressed, then the printed part properties, followed by properties directly relating to the application or functionality of the printed parts. Throughout, the focus was on using PA12 as a benchmark, investigating whether the inclusion of the additives changed any properties.

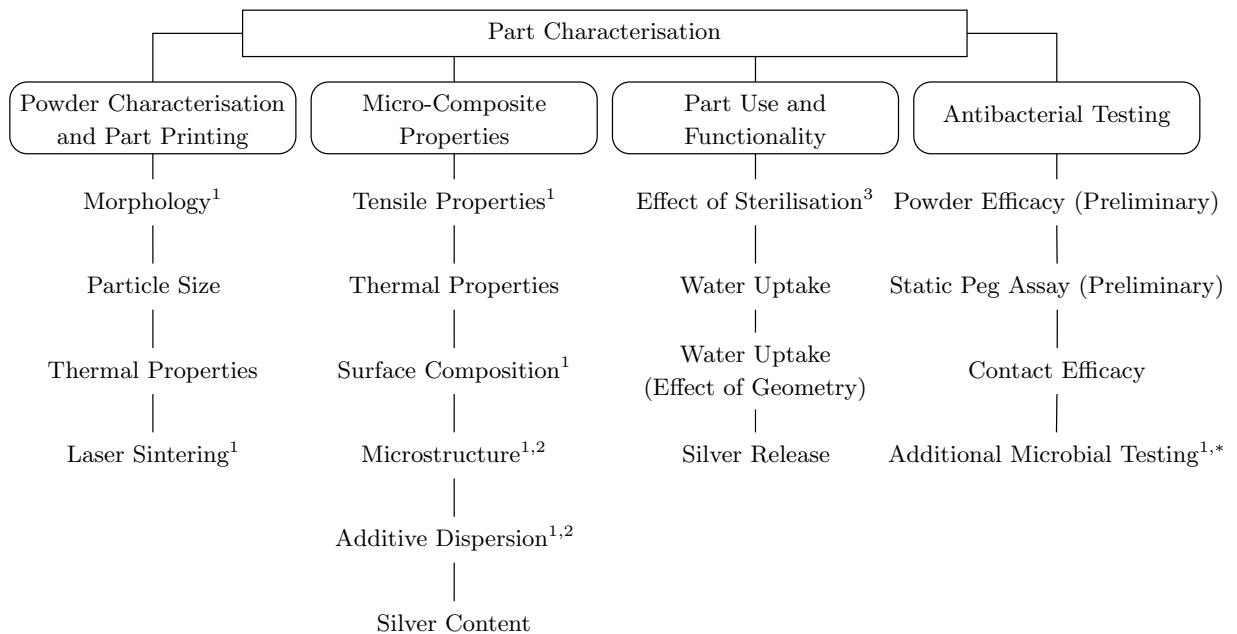


Figure 4.1: Commercially available silver phosphate additives chapter structure. ¹Published in [451] (data in [452]), ²Published in [260] (data in [453]), ³Published in [270], *Additional microbial testing carried out by Robert Turner. 🚫

Material Choice

Polyamide 12 (PA2200 – EOS) was chosen as a base material, due to its widespread use in LS composites (both commercially and in academic research – see Sections 2.6.4 and 2.6.5). Silver phosphate glass additives were chosen to add antimicrobial functionality to the printed parts, due to the customisable silver release, and the proclivity of PA12 to successfully incorporate glass additives in LS.

To maximise the repeatability and potential impact in industry, commercially available silver phosphate powders (B65003, B45003 – BioCote) were initially chosen in this chapter. These were chemically identical and differed only in size, with B65003 quoted as being $<40\ \mu\text{m}$ and B45003 $<10\ \mu\text{m}$. Each of these was incorporated into the powder feedstock at 1.0% by weight, higher than the manufacturer’s recommendation (0.3%), an overloading deemed to be reasonable to maximise any antimicrobial effect.

4.1 Powder Characterisation and Part Printing

This section focuses on the morphological and thermal characterisation of the powders, as well as the printing of the parts using Laser Sintering. By analysing the powders prior to printing, appropriate processing parameters could be chosen and potential problems could be identified.

4.1.1 Powder Morphology

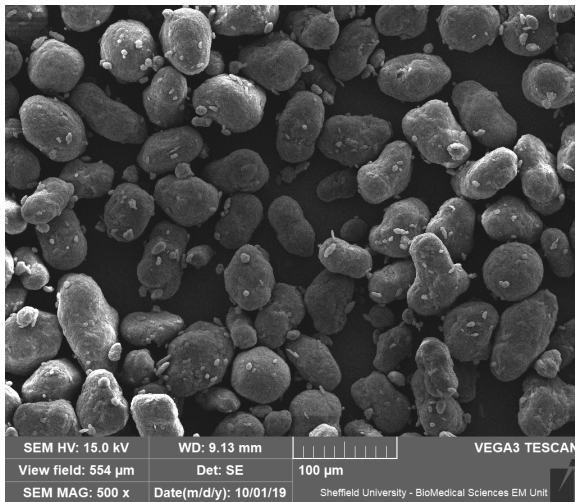
The morphology of the powders used in LS can have a large effect on their processability, particularly with respect to the flowability and packing density (see Section 2.2.2). Scanning Electron Microscopy (SEM) was therefore used to determine the shape of the powders give a general indication of their size. This section focuses on the polyamide powder (PA2200) and the larger of the two additives (B65003).

Methodology

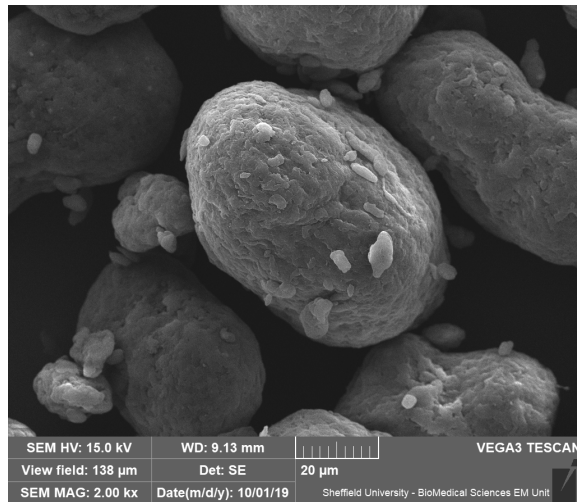
Small quantities of each powder were first attached to self-adhesive carbon pads, with the samples then gold sputter-coated using an Edwards S150B sputter coater. These were imaged using a TESCAN VEGA3 SEM, using an accelerating voltage of 15 kV and the detector set to measure secondary electrons.

Results

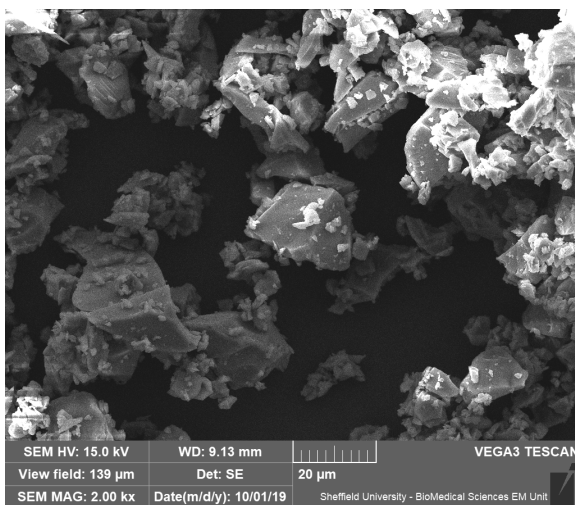
Views of the PA2200 powder can be seen in Figures 4.2a and 4.2b, where it can be seen that the grains have a rounded “potato-like” shape. The B65003 additive can be seen in Figures 4.2c and 4.2d, showing a much more angular and jagged shape.



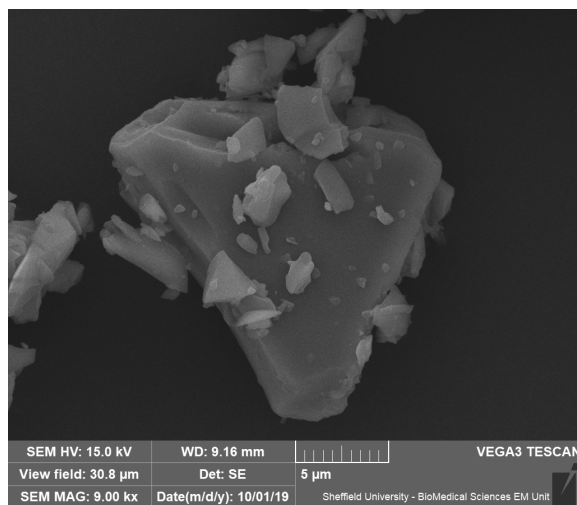
(a) PA2200.



(b) PA2200.



(c) B65003 [445].



(d) B65003.

Figure 4.2: Powder morphology obtained using SEM. 🌐

Discussion

Although the SEM images in Figure 4.2 show only an initial indication of both the shape and size, there is nothing present which would suggest an issue in terms of processability in LS. The angular shape of the B65003 was identified as a potential concern as it could hamper the flowability of the combined powders; however, since these are generally much smaller and far less prevalent than PA2200, this effect was thought to be negligible.

Due to the subtleties of the machine set up (such as the recoater blade profile and sweep direction, powder feed, and temperatures experienced), this effect could only be reliably confirmed during the powder deposition for a build in the LS machine (see Section 4.1.4). In terms of the efficacy of the additives, the angular shape could even prove to be advantageous as the particles could dissolve more quickly, releasing silver ions into the parts in a shorter time period; however, without directly equivalent particles with different morphologies, this cannot be confirmed.

4.1.2 Particle Size

The particle size distribution of the powder feedstock can have a large effect on the processability in LS (see Section 2.2.2), and the size of the incorporated additives are likely to affect the antimicrobial functionality of the printed parts. In order to determine a statistically valid size distribution of the powders, far more particles had to be analysed than in SEM. For this reason laser diffraction was used, with the larger sample size making it more representative of the overall powders.

Methodology

The size distribution of the powders was measured using a Mastersizer 3000 laser diffraction particle size analyser. Since the phosphate glasses are soluble in water, a dry dispersion unit was used for both B65003 and B45003. The refractive index of the glasses was not known, so a value was chosen for a material thought to be similar in composition (Tricalcium Phosphate) and a value of 1.627 used.

When measuring the polyamide 12 powder, the dry dispersion unit was found to be ineffective, as the particles tended to agglomerate together. For this reason, wet dispersion with additional ultrasonic agitation was used for PA2200, which was able to prevent the particles from agglomerating during the measurement. The refractive index of polyamide 12 (1.53) was used for the analysis.

The volume-based diameter metrics of D10, D50, and D90 (10%, 50%, and 90% along the cumulative distribution) were recorded, along with the average diameter weighted by volume (D[4,3]).

Results¹

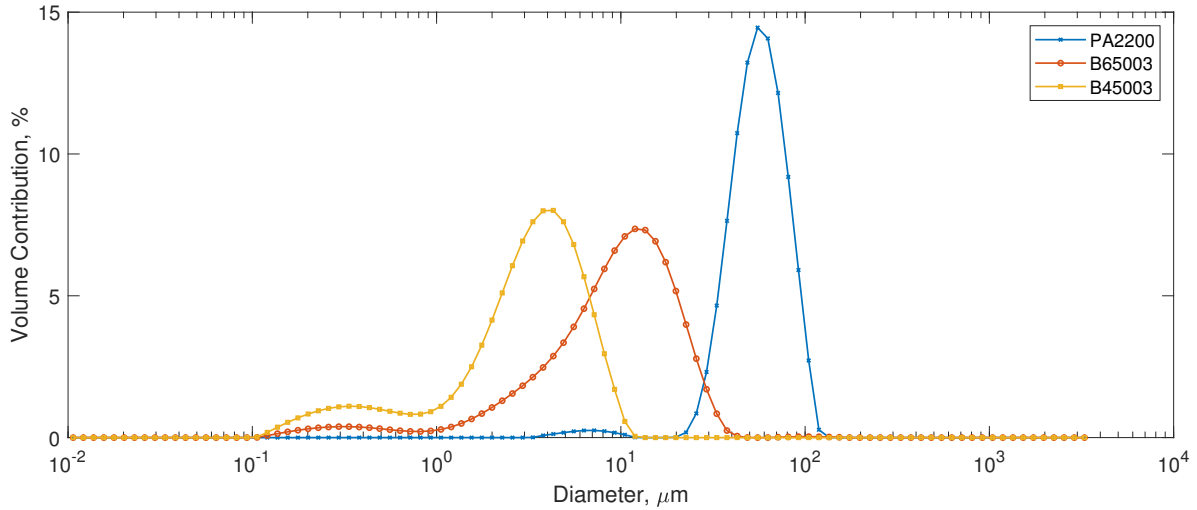
The results can be seen in Figure 4.3, with key values shown in Table 4.1. For each powder a minimum of 10 runs were carried out, with the mean values quoted here. The weighted residual (a measure of the amount of powder for the sample not measured in each run) was used to evaluate the validity of each run, with any runs showing a value greater than 1% discarded. Note that in Table 4.1, the D50 was specified by manufacturer of B65003, whereas for PA2200 the “average” size given was interpreted to be the D50.

| Glass Additive | D10 / μm | D50 / μm | D90 / μm | D[4,3] / μm | Weighted Residual / % |
|----------------|---------------------|------------------------|---------------------|------------------------|-----------------------|
| B65003 | 2.48 \pm 0.04 | 9.83 \pm 0.07 (10.5) | 21.1 \pm 0.4 | 11.1 \pm 0.5 | 0.81 \pm 0.04 |
| B45003 | 0.528 \pm 0.022 | 3.31 \pm 0.02 | 6.65 \pm 0.06 | 3.55 \pm 0.02 | 0.52 \pm 0.22 |
| PA2200* | 35.7 \pm 0.3 | 56.0 \pm 0.3 (56) | 84.7 \pm 0.6 | 57.9 \pm 0.4 | 0.56 \pm 0.02 |

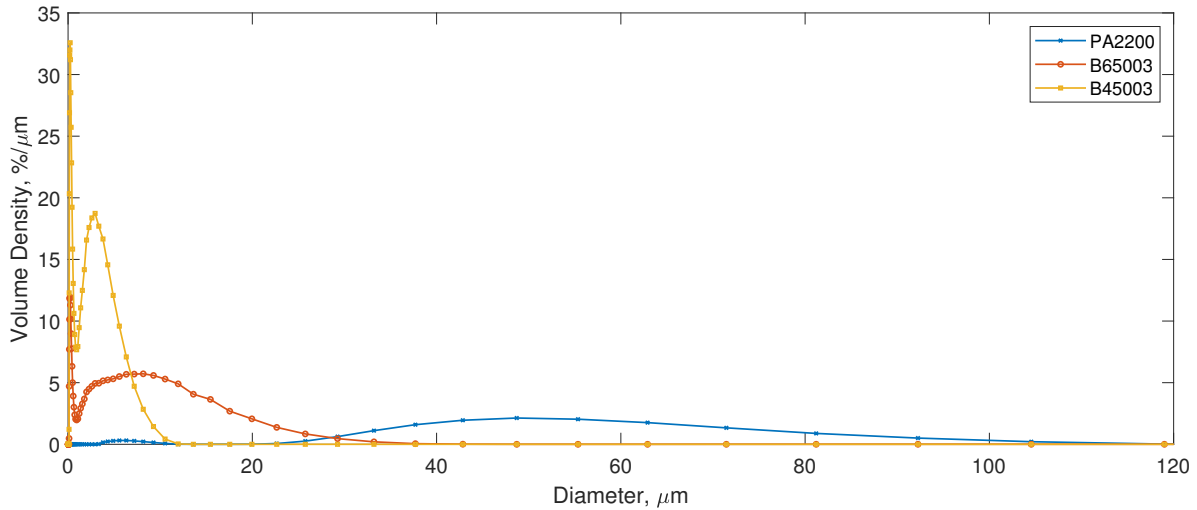
Table 4.1: Results from particle size analysis. Values in brackets are those quoted by the manufacturer. *wet dispersion + ultrasound.

The log scale shown in Figure 4.3a represents the data collected from the machine which grouped the volume contribution by equally sized log intervals (or bins). In order to show this on a linear scale, each measurement was normalised by the bin width to account for the uneven bin widths on a linear scale; subsequently, the area under the curves in Figure 4.3b represents the volume contribution of the particles.

¹The full results can be found in Appendix B.1, showing the D10, D50, D90, D[4,3], weighted residual, and plots of the size distribution for each of the 96 valid runs.



(a) Log scale – as measured from the Mastersizer 3000.



(b) Linear scale – normalised by bin width, with the area showing the volume contribution.

Figure 4.3: Results from particle size analysis of the polymer powder (PA2200), and the two commercially available silver phosphate additives used (B65003 and B45003). Shown are the averaged curves from all samples. 🚫

Discussion

All these results confirm the size distributions quoted by the manufacturers, as well as the sizes initially observed in the SEM imaging.

In terms of creating a composite powder feedstock for Laser Sintering (see Section 2.6.1), both of these glass powders would fall into the larger additive category. Practically, the larger size means that the simpler method of just mixing the two powders together could prove effective in creating a homogeneous mix, without the need for more complex and costly methods to be used.

For the smaller of the two additives (B45003), there were a large number of smaller, sub-micron sized particles detected (Figure 4.3), which could prove more challenging to distribute homogeneously throughout the feedstock. However, since the purpose of these is to create reservoirs of silver ions which are then free to move through the polyamide parts, some agglomeration of these smaller particles was not thought to have a significant impact on the efficacy of the printed parts. To test this, further sieving of the additives could be carried out with a 1 μm sieve to remove these smaller particles. However, since these only make up a small proportion of the additive particles by volume and two different particle size distributions were already being investigated, this was not explored in this research.

4.1.3 Thermal Properties

In order to establish a suitable processing window (see Section 2.2.1) for the selected materials, Differential Scanning Calorimetry (DSC) was used. This provided an initial check to determine whether the inclusion of the additives significantly changed the thermal behaviour of the PA2200 base material, thereby affecting the optimum processing parameters in LS.

Methodology

A schematic diagram of DSC is shown in Figure 4.4, the principle being that a sample and reference pan are heated at the same rate with the difference in energy required (heat flow) recorded. These measurements were subsequently used to determine the melting temperature (T_m), recrystallisation temperature (T_c), and crystallinity (X_c).

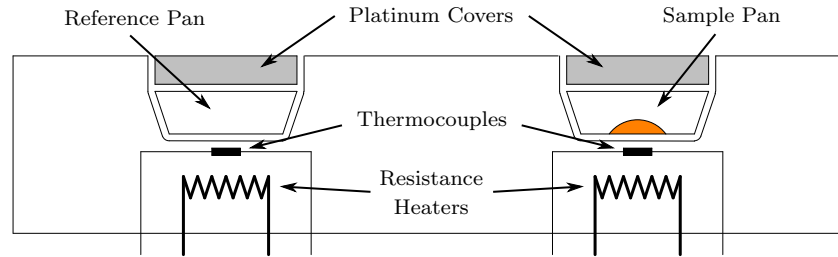


Figure 4.4: Schematic diagram of Differential Scanning Calorimetry (DSC) [15].

Approximately 10 mg of each powder was analysed using a Perkin Elmer DSC 8500. These were heated from 30–220°C at a rate of 10°C/min (as in [224, 240, 243]) and cooled back to 30°C at the same rate. By heating the powders to a temperature above those required to melt the powder (and therefore those expected to be experienced in LS), any phenomena occurring near those temperatures could be observed.

In addition to the phosphate-based additives, a sample of PA2200 was included for completeness, along with a 1% B65003 / 99% PA2200 mix (sample taken from a prepared 2 kg powder mix, prepared in a rotary tumbler using the method specified in Section 4.1.4), representative of the feedstock used; this allowed any changes in behaviour compared to PA2200 to be detected, and a suitable bed temperature for the build to be identified.

The T_m and T_c peaks were identified from the heat flow measurements, with the Pyris software used to determine the onset and end of the peaks (as in [224]), with a sigmoidal baseline used. The value of X_c was calculated using Equation 4.1 [240, 243], in this ΔH_m is the measured heat of melting, ΔH_m^∞ is the theoretical heat of melting for 100% crystalline polyamide 12 (taken to be 209.3 J/g [240, 243]), A_{peak} is the area under the peak (to a fitted baseline) and m_{sample} is the mass of the sample used.

$$\text{Percent Crystallinity} = X_c = \frac{\Delta H_m}{\Delta H_m^\infty} \quad \text{where,} \quad \Delta H_m = \frac{A_{\text{peak}}}{m_{\text{sample}}} \quad (4.1)$$

Results

An annotated example of a DSC heat flow measurement can be seen in Figure 4.5 for Virgin PA2200, with all the values measured within the DSC software shown. The heat flow curves for both PA2200 and PA2200 + 1% B65003 are shown in Figure 4.6a, with the measured curves for B65003 and B45003 shown in Figure 4.6b. In each of these, the predominantly PA2200 samples can be seen to be extremely similar, and both glass additives shown to behave identically to one another (no identifiable peaks in the temperature range tested). This corresponds to the expected behaviour of the additive, which has a quoted melting temperature of >600°C in the material datasheet.

The extracted results from the heat flow measurements can be seen in Table 4.2 for the predominantly polymer-based samples. In this, the onset and end of both the T_m and T_c peaks are shown, alongside the measured ΔH_m and calculated crystallinities (X_c). Here it can be seen that for both PA2200 and PA2200 + 1% B65003, the results are practically identical, with at most a 0.32°C difference in any of the recorded temperatures.

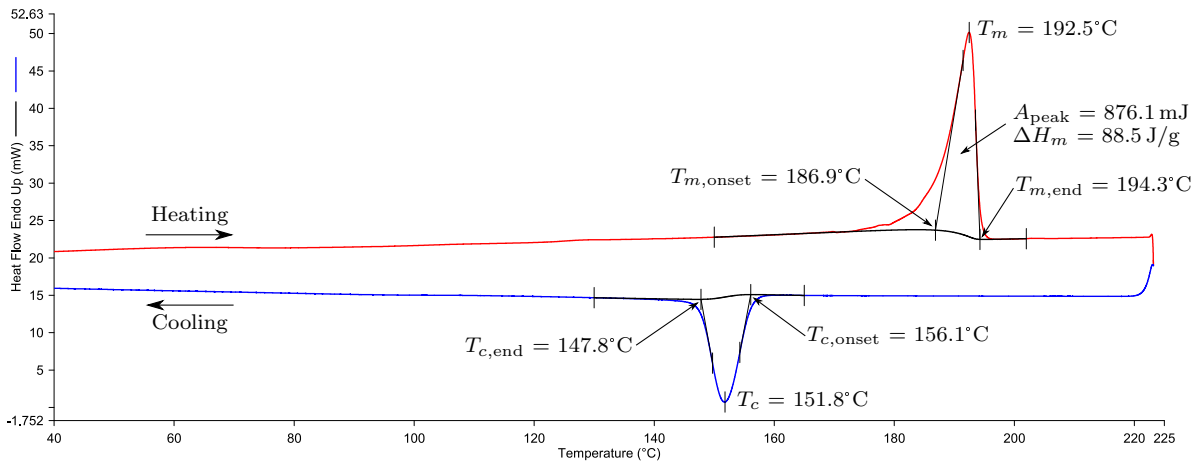
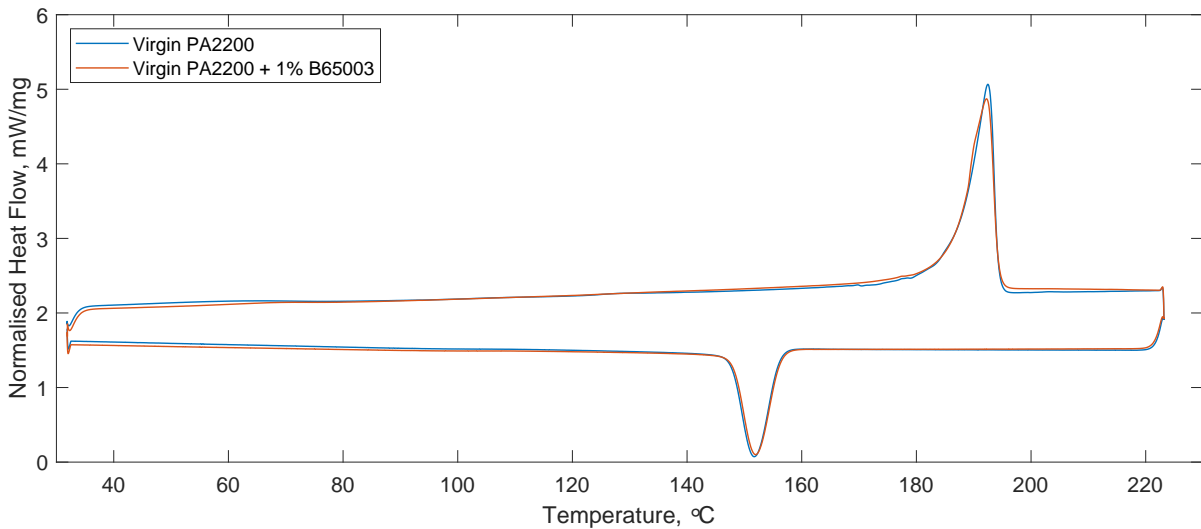
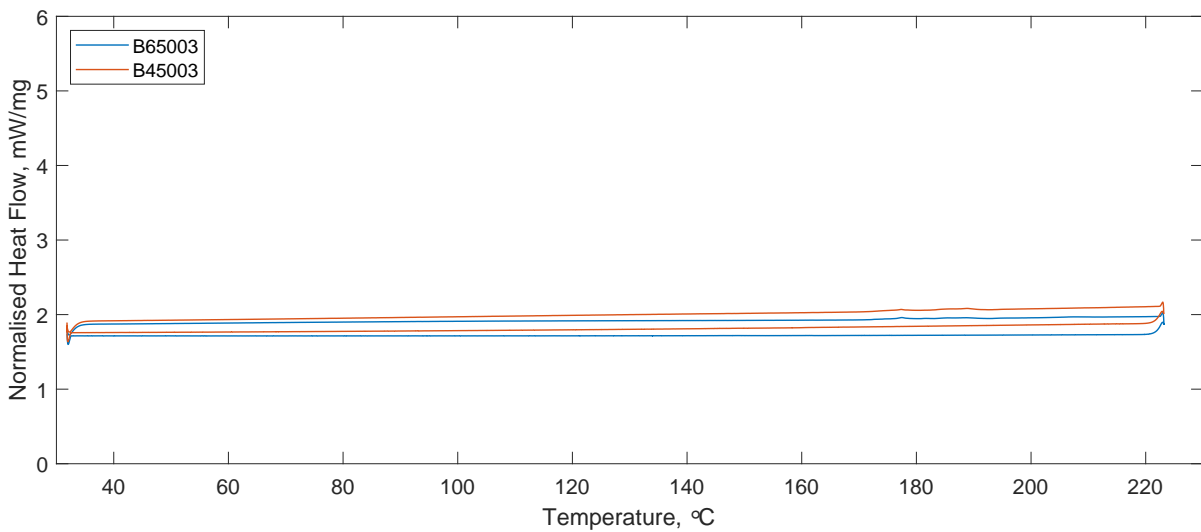


Figure 4.5: Example of a DSC curve for a powder sample processed in the software, split into heating (red) and cooling (blue), along with the values calculated. Shown is Virgin PA2200 powder. 🌐



(a) Virgin PA2200 and Virgin PA2200 + 1% B65003.



(b) B65003 and B45003.

Figure 4.6: Analysis of the powders from DSC. 🌐

| Material | $T_{m,onset}$ (°C) | T_m (°C) | $T_{m,end}$ (°C) | ΔH_m (J/g) | X_c (%) | $T_{c,onset}$ (°C) | T_c (°C) | $T_{c,end}$ (°C) |
|--------------------|-----------------------|---------------|---------------------|-----------------------|--------------|-----------------------|---------------|---------------------|
| PA2200 | 186.87 | 192.50 | 194.27 | 88.49 | 42.3 | 156.08 | 151.78 | 147.79 |
| PA2200 + 1% B65003 | 187.19 | 192.27 | 194.29 | 87.40 | 41.8 | 156.26 | 152.01 | 148.08 |

Table 4.2: DSC results for the polymer powder samples. Note that for B65003 and B45003, no peaks were observed in the temperature range tested.

Discussion

The PA2200-based measurements in Figures 4.5 and 4.6a can be seen to show exemplary behaviour for semi-crystalline polymers in LS (see Section 2.3.1). A narrow melt peak can be seen here (ideal for melting quickly with a laser), and a large processing window. This super-cooling window (the range between $T_{c,onset}$ – $T_{m,onset}$), suggests that for both the pure PA2200 and the composite powder feedstock, the same bed temperature can be used. To avoid the slight tail at the beginning of the melt peak, a temperature of 170°C was identified as a suitable starting point for the material.

As expected, no peaks were detected in the additives over the temperature range tested (see Figure 4.6b). These were expected to be stable up to temperatures much higher than those experienced during DSC (>600°C), suggesting that they should remain unaffected by the conditions in a Laser Sintering build.

The calculated values of crystallinity can be seen to be very similar for both PA2200 and PA2200 + 1% B65003, with values of 42.3% and 41.8% respectively. Although already close enough to each other not to suggest any significant differences in the build, the behaviour of B65003 (in Figure 4.6b) suggests that these could be even closer. Assuming the B65003 was not affected in any way throughout the experiment, removing the additive mass (1%) from the ΔH_m and X_c calculations enables the focus to be solely on PA2200. With this, the value of X_c becomes 42.2%, almost identical to the 42.3% measured for PA2200, further suggesting that the additive did not affect the melting behaviour.

4.1.4 Laser Sintering

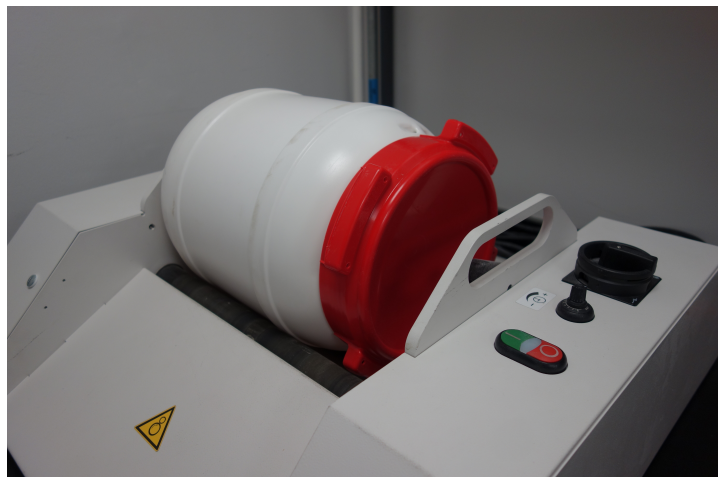
This section details the feedstock preparation, printing parameters (with potential issues), build setup, post-processing, and photos of the printed parts.

Materials

All of the parts were printed using an EOS Formiga P100 Laser Sintering machine, an industrial LS machine representative of those used more broadly in industry (Figure 4.7a). The standard build material for this is a polyamide 12 powder (commercial name PA2200 – EOS), usually mixed in a 50/50 ratio of virgin (new) and used powder; however, to maximise the repeatability, the additives here were mixed with 100% virgin PA2200. Two chemically identical additives from BioCote were used, namely B65003 (<40 µm diameter) and B45003 (<10 µm diameter).



(a) EOS – P100.



(b) EOS – mixing station P1.

Figure 4.7: Photos of the LS machine and powder mixing station. 🚫

For each test material, the PA2200 and silver glasses were first weighed out (usually 2 kg per build – virgin PA2200 weighed to 1.980 ± 0.05 kg, and the additive weighed to 20 ± 0.01 g), then subsequently mixed in a rotary tumbler (EOS – mixing station P1, Figure 4.7b) for approximately 100 minutes, with three acrylic blocks added to enhance mixing.

Printing Parameters

In order to allow for an effective comparison between the build materials, the build parameters used were kept the same for all the builds. The bed temperature identified in Section 4.1.3 was used (170°C), with multiple laser powers tested to determine the optimum parameters. For each material used, 9 test squares were first printed at differing laser powers to check for any excessive curling or smoking during printing; these were printed at 10, 12, 14, 16, 17, 18, 19, 20 and 21 W. During this initial test none of these powers displayed any curling or smoking, so the 21 W setting was chosen to match the standard parameters.

The standard parameters used to process PA2200 can be seen in Table 4.3, these optimised parameters were recommended in the manufacturer datasheet. In order to make an effective comparison between materials, these settings were used whenever possible. However, since an experimental material was used, the contours and edges were turned off while printing, minimising the potential causes of failures in the build and decreasing the number of parameters to optimise.

| | | |
|------------------|-----------------|---------------------|
| Preheat | Bed Temperature | 170°C |
| Hatching | Spacing | 0.25 mm |
| | Power | 21.0 W |
| | Scan Speed | 2500 mm/s |
| | Beam offset | 0.15 mm |
| | Layer height | 0.10 mm |
| Material Scaling | X direction | 3.2% |
| | Y direction | 3.3% |
| | Z(0) | 2.2% |
| | z(300) | 1.6% |

Table 4.3: Standard PA2200 Parameters.

Potential Issues

All the results of the powder characterisation suggest that the microcomposite feedstock should be processable in Laser Sintering; however, this was not a foregone conclusion. During the course of this research, other commercially available silver phosphate glass additives were trialled in addition to those from BioCote. However, these materials resulted in catastrophic failures during printing (see Figure 4.8) and were not able to produce parts using the standard PA2200 parameters. Other than the choice of additives, the methodology used was identical to that specified in the rest of this section.

In these builds, the combination of the material and parameters caused the scanned areas to recrystallise and curl during the build. Generally, a small amount of this is self-corrected by the machine, with the recoating blade able to push the parts down slightly and deposit a fresh layer of powder. However, when the curl is more severe, the parts are swept aside by the recoater blade, disrupting the build.

Full details of the experiments carried out with these additional commercially available additives can be found in Appendix C.3. This includes particle size analysis (with the smaller $< 5 \mu\text{m}$ size thought to contribute to the build failure), as well as further photos of the build and photos of the parts produced. Due to these issues, it was decided to focus solely on the BioCote additives previously specified.

Build Setup

An example build layout is shown in Figure 4.9, including parts designed for a range of different experiments. In order to ensure a valid comparison, the same build layout and machine parameters were used for each material. In all cases, a minimum of 1 mm separation was maintained between all parts to minimise the effect of adjacent parts on the properties. Full details of all the builds carried out over the course of this research can be found in Appendix A.1.

In all cases where the dimensions of the printed parts affected the testing carried out, the parts were measured to an accuracy of ± 0.01 mm, with multiple measurements taken and the mean values used for any subsequent calculations. Full details of these measurements can be found in Appendix A.2.

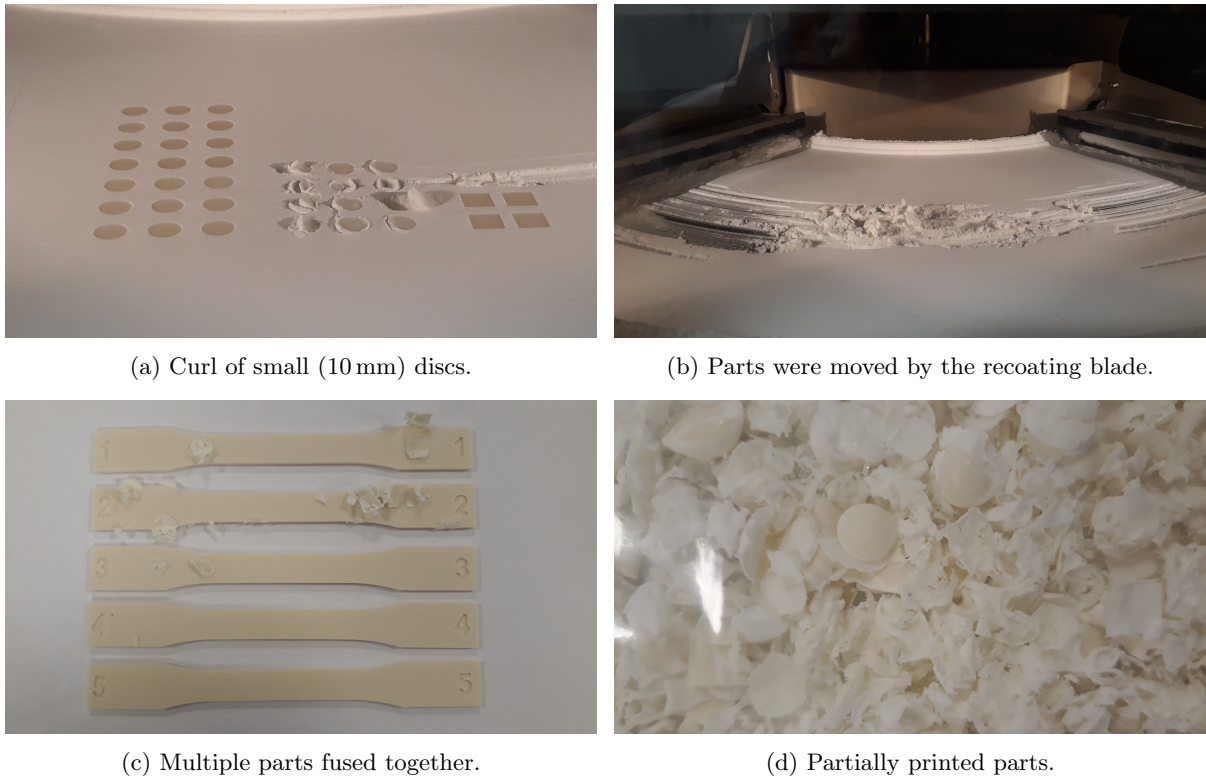


Figure 4.8: Photos of a failed build with 1% of a different commercial phosphate-based additive. Where (b) small parts curled slightly and were subsequently caught by the recoating blade (b), moving the parts and causing the build to fail, resulting in fused or incomplete parts (c) and (d). For more details see Appendix C.3.2. 🚫

Printing Observations

In the build, some slight curling was observed with 1.0% B45003 for smaller parts (such as 10 mm discs). While not sufficient to disrupt the build or significantly affect the geometry, this slight difference to both PA2200 and 1.0% B65003 suggests that this should be more closely monitored for any subsequent builds.

Post-Processing

To remove loose powder from the parts, the build cake was first sieved and parts cleaned with compressed air; this method was chosen to minimise potential sources of contamination to the surfaces. Smaller parts were processed in batches inside custom designed “cages” (see Figure 2.3a), reducing the amount of handling for each part (and potential sources of contamination), as well as drastically reducing the time required. For parts where no microbial testing was to be carried out (namely tensile test specimens), bead blasting was also used to aid in removing loose powder as is standard practice in LS.

Printed Parts

A photo showing a selection of printed test specimens in both the pure PA2200 and the microcomposite material (1% B65003) can be seen in Figure 4.10. In this, a slight colour difference between the two materials can be seen, with no discernible difference in the part geometries.

While this was a good indication that the material could be printed, to quantitatively analyse the mechanical properties of the part, other testing was required.

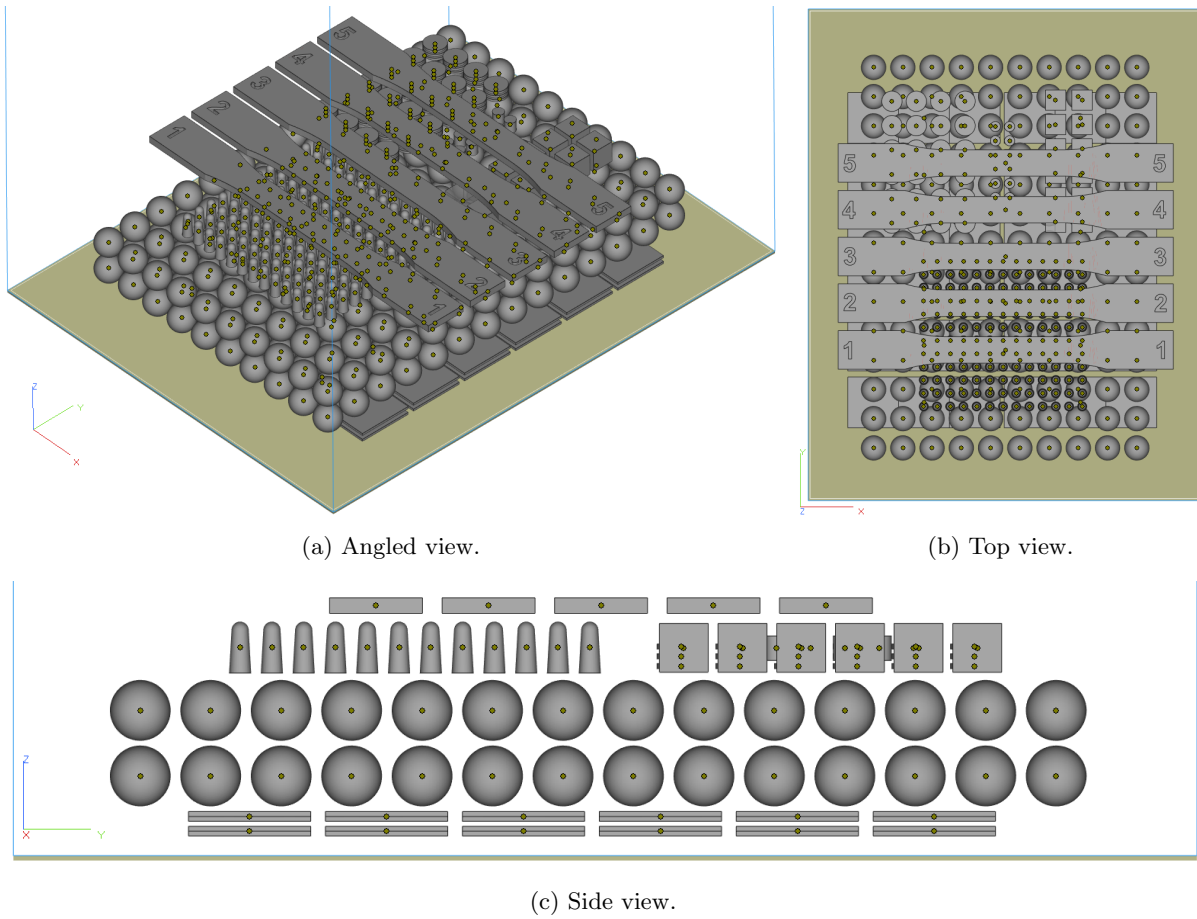


Figure 4.9: Build layout for builds 10–12, created in Magics 22.0. Including specimens for tensile testing, static peg assay tests, antibacterial testing, cytotoxicity testing, and micro-CT. 🚫

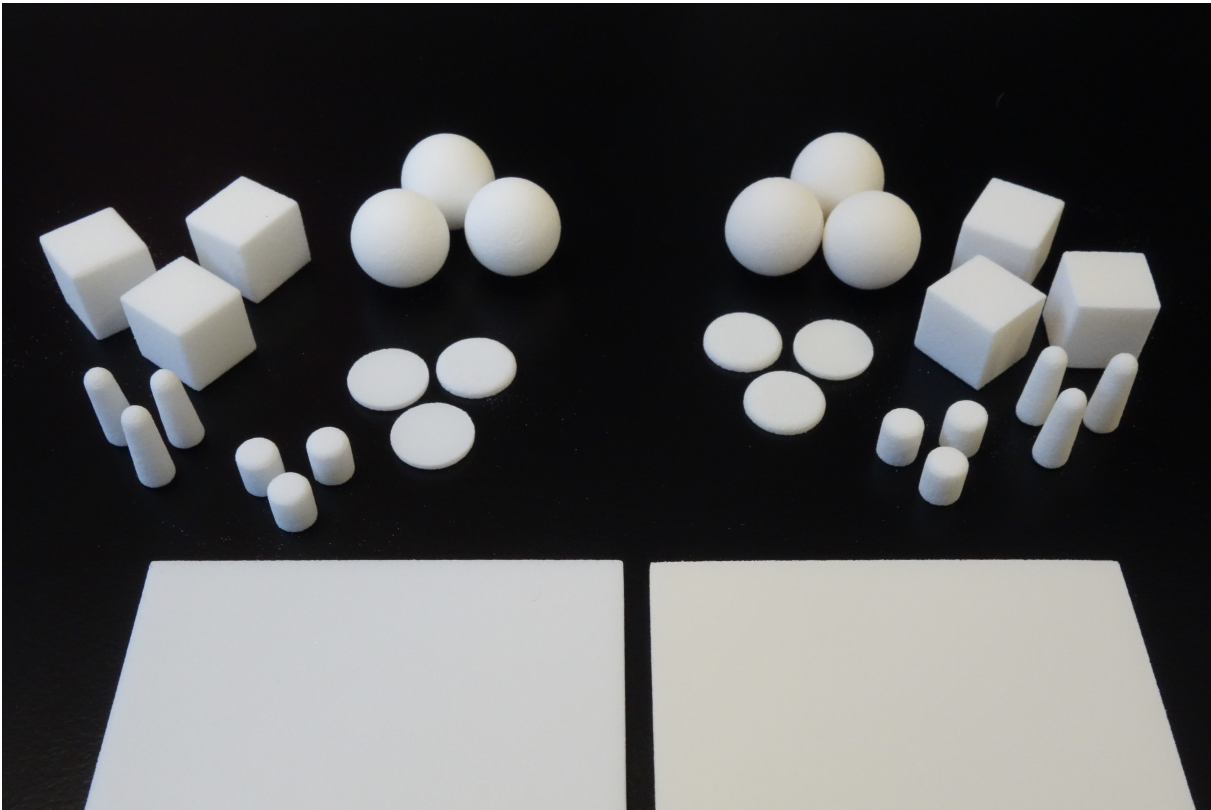


Figure 4.10: Photo of printed Virgin PA2200 parts (left) and 1.0% B65003 part (right) [451]. 🚫

4.2 Microcomposite Properties

This section focuses on characterising the physical properties and composition of the printed microcomposite material, with the mechanical properties and dispersion of the additive throughout the part of particular interest.

4.2.1 Tensile Properties^{2,3,4,5,6,7}

For a large proportion of the composites processed in LS, the purpose of the additives has been to alter the mechanical properties of the parts (see Sections 2.6.4 and 2.6.5). However, as the aim of this research was focused around adding functionality, rather than altering the mechanical performance, it was important to measure any effect that the additives might have on this.

Methodology

Testing was carried out using a Tinius Olsen 5K tensile testing machine with Laser Extensometer, a schematic of which is shown in Figure 4.11. The stress and strain values were collected using the “Horizon” software provided by Tinius Olsen.

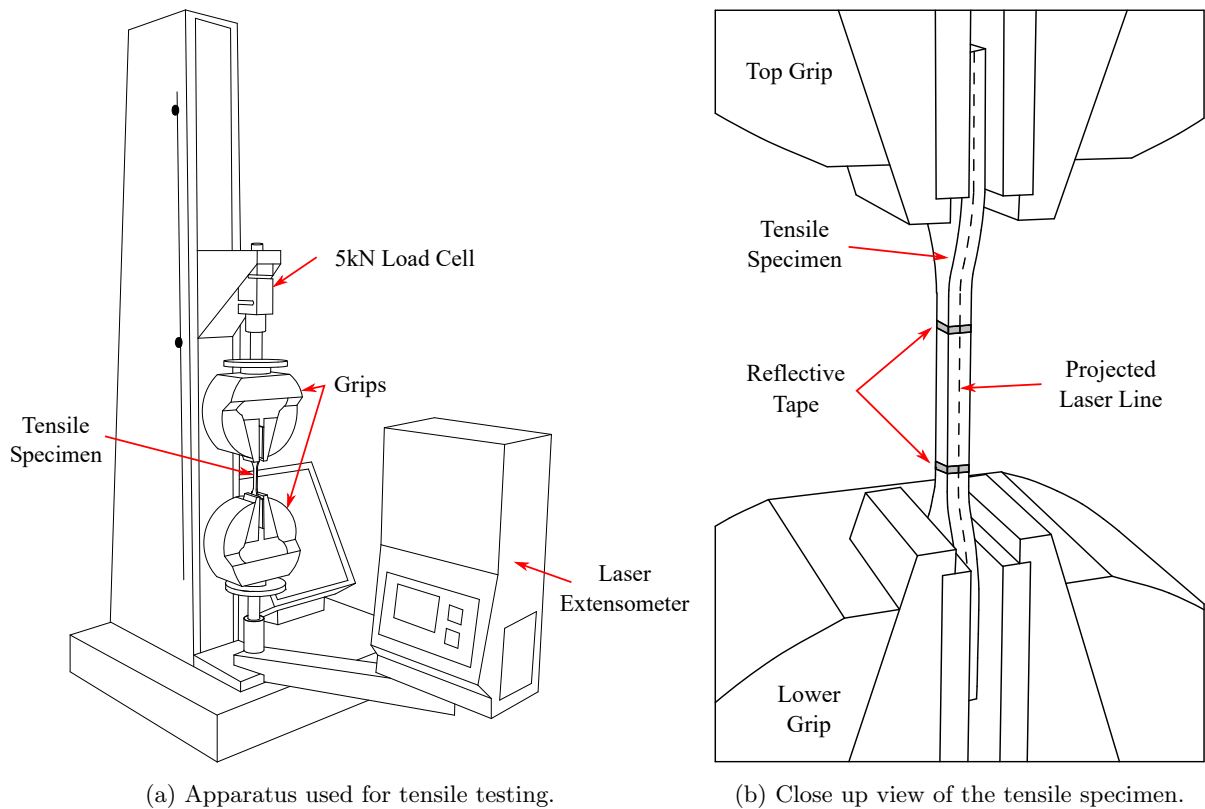


Figure 4.11: Schematic of the Tinius Olsen 5K apparatus used in tensile testing. 🚫

Tensile testing for each build material used was carried out in accordance with the methodology in ASTM D638 [454], with a type I specimen used; dimensions of this can be found in Figure 4.12, with a detailed protocol found in Appendix A.3. A minimum of 5 specimens were tested, with the Young’s Modulus (E), Ultimate Tensile Strength (σ_{uts}), and Elongation at Break (ε_{max}) determined to charac-

²Results in this section have been published in [451] (data available in [452]).

³Additional tensile testing was carried out throughout the project, utilising the same methodology as specified here. Details for all experiments are shown in Appendix C.1

⁴Additional experiments in Appendix C.1.1 focused on the effect of powder reuse (testing virgin PA2200, 50/50 used / virgin PA2200, and used PA2200 – no additives).

⁵Additional experiments in Appendix C.1.2 focused on the effect of additive loading (testing PA2200, 0.3% B45003, 0.3% B65003, 0.5% B65003, and 1% B65003).

⁶Additional experiments in Appendix C.1.3 show a preliminary experiment on the effect of steam autoclaving PA12 parts (then expanded on in Section 4.3.1).

⁷Additional experiments in Appendix C.1.4 detail trials of the microcomposite feedstock (1% B65003) in High Speed Sintering, and the comparison to LS.

terise the mechanical properties. The “Horizon” software was used to calculate E , with σ_{uts} and ε_{max} subsequently calculated from the stress-strain data using MATLAB.

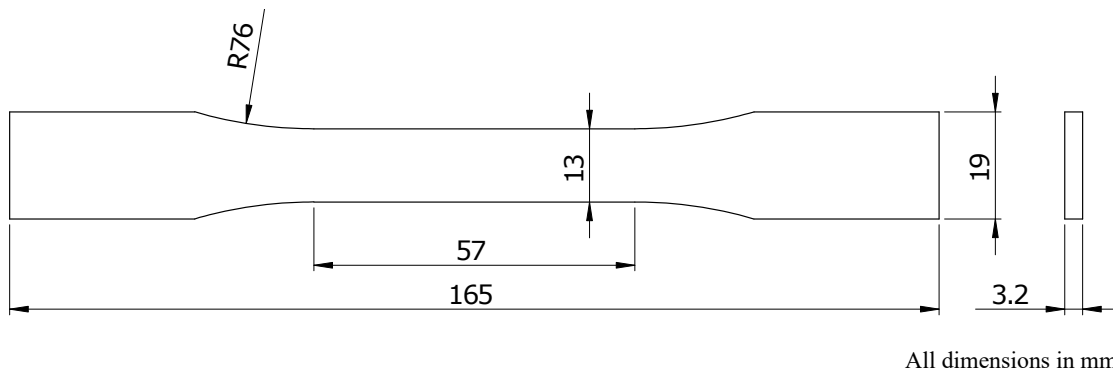


Figure 4.12: Nominal dimensions of the Type I test specimens used for tensile testing [451].

To create the test specimens, the 3D CAD model was converted into STL format and exported into Magics 22.0. The test specimens were positioned in the build area and labelled to track the position of individual specimens in the build; the labelling was positioned in the large end tabs so as not to affect the tensile testing. A minimum vertical spacing of 1 mm was kept between every part during the print, with the parts positioned away from the edges of the build area; see Appendix A.1 for build details.

Results⁸

The results from tensile testing can be seen in Figure 4.13, where the stress-strain curves can be seen for the individual specimens (Figure 4.13a) alongside the properties for the materials (Figures 4.13b–d). In this, the stress-strain curves for all the specimens tested appear to be very similar to one another, with the calculated properties confirming this, only showing small differences between the three materials.

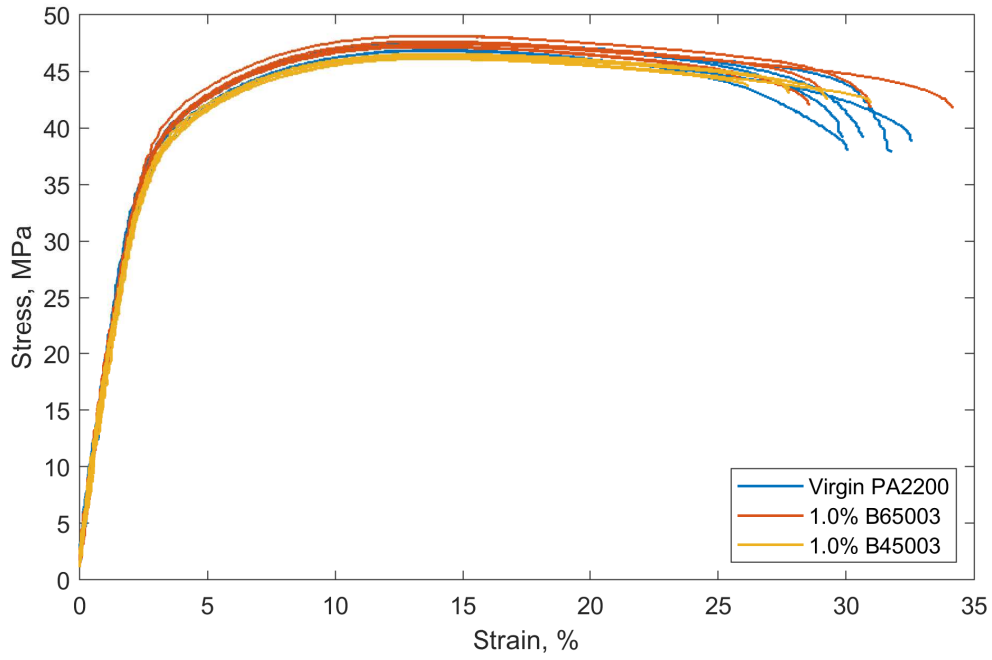
In order to determine whether there was a significant difference between the measured values, a 2 sample Welch’s t -test was carried out to compare the materials to each other. The resulting p -values are shown in Table 4.4, where a value of $p < 0.05$ indicates that the mean values were significantly different.

Discussion

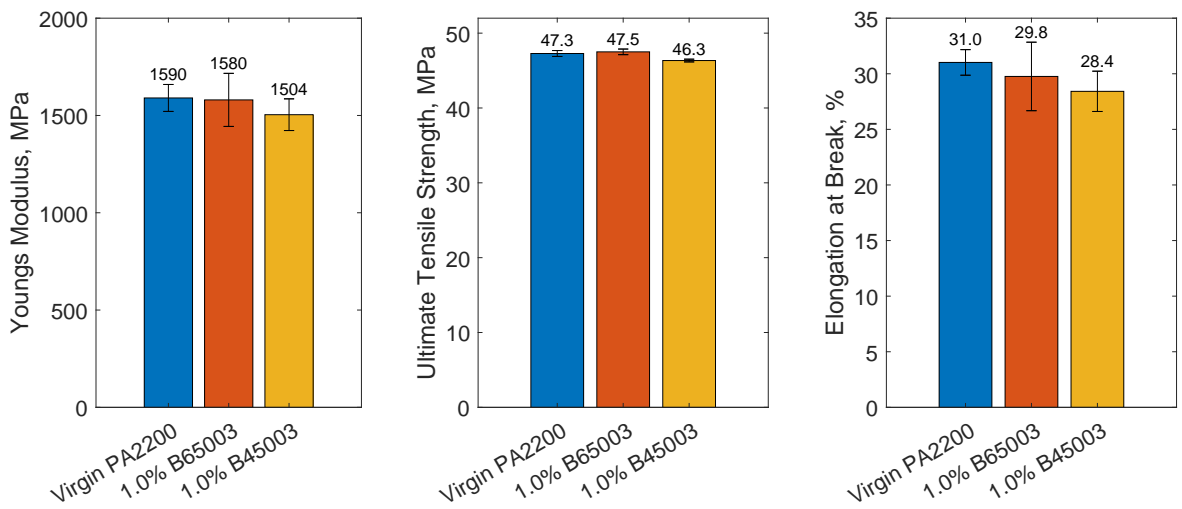
The results shown in Figure 4.13 appear very similar for all three materials; however, the results of the 2 sample t -tests (Table 4.4) show that there was a statistically significant difference in some cases. All the measured properties for Virgin PA2200 and 1.0% B65003 were shown to be equal, whereas the 1.0% B45003 showed slightly lower values of σ_{uts} and ε_{max} compared to the virgin PA2200. Although the numbers were shown to be statistically different, the magnitude of these differences were small; in a practical sense, this will likely render the differences unimportant.

In this research, the measured similarity between the PA2200 and the microcomposite parts constituted the ideal scenario, with the additives able to be incorporated for their added functionality without additional consideration needed for the mechanical properties. While any measured differences would not have been disastrous for the project, results of the tensile testing allowed further testing to focus on the microstructure and functionality, rather than on additional characterisation of the mechanical properties.

⁸Mean measurements of the tensile specimens printed in each build can be found in Appendix A.2.



(a) Stress-strain curves from tensile testing.



(b) Young's Modulus (E).

(c) Ultimate Tensile Strength (σ_{uts}).

(d) Elongation at Break (ϵ_{max}).

Figure 4.13: Results of the tensile testing, shown is the mean \pm standard deviation. 🚫

| | 1.0% B65003 | 1.0% B45003 |
|-------------|-------------|-------------|
| PA2200 | 0.889 | 0.111 |
| 1.0% B65003 | – | 0.323 |

(a) Young's Modulus.

| | 1.0% B65003 | 1.0% B45003 |
|-------------|-------------|--------------|
| PA2200 | 0.393 | 0.004 |
| 1.0% B65003 | – | 0.001 |

(b) Ultimate Tensile Strength.

| | 1.0% B65003 | 1.0% B45003 |
|-------------|-------------|--------------|
| PA2200 | 0.430 | 0.031 |
| 1.0% B65003 | – | 0.432 |

(c) Elongation at Break.

Table 4.4: Statistical comparison of tensile test data. Shown are p -values, where $p < 0.05$ (shown in bold) indicates a statistically significant difference.

4.2.2 Part Thermal Properties

Another check to determine whether the inclusion of the additives had changed any of the properties of the printed parts, was to determine their thermal properties using Differential Scanning Calorimetry (DSC).

Methodology

A description of DSC can be found in Section 4.1.3, with the same protocol used in this section. Samples were taken from the fracture surface of the tensile specimens (Section 4.2.1), with small pieces removed to make a total mass of approximately 7 μg . These were then processed in the same manner as the powders, with the heat flow measured from 30–220°C at a rate of 10°C/min and back to 30°C at the same rate.

Results

An annotated example of DSC heat flow measurements for a printed part is shown in Figure 4.14. Note that this is very similar to the powder measurements made in Section 4.1.3, with the difference of an additional peak ($T_{m,2}$) found after the first melt peak. The results for the pure PA2200 parts, and of the 1% B65003 and 1% B45003 microcomposites can be found in Figure 4.15, with all the curves showing very similar results.

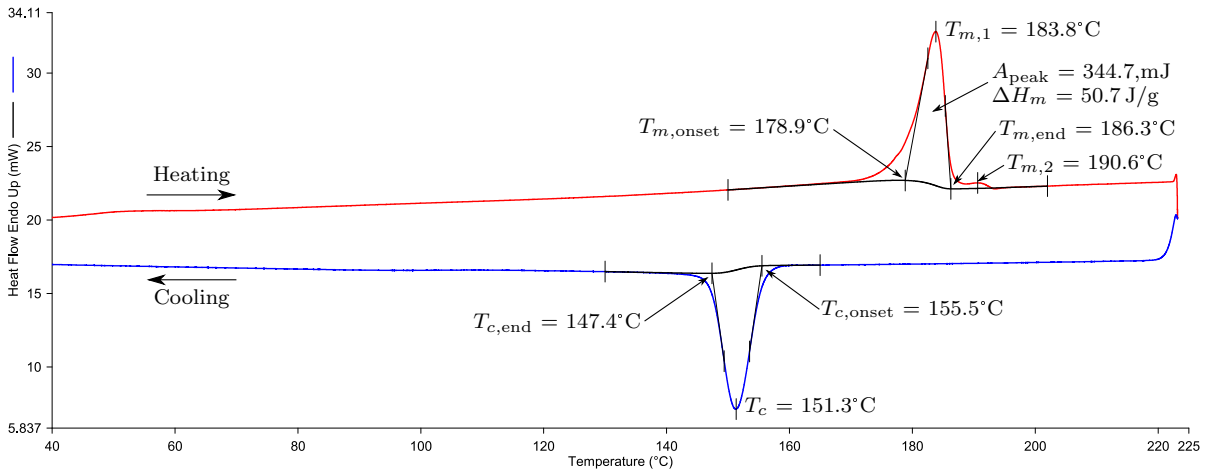


Figure 4.14: Example of a DSC curve for a printed part processed in the software, split into heating (red) and cooling (blue), along with the values calculated. Shown is a PA2200 + 1% B65003 part. 🚫

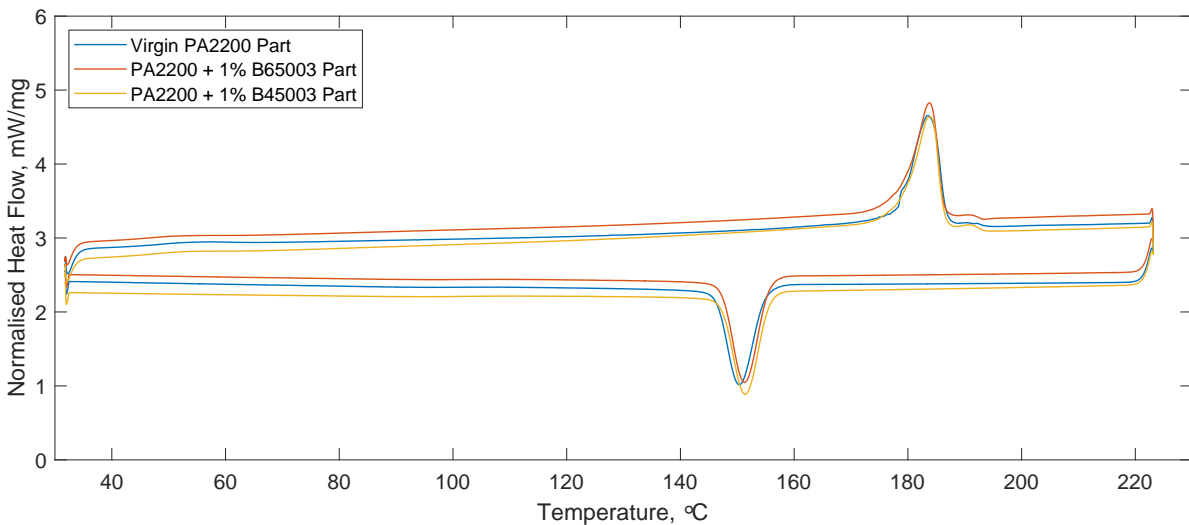


Figure 4.15: DSC of Laser Sintered parts, with PA2200, PA2200 with 1.0% B65003, and PA2200 with 1.0% B45003 shown. 🚫

The values extracted from the heat flow curves are shown in Table 4.5 alongside the calculated value of X_c (see Section 4.1.3 for details).

| Material | $T_{m,onset}$ (°C) | $T_{m,1}$ (°C) | $T_{m,end}$ (°C) | $T_{m,2}$ (°C) | ΔH_m (J/g) | X_c (%) | $T_{c,onset}$ (°C) | T_c (°C) | $T_{c,end}$ (°C) |
|--------------------|-----------------------|-------------------|---------------------|-------------------|-----------------------|--------------|-----------------------|---------------|---------------------|
| PA2200 | 178.02 | 183.53 | 186.79 | 190.35 | 54.22 | 25.9 | 154.90 | 150.45 | 146.41 |
| PA2200 + 1% B65003 | 178.85 | 183.84 | 186.27 | 190.62 | 50.69 | 24.2 | 155.51 | 151.32 | 147.38 |
| PA2200 + 1% B45003 | 178.82 | 184.02 | 186.40 | 190.80 | 52.01 | 24.8 | 155.67 | 151.43 | 147.35 |

Table 4.5: DSC results for the printed parts.

Discussion

For all the materials tested, the melting temperatures (onset, peak, and end) can be seen to be practically identical, with no significant differences shown. As well as suggesting that the inclusion of the additives did not affect these temperatures, this also suggests that the preparation of the samples did not have an effect on the results; with each sample comprised of small shavings of the parts made by hand with a scalpel. As a manual process, the uniformity of these shavings was not guaranteed, however the low levels of variation act to validate the method used.

The second melt peak ($T_{m,2}$) can be seen in all of the parts in Figure 4.15, a feature not previously seen in the powder testing. This is indicative that the powder was not fully melted during printing, with the different crystalline structure in the powder registering as distinct compared to the otherwise melted and recrystallised material (see Section 2.3.3 for more details). Although in an ideal process the parameters used in printing would result in complete melting of all the powder, the size of the measured secondary peaks is small, suggesting that the parameters used were close to an EMR of 1 and were appropriate for the material.

The crystallinity in microcomposites can be seen to be slightly lower than in PA2200, with values of 24.2% and 24.8% (for 1% B65003 and 1% B45003 respectively) compared to 25.9% for PA2200. As with the powder tests (Section 4.1.3), part of this difference can be explained simply by accounting for the additional, unreactive, mass of the glass additives; resulting in values of 24.4% and 25.1% for the surrounding polymer in the 1% B65003 and 1% B45003 microcomposites respectively. Although small, this difference could affect other properties in the part, such as the water uptake. Although not usually of much interest, the potential antimicrobial effect of the parts relies on the uptake of water and release of Ag^+ , making it relevant in this instance.

4.2.3 Surface Composition⁹

As an initial visual check of the additive dispersion on the surface of the printed parts, and to check that the additive had not been destroyed during printing, Scanning Election Microscopy (SEM) and Energy-dispersive X-ray Spectroscopy (EDX) were used. These allowed the particles to be identified visually from their morphology (with SEM) and through their chemical composition (with EDX).

Methodology

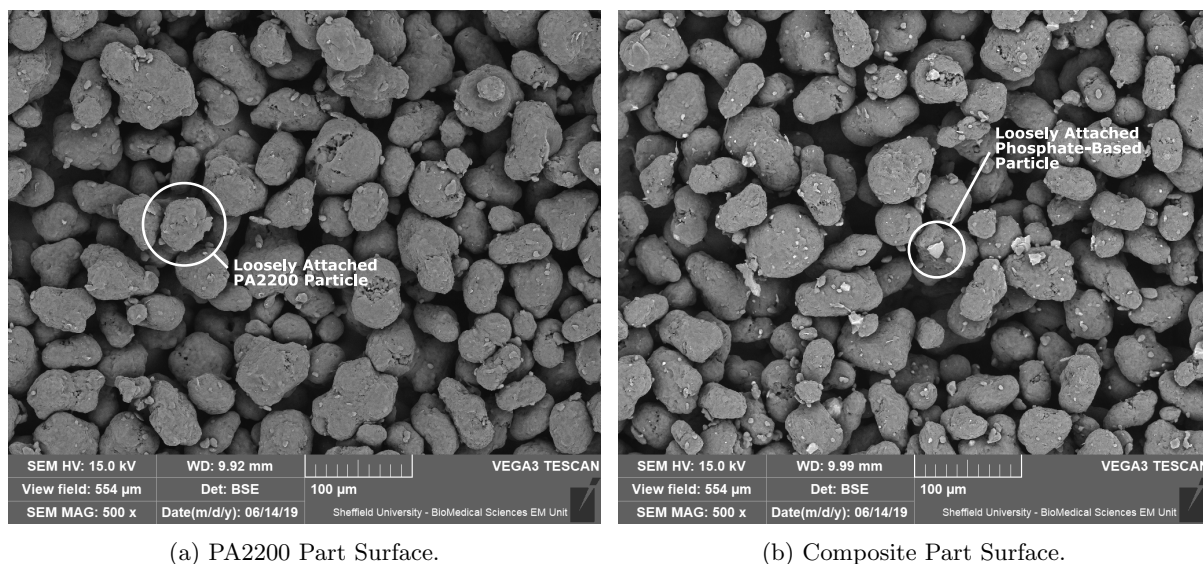
For both SEM and EDX of the printed parts, samples were first gold sputter-coated, then imaged using a TESCAN VEGA3 SEM with an accelerating voltage of 15 kV. In order to highlight the differences in materials, back-scattered electrons were detected. For EDX, the attached Oxford EDX analysis was used and whole area maps were produced of the elements detected by the software (AZtec, Oxford instruments).

Results

The SEM images of both a pure PA2200 part and a microcomposite part containing 1.0% B65003 are shown in Figure 4.16 [451]; by comparing these two images, the additive can be identified in Figure 4.16b as the brighter, more angular features.

A summary of the spectra detected with EDX for the B65003 powder and the PA2200 with 1.0% B65003 part is shown in Table 4.6. In this, it can be seen that although silver is present in the additive, it appears in relatively small amounts, too low to be detected in the EDX images of the printed part surfaces. For

⁹Results in this section have been published in [451].



(a) PA2200 Part Surface.

(b) Composite Part Surface.

Figure 4.16: SEM view of printed part surfaces, with a pure PA2200 part (a) and the composite part (b) where the additive can be seen to be brighter than the surrounding PA2200. Modified from [451].

| Sample | Weight percentage \pm Standard Deviation / % | | | | | | |
|----------------------|--|----------------|----------------|---------------|---------------|---------------|---------------|
| | O | C | P | Ti | Mg | Ca | Ag |
| B65003 | 63.6 \pm 0.4 | 16.5 \pm 0.4 | 12.6 \pm 0.1 | 0.0 \pm 0.0 | 3.5 \pm 0.0 | 2.9 \pm 0.0 | 0.9 \pm 0.1 |
| PA2200 + 1.0% B65003 | 72.5 \pm 0.1 | 27.1 \pm 0.1 | 0.2 \pm 0.0 | 0.1 \pm 0.0 | 0.0 \pm 0.0 | 0.0 \pm 0.0 | 0.0 \pm 0.0 |

Table 4.6: Elemental composition of B65003 and the composite part obtained from EDX analysis.

this reason, the distribution of Phosphorus, Oxygen, Calcium and Magnesium were instead used as a means of identifying the additive in the microcomposite part.

The maps of all the detectable elements are shown in Figure 4.17; with the original SEM image shown in Figure 4.17a and the individual element maps shown in Figures 4.17b–i. In these, the additive can be clearly identified in the maps of phosphorus, oxygen, calcium and magnesium (Figures 4.17d–g).

Discussion

Taking a closer look at Figure 4.17, each of the different element maps can be attributed to features which would be expected inside an LS part. The first two maps (Figures 4.17b,c) show the gold coating that was applied to the parts and detect the carbon present in the polyamide powder, both of which covers the entire map. Similarly, the traces of silicon and titanium (Figures 4.17h,i) are likely to be additives included in PA2200 by the manufacturer, as flow enhancers and whiteners respectively (see Section 2.6.4 for more on additives included in commercial LS powders).

From the EDX spectra (Table 4.6) it can be seen that although there are small amounts of silver present in the additive, the concentration is small enough that it does not register on the surface of the part. The other elements in the additive, namely Phosphorus, Oxygen, Calcium, and Magnesium, are therefore a better indicator of the additive location (shown in Figures 4.17d–g). Although the area analysed in these images is small, these show a relatively even dispersion of the additive over the part surface. While not a conclusive measure of the dispersion, as an initial indicator, these results do not suggest any major issues with the mixing of the powders or distribution of the additive.

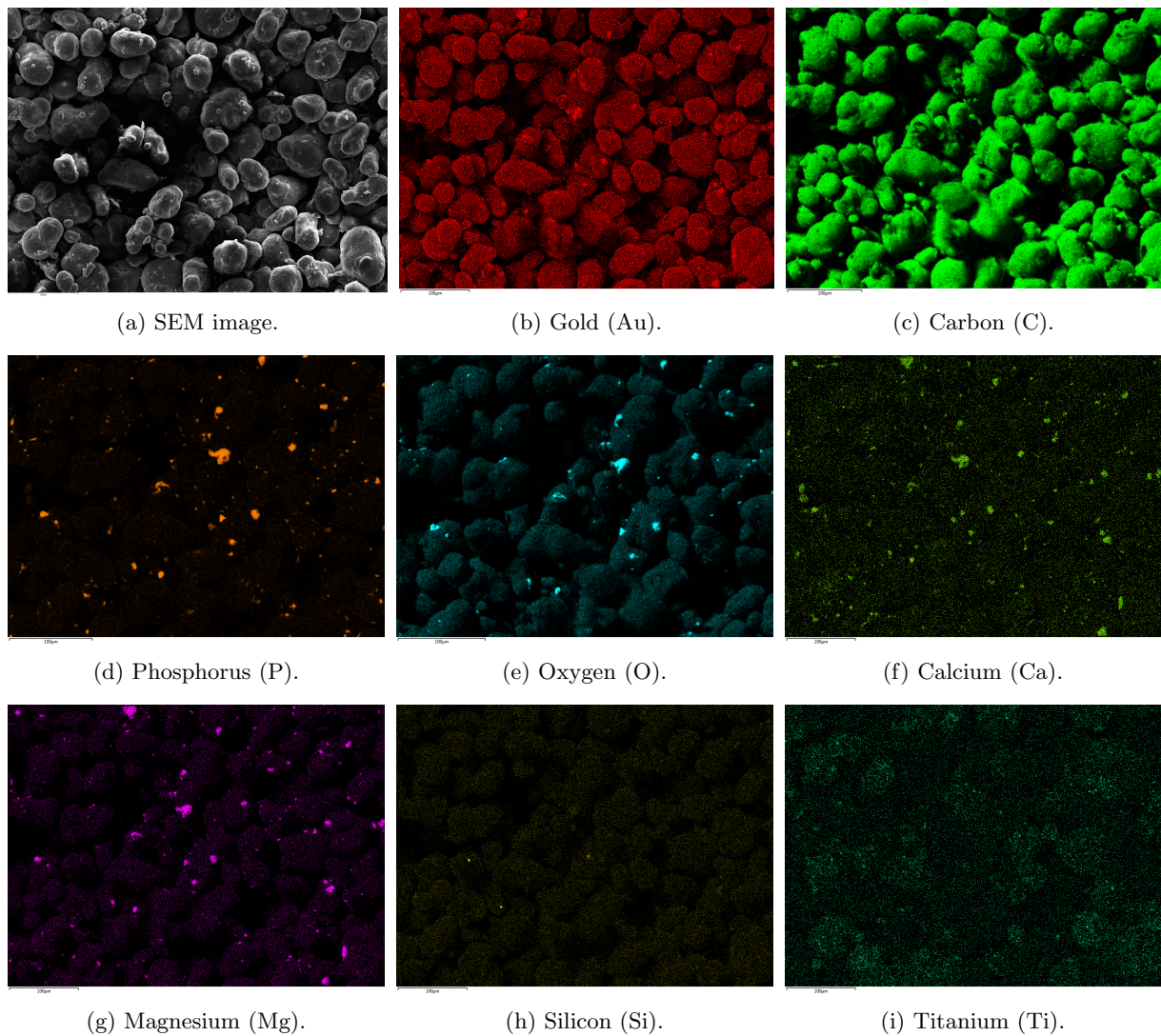


Figure 4.17: SEM and elemental maps on the surface of a microcomposite part obtained with EDX. Elements P, O, Ca, and Mg are indicative of the additive location, Au is from the gold coating of the samples, whereas Si and Ti are thought to be additional additives in the PA2200 powder from the manufacturer. 🚫

4.2.4 Microstructure

The focus of this section and Section 4.2.5 are on the use of X-Ray Computed Micro-Tomography (Micro-CT) to analyse the microcomposite parts. As this was a novel use of the technology, all the content shown here has been published in the Rapid Prototyping Journal as “Micro-CT for analysis of Laser Sintered microcomposites” [260] (data available in [453]), with additional content published in [451]. All experimental work and writing in this section was carried out by the author unless specified.

Methodology

To analyse the microstructure of the parts, micro-CT was used. The basic principle is shown in Figure 4.18, where multiple 2D x-ray images are taken through the side of a component at varying angles; these images are then reconstructed into an image stack of top-down views through the thickness of the part, which can then be used for analysis.

In order to minimise the potential for scanning artefacts [455], cylindrical specimens measuring 5×5 mm ($D \times L$) were created for scanning. A photo of the printed parts can be seen in Figure 4.19.

The parts were scanned using a Skyscan 1172 MicroCT Scanner; with the following parameters: voltage 40 kV, current $144 \mu\text{A}$, no filter, reconstructed voxel size $4.87 \mu\text{m}$, rotation 180° , rotation step 0.35° , and a total scan time of 18 minutes; the detector resolution was 4000×2000 pixels (binned to 2000×1024). For these parameters, the voltage and filter affect the ability of the x-ray beam to penetrate the sample;

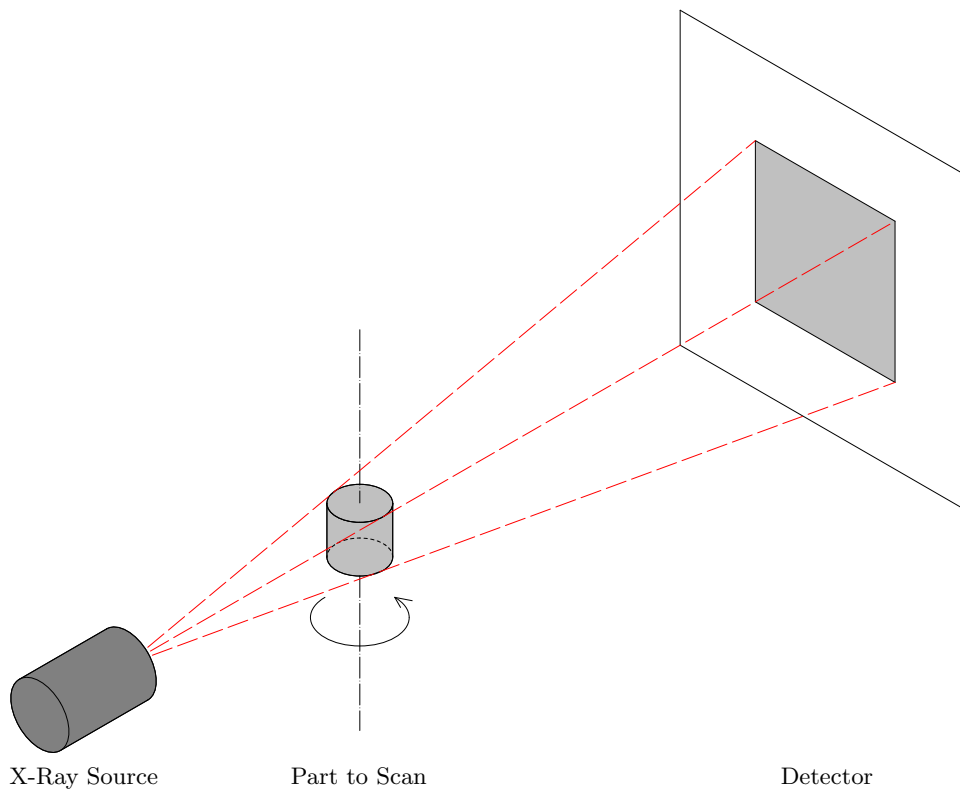


Figure 4.18: Schematic diagram of Micro-CT [260]. 🚫



Figure 4.19: Photo of the specimens printed for micro-CT scanning, showing (left to right) virgin PA2200, 1% B65003 and 1% B45003 [260]. 🚫

whereas the pixel size, rotation and rotation step affect the quality and clarity of the reconstructed data. The settings used here were selected based on a previous unpublished optimisation for a similar geometry and material (LS PA2200) carried out by another member of the research group.

Reconstruction and Thresholding

In order to analyse the microstructure of the parts, the scan data first had to be processed into a suitable form. This comprised of three steps, namely reconstruction of the raw data, selection of a region of interest (ROI), and applying a threshold to the greyscale image to obtain a binarised value. An example cross-sectional slice for each material is presented in Figure 4.20 at each of these stages.

The scan data were reconstructed in NRecon, with a contrast setting of 0–0.35 used to differentiate between PA2200 (part) and air (pores). The region of interest (ROI) was defined as a 3.5×2.5 mm (D×L) cylinder positioned in the centre of the specimen. The last step shown in Figure 4.20 was to apply a threshold to the ROI in each case; this was determined visually by the operator and varied depending on the focus of the analysis.

To analyse the individual pores, a threshold of 0–35 was applied to identify the pores as features. To

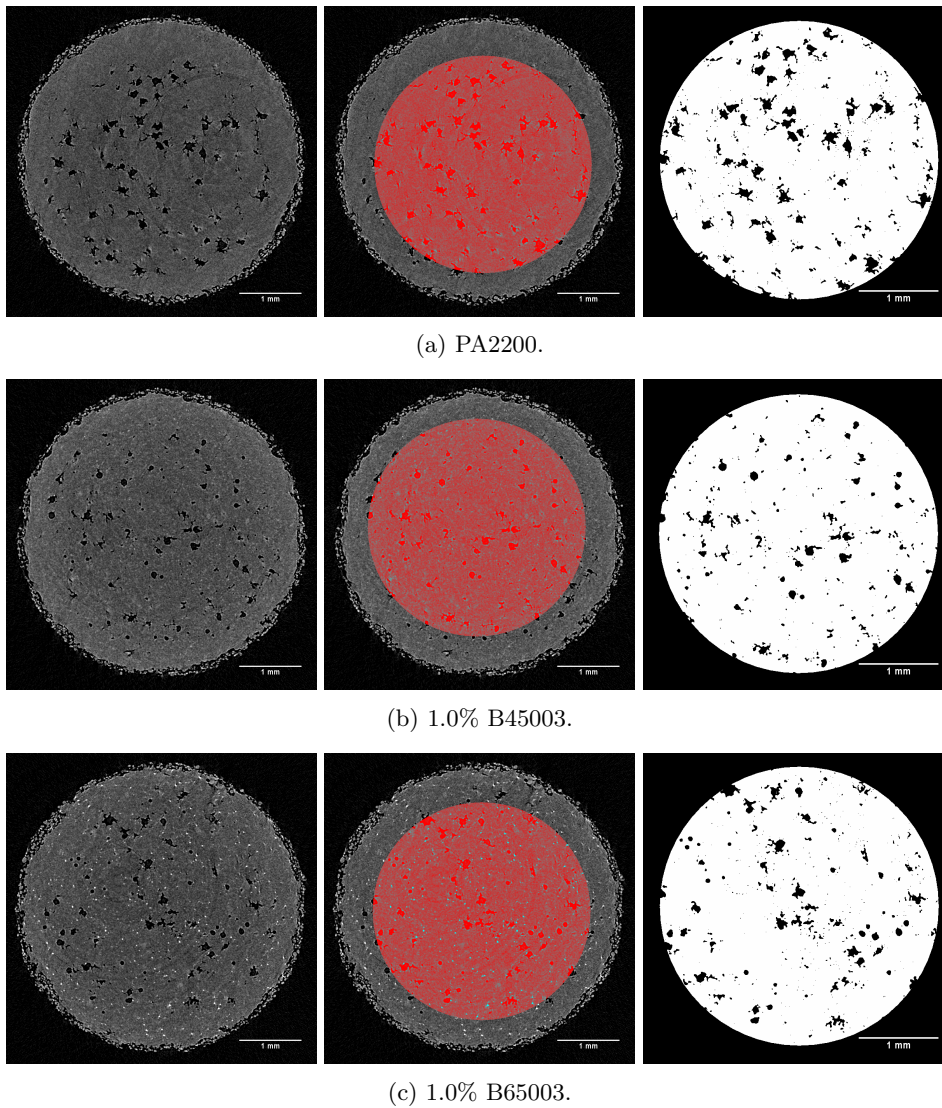


Figure 4.20: Example slices of the data from Micro-CT scanning. Showing (left to right), the reconstructed slice, ROI (shown in red), and pores (shown in black) [260].

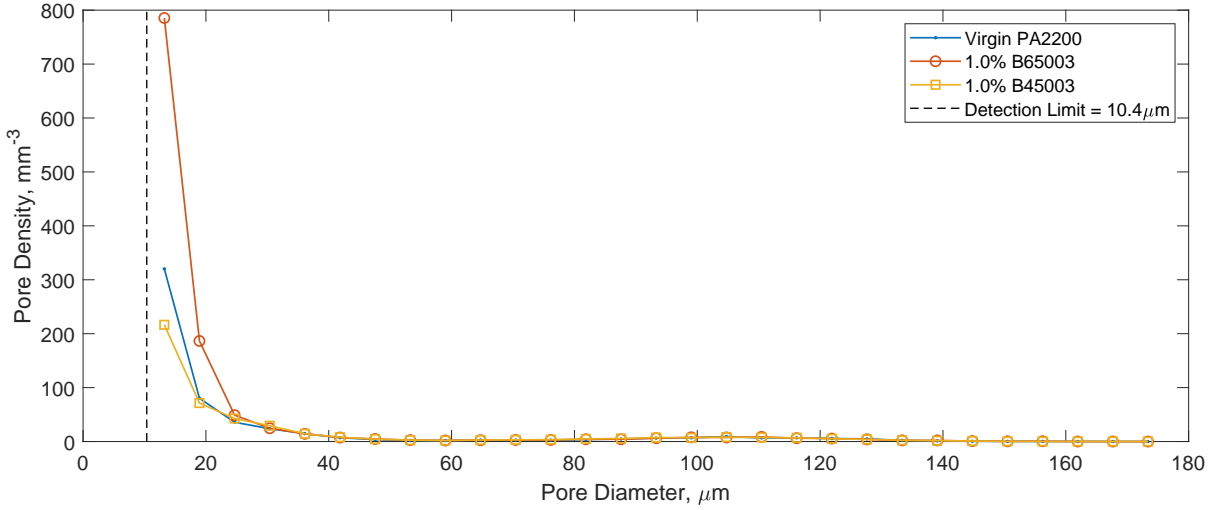
remove any noise from the scan data, a sweep was carried out to remove detected features < 8 voxels in size. The value of 8 voxels is commonly used as it represents a $2 \times 2 \times 2$ cube; another less common but equally valid value to use is 27 voxels ($3 \times 3 \times 3$) which eliminates even more features from the analysis [263, 304]. This criteria depends on the scan quality and noise levels. The combination of low-density parts and high scan quality used in this study resulted in low levels of noise, meaning that the smaller number of voxels could be used reliably.

Pore Size Distribution

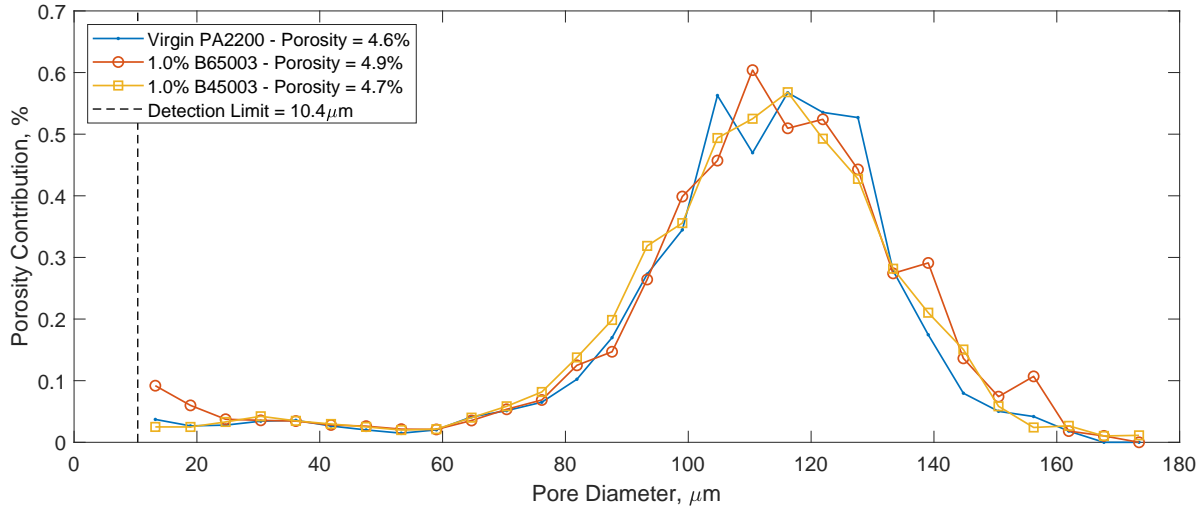
The porosity analysis was carried out using CTAn, with the volume (V_{actual}), major diameter (d_{maj} – the maximum distance between opposite walls) and surface area (A_{actual}) of each pore measured. The volume equivalent diameter (d_{vol}) was calculated from the measured volume using Equation 4.2; this was used to quantify the size of the features.

$$V_{\text{Sphere}} = \frac{4}{3}\pi \left(\frac{d_{\text{vol}}}{2}\right)^3 \Rightarrow d_{\text{vol}} = 2 \left(\frac{3V_{\text{actual}}}{4\pi}\right)^{\frac{1}{3}} \quad (4.2)$$

The results of the porosity analysis are shown in Figure 4.21, with all materials showing similar results. The measured values of d_{vol} are shown, with the overall porosity values (determined by summing all the values of d_{vol}) found to be 4.9%, 4.7% and 4.6% for the 1% B65003, 1% B45003 and Virgin PA2200 respectively.



(a) Diameter by density of pores.



(b) Diameter by volume contribution.

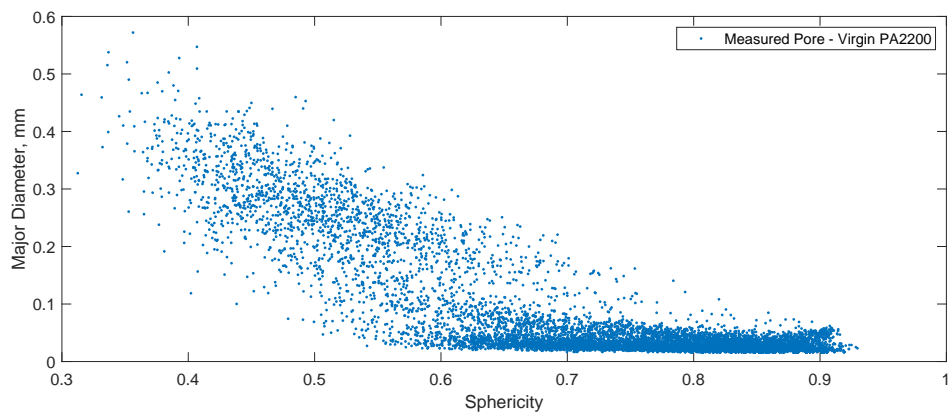
Figure 4.21: Pore volume equivalent diameters for Virgin PA2200, 1.0% B45003, and 1.0% B65003. Here it can be seen that there is no apparent difference in the porosity distributions for any of the tested materials [260].

Pore Morphology

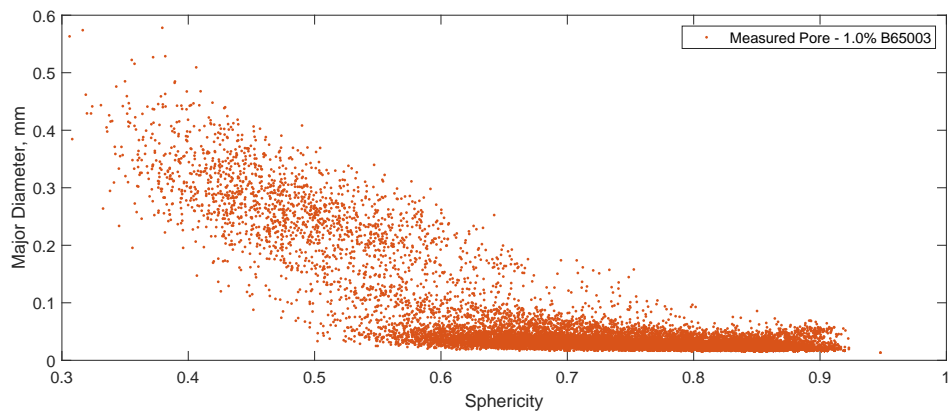
In this research, the sphericity (ψ) was used as the single metric to describe the feature morphology due to its simplicity. Other values including orientation, presence of trapped powder, and connectivity could also be chosen if more detail was required. The value of ψ was calculated from A_{actual} and the surface area of the volume equivalent sphere (A_{vol}) using Equation 4.3.

$$\psi = \frac{A_{\text{vol}}}{A_{\text{actual}}} = \frac{\pi d_{\text{vol}}^2}{A_{\text{actual}}} = \frac{\sqrt[3]{\pi(6V_{\text{actual}})^2}}{A_{\text{actual}}} \quad (4.3)$$

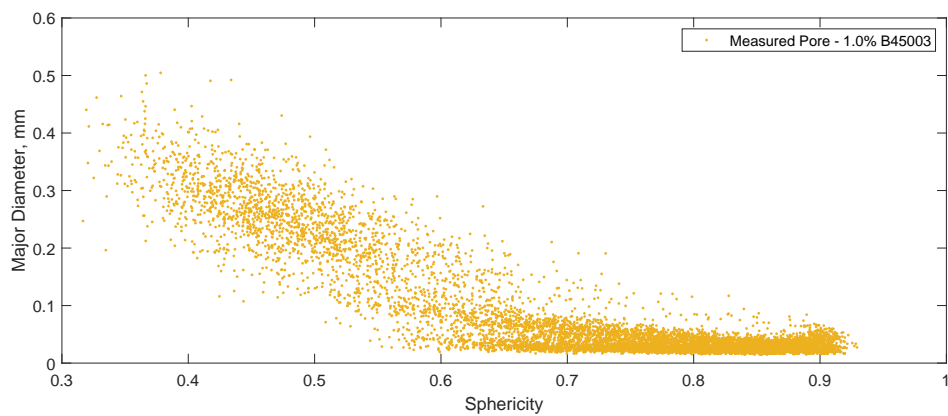
The measured sphericity (ψ) of the pores was found to relate to the major pore diameter (d_{maj}), with larger pores being less spherical. This is shown in Figure 4.22, where the relationship of ψ and d_{maj} is shown. For smaller pore sizes (those approaching the minimum detectable feature size), partial volume effects are likely to contribute to this trend, with the resolution of the scan creating an artificial smoothing effect. The reason for showing the major diameter of the pores, rather than the volume equivalent diameter, is due to the likely impact on the mechanical properties of the part. The pores within the parts can be approximated to act as cracks, meaning that the maximum (or major) diameter of the pore gives a value equivalent to the crack length; this is explored further in the next section.



(a) Virgin PA2200.



(b) 1% B65003.



(c) 1% B45003.

Figure 4.22: Relationship of Sphericity (ψ) and major pore diameter (d_{maj}). It can be seen that for all measured pores, there appears to be a negative correlation between the major diameter and the sphericity of the pores [260]. 🚫

Critical Pore Size

To determine whether the pore size was likely to have an impact on the mechanical properties of the printed parts, Linear Elastic Fracture Mechanics (LEFM) was used; a method which has been previously used for similar applications [238]. For this, the pores were assumed to behave as embedded cracks in a plate of infinite dimensions. The critical crack size (a_c) could then be calculated using Equation 4.4 [456] and could be compared to d_{maj} , to determine whether this presents an issue.

$$K_{Ic} = Y\sigma_f\sqrt{a_c\pi} \quad \Rightarrow \quad a_c = \frac{1}{\pi} \left(\frac{K_{Ic}}{Y\sigma_f} \right)^2 \quad (4.4)$$

In Equation 4.4, K_{Ic} is the critical stress intensity factor for a mode I crack in the case of plane strain, Y is the calibration function accounting for the crack geometry, and σ_f is the stress at fracture. The value of Y will vary depending on the exact geometry of each pore. While this is possible to obtain this from micro-CT data, a value of $Y = 1$ has been used here representative of a through thickness crack; in reality, the rounded edges of the pores mean this is likely to be lower and this is simulating the “worst case” scenario. The value of K_{Ic} can be determined experimentally for a given material, in this instance a value of $K_{Ic} = 3.25 \text{ MPa}\sqrt{\text{m}}$ was chosen, which was previously measured as the most critical value of K_{Ic} in LS PA2200 parts [457]. The stress at fracture has been arbitrarily chosen to be 40 MPa, a value slightly lower than the measured yield stress of the material, meaning that it represents a premature failure of the part in the elastic region. Using Equation 4.4, a critical crack length (a_c) of 2.1 mm was found, relating to a critical pore diameter (d_c) of 4.2 mm.

While this method provides an initial estimate of the effects on the mechanical properties, the positioning and proximity of the pores to one another will also have an effect. In order to accurately account for this, more detailed studies (such as the one carried out by [458]) would have to be performed based on the actual geometry derived from the scan data.

Discussion

The distribution of measured pore sizes (shown in Figure 4.21), show that the pore sizes which contribute the highest amount to the overall porosity are those between 60 - 160 μm ; both this, and the total porosity (4.9%), were found to be consistent with previous studies focused on pure PA2200 [238, 267]. The measured sphericity (ψ - shown in Figure 4.22), indicates that the smaller pores are more spherical. While it is likely that this is the case, it is worth noting that for small features, the smoothing effect of the surface fitting algorithm (the partial volume effect) could be artificially increasing this value [459]. This effect will decrease with larger features, but if analysing very small features (in terms of number of voxels) such as the included additives, cannot be ignored. It is also worth noting, that should a more in depth analysis of the porosity be required, a smaller voxel size could be used to obtain a more accurate result.

The relationship of ψ vs d_{maj} (shown in Figure 4.22), reinforces the importance of detecting larger pores as they are more likely to act as crack initiators. The reason for this is twofold and can be explained using the LEFM in Section 4.2.4. Firstly, a larger d_{maj} is more likely to approach d_c . Secondly, the lower value of sphericity could mean a less rounded pore, effectively increasing the value of Y as the pore elongates, causing it to act more as a linear crack. Visually, this means that the pores appearing in the top left portion of Figure 4.22 pose the largest risk of acting as crack initiators. However, the largest measured value of d_{maj} was 0.58 mm and as $d_{\text{maj}} \ll d_c$, the measured pore sizes are unlikely to lead to fast fracture of the part within the elastic region.

The key takeaway from both the measured pore size distributions and the sphericity / major diameter relationship in terms of the microcomposite functionality, is that no differences were detected between the PA2200 parts and the microcomposites. This reinforces the results of the tensile testing in Section 4.2.1, where a difference in the microstructure would likely relate to a measurable difference in the overall part properties. This means that regardless of how any differences in porosity might affect factors such as the water uptake (and subsequent Ag^+ elution), the addition of additives does not appear to have changed this in the parts produced.

4.2.5 Additive Dispersion

The wealth of information available from a single micro-CT scan is both immense and often underused. To obtain information such as the microstructure and porosity in printed parts, micro-CT is now becoming the “go to” method due to its accuracy and non-destructive nature. For the microcomposite materials presented here, this also presents a new opportunity, utilising the same scan data previously used to determine the microstructure in Section 4.2.4.

The dispersion of the additives within the printed parts was likely to have a large effect on any antimicrobial efficacy. While the SEM and EDX imaging provided an initial indication of this on the part surface (see Section 4.2.3), it provided no information about the dispersion throughout the part volume. With the proposed antimicrobial action relying on the presence of the additive throughout the part, this information could both validate the processes used to manufacture the parts, and provide quality control checks in any future applications.

This section focuses on the use of micro-CT to quantitatively analyse the additive dispersion throughout the printed parts; a novel approach in LS which has been published alongside Section 4.2.4 in [260].

Methodology

The analyses shown in this section utilise the same scan data that was presented in Section 4.2.4, with the methodology for the micro-CT scanning shown in Section 4.2.4. However for these analyses, rather than using the differences in density and chemical composition to distinguish the part from air, the differences between the additive and the polymer have been exploited to focus solely on the additive within the part.

To distinguish between PA2200 and the additive, the scan data were processed in a similar manner to Section 4.2.4, using a contrast setting of 0–0.1 for the reconstruction; and a threshold of 60–255 to identify the brighter voxels as features and obtain the binary images. Figure 4.23 shows example binarised data (the same slices shown Figure 4.20) focusing on the additive. From this, it can be seen that the voxel size was too large to identify the additive for the 1.0% B45003 (Figure 4.23b), which had a particle size of $<10\ \mu\text{m}$.

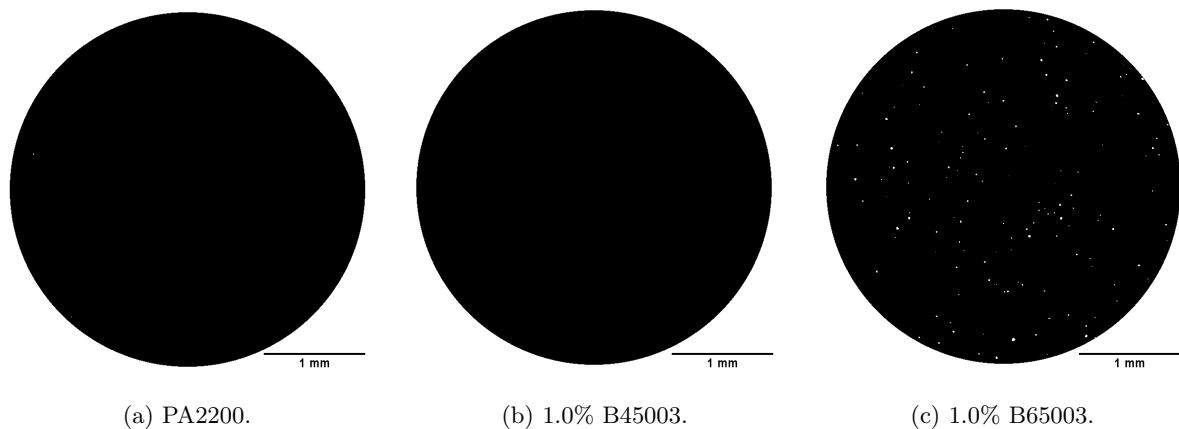


Figure 4.23: Example slices of the reconstructed and binarised data, showing the additive (in white) within the ROI. Here it can be seen that with the same post-processing, features were only identified for 1.0% B65003 (Figure 4.23c) [260]. 🚫

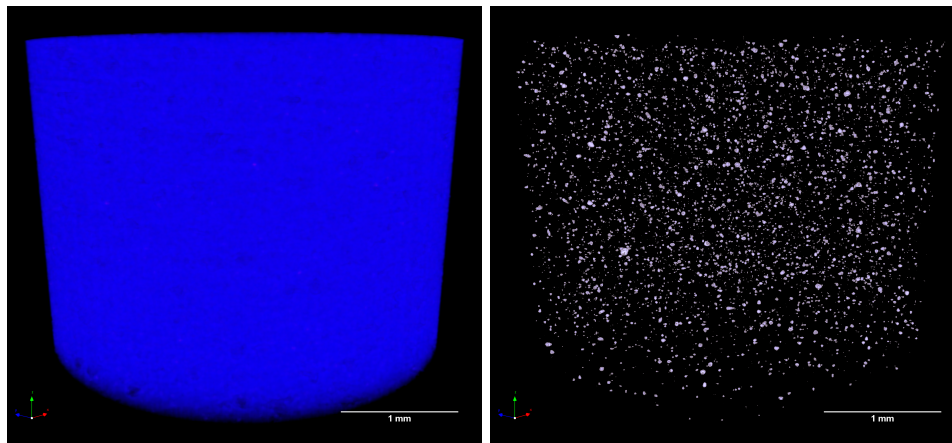
A 3D view of the scan data was created using CTvox to visualise the dispersion; this is shown in Figure 4.24, where the ROI is shown both with and without the base polymer.

From the 3D views of the data, a preliminary visual inspection of the additive was carried out. While the majority of particles appeared to be well dispersed, there were two larger “clumps” identified; one of these is shown for reference in Figure 4.25, both in the 2D reconstructed slice data and a 3D view.

While these initial observations provide a qualitative indication the the dispersion was reasonably homogeneous, further analysis was performed to obtain a quantitative measurement of the part microstructure.

Additive Analysis

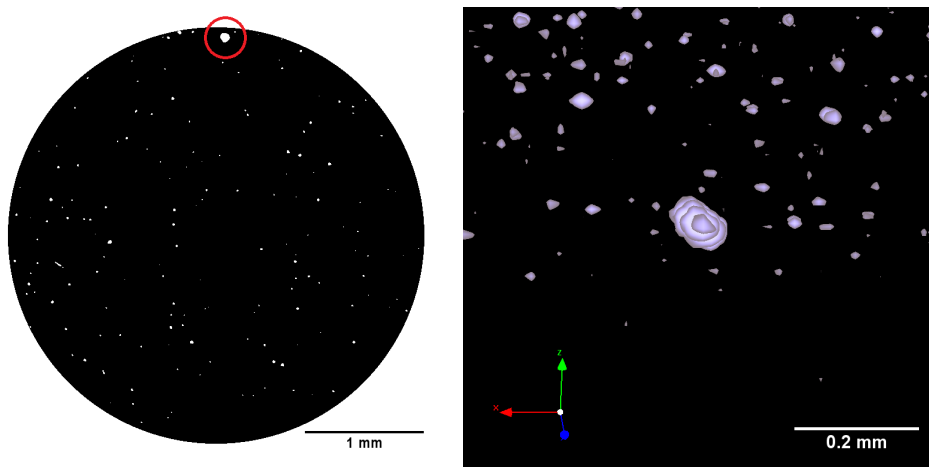
An individual object analysis was carried out on the binarised image, with the volume and positional data of each particle recorded. The analysis software used the marching cubes algorithm [460] to determine



(a) PA2200 shown in blue.

(b) Additive shown in grey.

Figure 4.24: 3D views of 1.0% B65003 scan data [260].



(a) Binarised 2D slice.

(b) 3D view.

Figure 4.25: Views of a “clump” of additive as identified from an initial visualisation of the scan data [260].

volume, making the smallest detectable feature (8 voxels) approximately $10.3\ \mu\text{m}$ in diameter for the chosen pixel size. This value represents the volume equivalent diameter of a smoothed $2 \times 2 \times 2$ voxel cube [459].

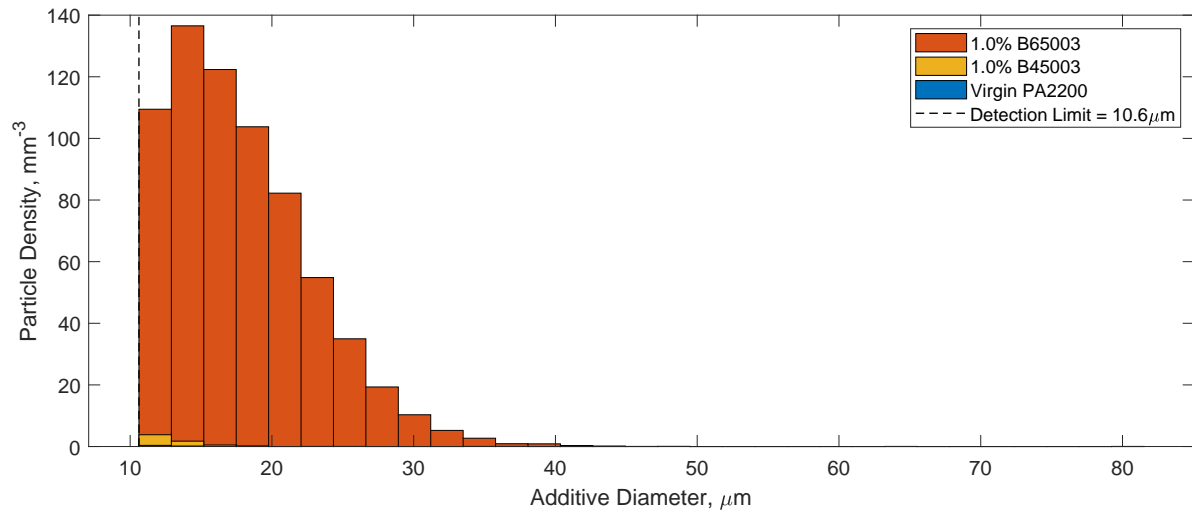
The individual particle diameters (d_{vol}) were determined in the part using the method in Section 4.2.4; these could then be compared to the pre-printed manufacturer’s specifications (diameter $< 40\ \mu\text{m}$) and the particle size analysis in Section 4.1.2 to determine whether coalescence occurred. The distribution of d_{vol} for the additive in each scan is shown in Figure 4.26; the data for each material have been superimposed onto the same graph so that a direct comparison is possible.

Spatial Analysis¹⁰

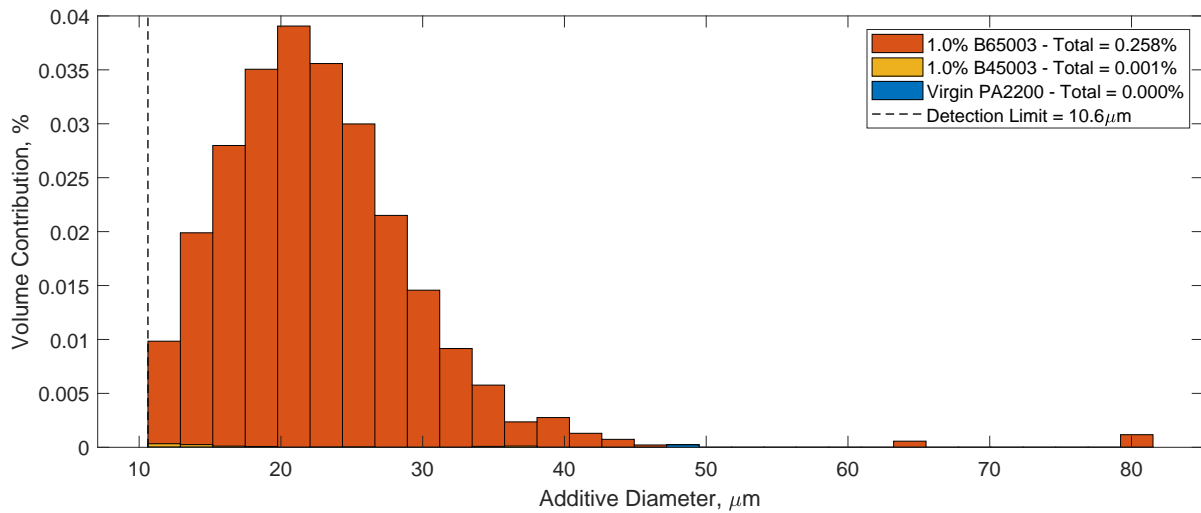
In order to determine whether the additive particles within the parts were randomly distributed, the individual particle centroids were analysed for Complete Spatial Randomness (CSR), which measures the distances of every point from every other point and compares them to a simulated randomly distributed dataset. The resulting pairwise correlation function was determined using the `spatstat` *R* package function `pcf3est` [461]. This was compared to the theoretical value (1 for a perfect distribution), as well as a simulated envelope of CSR results obtained by simulating 99 random distributions with a similar number of points and the same dimensions as the experimental data.

For the additive spatial analysis, a comparison was plotted (Figure 4.27) revealing that at length scales above about $90\ \mu\text{m}$ the distribution of additive particles conforms to CSR – the plot is close to the

¹⁰The analysis in this section was carried out by R. Turner and is included for completeness [260]



(a) Diameter by density of particles.



(b) Diameter by volume contribution.

Figure 4.26: Additive volume equivalent diameters for Virgin PA2200, 1.0% B45003, and 1.0% B65003 [260].

theoretical value and within the simulation envelope. At shorter length scales the line for experimental data falls below the simulation envelope. We propose that this is due to the physical size of the additive particles (and the PA2200 grains) making it impossible for centroids to be closer than a threshold value (of around the particle diameter).

Discussion

The scan parameters for both the additives analysed were kept the same throughout. For the larger additive (B65003), a high number of small particles were identified (Figure 4.26a) suggesting that there could be a large number of smaller particles which remained undetected. However, when compared with the volume contributions (Figure 4.26b), it can be seen that although these smaller particles may be many in number, the volume contribution of these smaller particles is small. Since detecting the presence of clumping and the dispersion of the majority of the additive throughout the part was of greatest interest, the voxel size was deemed to be sufficient for the analysis. On the other hand, the smaller additive (B45003) again showed a larger density of smaller particles, but the volume distribution did not appear to encapsulate the entire volume (which was expected to be similar in total volume to that of B65003); a smaller voxel size would therefore be required for this analysis.

To ensure that the analysis was actually detecting the additive, rather than some other feature in the material, the same analysis was run on a pure PA2200 sample (also shown in Figure 4.26). A small

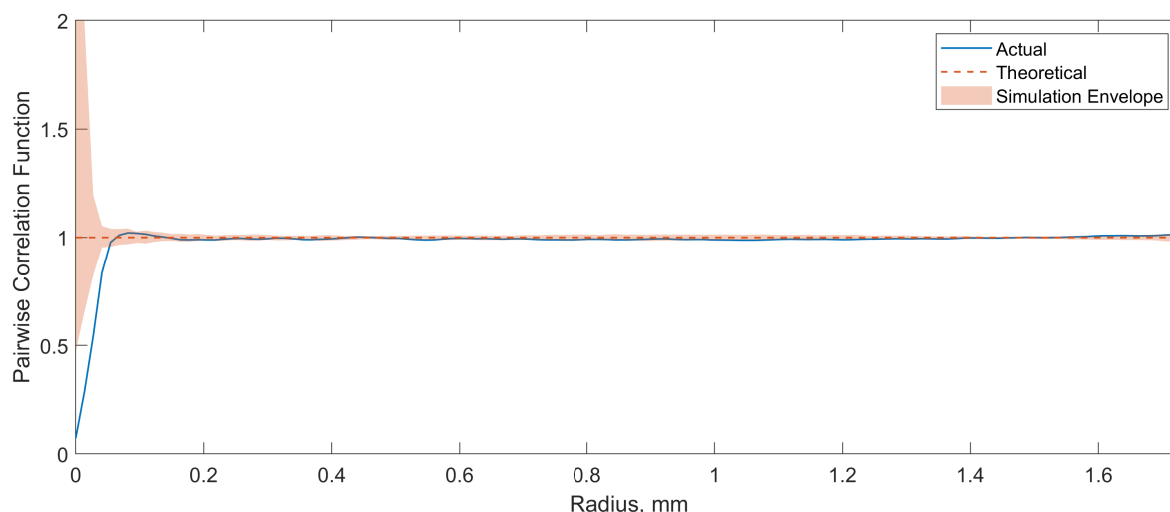


Figure 4.27: Complete Spatial Randomness (CSR) results for 1.0% B65003 [260].

number of features were detected with this, which are expected to be flow-enhancing additives included in the powder by the manufacturer [187, 236]. As these detected features were small in number and volume, the analysis was deemed to be valid.

An advantage of plotting the sizes by volume, rather than by number, was the ability to easily identify any agglomeration of the additive. The two peaks in Figure 4.26b present at $\approx 64 \mu\text{m}$ and $\approx 81 \mu\text{m}$ correspond to two “clumps” which were previously observed (the latter is shown in Figure 4.25). This volume distribution will also be independent of the voxel size used (provided the scan data is of sufficient quality), as frequency distributions can be deceptively weighted towards a large number of small particles.

From the spatial analysis, the key finding was that above $90 \mu\text{m}$ all the particles were randomly distributed. This means that all the properties affected by the additive distribution are also likely to be uniform above this length scale.

Practically, the additive analysis here validates the methods used to create the microcomposite parts; showing that the mixing of the powder feedstock was sufficient to homogenise the polymer / additive mixture, with no need to explore more complex methods of feedstock production (see Section 2.6.2). In terms of the potential antimicrobial efficacy, the results shown here crucially do not highlight any obstacles which might inhibit the proposed method of action, instead suggesting a uniform effect across the parts.

4.2.6 Silver Content

With the antimicrobial efficacy inherently linked to the amount of silver incorporated in the printing process, it was important to measure the actual amount present in the parts. There were two approaches to calculating this, one using the datasheet concentration of silver in the additive, and the other measuring the actual silver content from the printed parts experimentally.

Due to the more limited datasheet information for B45003, and the complexity of carrying out this experimentally, this section only analyses the microcomposite parts containing 1% B65003.

Methodology

The theoretical concentration of Ag^+ in the silver phosphate glass (as provided by BioCote) can be used to determine the theoretical concentration of Ag^+ in the printed parts. This calculation is shown in Equation 4.5.

$$\text{Concentration of } \text{Ag}^+ \text{ after sintering} = \frac{\text{Ag}^+ \text{ additive concentration in ppm}}{1,000,000} \times \text{Ratio of Additive} \quad (4.5)$$

To determine the concentration of Ag^+ in the parts experimentally, 1 cm^3 spheres were printed and analysed using Inductively Coupled Plasma Electrospray Mass Spectrometry (ICP-ESMS). For this, the

samples were obtained using nitric/perchloric acid digestion of the spheres. This technique measured the concentration of various metals in the parts, including silver.

Three spheres per material from random places in the build were analysed for their silver content. This provided a quantitative measurement of the amount of Ag^+ in the parts; however the dispersion of the additive within the part could not be measured using this method.

Results

The calculation of Ag^+ concentration for 1.0% B65003 using Equation 4.5 is shown in Equation 4.6; this calculates the w/w ratio of Ag^+ of the printed parts. The measured chemical composition of the parts is shown in Figure 4.28, with individual results shown in Appendix B.2.

$$\text{Concentration of } \text{Ag}^+ \text{ after sintering} = \frac{19,090}{1,000,000} \times 0.01 = 0.1909 \times 10^{-3} \Rightarrow 190.9 \text{ mg/kg} \quad (4.6)$$

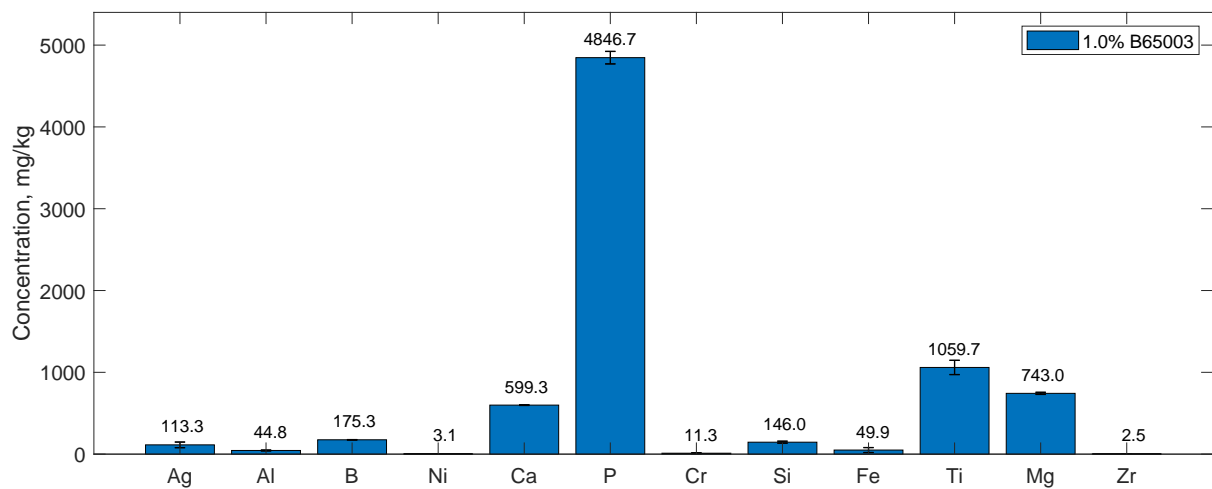


Figure 4.28: Chemical composition of the parts from ICP-ESMS analysis. 🚫

Discussion

The silver content measured using ICP-ESMS (shown in Figure 4.28) was found to be 113.3 mg/kg and was broadly similar to the predicted value of 190.9 mg/kg. The discrepancies in these values could be due to the random distribution of the additive within the build chamber, meaning that the small test specimens could be lower than the mean value for the entire build. A more likely cause of this, could be that the datasheet value was not representative of the additive used in the build. However, since the measured values are of the same order of magnitude, this discrepancy was not a cause for concern.

4.3 Part Use and Functionality

With the inherent properties of the microcomposite parts determined, the focus can now turn to characterising the properties directly relating to end-use applications and their functionality. This centres around testing the antimicrobial efficacy of the parts, with the effects of additional key processes (such as steam sterilisation) likely required in end-use applications investigated, as well as proxy measurements (such as water uptake and silver release) to more accurately determine the root causes of any differences identified.

4.3.1 Effect of Sterilisation

For any application where the initial sterility of the parts is important, the material must undergo a sterilisation process (see Section 3.3). The most common method used for this is steam sterilisation (carried out in an autoclave), with commercial marketing material for LS polyamide 12 parts often emphasising the ability of the parts to withstand the process [372, 462, 463]. Despite this, there is a remarkable lack of literature relating to the steam sterilisation of LS parts, especially in relation to the mechanical properties.

For this reason and after a preliminary experiment¹¹, it was decided to carry out a more rigorous investigation into the effects of steam sterilisation on the mechanical properties of LS parts. Due to the multitude of applications already employing this technique for polyamide 12 parts, as well as the previously observed similarities in the mechanical properties and microstructure between the polymer and the microcomposites, it was decided to focus solely on PA2200 parts; with the microcomposites expected to react in the same manner. By doing this, and by using the recommended material composition and printing parameters, it made the research more applicable to current uses, with the aim of increasing the impact.

This section investigates the effect of steam sterilisation on the mechanical properties of LS polyamide 12 parts, separately investigating the effects of autoclaving (temperature and moisture) and temperature alone on the properties. The reversibility of any changes in mechanical properties were investigated as an indicator of the root causes, and a methodology to simply measure the water content at the time of tensile testing is presented.

All the research presented here was planned, carried out, analysed, and written by the author and has been published in [270]. These results were also briefly discussed in [464].

Specimens and Tensile Testing

Tensile specimens were used in this experiment, with the same specifications and testing method used in Section 4.2.1. In total, 45 test specimens were built in a $1 \times 5 \times 9$ (XYZ) stack, in the same orientation (XY – with the longest dimension in the x-direction, parallel to the front of the machine), in the centre of a dedicated build. This ensured comparability between the samples; however it should be noted that parts built in other orientations are likely to have different properties. All parts were built with a 50/50 mix of virgin (unused) and used powder, a combination widely used in industry and recommended by the manufacturer. The default “performance” parameters for 50/50 PA2200 were used [465], these being laser power 21 W, scan spacing 0.25 mm, scan speed 2500 mm/s, layer height 100 μm and a bed temperature of 170°C. Excess powder was removed from the parts using bead blasting and compressed air.

Specimen Preparation

Some of the tensile test specimens were kept “as built”, while the remainder received a combination of either heating with steam, or heating only (henceforth referred to as the conditioning step), followed by a drying step prior to testing. These were chosen to determine the effect of autoclaving (Heat and Steam) and of heat only, with three drying methods chosen to identify the causes of any changes observed. The combinations of these sample sets are summarised in Table 4.7, where each label represents a set of $5 \times$ specimens.

Details for each of these conditioning and drying steps are shown here.

¹¹Details of the preliminary experiment can be found in Appendix C.1.3. In this, one set of tensile specimens was steam autoclaved and air-dried for 24 hours and compared to an “as built” set. A large difference was observed, so the samples were then oven-dried to explore whether this was significantly different between the two sets.

| | As Built | Heat and Steam | Heat Only |
|------------|----------|----------------|-----------|
| No Drying | A | B | C |
| Air-dried | D | E | F |
| Oven-dried | G | H | J |

Table 4.7: Combinations of conditioning (As Built, Heat and Steam, and Heat Only) and drying (No Drying, Air-dried, and Oven-dried) for each sample set.

Conditioning

To separately investigate the combined effects of autoclaving and of temperature alone, three different conditioning methods were used:

- As Built – no conditioning (control group).
- Heat and Steam – samples were subjected to steam at 121°C for 20 minutes. Specimens were placed in autoclave pouches for steam sterilisation, allowing them to remain sterile after removal from the autoclave.
- Heat Only – samples were heated to 121°C for 20 minutes (no steam).

The conditioning was carried out immediately after post-processing of the parts, with the autoclaving and heating taking place simultaneously to ensure comparability.

Drying

In order to test the reversibility of any changes, three methods of drying the specimens were investigated:

- No Drying – samples were tested immediately after conditioning, without any drying.
- Air-dried – samples were left uncovered in a non-dessicated environment for 7 days.
- Oven-dried – samples were held at 50°C for 7 days.

The “As Built – No Drying” specimens were used as a control group to compare all of the other combinations of conditioning and drying to, as this represented the standard properties after printing. The air-drying and oven-drying were fixed at 7 days to minimise any ageing effect. This was also expected to be sufficiently long to ensure the specimens held at 50°C reached their dried mass. As both these methods of drying were of equal length, tensile testing of all the “Oven-dried” and “Air-dried” samples could be carried out at the same time.

Water Content

In order to determine the water content at any given time t (w_t) during the sample conditioning and drying, a method was developed using two main approaches. When the dried mass of the specimens (m_{dried}) could be measured, the value of w_t could be calculated directly. Where m_{dried} could not be measured directly (whenever there was no oven-drying step before tensile testing), the initial water content of the build (w_{int}) was determined and used to calculate the value of m_{dried} , which could then be used to find w_t . Full details of each method are shown in Appendix B.3.1 and in [270].

To increase the accuracy of the measured water content value at the time of tensile testing (w_{test}), both the direct and indirect methods were used to calculate the pre- and post-test w_t . The mean of these was then used as the final value shown.

Note it was not possible to use the value of m_{dried} for the post-test specimens to calculate the pre-test water content. This was due to the tendency of polyamide 12 to fracture into more than 2 pieces during testing (see Figure 4.29); and as these small fragments could be easily lost, a comparison was not practical.



Figure 4.29: View of a fractured tensile test specimen [270]. 

Protocol Summary

An overview of the protocol used for the conditioning, testing, and drying of samples can be seen in Figure 4.30. This was developed to include all of the necessary measurements for the direct and indirect water content measurements¹².

Results^{13,14}

Mechanical Properties

The results of the tensile testing are shown in Figures 4.31 and 4.32, both as the raw data and the measured properties respectively. In Figure 4.31, it can be seen that all the stress-strain curves are broadly similar to one another, with the exception of the “Heat and Steam – No Drying” and “Heat and Steam – Air-dried”; which can be seen to be considerably different to the others, while following a similar profile.

In Figure 4.32, it is worth noting that all of the samples initially resembled the “As Built – No Drying”, with any subsequent changes due to the conditioning and drying. This initial value is therefore shown across all samples for comparison.

The properties shown in Figure 4.32 are again shown in Figure 4.33 with respect to w_{test} . A linear fit has been added, with the calculated R^2 value shown as a measure of the goodness of fit. The value of w_{int} was found to be $0.13 \pm 0.00\%$, and the value immediately after autoclaving was found to be $1.49 \pm 0.02\%$.

Discussion

From Figures 4.31 and 4.32, it can be clearly seen that there was a change in the mechanical properties after autoclaving (Heat and Steam). For these samples, E and σ_{uts} were initially lower than the as built values, whereas ε_{max} was significantly higher. These trends match those found in the literature for σ_{uts} and E , and agrees with the trend in ε_{max} where an increase in water content was not achieved under accelerated conditions. The samples which were exposed to heat only also showed the expected behaviour, with no significant change in the mechanical properties after exposure to the higher temperatures.

The reason for examining the different drying processes, was to determine the underlying cause of the differences observed. In the scenario where water content was the cause of any differences, logic dictates that after drying, the properties would revert to their original values. However, if these differences were caused by other factors (such as high temperatures), then this reversibility would not be expected. The results shown in Figures 4.31 and 4.32 clearly show that the “Heat and Steam” samples regain their original mechanical properties after oven-drying and partially regain them after air-drying. When combined with the lack of a difference in the “Heat Only”, this suggests that the causes of the differences were due to the water content of the parts.

This theory was further supported by the measured water content (shown in Figure 4.33), where all the mechanical properties show a negative trend with the measured w_{test} ; in this, the air-dried samples show a higher w_{test} than the oven-dried, whereas all the other samples have a similar water content. The samples initially exposed to the oven heating at 121°C , do not display a large divergence from the as built samples (Figure 4.32), again suggesting that the water content, rather than the temperature was the cause of the differences. Although a linear fit is shown in these results, similar experiments on injection moulded polyamide 6 samples [272], suggest that these trends may not in fact be linear. Further work could focus on measuring the effects of water content over a wider range of values to obtain a more accurate measure of the effects on the mechanical properties.

Throughout this experiment, the sterility of the parts after the initial steam sterilisation was not maintained. For practical applications, this would need to be investigated further to ensure that the parts remained sterile after conditioning. For oven-drying, this could be achieved by using autoclave bags / pouches during steam sterilisation (as in this experiment) and subsequently drying both the part and bag inside an oven. Alternatively for air-drying, this could be carried out in a class II biological safety cabinet, enabling the part to be uncovered while increasing the airflow over the part. However, it is worth noting that the time required to fully dry the parts is likely to be dependent on the geometry, meaning

¹²The protocol is shown in more detail in Appendix B.3, expanding on the calculation of the direct and indirect water content. Additional details are also shown in [270]

¹⁴Dimensions of the tensile specimens can be found in Appendix A.2, with the numerical values for the tensile properties shown in Appendix B.3.2.

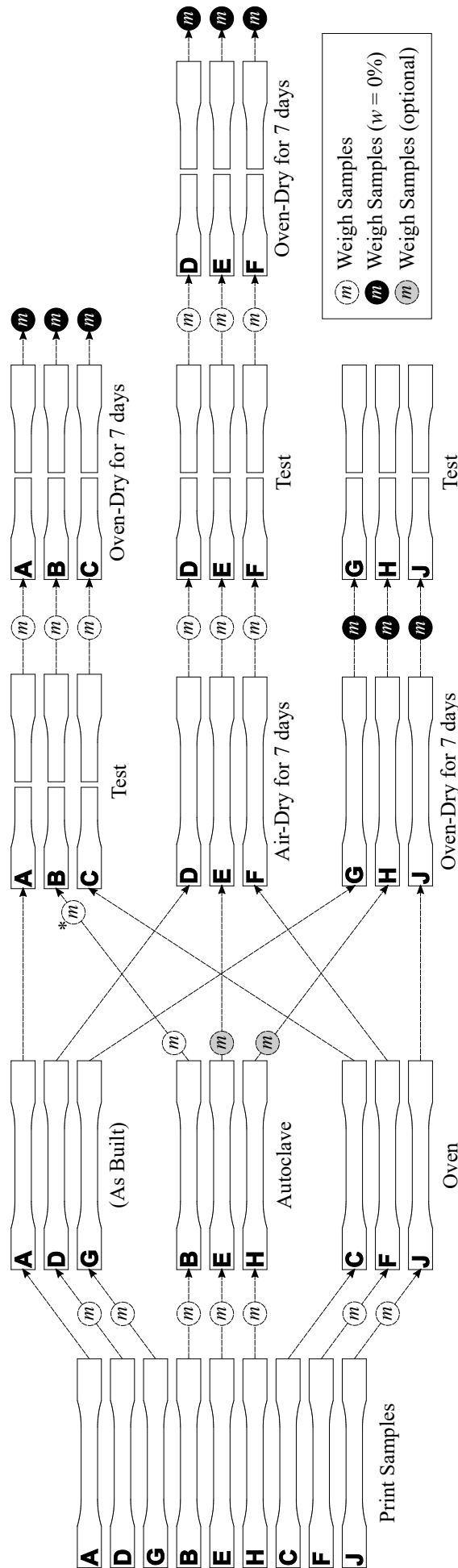


Figure 4.30: Overview of the protocol for conditioning and taking mass measurements. The additional pre-test measurement $*m$ was only taken as there was an 18 hour delay between autoclaving and testing [270]. $\bullet m$

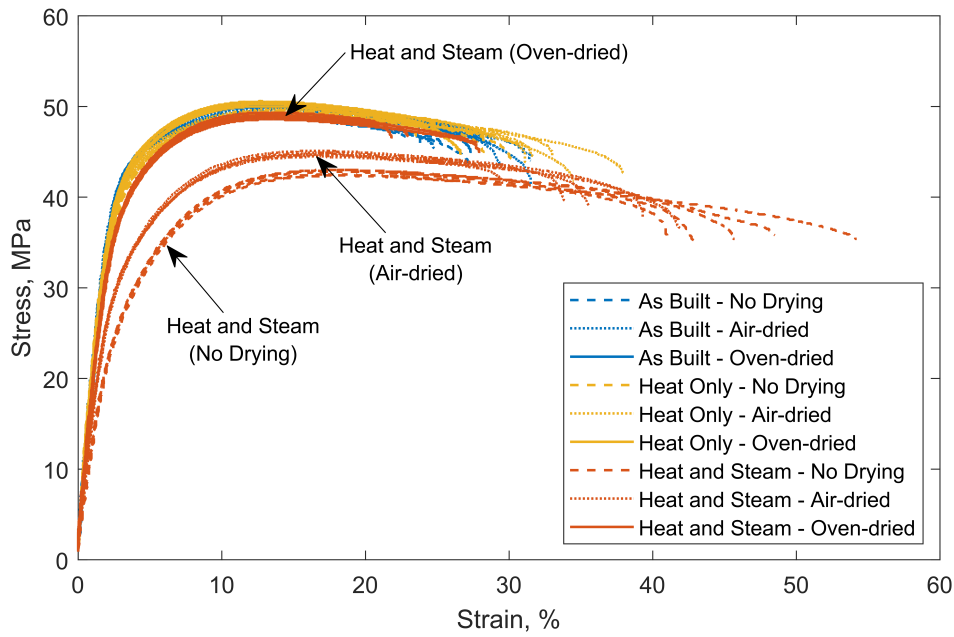


Figure 4.31: Stress-Strain data from tensile testing, with the results of all 45 test specimens shown. The majority of the curves can be seen to be similar, with “Heat and Steam – No Drying” and “Heat and Steam – Air-dried” samples appearing to be significantly different [270]. 🚫

it is not possible to determine a standard drying time. In these instances, repeated weighing of the part should be carried out, with the 0% water content achieved when the mass values plateau.

In terms of this project, these results clearly show that steam sterilisation can be used for the printed LS polymer and microcomposite parts for the antibacterial testing. This was later found to be crucial, with other sterilisation methods trialled potentially affecting the results of the experiments (see Section 4.4.3).

4.3.2 Water Uptake – Spherical Samples

The increased pressure and temperature inside an autoclave represents an extreme set of starting conditions the microcomposites could expect to undergo in real-life applications. However, not all of the uses of these materials are likely start this way, with the water uptake required to create the antimicrobial effect likely to be far slower than that shown in Section 4.3.1.

This section looks at the water uptake of printed parts submerged in water at room temperature and pressure. The time taken for the parts to become fully saturated gives an indication as to the minimum longevity of the antimicrobial functionality, with the water uptake also providing an initial estimate for the rate of silver release, with the two properties shown to be linked in Section 3.6.3.

Methodology

Test Specimens

In order to minimise the effects of varying geometry on the water uptake and the release of Ag^+ within a part (for example the effect of corners), a sphere was chosen as the test specimen geometry. Coupled with the agitation provided by a lab roller, this geometry also ensured an even application of the water as the sphere would constantly roll, thereby exposing the entire surface to the liquid.

The sphere was designed to have a volume (V_S) of 1 cm^3 , with the diameter (d_S) calculated as shown in Equation 4.7.

$$V = \frac{4}{3}\pi\left(\frac{d_S}{2}\right)^3 \Rightarrow d_S = 2\sqrt[3]{\frac{3}{4\pi}V}, \quad \text{for } V_S = 1 \text{ cm}^3, \quad d_S \approx 12.4 \text{ mm} \quad (4.7)$$

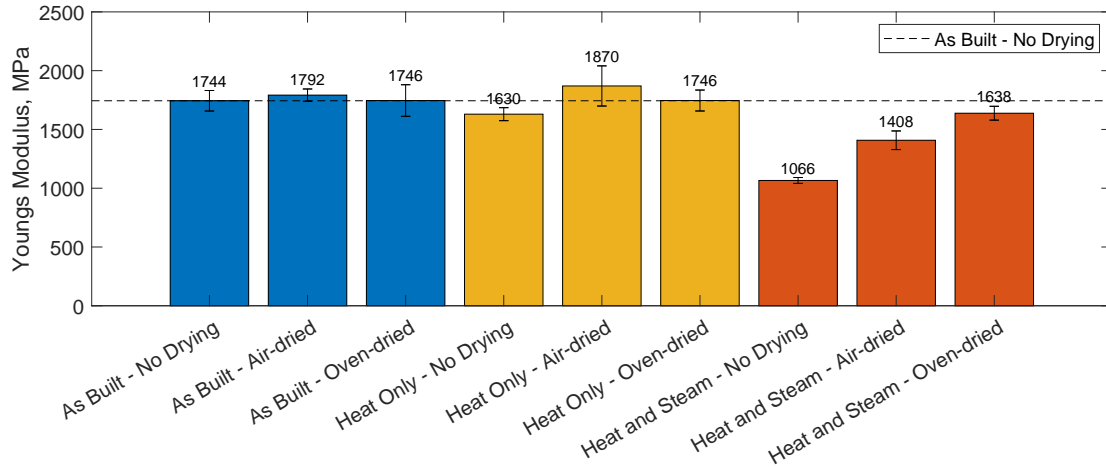
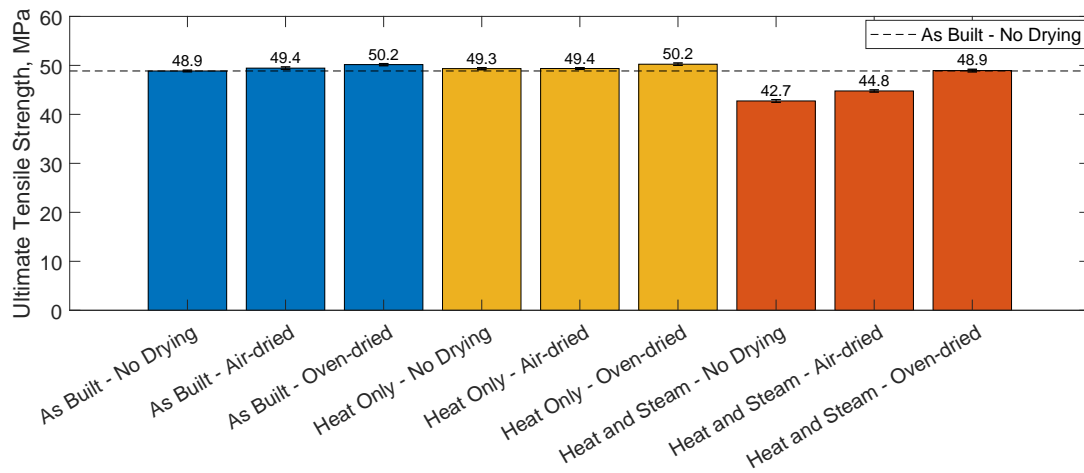
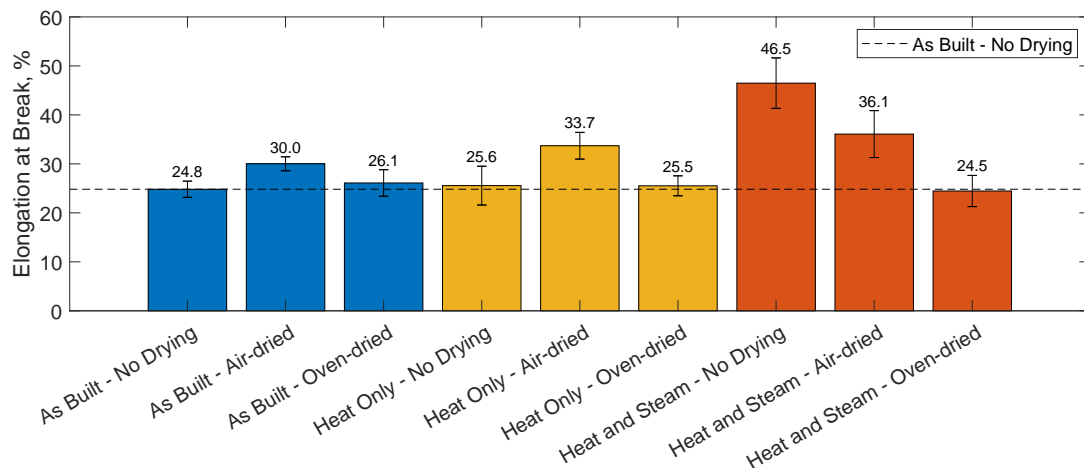
(a) Elastic Modulus (E).(b) Ultimate tensile strength (σ_{uts}).(c) Elongation at break (ϵ_{max}).

Figure 4.32: Tensile properties for all combinations of conditioning and drying, values are shown as the mean \pm standard deviation. Here it can be seen that the “Heat Only” samples do not show any significant difference to the “As Built” samples, whereas the “Heat and Steam” samples show a marked decrease in modulus, decrease in ultimate tensile strength and increase in elongation at break. These differences are shown to be reversed by the drying steps, with all of the oven-dried samples re-gaining their original mechanical properties [270]. 🚫

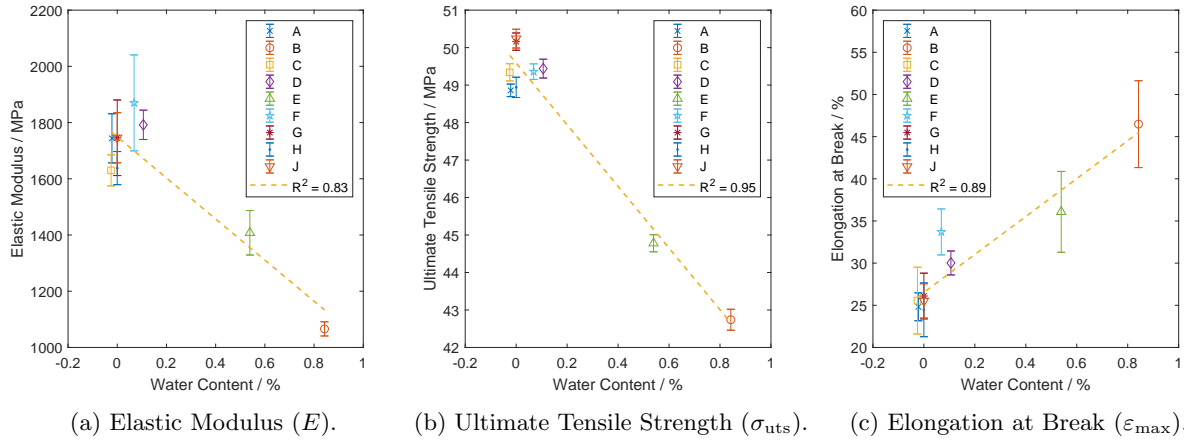


Figure 4.33: Effect of water content (w_{test}) on mechanical properties. Linear fits have been added, with the R^2 values showing a strong correlation between w_{test} and σ_{uts} , and a moderate correlation between w_{test} and both E and ε_{max} [270].

Experimental Procedure

The water uptake was determined by submerging the specimens (three per material) in deionised water and recording the mass at varying time points; a detailed protocol based on ASTM D570 [466] and BS EN ISO 62 [467] can be found in Appendix A.4.

Mass measurements were initially taken at 0, 1, 2, 4, 6, 8, 24, and 168 hours; with subsequent measurements carried out every 2 weeks until a constant mass was achieved. Prior to each measurement, the surface water was removed with a dry cloth (blue roll). The total mass uptake of the part (% w/w) was calculated from these measurements.

Diffusion Constant

The water uptake through the polymer was assumed to follow Fick's Law and as such, the experimental results were fitted to the theoretical curve for spheres as shown in Equation 4.8 [468]. In this, m_t is the mass recorded at time t , d_S is the sphere diameter, M_t is the water uptake, and D is the calculated diffusion coefficient. Note that this solution differs to those in the standards, as this is specifically for spherical geometries.

$$\frac{M_t}{M_\infty} = 1 - \frac{6}{\pi^2} \sum_{n=1}^{\infty} \frac{1}{n^2} \exp\left(-\frac{4Dn^2\pi^2t}{d_S^2}\right) \quad \text{where,} \quad M_t = m_t - m_{0h} \quad (4.8)$$

The initial phase of the sorption was also used to approximate the short-term diffusion constant (D_{int}), without the need for the mass at saturation (M_∞) to be reached. This was done by approximating Equation 4.8 in the region of $\frac{M_t}{M_\infty} < 0.2$, as shown in Equation 4.9 [469]; where C_1 is the gradient of $\frac{M_t}{M_\infty}$ against \sqrt{t} .

$$\text{For } \frac{M_t}{M_\infty} < 0.2, \quad \frac{M_t}{M_\infty} = \frac{12}{d_S} \left(\frac{D_{\text{int}}t}{\pi}\right)^{0.5} \Rightarrow \frac{M_t}{M_\infty} = C_1\sqrt{t} \quad (4.9)$$

The measured value of C_1 could therefore be used to calculate D_{int} using Equation 4.10.

$$C_1 = \frac{12}{d_S} \left(\frac{D_{\text{int}}}{\pi}\right)^{0.5} \Rightarrow D_{\text{int}} = \pi \left(\frac{C_1 d_S}{12}\right)^2 \quad (4.10)$$

Results¹⁵

The processed results are shown in Figure 4.34. The normalised values (relative to M_∞) of the mass uptake can be seen in Figures 4.34a–c, with Equation 4.8 fitted to these plots to determine the diffusion constant (D) over the entire experiment. In these the fitted curve was given an additional degree of freedom allowing the curve to start at “negative” times, allowing for a better fit and accounting for any residual water content after the initial drying period. To fit the curve, values of $n = 1$ to 200 were used for Equation 4.8. In the figures, an area corresponding to a mass measurement of ± 1 mg (or approximately 0.1%) is shown as a measure of whether the readings had converged.

In Figure 4.34d, the values of D_{int} were calculated using Equation 4.10. It is important to note that due to the relatively quick initial increase in mass and the small total mass uptake, it was not possible to restrict this calculation to values of $\frac{M_t}{M_\infty} < 0.2$; instead, values of $\frac{M_t}{M_\infty} < 0.35$ have been used.

The temperatures recorded throughout the experiment can be seen in Figure 4.34e, where slight fluctuations can be seen but the temperature remained within $22.3 \pm 3.0^\circ\text{C}$ for the duration.

The percentage mass increase is shown in Figure 4.34f, where the timepoints have been offset by the amount estimated by the fitted curves (the “negative” starting time) to allow for a more direct comparison of the fitted curves. The maximum percentage increase in mass for Virgin PA2200 was found to be 1.89%, 1.0% B65003 was 2.46%, and 1.0% B45003 was 2.05%.

Discussion

The diffusion rates (D) for the samples can be seen to be fairly similar for PA2200 and 1.0% B45003, with a slower rate found for 1.0% B65003. However, the mass measurements taken (Figures 4.34a–4.34c) do not conform perfectly to Fick’s Law; as this was a fundamental assumption, this could be a source of error in the value of D calculated with Equation 4.8. A possible explanation for the deviation from this is the porous nature of the printed parts, which were found to have porosities of 4.6–4.9% (see Section 4.2.4). The rapid initial increase in mass observed in Figures 4.34a–4.34c could therefore partially be caused by capillary action, rather than diffusion into the base polymer.

As previously mentioned, it was not possible to obtain a value of D_{int} using the constraints in Equation 4.9 due to the high rate of initial increase and the low overall uptake. As well as including measurements of $\frac{M_t}{M_\infty} > 0.2$, the subsequent lines of best fit plotted and used to calculate D_{int} were fitted to one data point only, further increasing the uncertainty of the obtained value. This suggests that for the geometries analysed here, the value of D_{int} cannot be relied upon for any meaningful analysis.

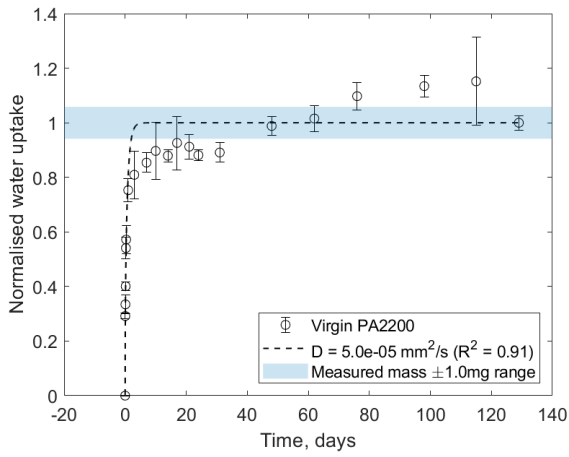
Variation was also seen in the mass over time, which was not expected. A possible explanation for this could have been temperature as this was not controlled during the experiment; for this reason, this has also been shown in Figure 4.34e where available (shown is the 24-hour moving average). There was no apparent correlation between temperature and mass, meaning that other factors were likely in effect. This was suspected to be the drying of the specimens’ surface, as this was performed by hand and was difficult to reproduce consistently. A solution to this could be to use larger specimens, where the mass of water removed from the surface would have less of an effect, or to use more samples to reduce the standard deviation.

The maximum water uptake (shown in Figure 4.34f), was found to be fairly similar for all three materials, but with both the microcomposites saturated at a higher value than the pure polymer. This suggests that the maximum water content of the additive is higher than that of the polymer, or potentially the additive could have partially dissolved, resulting in a higher porosity and therefore maximum water content. It is worth noting that even for the PA2200 samples, the final values were higher than expected in the literature (approximately 1.5% [442]). This could be due to the inherent porosity in LS samples, or could be due to insufficient drying of the samples during testing.

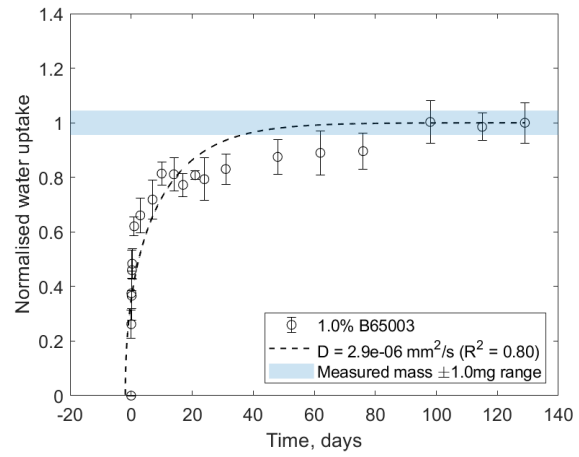
From the results collected here, the outlined procedure could be effective at identifying large differences in D , such as the ones present between different polymers. However, the large variation in the measured results makes it unsuitable for identifying small differences; although in future studies, a more thorough drying process could result in more accurate results.

In terms of the potential antimicrobial efficacy of the parts, the results here suggest that even though the smaller additive (B45003) might initially have an advantage over B65003, this is eventually offset by the total maximum water uptake. It is also possible that the larger voids left after the partial dissolution

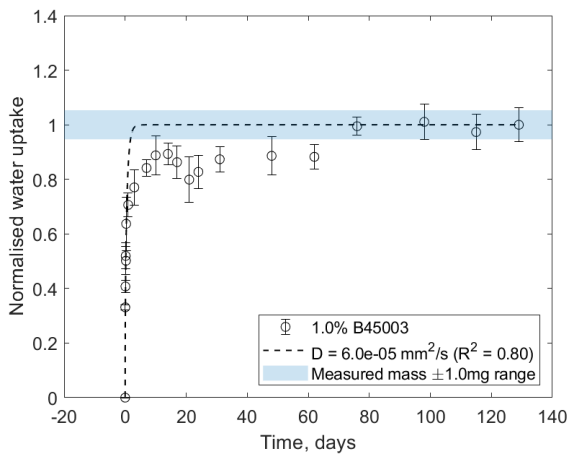
¹⁵Dimensions of the printed spheres can be found in Appendix A.2. Mass measurements for the samples taken throughout the experiment can be found in Appendix B.4.



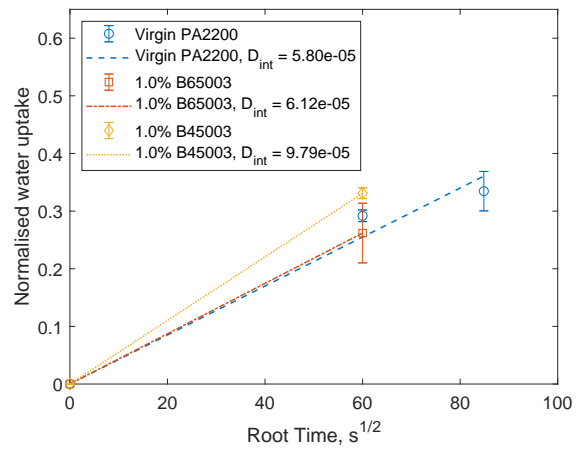
(a) Virgin PA2200 – Mass uptake.



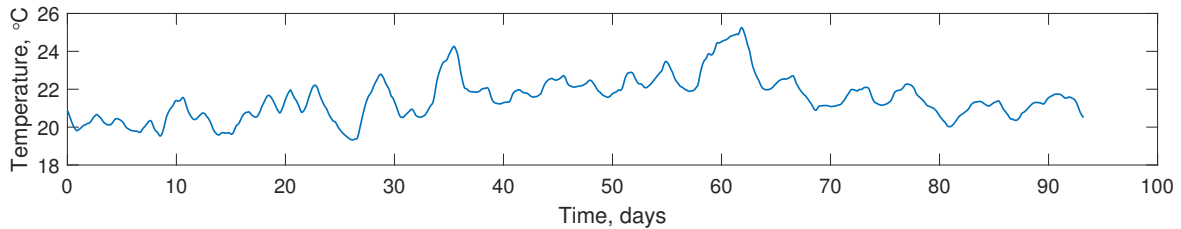
(b) 1.0% B65003 – Mass uptake.



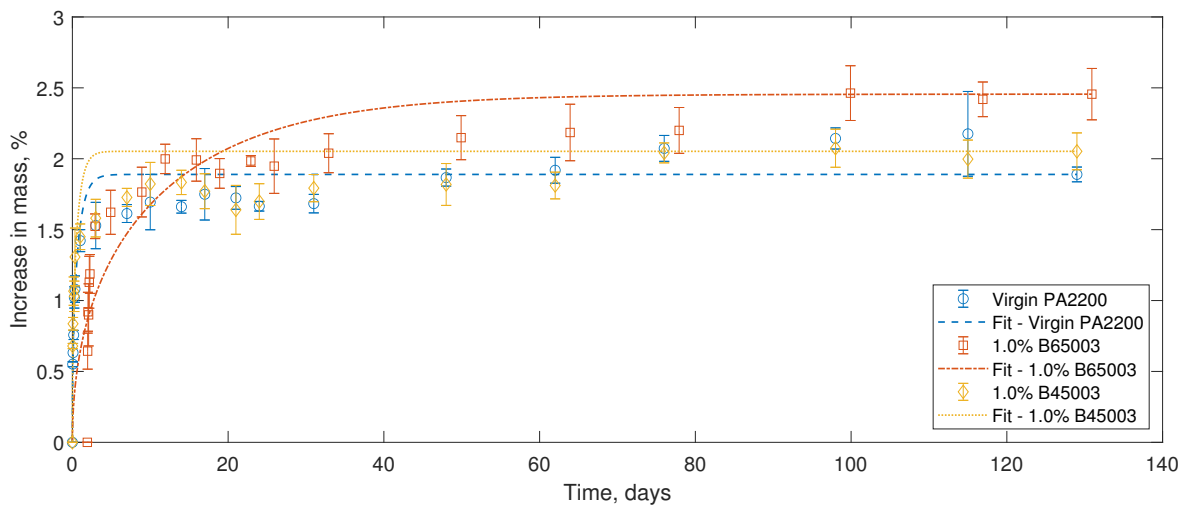
(c) 1.0% B45003 – Mass uptake.



(d) D_{int} calculated using Equation 4.10.



(e) Temperature measurements (24-hour moving average), remaining within $22.3 \pm 3.0^\circ\text{C}$.



(f) Percent increase in mass during water absorption testing, offset so the fitted curves start at zero.

Figure 4.34: Results of the water uptake test, with Equation 4.8 fitted. 🍷

of B65003, could result in the more effective release of Ag^+ from deeper within the parts at longer time periods. For these reasons, and the additional observed difficulties during printing (see Section 4.1.4), it was decided to primarily focus on the microcomposites containing 1.0% B65003 in subsequent tests.

4.3.3 Water Uptake – Effect of Geometry

While the results in Section 4.3.2 showed that there is a small, but measurable, difference in the behaviours of the microcomposites compared to PA2200, these results only cover one geometry. With potential applications of the microcomposites unlikely to focus solely on the production of 1 cm^3 spheres, it was decided to test the effects of different geometries on the water uptake of the parts.

In this section, six different geometries of test specimens were created in pure PA2200 and 1.0% B65003, with the water uptake measured over a 12-week period.¹⁶

Methodology

The methodology used here broadly reflects the one used for the spherical specimens in Section 4.3.2, with additional changes in the design of the test specimens, and in the experimental setup to enable the scalability for the number of samples needed.

Test Specimens

The design of the test specimens was based on the spheres previously used, with a single parameter changed to alter the sphericity (ψ , see Equation 4.3) of the parts. The concept revolved around decreasing the height of the spheres (essentially squashing them), but maintaining the same volume. To enable the resulting ellipsoids to fit inside the universals during testing, the width was kept constant; this resulted in the series of elongated ellipsoids with varying surface area and sphericity, shown in Figure 4.35.

Photos of the printed test specimens can be found in Figure 4.36, with the more elongated ellipsoids showing a much more prominent “start-stepping” effect due to the shallow gradients in the geometries. The measured dimensions of the ellipsoids can be found in Appendix A.2.

Protocol

The main protocol used was the same as in Section 4.3.2, with more attention on sufficiently drying the test specimens before weighing.

Due to the number of specimens intended to be tested simultaneously (originally intended to be around 80 samples), it became unfeasible to use a lab roller to agitate the samples during testing. To accommodate all the samples, it was decided to use gyro-rocker, which (after some provisional testing) was found to provide sufficient movement to expose the entire surface of the specimens to the water.

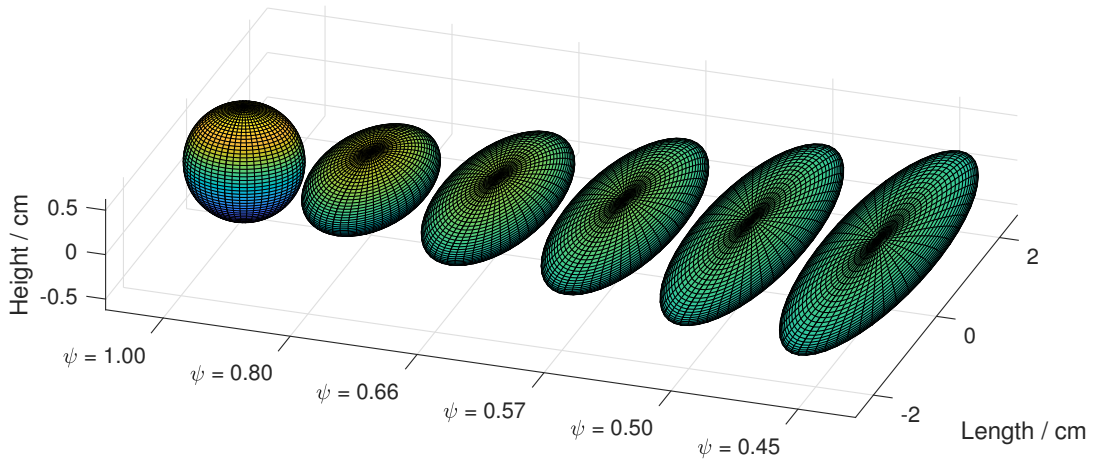
To fit all the specimens on a single gyro-rocker, racks were designed and printed in PLA with FDM to hold all the necessary samples. This was designed to hold standard 28 ml plastic universals so that the main section was perfectly horizontal, with the rack designed to fit on a Stuart mini gyro-rocker SSM3. Due to the maximum weight capacity of 3 kg, the racks were designed to be as lightweight as possible. The printed racks (shown in Figure 4.37) had the capacity for 84 universals (across six layers, weighing a total of 1.52 kg), with the weight low enough to allow each universal to hold a printed test specimen and up to 16.6 ml water.

In this experiment, due to a scaled back setup, only four layers of the rack were used, allowing for 20 ml water to be placed in each of the universals. The layout used can be seen in Figure 4.38, where additional spherical samples from Chapter 5 were run concurrently with the ellipsoids.

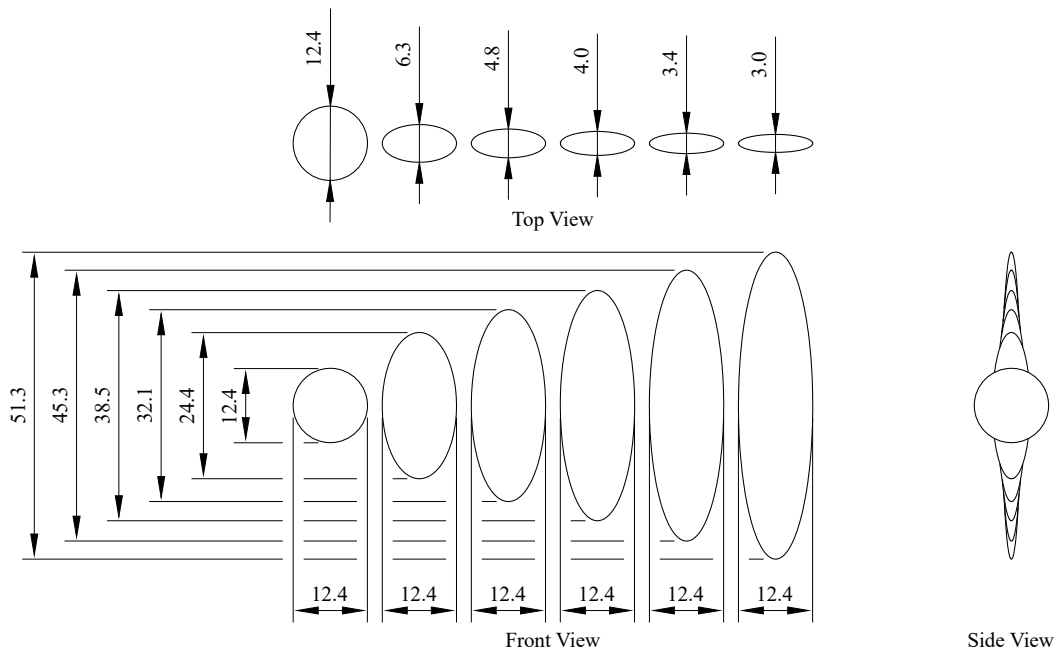
Results

The percentage mass uptake in the samples throughout the water uptake experiment can be seen in Figures 4.39a and 4.39b for PA2200 and 1% B65003 respectively. In this, it can be seen that for both materials, the water uptake was consistently higher for the more elongated ellipsoids. Temperatures throughout the experiment can be found in Section 5.3.1.

¹⁶This was originally intended as part of a much larger set of experiments, but was scaled back due to equipment availability and disruption due to the COVID-19 pandemic.

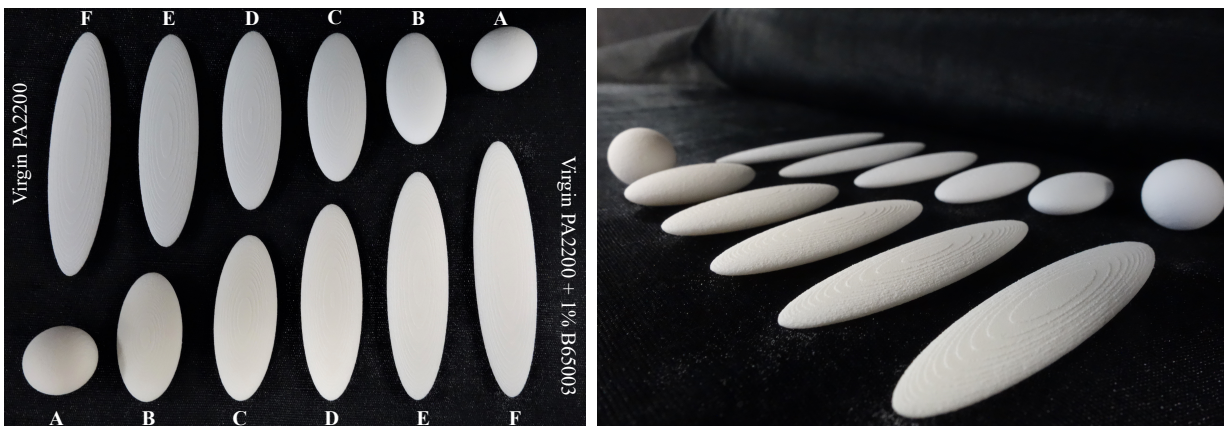


(a) 3D visualisation of the ellipsoid geometry and sphericity.



(b) Ellipsoids, all dimensions in mm.

Figure 4.35: Specifications of the ellipsoids used, with all samples designed to have the same volume. 🍎



(a) Top down view of the printed ellipsoids.

(b) Side view showing the “stair-stepping” effect.

Figure 4.36: Photos of the printed ellipsoids. 🍎

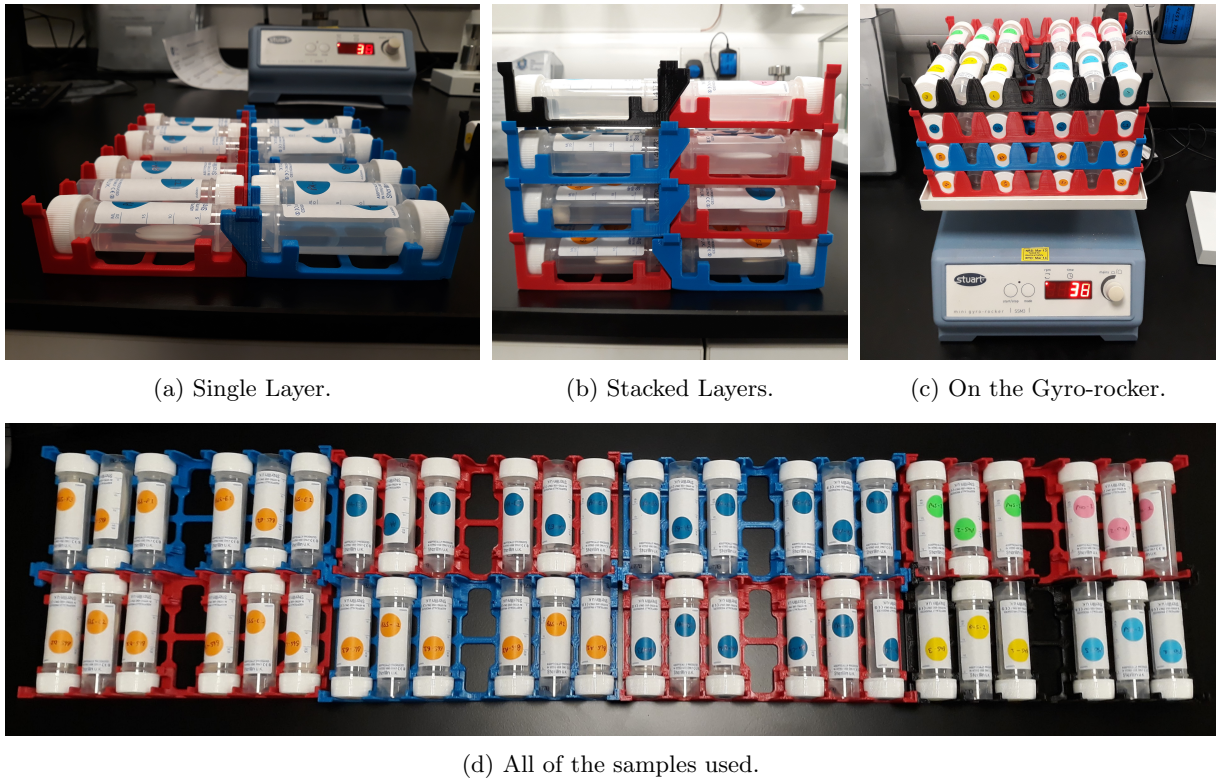


Figure 4.37: Racks designed for the water uptake experiments, with the plastic universals lying flat to ensure the optimum coverage of water on the parts. Printed with in PLA with FDM. 🚫

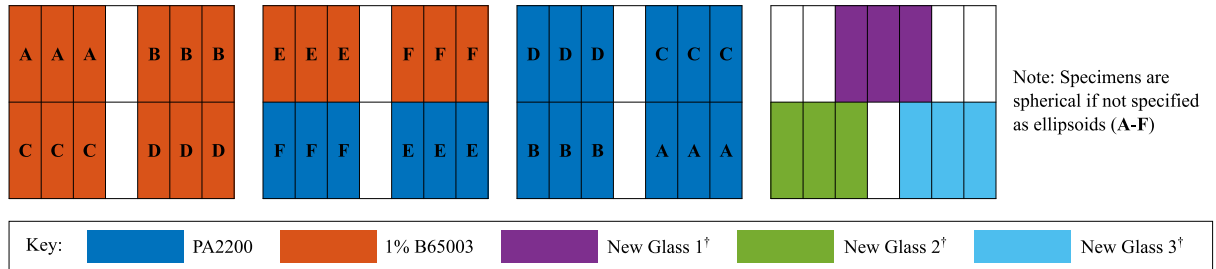


Figure 4.38: Experimental setup of the water uptake experiment, shown are layers in a rack designed to fit the gyro-rocker, with each cell representing one sample. [†]Additional samples from Chapter 5 are also shown, which will run concurrently to ensure comparability. 🚫

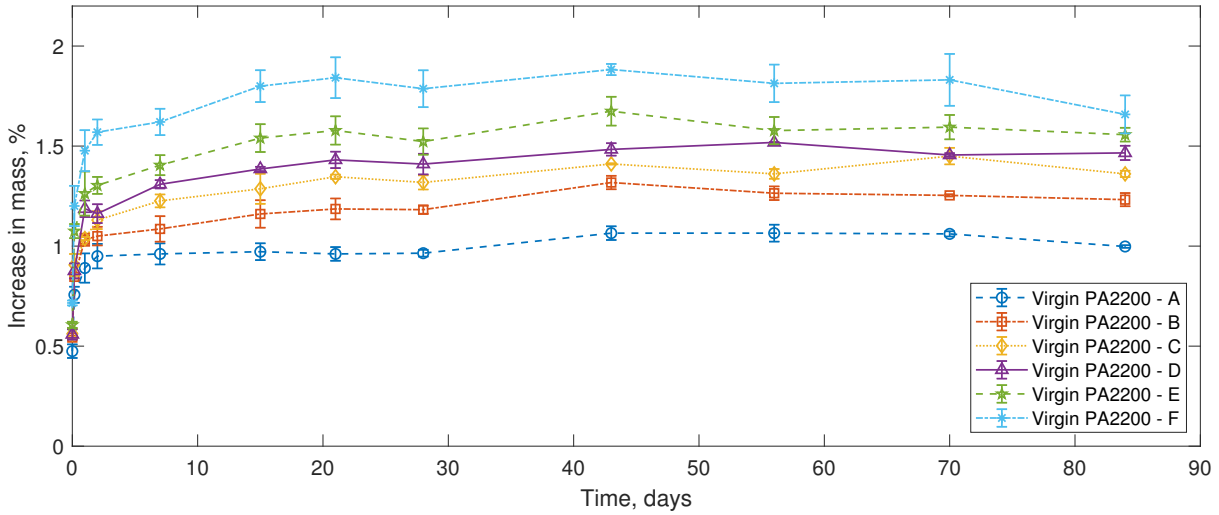
Note that due to an oversight in the procedure, samples were not dried prior to the experiment, with the values shown here instead based on the dried mass of the specimens after the experiment (samples were dried at 50°C for 18 days to ensure all the water had evaporated). The samples were, however, still thought to be comparable due to the closeness of the build dates (built on subsequent days) and identical storage conditions of the specimens prior to testing.

The water uptake from the final timepoint (12 weeks) is shown in Figures 4.39c and 4.39d relative to the measured surface area and sphericity of the specimens. The volume ($V_{\text{ellipsoid}}$) and surface area ($A_{\text{ellipsoid}}$) of the ellipsoids were calculated from the measured height (d_1), width (d_2) and length (d_3) of the samples¹⁷ using Equation 4.11; with the sphericity (ψ) subsequently calculated from $V_{\text{ellipsoid}}$ and $A_{\text{ellipsoid}}$ using Equation 4.3.

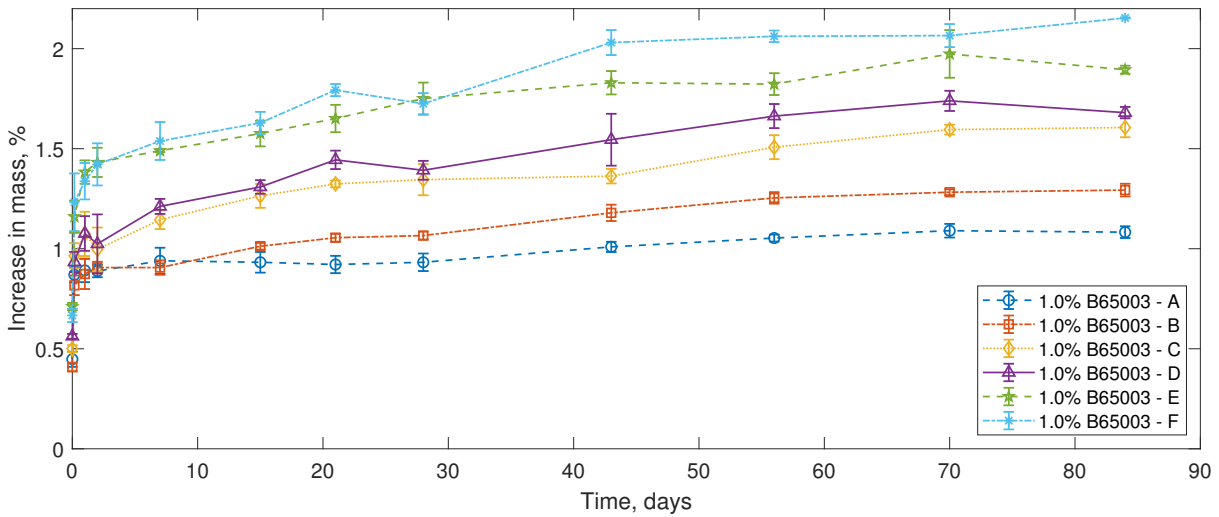
$$\text{Ellipsoid Volume:} \quad V_{\text{ellipsoid}} = \frac{4}{3}\pi r_1 r_2 r_3 \quad \text{where,} \quad r_1 = \frac{d_1}{2}, \quad r_2 = \frac{d_2}{2}, \quad r_3 = \frac{d_3}{2} \quad (4.11a)$$

$$\text{Ellipsoid Surface Area:} \quad A_{\text{ellipsoid}} \approx 4\pi \left(\frac{(r_1 r_2)^{1.6} + (r_1 r_3)^{1.6} + (r_2 r_3)^{1.6}}{3} \right)^{\frac{1}{1.6}} \quad (4.11b)$$

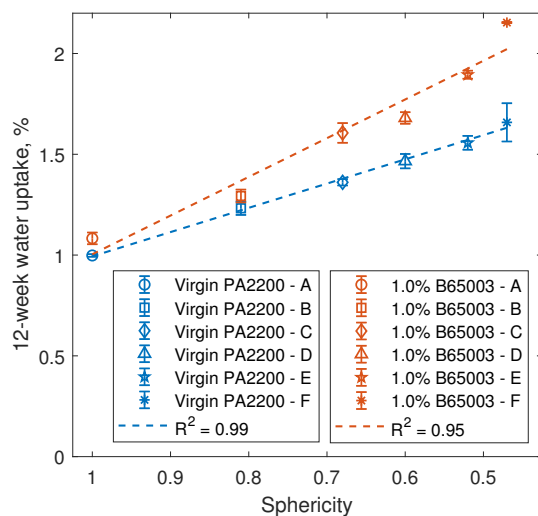
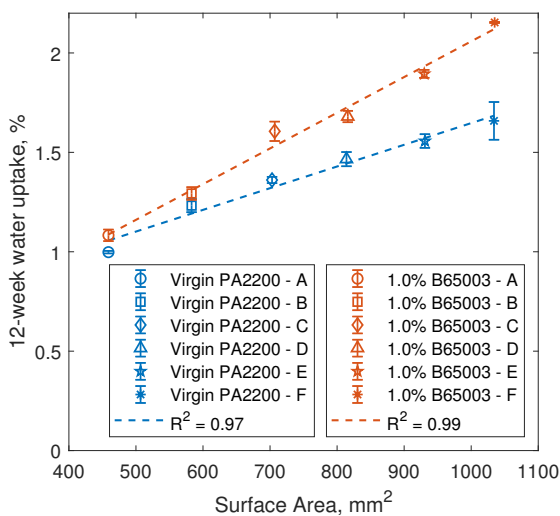
¹⁷The measured values of d_1 , d_2 , d_3 and the calculated values of $A_{\text{ellipsoid}}$, $V_{\text{ellipsoid}}$, and ψ for each geometry can be found in Appendix A.2.



(a) PA2200.



(b) 1% B65003.



(c) Correlation of maximum water uptake to surface area. (d) Correlation of maximum water uptake to sphericity.

Figure 4.39: Results of the water uptake test for the ellipsoidal samples, results are shown as the mean \pm standard deviation. 🚫

Discussion

The results in Figures 4.39a and 4.39b show that for both PA2200 and 1.0% B65003, the more elongated ellipsoids show a faster rate of water uptake, reaching higher water contents at much earlier timepoints. This was expected due to the larger surface area in the longer ellipsoids exposing more of the part to the water. Comparing between the materials, the 1.0% B65003 parts can be seen to consistently reach a higher water content than the PA2200 samples (also shown in Figures 4.39c and 4.39d), echoing the results found in Section 4.3.2.

Interestingly, the mass values for the different geometries did not plateau at the same value (shown in Figures 4.39c and 4.39d), which would be expected for complete saturation of the samples. A potential reason for this could be that the time period here was not sufficient to allow all the geometries to reach saturation, and that after a longer time all the mass uptake values would converge. Another possibility is that, despite the more diligent drying process, some remaining capillary action of the surface prevented the removal of all the water from the surface, a phenomenon which would be amplified by an increased surface area.

Comparing the results for PA2200 to those in Section 4.3.2 and to literature values, the results here can be seen to be much more in line with those previously reported, suggesting that the increased drying was effective in reducing the error in the experiment. This also shows in the smaller spread of results (standard deviation) for each timepoint.

In terms of the part functionality, this experiment confirms what was previously thought, that the spheres represent the “worst-case” scenario for any potential antimicrobial effect. For this reason, it was decided to only focus on the spherical specimens for all further testing.

4.3.4 Silver Release

All the powder and part characterisation carried out in this chapter so far have ultimately constituted a set of checks to identify any potential barriers to the use and function of the printed parts. With the parts shown to be useable in end-use applications, contain the antimicrobial additive, and absorb water to react with the additive; the final unknown before any microbial testing could take place, was to determine whether the parts were actually capable of releasing silver ions.

With the spherical test specimen geometry finalised, this section focuses on determining the amount of Ag^+ released from the microcomposite parts over 7 days. The experiment here uses the 1.0% B65003 spheres, with the conditions kept the same as the water uptake experiment in Section 4.3.2.

Methodology

To measure the maximum Ag^+ release of the parts, the methodology here was devised to simulate immersion in an infinite volume of water. To achieve this, the concentration of Ag^+ would have to be maintained at zero (or as close to zero as possible) on the surface of the sphere, facilitating the maximum rate of Ag^+ diffusion from the parts.

Since release into an infinite volume was not feasible to measure, the parts were immersed in 10 ml deionised water and moved to fresh water at each time point; effectively resetting the concentration of Ag^+ at the surface to zero. The release was measured over 1 week (168 hours), with measurements taken at 1, 2, 3, 8, 24, and 168 hours. The water was then analysed using ICP-ESMS to determine the concentration of Ag^+ , which was then converted into the mass of Ag^+ released per sphere.

Results

The Ag^+ release is shown in Figure 4.40, both as the total amount¹⁸ (Figure 4.40a) and as a rate of release (Figure 4.40b). In both of these, the amount is shown as the mass released and as a percentage of the total silver contained in the part, as measured in Section 4.2.6.

Discussion

For the time period analysed, the Ag^+ release in Figure 4.40 appeared to be relatively constant. However, the actual amounts of silver released were very small, totalling less than 1.5 μg per sphere over 1 week. While the concentration of Ag^+ released was not specified in the initial objectives, this is something that will have a direct effect on the antimicrobial efficacy of the parts.

¹⁸Measurements for individual samples are shown in Appendix B.5.

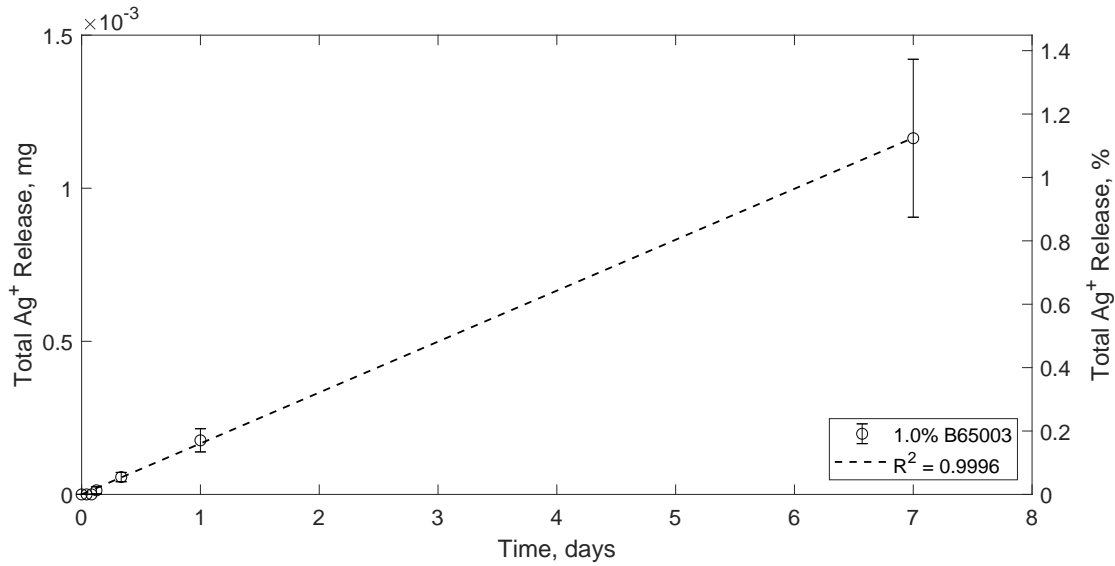
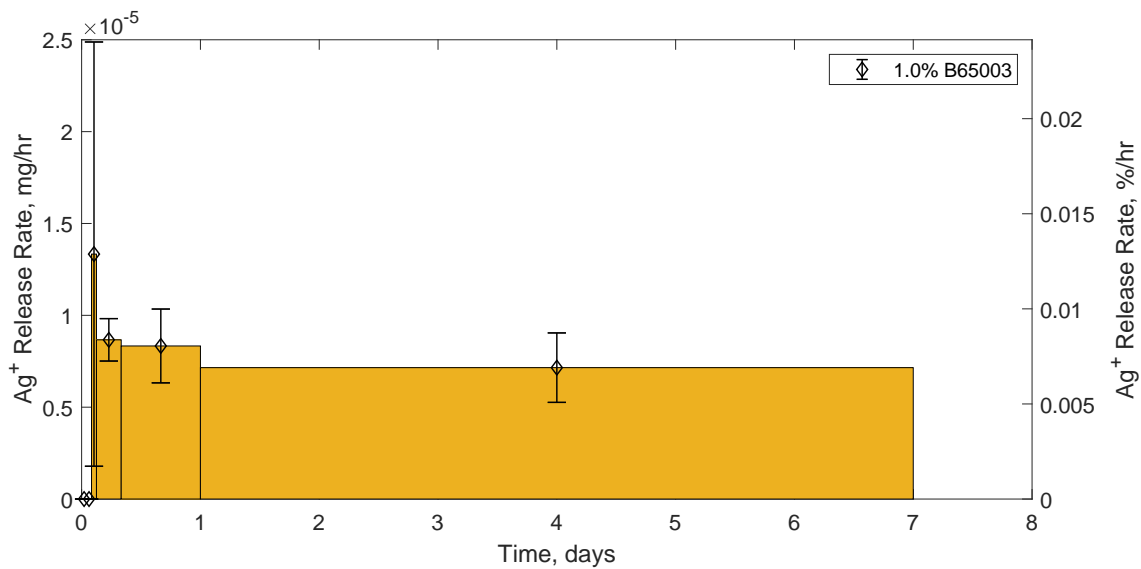
(a) Total Ag⁺ released in an infinite volume.(b) Ag⁺ release rate, where the area of the bars indicate the amount of Ag⁺ released.

Figure 4.40: Results of the Ag⁺ release experiment, shown as mass and a percentage of the total Ag⁺ content in the parts found using ICP in Section 4.2.6. 🚫

Regardless of the amounts measured over this time period, the fact that any amount of Ag⁺ was detected, proves that the concept has the potential to be effective, showing that the microcomposite parts are able to release silver into the surrounding environment. The experiments presented here only focused on one geometry, one additive, included at one level of loading. With the potential for all of these to have a significant effect on the rate of Ag⁺ and longevity of the effects, there are multiple potential avenues to explore.

4.4 Antibacterial Testing

So far, all the characterisation carried out has focused on the engineering properties of the parts, and their theorised antimicrobial efficacy based on proxy measurements. However, the only way to know for certain whether they had an antimicrobial effect, was to test how the printed parts interacted with microbes.

The challenge here was to develop protocols able to measure any antimicrobial effect. Although standards exist for measuring this, these are generally extremely specific and unworkable in the lab setup available. Adding to the confusion, the different definitions of “antimicrobial” (see Section 3.4.2) and the various strategies available (see Section 3.4.3) mean that manufacturers of antimicrobial materials use a wide range of tests, often cherry-picked to show the greatest difference for their product.

Throughout this project, various protocols were developed to measure the antimicrobial efficacy of the materials, making full use of the geometric freedom provided by Laser Sintering. These are detailed in this section, focusing on biofilm formation and the effect in the surrounding planktonic bacteria; with later testing also looking at the effect of the surrounding media and the cytotoxicity^{19,20,21}.

4.4.1 Bacterial Strains

Due to the differences between Gram-positive and Gram-negative bacteria (see Section 3.1.1), it was decided to test the antimicrobial efficacy against examples of both of these.

The chosen bacteria were clinical isolate strains of the Gram-positive *Staphylococcus aureus* S235 (referred to as *S. aureus* S235 or Sa S235), and Gram-negative *Pseudomonas aeruginosa* SOM1 (referred to as *P. aeruginosa* SOM1 or Pa SOM1), provided by the Charles Clifford Dental Hospital, Sheffield. Both of these are examples of commonly found, biofilm forming bacteria, which can cause significant infection, especially in immunocompromised patients.

Bacteria were maintained on stock Brain Heart Infusion (BHI) agar plates stored at 4°C. For experimental use, single colonies were picked from the plate and suspended in 15 ml BHI broth then incubated overnight at 37°C in a shaking incubator.

4.4.2 Preliminary Testing – Powder Efficacy

For the printed microcomposite materials, any antimicrobial effect was expected to be caused solely by the inclusion of the silver phosphate glass additives. For this reason, it was decided to first test the effectiveness of these additives before any testing on the parts was carried out.

The preliminary test in the section tracked the antimicrobial efficacy of both additives in nutrient-poor conditions (where the bacteria are suspended, without the nutrients required to grow) over 24 hours.

Methodology

In these tests 10 µg of each phosphate glass additive was analysed per sample, representing (approximately) the same amount found in 1 cm³ of the printed microcomposite materials. To ensure that there was no contamination in the testing, these were weighed out into glass universals (three samples per material), and sterilised in a steam autoclave at 121°C before testing.

Since this was a preliminary test, only one strain of bacteria was used (*S. aureus* S235); this was grown in BHI broth overnight in a shaking incubator (at 37°C). The overnight culture was diluted to an Optical Density at 600 nm (OD₆₀₀) of 0.01 in Phosphate Buffered Saline (PBS), before 5 ml of the diluted culture was added to each sample. The samples were incubated in a shaking incubator at 37°C, with 10 µl of the solution removed at each timepoint for analysis; with timepoints of 0, 3, and 24 hours chosen.

For each timepoint, a Miles and Misra serial dilution²² [363] was carried out to determine the number of Colony Forming Units (CFU) present; healthy bacteria in the samples capable of replicating themselves. Although labour intensive and time consuming, this is regarded as one of the most accurate methods of determining the antimicrobial efficacy, since the number of bacteria present is counted directly.

¹⁹Preliminary experiments also focused on sterilisation and contact efficacy, shown in Appendix C.2.

²⁰The preliminary experiment in Appendix C.2.1 qualitatively analysed the effectiveness of alcohol immersion (70% IMS) on the surface sterility.

²¹The preliminary experiment in Appendix C.2.2 used 10 mm discs to analyse the contact efficacy against planktonic *Staphylococcus aureus* S235 (with a refined version of this later used in Section 4.4.4).

²²A detailed protocol for a Miles and Misra serial dilution is shown in Appendix A.5

For this, a series of tenfold dilutions were carried out in PBS (10 μ l sample : 90 μ l PBS), before the resulting dilutions were plated out onto agar plates (20 μ l each time); these were allowed to dry, before being incubated at 37°C for 18–24 hours. After which, the bacterial colonies were large enough to be visible with the naked eye; by counting the number of separate colonies (indicating they originated from a single bacteria) in the lowest dilution, this could then be converted back to CFU/ml in the sample.

A schematic overview of the entire antimicrobial testing protocol for the powders is shown in Figure 4.41.

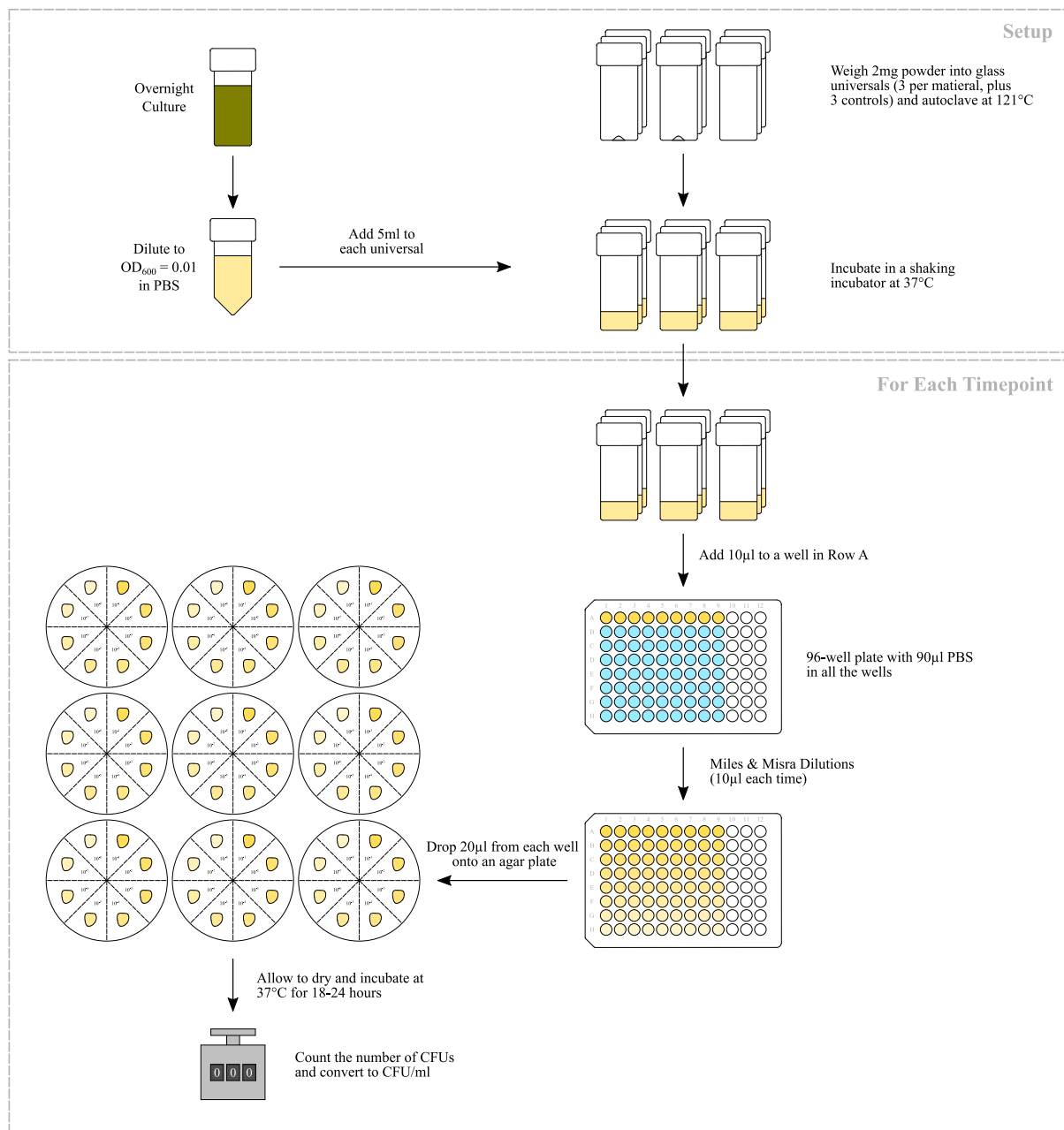


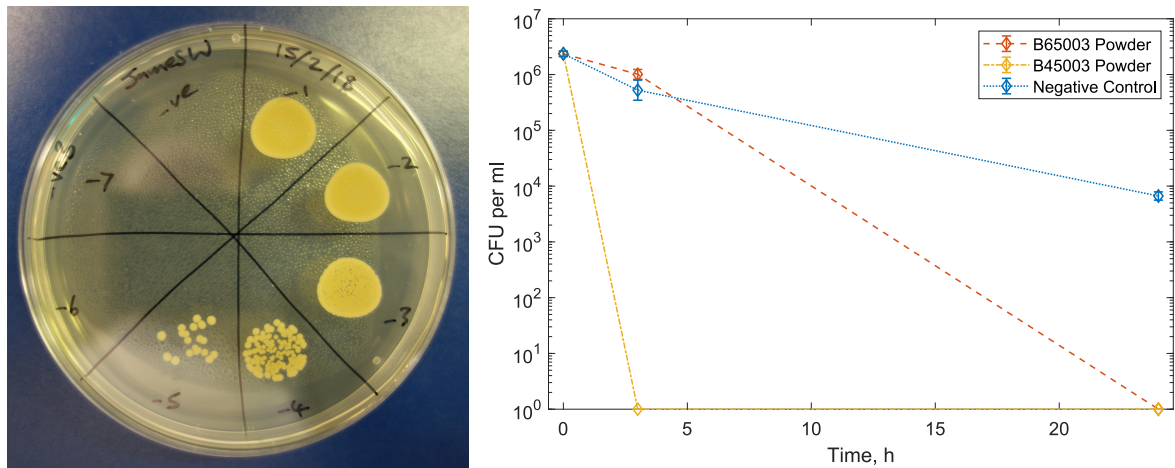
Figure 4.41: Protocol for the antibacterial testing of the powders, with timepoints. 🍷

Results

An example of a plated out Miles and Misra serial dilution after incubation is shown in Figure 4.42a, where the individual colonies become distinguishable at the higher dilutions (marked are the powers of 10 dilutions, for example -5 represents 10^{-5}). The results of the powder testing are shown in Figure 4.42b, where both glasses can be seen to completely kill *S. aureus* S235 in 24 hours.

Discussion

The results shown in Figure 4.42b show that both of the phosphate glasses have a very strong antimicrobial effect. Since both B45003 and B65003 are chemically identical, the differences observed here were thought



(a) Example Miles and Misra serial dilution, with 20 μ l plated out per dilution.

(b) Powder efficacy on *S. aureus* S235 in PBS (2 mg/ml powder). Results are geometric mean \times geometric standard error, zero values were given a value of 1 for analysis.

Figure 4.42: Results of the preliminary powder efficacy testing. 🚫

to be solely a result of the different particle size distributions, with the smaller additive (B45003) able to act more quickly in the PBS. With both of the powders proving effective, it was decided to proceed with testing for the microcomposite parts containing both B65003 and B45003.

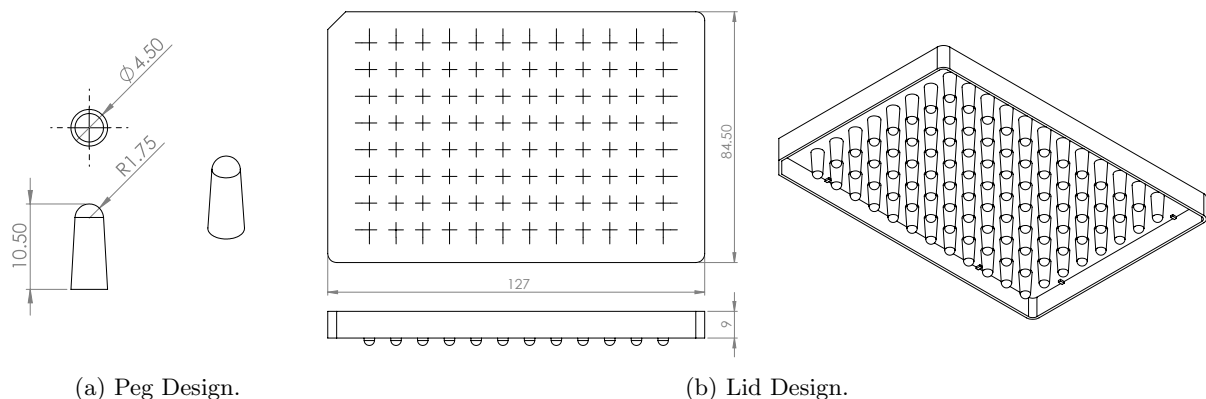
4.4.3 Preliminary Testing – Static Peg Assay

The first experiment performed to test the antimicrobial efficacy of the microcomposite parts was the static peg assay, against both *S. aureus* and *P. aeruginosa*. This new methodology was developed specifically based on the MBEC Peg Assay [470] to capitalise on the geometric freedom possible with laser sintering. The aim was to measure the formation of biofilms on the surface of the printed parts.

Methodology

Test Specimens

In order to test the antimicrobial efficacy of the laser sintered parts, pegs were designed as test specimens (shown in Figure 4.43a). These were designed to be glued onto a well plate lid and fit into a standard 96 well plate, allowing a constant contact area with the bacteria suspension below. Due to the low density of the printed parts, this also solved the issue of the LS parts floating on the surface of the media.



(a) Peg Design.

(b) Lid Design.

Figure 4.43: Design of the lid for the static peg assay. All dimensions in mm. 🚫

The design for these modified lids is shown in Figure 4.43b, showing the maximum number of pegs (96) able to be attached for a single 96-well-plate. For these preliminary experiments, the weighting of additive was also investigated, with loadings of 0.3% B45003, and 0.3%, 0.5% and 1.0% B65003 used. A photo of a typical completed lid to analyse these is shown in Figure 4.44, where the 5 materials were compared simultaneously (6 pegs per material).

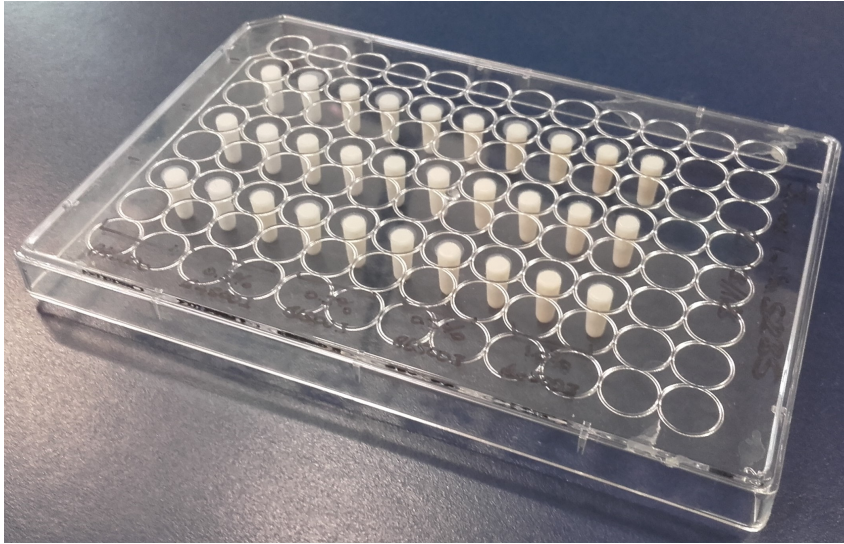
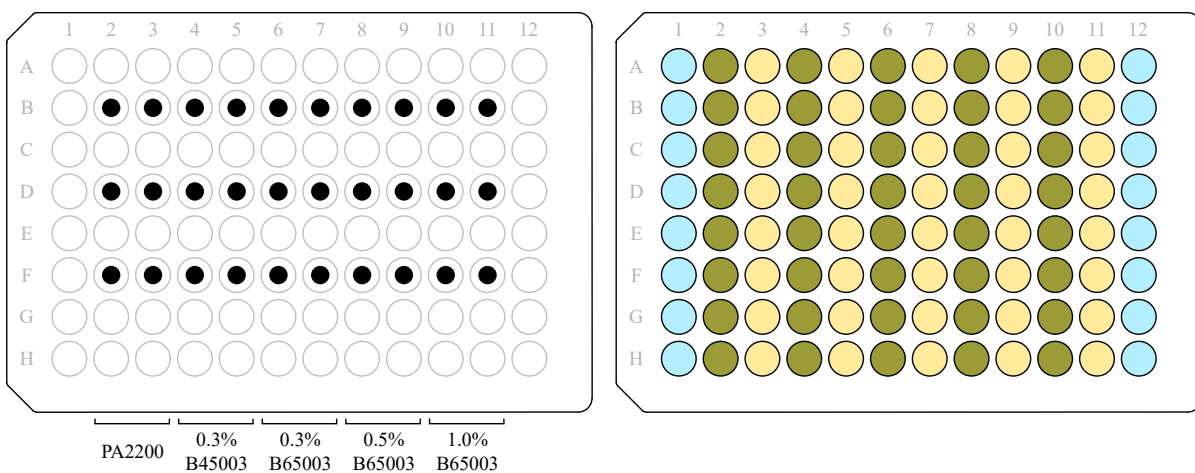


Figure 4.44: Completed peg lid (initial layout) for the static peg assay. 🦠

Protocol

The layout of pegs²³ on the lid and the corresponding wells in the well-plate are shown in Figure 4.45. Since the printing and gluing was not carried out in a sterile environment, sterilisation had to be carried out. Since the well-plate lids were not capable of withstanding the temperatures in a steam autoclave, this was done by submerging the modified peg lid in 70% Industrial Methylated Spirits (IMS) for 15 minutes (based on the preliminary experiment in Appendix C.2.1); with the lids then left to air-dry in a class II cabinet to prevent any subsequent contamination.

Pegs for each material were placed into two adjacent columns (see Figure 4.45), one of which contained 150 μl of the chosen bacteria (an overnight culture incubated at 37°C in BHI {Brain Heart Infusion}, diluted in BHI to an OD_{600} {Optical Density at 600 nm} of 0.01), and the other containing 150 μl BHI (without the bacteria) as a control. To limit the evaporation during incubation, 200 μl distilled water was placed in the outermost columns of the well-plate, with the plate and lid then wrapped in para-ply. Incubation took place in a shaking incubator at 37°C and 110 RPM for 24 hours.



(a) Layout of the pegs, with pegs in rows B, D and F. PA2200 pegs in columns 2–3, 0.3% B45003 in columns 4–5, 0.3% B65003 in columns 6–7, 0.5% B65003 in columns 8–9, and 1.0% B65003 in columns 10–11.

(b) Layout of the 96 well plate. Columns 2, 4, 6, 8 and 10 contain 150 μl of the culture at $\text{OD}_{600} = 0.01$, columns 3, 5, 7, 9 and 11 contain 150 μl broth only, and columns 1 and 12 contain 200 μl distilled water.

Figure 4.45: Layout of the modified peg lid and the 96-well-plate used in the experiment. 🦠

Three methods were used following incubation to indirectly measure the antimicrobial efficacy, each focusing on a separate aspect:

²³Dimensions of the printed pegs can be found in Appendix A.2, but did not form part of any subsequent analysis.

1. The Optical Density at 600 nm (OD_{600}) was measured across the well-plate. By comparing the differences in measurements from the wells with bacteria to the control wells, this was used as a proxy measurement for the number of planktonic bacteria present.
2. A PrestoBlue assay was used to measure the metabolic activity of the attached biofilm on the pegs. For this, following incubation, each peg was rinsed with 200 μ l PBS (in a separate 96-well-plate) before being submerged in 200 μ l PrestoBlue and incubated at 37°C for 15 minutes. The wells were then excited with light at 550 nm, with the fluorescence measured at 590 nm indicating the activity of the (living) cells.
3. Crystal Violet staining of the biofilms on the pegs was the final method used. The pegs were first rinsed with 200 μ l PBS, then submerged in 200 μ l crystal violet for 15 minutes to stain all of the cells on each peg. Excess stain was rinsed off with tap water, then left to dry overnight (in an incubator if necessary); with the pegs then immersed in 200 μ l of 30% acetic acid for 30 minutes to completely dissolve the stained cells. The absorbance (at 570 nm) was measured, giving a measure of the amount of cells (living or dead) present in the biofilm.

An overview of the protocol is shown in Figure 4.46, and summarised practically with detailed steps in Appendix A.6.

Results

The results from the static peg assay are shown in Figures 4.47 and 4.48. For the first repeat with each bacteria, large differences were seen between the PA2200 and the microcomposite parts. However, in these tests the pegs were positioned as in Figure 4.44 and it was suspected that evaporation at the edges could be the cause of the higher biofilm measurements on the outer pegs. To counteract this, the layout in Figure 4.45 was adopted, with distilled water placed in the empty wells and open containers of water placed in the incubator to raise the humidity. It should be noted that due to the variability in the growth of bacteria, experiments cannot be compared between repeats.

In Figure 4.47c, the negative values shown for the Crystal Violet stain indicate that the control pegs were measured as having more biomass than those in which the bacteria had been placed. Since all these were small in magnitude, this likely indicated that there was no biofilm formed on the pegs.

Photos of the wells after incubation, and of the pegs after incubation and crystal violet staining, are shown in Figures 4.49 and 4.50. In these, a clear difference can be seen between the bacteria-containing wells and the controls (BHI without bacteria).

Discussion

Effect on Planktonic Bacteria

The OD_{600} of the media in the wells, which would contain any planktonic bacteria after the pegs had been removed (Figures 4.47a and 4.48a), was used as a measure of the bacteria present after incubation, with no significant differences in either *S. aureus* S235 or *P. aeruginosa* SOM1 found between the PA2200 and the microcomposite pegs. A decrease in bacteria was found between the control wells and those containing pegs of all materials. This was thought to be due to the reduced surface area in the wells, limiting the amount of oxygen available, rather than an inherent antimicrobial efficacy of the PA2200. Further tests could be conducted anaerobically to test this.

Formation of Biofilms

The two methods used to quantify biofilm formation, were the cell viability on the pegs (Figures 4.47b and 4.48b) and crystal violet staining (Figures 4.47c and 4.48c). While these can be described as relatively crude tests when carried out individually, used together they give a quantitative indication of biofilm formation. In order to obtain more accurate results, individual pegs could be detached, sonicated and a Miles and Misra serial dilution (see Appendix A.5) carried out to determine the number of Colony Forming Units (CFU).

For the *S. aureus* S235, the cell viability assay (PrestoBlue – Figure 4.47b) showed no difference between the control pegs and those containing the silver additives. This, combined with the crystal violet results (Figure 4.47c – which showed no difference with the controls), indicated that no biofilms were formed on the pegs. The *P. aeruginosa* SOM1 assays (Figures 4.48b,c) produced a larger reading for the cell viability and the crystal violet, meaning that this was more likely to have formed a biofilm.

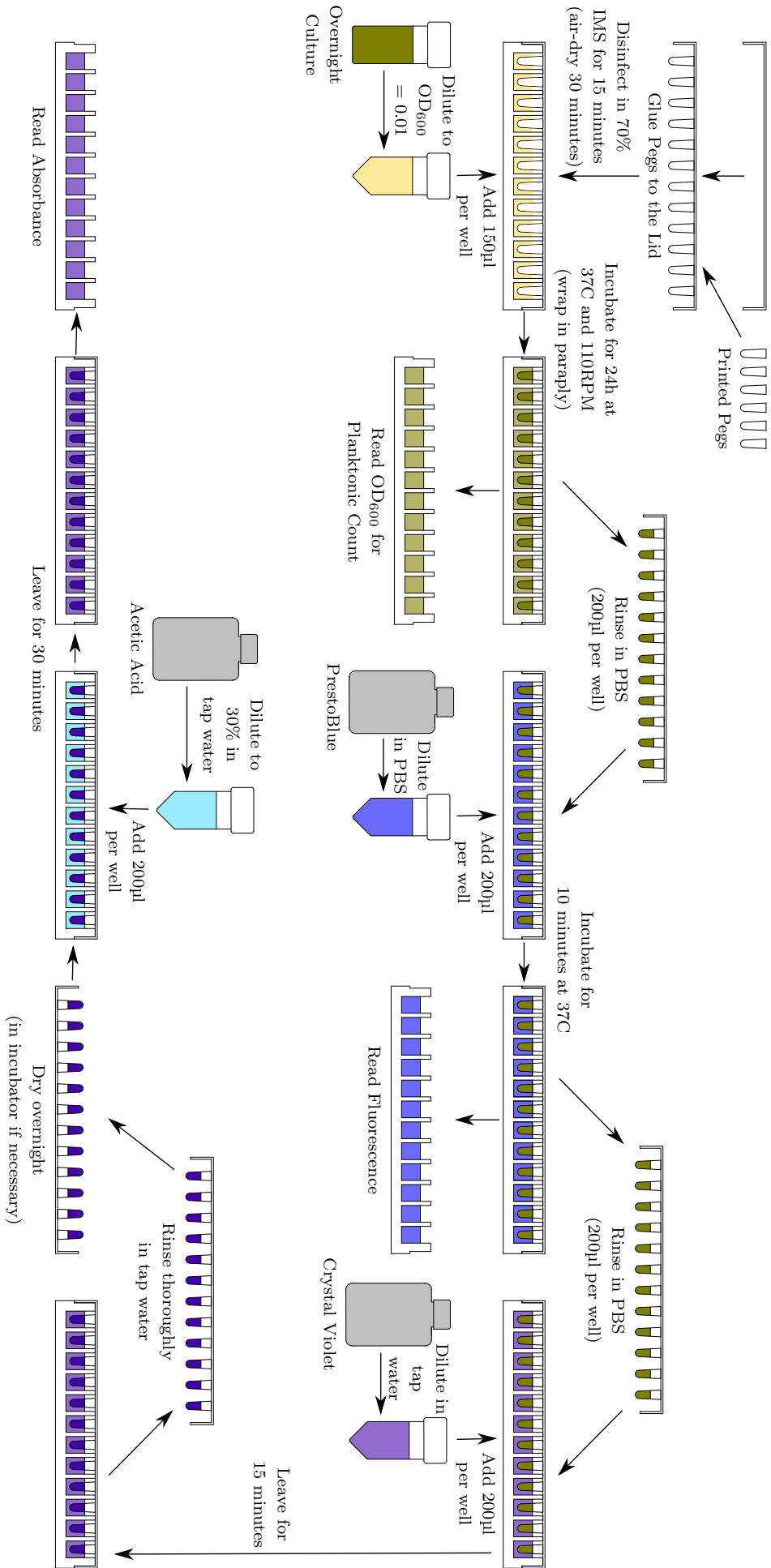

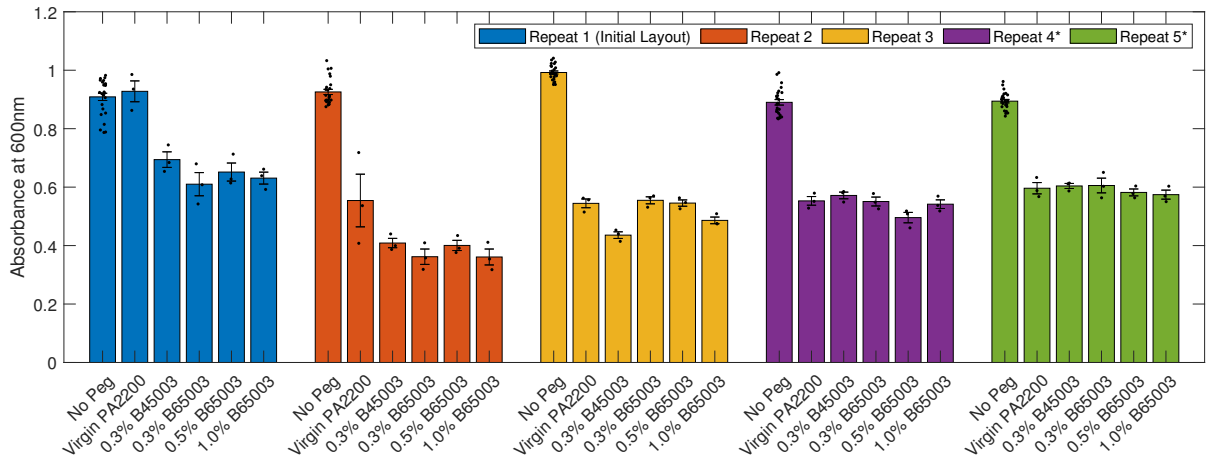
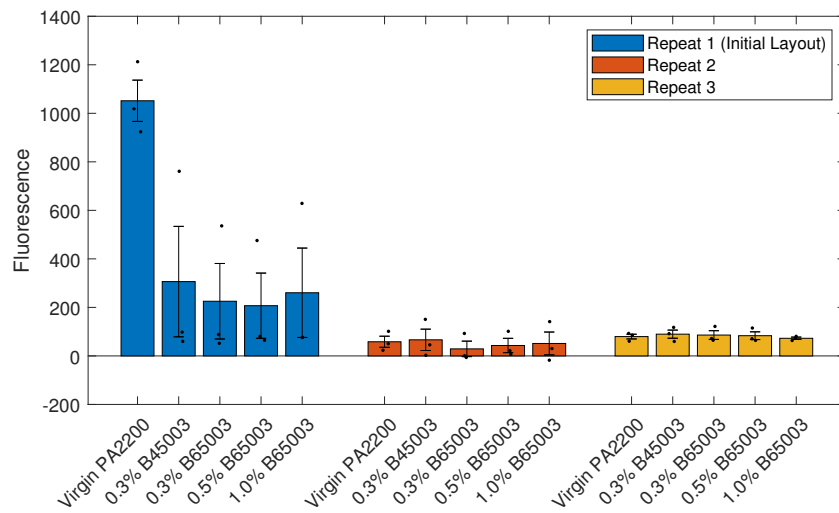


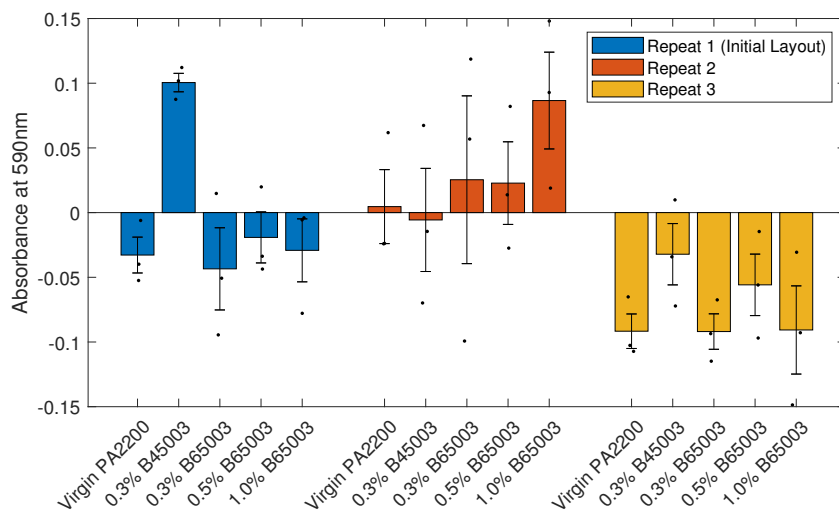
Figure 4.46: Protocol used in the static peg assay. 



(a) Optical density of the media, indicating growth of planktonic bacteria in the wells. Repeats marked (*) were carried out by R. Turner.

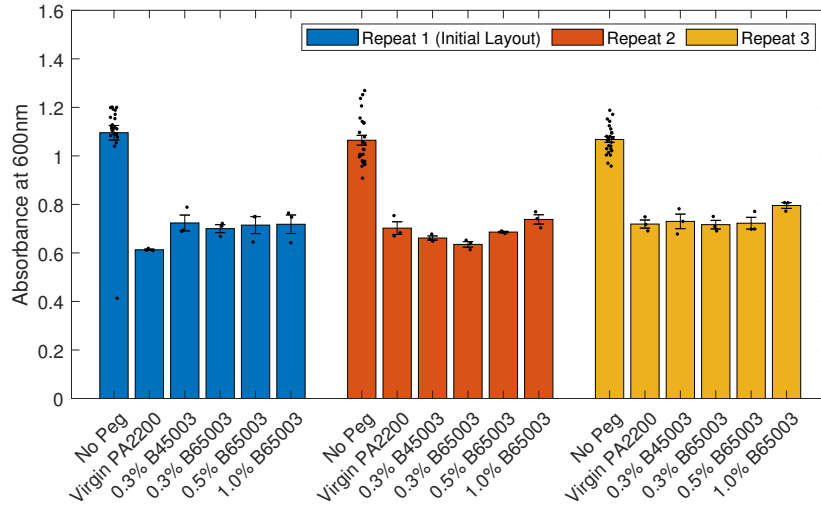


(b) Cell viability (PrestoBlue) assay, indicating cell viability of the attached biofilm.

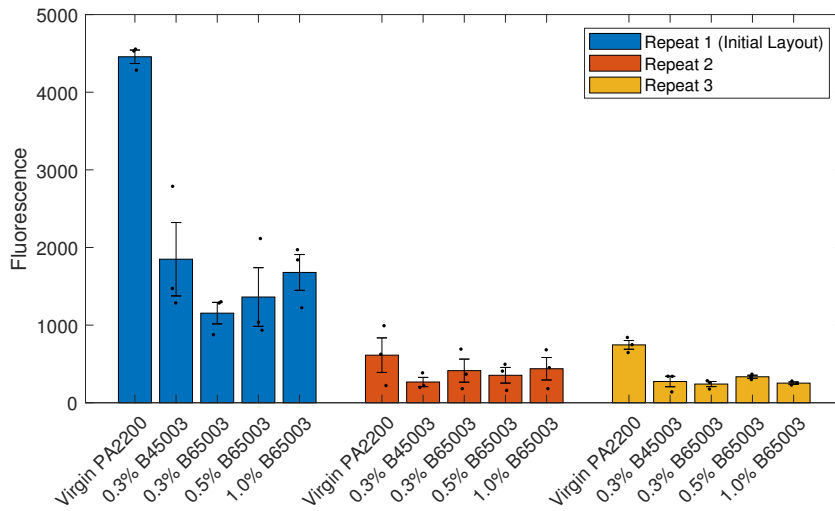


(c) Crystal violet staining, indicating the biomass of the attached biofilm.

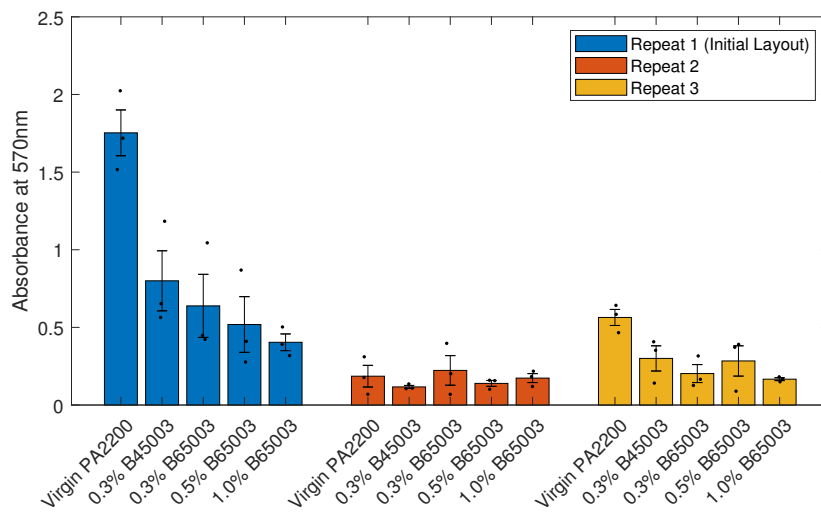
Figure 4.47: Results of the static peg assay after 24 hours incubation using *S. aureus* S235. Results are shown as the mean \pm standard error. 🚫



(a) Optical density of the media, indicating growth of planktonic bacteria in the wells.



(b) Cell viability (PrestoBlue) assay, indicating cell viability of the attached biofilm.



(c) Crystal violet staining, diluted $\times 10$, indicating the biomass of the attached biofilm.

Figure 4.48: Results of the static peg assay after 24 hours incubation using *P. aeruginosa* SOM1. Results are shown as the mean \pm standard error. 🚫

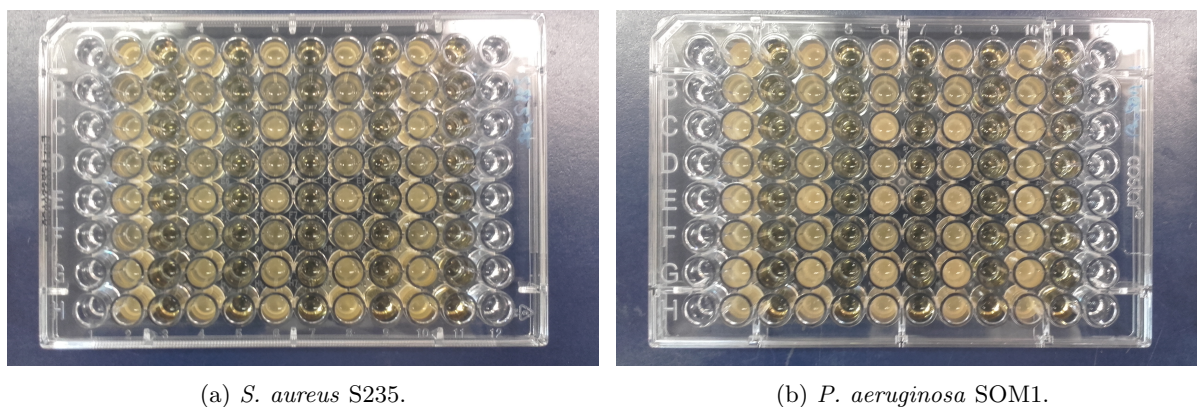
(a) *S. aureus* S235.(b) *P. aeruginosa* SOM1.

Figure 4.49: Photo of the planktonic bacteria in the wells after 24 hours incubation. The more opaque wells indicate bacterial growth. 🚫

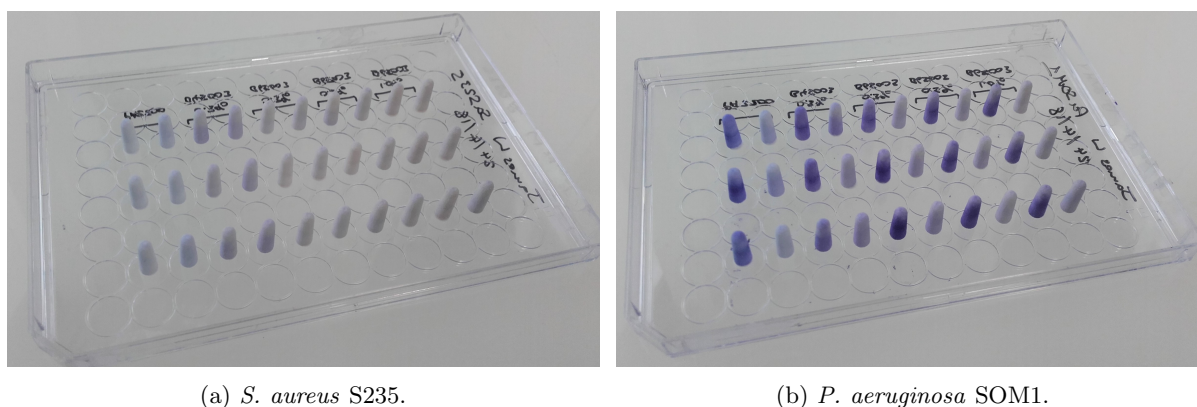
(a) *S. aureus* S235.(b) *P. aeruginosa* SOM1.

Figure 4.50: Crystal violet staining of the pegs after immersion in acetic acid, showing that some stain remained on the pegs even after dissolution. 🚫

Differences in cell viability and biomass were detected between the control pegs and the silver containing pegs for *P. aeruginosa* SOM1 (Figures 4.48b,c), suggesting that the inclusion of the additive could be having an antimicrobial effect. However, further tests would have to be carried out to confirm this. Modifications to the protocol could be made to obtain more definitive results, these could include changing the choice of media and incubation time.

Protocol – Critical Analysis

The static peg assay was designed as a high throughput method to analyse the biofilm formation on multiple materials simultaneously. The manufacture of the lids proved to be simple and repeatable with the use of a jig (printed with FDM) to hold the pegs in position during glueing, and the combination of tests carried out had the potential to give a clear indication of the antimicrobial efficacy. However, potential issues were identified during the experiments and during the subsequent analysis of the data; these centred on the crystal violet staining and the sterilisation of the parts.

Following the staining in crystal violet, the pegs had to be thoroughly rinsed in water to remove any excess stain. During this step, occasionally poorly attached biofilms would become detached from the pegs and be washed away; this was mostly avoidable with careful and gradual rinsing, but should be noted as a possible source of error. Another potential issue can be seen in Figure 4.50, where some of the stain can be seen on the pegs even after dissolution in acetic acid. This likely occurred during the drying time, with the hygroscopic polyamide 12 pegs absorbing some of the stain into the material, likely tempering the results.

The largest potential source of error was later identified as the sterilisation process (submersion in 70% IMS). With the results showing no significant differences between any of the materials, two explanations were thought to be likely; either there was no measurable difference in the antimicrobial efficacy between the materials, or another factor could be in play which had a greater effect on the bacteria than material. The hygroscopic nature of polyamide 12 was again considered here, with the possibility that some of the

IMS was absorbed into the pegs during sterilisation (then requiring a drying time longer than accounted for), which then leached out during testing.

Although the likelihood of this potential absorption and leaching of IMS was low, the potential “worst case” effect on the results was high. For this reason, it was decided that future experiments should avoid this method of sterilisation, instead using methods with less potential for contamination. The most commonly method used, both within the laboratory and more widely (see Section 3.3.2), is steam sterilisation. However, since the standard well-plate lids were not capable of withstanding the heat, and the effect on the glue used to attach the pegs was unknown, it was decided to switch to alternative methods for testing the antimicrobial efficacy.

4.4.4 Contact Efficacy (Planktonic)

In order to test the antimicrobial efficacy of the microcomposite parts on the surrounding environment, the methodology in this section was developed. To accommodate the use of steam sterilisation, individual parts were tested for each material, rather than a larger test specimen comprised of multiple materials (such as the peg lids in Section 4.4.3). This section focuses on measuring the antimicrobial efficacy of the parts on bacteria in nutrient-poor media.

Methodology

In its simplest form, the protocol used here revolved around immersing the parts in a bacteria-containing suspension and measuring the effect on the bacteria. This approach was significantly less scalable than that used in the static peg assay, but eliminated the uncertainty from the sterilisation and led to more accurate results.

Since the main method of action for the parts was thought to be elution of Ag^+ (rather than through direct contact with the surface), the 1 cm^3 spheres were used for the testing, with three spheres used per material per repeat. The water uptake and silver release had been previously been characterised for this geometry (see Sections 4.3.2 and 4.3.4), allowing for a direct comparison between the measured values and the antimicrobial efficacy.

The protocol was based on the preliminary powder efficacy method (Section 4.4.2), with the spheres first placed in autoclave bags and steam sterilised at 121°C . These were then combined with 5 ml PBS containing the bacteria (grown overnight in BHI at 37°C) diluted to an OD_{600} of 0.01; before being incubated in a shaking incubator at 37°C . At timepoints of 0, 3, and 24 hours, 10 μl of the surrounding media was removed, and a Miles and Misra serial dilution carried out to determine the number of CFU/ml.

An overview of the protocol used is shown in Figure 4.51

Results

The results of the contact efficacy against *S. aureus* S235 are shown in Figure 4.52, where the parts can be seen to display some amount of antimicrobial activity after 24 hours. The reduction in bacteria is generally relatively small, with the largest differences found for 1% B45003, with 4-log and 2-log reductions shown in repeats 2 and 3. After 24 hours, all the repeats for 1% B45003 showed significantly lower number of bacteria compared to PA2200 (p -values of 0.040, 0.001, and 0.005 for the three repeats {log-values analysed}); with the values for 1% B65003 showing no significant difference from PA2200.

Note that this protocol was originally planned to be repeated with *P. aeruginosa* SOM1. However, additional antimicrobial testing was also being carried out on the microcomposites by R. Turner (see Section 4.4.5), with the overlap sufficient to make this unnecessary.

Discussion

The results shown in Figure 4.52 echo those of the powder testing (Section 4.4.2), with the microcomposites containing 1% B45003 generally displaying a greater reduction in CFU/ml compared to 1% B65003. Interestingly, after 24 hours, the majority of samples containing spheres of any material showed a statistically significant reduction in bacteria compared to the control. This could have been caused by the impact of the spheres in the shaking incubator, or the reduced oxygen available at the surface (due to the part of the floating sphere in contact with the air). These tests also only tell part of the story, as some of the planktonic bacteria were likely to have attached to the LS parts to form a biofilm, thus reducing the planktonic count in the surrounding media.

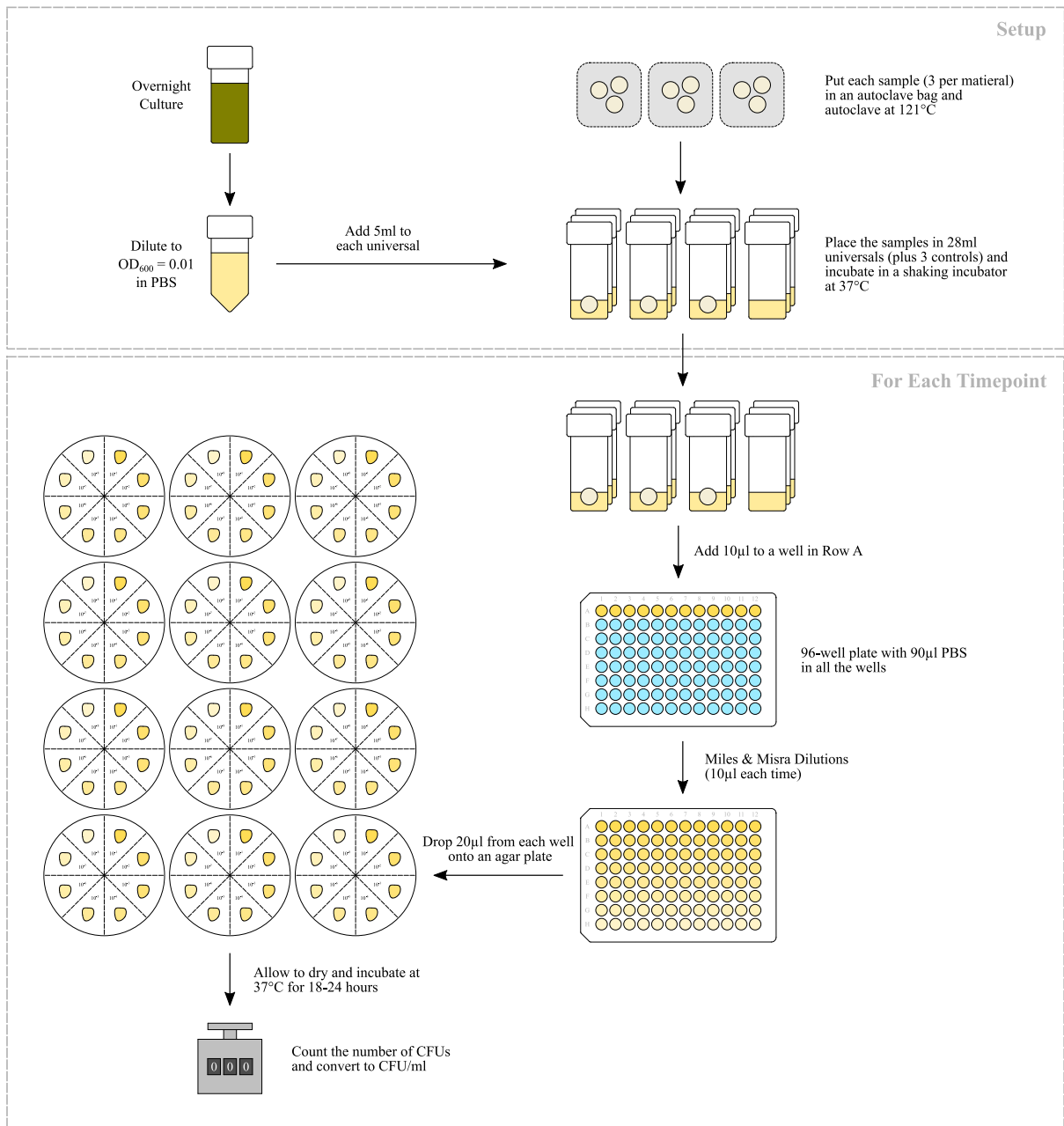
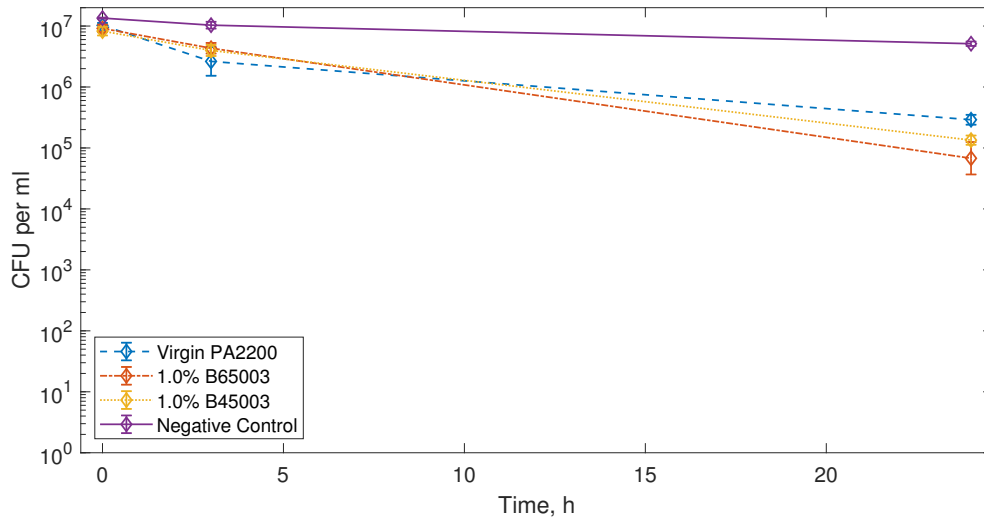
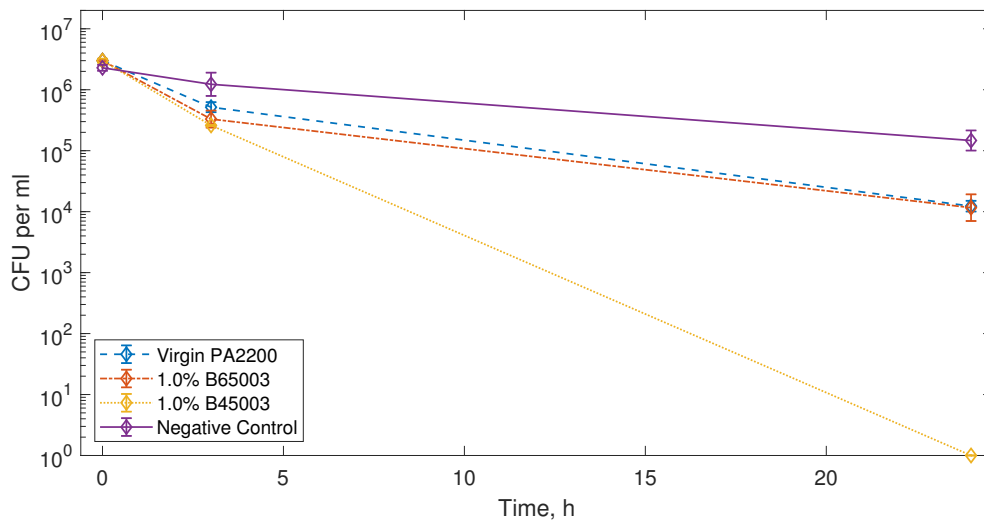


Figure 4.51: Protocol for the antibacterial contact testing of the microcomposite parts, with timepoints. 🚫

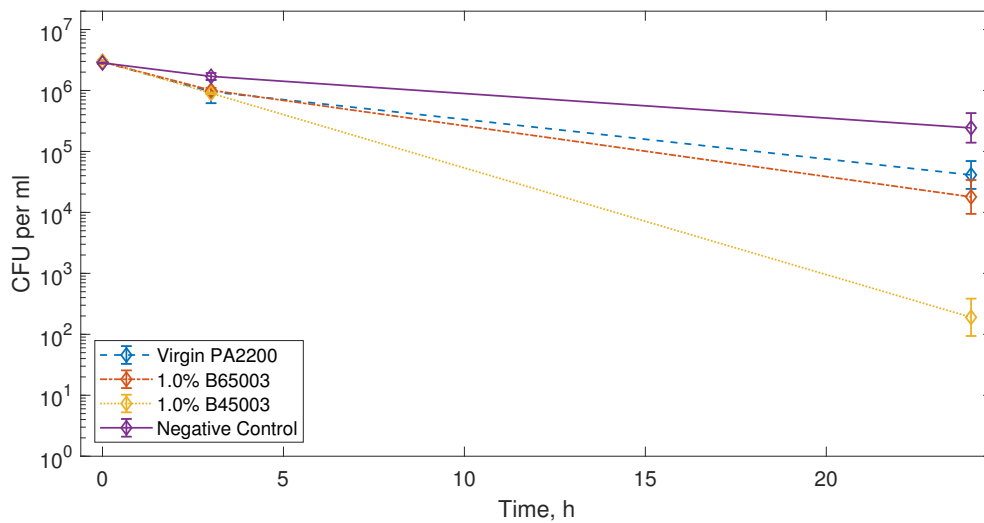
Despite the higher efficacy of B45003 measured here, it was decided to focus on B65003 in subsequent tests. This was primarily based on the processability of the feedstock in LS (see Section 4.1.4), rather than on the antimicrobial efficacy, as well as the results of the water uptake experiments (as discussed in Section 4.3.2).



(a) Repeat 1 – Plastic Universals.



(b) Repeat 2 – Glass Universals. Measured zero values were given a value of 1 for analysis.



(c) Repeat 3 – Glass Universals.

Figure 4.52: Part effectiveness against *S. aureus* S235, with 1 sphere in 5 ml PBS. Results are geometric mean * geometric standard error. 🍷

4.4.5 Additional Microbial Testing (carried out by R. Turner)

The majority of the antibacterial testing carried out on the 1% B65003 microcomposites, was performed by Robert (Bob) Turner as part of a 1-year Research Assistant position. Key data from this is included here to give a more complete picture of the antimicrobial efficacy, which has also been published in [451, 452].

The antibacterial tests in this section were designed and planned in close collaboration with the author, with similar methods to Section 4.4.4 used. Raw data was obtained with permission from [452], with all subsequent analysis carried out by the author.

Nutrient-Poor Media

The contact efficacy on suspended bacteria was determined using a paired back version of the time course in Section 4.4.4, with additional steps to analyse the effect on biofilm formation. A further non-contact test was carried out to determine whether contact with the microcomposite was necessary to have an antimicrobial effect.

Methodology

For the contact tests, 1 cm³ spheres were autoclaved inside glass universals, before 5 ml PBS (inoculated with an overnight culture in BHI of the chosen bacteria to an OD₆₀₀ = 0.01) was added, these were then incubated at 37°C and 110 RPM for 24 hours. After this, the spheres were removed, washed twice in PBS to remove any loosely attached bacteria, then vortexed (agitated vigorously) for 30 seconds in 2 ml PBS to release the biofilm. A serial dilution was carried out on both the planktonic bacteria and the detached biofilm, recording the number of CFUs/ml for each.

To determine whether these effects were solely contact-dependent, additional non-contact tests were carried out. For these, the spheres were incubated with 5 ml PBS (at 37°C and 110 RPM) for 24 hours, before the spheres were removed and bacteria added to make an OD₆₀₀ = 0.01; these were then incubated for a further 24 hours before a serial dilution was performed to count the CFUs. With this method, the only possible method of antimicrobial activity was through the prior elution of antimicrobial particles into the PBS.

Results

The results of the contact testing can be seen in Figures 4.53a–d, both for the effect on planktonic bacteria and the attached biofilm. In these, a marked reduction in planktonic CFU can be seen for both *S. aureus* S235 and *P. aeruginosa* SOM1; showing a 3.5-log ($p = 0.001$) and 2.5-log ($p = 0.000$) reduction respectively. A large antimicrobial effect can also be seen with the biofilms; however the spread of results for *S. aureus*, mean that although 4/9 samples showed no viable CFUs, this difference was not statistically significant.

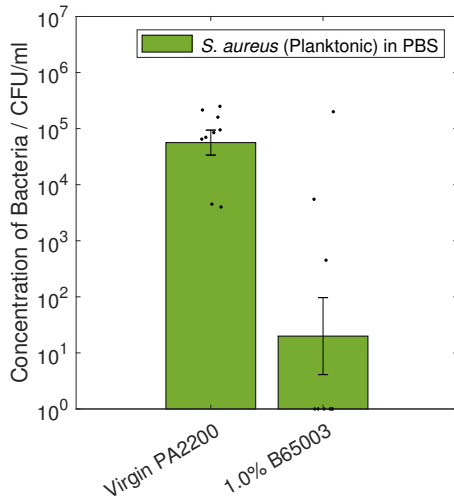
The results of the non-contact tests are shown in Figure 4.53e. Carried out as a preliminary test, this only focused on *S. aureus* S235, with a large reduction (3.8-log, $p = 0.000$) in CFU found.

For all the experiments shown in Figure 4.53, the full results split into individual repeats can be found in Appendix B.6.1.

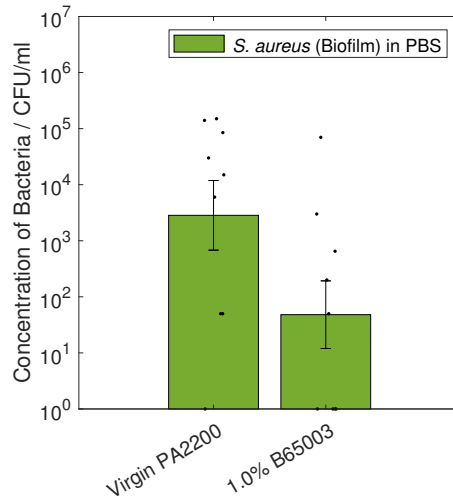
Discussion

These results (Figure 4.53) clearly show that the 1% B65003 microcomposites have a significant antimicrobial effect in nutrient-poor environments. Comparing between the contact and non-contact data, the results in Figure 4.53e suggest that the main method of the antimicrobial efficacy was through the elution of Ag⁺, with no direct contact needed with the part surface needed. This confirms the method of action proposed in Section 3.7.6 for silver-containing microcomposite materials.

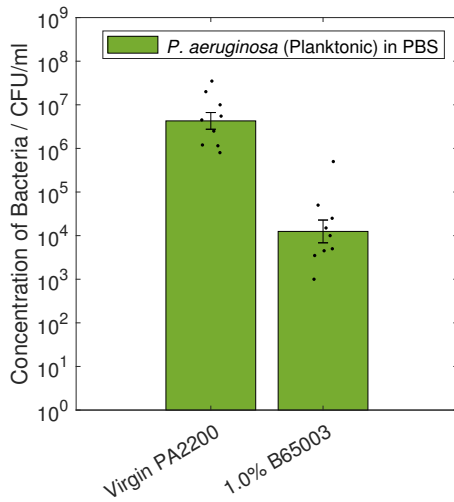
One aspect which was not shown with these tests, was whether the inclusion of a PA2200 part affects the CFU in any way. Although no difference would be expected from a negative control (a bacterial suspension without an LS sphere), this additional information would further validate the efficacy of the microcomposite.



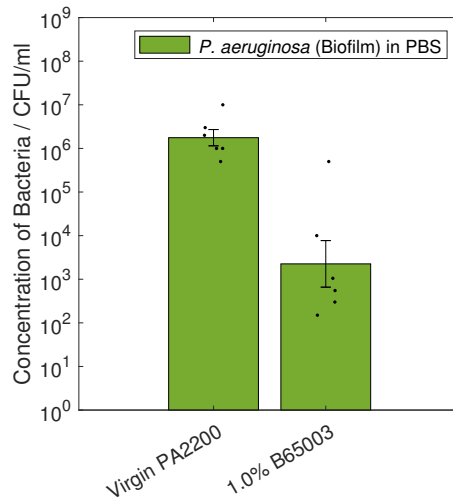
(a) *S. aureus* S235 (Planktonic) in PBS; showing a 3.5-log reduction, $p = \mathbf{0.001}$.



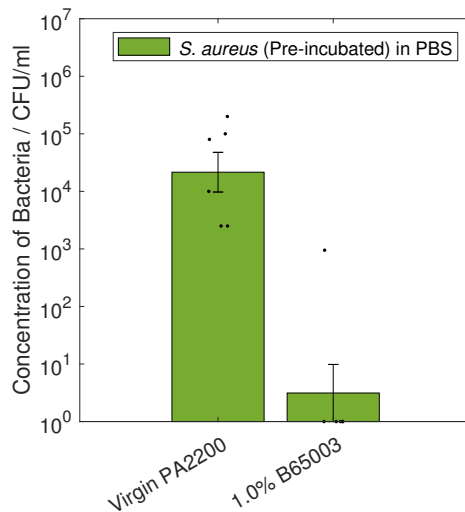
(b) *S. aureus* S235 (Biofilm) in PBS; showing a 1.8-log reduction, $p = 0.058$.



(c) *P. aeruginosa* SOM1 (Planktonic) in PBS; showing a 2.5-log reduction, $p = \mathbf{0.000}$.



(d) *P. aeruginosa* SOM1 (Biofilm) in PBS; showing a 2.9-log reduction, $p = \mathbf{0.002}$.



(e) *S. aureus* S235 (Planktonic) in PBS pre-incubated with a microcomposite sphere; showing a 3.8-log reduction, $p = \mathbf{0.000}$.

Figure 4.53: Additional antimicrobial testing in nutrient-poor media. Results shown are geometric mean \times geometric standard error, measured zero values were given a value of 1 for analysis. Log differences and p -values are shown, with statistically different results (< 0.05) shown in bold [451]. 🚫

Nutrient-Rich Media

While tests in PBS were a good representation of scenarios where contact with nutrient-poor liquids (such as water) is likely, a major use case of antimicrobial materials is in nutrient-rich media. An extreme example of this is for use cases inside the body, with blood being an example of a nutrient-rich media.

Methodology

To test the contact efficacy with a nutrient-rich media, Brain Heart Infusion (BHI) was used, otherwise utilising the same methodology as in the nutrient-poor media experiments.

The literature suggested that interaction with thiols in the blood could lead to silver having a reduced antimicrobial efficacy [471]. To test for this additional experiments, with 1 mM glutathione added to PBS, were carried out to determine the cause of any differences found with BHI.

Results

The results of the contact tests in BHI are shown in Figures 4.54a–d, both for the planktonic and biofilm data of *S. aureus* S235 and *P. aeruginosa* SOM1. In this, it can be seen that there was no significant difference in any of the results, with no antimicrobial effect measured.

The results of the contact tests in PBS with 1 mM glutathione are shown in Figures 4.54e,f, with no significant difference seen for planktonic *S. aureus* and a slight increase in CFU seen for the biofilm data. Note that as a proof-of-concept experiment, this was only carried out on *S. aureus* S235.

For all the experiments shown in Figure 4.54, the full results split into individual repeats can be found in Appendix B.6.2.

Discussion

These results in Figures 4.54a–d clearly show that components in the nutrient-rich media disrupt the antimicrobial efficacy of the microcomposite parts. While more repeats would have to be carried out to prove this conclusively (only one repeat was carried out with *S. aureus* and two with *P. aeruginosa*), this strongly suggests that any potential use cases for the microcomposite materials would be better suited to nutrient-poor conditions, rather than in nutrient-rich environments (such as those around implants).

The effects seen in nutrient-rich media were also seen in PBS with 1 mM glutathione (Figures 4.54e,f), confirming that the thiols present were the cause of the decreased levels of antimicrobial efficacy.

Cytotoxicity

Since any microcomposite parts made are likely to come into contact with humans or animals, the cytotoxicity (how toxic the parts are to mammalian cells) was important to establish.

Methodology

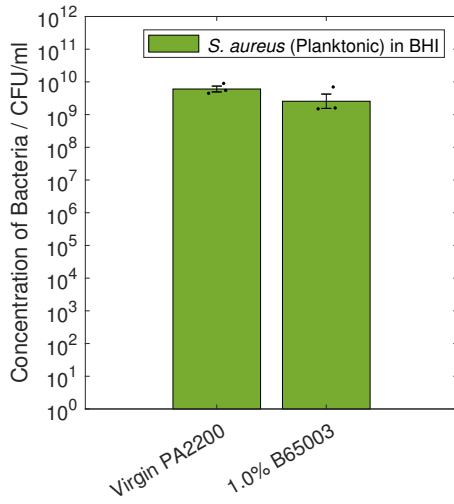
The full methodology for these tests can be found in [451], with only the key points shown here. Testing was carried out by R. Turner and T. Paterson.

In this experiment, human primary dermal fibroblasts isolated from donor skin were grown and exposed to LS discs in a 12-well plate for 24 hours, encouraging attachment and growth on the part surface. A PrestoBlue assay was carried out (as in Section 4.4.3), with cells excited at 535 nm and emission measured at 590 nm. The resulting fluorescence measurement was proportional to the cell metabolic activity.

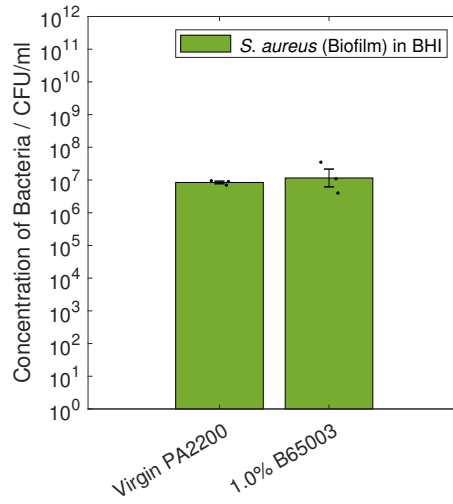
Results and Discussion

The results of the cytotoxicity experiments can be seen in Figure 4.55, where no significant difference can be seen for any of the measured materials.

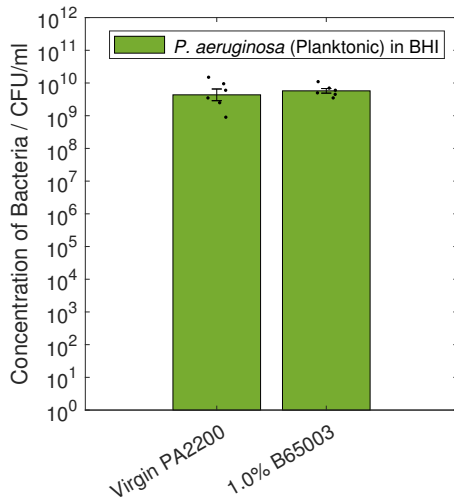
The values shown in Figure 4.55 show that neither the pure PA2200 parts or the 1% B65003 parts have any cytotoxic effect on human cells. This was crucial for any potential use case of the microcomposite materials, since any effect against mammalian cells would make them much more hazardous to use, severely limiting the potential applications. The results here show that the levels of Ag⁺ released from the parts were sufficient to have a substantial effect against bacteria, without affecting mammalian cells.



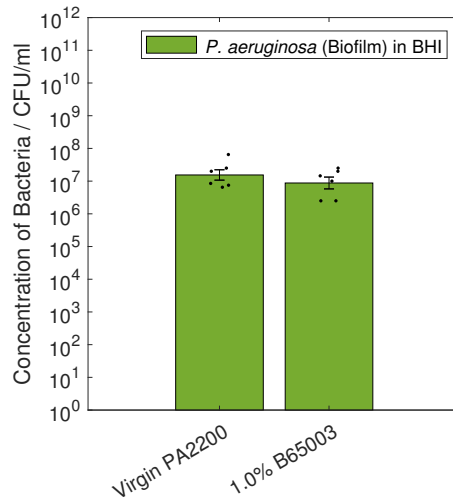
(a) *S. aureus* S235 (Planktonic) in BHI; showing a 0.4-log reduction, $p = 0.223$.



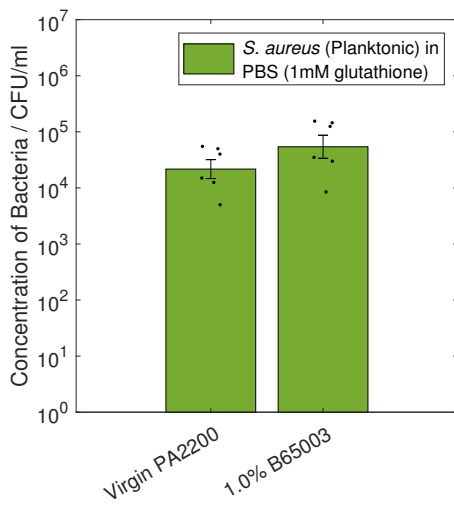
(b) *S. aureus* S235 (Biofilm) in BHI; showing a 0.1-log increase, $p = 0.666$.



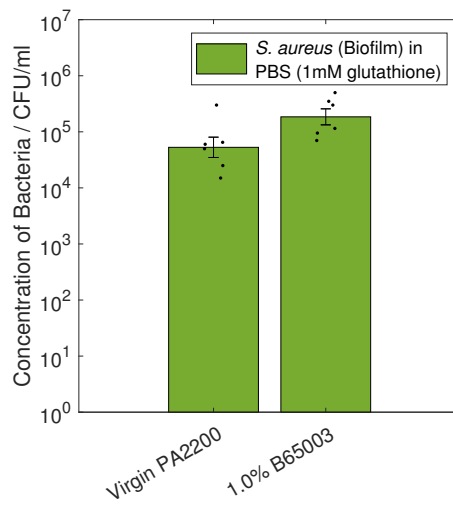
(c) *P. aeruginosa* SOM1 (Planktonic) in BHI; showing a 0.1-log increase, $p = 0.547$.



(d) *P. aeruginosa* SOM1 (Biofilm) in BHI; showing a 0.2-log reduction, $p = 0.332$.



(e) *S. aureus* S235 (Planktonic) in PBS with 1mM glutathione; showing a 0.4-log increase, $p = 0.167$.



(f) *S. aureus* S235 (Biofilm) in PBS with 1mM glutathione; showing a 0.5-log increase, $p = \mathbf{0.041}$.

Figure 4.54: Additional antimicrobial testing in nutrient-rich media. Results shown are geometric mean * geometric standard error. Log differences and p -values are shown, with statistically different results (< 0.05) shown in bold [451].

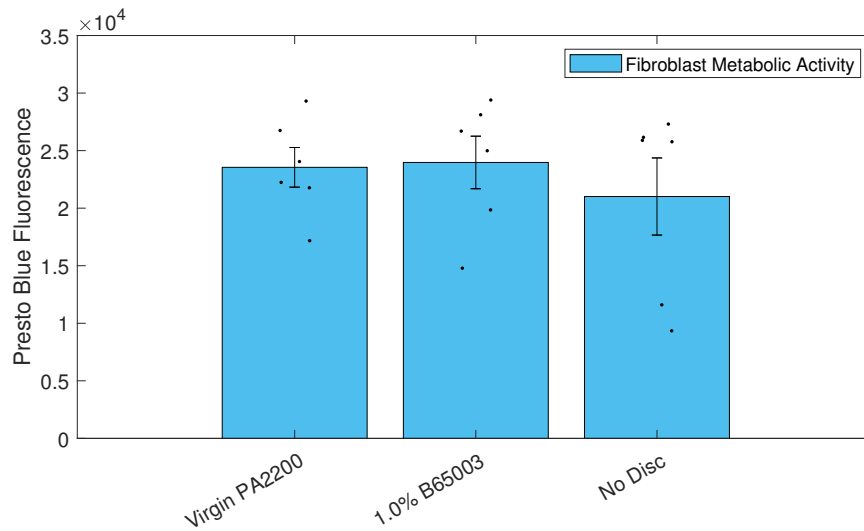


Figure 4.55: Cytotoxicity test results with human fibroblasts. Results shown are the mean \pm standard error [451]. 🚫

4.5 Chapter Summary

A brief summary of the experiments carried out in this chapter is included here, with reference to which research question (see Section 3.7.3) they contributed to answering. A more detailed discussion of these results can be found in Chapter 6.

RQ 1 Can powder feedstocks containing silver-doped phosphate-based additives be effectively processed in Laser Sintering?

This question is addressed in Section 4.1, with experiments focusing on the powder characterisation and the printing of the composite feedstock in LS.

Section 4.1.1 Analysed the morphology of the polymer powder and the additives used, using SEM.

Section 4.1.2 Measured the particle size distribution for all the powders used, using laser diffraction.

Section 4.1.3 Measured the thermal properties of the polymer and additive, using DSC.

Section 4.1.4 Focused on the build setup, creating the composite powder feedstock, and processing the feedstock in Laser Sintering.

RQ 2 Does the addition of these additives affect the Engineering properties of the parts, and are these sufficiently dispersed throughout the part?

This question is addressed in Section 4.2, focusing on the inherent properties of the printed parts.

Section 4.2.1 Measured the mechanical properties of the printed microcomposite parts, using tensile testing.

Section 4.2.2 Analysed the thermal properties of the printed parts, using DSC.

Section 4.2.3 Measured the chemical composition of the additives and qualitatively analysed the dispersion of the additive on the part surface, using EDX.

Section 4.2.4 Analysed the microstructure of the parts to determine any effect on the porosity, using Micro-CT.

Section 4.2.5 Quantitatively analysed the dispersion of the additive within the part, using Micro-CT.

Section 4.2.6 Measured the mineral composition of the printed parts to verify the incorporation of silver, using ICP-ESMS.

RQ 3 Do the printed parts absorb water and release silver ions, and how does this compare to similar materials manufactured with other processes?

This question is addressed in Section 4.3, focusing on the behaviour of the parts in relation to specific external factors relevant to the antimicrobial performance.

Section 4.3.1 Investigated the effect and reversibility of steam sterilisation on the mechanical properties of LS PA12 parts.

Section 4.3.2 Measured the water uptake for the printed microcomposite parts.

Section 4.3.3 Investigated whether the geometry of the parts affected the water uptake characteristics.

Section 4.3.4 Measured the release rate of Ag^+ into water, using ICP-ESMS.

RQ 4 Do the printed parts show display significant antibacterial functionality, against representative and problematic strains of bacteria?

This question is addressed in Section 4.4, focusing on developing suitable test methods and determining the antibacterial efficacy and cytotoxicity of the printed parts.

Section 4.4.1 Specified the bacterial strains (one Gram-positive and one Gram-negative) used.

Section 4.4.2 Measured the efficacy of the additives (preliminary experiment), tested against *S. aureus*.

Section 4.4.3 Developed a preliminary methodology for determining the effect on biofilm formation and planktonic cells, using a static peg assay.

Section 4.4.4 Developed a method to measure the contact efficacy (planktonic), tested against *S. aureus*.

Section 4.4.5 Detailed additional microbial testing carried out by R. Turner on the printed parts. Measuring the contact efficacy against biofilm formation and planktonic cells of the parts in nutrient-poor and nutrient-rich media, the non-contact efficacy in nutrient-poor media, and the cytotoxicity against human cells.

Chapter 5

Custom-Made Silver Phosphate Additives

The part characterisation and antibacterial tests carried out in Chapter 4, proved the concept that silver phosphate-containing LS parts can have an antimicrobial effect. However, with the commercial additive, there was little control over the composition of the phosphate glass. This meant that it was not clear what characteristics of the additive would be desirable, or which would have a significant effect on the antimicrobial efficacy of the printed parts.

The characteristics of the additives thought to have the largest effect on the amount of silver released (and therefore the antimicrobial efficacy), were the amount of silver in the additives, and their degradation rate. Both of these properties have the potential to affect the longevity of any antimicrobial efficacy, as well as the strength of any biocidal effect measured.

The initial focus chosen was the degradation rate of the additives, as it was unclear whether this would have a significant effect, or whether the rate of water diffusion through the polymer matrix would prove to be the limiting factor. While the concentration of silver could increase the silver release, the concentration used here was close to the maximum possible to incorporate into a phosphate-based glass (approximately 2 mol%, above which metallic silver would form [472]), thus limiting the potential benefits.

In this chapter, three custom silver phosphate glass compositions were created in order to determine whether the additive degradation rate had a significant effect on the silver ion release. All three of these additives were intended to contain the same amount of silver, and were designed to be comparable with those analysed in Chapter 4. The chapter structure is shown in Figure 5.1, following a similar experimental plan as Chapter 4.

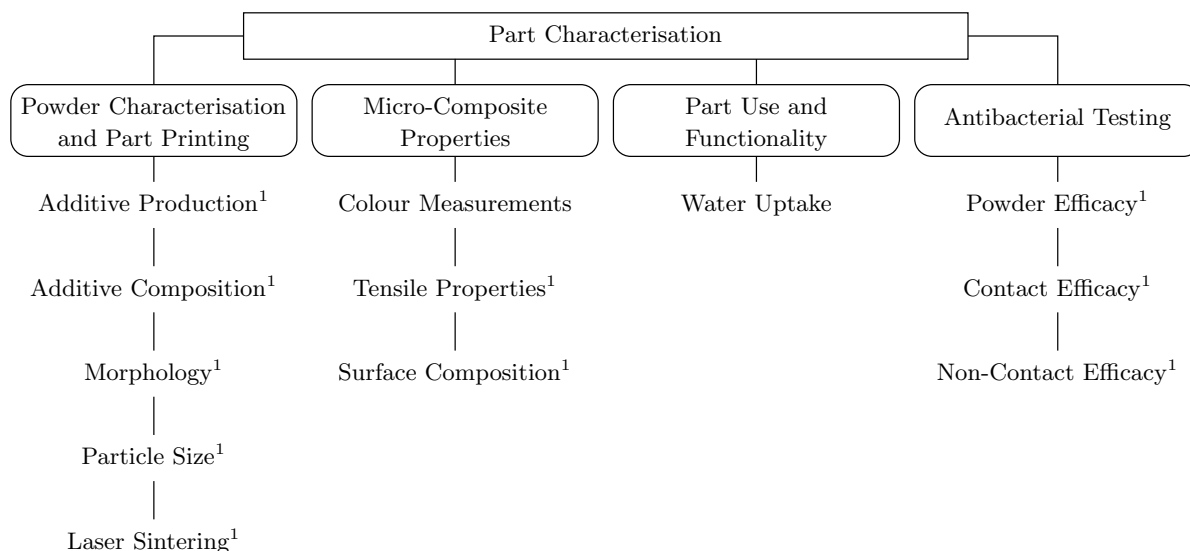


Figure 5.1: Custom-made silver phosphate additives chapter structure. ¹Published in [445]. 🇬🇧

5.1 Powder Characterisation and Part Printing

Similarly to the antibacterial testing, the methodology used here was approached from an Engineering perspective, with no prior knowledge of glass design or manufacture. The methodology and formulations shown in this section are a result of consultations with experts in material science, with the designs mostly based on personal experience.

5.1.1 Additive Production¹

The custom glasses shown in this section were designed in collaboration with Dr. Ifty Ahmed (University of Nottingham), and were manufactured by Md Towhidul Islam (University of Nottingham). The design of these was based on the measured composition of B65003 (Table 4.6), the manufacturer’s measurement of silver content in B65003 (1.9%), and personal experience.

Additive Design

In its pure form phosphate dissolves quickly, however by adding other oxides (such as Na₂O, CaO, and MgO) in varying proportions, the release rate could be tailored; creating an approximately linear dissolution rate (and associated release of Ag⁺) over its lifetime [446,448].

The proportions of P₂O₅ and MgO were altered here to create glass compositions with different degradation rates; with decreased levels of P₂O₅ and increased levels of MgO both previously shown to reduce the degradation rate in water [473,474]. The amounts of Ag₂O were designed to be kept constant, as increasing this has also been shown to affect the structure of phosphate-based glasses, increasing their strength and decreasing degradation rates [448–450].

The three chosen glasses were in the system of (50-*x*)P₂O₅-(14+*x*)MgO-16CaO-18Na₂O-2Ag₂O (where *x* = 0, 5, 10), as shown in Table 5.1. This was used to denote the three formulations as P40, P45, and P50, proportions previously used for research into similar glasses [475].

| Glass Name (abbreviation) | Glass Formulation / mol% | | | | |
|---------------------------|-------------------------------|------|------|-------------------|-------------------|
| | P ₂ O ₅ | MgO | CaO | Na ₂ O | Ag ₂ O |
| P40Mg24Ca16Na18Ag2 (P40) | 40 | 24 | 16 | 18 | 2 |
| P45Mg19Ca16Na18Ag2 (P45) | 45 | 19 | 16 | 18 | 2 |
| P50Mg14Ca16Na18Ag2 (P50) | 50 | 14 | 16 | 18 | 2 |
| B65003* | 48.0 | 34.0 | 17.1 | – | 1.0 |

Table 5.1: Custom additive oxide compositions by molar percentage. *included for comparison, calculated from the measured EDX spectrum (Table 4.6), see Section 5.1.2 for details.

Manufacturing

To manufacture the glasses, the precursors (shown in Table 5.2) were weighed and mixed to achieve the formulations in Table 5.1, before being transferred to a quartz crucible (VWR International) and placed in a furnace. The precursors were heated at a rate of 10°C/min, held at 350°C for 0.5 hours to remove any H₂O, then heated further and held at 1150°C for 1.5 hours to achieve full melting. The resulting molten glass was then poured onto a steel plate and allowed to cool to room temperature. The glass was subsequently ground using a Retsch PM 100 ball mill, and sieved to obtain a <45 µm powder.

| Precursor | Chemical Composition | Manufacturer |
|---|--|---------------|
| Sodium dihydrogen phosphate | NaH ₂ PO ₄ | Sigma Aldrich |
| Magnesium hydrogen phosphate trihydrate | MgHPO ₄ · 3H ₂ O | Sigma Aldrich |
| Calcium hydrogen phosphate | CaHPO ₄ | Sigma Aldrich |
| Phosphorous pentoxide | P ₂ O ₅ | Sigma Aldrich |
| Silver phosphate | Ag ₃ PO ₄ | Alfa Aesar |

Table 5.2: Precursors used to manufacture the custom glasses.

Photos of the three additives produced can be seen in Figure 5.2, with all of the glasses similar in appearance and colour.

¹Due to COVID-19 delays and restrictions, there was no opportunity for any iterations of the additives.

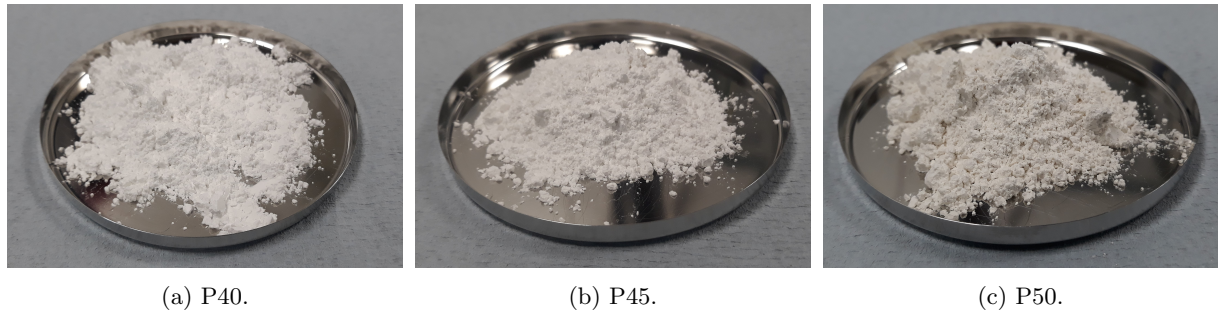


Figure 5.2: Photos of the three custom silver phosphate glass additives produced, each amount shown is approximately 20 g. 🚫

5.1.2 Additive Composition

In order to determine the composition of the manufactured custom additives, EDX was used. This was carried out on each of the three powders, obtaining an elemental spectrum (by weight) for each. These were then used to determine the oxide composition for each of the glasses.

Methodology

The same methodology as Section 4.2.3 was used for the EDX scanning, utilising a 15kV accelerating voltage and detecting back-scattered electrons. Once obtained, the measured weight% compositions percentages were converted to atomic% compositions using their atomic masses [476]. Using these, the molar% of each oxide was calculated based on the atomic% of each element (P, Mg, Ca, Na, Ag).

Results

The measured weight% compositions are shown in Table 5.3 alongside the expected values described in Section 5.1.1. These were then converted into their atomic% (Table 5.4), before the glass oxide composition was determined (shown in Table 5.5). For both these steps, the analysis of B65003 (measured in Section 4.2.3) has been included for comparison.

| Element | P40 / weight% | | P45 / weight% | | P50 / weight% | | B65003 |
|---------|---------------|----------|---------------|----------|---------------|----------|----------|
| | Expected | Actual | Expected | Actual | Expected | Actual | Actual |
| P | 27.8 | 26.6±0.2 | 29.6 | 30.7±0.3 | 31.2 | 29.9±0.2 | 15.1±0.1 |
| Mg | 6.6 | 6.1±0.1 | 4.9 | 4.6±0.1 | 3.4 | 3.1±0.1 | 4.2±0.0 |
| Ca | 7.2 | 5.8±0.1 | 6.8 | 6.3±0.1 | 6.5 | 5.5±0.1 | 3.5±0.0 |
| Na | 9.3 | 8.1±0.1 | 8.8 | 7.5±0.1 | 8.3 | 7.5±0.1 | 0.0±0.0 |
| Ag | 2.4 | 5.2±0.1 | 2.3 | 3.6±0.1 | 2.2 | 3.4±0.1 | 1.1±0.1 |
| O | 46.7 | 48.3±0.4 | 47.6 | 47.3±0.4 | 48.4 | 50.6±0.4 | 76.2±0.5 |

Table 5.3: Elemental weight% compositions of the custom additives from EDX analysis, results are shown as mean ± standard deviation.

| Element | P40 / atomic% | | P45 / atomic% | | P50 / atomic% | | B65003 |
|---------|---------------|--------|---------------|--------|---------------|--------|--------|
| | Expected | Actual | Expected | Actual | Expected | Actual | Actual |
| P | 19.1 | 18.4 | 20.3 | 21.3 | 21.4 | 20.3 | 8.8 |
| Mg | 5.7 | 5.4 | 4.3 | 4.1 | 3.0 | 2.7 | 3.1 |
| Ca | 3.8 | 3.1 | 3.6 | 3.4 | 3.4 | 2.9 | 1.6 |
| Na | 8.6 | 7.5 | 8.1 | 7.0 | 7.7 | 6.8 | 0.0 |
| Ag | 0.5 | 1.0 | 0.5 | 0.7 | 0.4 | 0.7 | 0.2 |
| O | 62.2 | 64.6 | 63.2 | 63.6 | 64.1 | 66.6 | 86.3 |

Table 5.4: Atomic% compositions for each additive, calculated from Table 5.3. Values of atomic mass (in Da) used to convert between weight% and atomic% [476]: P (30.973762), Mg (24.305), Ca (40.08), Na (22.9897693), Ag (107.868), O (15.999).

| Oxide | P40 Composition / mol% | | P45 Composition / mol% | | P50 Composition / mol% | | B65003 |
|-------------------------------|------------------------|--------|------------------------|--------|------------------------|--------|--------|
| | Expected | Actual | Expected | Actual | Expected | Actual | Actual |
| P ₂ O ₅ | 40 | 41.8 | 45 | 48.5 | 50 | 52.1 | 48.0 |
| MgO | 24 | 24.6 | 19 | 18.5 | 14 | 13.7 | 34.0 |
| CaO | 16 | 14.1 | 16 | 15.4 | 16 | 14.9 | 17.1 |
| Na ₂ O | 18 | 17.1 | 18 | 15.9 | 18 | 17.5 | – |
| Ag ₂ O | 2 | 2.3 | 2 | 1.6 | 2 | 1.7 | 1.0 |

Table 5.5: Oxide compositions (molar%) of each custom additive calculated from Table 5.4.

Discussion

The measured compositions of the three custom additives (Tables 5.3–5.5), show that there was a measurable deviation from the desired compositions. Of these, the phosphate (P₂O₅ – affecting the additive dissolution rate) and silver content (Ag – affecting the total amount of Ag⁺ which can be released) are likely to be the most important, directly affecting the antimicrobial efficacy.

The phosphate content (specified by molar%) was designed to vary between the three additives, with the dissolution rate of the glasses expected to be proportional to this. Despite the measured values not matching those intended, there was still a good spread of values (41.8%, 48.5%, and 52.1%) which would still enable a comparison between different dissolution rates. However, the silver content (intended to be 2% by weight for all three additives), also varied considerably between 3.4% for P50, up to 5.2% for P40.

In terms of the expected antimicrobial efficacy, for a given silver content one would expect a faster dissolving additive to have a greater effect, as it can release Ag⁺ at a higher rate. On the other hand, this should also be the case for an additive with a higher Ag content. In terms of these powders, this therefore means that since the Ag content of P45 and P50 are similar, the effect of the dissolution rate between them can be observed; however, the higher Ag content in P40 is likely to counteract the effects of a slower dissolution rate (as was the case in [449]).

5.1.3 Morphology

As with the commercial additives, SEM was carried out to determine the morphology of the additives. Here, the same methodology as Section 4.1.1 has been used to obtain the images shown in Figure 5.3.

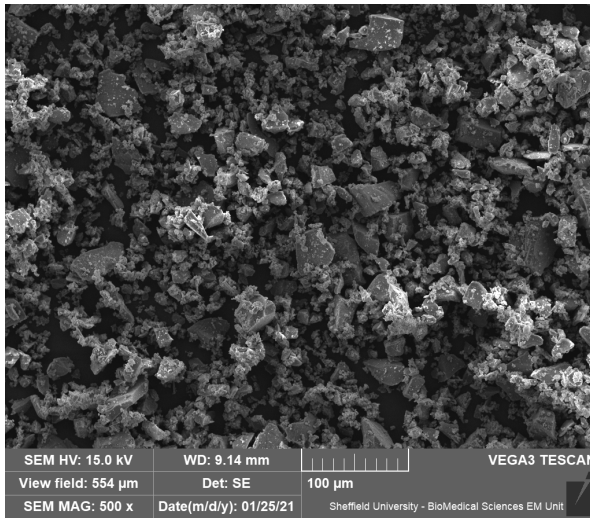
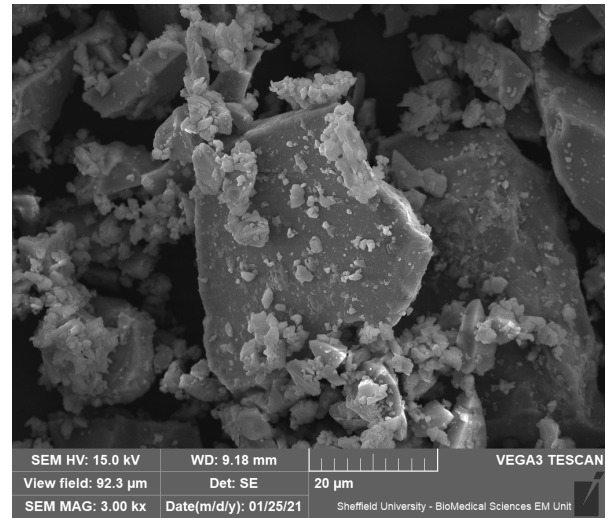
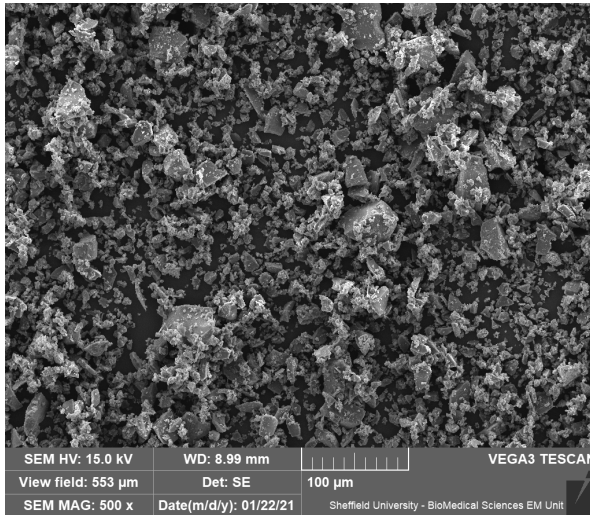
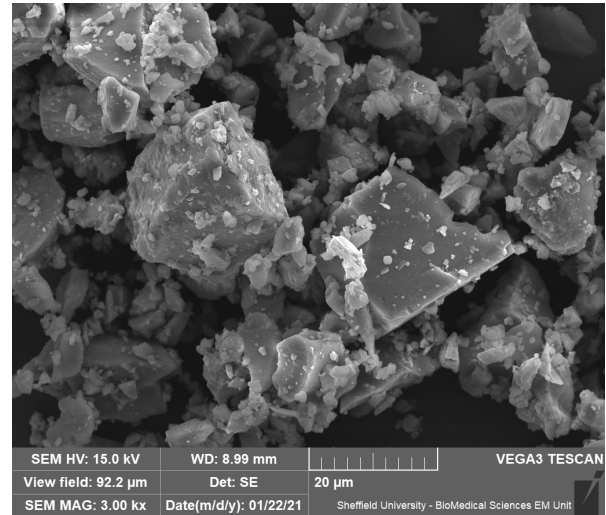
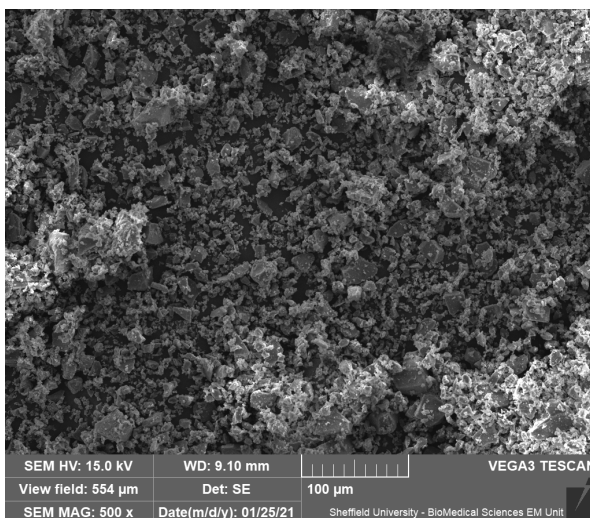
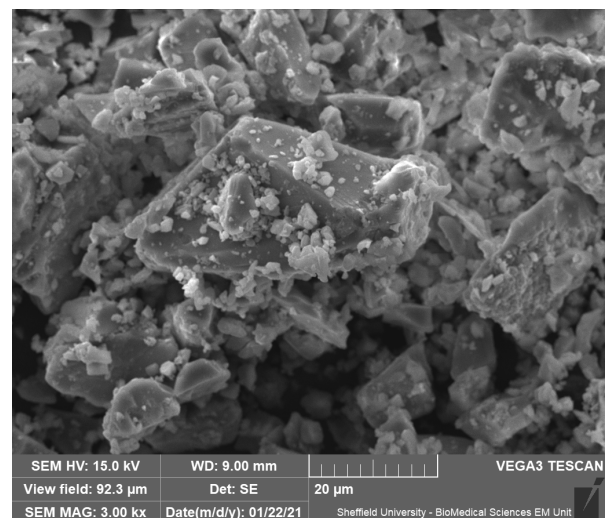
(a) P40 – $\times 500$.(b) P40 – $\times 3k$.(c) P45 – $\times 500$.(d) P45 – $\times 3k$.(e) P50 – $\times 500$.(f) P50 – $\times 3k$.

Figure 5.3: SEM images of the custom additives. 🚫

Discussion

For all of the glass powders shown in Figure 5.3, these can be seen to be very similar both in shape and size to each other. The morphology of these is also very similar to that of the commercial B65003 additive (see Section 4.1.1), with the distinctive jagged edges to the powder particles.

In terms of the performance of these additives, this similarity was essential for comparing the chemical compositions, rather than the morphology or particle size (previously shown to have a significant effect with the commercial additives – see Section 4.4.4). The SEM images shown here suggest that the manufacturing processes used to create the powders were consistent between the glasses, and that this should therefore not be the cause of any differences in the antimicrobial efficacy.

5.1.4 Particle Size

Although the SEM images suggested that all of the glasses were a similar size and shape, this only focused on a small amount of powder. Since even a small change in particle size can have a significant impact on the efficacy, Laser Diffraction was again used to measure the particle size distribution in the glass powders.

Methodology

In order to ensure comparability, the same methodology as Section 4.1.2 was used, with a dry dispersion unit used for the custom glasses. As for the commercial glasses, a refractive index of 1.627 (for Tricalcium Phosphate) was used for the analysis.

Results

The results of the particle size analysis are shown in Figure 5.4, with key values shown in Table 5.6. The values for B65003 have been included here for comparison.

| Glass Additive | D10 / μm | D50 / μm | D90 / μm | D[4,3] / μm | Weighted Residual / % |
|----------------|---------------------|---------------------|---------------------|------------------------|-----------------------|
| B65003 | 2.48 \pm 0.04 | 9.83 \pm 0.07 | 21.1 \pm 0.4 | 11.1 \pm 0.5 | 0.81 \pm 0.04 |
| P40 | 1.93 \pm 0.07 | 15.5 \pm 0.2 | 41.3 \pm 0.9 | 18.9 \pm 0.3 | 0.58 \pm 0.04 |
| P45 | 2.10 \pm 0.02 | 14.8 \pm 0.1 | 40.6 \pm 0.6 | 18.5 \pm 0.2 | 0.56 \pm 0.09 |
| P50 | 1.74 \pm 0.02 | 13.0 \pm 0.1 | 39.4 \pm 0.4 | 17.2 \pm 0.1 | 0.83 \pm 0.17 |

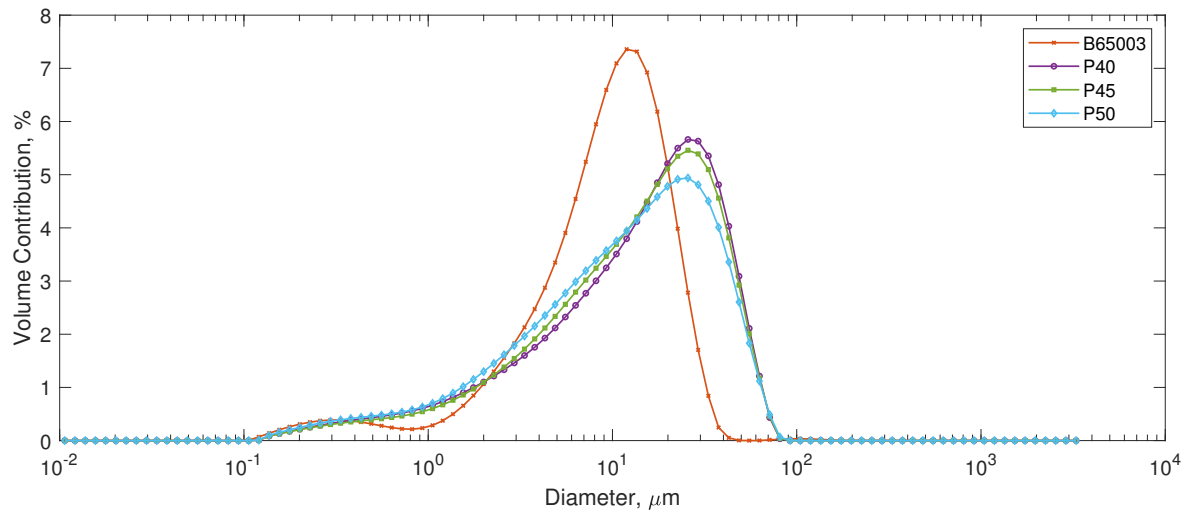
Table 5.6: Particle sizes.

Discussion

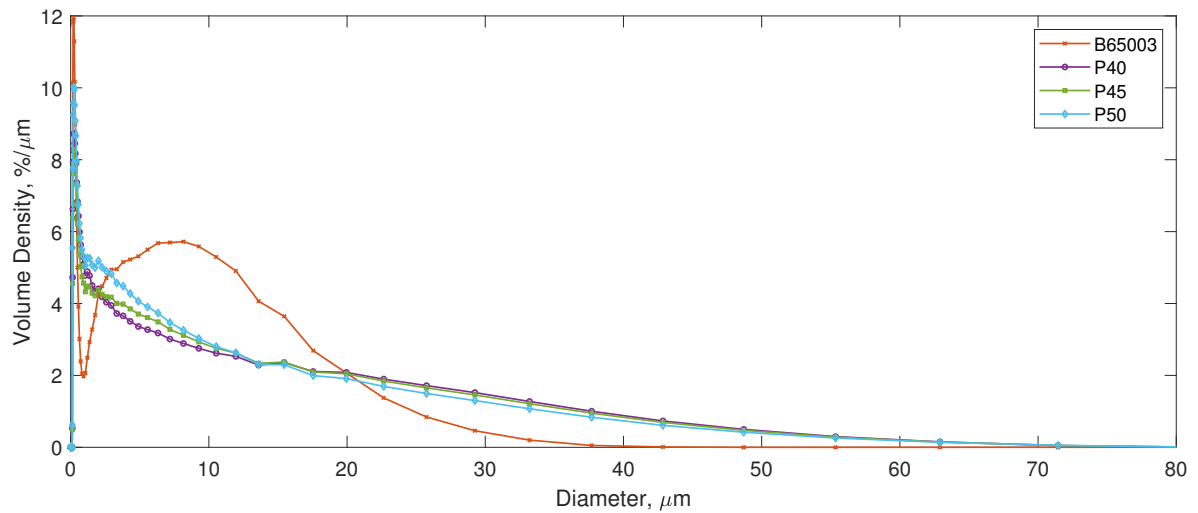
Although the aim was to replicate the morphology of the commercial powder (B65003) as closely as possible, some changes had to be made due to the availability of equipment. In terms of the particle size, this revolved around the standard sieve sizes available, with a 45 μm sieve used for the custom additives; a close match to the <40 μm specification of B65003. As expected, all three of the custom glasses were shown to be larger in size than the commercial additive (see Table 5.6), with the average particle sizes (D50) measured as 13.0–15.5 μm compared to 9.8 μm .

The shape of the distributions can also be seen to be different in Figure 5.4, with a longer tail off in the custom glasses where a greater proportion of smaller particles were measured compared to B65003. This difference is suspected to be due to additional sieving steps carried out in the commercial additives, removing smaller particles (then sold separately, for example as B45003). For the custom additives, the dramatic reduction in the yield this would bring about, coupled with the increased production time and high cost of consumables, meant that this was impractical to replicate.

Comparing the custom glasses to each other, the shape of the distributions (Figure 5.4) can be seen to be very similar for all three, with a subtly smaller size measured for P50. Although this slight difference could affect the efficacy of the powder, this would only act to increase the dissolution rate, which was already intended to be the highest in P50. Considering both this and the overwhelming similarities between the distributions, the results shown here suggest that the particle size is not likely to significantly affect the antimicrobial efficacy of the powders.



(a) Log scale – as measured from the Mastersizer 3000.



(b) Linear - normalised by bin width (area represents total volume)

Figure 5.4: All glass - average curves for the samples. B65003 included for comparison. 🚫

5.1.5 Laser Sintering

With the custom additives manufactured and characterised, the next crucial step was to determine whether the additives could be incorporated into the PA2200 powder and processed in Laser Sintering.

Part Printing

All of the Laser Sintering for the custom glass micro-composites was carried out using an EOS P100, using the methodology in Section 4.1.4. The custom glasses were mixed into the powder feedstock using a rotary tumbler, these were incorporated at 1% by mass (to match that of the commercial additives in Chapter 4). The standard parameters for PA2200 were found to be suitable for the PA2200 / phosphate glass feedstock and were again used for printing.

Photos taken during each of the builds can be seen in Figure 5.5. All the parts printed without any observable issues (such as curl or excessive smoking), validating the use of the standard PA2200 parameters. For the scanned areas of the build, there was a noticeable difference in colour for the additive-containing powders (shown in Figure 5.5), although this did not appear to affect the build.

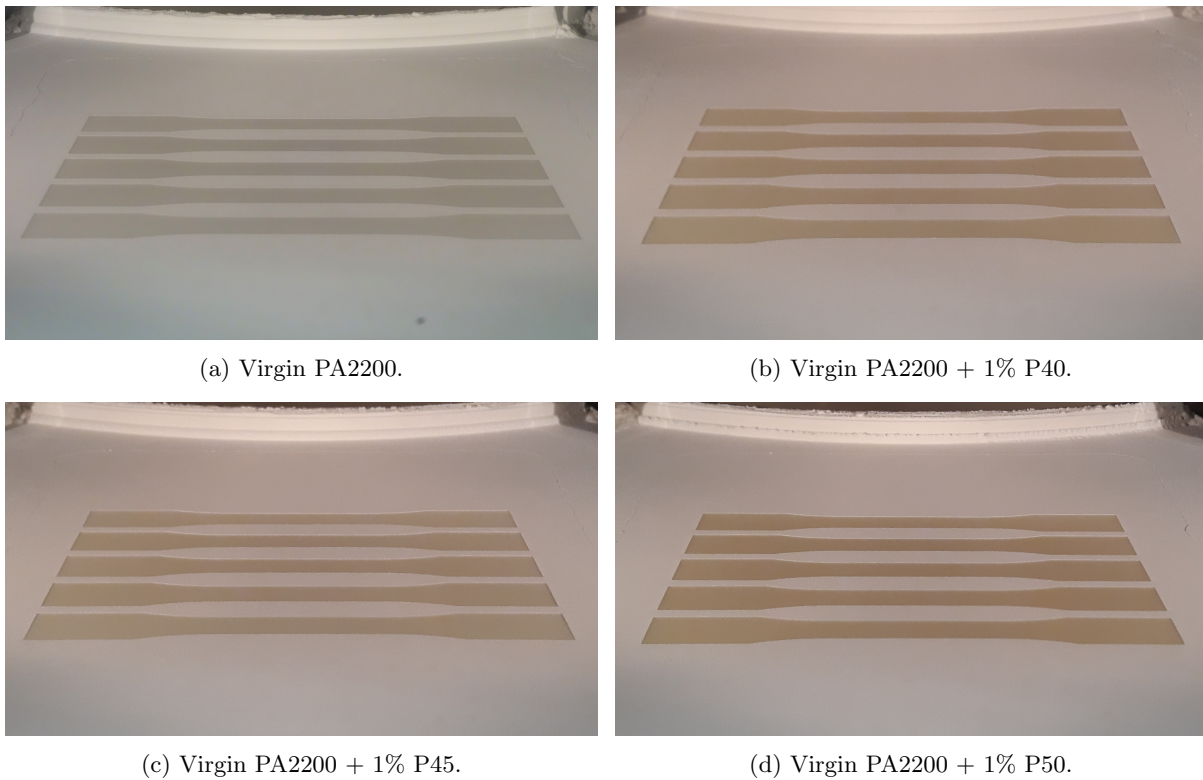


Figure 5.5: Photos of the four materials taken during Laser Sintering. 🚫

Printed Parts

As in the previous chapter, powder was removed from the tensile test specimens through a combination of bead-blasting and compressed air jets; compressed air only was used for all other specimens to avoid contamination. Photos of post-processed parts containing the custom additives can be seen in Figure 5.6. Apart from the obvious differences in colour, no discernable dissimilarities were observed between builds.



Figure 5.6: Photo of the equivalent part from all 3 builds containing the custom additives and one without additives. Shown are (top to bottom), virgin PA2200 + 1% P50, virgin PA2200 + 1% P45, virgin PA2200 + 1% P40, virgin PA2200. 🚫

5.2 Micro-Composite Properties

5.2.1 Colour Measurements

The colour difference between the microcomposite and pure PA2200 parts was seen to be significant during printing. For this reason, the colour of all the parts was measured quantitatively to accurately characterise this.

Methodology

Colour measurements were carried out using a PCE-RGB2 Color Meter from PCE Instruments. The tensile specimens produced were used for analysis as they could be arranged to create a flat surface large enough to cover the sensor in the colour analyser probe (see Figure 5.7a). Since this layout could position the colour sensor above a joint between samples, 10 × RGB measurements were taken from slightly different positions while ensuring that the entirety of the probe was covered (see Figure 5.7b for an example position).



(a) Layout of tensile specimens. (b) Example position of the probe. (c) Offset of the colour probe.

Figure 5.7: Setup used for colour measurements. 🚫

Before use, the colour meter first had to be calibrated to a white sample. Two different calibration standards were used here, these being a white card sample provided by PCE Instruments and a spectralon white standard. Note that since the spectralon sample was smaller than the outer rim on the probe (see Figure 5.7c), this had to be positioned closer to the light source and sensors than for the card calibration.

Results

The results can be seen in Table 5.7, with the individual results (RGB values for each measurement) shown in Appendix B.7. This shows both the card and spectralon calibrations, with the card sample visually appearing closer to the true colour of the samples.

Discussion

The use of a colour meter to record the colour of the materials was undoubtedly more accurate than simply taking photographs of the parts. However, there were some potential sources of error that should be noted which could have affected the values shown in Table 5.7; arising from the sample surface and the calibration.

The issue with the part surface comes both from the “powdery” surface seen with LS parts (see Section 2.1.3), and the fact that multiple parts had to be assembled to create an area large enough to cover the probe. The scattering of light on the uneven surface and the likelihood of gaps and shadows in between parts had the potential to affect the readings. The effect of the surface roughness was unavoidable, however to minimise the effect of part boundaries multiple measurements were taken in different places, with the averaged values shown in Table 5.7.

The white sample calibration was shown to have a large effect on the measured colour values (Table 5.7), with two calibrations used here. The most noticeable difference here is the measured brightness (or luminosity) of the parts, with the white card calibration recording markedly brighter colours. There are two likely reasons for this, the measurement distance from the light source and detector, and the

| Material | Card Sample Calibration | | | Spectralon Calibration* | | |
|----------|-------------------------|------------|-----------|-------------------------|------------|-----------|
| | Colour | RGB Values | Hex Value | Colour | RGB Values | Hex Value |
| PA2200 | | R 1023 ± 0 | | | R 819 ± 9 | |
| | | G 1023 ± 0 | #FFFFFF8 | | G 822 ± 8 | #CCDCB |
| | | B 994 ± 5 | | | B 813 ± 10 | |
| 1% P40 | | R 660 ± 12 | | | R 525 ± 7 | |
| | | G 600 ± 12 | #A5967B | | G 478 ± 6 | #837764 |
| | | B 495 ± 16 | | | B 400 ± 8 | |
| 1% P45 | | R 616 ± 9 | | | R 475 ± 10 | |
| | | G 558 ± 10 | #9A8B70 | | G 437 ± 9 | #766D5A |
| | | B 450 ± 11 | | | B 361 ± 8 | |
| 1% P50 | | R 559 ± 9 | | | R 429 ± 10 | |
| | | G 501 ± 9 | #8A7D6A | | G 394 ± 9 | #6B6255 |
| | | B 426 ± 8 | | | B 341 ± 10 | |

Table 5.7: Colours values measured for the four materials. RGB values were measured in 10-bit (/1023) and are shown as the mean ± standard deviation, hex values shown are based on the mean. *Spectralon calibration was carried out closer to the sensor than all other measurements.

actual whiteness of the card sample. The distance was thought to be key here, as a sample closer to the light / detector is likely to reflect a higher proportion of the light back, rather than scattering to the surroundings and leading to a brighter reading. Although likely to be closer to “true white”, the white card calibrated samples were deemed to be closer to reality due to the difference in distance.

Ultimately, although interesting and useful for future design and application of the microcomposite material, the colour of the parts was not seen as critical to the function of the parts.

5.2.2 Tensile Properties

To determine whether the additives affected the mechanical properties of the printed parts, tensile testing was again carried out.

Methodology

The same methodology as the previous chapter (see Section 4.2.1) was used here, using a Tinius Olsen 5K with Laser Extensometer and type I specimens [454].

Results

The results of the tensile testing can be seen in Figure 5.8, both as the raw stress-strain curves (Figure 5.8a) and comparing the measured values of E , σ_{uts} , and ϵ_{max} (Figures 5.8b–d). Dimensions of the printed parts can be found in Appendix A.2.

A 2-sample Welch’s t -test was once again used to determine whether there were any statistically significant differences in the measured values; the results of which are shown in Table 5.8a, where a p value of $p < 0.05$ indicates the means are significantly different.

| | 1% P40 | 1% P45 | 1% P50 |
|--------|--------|--------|--------|
| PA2200 | 0.638 | 0.208 | 0.152 |
| 1% P40 | – | 0.271 | 0.171 |
| 1% P45 | – | – | 0.939 |

(a) Young’s Modulus.

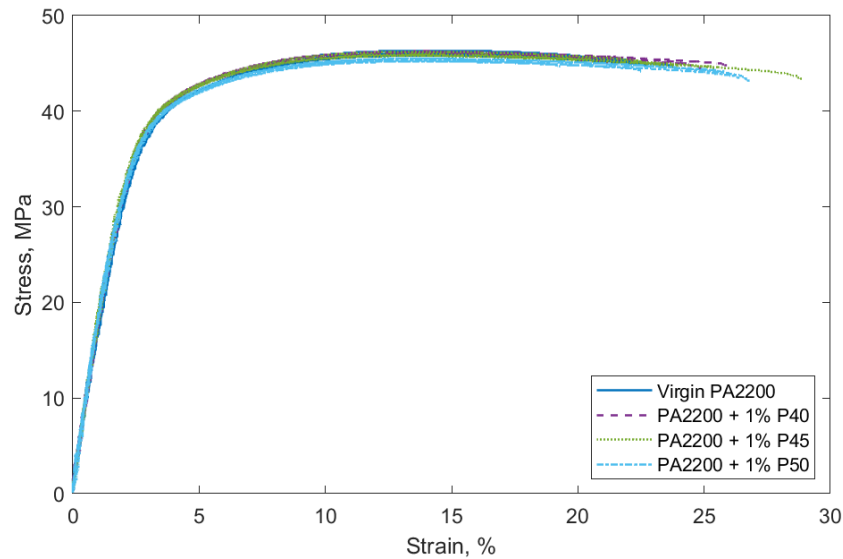
| | 1% P40 | 1% P45 | 1% P50 |
|--------|--------|--------------|--------------|
| PA2200 | 0.154 | 0.503 | 0.000 |
| 1% P40 | – | 0.032 | 0.000 |
| 1% P45 | – | – | 0.000 |

(b) Ultimate Tensile Strength.

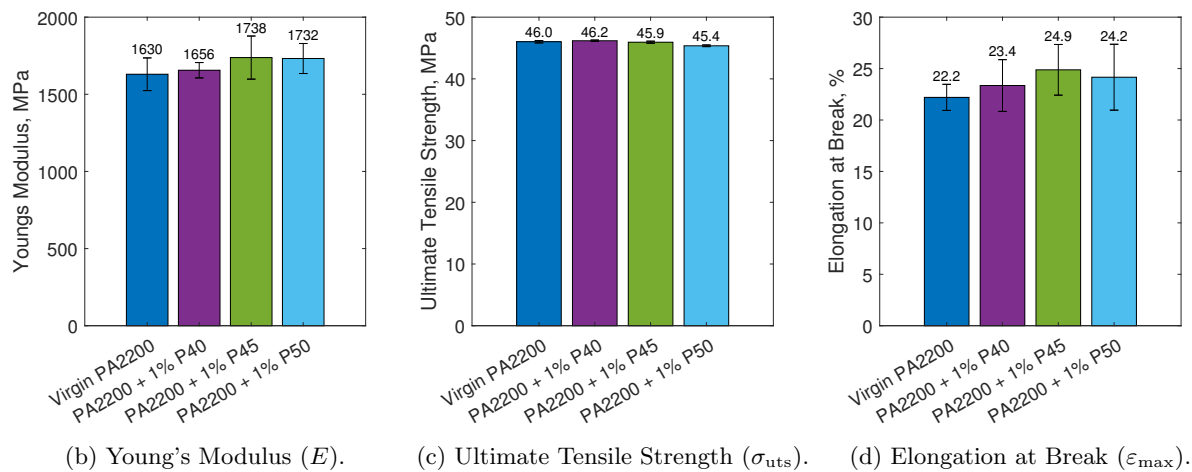
| | 1% P40 | 1% P45 | 1% P50 |
|--------|--------|--------|--------|
| PA2200 | 0.396 | 0.074 | 0.257 |
| 1% P40 | – | 0.361 | 0.670 |
| 1% P45 | – | – | 0.701 |

(c) Elongation at Break.

Table 5.8: Statistical comparison of tensile test data. Shown are p -values, where $p < 0.05$ (shown in bold) indicates a statistically significant difference.



(a) Stress-strain curves from tensile testing.

(b) Young's Modulus (E).(c) Ultimate Tensile Strength (σ_{uts}).(d) Elongation at Break (ϵ_{max}).Figure 5.8: Results of the tensile testing. With (b)–(d) showing the mean \pm standard deviation. 🚫

Discussion

In the stress-strain plots (Figure 5.8a), it can be seen that all of the materials follow a very similar shape with no major differences between any of the specimens tested. This is supported by the values of E , σ_{uts} , and ϵ_{max} (Figures 5.8b–d), which again show very similar values for all the materials tested. The combination of these, means that in terms of design and potential use cases, these additives can be incorporated into the feedstock for existing designs, without the need for any alterations.

The statistical analysis shown in Table 5.8, shows that the only statistically significant difference in any of the properties is the value of σ_{uts} for 1% P50. However, it is important to note that although statistically significant, this only represents a difference of 0.6 MPa from the PA2200 specimens. Practically, this would not be sufficient a decrease in properties to warrant changing the design in the majority of applications.

5.2.3 Surface Composition

Although the proposed method of action for the microcomposite parts did not rely upon an even surface distribution of silver-containing additives, this gives an indication of the dispersion of the additive throughout the volume and can show other features that might otherwise be missed. The main focus of this section, was to detect whether any of the additives were present on the surface, while also checking for any additional additives or contaminants.

Methodology

This section follows the same methodology as Section 4.2.3, with SEM used to inspect the morphology of the part surface, and EDX used to further identify features shown in the SEM images. Test specimens measuring $8 \times 8 \times 1$ mm were printed for this purpose, with SEM scans and elemental maps of the surface obtained.

Results

SEM images of parts containing the three custom additives are shown in Figure 5.9, with key features annotated. The elemental maps from EDX for a part containing 1% P50 are shown in Figure 5.10, with all of the other microcomposites showing similar results.

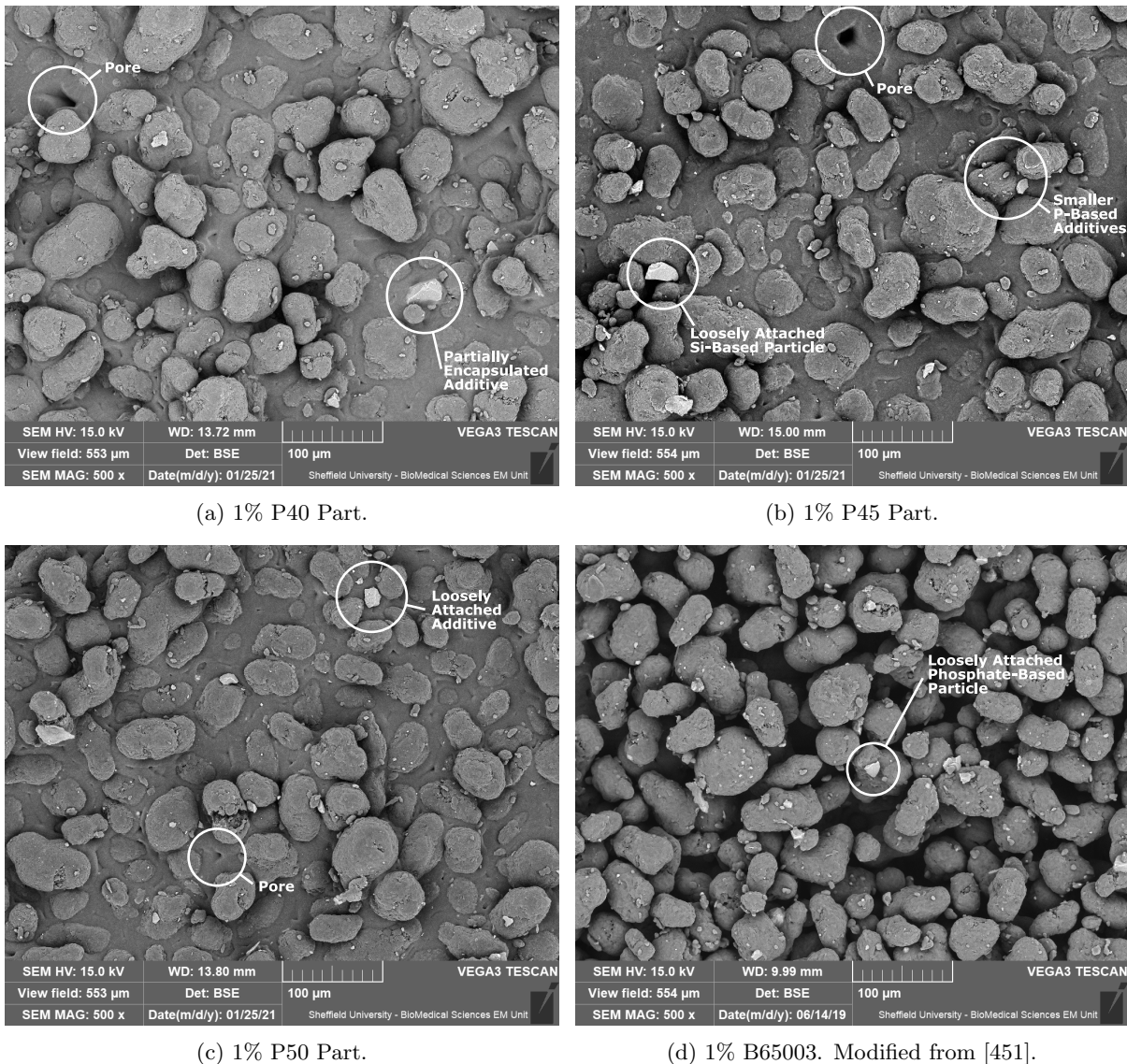


Figure 5.9: SEM images of the microcomposite surfaces containing the custom additives (1% B65003 included for comparison). The brighter features are additives, with the majority of the smaller additives present over the entire surface found to be the custom-made phosphorus-based additives. All features identified were found on all three materials. 🚫

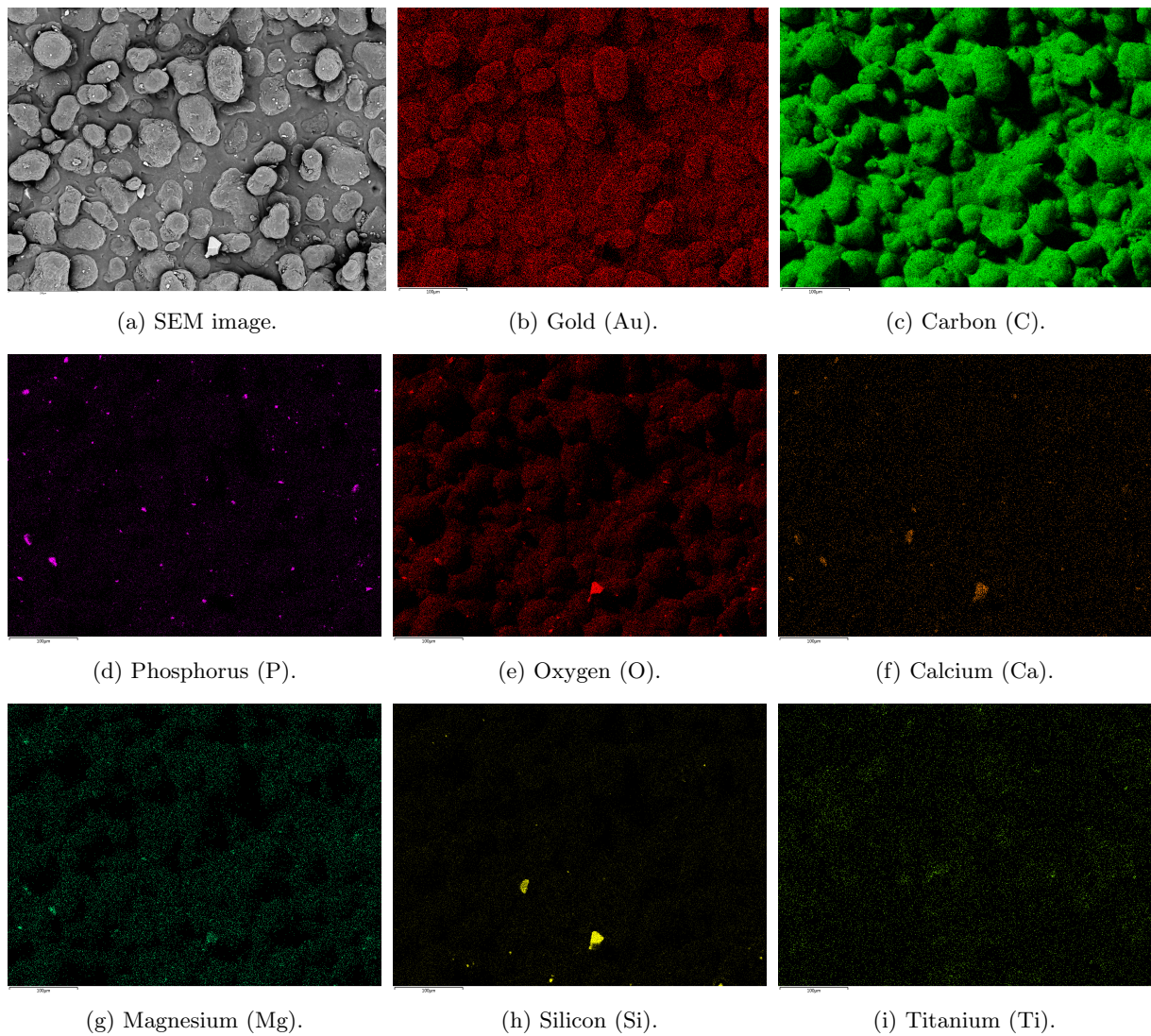


Figure 5.10: P50 Part – SEM and elemental maps on the surface of a microcomposite part obtained with EDX. Elements P, O, Ca, and Mg are indicative of the additive location. Au is from the gold coating of the samples, Si and Ti are thought to be additional additives in the PA2200 powder from the manufacturer and post-printing contaminants. 🚫

Discussion

The SEM images of P40, P45, and P50 (Figures 5.9a–c), show a number of key features which one would expect to see on the surface of LS parts, these being a combination of partially melted powder particles, fully melted areas, and “open” pores leading inside the parts in the fully melted areas. Extending this to features which would be expected in composite materials, the presence of both partially encapsulated and loosely attached additive particles can be seen on all the scans. For all these, this shows that the additive has been successfully incorporated into the parts, with no obvious effects on the microstructure of the surface.

This appears to be in contrast to the scan of the commercial additive (Figure 5.9d), where few of these features can be seen and there is no evidence of melted areas. Due to the measured properties of the part (including tensile strength), these areas must be present, suggesting that these are simply obscured by loose powder on the surface of the 1% B65003 parts. This could be due to incomplete powder removal, or could be a result of scanning a differently oriented surface in the LS build. For the custom additives, the top surface was scanned, whereas for the B65003 part the orientation was unknown. It is possible that the bottom surface of the LS part was scanned, these generally have more partially attached particles, which could explain the apparently loose PA2200 particles shown in Figure 5.9d.

Combining these with EDX measurements (such as those in Figure 5.10), it was possible to further characterise the additives in the SEM images. In all the microcomposite scans, phosphate-based particles

were identified across the surface, suggesting that the mixing of the powder feedstock was successful and the additives were relatively evenly dispersed. In some images, larger, loosely attached, silicon-based particles were also detected. Since none of these were detected encapsulated in the parts, these were suspected to be contamination after printing, possibly during powder removal or in transport to SEM scanning.

The evenness of the additive dispersion measured for these parts, as well as the similarity both to each other and the commercial additive (see Section 4.2.3), suggest that this should not be the cause of any differences in antimicrobial efficacy. Although shown in two of the scans here (Figures 5.9b and 5.10), the silicon-based contaminants were rarely seen on the parts' surface, with these also unlikely to affect the performance of the parts.

5.3 Part Use and Functionality

5.3.1 Water Uptake

As with the commercially available additives, the water uptake was measured for the microcomposites containing the custom glasses. With the water uptake providing an estimate of the amount of silver released from the parts during use, the main focus here was to detect any large differences between the three custom glass compositions.

Methodology

The same spherical test specimen geometry from Section 4.3.2 was again used here, with the same method used to calculate the diffusion constant (D) from Fick's law. The protocol from Section 4.3.3 was used throughout, with the samples held in the custom racks made for the gyro-rocker, and with the experiments run concurrently with the effect of geometry samples.

Results

The normalised mass uptake (relative to the 12-week timepoint) for all the microcomposites² can be seen in Figures 5.11a–c, with the spherical 1.0% B65003 and PA2200 samples from Section 4.3.3 shown in Figures 5.11d and 5.11e for comparison. For all of these, Equation 4.8 was fitted to the mass values to determine the value of D , a comparison of which is shown in Figure 5.11f.

Note that due to an oversight in the procedure, the samples were not dried before the start of the experiment; the values shown were instead calculated relative to the dried mass after the experiment (the samples were dried at 50°C for 18 days to ensure all the water had evaporated). Despite this, the three custom microcomposites were thought to be comparable due to the closeness of the build dates (built on subsequent days) and identical storage conditions of the sample parts. To account for the non-zero water contents at the beginning of the experiment, the fitted curve was given additional freedom to start at “negative” times (as in Section 4.3.2).

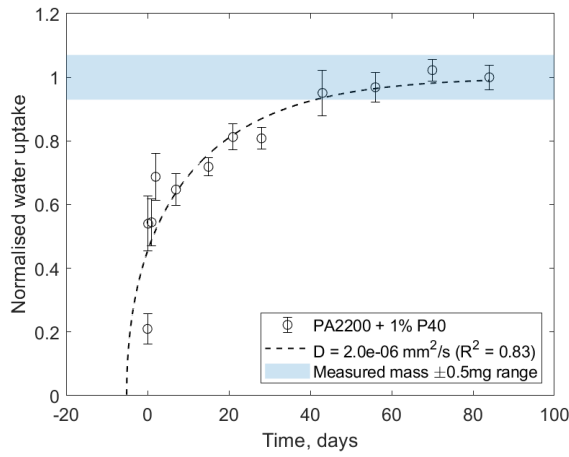
The percentage water uptake for the parts tested is shown in Figure 5.12, with the measured values offset so that the fitted curves start at zero.

Discussion

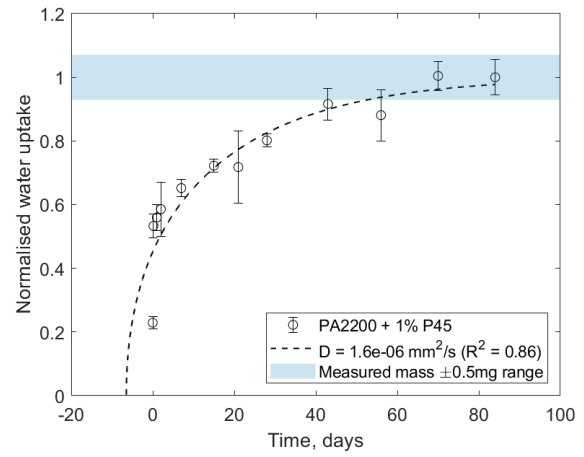
The results in Figures 5.11 and 5.12, show that all three of the microcomposites containing the custom glasses displayed very similar behaviours across the time measured. This also closely matches the properties of the 1.0% B65003 part, suggesting that both the commercial and custom glasses have a similar effect on the overall uptake of the parts, likely with the rate of diffusion through the PA2200 (rather than the additives) being the limiting factor here.

Looking at the fitted values of Fick's law in Figure 5.11, it can be seen that the values for the microcomposites appear strikingly different to the pure PA2200 parts in Figure 5.11e. However, the source of the differences here was thought to be due largely to do with the fact that the samples were not dried before the start of the experiment, rather than due to inherent differences with PA2200. While the the custom microcomposites were all built in within three days of each other (and the PA2200 and 1.0% B65003 parts within two days of each other), there was a large gap of approximately 21 months in between the two sets of builds. Although the parts were kept in sealed containers before use, the PA2200 and 1.0% B65003 parts showed a higher starting water content. This was thought to create additional issues when fitting

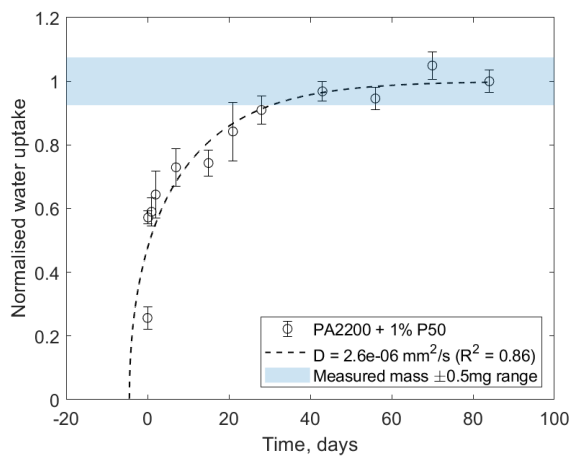
²Dimensions of the printed spheres (d_S , A_S , and V_S) can be found in Appendix A.2.



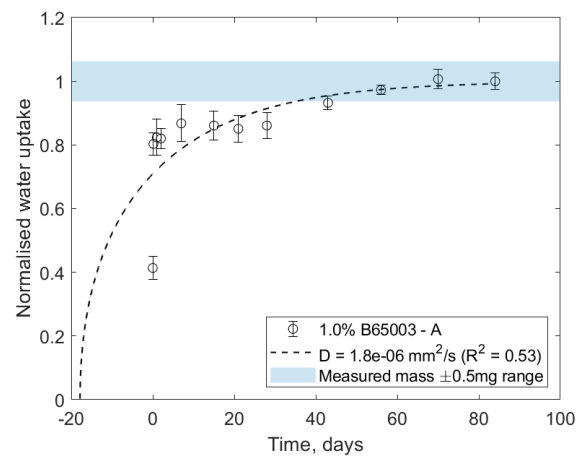
(a) 1% P40 – Mass uptake.



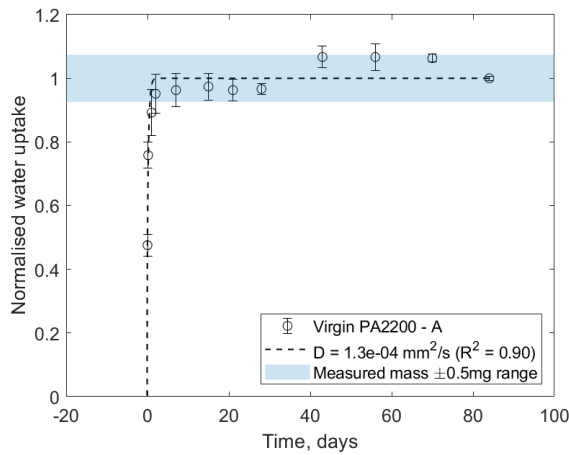
(b) 1% P45 – Mass uptake.



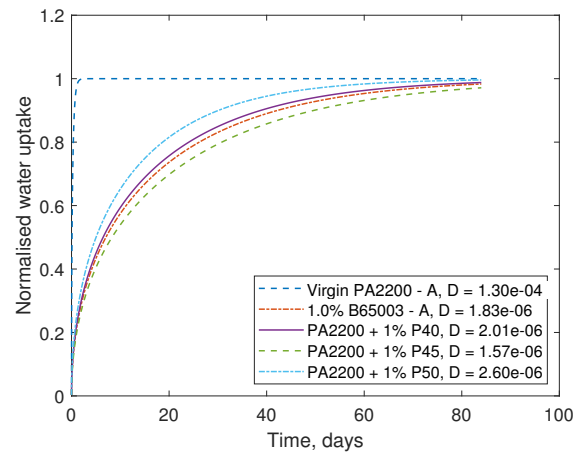
(c) 1% P50 – Mass uptake.



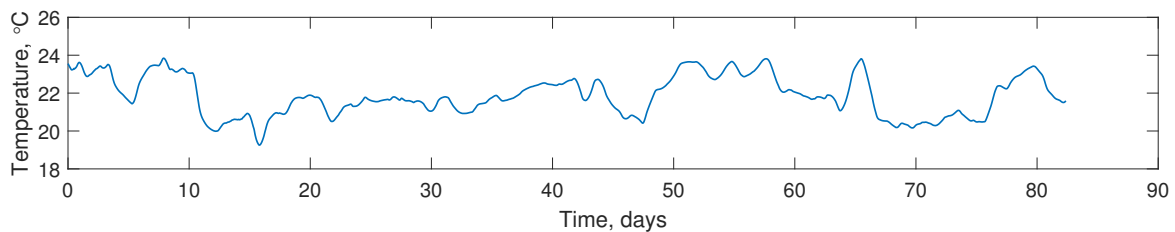
(d) 1% B65003 – Mass uptake.



(e) Virgin PA2200 – Mass uptake.



(f) Comparison of the fitted values of D .



(g) Temperature measurements (24-hour moving average), remaining within $21.5 \pm 2.3^\circ\text{C}$.

Figure 5.11: Results of the water uptake test, with Equation 4.8 fitted. Results from Section 4.3.2 (spherical samples only) for PA2200 and 1% B65003 have been included here for comparison. 🚫

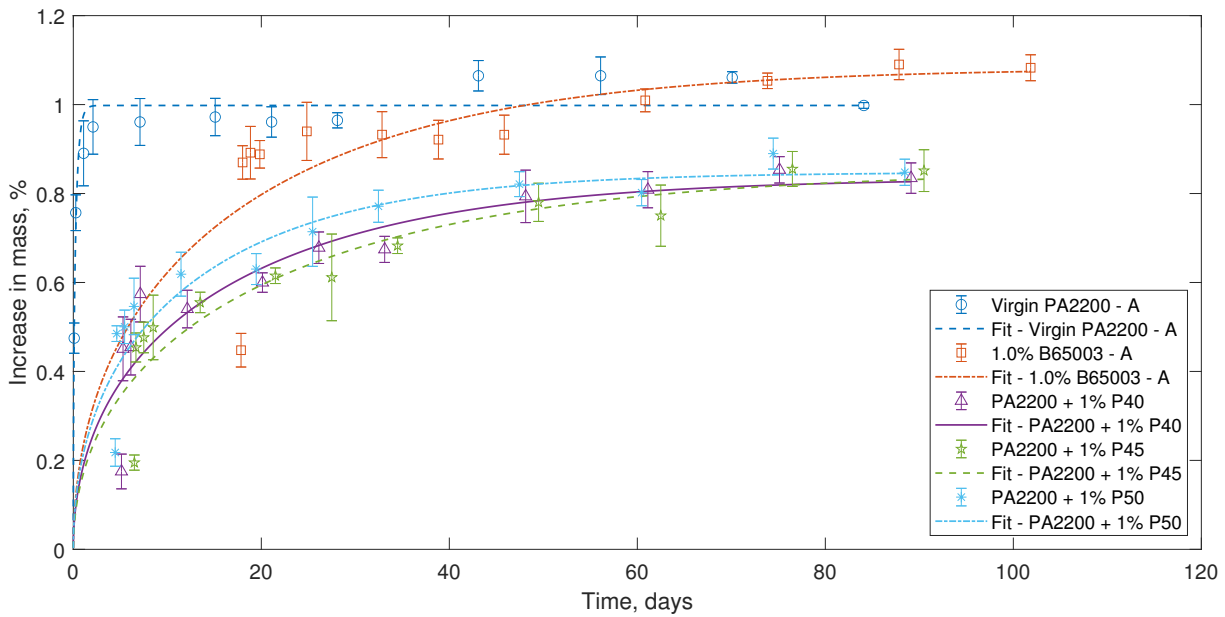


Figure 5.12: Percent increase in mass during water absorption testing. Due to the non-zero starting water content, the times have been offset by the estimated zero water content time (obtained from the fitted Fick's law curve). The results for PA2200 and 1% B65003 (from Section 4.3.3, carried out concurrently) are also shown here for comparison. 🚫

the curves, with a poor fit for 1.0% B65003 ($R^2 = 0.53$) and an unrealistically high value of D calculated for pure PA2200. This could have also explained the higher 12-week water contents compared to the custom additives (shown in Figure 5.12), otherwise seen to be practically identical for the three custom microcomposites.

Despite the issues preventing comparison with the commercial additives, comparisons between the custom additives was possible. Crucially, in terms of the functionality of the parts, the similarities shown suggest that the water uptake is unlikely to be the cause of any differences in the antimicrobial efficacy.

5.4 Antibacterial Testing

In order to test the antimicrobial efficacy of the microcomposites, testing was carried out based on the methods used in Section 4.4.5 [451]. These had previously shown that the efficacy was likely to be negligible in nutrient-rich conditions due to the interactions between silver ions and thiols in nutrient-rich media. For this reason (and due to restricted lab access during the COVID-19 pandemic), determining the efficacy in nutrient-poor conditions was prioritised, with all the testing carried out here focused on this.

As part of these experiments, a rack for the shaking incubator was designed and printed (Figure 5.13) to cope with the large number of samples in each repeat.



(a) As installed in the incubator.

(b) In use for 2 simultaneous repeats.

Figure 5.13: Shaking incubator rack designed to contain 30 glass universals, enough for 2 simultaneous repeats of either the powder or non-contact efficacy experiments. Printed in PLA using FDM. 🚫

5.4.1 Powder Efficacy

Before testing the efficacy of the microcomposite parts, the powder was tested in isolation to determine the maximum possible effectiveness of the parts. By testing the powder directly, this not only provided the maximum surface area (for a faster dissolution speed), it also exposed all of the additive at once; rather than the water having to diffuse through (and then back out of) the microcomposite parts to have an antimicrobial effect.

Methodology

In order to make a direct comparison with the printed microcomposite spheres, the testing conditions and amount of additive were kept as close as possible to the part testing. Since each sphere had a mass of approximately 1 g and contained 1% additive, 10 mg of the raw additive was used, representing the approximate total amount in each sphere.

The custom glasses were weighed out into glass universals to an accuracy of 10–12 μg , before being sterilised (in a steam autoclave at 121°C); three samples were prepared per material per repeat. The chosen bacteria (clinical isolates *P. aeruginosa* SOM1 and *S. aureus* S235) were grown in BHI, with the overnight cultures diluted to an OD_{600} of 0.01 in PBS; 5 ml of these were added to each sample and incubated in a shaking incubator (150 RPM at 37°C) for 24 hours. Following this, 10 μl of the powder/bacteria suspension was taken from each sample and a Miles and Misra serial dilution carried out to determine the number of CFUs (see Appendix A.5 for more details). The full protocol is shown in Figure 5.14.

Results

The results from the powder testing can be seen in Figure 5.15, where all of the silver phosphate glass powders can be seen to be extremely effective against both *S. aureus* and *P. aeruginosa*. Calculated p -values from a Welch's t -test are shown in Table 5.9, with statistically significant differences shown in bold.

In Figure 5.15a, all of the glass powders can be seen to have a significant antimicrobial effect on *S. aureus* S235; with 6.0-log, 6.0-log and 5.9-log reductions measured for P40, P45 and P50 respectively. A similarly large effect can be seen in Figure 5.15b against *P. aeruginosa* SOM1, with 6.5-log, 6.5-log and 6.4-log

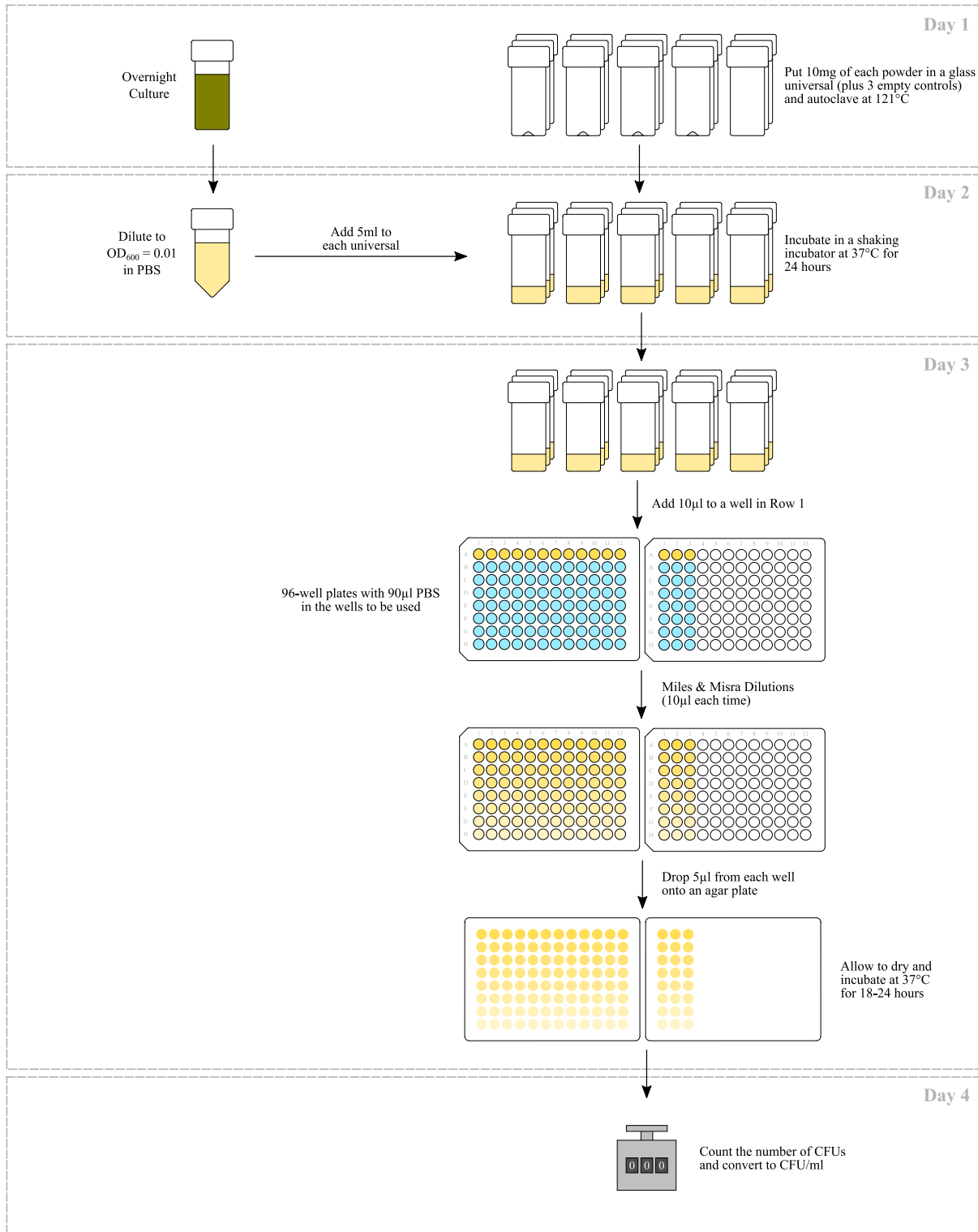
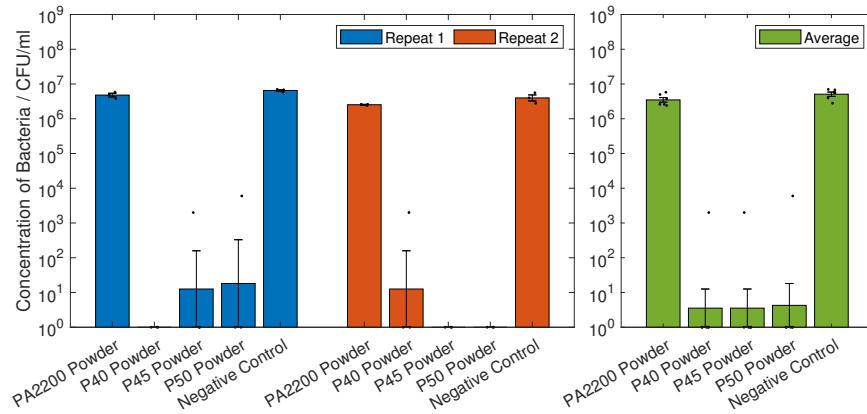


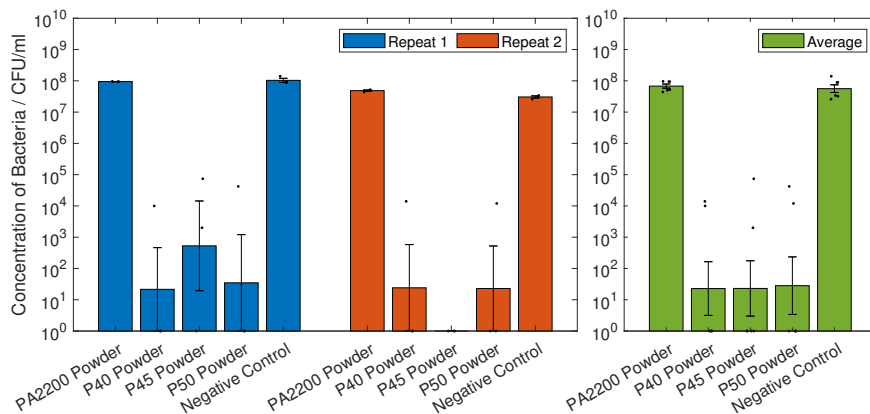
Figure 5.14: Powder protocol (planktonic), divided into days of activities. Note that for all of the antibacterial protocols in this chapter, a smaller volume of the dilution was spotted onto agar plates compared to the serial dilutions in Chapter 4 to allow a higher throughput of samples. 🍷

reductions measured for P40, P45 and P50. It is worth noting that for both strains of bacteria, the PA2200 powder showed no significant difference to the negative controls.

During the testing, visible differences were observed for the different powders after incubation, photos of which are shown in Figure 5.16.



(a) *S. aureus* S235 (Planktonic) in PBS with 10 mg powder (2 mg/ml).



(b) *P. aeruginosa* SOM1 (Planktonic) in PBS with 10 mg powder (2 mg/ml).

Figure 5.15: Powder PBS Tests. Results shown are geometric mean \times geometric standard error, measured zero values were given a value of 1 for analysis. Powders were all weighed within 10–12 mg. 🚫

| | P40 Powder | P45 Powder | P50 Powder | Control |
|---------------|--------------|--------------|--------------|--------------|
| PA2200 Powder | 0.000 | 0.000 | 0.000 | 0.103 |
| P40 Powder | – | 1.000 | 0.926 | 0.000 |
| P45 Powder | – | – | 0.926 | 0.000 |
| P50 Powder | – | – | – | 0.000 |

(a) *S. aureus* S235 (Planktonic).

| | P40 Powder | P45 Powder | P50 Powder | Control |
|---------------|--------------|--------------|--------------|--------------|
| PA2200 Powder | 0.001 | 0.001 | 0.001 | 0.575 |
| P40 Powder | – | 0.997 | 0.943 | 0.001 |
| P45 Powder | – | – | 0.946 | 0.001 |
| P50 Powder | – | – | – | 0.001 |

(b) *P. aeruginosa* SOM1 (Planktonic).

Table 5.9: Statistical comparison of powder PBS testing data in Figure 5.15 (log-values). Shown are p -values, where $p < 0.05$ (shown in bold) indicates a statistically significant difference.

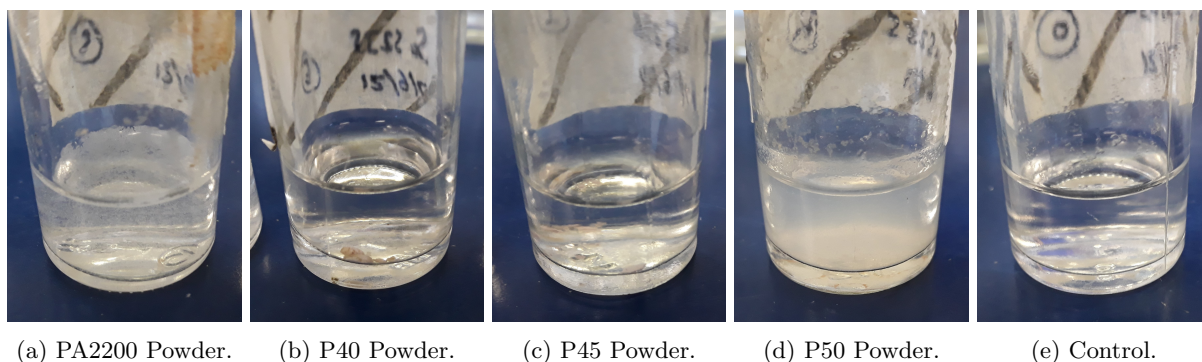


Figure 5.16: Photos from the powder PBS tests taken after 24 hours incubation with *S. aureus* S235. In this, the polymer powder (a) was unaffected by the autoclaving and incubation, remaining dispersed as a powder; the P40 powder (b) turned slightly brown and agglomerated together; the P45 powder (c) also agglomerated but displayed less of a colour change; whereas the P50 powder (d) appeared to dissolve completely. 🚫

Discussion

For all three of the custom additives tested, the reduction in both *S. aureus* and *P. aeruginosa* measured (Figure 5.15) shows the powders are extremely antimicrobial, typically displaying a 6-log reduction or more in the measured CFUs. This quantifies the upper limit of the effectiveness expected from the microcomposite parts; however, since such a large difference was detected for all the powders, they were all predicted to have at least some antimicrobial effect.

The reactions of the powders to incubation in PBS can be seen in Figure 5.16. As expected, the PA2200 powder was not visibly affected, however the three custom glasses all displayed slightly different behaviours. For P40 and P45, these agglomerated together during autoclaving, with P40 turning a darker colour, likely due to the increased silver content and subsequent oxidation. The P50 was not distinguishable as a powder after 24 hours incubation, suggesting that (as per the additive design) this dissolved much more quickly. Although not conclusive, this suggests that the changes in glass formulation did result in significantly different dissolution rates.

5.4.2 Contact Efficacy

Knowing that the additive has a significant antimicrobial effect, the microcomposite parts were subsequently tested in the same manner. For the contact testing, two aspects were investigated in parallel, with both the planktonic bacteria surrounding the parts, and the biofilm formation of the part surface measured.

Methodology

The protocol used here was designed to replicate that used in Section 4.4.5, with some changes included to increase the reliability of the results and allow for a higher throughput of samples. These included adding a negative control (no microcomposite part) and reducing the volume of the serial dilutions spotted onto agar (5 μ l compared to 20 μ l) to enable testing of a large number of samples simultaneously.

As in Sections 4.4.4 and 4.4.5, 1 cm³ spheres were printed and used for the antibacterial testing, representing the “worst case scenario” for the volume to surface area ratio and a uniform absorption of water across the part. Three spheres per material per repeat were used, with each one placed in a glass universal and sterilised (steam autoclave at 121°C) before use. For the contact tests, the bacteria (*P. aeruginosa* SOM1 and *S. aureus* S235) were grown overnight in BHI before being diluted to an OD₆₀₀ of 0.01 in PBS; 5 ml of these were added to each sample and incubated in a shaking incubator (either 150, 175 or 210 RPM depending on availability, at 37°C) for 24 hours.

After the incubation, 10 μ l of the surrounding media was taken from each sample to measure the planktonic bacteria, with a Miles and Misra serial dilution carried out to determine the number of CFUs. To isolate the biofilm attached to the part surface, the remaining media was removed and each sphere rinsed twice with fresh PBS (5 ml each time) to remove loosely attached bacteria. 2 ml PBS was then added and each sphere was vortexed at the highest setting for 30 seconds to remove the attached biofilm. As with the planktonic bacteria, 10 μ l of the resulting suspension was removed, with a Miles and Misra serial

dilution carried out to count the CFUs.

The full protocol is shown in Figure 5.17, combining both the planktonic and biofilm measurements.

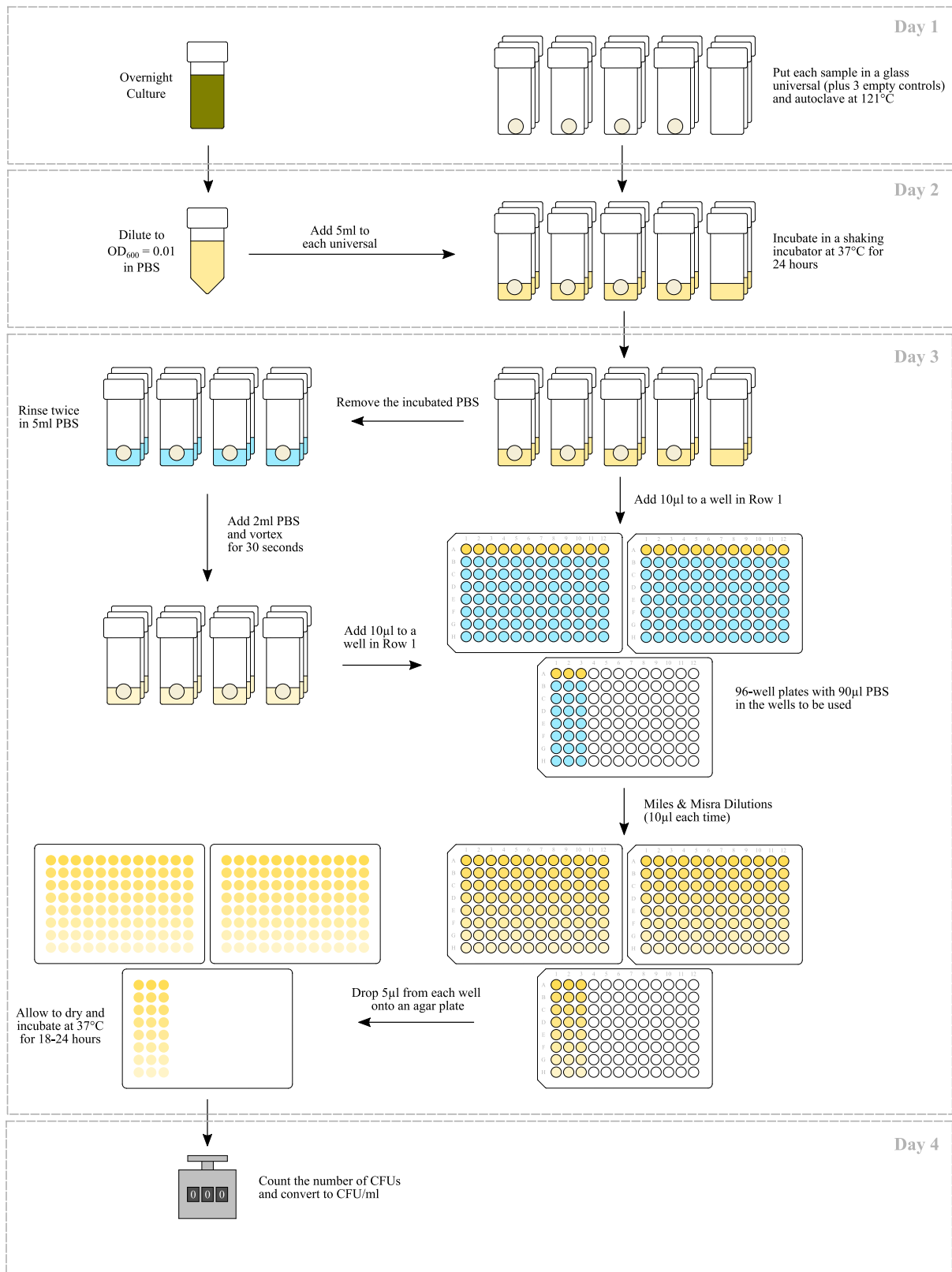


Figure 5.17: Contact protocol (planktonic and biofilms), divided into days of activities. 

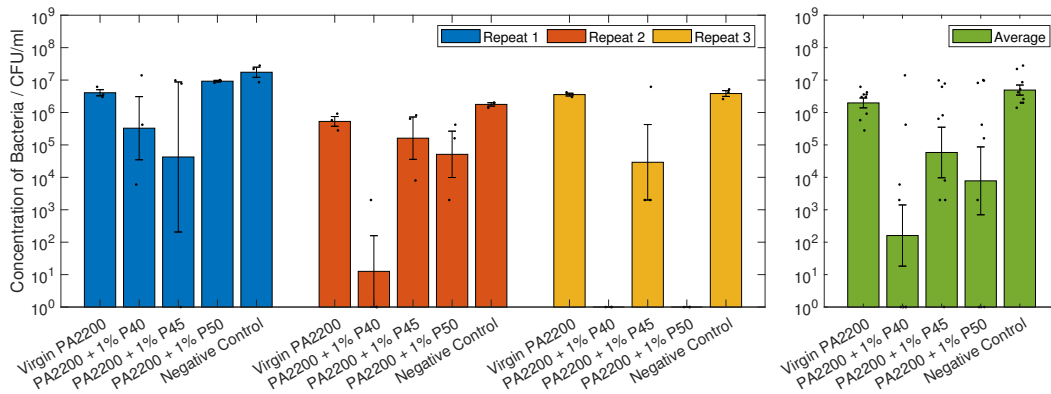
Results

Results of the contact testing for *S. aureus* S235 are shown in Figure 5.18, showing both the planktonic and biofilm data. The the calculated p -values (from a Welch's t -test) comparing all of the tested materials

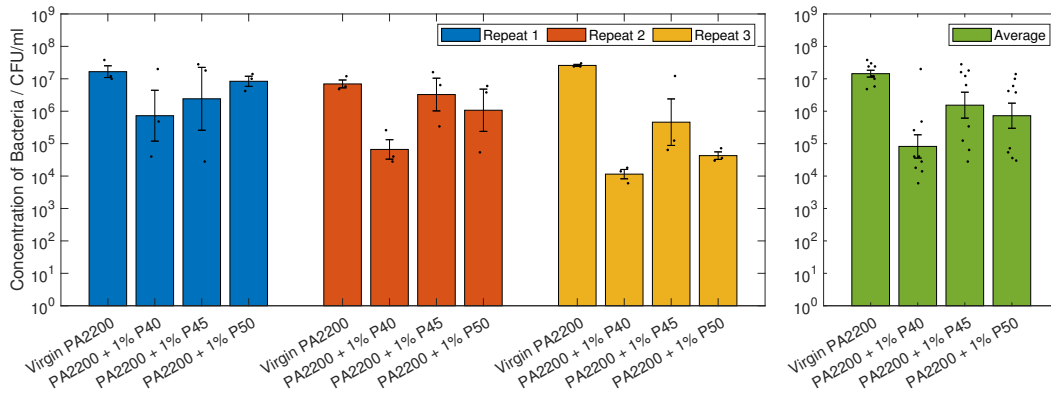
are shown in Table 5.10, with statistically different values shown in bold.

For the *S. aureus* planktonic results (Figure 5.18a), reductions in CFU compared to PA2200 can be seen for all of the microcomposite materials, with 4.1-log, 1.5-log and 2.4-log reductions seen for 1% P40, 1% P45 and 1% P50 respectively. However due to the variation in the measured values, only 1% P40 displayed a statistically significant reduction ($p = 0.002$), with 1% P50 only just above the 0.05 threshold ($p = 0.051$). It should be noted that all of the microcomposites showed a significant reduction compared to the negative control.

The *S. aureus* biofilm data (shown in Figure 5.18b), displayed statistically significant reductions in CFU for all of the microcomposites compared to PA2200. These can be seen as a 2.2-log reduction for 1% P40 ($p = 0.000$), 1.0-log for 1% P45 ($p = 0.043$) and 1.3-log for 1% P50 ($p = 0.010$).



(a) *S. aureus* S235 (Planktonic) in PBS.



(b) *S. aureus* S235 (Biofilm) in PBS.

Figure 5.18: *S. aureus* S235 Contact PBS Tests. Results shown are geometric mean * geometric standard error, measured zero values were given a value of 1 for analysis. An additional repeat of *S. aureus* S235 was also carried out but was contaminated and could not be used. 🚫

| | 1% P40 | 1% P45 | 1% P50 | Control |
|--------|--------------|--------|--------------|--------------|
| PA2200 | 0.002 | 0.088 | 0.051 | 0.087 |
| 1% P40 | – | 0.053 | 0.249 | 0.001 |
| 1% P45 | – | – | 0.513 | 0.040 |
| 1% P50 | – | – | – | 0.028 |

(a) *S. aureus* S235 (Planktonic).

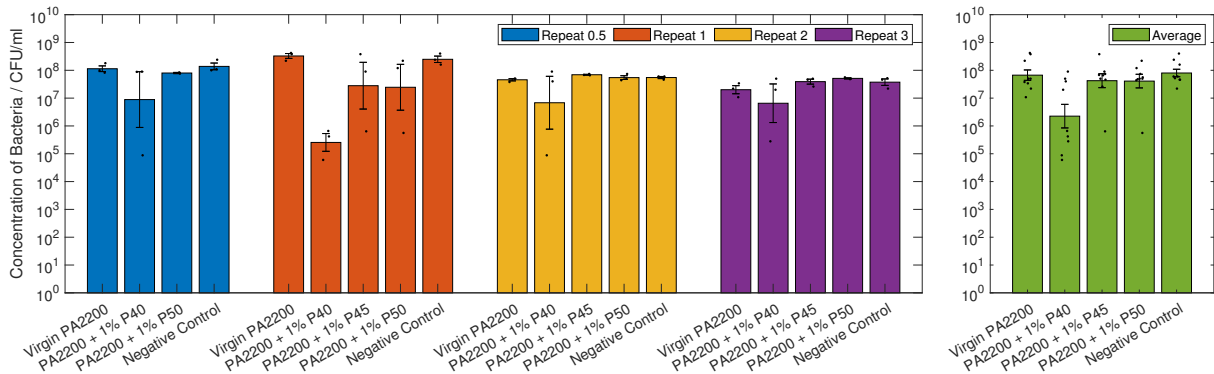
| | 1% P40 | 1% P45 | 1% P50 |
|--------|--------------|--------------|--------------|
| PA2200 | 0.000 | 0.043 | 0.010 |
| 1% P40 | – | 0.031 | 0.092 |
| 1% P45 | – | – | 0.567 |

(b) *S. aureus* S235 (Biofilm).

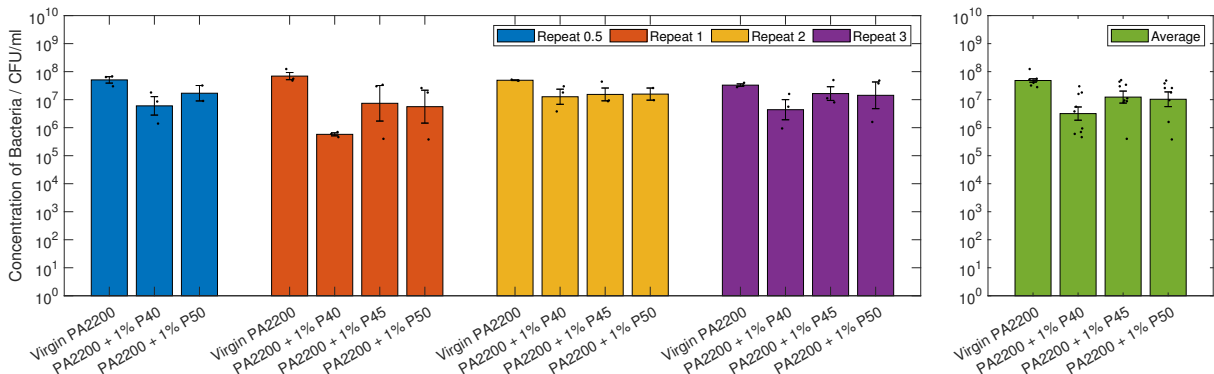
Table 5.10: Statistical comparison of *S. aureus* S235 contact testing data in Figure 5.18 (log-values). Shown are p -values, where $p < 0.05$ (shown in bold) indicates a statistically significant difference.

The results of the contact efficacy test for *P. aeruginosa* SOM1 are shown in Figure 5.19, both for the planktonic and biofilm data. The calculated p -values comparing all the materials are shown in Table 5.11.

In the planktonic data (Figure 5.19a), it can be seen that all the microcomposites display a small reduction in CFU compared to PA2200, with the only statistically significant reduction measured in 1% P40 (1.5-log, $p = 0.009$). Similarly for the biofilm data in Figure 5.19b, 1% P40 shows the largest reduction in CFU (1.2-log, $p = 0.001$), with smaller but still statistically significant differences measured in 1% P45 (0.6-log, $p = 0.025$) and 1% P50 (0.7-log, $p = 0.039$).



(a) *P. aeruginosa* SOM1 (Planktonic) in PBS.



(b) *P. aeruginosa* SOM1 (Biofilm) in PBS.

Figure 5.19: *P. aeruginosa* SOM1 Contact PBS Tests. Results shown are geometric mean * geometric standard error. In repeat 0.5, some of the lids on the universals became unscrewed in the shaking incubator and could not be used (omitted here); this repeat has been excluded from the averages shown. 🚫

| | 1% P40 | 1% P45 | 1% P50 | Control |
|--------|--------------|--------------|--------------|--------------|
| PA2200 | 0.009 | 0.534 | 0.499 | 0.742 |
| 1% P40 | – | 0.023 | 0.023 | 0.006 |
| 1% P45 | – | – | 0.968 | 0.350 |
| 1% P50 | – | – | – | 0.318 |

(a) *P. aeruginosa* SOM1 (Planktonic).

| | 1% P40 | 1% P45 | 1% P50 |
|--------|--------------|--------------|--------------|
| PA2200 | 0.001 | 0.025 | 0.039 |
| 1% P40 | – | 0.084 | 0.169 |
| 1% P45 | – | – | 0.823 |

(b) *P. aeruginosa* SOM1 (Biofilm).

Table 5.11: Statistical comparison of *P. aeruginosa* SOM1 contact testing data in Figure 5.19 (log-values). Shown are p -values, where $p < 0.05$ (shown in bold) indicates a statistically significant difference.

Photos of the spheres immersed in 5 ml PBS can be seen in Figure 5.20, where the volume of PBS can be seen to be sufficient to cover the parts. For all of these, the parts floated in the PBS, with the agitation in the shaking incubator ensuring an even exposure of the part surface.



(a) PA2200 Sphere. (b) 1% P40 Sphere. (c) 1% P45 Sphere. (d) 1% P50 Sphere. (e) Control.

Figure 5.20: Photos from the part PBS tests, showing the immersion of the microcomposite spheres. 🚫

Discussion

Antimicrobial Efficacy

For all the microcomposites containing the custom silver phosphate glasses, the contact efficacy testing measured an antimicrobial effect, both against *S. aureus* S235 and *P. aeruginosa* SOM1. For all the tests carried out, a general trend was observed of 1% P40 showing the largest antimicrobial efficacy, followed by 1% P50, and with 1% P45 the least effective.

The only microcomposite to consistently show statistically significant reductions in CFU (planktonic and biofilm) was 1% P40, consistently outperforming the other glasses. This can be explained based on the measured composition of the glasses (Section 5.1.2), where P40 was found to contain a much higher amount of silver (5.2% by weight) compared to P45 and P50 (3.6% and 3.4%). Interestingly, this increase in performance was observed despite P40 being (theoretically, based on the measured phosphorus content) the slowest to dissolve of the three glasses. This suggests that the difference in silver content between the glasses was sufficient enough to negate the effects of a slower dissolution rate.

Whereas only 1% P40 showed significant reduction in CFU for the planktonic bacteria, all the microcomposites showed statistically significant reductions in the biofilm formation on the parts (Figures 5.18 and 5.19). As expected, the biofilm data for both *S. aureus* and *P. aeruginosa* show the same trends as the planktonic data, with a clear link between the two aspects. However the variability in the results for the biofilms was lower than the planktonic, particularly for PA2200, resulting in the lower *p*-values measured. In Figure 5.19, 1% P45 and 1% P50 can be seen to have a negligible effect on planktonic *P. aeruginosa* SOM1; similarly for the biofilm data, although statistically significant, the reductions here are small (0.6-log and 0.7-log), only showing a limited effect on the biofilms.

Sample Variation

In all of the tests (most notably in Figure 5.18a), a large spread in the measured CFU count can be seen for the microcomposite parts. Since this variation is much greater in the microcomposites, compared to either the PA2200 control or the negative control, it can be assumed that this variation was due to differences in the antimicrobial efficacy of each sphere for that sample. There are several potential causes of this, based both around the printed spheres and potential variation in the bacteria and testing.

Focusing first on the material composition, the dispersion of the additives throughout the parts was not measured for the custom glass microcomposites. Due to the similarities between the custom commercial glasses previously identified, it was assumed that the preparation of the powder feedstock for LS would be sufficient to create a homogeneous distribution throughout the parts (as shown with micro-CT in Section 4.2.5). Regardless of whether the custom glasses showed more agglomeration in printing or not (or even if they were incorporated with a truly random distribution), it is possible that in some of the

parts had a higher concentration of the additives on or near the surface. However, the overall (or bulk) composition of the parts was expected to be very similar across the build, meaning that any short-term differences arising from this are likely to be mitigated as more of the part is saturated with water.

As bacteria are living organisms there is always likely to be some variation in the results, necessitating the multiple repeats carried out here. To control this across the testing, in each repeat the bacteria were grown from a single colony, minimising the potential for mutations in the bacterial strain to have an effect; the results for each repeat have also been shown separately throughout. This variability in growth was most noticeable in the overnight cultures, which despite similar conditions showed a large variation in growth, with measured OD₆₀₀ values of 1.84–2.43 for *S. aureus* S235 and 0.57–2.09 for *P. aeruginosa* SOM1. Another cause of variation could be the length of time between autoclaving the parts and incubation, with a longer time allowing more water to be absorbed or to dry out; to counter this, all the parts were autoclaved at similar times (<20 hours before incubation).

5.4.3 Non-Contact Efficacy

Since the proposed method of action for the microcomposite parts was based on the elution of antimicrobial silver ions into the surrounding environment, non-contact testing was carried out on the spheres to quantify this effect.

Methodology

As with the contact efficacy protocols, the non-contact protocol is based on the one used in Section 4.4.5, with the same modifications as the contact protocol (Section 5.4.2) made here.

The 1 cm³ spheres were again used, with three spheres used per material per repeat; these were placed in glass universals and sterilised (steam autoclave at 121°C) before use. For the non-contact testing, 5 ml PBS was added to each sample and incubated in a shaking incubator (150 RPM at 37°C) for 24 hours, after which the spheres were removed. The bacteria of interest (*P. aeruginosa* SOM1 and *S. aureus* S235 – grown overnight in BHI), were then added into each universal to make an OD₆₀₀ of 0.01. These were incubated for a further 24 hours in a shaking incubator (150 RPM at 37°C) for 24 hours, after which 10 µl of each suspension was removed, and a Miles and Misra dilution carried out to count the CFUs. The full non-contact protocol is shown in Figure 5.21.

Results

The results of the non-contact testing can be seen in Figure 5.22 for both *S. aureus* S235 and *P. aeruginosa* SOM1. Calculated *p*-values (Welch's *t*-test) are shown in Table 5.12, with statistically significant differences shown in bold.

In Figure 5.22a, the microcomposites can all be seen to have statistically significant effect against *S. aureus* S235. Here it can be seen that 1% P40 shows the largest reduction in CFU (1.3-log, *p* = 0.000), followed by 1% P50 (0.9-log, *p* = 0.002) and 1% P45 (0.7-log, *p* = 0.000).

For *P. aeruginosa* SOM1 (Figure 5.22b), only two of the microcomposites were seen to have a significant effect on the CFU. In this, 1% P45 can be seen to have the largest reduction (2.2-log, *p* = 0.000) followed by 1% P40 (1.8-log, *p* = 0.002), no significant difference can be seen for 1% P50.

Discussion

The non-contact tests shown in Figure 5.22 clearly show that the microcomposite parts have an antimicrobial effect on the surrounding environment, even without contact with the surface. This supports the theory that the majority of this effect was due to the elution of Ag⁺ into the surrounding media.

For *S. aureus* S235, the trend seen in Figure 5.22a is the same as the one seen with the contact tests, again with 1% P40 showing the largest reduction (1.3-log) in CFU. Despite all of the microcomposites showing statistically significant differences, the effect for 1% P45 and 1% P50 is lower (0.9-log and 0.7-log), again suggesting that the increased silver content of P40 outweighs the slower rate of dissolution.

Interestingly for *P. aeruginosa* SOM1 (Figure 5.22b), the largest antimicrobial effect was observed with 1% P45 (2.2-log reduction), making it comparable to the efficacy of 1% P40 (1.8-log reduction). This stands in contrast to all the other antimicrobial testing carried out, suggesting that (although it is possible that other factors are in play), this could just be due to the random variation in the testing or the parts. As seen with the contact testing, 1% P50 showed no significant efficacy against *P. aeruginosa*.

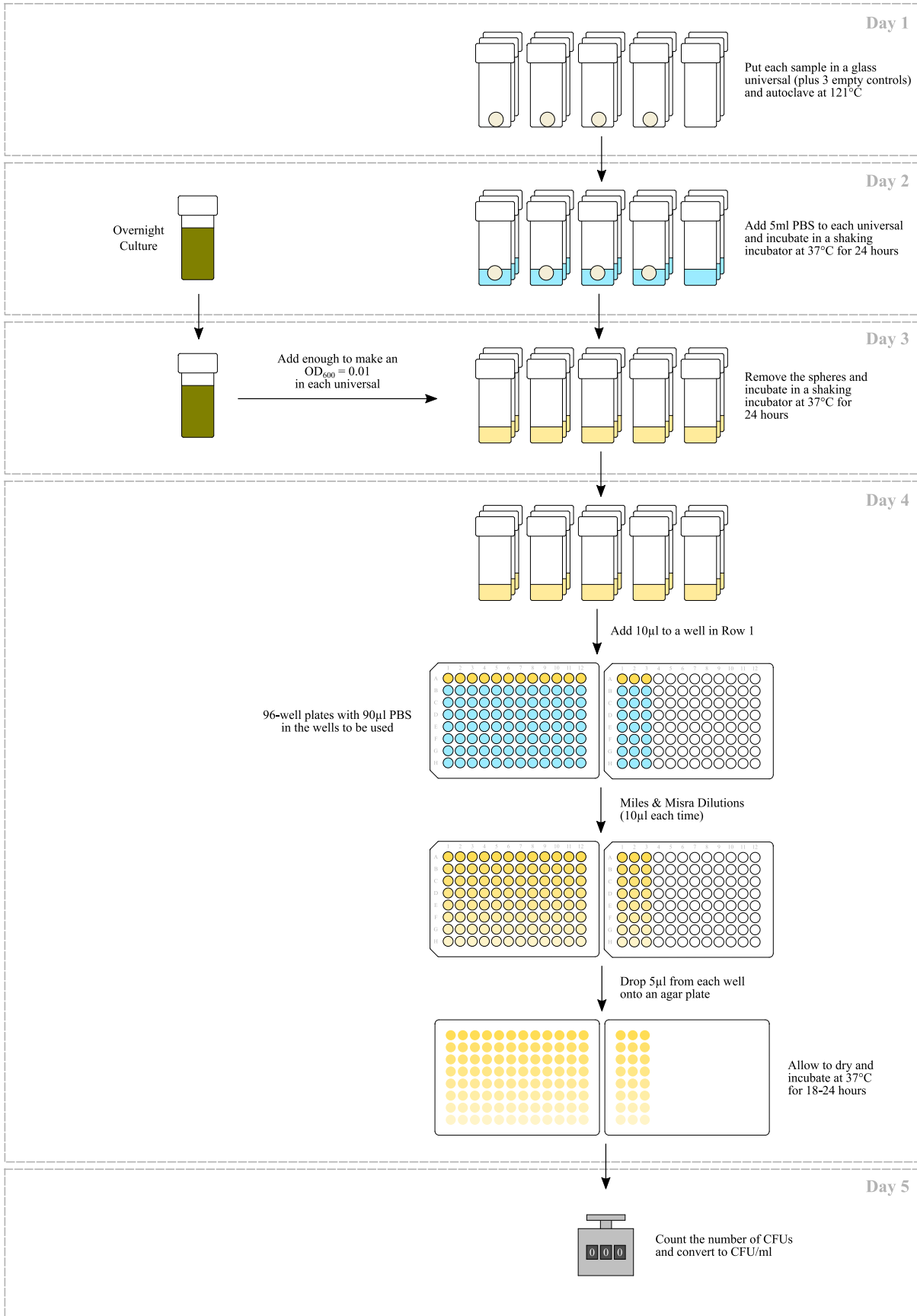
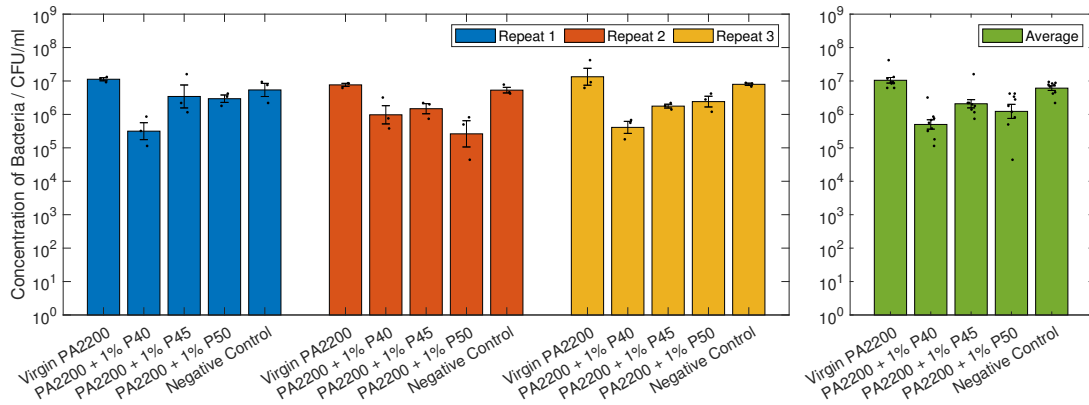
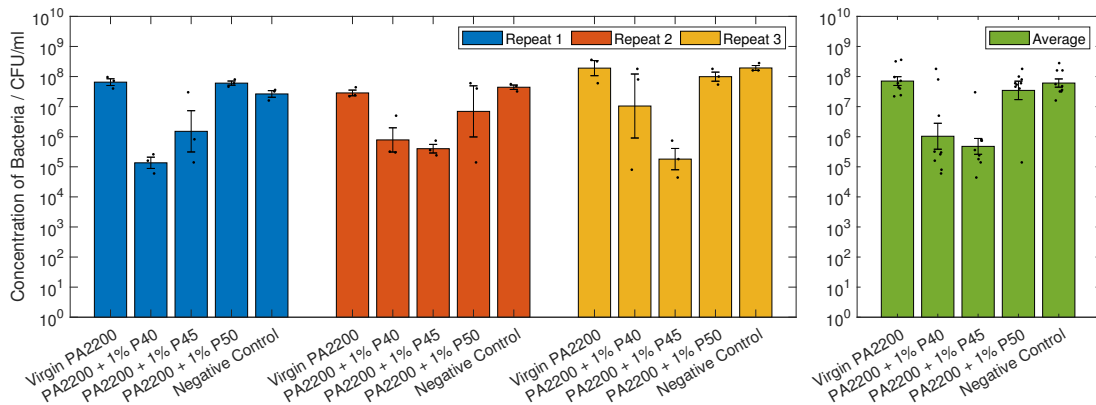


Figure 5.21: Non-contact protocol (planktonic), divided into days of activities. 🤖



(a) *S. aureus* S235 (Planktonic) in PBS pre-incubated with a microcomposite sphere.



(b) *P. aeruginosa* SOM1 (Planktonic) in PBS pre-incubated with a microcomposite sphere.

Figure 5.22: Non-contact PBS Tests. Results shown are geometric mean * geometric standard error. 🚫

| | 1% P40 | 1% P45 | 1% P50 | Control |
|--------|--------------|--------------|--------------|--------------|
| PA2200 | 0.000 | 0.000 | 0.002 | 0.046 |
| 1% P40 | – | 0.004 | 0.145 | 0.000 |
| 1% P45 | – | – | 0.367 | 0.006 |
| 1% P50 | – | – | – | 0.011 |

(a) *S. aureus* S235 (Planktonic).

| | 1% P40 | 1% P45 | 1% P50 | Control |
|--------|--------------|--------------|--------------|--------------|
| PA2200 | 0.002 | 0.000 | 0.380 | 0.747 |
| 1% P40 | – | 0.517 | 0.012 | 0.003 |
| 1% P45 | – | – | 0.000 | 0.000 |
| 1% P50 | – | – | – | 0.482 |

(b) *P. aeruginosa* SOM1 (Planktonic).

Table 5.12: Statistical comparison of the non-contact test data in Figure 5.22 (log-values). Shown are *p*-values, where *p* < 0.05 (shown in bold) indicates a statistically significant difference.

5.5 Chapter Summary

The results in this section are briefly summarised here, with reference to the research question (see Section 3.7.3) they contribute to. Note that all of this chapter falls under RQ 5, with the summary here also dividing up the results according to RQ 1–RQ 4. A more detailed discussion can be found in Chapter 6.

RQ 5 Can the customisability of phosphate-based glasses be exploited to tailor the effectiveness of the additives, and the printed microcomposite parts?

This question is addressed throughout Chapter 5, with the experiments common to those used in Chapter 4 grouped below.

Section 5.1.1 Detailed the design and manufacturing of the custom phosphate-based glass additives, based on the commercial additives.

RQ 1 Can powder feedstocks containing silver-doped phosphate-based additives be effectively processed in Laser Sintering?

This question is addressed in Section 5.1, with experiments focusing on the powder characterisation and the printing of the composite feedstock in LS.

Section 5.1.2 Measured the composition of the custom additives, using EDX.

Section 5.1.3 Analysed the morphology of the custom glass additives, using SEM.

Section 5.1.4 Measured the particle size distribution of the custom glass additives, using laser diffraction.

Section 5.1.5 Focused on the processing of the composite feedstock in Laser Sintering.

RQ 2 Does the addition of these additives affect the Engineering properties of the parts, and are these sufficiently dispersed throughout the part?

This question is addressed in Section 5.2, focusing on the inherent properties of the printed parts.

Section 5.2.1 Measured the colour of the printed microcomposites.

Section 5.2.2 Determined the mechanical properties of the printed parts, using tensile testing.

Section 5.2.3 Qualitatively analysed the surface features and additive dispersion on the part surface, using SEM and EDX.

RQ 3 Do the printed parts absorb water and release silver ions, and how does this compare to similar materials manufactured with other processes?

This question is addressed in Section 5.3, focusing on the behaviour of the parts in relation to specific external factors relevant to the antimicrobial performance.

Section 5.3.1 Measured the water uptake characteristics of the printed parts.

RQ 4 Do the printed parts show display significant antibacterial functionality, against representative and problematic strains of bacteria?

This question is addressed in Section 5.4, focusing on determining the antibacterial efficacy of the printed parts in nutrient-poor conditions.

Section 5.4.1 Measured the antibacterial efficacy of the custom additives (theoretical upper limit) against *S. aureus* and *P. aeruginosa*.

Section 5.4.2 Measured the contact efficacy (against biofilm formation and planktonic cells) of the printed parts.

Section 5.4.3 Measured the non-contact efficacy (planktonic cells) of the printed parts.

Chapter 6

Conclusions

6.1 Achievement of the Overall Aims

The aim of this research was to investigate the effectiveness of incorporating silver-containing additives to create intrinsically antimicrobial printed parts in Laser Sintering. Through the use of phosphate-based glasses, this was successfully achieved, with the resultant polyamide 12 / silver phosphate microcomposite parts able to release potent silver ions into their surroundings for a strong antimicrobial effect.

Microcomposite parts printed in this manner displayed a strong efficacy against both Gram-positive and Gram-negative bacteria (*Staphylococcus aureus* and *Pseudomonas aeruginosa*) under certain conditions, such as in nutrient-poor media, showing reductions in both planktonic bacteria and biofilm formation.

The methods outlined here were used to create phosphate-based glasses with different compositions, allowing for a tailored release rate of silver ions, and achieving similar results to the commercially available additives. In some cases, there appeared to be some difference in efficacy between Gram-positive and Gram-negative bacteria, with the amount of silver in the additives seemingly more important than the dissolution rate.

Practically, this research has shown that antimicrobial functionality can be added into Laser Sintered parts using this method, without affecting the mechanical properties. This allows for easy adoption of the microcomposite material, without the need to redesign parts or change parameters in the Laser Sintering process. The antimicrobial functionality is thought to be strongest in applications which directly contact water, with a lower efficacy potentially possible in humid conditions.

Alongside the antimicrobial functionality, this research demonstrated the ability of micro-CT to quantitatively analyse the additive distribution in a Laser Sintered microcomposite for the first time; showing the breadth of information available from a single scan and validating the production method. The effects and reversibility of a single steam sterilisation cycle on Laser Sintered parts were also investigated for the first time; with significant effects on the mechanical properties found and linked to the water content, and shown to be fully reversible through drying steps.

6.2 Summary of Work and Contributions to Knowledge

Here, each of the project objectives (specified in Section 3.7.4) are individually addressed. This includes a summary of the work carried out, the significance, and the contributions to knowledge.

RQ 1 Processability in Laser Sintering (Commercial Additives)

Objective 1. A base polymer of PA12 was chosen, as the most widely used and well understood material in Laser Sintering. Two commercially available, silver-containing phosphate-based additives were chosen, differing from each other only in size.

The choice of materials here represents the first instance of silver-containing additives or phosphate-based additives for use in LS. By initially focusing solely on commercially available materials, it makes the outcomes for any of the research more accessible to industry (therefore increasing the potential short-term impact) and more reproducible (lowering the threshold for further work in academia to occur).

Objective 1a. The morphology, particle size, and thermal properties of the PA12 polymer powder and the phosphate-based additives were characterised; with the chemical composition of the additives also measured. The results of the additive characterisation did not reveal any potential issues with regards to its processability in LS.

While the characterisation of PA12 for LS has been extensively investigated previously, it is predominantly included here for completeness with no significant addition to knowledge. Instead the novelty arises from the characterisation of the additives, which although interesting in isolation, could also be used as a reference to base any custom-made additives on.

Objective 2. The composite feedstocks used in this project were created simply by mechanical mixing of the two powders (polymer and additive).

Mechanical mixing is the simplest method available for creating a composite polymer feedstock, it is also the most accessible to both industry and academia, with the lowest capital cost and level of expertise required. However, the potential for agglomeration and poor dispersion of the additive within the part is high, with further analysis needed to validate the process. In this project, micro-CT was subsequently used for this purpose (see *Objective 4c*), providing sufficient justification for the use of mechanical mixing. As a result, the combination of a commercially available additive and the simplicity of mechanical mixing, means the composite powder feedstock can be easily reproduced at low cost (both in industry and academia).

Objective 3. The composite powder feedstock was successfully processed in Laser Sintering, with the standard parameters for PA12 used to create microcomposite parts.

In addition to the fact that the feedstock could be processed to form parts at all, the key point here was that the default parameters for PA12 could be used, without the need for any adjustment. While this may seem insignificant from a research setting where open machines are widespread, the vast majority of LS machines in industry are almost entirely locked down, allowing for the selection of only a few different parameter sets. This is therefore of most significance to end-users of LS in industry, with the research here suggesting that this easily reproducible composite feedstock can be processed in industrial LS machines, without the need for an open setup.

RQ 2 Engineering Properties (Commercial Additives)

Objective 4. For all of the characterisation carried out on the microcomposite parts, equivalent parts made out of the pure polymer (PA12 only) were also produced, allowing for a comparison to be made. For all of the tests carried out, no significant differences to the pure polymer parts were detected.

Objective 4a. The mechanical properties of the microcomposites showed no significant differences to the pure polymer parts.

This is perhaps the most significant aspect of the characterisation from an Engineering perspective. It means that for functional end-use applications of the printed parts, the composite powder feedstock can be used, without having to alter the design to account for any changes in mechanical properties. Combined with the ease and reproducibility of creating the composite powder feedstock, this means that the combination of materials specified here can most likely be applied directly in industry, at low cost, without the need for additional or open machinery, and with no design changes needed.

Objective 4b. A DSC trace of the printed parts revealed a slight, but largely insignificant decrease in the crystallinity of the microcomposite parts, compared to the pure polymer.

In this instance, the minimal difference in crystallinity could be advantageous in that significant changes in this would have likely affected the mechanical properties of the printed parts. That being said, a significant reduction in crystallinity could increase the water uptake rate of the printed parts, potentially leading to a higher release rate of silver from the parts, and a higher antimicrobial efficacy.

Objective 4c. Micro-CT was used to quantitatively analyse the porosity and additive dispersion in the printed parts. There was no change to the part microstructure (porosity) in the microcomposite parts; the additive was found to be randomly dispersed throughout the volume.

While the analysis of the porosity in this manner had been previously investigated (included for completeness here), this step was significant both in terms of the production of the microcomposites in this project, as well as a stand-alone contribution to the knowledge in academia. The similarity in the porosity analysis to the pure polymer parts goes further to explaining why no changes in the mechanical properties

were found, while partly redundant in this project, a similar approach could be used for production parts as a means of non-destructively analysing the properties.

The additive analysis for the microcomposite parts represents the first instance of micro-CT being used to quantitatively analyse the additives inside an LS part. The novelty of this resulted in a journal publication [260]; with the concept suitable for use in industry as a quality control method, highlighting the versatility of micro-CT and the range of information available from a single scan. In this project, the random dispersion this revealed validated the use of mechanical mixing to create the composite powder feedstock; meaning that a more complex (and costly) method of creating the feedstock was not required.

Objective 4d. The expected amount of silver was measured inside the printed microcomposite parts, showing that it was successfully incorporated.

The analysis of the printed parts did reveal a significant difference between the expected and measured amounts of silver in the parts; however, the small size of the samples and the likely inaccuracy of the datasheet value for the silver content quoted meant that the similarity (same order of magnitude) was not a cause for concern here. This measured value for the silver content in the printed parts could then be used to contextualise any subsequent silver release rates measured, allowing for the values to be expressed as an estimated percentage of the total in the parts.

RQ 3 Situational Properties (Commercial Additives)

Objective 5. Based on the literature and on observations in preliminary experiments, three aspects relevant to the use and antimicrobial functionality of the microcomposite parts were investigated here. These being the effect of steam sterilisation, the water uptake characteristics of the parts, and the release rate of silver ions from the parts.

Objective 5a. Steam sterilisation was shown to have a large effect on the mechanical properties of the printed parts, with the effects reversible with subsequent drying steps.

This step represents a significant contribution to knowledge, being the first investigation on the effect of a single steam sterilisation cycle on the mechanical properties, and the first investigating the reversibility of the changes through additional drying steps. In terms of the impact in academia, a journal publication was published based on this research [270], further adding to the literature on both the effect of autoclaving and the effect of water content on LS PA12 parts. In terms of industry impact, this both confirms and dispels some of the claims about the ability of LS PA12 to withstand the conditions in steam sterilisation. While obviously the parts survived the process, additional information covering the effects on mechanical properties and the need for subsequent drying steps in applications where the mechanical properties are critical, should be added to these claims.

Objective 5b. The water uptake of the parts was measured as an indication of silver release, with the LS parts showing a higher water diffusion rate than injection moulded polyamide 12.

The water diffusion rates measured in this experiment were markedly higher than those measured in injection moulded PA12, thought to be mainly a result of capillary action on the surface of the parts, as well as the porosity of the material. Both of these features are difficult to achieve with injection moulding, suggesting that LS could be a more effective method of producing parts with water-dependent antibacterial functionality than IM.

Although potentially a good indicator of the silver ion release rate, another unintentional outcome of this experiment was to highlight the variability in the results, and therefore potential flaws in the method for detecting small differences. This was mainly attributed to the difficulty of drying the specimens in a repeatable manner by hand, with additional changes noted for further use of this method. However, in this case the method was not sensitive enough to distinguish any differences between the printed parts tested.

Objective 5c. The release of silver ions from the parts into water was measured, showing a constant release rate over 7 days.

Although only conducted over a short time period (7 days) the release of silver ions was significant in terms of the viability of the material. This proved that the concept was possible, and that the silver in the part was able to be released. The rates measured were also higher than similar compression moulded samples, further indicating that the use of LS could prove more effective in the production of these type of antimicrobial materials.

RQ 4 Antimicrobial Properties (Commercial Additives)

Objective 6. Methods for measuring the antimicrobial efficacy of the printed parts were developed for this project, in consultation with experts in Microbiology. These focused on testing the effect on biofilm formation as well as on planktonic cells, testing against clinical isolates of representative and problematic pathogens (Gram-positive *Staphylococcus aureus* S235 and Gram-negative *Pseudomonas aeruginosa*).

Although not all of the methods developed here were effective and insightful (denoted as preliminary experiments), the final methods developed towards the end of this section (subsequently used in Chapter 5) were robust and repeatable. The instances where issues were discovered with the testing procedures all provided insights into how the materials worked, with more rigorous tests devised as a result.

Objective 6a. The powder feedstock was found to be highly antimicrobial in nutrient-poor conditions.

These relatively simple tests provided an upper limit for the potential antibacterial effect of the additives, with the immediate exposure to water over a large surface area expected to yield a far greater effect than when encased in the parts. With such a large effect seen with the powders, at least some level of antimicrobial functionality was expected to be seen from the microcomposite parts.

Objective 6b. The microcomposite parts showed both bactericidal and antibiofouling effects (planktonic and biofilm) for both Gram-positive and Gram-negative bacteria (*S. aureus* and *P. aeruginosa*) in nutrient-poor conditions, even with no direct contact.

The tests carried out in these conditions are the most significant for the printed microcomposite parts, with the largest antimicrobial effects expected (and subsequently measured) in these experiments. The effectiveness of the parts with no direct contact (pre-incubated and removed before exposure to the bacteria) confirms the method of action, that the silver ions were released from the parts into the surrounding media, rather than having a bactericidal effect through contact methods. The nutrient-poor conditions also suggest potentially suitable environments for applications, where constant or intermittent contact with water is required to achieve the desired antimicrobial effect.

Objective 6c. No antimicrobial effect was measured in nutrient-rich conditions, due to the interaction of silver with thiols in the media.

Although the parts did not display any antibacterial efficacy in these environments, these experiments were still significant in terms of identifying the limitations of the material; and confirming the interaction of silver and thiols presented in the literature. For this project, the results suggest that the parts are not effective in nutrient-rich environments, such as blood. In terms of potential applications, this rules out the use of the material for internal implants, while the use for external aids such as braces or prostheses (where there is likely intermittent contact with liquids such as water or sweat) is still an option.

Objective 7. The results show that it was possible to create an antimicrobial material for Laser Sintering using silver-containing additives.

This conclusion, formed from all the results in Objectives 1–6, is significant both in academia and more widely. The results of these have been published in a high impact journal [451], with the paper and accompanying press release gaining significant media attention from over 50 national and international outlets (see Appendix D for more details on publications arising from this).

The conclusion of the parts containing the commercial additives is that the hypothesis presented in Section 3.7.6, detailing the proposed release method of silver ions from Laser Sintered PA12 parts, is correct. The results show that the composite powder feedstock can be processed in LS, absorb water and release silver ions (at a faster rate than equivalent injection moulded parts), and have significant antibiofouling and bactericidal effects. Additional testing also confirmed that the materials did not have a cytotoxic effect against human cells, showing they are safe to be used and handled. This therefore proved the concept, allowing for further development of the parts, with respect to the amount of silver required to be released and the factors affecting this.

Going forward, from observations during printing, the larger of the two additive sizes was identified as the more reliable to process (with parts made with the smaller additives showing signs of curl in the prints). The dispersion of these larger additives was also measured to be sufficiently random within the parts, with no significant difference in the water uptake (indicative of silver release) between the two additive sizes found. The additive loading was found to be sufficient in creating a strong antimicrobial effect, although the effect of changing the properties of the additives (such as silver content or dissolution rate) was still unclear.

RQ 5 Tailored Additives

Objective 8. Three silver-containing phosphate-based glasses (P40, P45 and P50) were designed based on the commercial additive, in consultation with experts in Materials Science. These were designed with different amounts of phosphate to achieve different degradation rates. The amount of silver was designed to be constant between all the glasses, although some differences were measured after production. The glasses were ground into a powder and sieved to resemble the larger of the two commercial additives.

This represents the first use of these methods of phosphate glass manufacture to create tailored additives for use in Laser Sintering. As such, they constitute a significant addition to knowledge, with a journal publication published [445] based on this and the subsequent testing carried out on the printed parts.

The characterisation of the custom additives showed that the morphology, particle size, and the general composition had closely replicated that of the commercial additive, suggesting that there should not be any effect on the processability of the feedstock based on these. However, the characterisation of the additive composition revealed some differences in the silver content for the three additives, compared to the desired amounts. This slight variation in composition is common with the methods used; however, due to the high cost of consumables and restrictions due to COVID-19, it was not possible to produce further iterations of the glasses to closer match the desired specification.

These differences in both the dissolution rate and silver content made finding a correlation between any observed differences and the dissolution rate or the silver content impractical, with the changes in composition often acting against each other. Despite this, the three additives produced were significantly different to one another to warrant testing, even if broader generalisations about the key properties of the additives might not be possible to make.

Objective 9. The processability in Laser Sintering, Engineering properties, situational properties, and antibacterial properties for the custom-made additives was determined using the same methods as for the commercial additive where possible. These are further divided according to Objectives 2–7 here, where only the methods identified as providing a meaningful insight into the performance of the microcomposite parts were used. Note that where the results mirrored that of the commercial additive, the discussion points are the same and have not been repeated here.

(Objective 2). Composite powder feedstocks were created by physical mixing of polyamide 12 powder and the custom-made silver phosphate glass powders, as with the commercial additives.

(Objective 3). All three custom feedstocks were successfully processed in Laser Sintering using standard polyamide 12 parameters, with colour changes observed in the parts.

The processability of all three custom additives in LS was a significant milestone in the project, as it validated the hypothesised behaviour of the glasses based on their similarity to the commercial additives. As mentioned previously, the use of standard parameters for PA12 was also significant here, allowing for the feedstock to be processed in a wider range of industrial LS machines. The colour change observed in the printed parts was quantified for completeness, although it is unlikely to affect the choice of using the additive unless the aesthetics are critical to the design.

(Objective 4). The Engineering properties of the printed microcomposite parts were measured, with no significant differences to the pure polymer parts found.

Characterisation of the thermal properties (*Objective 4b*) was not carried out here, as the differences with the commercial additives were small, and the results not thought to have a significant effect on the antimicrobial properties. The silver content of the parts (*Objective 4d*) was also not carried out here, due to restricted lab access during COVID-19.

(Objective 4a). The mechanical properties of all the microcomposite materials showed no statistical difference to those of the pure polymer.

(Objective 4c). The additives were qualitatively observed as dispersed on the part surface, and assumed to be randomly dispersed throughout the volume based on the similarities to the commercial powder.

Due to the similarities with the commercial additives, it was decided that characterising the additive dispersion with micro-CT was unnecessary. This was instead qualitatively addressed using SEM and EDX, allowing for analysis of the part surface. Although the internal microstructure of the parts was not measured, the scans of the part surface revealed far more of the expected features on the surface of an LS part (melted areas, partially melted particles, partially encapsulated additive particles, and open pores) than with the commercial additive. However, this was thought to be due to differences in the orientation of the surface scanned, rather than any inherent differences in the printed parts.

(Objective 5). To characterise the situational properties of the custom microcomposite parts, the water uptake was measured.

Although some of the other experiments used for the commercial additives (such as measuring the silver release – Objective 5c) would have provided a deeper insight into the performance of the parts, it was not possible to carry these out. This was due to the significantly reduced access to labs due to COVID-19, with the scale of the experiments and the significant cost involved with outsourcing these tests making them infeasible to perform. The behaviour of the microcomposites was expected to be the same as for pure PA12 parts, so the effect of steam sterilisation (Objective 5a) was not investigated again here.

(Objective 5b). The water uptake was measured, with no differences found between any of the custom microcomposite parts.

Despite the improvements made based on the water uptake tests carried out previously, human error meant that the results from this could not be used to definitively characterise the parts or make a comparison to parts made from the pure polymer or the commercial additive. However, a comparison between the custom microcomposites was possible, with the differences small enough to suggest that any changes in antimicrobial efficacy were unlikely to be caused by differences in water uptake.

(Objective 6). The antibacterial testing carried out on the custom additives focuses solely on the efficacy in nutrient-poor conditions, using the methods developed for the commercial additives.

From the experiments carried out in nutrient-rich conditions previously, it was decided to focus solely on the efficacy in nutrient-poor conditions, as these were likely to display the largest effect. The methods used mirrored those used previously, with additional steps added to increase the reliability and robustness of the experiments. These included adding a negative control sample for all tests, and ensuring that three repeats were carried out for each experiment (as is best practice).

(Objective 6a). All three custom glass powders were found to have a strong antimicrobial effect against both Gram-positive and Gram-negative bacteria (*S. aureus* and *P. aeruginosa*) in nutrient-poor conditions.

Again representing the upper bound on the effectiveness of the additives produced, the powders all displayed significant antimicrobial properties. This suggested that any parts containing the custom additives were also likely to display some level of antimicrobial functionality.

(Objective 6b). Only microcomposite parts containing P40 were seen to have a statistically significant antimicrobial effect on planktonic bacteria (*S. aureus* and *P. aeruginosa*) compared to the pure polymer, thought to be due to the slightly higher silver content. All the microcomposite parts showed a statistically significant reduction in biofilm formation (*S. aureus* and *P. aeruginosa*) on the part surface. All the microcomposite parts displayed a bactericidal effect with pre-incubated (non-contact) tests with *S. aureus*, with P40 and P45 also showing an effect against *P. aeruginosa*.

While the differences in the additive composition from the initial design might have slightly clouded the results obtained here, the at least one of the formulations created (P40) showed consistently significant antimicrobial functionality. This significant result shows that it was possible to create custom additives to add antimicrobial functionality to Laser Sintered parts, using the methods outlined in this research. By transparently displaying the method here, this builds on the results from the commercial additives, as it gives a deeper insight into what is involved with creating such a material.

This is significant both in academia (with the journal publication adding to the knowledge in this area [445]) and in industry, where additive manufacturers can use this method directly to replicate the materials described in this research.

(Objective 7). This research shows that it is possible to tailor properties of silver-doped phosphate-based glass additives to an extent, to alter the antimicrobial properties of microcomposite PA12 parts made using Laser Sintering.

The results for the three custom glasses show that, although not originally specified as an objective, the antimicrobial efficacy of the parts is more sensitive to the silver content of the additives than their degradation rate. This knowledge can be built on in further work, with the potential to further elucidate on the key properties of the additive composition in future work.

6.3 Obstacles to Completion

Undoubtedly, the largest obstacles overcome in the completion of this project revolved around a lack of prior knowledge in Microbiology and Materials Science (among many other topics). With both of these being fundamental to the project, the approach used here was fundamentally collaborative, with efforts made to work with experts in these fields. As well as being able to suggest different methodologies and offer practical advice on carrying these out, this opened up the possibility to work in laboratories across different departments, faculties and universities. With such a multidisciplinary project as this, I am of the firm belief that this was the best (and only) possible way to complete the research in the time allocated.

The disruption caused by the COVID-19 pandemic cannot be ignored in a section such as this. As mentioned throughout this thesis, the restricted lab access and necessity to work from home for long periods of time, did impact the amount of experimental work which could be carried out in the second half of this project. For the most part, this did not affect the overall plans, with some experiments able to be carried out by external parties (such as the manufacture of the glasses) and others able to be scheduled in such a way that they were possible to carry out in person. This meant that (other than slightly extending the duration of the research) all of the necessary practical work was carried out, with only some additional testing unable to be performed.

6.4 Significance and Potential for Impact

In terms of academic significance, multiple stand-alone aspects of this thesis have been sufficiently novel and rigorous to be published in peer reviewed academic journals (for full details, see Appendix D). These have included the first academic research carried out into antimicrobial materials for Laser Sintering [451], the first instance of micro-CT being used to quantitatively analyse the additives inside LS microcomposite parts [260], the first research into the effects and reversibility of steam sterilisation on LS parts [270], and the first instance of manufacturing tailored glass additives to create antimicrobial LS parts [445]. These comprise the majority of the work presented in this thesis, allowing a greater dissemination of the work, and drastically increasing the potential for further work to be carried out based on this.

In terms of the potential impact in industry, the success of the methods used here mean that barriers to entry for adopting these microcomposites are relatively low. The use of commercial powders and machines, mean that the materials here can be directly recreated; in terms of the powder feedstock, the use of physical mixing means it simple to create at a low cost; the ability of the feedstock to be processed using standard PA12 parameters, means that a wider range of industrial LS machines can be used; and the lack of any changes in the mechanical properties, mean that the microcomposites can be used without changing the part designs. Overall, this both enables the use of the exact materials specified here, and raises awareness of antimicrobial materials more generally.

The additional (and largely unexpected) impact from this work in industry, relates to the use of micro-CT and the effect of steam sterilisation. As a non-destructive method for quantitatively analysing microcomposite parts, micro-CT can be used with the methods outlined here to validate the choice and consistency of production method for composite polymer feedstocks. The effect of autoclaving can also be applied here, as further guidance on drying methods and the effect on the mechanical properties would lead to more complete design guides and marketing information, when aiming the sale of LS PA12 materials towards medical applications.

6.5 Further Work

As with any PhD, there are additional experiments which could be carried out to continue research in this area. The most relevant of these are briefly summarised here, with suggestions of methodologies to use and what these might show.

Long Term Measurements of Silver Release

In this report, the short-term silver release into water was measured over 7 days (see Section 4.3.4). As these microcomposites are expected to be effective for long (100+ days) periods of time, the intention was to measure the long-term release alongside the water uptake measurements in Sections 4.3.3 and 5.3.1. Although this was not possible due to COVID-19 restrictions, this would provide a good indication as to the lifespan and effectiveness of the material.

To achieve this, the same methodology as Section 4.3.4 could be used, with the potential to use the same detection method (ICP-ESMS) or using a less expensive method such as a silver specific electrode. For either of these, the water uptake could be measured using the method in Section 4.3.2 to establish a more direct link between the two properties. The expected relationship would be proportional, matching the literature for similar materials (see Figure 3.17).

Different Bacteria and Other Microbes

While *S. aureus* and *P. aeruginosa* are a good starting point for antimicrobial testing, further testing could be carried out with other microorganisms. This could include a broader range of bacteria (for example the ESKAPE pathogens), as well as fungi (such as *Candida* and *Aspergillus*), or even combinations of these for mixed biofilms. Additional strains could also be investigated for particular traits, such as *S. aureus* SH1000 for increased biofilm formation (compared to S235 analysed here).

The recommendation here would be to use the methods used in Chapter 5, allowing for the measurement of both planktonic cells and biofilm formation. For each of the microorganisms chosen, the exact temperatures would have to reflect the optimum conditions needed. Due to the wide-ranging effectiveness of silver, an antimicrobial effect would be expected to some extent for all of the microorganisms suggested here.

Additional Bacterial Testing

Changes to the antibacterial testing could also be made to encourage more biofilm formation and represent more realistic conditions. This could include running the tests for longer (48 hours for biofilm growth), using lower shaking speeds, or investigating the effects under constant flow.

In terms of a scaleable test, a modified version of the static peg assay (Section 4.4.3) could be developed. This would have to be manufactured from materials capable of withstanding the temperatures in an autoclave, to ensure there is no residual contamination from the sterilisation process. For more realistic representation, the biofilms could be grown under a constant flow. This could be done in a low-shear, gravity fed system such as the one outlined in [477]; or under a high shear condition, such as the method outlined in [478].

Additive Loading

The loading of the additives was briefly addressed in Section 4.4.3 and Appendix C.1.2, before a fixed 1% by mass was used for all subsequent experiments. As this was not investigated in depth, further research could be carried out to establish the maximum amount processable in LS, and to investigate the effects this has on the properties and antimicrobial functionality of the printed parts.

With the silver content of the tailored glasses close to the theoretical maximum for glass-forming amounts, the most effective way of increasing the amount of silver (and therefore rate of Ag^+ release) in the part, is by increasing the additive loading. In its simplest form, these experiments could focus on the processability in LS and the effect on the mechanical properties. However, should a more in depth analysis be required; further testing of the Engineering properties, situational properties, and antimicrobial efficacy could be carried out as laid out in this thesis.

Different Base Polymer

The widespread use of PA12 in LS made it an obvious starting point for this testing. However, with the performance of the part so closely linked to the water uptake of the polymers, a polyamide with a higher maximum water content might provide a higher Ag^+ release rate and therefore a stronger antimicrobial effect. These could include materials such as PA6 or PA6,6, which have already been established as suitable materials for LS.

For these materials, the rate of water uptake is the key difference to the PA12 used here. For any experiments carried out to determine the processability in LS, the Engineering properties, or the antimicrobial efficacy; additional testing should focus on measuring the water uptake and determining the diffusion coefficient. In terms of the practicalities of this, LS machines with higher temperature capabilities (higher bed temperatures) are likely required to process materials such as PA11 and PA6,6.

Laser Sintering Parameters

An alternative option to choosing different base materials could be to change the parameters used during printing to change the part properties. This could involve optimising the properties for Ag^+ release (rather than the mechanical properties), potentially by intentionally increasing the porosity / decrease the porosity to allow for more water penetration into the parts, and increased accessibility of the additive.

Although this goes against the usual optimisation of LS parts, by lowering the energy density in the parts (lowering the laser power / faster scan speed etc. – see Section 2.3.2), less of the feedstock will be melted during printing. This would create a weaker part, but with a higher porosity and more open pores, allowing for a much higher maximum water content and a higher rate of water absorption. This would allow a faster access to the additives embedded in the parts, allowing for the Ag^+ producing reaction to occur sooner and reduce the initial delay in the release of Ag^+ .

Effect of Pre-Wetting

Another method which could be used to determine the long-term effectiveness of the microcomposites, would be to soak the samples in water for varying amounts of time before testing the antimicrobial efficacy. In the short-term, this would give an insight as to whether this “kick starts” the release of silver, leading to a stronger efficacy straight away. In the long-term, the immersion of the samples in water (in the same way as the water uptake experiments in Section 4.3.2) would represent a longer use case, depleting some of the silver reserves inside the parts before testing.

Following this pre-wetting, the same methods of antibacterial testing as used in Chapter 5 should be used. These will give an accurate representation of the effect on planktonic cells, and on the biofilm formation on the printed parts.

References

- [1] *Standard Terminology for Additive Manufacturing – General Principles – Terminology*, ASTM International Std. ASTM ISO/ASTM52900-15, 2015. [Online]. Available: <https://doi.org/10.1520/ISOASTM52900-15> [Accessed: 9-11-2017].
- [2] I. Gibson *et al.*, “Introduction and basic principles,” in *Additive Manufacturing Technologies: 3D Printing, Rapid Prototyping, and Direct Digital Manufacturing*, 2nd ed. New York: Springer, 2015, ch. 1, pp. 1–18.
- [3] R. Hague, “Unlocking the design potential of rapid manufacturing,” in *Rapid manufacturing: an industrial revolution for the digital age*. Chichester, England: John Wiley, 2006, ch. 2, pp. 5–18.
- [4] T. T. Wohlers and T. Gornet, “History of additive manufacturing,” in *Wohlers Report 2017: 3D printing and Additive Manufacturing State of the Industry Annual Worldwide Progress Report*. Fort Collins: Wohlers Associates, 2017, pt. 1, pp. 15–33. [Online]. Available: <http://wohlersassociates.com/history2017.pdf> [Accessed: 23-11-2017].
- [5] K. Stevenson. (2014, Dec. 9) *Blueprinter Update*. [Online]. Available: <http://www.fabbaloo.com/blog/2014/12/7/blueprinter-update> [Accessed: 24-11-2017].
- [6] HP. (2017) *The 3D printer revolution starts now – meet the mighty HP Voxel*. [Online]. Available: <http://www8.hp.com/uk/en/printers/3d-printers.html> [Accessed: 13-11-2017].
- [7] Voxeljet. (2017) *Voxeljet unveils new 3D printing technology*. [Online]. Available: <http://www.voxeljet.com/unternehmen/news/voxeljet-introduces-high-speed-sintering-process/> [Accessed: 24-11-2017].
- [8] C. Hull, “Apparatus for production of three-dimensional objects by stereolithography,” U.S. Patent 4,575,330, Mar. 11, 1986. [Online]. Available: <https://www.google.com/patents/US4575330> [Accessed: 9-11-2017].
- [9] N. Hopkinson, “Lecture – Additive Manufacturing: Overview and History,” in *MEC304 Manufacturing Systems*, The University of Sheffield, Oct. 16 2015.
- [10] R. I. Campbell, “Customer input and customisation,” in *Rapid manufacturing: an industrial revolution for the digital age*. Chichester, England: John Wiley, 2006, ch. 3, pp. 19–37.
- [11] L. E. André *et al.*, “QuickCast foundry experience,” in *Stereolithography and other RP&M technologies: from rapid prototyping to rapid tooling*. Dearborn, Mich.: New York: Society of Manufacturing Engineers; American Society of Mechanical Engineers, 1996, ch. 7, pp. 209–238.
- [12] T. T. Wohlers *et al.*, “Introduction,” in *Wohlers Report 2017: 3D printing and Additive Manufacturing State of the Industry Annual Worldwide Progress Report*. Fort Collins: Wohlers Associates, 2017, pt. 1, pp. 15–33.
- [13] T. T. Wohlers *et al.*, “Industries, applications, and regions,” in *Wohlers report 2018: 3D printing and additive manufacturing state of the industry annual worldwide progress report*. Fort Collins: Wohlers Associates, 2018, pt. 1, pp. 21–32.
- [14] I. Gibson *et al.*, “Generalized additive manufacturing process chain,” in *Additive Manufacturing Technologies: 3D Printing, Rapid Prototyping, and Direct Digital Manufacturing*, 2nd ed. New York: Springer, 2015, ch. 3, pp. 43–62.
- [15] J. R. Wingham, “Effect of colour on the performance of 3D printing materials,” M.Eng. thesis, Department of Mechanical Engineering, University of Sheffield, England, Apr. 2017.
- [16] M. Eisenberg, “3D printing for children: What to build next?” *International Journal of Child-Computer Interaction*, vol. 1, no. 1, pp. 7–13, 2013. [Online]. Available: <http://www.sciencedirect.com/science/article/pii/S2212868912000050>
- [17] P. F. Jacobs, “Introduction,” in *Stereolithography and other RP&M technologies: from rapid prototyping to rapid tooling*. Dearborn, Mich. : New York: Society of Manufacturing Engineers ; American Society of Mechanical Engineers, 1996, ch. 1, pp. 1–28.
- [18] *Standard Specification for Additive Manufacturing File Format (AMF) Version 1.2*, ASTM International Std. ASTM ISO/ASTM52915-16, 2016. [Online]. Available: <https://doi.org/10.1520/ISOASTM52915-16> [Accessed: 30-11-2017].

- [19] T. T. Wohlers *et al.*, “Industries, applications, and regions,” in *Wohlers report 2016: 3D printing and additive manufacturing state of the industry annual worldwide progress report*. Fort Collins: Wohlers Associates, 2016, pt. 1, pp. 19–30.
- [20] 3MF Consortium. (no date) *Enabling the full potential of 3D Printing*. [Online]. Available: <https://3mf.io/> [Accessed: 30-11-2017].
- [21] W. Gao *et al.*, “The status, challenges, and future of additive manufacturing in engineering,” *Computer-Aided Design*, vol. 69, pp. 65–89, 2015. [Online]. Available: <https://doi.org/10.1016/j.cad.2015.04.001> [Accessed: 9-10-2017].
- [22] C. Tuck and R. Hague, “Management and implementation of rapid manufacturing,” in *Rapid manufacturing: an industrial revolution for the digital age*. Chichester, England: John Wiley, 2006, ch. 10, pp. 159–174.
- [23] J. B. Naylor *et al.*, “Leagility: Integrating the lean and agile manufacturing paradigms in the total supply chain,” *International Journal of Production Economics*, vol. 62, no. 1, pp. 107–118, 1999. [Online]. Available: [https://doi.org/10.1016/S0925-5273\(98\)00223-0](https://doi.org/10.1016/S0925-5273(98)00223-0) [Accessed: 12-12-2017].
- [24] T. T. Wohlers *et al.*, “Final part production,” in *Wohlers Report 2017: 3D printing and Additive Manufacturing State of the Industry Annual Worldwide Progress Report*. Fort Collins: Wohlers Associates, 2017, pt. 5, pp. 176–201.
- [25] J. K. Watson and K. M. B. Taminger, “A decision-support model for selecting additive manufacturing versus subtractive manufacturing based on energy consumption,” *Journal of Cleaner Production*, 2015. [Online]. Available: <https://doi.org/10.1016/j.jclepro.2015.12.009> [Accessed: 08-12-2017].
- [26] P. C. Priarone and G. Ingarao, “Towards criteria for sustainable process selection: On the modelling of pure subtractive versus additive/subtractive integrated manufacturing approaches,” *Journal of Cleaner Production*, vol. 144, pp. 57–68, 2017. [Online]. Available: <https://doi.org/10.1016/j.jclepro.2016.12.165> [Accessed: 08-12-2017].
- [27] H. Paris *et al.*, “Comparative environmental impacts of additive and subtractive manufacturing technologies,” *CIRP Annals*, vol. 65, no. 1, pp. 29–32, 2016. [Online]. Available: <https://doi.org/10.1016/j.cirp.2016.04.036> [Accessed: 08-12-2017].
- [28] R. Huang *et al.*, “Energy and emissions saving potential of additive manufacturing: the case of lightweight aircraft components,” *Journal of Cleaner Production*, vol. 135, pp. 1559–1570, 2016. [Online]. Available: <https://doi.org/10.1016/j.jclepro.2015.04.109> [Accessed: 08-12-2017].
- [29] Shapeways. (no date) *Silver Material Information*. [Online]. Available: <https://www.shapeways.com/materials/silver> [Accessed: 07-12-2017].
- [30] T. T. Wohlers *et al.*, “Processes and materials,” in *Wohlers report 2016: 3D printing and additive manufacturing state of the industry annual worldwide progress report*. Fort Collins: Wohlers Associates, 2016, pt. 2, pp. 33–66.
- [31] N. Hopkinson and P. Dickens, “Analysis of rapid manufacturing – using layer manufacturing processes for production,” *Proceedings of the Institution of Mechanical Engineers, Part C: Journal of Mechanical Engineering Science*, vol. 217, no. 1, pp. 31–39, 2003. [Online]. Available: <https://doi.org/10.1243/095440603762554596> [Accessed: 12-12-2017].
- [32] G. D. Kim and Y. T. Oh, “A benchmark study on rapid prototyping processes and machines: Quantitative comparisons of mechanical properties, accuracy, roughness, speed, and material cost,” *Proceedings of the Institution of Mechanical Engineers, Part B: Journal of Engineering Manufacture*, vol. 222, no. 2, pp. 201–215, 2008. [Online]. Available: <https://doi.org/10.1243/09544054JEM724> [Accessed: 15-11-2016].
- [33] T. T. Wohlers *et al.*, “Research and development,” in *Wohlers Report 2017: 3D printing and Additive Manufacturing State of the Industry Annual Worldwide Progress Report*. Fort Collins: Wohlers Associates, 2017, pt. 7, pp. 236–288.
- [34] RepRap. *RepRap Project*. [Online]. Available: <http://reprap.org/> [Accessed: 9-11-2016].
- [35] N. Hopkinson *et al.*, “Introduction to rapid manufacturing,” in *Rapid manufacturing: an industrial revolution for the digital age*. Chichester, England: John Wiley, 2006, ch. 1, pp. 1–4.
- [36] I. Gibson, “Rapid prototyping for medical applications,” in *Advanced manufacturing technology for medical applications: reverse engineering, software conversion, and rapid prototyping*. Chichester, England: John Wiley, 2005, ch. 1, pp. 1–14.
- [37] T. Wohlers *et al.*, “Introduction,” in *Wohlers Report 2022: 3D printing and Additive Manufacturing Global State of the Industry*. Washington, DC: ASTM International, 2022, pt. 1, pp. 18–76.
- [38] V. Waran *et al.*, “Utility of multimaterial 3D printers in creating models with pathological entities to enhance the training experience of neurosurgeons,” *Journal of Neurosurgery*, vol. 120, no. 2, pp. 489–492, 2014. [Online]. Available: <https://doi.org/10.3171/2013.11.JNS131066> [Accessed: 06-12-2017].
- [39] A. M. Christensen and S. M. Humphries, “Role of rapid digital manufacture in planning and implementation of complex medical treatments,” in *Advanced manufacturing technology for medical applications: reverse engineering, software conversion, and rapid prototyping*. Chichester, England: John Wiley, 2005, ch. 2, pp. 15–30.

- [40] LGM Models. (2017) *Sales Models*. [Online]. Available: <http://www.lgm3d.com/products/sales-models> [Accessed: 06-12-2017].
- [41] C. Nicholson. (2014, Jan. 22) *3D-Printed Brain Surgery*. [Online]. Available: <http://www.core77.com/posts/26200/3D-Printed-Brain-Surgery> [Accessed: 06-12-2017].
- [42] D. Karalekas and A. Agelopoulos, "On the use of stereolithography built photoelastic models for stress analysis investigations," *Materials & Design*, vol. 27, no. 2, pp. 100–106, 2006. [Online]. Available: <https://doi.org/10.1016/j.matdes.2004.09.028> [Accessed: 04-12-2017].
- [43] W. Steinchen and A. Hirchenhain, "Fotopolymere der stereolithografie als spannungsoptische werkstoffekalibrierung und anwendung für ebene und räumliche untersuchungen," *Forschung im Ingenieurwesen*, vol. 59, no. 7, pp. 153–159, 1993. [Online]. Available: <https://doi.org/10.1007/BF02561024> [Accessed: 04-12-2017].
- [44] P. F. Jacobs, "Special applications of RP&M," in *Stereolithography and other RP&M technologies: from rapid prototyping to rapid tooling*. Dearborn, Mich.: New York: Society of Manufacturing Engineers; American Society of Mechanical Engineers, 1996, ch. 12, pp. 317–348.
- [45] J. D. Curtis *et al.*, "On the use of stereolithography for the manufacture of photoelastic models," *Experimental Mechanics*, vol. 43, no. 2, pp. 148–162, 2003. [Online]. Available: <https://doi.org/10.1007/BF02410496> [Accessed: 04-12-2017].
- [46] K. R. Denton and S. B. O'Reilly, "Hard tooling applications of RP&M," in *Stereolithography and other RP&M technologies: from rapid prototyping to rapid tooling*. Dearborn, Mich.: New York: Society of Manufacturing Engineers; American Society of Mechanical Engineers, 1996, ch. 12, pp. 293–316.
- [47] V. Petrovic *et al.*, "Additive layered manufacturing: sectors of industrial application shown through case studies," *International Journal of Production Research*, vol. 49, no. 4, pp. 1061–1079, 2011. [Online]. Available: <https://doi.org/10.1080/00207540903479786> [Accessed: 07-12-2017].
- [48] HRS Flow. (no date) *SLM inserts – Selective Laser Melting*. [Online]. Available: <https://www.hrsflow.com/eng/prodotti/slm-inserts-selective-laser-melting/slm-inserts-selective-laser-melting.php> [Accessed: 07-12-2017].
- [49] I. Gibson *et al.*, "Rapid tooling," in *Additive Manufacturing Technologies: 3D Printing, Rapid Prototyping, and Direct Digital Manufacturing*, 2nd ed. New York: Springer, 2015, ch. 18, pp. 437–449.
- [50] A. Christensen and N. Wake, "Medical applications," in *Wohlers report 2019: 3D printing and additive manufacturing state of the industry*. Fort Collins: Wohlers Associates, 2019, pt. 1, pp. 35–40.
- [51] P. D'Urso, "Biomodelling," in *Advanced manufacturing technology for medical applications: reverse engineering, software conversion, and rapid prototyping*. Chichester, England: John Wiley, 2005, ch. 3, pp. 31–58.
- [52] S. Galjaard *et al.*, "Optimizing structural building elements in metal by using additive manufacturing," in *Proceedings of the International Association for Shell and Spatial Structures (IASS) Symposium 2015*, 2015. [Online]. Available: https://www.researchgate.net/profile/Salome_Galjaard/publication/283634852_Optimizing_Structural_Building_Elements_in_Metal_by_using_Additive_Manufacturing/links/5641c19308aec448fa61d215.pdf [Accessed: 14-12-2017].
- [53] HRL Laboratories. (2011, Nov. 17) *HRL Researchers Develop World's Lightest Material*. [Online]. Available: <http://www.hrl.com/news/2011/11/17/hrl-researchers-develop-worlds-lightest-material> [Accessed: 14-12-2017].
- [54] GE Aviation. (2017) *Advanced Turboprop*. [Online]. Available: <https://www.geaviation.com/bga/engines/advanced-turboprop> [Accessed: 14-12-2017].
- [55] S. Anson. (2013, Jan. 1) *PEKK Pioneer*. [Online]. Available: <http://oxfordpm.com/news-events/opm-in-the-news?id=339726/pekk-pioneer> [Accessed: 15-12-2017].
- [56] T. A. Schaedler *et al.*, "Ultralight metallic microlattices," *Science*, vol. 334, no. 6058, pp. 962–965, 2011. [Online]. Available: <http://science.sciencemag.org/content/334/6058/962>
- [57] T. Kellner. (2017, Nov. 12) *New One-Of-A-Kind Turboprop Engine Delivers Jet-Like Simplicity To Pilots*. [Online]. Available: <https://www.ge.com/reports/new-one-kind-turboprop-engine-delivers-jet-like-simplicity-pilots/> [Accessed: 12-12-2017].
- [58] O. L. A. Harrysson and D. R. Cormier, "Direct fabrication of custom orthopedic implants using electron beam melting technology," in *Advanced manufacturing technology for medical applications: reverse engineering, software conversion, and rapid prototyping*. Chichester, England: John Wiley, 2005, ch. 9, pp. 191–206.
- [59] J. Wallace *et al.*, "Validating continuous digital light processing (cDLP) additive manufacturing accuracy and tissue engineering utility of a dye-initiator package," *Biofabrication*, vol. 6, no. 1, p. 015003, 2014. [Online]. Available: <http://dx.doi.org/10.1088/1758-5082/6/1/015003> [Accessed: 9-11-2017].
- [60] B. N. Turner *et al.*, "A review of melt extrusion additive manufacturing processes: I. process design and modeling," *Rapid Prototyping Journal*, vol. 20, no. 3, pp. 192–204, 2014. [Online]. Available: <https://doi.org/10.1108/RPJ-01-2013-0012> [Accessed: 9-11-2017].

- [61] CustomPartNet. (2008) *Fused Deposition Modeling (FDM)*. [Online]. Available: <http://www.custompartnet.com/wu/fused-deposition-modeling> [Accessed: 9-11-2017].
- [62] D. Espalin *et al.*, “Multi-material, multi-technology FDM: exploring build process variations,” *Rapid Prototyping Journal*, vol. 20, no. 3, pp. 236–244, 2014. [Online]. Available: <https://doi.org/10.1108/RPJ-12-2012-0112> [Accessed: 9-11-2017].
- [63] W. R. Priedeman and A. L. Brosch, “Soluble material and process for three-dimensional modeling,” U.S. Patent 6,790,403, Sep. 14, 2004. [Online]. Available: <https://www.google.com/patents/US6790403> [Accessed: 9-11-2017].
- [64] J. L. Lombardi *et al.*, “Water soluble rapid prototyping support and mold material,” U.S. Patent 6,070,107, May 30, 2000. [Online]. Available: <https://www.google.co.uk/patents/US6070107> [Accessed: 9-11-2017].
- [65] CustomPartNet. (2008) *Jetted Photopolymer*. [Online]. Available: <http://www.custompartnet.com/wu/jetted-photopolymer> [Accessed: 10-11-2017].
- [66] S. Meteyer *et al.*, “Energy and material flow analysis of binder-jetting additive manufacturing processes,” *Procedia CIRP*, vol. 15, no. Supplement C, pp. 19–25, 2014. [Online]. Available: <https://doi.org/10.1016/j.procir.2014.06.030> [Accessed: 17-11-2017].
- [67] CustomPartNet. (2008) *3D Printing*. [Online]. Available: <http://www.custompartnet.com/wu/3d-printing> [Accessed: 13-11-2017].
- [68] D. Günther and F. Mögele, “Additive manufacturing of casting tools using powder-binder-jetting technology,” in *New Trends in 3D Printing*, I. Shishkovsky, Ed. InTech, 2016, ch. 3, pp. 53–86. [Online]. Available: <https://doi.org/10.5772/62532> [Accessed: 17-11-2017].
- [69] R. A. Giordano *et al.*, “Mechanical properties of dense polylactic acid structures fabricated by three dimensional printing,” *Journal of Biomaterials Science, Polymer Edition*, vol. 8, no. 1, pp. 63–75, 1997. [Online]. Available: <http://dx.doi.org/10.1163/156856297X00588> [Accessed: 15-11-2017].
- [70] B. R. Utela *et al.*, “Development process for custom three-dimensional printing (3DP) material systems,” *Journal of Manufacturing Science and Engineering*, vol. 132, no. 1, p. 011008, 2010. [Online]. Available: <http://dx.doi.org/10.1115/1.4000713> [Accessed: 17-11-2017].
- [71] S. Pak *et al.*, “Laminated object manufacturing,” in *Stereolithography and other RP&M technologies: from rapid prototyping to rapid tooling*. Dearborn, Mich.: New York: Society of Manufacturing Engineers; American Society of Mechanical Engineers, 1996, ch. 14, pp. 317–348.
- [72] J. Park *et al.*, “Characterization of the laminated object manufacturing (LOM) process,” *Rapid Prototyping Journal*, vol. 6, no. 1, pp. 36–50, 2000. [Online]. Available: <https://doi.org/10.1108/13552540010309868> [Accessed: 18-11-2017].
- [73] B. Mueller and D. Kochan, “Laminated object manufacturing for rapid tooling and patternmaking in foundry industry,” *Computers in Industry*, vol. 39, no. 1, pp. 47–53, 1999. [Online]. Available: [https://doi.org/10.1016/S0166-3615\(98\)00127-4](https://doi.org/10.1016/S0166-3615(98)00127-4) [Accessed: 18-11-2017].
- [74] S. Upcraft and R. Fletcher, “The rapid prototyping technologies,” *Assembly Automation*, vol. 23, no. 4, pp. 318–330, 2003. [Online]. Available: <https://doi.org/10.1108/01445150310698634> [Accessed: 18-11-2017].
- [75] Mcor. (2017) *Mcor ARKe*. [Online]. Available: <http://www.mcor technologies.com/3d-printers/arke-3d-photorealistic-colour-printer/> [Accessed: 15-11-2017].
- [76] CustomPartNet. (2008) *Laminated Object Manufacturing (LOM)*. [Online]. Available: <http://www.custompartnet.com/wu/laminated-object-manufacturing> [Accessed: 13-11-2017].
- [77] A. Hehr and M. J. Dapino, “Dynamics of ultrasonic additive manufacturing,” *Ultrasonics*, vol. 73, no. Supplement C, pp. 49–66, 2017. [Online]. Available: <https://doi.org/10.1016/j.ultras.2016.08.009> [Accessed: 18-11-2017].
- [78] C. Y. Kong *et al.*, “Ultrasonic consolidation for embedding sma fibres within aluminium matrices,” *Composite Structures*, vol. 66, no. 1, pp. 421–427, 2004. [Online]. Available: <https://doi.org/10.1016/j.compstruct.2004.04.064> [Accessed: 18-11-2017].
- [79] W. E. Frazier, “Metal additive manufacturing: A review,” *Journal of Materials Engineering and Performance*, vol. 23, no. 6, pp. 1917–1928, 2014. [Online]. Available: <https://doi.org/10.1007/s11665-014-0958-z> [Accessed: 20-11-2017].
- [80] B. E. Carroll *et al.*, “Anisotropic tensile behavior of ti–6al–4v components fabricated with directed energy deposition additive manufacturing,” *Acta Materialia*, vol. 87, no. Supplement C, pp. 309–320, 2015. [Online]. Available: <https://doi.org/10.1016/j.actamat.2014.12.054> [Accessed: 20-11-2017].
- [81] Loughborough University. (no date) *About Additive Manufacturing*. [Online]. Available: <http://www.lboro.ac.uk/research/amrg/about/> [Accessed: 13-11-2017].
- [82] B. Bradley, “Metal AM part production,” in *Wohlers report 2016: 3D printing and additive manufacturing state of the industry annual worldwide progress report*. Fort Collins: Wohlers Associates, 2016, pt. 5, pp. 183–188.

- [83] D. D. Gu *et al.*, “Laser additive manufacturing of metallic components: materials, processes and mechanisms,” *International Materials Reviews*, vol. 57, no. 3, pp. 133–164, 2012. [Online]. Available: <http://dx.doi.org/10.1179/1743280411Y.0000000014> [Accessed: 20-11-2017].
- [84] Materialgeez. (2008) *Selective laser melting system schematic*. [Online]. Available: https://commons.wikimedia.org/wiki/File:Selective_laser_melting_system_schematic.jpg#filelinks [Accessed: 14-11-2017].
- [85] T. Wohlers *et al.*, “Industry growth,” in *Wohlers Report 2022: 3D printing and Additive Manufacturing Global State of the Industry*. Washington, DC: ASTM International, 2022, pt. 3, pp. 127–174.
- [86] T. Wohlers *et al.*, “Materials and processes,” in *Wohlers Report 2022: 3D printing and Additive Manufacturing Global State of the Industry*. Washington, DC: ASTM International, 2022, pt. 2, pp. 77–126.
- [87] B. Khoshnevis *et al.*, “SIS – a new SFF method based on powder sintering,” *Rapid Prototyping Journal*, vol. 9, no. 1, pp. 30–36, 2003. [Online]. Available: <https://doi.org/10.1108/13552540310455638> [Accessed: 4-10-2017].
- [88] B. Asiabanpour *et al.*, “Advancements in the SIS process,” in *Solid Freeform Fabrication Symposium*, 2003, pp. 25–38. [Online]. Available: <http://sffsymposium.engr.utexas.edu/Manuscripts/2003/2003-03-Asiabanpour.pdf> [Accessed: 4-10-2017].
- [89] B. Asiabanpour *et al.*, “An experimental study of surface quality and dimensional accuracy for selective inhibition of sintering,” *Rapid Prototyping Journal*, vol. 10, no. 3, pp. 181–192, 2004. [Online]. Available: <https://doi.org/10.1108/13552540410539003> [Accessed: 9-10-017].
- [90] B. Khoshnevis *et al.*, “Metallic part fabrication using selective inhibition sintering (SIS),” *Rapid Prototyping Journal*, vol. 18, no. 2, pp. 144–153, 2012. [Online]. Available: <https://doi.org/10.1108/13552541211212122> [Accessed: 15-11-2017].
- [91] B. Asiabanpour *et al.*, “Advancements in the selective inhibition sintering process development,” *Virtual and Physical Prototyping*, vol. 1, no. 1, pp. 43–52, 2006. [Online]. Available: <http://dx.doi.org/10.1080/17452750500289910> [Accessed: 15-11-2017].
- [92] B. Wendel *et al.*, “Additive processing of polymers,” *Macromolecular Materials and Engineering*, vol. 293, no. 10, pp. 799–809, 2008. [Online]. Available: <http://dx.doi.org/10.1002/mame.200800121> [Accessed: 27-11-2017].
- [93] C. K. Chua *et al.*, “Powder-based rapid prototyping systems,” in *Rapid prototyping: principles and applications*, 3rd ed. Singapore: World Scientific, 2010, ch. 5, pp. 199–300.
- [94] N. Hopkinson and P. Dickens, “Emerging rapid manufacturing processes,” in *Rapid manufacturing: an industrial revolution for the digital age*. Chichester, England: John Wiley, 2006, ch. 5, pp. 55–80.
- [95] D. Rietzel *et al.*, “Funktionalisierte bauteile durch selektives maskensintern,” *RTEjournal - Forum für Rapid Technologie*, vol. 6, no. 1, 2010. [Online]. Available: <http://nbn-resolving.de/urn:nbn:de:0009-2-22154> [Accessed: 27-11-2017].
- [96] A. Ø. Hartmann and F. W. Tjellesen, “Three-dimensional printer,” U.S. Patent 9,421,715, Aug. 23, 2016. [Online]. Available: <https://www.google.com/patents/US9421715> [Accessed: 15-11-2017].
- [97] M. Baumers *et al.*, “Selective heat sintering versus laser sintering: Comparison of deposition rate, process energy consumption and cost performance,” *Solid Freeform Fabrication Symposium*, pp. 109–121, 2015. [Online]. Available: <https://sffsymposium.engr.utexas.edu/sites/default/files/2015/2015-9-Baumers.pdf> [Accessed: 10-10-2017].
- [98] A. Wheeler. (2015, Jun. 3) *New M3 blueprinter features SHS 3D printing technology*. [Online]. Available: <https://3dprintingindustry.com/news/new-m3-blueprinter-features-shs-printing-technology-50412/> [Accessed: 15-11-2017].
- [99] D. O’Connor. (2016, Sep. 8) *Blueprinter files for bankruptcy*. [Online]. Available: <https://www.tctmagazine.com/3d-printing-news/blueprinter-files-for-bankruptcy/> [Accessed: 15-11-2017].
- [100] N. Hopkinson and P. Erasenthiran, “High speed sintering – early research into a new rapid manufacturing process,” in *Solid Freeform Fabrication Symposium*, 2004, pp. 312–320. [Online]. Available: <http://edge.rit.edu/content/P10551/public/SFF/SFF%202004%20Proceedings/SFF%20Papers%202004/31-Hopkinson.pdf> [Accessed: 28-09-2017].
- [101] H. R. Thomas *et al.*, “High speed sintering – continuing research into a new rapid manufacturing process,” in *Solid Freeform Fabrication Symposium*, 2006, pp. 682–691. [Online]. Available: <https://sffsymposium.engr.utexas.edu/Manuscripts/2006/2006-59-Thomas.pdf> [Accessed: 28-09-2017].
- [102] C. Majewski *et al.*, “Effect of infra-red power level on the sintering behaviour in the high speed sintering process,” *Rapid Prototyping Journal*, vol. 14, no. 3, pp. 155–160, 2008. [Online]. Available: <https://doi.org/10.1108/13552540810878012> [Accessed: 28-09-2017].
- [103] A. Ellis *et al.*, “Materials for high speed sintering,” *Journal of Materials Research*, vol. 29, no. 17, pp. 2080–2085, 2014. [Online]. Available: <https://doi.org/10.1557/jmr.2014.156> [Accessed: 29-09-2017].
- [104] F. Norazman and N. Hopkinson, “Effect of sintering parameters and flow agent on the mechanical properties of high speed sintered elastomer,” *Journal of Manufacturing Science and Engineering*, vol. 136, no. 6, p. 061006, 2014. [Online]. Available: <http://dx.doi.org/10.1115/1.4028482> [Accessed: 29-09-2017].

- [105] C. E. Majewski *et al.*, “Effect of bed temperature and infra-red lamp power on the mechanical properties of parts produced using high-speed sintering,” *Virtual and Physical Prototyping*, vol. 2, no. 2, pp. 103–110, 2007. [Online]. Available: <http://dx.doi.org/10.1080/17452750701520915> [Accessed: 29-09-2017].
- [106] A. Ellis *et al.*, “The effect of build orientation and surface modification on mechanical properties of high speed sintered parts,” *Surface Topography: Metrology and Properties*, vol. 3, no. 3, p. 034005, 2015. [Online]. Available: <http://stacks.iop.org/2051-672X/3/i=3/a=034005> [Accessed: 2-10-2017].
- [107] M. Fahad and N. Hopkinson, “Evaluation and comparison of geometrical accuracy of parts produced by sintering-based additive manufacturing processes,” *The International Journal of Advanced Manufacturing Technology*, vol. 88, no. 9, pp. 3389–3394, 2017. [Online]. Available: <https://doi.org/10.1007/s00170-016-9036-z> [Accessed: 4-10-2017].
- [108] M. J. Thompson *et al.*, “Investigating dielectric properties of sintered polymers for rapid manufacturing,” in *Solid Freeform Fabrication Symposium*, 2008, pp. 4–6. [Online]. Available: <http://edge.rit.edu/content/P10551/public/SFF/SFF%202008%20Proceedings/Manuscripts/2008-08-Thompson.pdf> [Accessed: 3-10-2017].
- [109] A. Ellis *et al.*, “High speed sintering: Assessing the influence of print density on microstructure and mechanical properties of nylon parts,” *Additive Manufacturing*, vol. 1, pp. 48–51, 2014. [Online]. Available: <https://doi.org/10.1016/j.addma.2014.07.003> [Accessed: 29-09-2017].
- [110] C. J. Noble *et al.*, “Effect of greyscale/print density on the properties of high speed sintered nylon 12,” in *Solid Freeform Fabrication Symposium*, 2014. [Online]. Available: <http://sffsymposium.engr.utexas.edu/sites/default/files/2014-013-Noble.pdf> [Accessed: 9-10-2017].
- [111] L. Fox *et al.*, “Use of an alternative ink in the high speed sintering process,” in *Solid Freeform Fabrication Symposium*, 2015, pp. 456–463. [Online]. Available: <https://sffsymposium.engr.utexas.edu/sites/default/files/2015/2015-36-Fox.pdf> [Accessed: 3-10-2017].
- [112] HP Development Company. (2022) *HP Jet Fusion 4200 3D Printing Solution – Product Documentation User Guide*. [Online]. Available: <https://support.hp.com/gb-en/product/hp-jet-fusion-3d-4200-printer/11461058/manuals> [Accessed: 23-05-2022].
- [113] HP Development Company. (2022) *HP 3D Printing materials*. [Online]. Available: <https://www.hp.com/uk-en/printers/3d-printers/materials> [Accessed: 07-06-2022].
- [114] C. Cai *et al.*, “Comparative study on 3d printing of polyamide 12 by selective laser sintering and multi jet fusion,” *Journal of Materials Processing Technology*, vol. 288, p. 116882, 2021. [Online]. Available: <https://doi.org/10.1016/j.jmatprotec.2020.116882> [Accessed: 21-04-2022].
- [115] H. J. O’Connor *et al.*, “Evaluation of the mechanical performance of polymer parts fabricated using a production scale multi jet fusion printing process,” *Additive Manufacturing*, vol. 22, pp. 381–387, 2018. [Online]. Available: <https://doi.org/10.1016/j.addma.2018.05.035> [Accessed: 21-04-2022].
- [116] CustomPartNet. (2008) *Selective Laser Sintering*. [Online]. Available: <http://www.custompartnet.com/wu/selective-laser-sintering> [Accessed: 13-11-2017].
- [117] Senvol, “Senvol database: industrial additive manufacturing machines and materials,” Database, 2022. [Online]. Available: <http://senvol.com/database/> [Accessed: 31-01-2022].
- [118] S. Yuan *et al.*, “Polymeric composites for powder-based additive manufacturing: Materials and applications,” *Progress in Polymer Science*, vol. 91, pp. 141–168, 2019. [Online]. Available: <https://doi.org/10.1016/j.progpolymsci.2018.11.001> [Accessed: 27-11-2019].
- [119] X. Wang *et al.*, “3d printing of polymer matrix composites: A review and prospective,” *Composites Part B: Engineering*, vol. 110, pp. 442–458, 2017, [Accessed: 02-02-2022].
- [120] D. L. Bourell, “Sintering in laser sintering,” *JOM*, vol. 68, no. 3, pp. 885–889, 2016. [Online]. Available: <https://doi.org/10.1007/s11837-015-1780-2> [Accessed: 22-11-2019].
- [121] Department of Mechanical Engineering. (2012, Dec. 6,) *Selective Laser Sintering, Birth of an Industry*. The University of Texas at Austin. [Online]. Available: <https://www.me.utexas.edu/news/news/selective-laser-sintering-birth-of-an-industry> [Accessed: 04-12-2019].
- [122] Materialise Magics. (2020) *The most powerful data & build preparation software*. Purple Platypus. [Online]. Available: <https://purpleplatypus.com/materialise-magics/> [Accessed: 12-5-2020].
- [123] M. Ruffo *et al.*, “Cost estimation for rapid manufacturing – laser sintering production for low to medium volumes,” *Proceedings of the Institution of Mechanical Engineers, Part B: Journal of Engineering Manufacture*, vol. 220, no. 9, pp. 1417–1427, 2006. [Online]. Available: <https://doi.org/10.1243/09544054JEM517> [Accessed: 11-12-2019].
- [124] ProtoCam. (2020) *Selective laser sintering*. [Online]. Available: <https://www.protocam.com/additive-manufacturing-services/selective-laser-sintering-sls/> [Accessed: 4-5-2020].
- [125] Prodways. (2020) *PA12-GFX 2550*. [Online]. Available: <https://www.prodways.com/en/material/pa12-gfx-2550/> [Accessed: 1-5-2020].

- [126] New Balance. (2015, Nov. 19) *New Balance launches first 3D printed running shoe*. [Online]. Available: <https://newbalance.newsmarket.com/LATEST-NEWS/ALL/new-balance-launches-first-3d-printed-running-shoe/s/945ADE0F-1185-4CE0-AE3B-A857F8D2A445> [Accessed: 4-5-2020].
- [127] C. Lestrangle, "Effect of surface roughness on quality perception of laser sintered (LS) parts," Ph.D. thesis, The University of Sheffield, October 2016. [Online]. Available: <https://etheses.whiterose.ac.uk/17349/> [Accessed: 07-06-2022].
- [128] M. Launhardt *et al.*, "Detecting surface roughness on SLS parts with various measuring techniques," *Polymer Testing*, vol. 53, pp. 217–226, 2016. [Online]. Available: <https://doi.org/10.1016/j.polymertesting.2016.05.022> [Accessed: 13-06-2018].
- [129] EOS. (2020) *Material management for additive manufacturing with plastics*. [Online]. Available: <https://www.eos.info/en/additive-manufacturing/3d-printing-plastic/eos-polymer-systems/material-management-plastic-3d-printing> [Accessed: 10-06-2020].
- [130] T. T. Wohlers *et al.*, "System producers," in *Wohlers report 2019: 3D printing and additive manufacturing state of the industry*. Fort Collins: Wohlers Associates, 2019, pt. 3, pp. 84–161.
- [131] Sintratec. (2019) *Sintratec Kit*. [Online]. Available: <https://sintratec.com/product/sintratec-kit/> [Accessed: 05-12-2019].
- [132] M. Tomanik *et al.*, "Mechanical and structural evaluation of the PA12 desktop selective laser sintering printed parts regarding printing strategy," *3D Printing and Additive Manufacturing*, vol. 0, no. 0, p. null, 0. [Online]. Available: <https://doi.org/10.1089/3dp.2020.0111> [Accessed: 29-03-2021].
- [133] Xometry. (2020) *The complete guide to 3D printing*. [Online]. Available: <https://www.xometry.com/ultimate-guide/complete-3d-printing-guide> [Accessed: 1-5-2020].
- [134] Formlabs. (2020) *Guide to selective laser sintering (SLS) 3D printing*. [Online]. Available: <https://formlabs.com/eu/blog/what-is-selective-laser-sintering/> [Accessed: 1-5-2020].
- [135] CRP Technology. (2019) *Manufacturing of Tiltrotor AW609 wind tunnel model via SLS and Windform*. [Online]. Available: <https://www.crptechnology.com/tiltrotor-aw609-wind-tunnel-model-sls-windform/> [Accessed: 28-4-2020].
- [136] 3D People. (2020) *3D printing for architecture models*. [Online]. Available: <https://www.3dpeople.uk/architecture> [Accessed: 30-4-2020].
- [137] O. Asensio. (2020) *3D rex*. [Online]. Available: <http://www.octavioasensio.com/work#/3d-rex/> [Accessed: 29-4-2020].
- [138] B. Redwood *et al.*, "3D printing technologies and materials," in *The 3D printing handbook – technologies, design and applications*. Arnhem, The Netherlands: Coers & Roest, 2018, pt. 1, pp. 16–143.
- [139] Prodartis. (2016, May 16) *Long-haul flight with laser-sintered battery cooling system*. [Online]. Available: <https://www.additively.com/en/showcase/en/prodartis-ag-long-haul-flight-with-laser-sintered-battery-cooling-system> [Accessed: 28-4-2020].
- [140] Rehook. (2019) *Rehook*. [Online]. Available: <https://www.rehook.bike/> [Accessed: 05-12-2019].
- [141] 3DPrintUK. (2016) *3D printing alternative to injection moulding*. [Online]. Available: <https://www.3dprint-uk.co.uk/alternative-to-injection-moulding-or-cnc/> [Accessed: 1-5-2020].
- [142] Summit ID. (2020) *Skateboard*. [Online]. Available: <http://www.summitid.com/#/skateboard/> [Accessed: 28-4-2020].
- [143] TCT Magazine. (2015, Dec. 9) *Jay Leno turns to 3D printing to restore part on EcoJet concept car*. [Online]. Available: <https://www.tctmagazine.com/prsnlz/jay-leno-restores-ecojet-car-part-3d-systems-technologies/> [Accessed: 1-5-2020].
- [144] B. Redwood *et al.*, "Applications of 3D printing," in *The 3D printing handbook – technologies, design and applications*. Arnhem, The Netherlands: Coers & Roest, 2018, pt. 3, pp. 226–285.
- [145] 3DPrintUK. (2016) *Low volume production calculator*. [Online]. Available: <https://www.3dprint-uk.co.uk/low-volume-production-calculator/> [Accessed: 5-5-2020].
- [146] J. Evill. (2013) *A New Way to Heal Broken Bones: An Exoskeletal 3D Printed Cast of bones*. [Online]. Available: <https://www.arch2o.com/new-way-heal-broken-bones-3d-printed-cast-3d-molds-exoskeletal/> [Accessed: 28-4-2020].
- [147] Summit ID. (2020) *Ekso Bionics*. [Online]. Available: <http://www.summitid.com/#/ekso-bionics/> [Accessed: 28-4-2020].
- [148] Summit ID. (2020) *Scoliosis*. [Online]. Available: <http://www.summitid.com/#/scoliosis/> [Accessed: 12-3-2020].
- [149] Summit ID. (2020) *Prosthetic Fairings*. [Online]. Available: <http://www.summitid.com/#/fairings-1/> [Accessed: 28-4-2020].
- [150] Summit ID. (2020) *Transfemoral Prosthetic Concept #3*. [Online]. Available: <http://www.summitid.com/#/concept3/> [Accessed: 28-4-2020].

- [151] NHS. (2020) *Scoliosis – Overview*. [Online]. Available: <https://www.nhs.uk/conditions/scoliosis/> [Accessed: 6-5-2020].
- [152] Scoliosis Association UK. (2014) *Bracing*. [Online]. Available: <https://www.sauk.org.uk/scoliosis-treatment/bracing> [Accessed: 6-5-2020].
- [153] S. Summit. (2011, Nov.) *Beautiful artificial limbs*. TEDxCambridge. [Online]. Available: https://www.ted.com/talks/scott_summit_beautiful_artificial_limbs/up-next [Accessed: 6-5-2020].
- [154] K. Oyama *et al.*, “Endoscopic endonasal cranial base surgery simulation using an artificial cranial base model created by selective laser sintering,” *Neurosurgical review*, vol. 38, no. 1, pp. 171–178, 2015. [Online]. Available: <https://doi.org/10.1007/s10143-014-0580-4> [Accessed: 29-4-2020].
- [155] Cavendish Imaging. (2020) *3D printed anatomical models*. [Online]. Available: <https://www.cavendishimaging.com/3d-printing/> [Accessed: 29-4-2020].
- [156] G. Maza *et al.*, “Surgical simulation of a catastrophic internal carotid artery injury: a laser-sintered model,” *International Forum of Allergy & Rhinology*, vol. 9, no. 1, pp. 53–59, 2019. [Online]. Available: <https://doi.org/10.1002/alr.22178> [Accessed: 29-4-2020].
- [157] DePuy Synthes. (2016) *Patient-specific surgical guides*. [Online]. Available: <https://www.jnjmedicaldevices.com/en-EMEA/service-details/patient-specific-surgical-guides> [Accessed: 28-4-2020].
- [158] W. Y. Zhou *et al.*, “Selective laser sintered poly(l-lactide)/carbonated hydroxyapatite nanocomposite scaffolds: A bottom-up approach,” in *Advances in Diverse Industrial Applications of Nanocomposites*, B. Reddy, Ed. Rijeka: IntechOpen, 2011, ch. 10. [Online]. Available: <https://doi.org/10.5772/14683> [Accessed: 05-12-2019].
- [159] A. Awad *et al.*, “3d printed pellets (miniprintlets): A novel, multi-drug, controlled release platform technology,” *Pharmaceutics*, vol. 11, no. 4, p. 148, 2019. [Online]. Available: <https://doi.org/10.3390/pharmaceutics11040148> [Accessed: 02-12-2019].
- [160] Y. Zhang *et al.*, “In vitro biocompatibility of hydroxyapatite-reinforced polymeric composites manufactured by selective laser sintering,” *Journal of Biomedical Materials Research Part A*, vol. 91A, no. 4, pp. 1018–1027, 2009. [Online]. Available: <https://doi.org/10.1002/jbm.a.32298> [Accessed: 28-11-2019].
- [161] G. Lee and J. W. Barlow, “Selective laser sintering of bioceramic materials for implants,” in *Proceedings of the solid freeform fabrication symposium, Austin, TX, 1993*, pp. 376–380. [Online]. Available: <http://www.dtic.mil/get-tr-doc/pdf?AD=ADA27718#page=386> [Accessed: 05-12-2017].
- [162] K. Tan *et al.*, “Scaffold development using selective laser sintering of polyetheretherketone–hydroxyapatite biocomposite blends,” *Biomaterials*, vol. 24, no. 18, pp. 3115–3123, 2003. [Online]. Available: [https://doi.org/10.1016/S0142-9612\(03\)00131-5](https://doi.org/10.1016/S0142-9612(03)00131-5) [Accessed: 21-11-2019].
- [163] C. K. Chua *et al.*, “Development of tissue scaffolds using selective laser sintering of polyvinyl alcohol/hydroxyapatite biocomposite for craniofacial and joint defects,” *Journal of Materials Science: Materials in Medicine*, vol. 15, no. 10, pp. 1113–1121, 2004. [Online]. Available: <https://doi.org/10.1023/B:JMSM.0000046393.81449.a5> [Accessed: 21-11-2019].
- [164] L. Hao *et al.*, “Selective laser sintering of hydroxyapatite reinforced polyethylene composites for bioactive implants and tissue scaffold development,” *Proceedings of the Institution of Mechanical Engineers, Part H: Journal of Engineering in Medicine*, vol. 220, no. 4, pp. 521–531, 2006. [Online]. Available: <https://doi.org/10.1243/09544119JEIM67> [Accessed: 21-11-2019].
- [165] B. Duan *et al.*, “Three-dimensional nanocomposite scaffolds fabricated via selective laser sintering for bone tissue engineering,” *Acta Biomaterialia*, vol. 6, no. 12, pp. 4495–4505, 2010. [Online]. Available: <http://www.sciencedirect.com/science/article/pii/S1742706110002904> [Accessed: 19-10-2017].
- [166] Smith & Nephew. (2009) *Biocompatibility of Medical Grade Nylon*. [Online]. Available: https://www.smith-nephew.com/global/assets/pdf/products/surgical/visionaire_biocompatibility_nylon_whitepaper_71281643.pdf [Accessed: 02-12-2019].
- [167] C. Leiggenger *et al.*, “A selective laser sintering guide for transferring a virtual plan to real time surgery in composite mandibular reconstruction with free fibula osseous flaps,” *International Journal of Oral and Maxillofacial Surgery*, vol. 38, no. 2, pp. 187–192, 2009. [Online]. Available: <https://doi.org/10.1016/j.ijom.2008.11.026> [Accessed: 01-04-2019].
- [168] I. Gibson, *Advanced manufacturing technology for medical applications: reverse engineering, software conversion, and rapid prototyping*. Chichester, England: John Wiley, 2005.
- [169] J. Peels, “Desktop 3D printers,” in *Wohlers report 2016: 3D printing and additive manufacturing state of the industry annual worldwide progress report*. Fort Collins: Wohlers Associates, 2016, pt. 3, pp. 132–139.
- [170] G. V. Salmoria *et al.*, “The effects of laser energy density and particle size in the selective laser sintering of polycaprolactone/progesterone specimens: morphology and drug release,” *The International Journal of Advanced Manufacturing Technology*, vol. 66, no. 5-8, pp. 1113–1118, 2013. [Online]. Available: <https://doi.org/10.1007/s00170-012-4393-8> [Accessed: 04-06-2020].
- [171] 3DPrintUK. (2016) *Brushtec 3D printed jig manufacture*. [Online]. Available: <https://www.3dprint-uk.co.uk/portfolio-item/brushtec-3dprinted-jig-manufacture/> [Accessed: 4-5-2020].

- [172] B. Trapp. (2019) *SLS for durable and cost-effective normalized CNC fixtures*. 3D Systems. [Online]. Available: <https://www.3dsystems.com/blog/2019/2019-04/sls-durable-and-cost-effective-normalized-cnc-fixtures> [Accessed: 1-5-2020].
- [173] CRP Meccanica. (2020) *Rapid casting*. [Online]. Available: <https://www.crpmeccanica.com/rapid-casting/> [Accessed: 1-5-2020].
- [174] J. Yang *et al.*, “Selective laser sintering of hips and investment casting technology,” *Journal of Materials Processing Technology*, vol. 209, no. 4, pp. 1901–1908, 2009. [Online]. Available: <https://doi.org/10.1016/j.jmatprotec.2008.04.056> [Accessed: 04-06-2020].
- [175] Steve Marsel Studio. (2014) *Kinematic Dress 1*. Nervous System. [Online]. Available: <https://n-e-r-v-o-u-s.com/projects/albums/kinematics-dress-1/> [Accessed: 4-5-2020].
- [176] A. Wipprecht. (2020) *Fashiontech*. [Online]. Available: <http://www.anoukwipprecht.nl/> [Accessed: 12-3-2020].
- [177] T. T. Wohlers *et al.*, “Industry growth,” in *Wohlers Report 2017: 3D printing and Additive Manufacturing State of the Industry Annual Worldwide Progress Report*. Fort Collins: Wohlers Associates, 2017, pt. 4, pp. 148–175.
- [178] T. T. Wohlers *et al.*, “Industry growth,” in *Wohlers Report 2018: 3D printing and Additive Manufacturing State of the Industry Annual Worldwide Progress Report*. Fort Collins: Wohlers Associates, 2018, pt. 4, pp. 142–172.
- [179] T. T. Wohlers *et al.*, “Industry growth,” in *Wohlers report 2019: 3D printing and additive manufacturing state of the industry*. Fort Collins: Wohlers Associates, 2019, pt. 4, pp. 162–195.
- [180] D. Drummer *et al.*, “Polymer blends for selective laser sintering: Material and process requirements,” *Physics Procedia*, vol. 39, pp. 509–517, 2012, laser Assisted Net shape Engineering 7 (LANE 2012). [Online]. Available: <https://doi.org/10.1016/j.phpro.2012.10.067> [Accessed: 27-08-2019].
- [181] G. Salmoria *et al.*, “Characterization of pa12/pbt specimens prepared by selective laser sintering,” *Optics & Laser Technology*, vol. 98, pp. 92–96, 2018. [Online]. Available: <https://doi.org/10.1016/j.optlastec.2017.07.044> [Accessed: 21-11-2019].
- [182] J.-P. Kruth *et al.*, “Consolidation phenomena in laser and powder-bed based layered manufacturing,” *CIRP Annals-Manufacturing Technology*, vol. 56, no. 2, pp. 730–759, 2007. [Online]. Available: <https://doi.org/10.1016/j.cirp.2007.10.004> [Accessed: 4-10-2017].
- [183] P. Shipton, “Materials selection for medical devices (part 1),” presented at the Introduction to Plastics and Rubber Materials in Medical Devices, Smithers Rapra, Shawbury, UK, pp. 90–124, Dec. 6 2018.
- [184] Y. Shi *et al.*, “Study of the selective laser sintering of polycarbonate and postprocess for parts reinforcement,” *Proceedings of the Institution of Mechanical Engineers, Part L: Journal of Materials: Design and Applications*, vol. 221, no. 1, pp. 37–42, 2007. [Online]. Available: <https://doi.org/10.1243/14644207JMDA65> [Accessed: 21-11-2019].
- [185] J. C. Nelson *et al.*, “Model of the selective laser sintering of bisphenol-a polycarbonate,” *Industrial & Engineering Chemistry Research*, vol. 32, no. 10, pp. 2305–2317, 1993. [Online]. Available: <https://doi-org.sheffield.idm.oclc.org/10.1021/ie00022a014> [Accessed: 21-11-2019].
- [186] C. Yan *et al.*, “Investigation into the selective laser sintering of styrene-acrylonitrile copolymer and postprocessing,” *The International Journal of Advanced Manufacturing Technology*, vol. 51, no. 9, pp. 973–982, 2010. [Online]. Available: <https://doi.org/10.1007/s00170-010-2681-8> [Accessed: 27-11-2019].
- [187] R. Goodridge *et al.*, “Laser sintering of polyamides and other polymers,” *Progress in Materials Science*, vol. 57, no. 2, pp. 229–267, 2012. [Online]. Available: <https://doi.org/10.1016/j.pmatsci.2011.04.001> [Accessed: 28-09-2017].
- [188] J. T. Rimell and P. M. Marquis, “Selective laser sintering of ultra high molecular weight polyethylene for clinical applications,” *Journal of Biomedical Materials Research*, vol. 53, no. 4, pp. 414–420, 2000. [Online]. Available: [https://doi.org/10.1002/1097-4636\(2000\)53:4%3C414::AID-JBM16%3E3.0.CO;2-M](https://doi.org/10.1002/1097-4636(2000)53:4%3C414::AID-JBM16%3E3.0.CO;2-M) [Accessed: 21-11-2019].
- [189] D. W. Hutmacher, “Scaffold-based tissue engineering – design and fabrication of matrices using solid freeform fabrication techniques,” in *Advanced manufacturing technology for medical applications: reverse engineering, software conversion, and rapid prototyping*. Chichester, England: John Wiley, 2005, ch. 8, pp. 163–190.
- [190] T. Niino and H. Yamada, “Transparentization of SLS processed SMMA copolymer parts by infiltrating a thermosetting epoxy resin with tuned refractive index,” in *Solid Freeform Fabrication Symposium*, 2005, pp. 208–216. [Online]. Available: <https://sffsymposium.engr.utexas.edu/Manuscripts/2005/2005-19-Niino.pdf> [Accessed: 27-11-2019].
- [191] Y. Shi *et al.*, “Experimental investigation into the selective laser sintering of high-impact polystyrene,” *Journal of Applied Polymer Science*, vol. 108, no. 1, pp. 535–540, 2008. [Online]. Available: <https://doi.org/10.1002/app.27686> [Accessed: 23-06-2020].
- [192] M. Schmidt *et al.*, “Laser based additive manufacturing in industry and academia,” *CIRP Annals*, vol. 66, no. 2, pp. 561–583, 2017. [Online]. Available: <https://doi.org/10.1016/j.cirp.2017.05.011> [Accessed: 10-10-2017].

- [193] S. Berretta *et al.*, “Processability of PEEK, a new polymer for high temperature laser sintering (HT-LS),” *European Polymer Journal*, vol. 68, pp. 243–266, 2015. [Online]. Available: <https://doi.org/10.1016/j.eurpolymj.2015.04.003> [Accessed: 19-09-2018].
- [194] O. Ghita *et al.*, “Physico-chemical behaviour of poly (ether ketone) (PEK) in high temperature laser sintering (HT-LS),” *Journal of Materials Processing Technology*, vol. 214, no. 4, pp. 969–978, 2014. [Online]. Available: <https://doi.org/10.1016/j.jmatprotec.2013.11.007> [Accessed: 19-09-2018].
- [195] W. Huang *et al.*, “Microstructure, mechanical, and biological properties of porous poly (vinylidene fluoride) scaffolds fabricated by selective laser sintering,” *International Journal of Polymer Science*, vol. 2015, 2015. [Online]. Available: <http://dx.doi.org/10.1155/2015/132965> [Accessed: 22-11-2019].
- [196] H. Zhang *et al.*, “Study on laser sintering of pine/co-PES composites and the investment casting process,” *Rapid Prototyping Journal*, vol. 25, no. 8, pp. 1349–1358, 2019. [Online]. Available: <http://dx.doi.org/10.1108/RPJ-01-2019-0019> [Accessed: 27-11-2019].
- [197] J. M. Williams *et al.*, “Bone tissue engineering using polycaprolactone scaffolds fabricated via selective laser sintering,” *Biomaterials*, vol. 26, no. 23, pp. 4817–4827, 2005. [Online]. Available: <https://doi.org/10.1016/j.biomaterials.2004.11.057> [Accessed: 21-11-2019].
- [198] R. L. Simpson *et al.*, “Development of a 95/5 poly(L-lactide-co-glycolide)/hydroxylapatite and β -tricalcium phosphate scaffold as bone replacement material via selective laser sintering,” *Journal of Biomedical Materials Research Part B: Applied Biomaterials*, vol. 84B, no. 1, pp. 17–25, 2008. [Online]. Available: <https://doi.org/10.1002/jbm.b.30839> [Accessed: 11-06-2020].
- [199] A. Mazzoli, “Selective laser sintering in biomedical engineering,” *Medical & Biological Engineering & Computing*, vol. 51, no. 3, pp. 245–256, 2013. [Online]. Available: <https://doi.org/10.1007/s11517-012-1001-x> [Accessed: 19-10-2017].
- [200] J. Schmidt *et al.*, “Optimized polybutylene terephthalate powders for selective laser beam melting,” *Chemical Engineering Science*, vol. 156, pp. 1–10, 2016. [Online]. Available: <https://doi.org/10.1016/j.ces.2016.09.009> [Accessed: 21-11-2019].
- [201] K. C. Chuang *et al.*, “Challenges in laser sintering of melt-processable thermoset imide resin,” in *The Composites and Advanced Materials Expo*, 2016. [Online]. Available: <https://ntrs.nasa.gov/archive/nasa/casi.ntrs.nasa.gov/20160011504.pdf> [Accessed: 22-11-2019].
- [202] G. Vasquez *et al.*, “A targeted material selection process for polymers in laser sintering,” *Additive Manufacturing*, vol. 1–4, pp. 127–138, 2014, Inaugural Issue. [Online]. Available: <https://doi.org/10.1016/j.addma.2014.09.003> [Accessed: 13-06-2018].
- [203] L. Verbelen *et al.*, “Analysis of the material properties involved in laser sintering of thermoplastic polyurethane,” *Additive Manufacturing*, vol. 15, pp. 12–19, 2017. [Online]. Available: <https://doi.org/10.1016/j.addma.2017.03.001> [Accessed: 9-10-2017].
- [204] J. M. G. Cowie and V. Arrighi, “The crystalline state and partially ordered structures,” in *Polymers: Chemistry and Physics of Modern Materials*, 3rd ed. Boca Raton, United States: Taylor & Francis Group, 2007, ch. 11, pp. 279–320. [Online]. Available: <https://ebookcentral.proquest.com/lib/sheffield/detail.action?docID=1449424> [Accessed: 19-06-2020].
- [205] HCL Technologies. (2019) *Plastic material selection – it’s a jungle out there!* [Online]. Available: <https://dfmpro.com/2017/07/14/plastic-material-selection-its-a-jungle-out-there/> [Accessed: 25-11-2019].
- [206] I. Gibson and D. Shi, “Material properties and fabrication parameters in selective laser sintering process,” *Rapid Prototyping Journal*, vol. 3, no. 4, pp. 129–136, 1997. [Online]. Available: <https://doi.org/10.1108/13552549710191836> [Accessed: 11-02-2019].
- [207] L. W. McKeen, “Polyamides (nylons),” in *Plastics Failure Analysis and Prevention*, 2nd ed., ser. PDL Handbook Series. Oxford, England: Elsevier, 2009, pp. 197–262.
- [208] L. Verbelen *et al.*, “Characterization of polyamide powders for determination of laser sintering processability,” *European Polymer Journal*, vol. 75, no. Supplement C, pp. 163–174, 2016. [Online]. Available: <https://doi.org/10.1016/j.eurpolymj.2015.12.014> [Accessed: 19-10-2017].
- [209] T. L. Starr *et al.*, “The effect of process conditions on mechanical properties of laser-sintered nylon,” *Rapid Prototyping Journal*, vol. 17, no. 6, pp. 418–423, 2011. [Online]. Available: <https://doi.org/10.1108/13552541111184143> [Accessed: 9-10-2017].
- [210] H. Scholten and W. Christoph, “Use of a nylon-12 for selective laser sintering,” U.S. Patent 6,245,281, Jun. 12, 2001. [Online]. Available: <https://patents.google.com/patent/US6245281B1/en> [Accessed: 06-12-2019].
- [211] S. Berretta *et al.*, “Morphology of polymeric powders in laser sintering (LS): From polyamide to new PEEK powders,” *European Polymer Journal*, vol. 59, pp. 218–229, 2014. [Online]. Available: <https://doi.org/10.1016/j.eurpolymj.2014.08.004> [Accessed: 27-08-2019].
- [212] E. Gallino, “Characterization tools for evaluating powders for selective laser sintering,” presented at a Freeman Technology webinar, RICOH UK, Jun. 2 2020.

- [213] EagleAngle Eyes. (2020) *Raw potato at market*. [Online]. Available: <https://www.shutterstock.com/image-photo/raw-potato-market-749008465> [Accessed: 05-06-2020].
- [214] alantobey. (2018) *Bin of cauliflower heads*. [Online]. Available: <https://www.gettyimages.co.uk/detail/photo/bin-of-cauliflower-heads-royalty-free-image/182240577> [Accessed: 05-06-2020].
- [215] Netafim. (2020) *Meet demand with better tomatoes*. [Online]. Available: <https://www.netafimindia.com/crop-knowledge/tomato/> [Accessed: 05-06-2020].
- [216] C. Pochin. (2019, Aug. 17) *Kellogg's Corn Flakes' rather rude 'origin story' shocks thousands*. [Online]. Available: <https://www.irishmirror.ie/news/weird-news/kelloggs-corn-flakes-rude-origin-18953821> [Accessed: 05-06-2020].
- [217] B. Van der Schueren and J.-P. Kruth, "Powder deposition in selective metal powder sintering," *Rapid Prototyping Journal*, vol. 1, no. 3, pp. 23–31, 1995. [Online]. Available: <https://doi.org/10.1108/13552549510094241> [Accessed: 13-03-2020].
- [218] T. Gornet *et al.*, "Characterization of selective laser sintering materials to determine process stability," in *Solid Freeform Fabrication Symposium*, 2002, pp. 546–553. [Online]. Available: <http://utw10945.utweb.utexas.edu/Manuscripts/2002/2002-62-Gornet.pdf> [Accessed: 22-05-2020].
- [219] D. L. Bourell *et al.*, "Performance limitations in polymer laser sintering," *Physics Procedia*, vol. 56, pp. 147–156, 2014, 8th International Conference on Laser Assisted Net Shape Engineering LANE 2014. [Online]. Available: <https://doi.org/10.1016/j.phpro.2014.08.157> [Accessed: 07-09-2018].
- [220] P. Chen *et al.*, "Investigation into the processability, recyclability and crystalline structure of selective laser sintered polyamide 6 in comparison with polyamide 12," *Polymer Testing*, vol. 69, pp. 366–374, 2018. [Online]. Available: <https://doi.org/10.1016/j.polymertesting.2018.05.045> [Accessed: 20-03-2019].
- [221] K. Wudy and D. Drummer, "Aging effects of polyamide 12 in selective laser sintering: Molecular weight distribution and thermal properties," *Additive Manufacturing*, vol. 25, pp. 1–9, 2019. [Online]. Available: <https://doi.org/10.1016/j.addma.2018.11.007> [Accessed: 13-08-2019].
- [222] P. Chen *et al.*, "Systematical mechanism of polyamide-12 aging and its micro-structural evolution during laser sintering," *Polymer Testing*, vol. 67, pp. 370–379, 2018. [Online]. Available: <https://doi.org/10.1016/j.polymertesting.2018.03.035> [Accessed: 20-03-2019].
- [223] B. Haworth *et al.*, "Shear viscosity measurements on polyamide-12 polymers for laser sintering," *Rapid Prototyping Journal*, vol. 19, no. 1, pp. 28–36, 2013. [Online]. Available: <https://doi.org/10.1108/13552541311292709> [Accessed: 30-11-2018].
- [224] S. Dadbakhsh *et al.*, "Effect of PA12 powder reuse on coalescence behaviour and microstructure of SLS parts," *European Polymer Journal*, vol. 92, no. Supplement C, pp. 250–262, 2017. [Online]. Available: <https://doi.org/10.1016/j.eurpolymj.2017.05.014> [Accessed: 19-10-2017].
- [225] D. T. Pham *et al.*, "Deterioration of polyamide powder properties in the laser sintering process," *Proceedings of the Institution of Mechanical Engineers, Part C: Journal of Mechanical Engineering Science*, vol. 222, no. 11, pp. 2163–2176, 2008. [Online]. Available: <https://doi.org/10.1243/09544062JMES839> [Accessed: 11-02-2019].
- [226] S. Kumar and A. Czekanski, "Development of filaments using selective laser sintering waste powder," *Journal of Cleaner Production*, vol. 165, pp. 1188–1196, 2017. [Online]. Available: <https://doi.org/10.1016/j.jclepro.2017.07.202> [Accessed: 20-03-2019].
- [227] 3D Hubs. (2020) *What is 3D printing? The definitive guide*. [Online]. Available: <https://www.3dhubs.com/guides/3d-printing/> [Accessed: 12-5-2020].
- [228] B. Redwood *et al.*, "Designing for 3D printing," in *The 3D printing handbook – technologies, design and applications*. Arnhem, The Netherlands: Coers & Roest, 2018, pt. 2, pp. 144–225.
- [229] M. Pavan *et al.*, "On the influence of inter-layer time and energy density on selected critical-to-quality properties of PA12 parts produced via laser sintering," *Polymer Testing*, vol. 61, pp. 386–395, 2017. [Online]. Available: <https://doi.org/10.1016/j.polymertesting.2017.05.027> [Accessed: 07-09-2018].
- [230] B. Caulfield *et al.*, "Dependence of mechanical properties of polyamide components on build parameters in the sls process," *Journal of Materials Processing Technology*, vol. 182, no. 1, pp. 477–488, 2007. [Online]. Available: <https://doi.org/10.1016/j.jmatprotec.2006.09.007> [Accessed: 19-09-2018].
- [231] S. Rösenberg *et al.*, "Mechanical and physical properties – a way to assess quality of laser sintered parts," in *Solid Freeform Fabrication Symposium*, 2011, pp. 239–251. [Online]. Available: <https://sffsymposium.engr.utexas.edu/Manuscripts/2011/2011-19-Ruesenberg.pdf> [Accessed: 19-09-2018].
- [232] C. Majewski and N. Hopkinson, "Effect of section thickness and build orientation on tensile properties and material characteristics of laser sintered nylon-12 parts," *Rapid Prototyping Journal*, vol. 17, no. 3, pp. 176–180, 2011. [Online]. Available: <https://doi.org/10.1108/13552541111124743> [Accessed: 13-06-2018].
- [233] A. Wegner and G. Witt, "Adjustment of isotropic part properties in laser sintering based on adapted double laser exposure strategies," *Optics & Laser Technology*, vol. 109, pp. 381–388, 2019. [Online]. Available: <https://doi.org/10.1016/j.optlastec.2018.08.017> [Accessed: 30-07-2019].

- [234] M. Vasquez *et al.*, “Optimum sintering region for laser sintered nylon-12,” *Proceedings of the Institution of Mechanical Engineers, Part B: Journal of Engineering Manufacture*, vol. 225, no. 12, pp. 2240–2248, 2011. [Online]. Available: <https://doi.org/10.1177/0954405411414994> [Accessed: 12-11-2019].
- [235] M. Vasquez *et al.*, “Methods for quantifying the stable sintering region in laser sintered polyamide-12,” *Polymer Engineering & Science*, vol. 53, no. 6, pp. 1230–1240, 2013. [Online]. Available: <http://dx.doi.org/10.1002/pen.23386> [Accessed: 12-06-2018].
- [236] S. Dupin *et al.*, “Microstructural origin of physical and mechanical properties of polyamide 12 processed by laser sintering,” *European Polymer Journal*, vol. 48, no. 9, pp. 1611–1621, 2012. [Online]. Available: <https://doi.org/10.1016/j.eurpolymj.2012.06.007> [Accessed: 27-07-2018].
- [237] T. Stichel *et al.*, “A round robin study for selective laser sintering of polyamide 12: Microstructural origin of the mechanical properties,” *Optics & Laser Technology*, vol. 89, pp. 31–40, 2017. [Online]. Available: <https://doi.org/10.1016/j.optlastec.2016.09.042> [Accessed: 07-09-2018].
- [238] T. Stichel *et al.*, “A round robin study for selective laser sintering of polymers: Back tracing of the pore morphology to the process parameters,” *Journal of Materials Processing Technology*, vol. 252, pp. 537–545, 2018. [Online]. Available: <https://doi.org/10.1016/j.jmatprotec.2017.10.013> [Accessed: 07-09-2018].
- [239] R. Morgan *et al.*, “Density analysis of direct metal laser re-melted 316L stainless steel cubic primitives,” *Journal of Materials Science*, vol. 39, no. 4, pp. 1195–1205, 2004. [Online]. Available: <https://doi.org/10.1023/B:JMSS.0000013875.62536.f4> [Accessed: 26-09-2019].
- [240] H. Zarringhalam *et al.*, “Degree of particle melt in nylon-12 selective laser-sintered parts,” *Rapid Prototyping Journal*, vol. 15, no. 2, pp. 126–132, 2009. [Online]. Available: <https://doi.org/10.1108/13552540910943423> [Accessed: 13-06-2018].
- [241] C. Majewski *et al.*, “Effect of the degree of particle melt on mechanical properties in selective laser-sintered nylon-12 parts,” *Proceedings of the Institution of Mechanical Engineers, Part B: Journal of Engineering Manufacture*, vol. 222, no. 9, pp. 1055–1064, 2008. [Online]. Available: <https://doi.org/10.1243/09544054JEM1122> [Accessed: 13-06-2018].
- [242] H. Zarringhalam *et al.*, “Effects of processing on microstructure and properties of sls nylon 12,” *Materials Science and Engineering: A*, vol. 435–436, pp. 172–180, 2006. [Online]. Available: <https://doi.org/10.1016/j.msea.2006.07.084> [Accessed: 11-11-2019].
- [243] N. Hopkinson *et al.*, “Quantifying the degree of particle melt in selective laser sintering,” *CIRP Annals*, vol. 58, no. 1, pp. 197–200, 2009. [Online]. Available: <https://doi.org/10.1016/j.cirp.2009.03.001> [Accessed: 13-06-2018].
- [244] H. Zarringhalam, “Investigation into crystallinity and degree of particle melt in selective laser sintering,” Ph.D. thesis, Loughborough University, 2007. [Online]. Available: <https://hdl.handle.net/2134/7960> [Accessed: 22-05-2020].
- [245] C. E. Majewski *et al.*, “Effects of degree of particle melt and crystallinity in SLS nylon-12 parts,” in *Solid Freeform Fabrication Symposium*, 2008, pp. 45–54. [Online]. Available: <https://sffsymposium.engr.utexas.edu/Manuscripts/2008/2008-05-Majewski.pdf> [Accessed: 18-11-2019].
- [246] T. Wohlers *et al.*, “Final part production,” in *Wohlers Report 2022: 3D printing and Additive Manufacturing Global State of the Industry*. Washington, DC: ASTM International, 2022, pt. 4, pp. 175–246.
- [247] J. M. G. Cowie and V. Arrighi, “Structure–property relations,” in *Polymers: Chemistry and Physics of Modern Materials*, 3rd ed. Boca Raton, United States: Taylor & Francis Group, 2007, ch. 15, pp. 409–454. [Online]. Available: <https://ebookcentral.proquest.com/lib/sheffield/detail.action?docID=1449424> [Accessed: 19-06-2020].
- [248] Y. Kong and J. Hay, “The enthalpy of fusion and degree of crystallinity of polymers as measured by DSC,” *European Polymer Journal*, vol. 39, no. 8, pp. 1721–1727, 2003. [Online]. Available: [https://doi.org/10.1016/S0014-3057\(03\)00054-5](https://doi.org/10.1016/S0014-3057(03)00054-5) [Accessed: 19-06-2020].
- [249] PostProcess Technologies. (2018) *Guide to SLS & MJF automated powder removal with innovative Fusillade technology*. [Online]. Available: <https://www.javelin-tech.com/3d/post-processing-sls-mjf-powder-removal/> [Accessed: 09-06-2022].
- [250] Dyemansion. (2019) *Dyemansion Powershot C*. [Online]. Available: <https://dyemansion.com/en/products/powershot-c/> [Accessed: 14-11-2019].
- [251] Materialise. (2019) *Polyamide (SLS) – colors & finishes*. [Online]. Available: <https://i.materialise.com/en/3d-printing-materials/polyamide/colors-finishes> [Accessed: 15-11-2019].
- [252] DyeMansion. (2019) *DyeMansion powerfuse S*. [Online]. Available: <https://dyemansion.com/en/products/powerfuse-s/> [Accessed: 20-11-2019].
- [253] N. Crane *et al.*, “Impact of chemical finishing on laser-sintered nylon 12 materials,” *Additive Manufacturing*, vol. 13, pp. 149–155, 2017. [Online]. Available: <https://doi.org/10.1016/j.addma.2016.10.001> [Accessed: 28-08-2018].
- [254] H. Zarringhalam and N. Hopkinson, “Post-processing of duraform parts for rapid manufacture,” in *Solid Freeform Fabrication Symposium*, 2003, pp. 596–606. [Online]. Available: <https://sffsymposium.engr.utexas.edu/Manuscripts/2003/2003-57-Zarringhalam.pdf> [Accessed: 18-11-2019].

- [255] Prosilas. (2019) *Metal Plating*. [Online]. Available: <https://www.prosilas.com/en/portfolio-items/metal-plating/> [Accessed: 15-11-2019].
- [256] SAT Plating. (2019) *3D Prototyping*. [Online]. Available: <https://www.satplating.com/plating-plastics/3d-prototyping/> [Accessed: 15-11-2019].
- [257] Sharretts Plating Company. (2019) *SLS Plastics*. [Online]. Available: <https://www.sharrettsplating.com/base-materials/sls-plastics-plating> [Accessed: 18-11-2019].
- [258] W. Zhu *et al.*, “A novel method based on selective laser sintering for preparing high-performance carbon fibres/polyamide12/epoxy ternary composites,” *Scientific reports*, vol. 6, p. 33780, 2016. [Online]. Available: <https://doi.org/10.1038/srep33780> [Accessed: 02-12-2019].
- [259] T. Niino and H. Yamada, “Preliminary study for transparentization of sls parts by resin infiltration,” in *Solid Freeform Fabrication Symposium*, 2004, pp. 236–243. [Online]. Available: <https://sffsymposium.engr.utexas.edu/Manuscripts/2004/2004-24-Niino.pdf> [Accessed: 18-11-2019].
- [260] J. R. Wingham *et al.*, “Micro-CT for analysis of laser sintered micro-composites,” *Rapid Prototyping Journal*, vol. 26, no. 4, pp. 649–657, 2020. [Online]. Available: <https://doi.org/10.1108/RPJ-08-2019-0211> [Accessed: 28-1-2020].
- [261] A. Thompson *et al.*, “X-ray computed tomography for additive manufacturing: a review,” *Measurement Science and Technology*, vol. 27, no. 7, p. 072001, 2016. [Online]. Available: <http://stacks.iop.org/0957-0233/27/i=7/a=072001> [Accessed: 27-07-2018].
- [262] L. D. Chiffre *et al.*, “Industrial applications of computed tomography,” *CIRP Annals*, vol. 63, no. 2, pp. 655–677, 2014. [Online]. Available: <https://doi.org/10.1016/j.cirp.2014.05.011> [Accessed: 19-09-2018].
- [263] M. Pavan *et al.*, “CT-based quality control of laser sintering of polymers,” *Case Studies in Nondestructive Testing and Evaluation*, vol. 6, pp. 62–68, 2016, special Issue: Industrial computed tomography. [Online]. Available: <https://doi.org/10.1016/j.csn.2016.04.004> [Accessed: 07-09-2018].
- [264] A. Jansson and L. Pejryd, “Characterisation of carbon fibre-reinforced polyamide manufactured by selective laser sintering,” *Additive Manufacturing*, vol. 9, pp. 7–13, 2016. [Online]. Available: <https://doi.org/10.1016/j.addma.2015.12.003> [Accessed: 07-09-2018].
- [265] W. Dewulf *et al.*, “Using x-ray computed tomography to improve the porosity level of polyamide-12 laser sintered parts,” *CIRP Annals*, vol. 65, no. 1, pp. 205–208, 2016. [Online]. Available: <https://doi.org/10.1016/j.cirp.2016.04.056> [Accessed: 07-09-2018].
- [266] B. V. Hooreweder and J.-P. Kruth, “High cycle fatigue properties of selective laser sintered parts in polyamide 12,” *CIRP Annals*, vol. 63, no. 1, pp. 241–244, 2014. [Online]. Available: <https://doi.org/10.1016/j.cirp.2014.03.060> [Accessed: 07-09-2018].
- [267] D. Rouholamin and N. Hopkinson, “An investigation on the suitability of micro-computed tomography as a non-destructive technique to assess the morphology of laser sintered nylon 12 parts,” *Proceedings of the Institution of Mechanical Engineers, Part B: Journal of Engineering Manufacture*, vol. 228, no. 12, pp. 1529–1542, 2014. [Online]. Available: <https://doi.org/10.1177/0954405414522209> [Accessed: 19-09-2018].
- [268] M. Pavan *et al.*, “Investigating the influence of x-ray CT parameters on porosity measurement of laser sintered PA12 parts using a design-of-experiment approach,” *Polymer Testing*, vol. 66, pp. 203–212, 2018. [Online]. Available: <https://doi.org/10.1016/j.polymertesting.2018.01.037> [Accessed: 07-09-2018].
- [269] G. Flodberg *et al.*, “Pore analysis and mechanical performance of selective laser sintered objects,” *Additive Manufacturing*, vol. 24, pp. 307–315, 2018. [Online]. Available: <https://doi.org/10.1016/j.addma.2018.10.001> [Accessed: 13-08-2019].
- [270] J. R. Wingham *et al.*, “Effect of steam autoclaving on laser sintered polyamide 12,” *Rapid Prototyping Journal*, vol. 27, no. 1, pp. 45–52, 2020. [Online]. Available: <https://doi.org/10.1108/RPJ-11-2019-0288> [Accessed: 12-11-2020].
- [271] H. Batzer and U. T. Kreibich, “Influence of water on thermal transitions in natural polymers and synthetic polyamides,” *Polymer Bulletin*, vol. 5, no. 11, pp. 585–590, 1981. [Online]. Available: <https://doi.org/10.1007/BF00255296> [Accessed: 11-02-2019].
- [272] N. Jia and V. A. Kagan, “Mechanical performance of polyamides with influence of moisture and temperature – accurate evaluation and better understanding,” in *Plastics Failure Analysis and Prevention*, ser. Plastics Design Library, J. Moalli, Ed. Norwich, NY: William Andrew Publishing, 2001, pp. 95–104. [Online]. Available: <https://doi.org/10.1016/B978-188420792-1.50014-7> [Accessed: 20-03-2019].
- [273] J. J. Rajesh *et al.*, “Effect of water absorption on erosive wear behaviour of polyamides,” *Journal of Materials Science*, vol. 37, no. 23, pp. 5107–5113, 2002. [Online]. Available: <https://doi.org/10.1023/A:1021012404839> [Accessed: 21-03-2019].
- [274] L. Razumovskii *et al.*, “Sorption of water by aliphatic polyamides. review,” *Polymer Science U.S.S.R.*, vol. 27, no. 4, pp. 751–768, 1985. [Online]. Available: [https://doi.org/10.1016/0032-3950\(85\)90411-3](https://doi.org/10.1016/0032-3950(85)90411-3) [Accessed: 20-03-2019].
- [275] M. Kurokawa *et al.*, “Performance of plastic gear made of carbon fiber reinforced polyamide 12,” *Wear*, vol. 254, no. 5, pp. 468–473, 2003. [Online]. Available: [https://doi.org/10.1016/S0043-1648\(03\)00020-6](https://doi.org/10.1016/S0043-1648(03)00020-6) [Accessed: 11-02-2019].

- [276] X. Fan *et al.*, “Experimental investigations and model study of moisture behaviors in polymeric materials,” *Microelectronics Reliability*, vol. 49, no. 8, pp. 861–871, 2009. [Online]. Available: <https://doi.org/10.1016/j.microrel.2009.03.006> [Accessed: 21-03-2019].
- [277] R. Goodridge *et al.*, “Effect of long-term ageing on the tensile properties of a polyamide 12 laser sintering material,” *Polymer Testing*, vol. 29, no. 4, pp. 483–493, 2010. [Online]. Available: <https://doi.org/10.1016/j.polymertesting.2010.02.009> [Accessed: 30-11-2018].
- [278] W. Cooke *et al.*, “Anisotropy, homogeneity and ageing in an sls polymer,” *Rapid Prototyping Journal*, vol. 17, no. 4, pp. 269–279, 2011. [Online]. Available: <https://doi.org/10.1108/13552541111138397> [Accessed: 30-11-2018].
- [279] E. Moeskops *et al.*, “Creep behaviour of polyamide in selective laser sintering,” in *Solid Freeform Fabrication Symposium*, 2004, pp. 60–67. [Online]. Available: <http://sffsymposium.engr.utexas.edu/Manuscripts/2004/2004-07-Moeskops.pdf> [Accessed: 11-02-2019].
- [280] R. Seltzer *et al.*, “Effect of water conditioning on the fracture behavior of PA12 composites processed by selective laser sintering,” *Materials Science and Engineering: A*, vol. 528, no. 22, pp. 6927–6933, 2011. [Online]. Available: <https://doi.org/10.1016/j.msea.2011.05.045> [Accessed: 20-03-2019].
- [281] A. Salazar *et al.*, “Monotonic loading and fatigue response of a bio-based polyamide PA11 and a petrol-based polyamide PA12 manufactured by selective laser sintering,” *European Polymer Journal*, vol. 59, pp. 36–45, 2014. [Online]. Available: <https://doi.org/10.1016/j.eurpolymj.2014.07.016> [Accessed: 20-03-2019].
- [282] M. J. Haerst *et al.*, “Ageing processes in laser sintered and injection moulded PA12 following hygienic reprocessing,” *Rapid Prototyping Journal*, vol. 21, no. 3, pp. 279–286, 2015. [Online]. Available: <https://doi.org/10.1108/RPJ-06-2013-0061> [Accessed: 27-03-2019].
- [283] M. Blattmeier *et al.*, “Influence of surface characteristics on fatigue behaviour of laser sintered plastics,” *Rapid Prototyping Journal*, vol. 18, no. 2, pp. 161–171, 2012. [Online]. Available: <https://doi.org/10.1108/13552541211212140> [Accessed: 27-08-2019].
- [284] B. Van Hooreweder *et al.*, “Microstructural characterization of SLS-PA12 specimens under dynamic tension/compression excitation,” *Polymer Testing*, vol. 29, no. 3, pp. 319–326, 2010. [Online]. Available: <https://doi.org/10.1016/j.polymertesting.2009.12.006> [Accessed: 19-06-2020].
- [285] G. V. Salmoria *et al.*, “Microstructural and mechanical characterization of PA12/MWCNTs nanocomposite manufactured by selective laser sintering,” *Polymer Testing*, vol. 30, no. 6, pp. 611–615, 2011. [Online]. Available: <https://doi.org/10.1016/j.polymertesting.2011.04.007> [Accessed: 19-10-2017].
- [286] A. Salazar *et al.*, “Fatigue crack growth of sls polyamide 12: Effect of reinforcement and temperature,” *Composites Part B: Engineering*, vol. 59, pp. 285–292, 2014. [Online]. Available: <https://doi.org/10.1016/j.compositesb.2013.12.017> [Accessed: 13-09-2018].
- [287] A. S. Shackelford *et al.*, “Degradation of laser sintered nylon-12 parts due to accelerated exposure to ultraviolet radiation,” *Additive Manufacturing*, vol. 46, p. 102132, 2021. [Online]. Available: <https://doi.org/10.1016/j.addma.2021.102132> [Accessed: 28-06-2021].
- [288] Microfol Compounding. (2020) *Perfectly adapted material mixtures with additives*. [Online]. Available: <https://www.microfol.de/en/mycompounds/additive.php> [Accessed: 6-1-2020].
- [289] J. P. Schultz *et al.*, “Selective laser sintering of nylon 12-peek blends formed by cryogenic mechanical alloying,” *Solid Freeform Fabrication Symposium*, pp. 119–124, 2000. [Online]. Available: <https://sffsymposium.engr.utexas.edu/Manuscripts/2000/2000-15-Schultz.pdf> [Accessed: 16-12-2019].
- [290] B. Chen *et al.*, “Poly aryl ether ketones (PAEKs) and carbon-reinforced PAEK powders for laser sintering,” *Journal of Materials Science*, vol. 52, no. 10, pp. 6004–6019, 2017. [Online]. Available: <https://doi.org/10.1007/s10853-017-0840-0> [Accessed: 16-12-2019].
- [291] J. Schmidt *et al.*, “A novel process route for the production of spherical LBM polymer powders with small size and good flowability,” *Powder Technology*, vol. 261, pp. 78–86, 2014. [Online]. Available: <https://doi.org/10.1016/j.powtec.2014.04.003> [Accessed: 16-12-2019].
- [292] Y. Chunze *et al.*, “A nanosilica/nylon-12 composite powder for selective laser sintering,” *Journal of Reinforced Plastics and Composites*, vol. 28, no. 23, pp. 2889–2902, 2009. [Online]. Available: <https://doi.org/10.1177/0731684408094062> [Accessed: 13-12-2019].
- [293] K. Shahzad *et al.*, “Preparation and indirect selective laser sintering of alumina/PA microspheres,” *Ceramics International*, vol. 38, no. 2, pp. 1241–1247, 2012. [Online]. Available: <https://doi.org/10.1016/j.ceramint.2011.08.055> [Accessed: 13-12-2019].
- [294] H. C. Kim *et al.*, “Synthesis of PA12/functionalized GNP nanocomposite powders for the selective laser sintering process,” *Journal of Composite Materials*, vol. 47, no. 4, pp. 501–509, 2013. [Online]. Available: <https://doi.org/10.1177/0021998312441812> [Accessed: 13-12-2019].
- [295] S.-D. Yeo and E. Kiran, “Formation of polymer particles with supercritical fluids: A review,” *The Journal of Supercritical Fluids*, vol. 34, no. 3, pp. 287–308, 2005. [Online]. Available: <https://doi.org/10.1016/j.supflu.2004.10.006> [Accessed: 16-12-2019].

- [296] N. Mys *et al.*, “Processing of syndiotactic polystyrene to microspheres for part manufacturing through selective laser sintering,” *Polymers*, vol. 8, no. 11, p. 383, 2016. [Online]. Available: <https://doi.org/10.3390/polym8110383> [Accessed: 13-12-2019].
- [297] S. Faselow *et al.*, “Production of spherical wax and polyolefin microparticles by melt emulsification for additive manufacturing,” *Chemical Engineering Science*, vol. 141, pp. 282–292, 2016. [Online]. Available: <https://doi.org/10.1016/j.ces.2015.11.019> [Accessed: 16-12-2019].
- [298] G. Nelson, “Microencapsulated colourants for technical textile application,” in *Advances in the Dyeing and Finishing of Technical Textiles*, M. Gulrajani, Ed. Woodhead Publishing, 2013, pp. 78–104. [Online]. Available: <https://doi.org/10.1533/9780857097613.1.78> [Accessed: 13-12-2019].
- [299] A. N. M. B. El-hoshoudy, “Emulsion polymerization mechanism,” *Recent Research in Polymerization*, pp. 3–12, 2018. [Online]. Available: <https://doi.org/10.5772/intechopen.72143> [Accessed: 13-12-2019].
- [300] S. Eshraghi *et al.*, “Processing and properties of electrically conductive nanocomposites based on polyamide-12 filled with exfoliated graphite nanoplatelets prepared by selective laser sintering,” *International Journal of Precision Engineering and Manufacturing*, vol. 14, no. 11, pp. 1947–1951, 2013. [Online]. Available: <https://doi.org/10.1007/s12541-013-0264-y> [Accessed: 13-12-2019].
- [301] S. Kenzari *et al.*, “Quasicrystal–polymer composites for selective laser sintering technology,” *Materials & Design*, vol. 35, pp. 691–695, 2012. [Online]. Available: <https://doi.org/10.1016/j.matdes.2011.10.032> [Accessed: 13-12-2019].
- [302] H. Chung and S. Das, “Functionally graded nylon-11/silica nanocomposites produced by selective laser sintering,” *Materials Science and Engineering: A*, vol. 487, no. 1, pp. 251–257, 2008. [Online]. Available: <https://doi.org/10.1016/j.msea.2007.10.082> [Accessed: 19-10-2017].
- [303] A. du Plessis *et al.*, “Quality investigation of 3D printer filament using laboratory x-ray tomography,” *3D Printing and Additive Manufacturing*, vol. 3, no. 4, pp. 262–267, 2016. [Online]. Available: <https://doi.org/10.1089/3dp.2016.0011>
- [304] A. du Plessis *et al.*, “X-ray microcomputed tomography in additive manufacturing: A review of the current technology and applications,” *3D Printing and Additive Manufacturing*, vol. 5, no. 3, pp. 227–247, 2018. [Online]. Available: <https://doi.org/10.1089/3dp.2018.0060> [Accessed: 29-08-2018].
- [305] A. du Plessis and S. G. le Roux, “Standardized x-ray tomography testing of additively manufactured parts: A round robin test,” *Additive Manufacturing*, vol. 24, pp. 125–136, 2018. [Online]. Available: <https://doi.org/10.1016/j.addma.2018.09.014> [Accessed: 08-10-2019].
- [306] A. du Plessis *et al.*, “X-ray computed tomography of consumer-grade 3d-printed parts,” *3D Printing and Additive Manufacturing*, vol. 2, no. 4, pp. 190–195, 2015. [Online]. Available: <https://doi.org/10.1089/3dp.2015.0015> [Accessed: 09-10-2019].
- [307] E. Chlebus *et al.*, “Titanium alloyed with rhenium by selective laser melting,” *Materials Science and Engineering: A*, vol. 620, pp. 155–163, 2015. [Online]. Available: <https://doi.org/10.1016/j.msea.2014.10.021> [Accessed: 27-07-2018].
- [308] T. Dzogbewu *et al.*, “Optimal process parameters for in situ alloyed Ti15Mo structures by laser powder bed fusion,” in *Proceedings of 28th SFF Symposium*, 2017, pp. 75–96. [Online]. Available: <https://sffsymposium.engr.utexas.edu/sites/default/files/2017/Manuscripts/OptimalProcessParametersforInSituAlloyedTi1.pdf> [Accessed: 23-07-2019].
- [309] EOS. (2019) *EOS plastic materials for additive Manufacturing*. [Online]. Available: <https://www.eos.info/material-p> [Accessed: 17-12-2019].
- [310] BASF 3D Printing Solutions. (2019) *Powder bed fusion product information*. [Online]. Available: https://www.basf.com/global/images/about-us/locations/europe/german-companies/b3dps/documents/powders/BASF_3D_Printing_Powders_Brochure.pdf [Accessed: 17-12-2019].
- [311] Advanced Laser Materials. (2019) *Materials that help bring your ideas to reality*. [Online]. Available: <https://alm-llc.com/products/> [Accessed: 17-12-2019].
- [312] Prodways. (2019) *3D printing polymer powders*. [Online]. Available: <https://www.prodways.com/en/type/plastic-powders/> [Accessed: 17-12-2019].
- [313] 3D Systems. (2019) *SLS materials guide*. [Online]. Available: https://www.3dsystems.com/sites/default/files/2019-07/3DSystems_SLS_Material_Guide_Infographic.pdf [Accessed: 17-12-2019].
- [314] Eplus 3D. (2019) *Material*. [Online]. Available: <http://www.eplus3d.com/en/materials.html> [Accessed: 17-12-2019].
- [315] Diamond Plastics. (2019) *Products*. [Online]. Available: <http://www.diamond-plastics.de/en/products/> [Accessed: 17-12-2019].
- [316] Farsoon Technologies. (2019) *Polymer Laser Sintering Solution*. [Online]. Available: http://en.farsoon.com/solution_list_01.html [Accessed: 17-12-2019].
- [317] CRP Technology. (2019) *Additive manufacturing with windform, taking 3D printing to the next level*. [Online]. Available: <https://www.crptechnology.com/windform-3d-printing-materials/> [Accessed: 17-12-2019].

- [318] I. Shishkovsky and V. Scherbakov, "Selective laser sintering of biopolymers with micro and nano ceramic additives for medicine," *Physics Procedia*, vol. 39, pp. 491–499, 2012, laser Assisted Net shape Engineering 7 (LANE 2012). [Online]. Available: <https://doi.org/10.1016/j.phpro.2012.10.065> [Accessed: 02-06-2020].
- [319] I. V. Shishkovsky and Y. G. Morozov, "Laser assisted fabrication of porous polymer mems with nano structured additives," *MRS Proceedings*, vol. 1312, pp. mrsf10–1312–ii10–07, 2011. [Online]. Available: <https://doi.org/10.1557/opl.2011.122> [Accessed: 03-06-2020].
- [320] B. Badrinarayan and J. W. Barlow, "Selective laser sintering of a copper-PMMA system," in *Solid Freeform Fabrication Symposium*, 1991, pp. 245–250. [Online]. Available: <https://sffsymposium.engr.utexas.edu/Manuscripts/1991/1991-28-Badrinarayan.pdf> [Accessed: 01-06-2020].
- [321] I. Shishkovsky *et al.*, "Laser sinterability and characterization of oxide nano ceramics reinforced to biopolymer matrix," *The International Journal of Advanced Manufacturing Technology*, vol. 78, pp. 449–455, 2015. [Online]. Available: <https://doi.org/10.1007/s00170-014-6633-6> [Accessed: 03-06-2020].
- [322] K. Subramanian *et al.*, "Selective laser sintering of alumina with polymer binders," *Rapid Prototyping Journal*, vol. 1, no. 2, pp. 24–35, 1995. [Online]. Available: <https://doi.org/10.1108/13552549510086844> [Accessed: 01-06-2020].
- [323] K. Shahzad *et al.*, "Additive manufacturing of zirconia parts by indirect selective laser sintering," *Journal of the European Ceramic Society*, vol. 34, no. 1, pp. 81–89, 2014. [Online]. Available: <https://doi.org/10.1016/j.jeurceramsoc.2013.07.023> [Accessed: 01-06-2020].
- [324] M. S. Wahab *et al.*, "Development of polymer nanocomposites for rapid prototyping process," in *Proceedings of the World Congress on Engineering*, vol. 2, 2009. [Online]. Available: http://iaeng.org/publication/WCE2009/WCE2009_pp1499-1504.pdf [Accessed: 01-06-2020].
- [325] H. Chung and S. Das, "Processing and properties of glass bead particulate-filled functionally graded nylon-11 composites produced by selective laser sintering," *Materials Science and Engineering: A*, vol. 437, no. 2, pp. 226–234, 2006. [Online]. Available: <https://doi.org/10.1016/j.msea.2006.07.112> [Accessed: 04-09-2019].
- [326] Y. Wang *et al.*, "Glass bead filled polyetherketone (PEK) composite by high temperature laser sintering (HT-LS)," *Materials & Design*, vol. 83, pp. 545–551, 2015. [Online]. Available: <https://doi.org/10.1016/j.matdes.2015.06.005> [Accessed: 27-11-2019].
- [327] J. Koo *et al.*, "Polyamide nanocomposites for selective laser sintering," in *Solid Freeform Fabrication Symposium*, 2006, pp. 392–409. [Online]. Available: <http://edge.rit.edu/edge/P10551/public/SFF/SFF%202006%20Proceedings/Manuscripts/36-Koo.pdf> [Accessed: 19-10-2017].
- [328] B. Chen *et al.*, "A primary study into graphene/polyether ether ketone (PEEK) nanocomposite for laser sintering," *Applied Surface Science*, vol. 428, pp. 1018–1028, 2018. [Online]. Available: <https://doi.org/10.1016/j.apsusc.2017.09.226> [Accessed: 20-09-2018].
- [329] R. B. Booth *et al.*, "Methods and systems for fabricating fire retardant materials," U.S. Patent 8,236,418, Aug. 7, 2012. [Online]. Available: <https://patents.google.com/patent/US8236418B2/en> [Accessed: 28-11-2019].
- [330] K. Jiang *et al.*, "Study on the microstructure and binding mechanisms of selective laser sintered wood plastic composite," in *Solid Freeform Fabrication Symposium*, 2013, pp. 497–504. [Online]. Available: <https://sffsymposium.engr.utexas.edu/Manuscripts/2013/2013-39-Jiang.pdf> [Accessed: 22-11-2019].
- [331] L. Lanzl *et al.*, "Selective laser sintering of copper filled polyamide 12: Characterization of powder properties and process behavior," *Polymer Composites*, vol. 40, no. 5, pp. 1801–1809, 2019. [Online]. Available: <https://onlinelibrary.wiley.com/doi/abs/10.1002/pc.24940> [Accessed: 28-11-2019].
- [332] A. Mazzoli *et al.*, "Characterization of an aluminum-filled polyamide powder for applications in selective laser sintering," *Materials & Design*, vol. 28, no. 3, pp. 993–1000, 2007. [Online]. Available: <https://doi.org/10.1016/j.matdes.2005.11.021> [Accessed: 28-11-2019].
- [333] C. Yan *et al.*, "Preparation and selective laser sintering of nylon-12 coated metal powders and post processing," *Journal of Materials Processing Technology*, vol. 209, no. 17, pp. 5785–5792, 2009. [Online]. Available: <https://doi.org/10.1016/j.jmatprotec.2009.06.010> [Accessed: 01-06-2020].
- [334] P. Forderhase *et al.*, "The development of a SLS composite material," in *Solid Freeform Fabrication Symposium*, 1995, pp. 287–297. [Online]. Available: <https://sffsymposium.engr.utexas.edu/Manuscripts/1995/1995-34-Forderhase.pdf> [Accessed: 04-09-2019].
- [335] K. Wudy *et al.*, "Selective laser sintering of filled polymer systems: Bulk properties and laser beam material interaction," *Physics Procedia*, vol. 83, pp. 991–1002, 2016, laser Assisted Net Shape Engineering 9 International Conference on Photonic Technologies Proceedings of the LANE 2016 September 19-22, 2016 Fürth, Germany. [Online]. Available: <https://doi.org/10.1016/j.phpro.2016.08.104> [Accessed: 27-08-2019].
- [336] K. Hon and T. Gill, "Selective laser sintering of SiC/polyamide composites," *CIRP Annals*, vol. 52, no. 1, pp. 173–176, 2003. [Online]. Available: [https://doi.org/10.1016/S0007-8506\(07\)60558-7](https://doi.org/10.1016/S0007-8506(07)60558-7) [Accessed: 04-09-2019].

- [337] P. K. Jain *et al.*, “Selective laser sintering of clay-reinforced polyamide,” *Polymer Composites*, vol. 31, no. 4, pp. 732–743, 2010. [Online]. Available: <https://doi.org/10.1002/pc.20854> [Accessed: 28-11-2019].
- [338] M. Yan *et al.*, “Hierarchically porous materials prepared by selective laser sintering,” *Materials & Design*, vol. 135, pp. 62–68, 2017. [Online]. Available: <https://doi.org/10.1016/j.matdes.2017.09.015> [Accessed: 7-1-2020].
- [339] C. Yan *et al.*, “Preparation, characterisation and processing of carbon fibre/polyamide-12 composites for selective laser sintering,” *Composites Science and Technology*, vol. 71, no. 16, pp. 1834–1841, 2011. [Online]. Available: <https://doi.org/10.1016/j.compscitech.2011.08.013> [Accessed: 19-10-2017].
- [340] R. Goodridge *et al.*, “Processing of a polyamide-12/carbon nanofibre composite by laser sintering,” *Polymer Testing*, vol. 30, no. 1, pp. 94–100, 2011. [Online]. Available: <https://doi.org/10.1016/j.polymertesting.2010.10.011> [Accessed: 19-10-2017].
- [341] S. R. Athreya *et al.*, “Processing and characterization of a carbon black-filled electrically conductive nylon-12 nanocomposite produced by selective laser sintering,” *Materials Science and Engineering: A*, vol. 527, no. 10, pp. 2637–2642, 2010. [Online]. Available: <https://doi.org/10.1016/j.msea.2009.12.028> [Accessed: 19-10-2017].
- [342] S. R. Athreya *et al.*, “Mechanical and microstructural properties of nylon-12/carbon black composites: Selective laser sintering versus melt compounding and injection molding,” *Composites Science and Technology*, vol. 71, no. 4, pp. 506–510, 2011. [Online]. Available: <https://doi.org/10.1016/j.compscitech.2010.12.028> [Accessed: 4-10-2017].
- [343] S. R. Athreya *et al.*, “Microstructure, thermomechanical properties, and electrical conductivity of carbon black-filled nylon-12 nanocomposites prepared by selective laser sintering,” *Polymer Engineering & Science*, vol. 52, no. 1, pp. 12–20, 1 2012. [Online]. Available: <https://doi.org/10.1002/pen.22037> [Accessed: 11-02-2019].
- [344] H. C. Kim *et al.*, “Synthesis of PA12/functionalized GNP nanocomposite powders for the selective laser sintering process,” *Journal of Composite Materials*, vol. 47, no. 4, pp. 501–509, 2013. [Online]. Available: <https://doi.org/10.1177/0021998312441812> [Accessed: 04-06-2020].
- [345] Graphite Additive Manufacturing. (2019) *Quality 3D printing*. [Online]. Available: <https://www.graphite-am.co.uk/> [Accessed: 05-12-2019].
- [346] G. Salmoria *et al.*, “Rapid manufacturing of PA/HDPE blend specimens by selective laser sintering: Microstructural characterization,” *Polymer Testing*, vol. 26, no. 3, pp. 361–368, 2007. [Online]. Available: <https://doi.org/10.1016/j.polymertesting.2006.12.002> [Accessed: 15-5-2020].
- [347] Y. A. C. Jande, “Manufacturing and characterization of uniformly porous and graded porous polymeric structures via selective laser sintering,” M.Sc. thesis, The graduate school of natural and applied sciences, Middle East Technical University, Dec. 2009. [Online]. Available: <http://citeseerx.ist.psu.edu/viewdoc/download?doi=10.1.1.632.8020&rep=rep1&type=pdf> [Accessed: 23-06-2020].
- [348] Microbiology Society. (2021) *Bacteria*. [Online]. Available: <https://microbiologysociety.org/why-microbiology-matters/what-is-microbiology/bacteria.html> [Accessed: 25-10-2021].
- [349] M. Madigan *et al.*, “The foundations of microbiology,” in *Brock Biology of Microorganisms*, 14th ed. Harlow, England: Pearson, 2015, unit 1, pp. 25–206.
- [350] T. J. Beveridge and L. L. Graham, “Surface layers of bacteria,” *Microbiological Reviews*, vol. 55, no. 4, pp. 684–705, 1991. [Online]. Available: <https://doi.org/10.1128/mr.55.4.684-705.1991> [Accessed: 21-10-2021].
- [351] T. J. Silhavy *et al.*, “The bacterial cell envelope,” *Cold Spring Harbor perspectives in biology*, vol. 2, no. 5, p. a000414, 2010. [Online]. Available: <https://doi.org/10.1101/cshperspect.a000414> [Accessed: 21-10-2021].
- [352] M. B. Miller and B. L. Bassler, “Quorum sensing in bacteria,” *Annual Review of Microbiology*, vol. 55, no. 1, pp. 165–199, 2001. [Online]. Available: <https://doi.org/10.1146/annurev.micro.55.1.165> [Accessed: 19-03-2021].
- [353] T. Defoirdt *et al.*, “Disruption of bacterial quorum sensing: an unexplored strategy to fight infections in aquaculture,” *Aquaculture*, vol. 240, no. 1, pp. 69–88, 2004. [Online]. Available: <https://doi.org/10.1016/j.aquaculture.2004.06.031> [Accessed: 12-06-2019].
- [354] M. Madigan *et al.*, “Genomics, genetics, and virology,” in *Brock Biology of Microorganisms*, 14th ed. Harlow, England: Pearson, 2015, unit 2, pp. 207–370.
- [355] Y. Dong *et al.*, “A novel bio-carrier fabricated using 3D printing technique for wastewater treatment,” *Scientific reports*, vol. 5, p. 12400, 2015. [Online]. Available: <https://doi.org/10.1038/srep12400> [Accessed: 20-12-2019].
- [356] W. S. Tan *et al.*, “Comparison of solid, liquid and powder forms of 3D printing techniques in membrane spacer fabrication,” *Journal of Membrane Science*, vol. 537, pp. 283–296, 2017. [Online]. Available: <https://doi.org/10.1016/j.memsci.2017.05.037> [Accessed: 7-1-2020].
- [357] R. D. Turner *et al.*, “Interactions between microbes and laser sintered polymers,” presented at the Solid Freeform Fabrication Symposium, Aug. 15, 2018.

- [358] Antimicrobial Resistance Collaborators, “Global burden of bacterial antimicrobial resistance in 2019: a systematic analysis,” *The Lancet*, vol. 399, no. 10325, pp. 629–655, 2022. [Online]. Available: [https://doi.org/10.1016/S0140-6736\(21\)02724-0](https://doi.org/10.1016/S0140-6736(21)02724-0) [Accessed: 20-01-2022].
- [359] Interagency Coordination Group on Antimicrobial Resistance, “No time to wait: Securing the future from drug-resistant infections,” World Health Organization, Report to the Secretary-General of the United Nations, Apr. 2019. [Online]. Available: <https://www.who.int/publications/i/item/no-time-to-wait-securing-the-future-from-drug-resistant-infections> [Accessed: 25-10-2021].
- [360] J. O’Neill. (2016, May 16.) *Tackling drug-resistant infections globally: final report and recommendations*. The Review on Antimicrobial Resistance. [Online]. Available: <https://amr-review.org/Publications.html> [Accessed: 22-02-2019].
- [361] A. Molnar, “Antimicrobial resistance awareness and games,” *Trends in Microbiology*, vol. 27, no. 1, pp. 1–3, 2019. [Online]. Available: <https://doi.org/10.1016/j.tim.2018.09.007> [Accessed: 22-02-2019].
- [362] M. A. B. Lucien *et al.*, “Antibiotics and antimicrobial resistance in the COVID-19 era: Perspective from resource-limited settings,” *International Journal of Infectious Diseases*, vol. 104, pp. 250–254, 2021. [Online]. Available: <https://doi.org/10.1016/j.ijid.2020.12.087> [Accessed: 25-10-2021].
- [363] A. A. Miles *et al.*, “The estimation of the bactericidal power of the blood,” *Epidemiology and Infection*, vol. 38, no. 6, pp. 732–749, 1938. [Online]. Available: <https://doi.org/10.1017/s002217240001158x> [Accessed: 18-06-2021].
- [364] J. J. Perkins, “Chemical disinfection,” in *Principles and Methods of Sterilization in Health Sciences*, 2nd ed. Springfield, Illinois: Charles C Thomas, 1969, ch. 14, pp. 327–344.
- [365] W. A. Rutala *et al.* (2017, Feb.) *Guideline for Disinfection and Sterilization in Healthcare Facilities, 2008*. CDC: Centers for Disease Control and Prevention. [Online]. Available: <https://www.cdc.gov/infectioncontrol/guidelines/disinfection/> [Accessed: 07-02-2018].
- [366] E. H. Spaulding, “Chemical disinfection of medical and surgical materials,” in *Disinfection, sterilization and preservation*, C. Lawrence and S. S. Block, Eds. Philadelphia: Lea & Febiger, 1968, pp. 517–531.
- [367] W. A. Rutala and D. J. Weber, “Disinfection and sterilization in health care facilities: What clinicians need to know,” *Clinical Infectious Diseases*, vol. 39, no. 5, pp. 702–709, 2004. [Online]. Available: <http://dx.doi.org/10.1086/423182> [Accessed: 08-02-2018].
- [368] M. Forrest, “Sterilisation of rubbers and plastics & packaging of sterile devices,” presented at the Introduction to Plastics and Rubber Materials in Medical Devices, Smithers Rapra, Shawbury, UK, pp. 140–176, Dec. 7 2018.
- [369] J. J. Perkins, “Dry heat sterilization,” in *Principles and Methods of Sterilization in Health Sciences*, 2nd ed. Springfield, Illinois: Charles C Thomas, 1969, ch. 12, pp. 286–311.
- [370] M. J. George and R. H. Crawford, “The effects of dry heat sterilization on parts using selective laser sintering,” in *Solid Freeform Fabrication Symposium*, 2010, pp. 312–320. [Online]. Available: <https://sffsymposium.engr.utexas.edu/Manuscripts/2010/2010-77-George.pdf> [Accessed: 08-07-2019].
- [371] M. Dion and W. Parker, “Steam sterilization principles,” *Pharmaceutical Engineering*, vol. 33, no. 6, 2013. [Online]. Available: https://www.ispe.gr.jp/ISPE/07_public/pdf/201504_en.pdf [Accessed: 12-02-2018].
- [372] M. Johnson, “Common sterilization methods and 3D Systems’ plastic 3D printing materials,” 3D Systems, Whitepaper, 2021. [Online]. Available: <https://www.3dsystems.com/sterilization-methods-plastic-materials> [Accessed: 16-06-2022].
- [373] S. P. Krishnan *et al.*, “A review of rapid prototyped surgical guides for patient-specific total knee replacement,” *The Journal of bone and joint surgery. British volume*, vol. 94-B, no. 11, pp. 1457–1461, 2012. [Online]. Available: <https://doi.org/10.1302/0301-620X.94B11.29350> [Accessed: 24-06-2020].
- [374] M. T. Mubarak *et al.*, “Evaluation of sterilization methods for medical devices,” in *2019 Advances in Science and Engineering Technology International Conferences (ASET)*, 2019, pp. 1–4. [Online]. Available: <https://doi.org/10.1109/ICASET.2019.8714223> [Accessed: 16-06-2022].
- [375] A. Wegner, “Cross-linking of laser sintered polyamide 12 and polyethylene parts by gamma irradiation,” in *AIP Conference Proceedings*, vol. 1914, no. 1, 2017, p. 190005. [Online]. Available: <https://doi.org/10.1063/1.5016794> [Accessed: 27-10-2021].
- [376] W. J. Rogers, *Healthcare Sterilisation: Challenging Practices*. Shawbury, UK: Smithers Rapra, 2014, vol. 2.
- [377] R. S. Donofrio *et al.*, “Are we aware of microbial hotspots in our household?” *Journal of Environmental Health*, vol. 75, no. 2, pp. 12–19, 2012. [Online]. Available: <http://www.jstor.org/stable/26329462> [Accessed: 15-10-2018].
- [378] K. Page *et al.*, “Antimicrobial surfaces and their potential in reducing the role of the inanimate environment in the incidence of hospital-acquired infections,” *Journal of Materials Chemistry*, vol. 19, pp. 3819–3831, 2009. [Online]. Available: <http://dx.doi.org/10.1039/B818698G> [Accessed: 30-10-2018].
- [379] J. Hasan *et al.*, “Antibacterial surfaces: the quest for a new generation of biomaterials,” *Trends in Biotechnology*, vol. 31, no. 5, pp. 295–304, 2013. [Online]. Available: <https://doi.org/10.1016/j.tibtech.2013.01.017> [Accessed: 29-10-2018].

- [380] C. Adlhart *et al.*, “Surface modifications for antimicrobial effects in the healthcare setting: a critical overview,” *Journal of Hospital Infection*, vol. 99, no. 3, pp. 239–249, 2018. [Online]. Available: <https://doi.org/10.1016/j.jhin.2018.01.018> [Accessed: 15-10-2018].
- [381] V. Truong *et al.*, “Air-directed attachment of coccoid bacteria to the surface of superhydrophobic lotus-like titanium,” *Biofouling*, vol. 28, no. 6, pp. 539–550, 2012. [Online]. Available: <https://doi.org/10.1080/08927014.2012.694426> [Accessed: 30-10-2018].
- [382] H. Zhu *et al.*, “Adhesion behaviors on superhydrophobic surfaces,” *Chemical Communications*, vol. 50, pp. 3900–3913, 2014. [Online]. Available: <http://dx.doi.org/10.1039/C3CC47818A> [Accessed: 30-10-2018].
- [383] J. Jordan. (2016, Sep. 5) *The lotus leaf: how nature makes water-repellent materials*. [Online]. Available: <https://www.jeremyjordan.me/lotus-leaf-how-nature-makes-water-repellant-materials/> [Accessed: 5-11-2018].
- [384] W. Zhao *et al.*, “Grafting zwitterionic polymer brushes via electrochemical surface-initiated atomic-transfer radical polymerization for anti-fouling applications,” *Journal of Materials Chemistry B*, vol. 2, pp. 5352–5357, 2014. [Online]. Available: <http://dx.doi.org/10.1039/C4TB00816B> [Accessed: 5-11-2017].
- [385] C. Liu *et al.*, “Mitigation of biofilm development on thin-film composite membranes functionalized with zwitterionic polymers and silver nanoparticles,” *Environmental Science & Technology*, vol. 51, no. 1, pp. 182–191, 2017. [Online]. Available: <https://doi.org/10.1021/acs.est.6b03795> [Accessed: 30-10-2018].
- [386] L. Shen *et al.*, “Asymmetric free-standing film with multifunctional anti-bacterial and self-cleaning properties,” *ACS Applied Materials & Interfaces*, vol. 4, no. 9, pp. 4476–4483, 2012. [Online]. Available: <https://doi.org/10.1021/am301118f> [Accessed: 30-10-2018].
- [387] S. Pogodin *et al.*, “Biophysical model of bacterial cell interactions with nanopatterned cicada wing surfaces,” *Biophysical Journal*, vol. 104, no. 4, pp. 835–840, 2013. [Online]. Available: <https://doi.org/10.1016/j.bpj.2012.12.046> [Accessed: 30-10-2018].
- [388] K. Lewis and A. M. Klibanov, “Surpassing nature: rational design of sterile-surface materials,” *Trends in Biotechnology*, vol. 23, no. 7, pp. 343–348, 2005. [Online]. Available: <https://doi.org/10.1016/j.tibtech.2005.05.004>
- [389] Z. Hosseinioust *et al.*, “Bacterial capture efficiency and antimicrobial activity of phage-functionalized model surfaces,” *Langmuir*, vol. 27, no. 9, pp. 5472–5480, 2011. [Online]. Available: <https://doi.org/10.1021/la200102z> [Accessed: 6-11-2018].
- [390] E. P. Ivanova *et al.*, “Natural bactericidal surfaces: Mechanical rupture of pseudomonas aeruginosa cells by cicada wings,” *Small*, vol. 8, no. 16, pp. 2489–2494, 8 2012. [Online]. Available: <https://doi.org/10.1002/sml.201200528> [Accessed: 6-11-2018].
- [391] V. Kumar *et al.*, “Development of silver nanoparticle loaded antibacterial polymer mesh using plasma polymerization process,” *Journal of Biomedical Materials Research Part A*, vol. 101A, no. 4, pp. 1121–1132, 2013. [Online]. Available: <https://doi.org/10.1002/jbm.a.34419> [Accessed: 12-10-2017].
- [392] X. Laloyaux *et al.*, “Temperature-responsive polymer brushes switching from bactericidal to cell-repellent,” *Advanced Materials*, vol. 22, no. 44, pp. 5024–5028, 2010. [Online]. Available: <https://doi.org/10.1002/adma.201002538> [Accessed: 09-03-2021].
- [393] J. Yue *et al.*, “3D-printable antimicrobial composite resins,” *Advanced Functional Materials*, vol. 25, no. 43, pp. 6756–6767, 11 2015. [Online]. Available: <https://doi.org/10.1002/adfm.201502384> [Accessed: 15-02-2019].
- [394] M. van de Lagemaat *et al.*, “Comparison of methods to evaluate bacterial contact-killing materials,” *Acta Biomaterialia*, vol. 59, pp. 139–147, 2017. [Online]. Available: <https://doi.org/10.1016/j.actbio.2017.06.042> [Accessed: 15-10-2018].
- [395] Z. Hosseinioust *et al.*, “Going viral: Designing bioactive surfaces with bacteriophage,” *Colloids and Surfaces B: Biointerfaces*, vol. 124, pp. 2–16, 2014, biointerfaces: Global Perspectives. [Online]. Available: <https://doi.org/10.1016/j.colsurfb.2014.05.036> [Accessed: 6-11-2018].
- [396] D. Campoccia *et al.*, “A review of the biomaterials technologies for infection-resistant surfaces,” *Biomaterials*, vol. 34, no. 34, pp. 8533–8554, 2013. [Online]. Available: <https://doi.org/10.1016/j.biomaterials.2013.07.089> [Accessed: 26-10-2018].
- [397] J. A. Lemire *et al.*, “Antimicrobial activity of metals: mechanisms, molecular targets and applications,” *Nature Reviews Microbiology*, vol. 11, no. 6, pp. 371–384, 2013. [Online]. Available: <https://doi.org/10.1038/nrmicro3028> [Accessed: 08-11-2021].
- [398] V. V. Komnatny *et al.*, “Bacteria-triggered release of antimicrobial agents,” *Angewandte Chemie International Edition*, vol. 53, no. 2, pp. 439–441, 2014. [Online]. Available: <https://doi.org/10.1002/anie.201307975> [Accessed: 09-11-2021].
- [399] S. Liu *et al.*, “Antibacterial activity of graphite, graphite oxide, graphene oxide, and reduced graphene oxide: Membrane and oxidative stress,” *ACS Nano*, vol. 5, no. 9, pp. 6971–6980, 2011. [Online]. Available: <https://doi.org/10.1021/nn202451x> [Accessed: 12-06-2019].

- [400] Copper3D. (2017) *Antimicrobial performance*. [Online]. Available: <https://copper3d.com/antimicrobial-performance/> [Accessed: 15-11-2021].
- [401] J. M. Zuniga, “3D printed antibacterial prostheses,” *Applied Sciences*, vol. 8, no. 9, p. 1651, 2018. [Online]. Available: <https://doi.org/10.3390/app8091651> [Accessed: 10-07-2020].
- [402] J. M. Zuniga and M. Thompson, “Applications of antimicrobial 3D printing materials in space,” *Journal of 3D Printing in Medicine*, vol. 3, no. 1, pp. 5–9, 2019. [Online]. Available: <https://doi.org/10.2217/3dp-2019-0001> [Accessed: 10-07-2020].
- [403] A. Lo. (2019, Sep. 13) *NASA’s antimicrobial space challenge incites students to 3D print off-earth medical devices and space tools*. 3D Printing Industry. [Online]. Available: <https://3dprintingindustry.com/news/nasas-antimicrobial-space-challenge-invites-students-to-3d-print-off-earth-medical-devices-and-space-tools-161644/> [Accessed: 10-07-2020].
- [404] J. Y. Wong and A. C. Pfahnl, “3D printing of surgical instruments for long-duration space missions,” *Aviation, Space, and Environmental Medicine*, vol. 85, no. 7, pp. 758–763, 2014. [Online]. Available: <https://doi.org/10.3357/ASEM.3898.2014> [Accessed: 10-07-2020].
- [405] B. J. Tiimob *et al.*, “Nanoengineered eggshell–silver tailored copolyester polymer blend film with antimicrobial properties,” *Journal of agricultural and food chemistry*, vol. 65, no. 9, pp. 1967–1976, 2017. [Online]. Available: <https://doi.org/10.1021/acs.jafc.7b00133> [Accessed: 06-07-2020].
- [406] Z. Muwaffak *et al.*, “Patient-specific 3D scanned and 3D printed antimicrobial polycaprolactone wound dressings,” *International Journal of Pharmaceutics*, vol. 527, no. 1, pp. 161–170, 2017. [Online]. Available: <https://doi.org/10.1016/j.ijpharm.2017.04.077> [Accessed: 10-07-2020].
- [407] Y. Zhang *et al.*, “3D-printed bioceramic scaffolds with antibacterial and osteogenic activity,” *Biofabrication*, vol. 9, no. 2, p. 025037, 2017. [Online]. Available: <https://doi.org/10.1088%2F1758-5090%2F9a6ed6> [Accessed: 06-07-2020].
- [408] S. W. Pattinson and A. J. Hart, “Additive manufacturing of cellulosic materials with robust mechanics and antimicrobial functionality,” *Advanced Materials Technologies*, vol. 2, no. 4, p. 1600084, 2017. [Online]. Available: <https://doi.org/10.1002/admt.201600084> [Accessed: 19-10-2021].
- [409] D. Puppi *et al.*, “Levofloxacin-loaded star poly (ϵ -caprolactone) scaffolds by additive manufacturing,” *Journal of Materials Science: Materials in Medicine*, vol. 27, no. 3, p. 44, 2016. [Online]. Available: <https://doi.org/10.1007/s10856-015-5658-1> [Accessed: 06-07-2020].
- [410] N. Sandler *et al.*, “Towards fabrication of 3D printed medical devices to prevent biofilm formation,” *International Journal of Pharmaceutics*, vol. 459, no. 1, pp. 62–64, 2014. [Online]. Available: <https://doi.org/10.1016/j.ijpharm.2013.11.001> [Accessed: 06-07-2020].
- [411] M. Nagrath *et al.*, “Functionalized prosthetic interfaces using 3D printing: Generating infection-neutralizing prosthesis in dentistry,” *Materials Today Communications*, vol. 15, pp. 114–119, 2018. [Online]. Available: <https://doi.org/10.1016/j.mtcomm.2018.02.016> [Accessed: 28-08-2018].
- [412] Y. Yang *et al.*, “Anti-infective efficacy, cytocompatibility and biocompatibility of a 3D-printed osteoconductive composite scaffold functionalized with quaternized chitosan,” *Acta Biomaterialia*, vol. 46, pp. 112–128, 2016. [Online]. Available: <https://doi.org/10.1016/j.actbio.2016.09.035> [Accessed: 06-07-2020].
- [413] J. Wang *et al.*, “Stereolithographic (SLA) 3D printing of oral modified-release dosage forms,” *International Journal of Pharmaceutics*, vol. 503, no. 1, pp. 207–212, 2016. [Online]. Available: <https://doi.org/10.1016/j.ijpharm.2016.03.016> [Accessed: 06-07-2020].
- [414] Z. Li *et al.*, “Antimicrobial thiol–ene–acrylate photosensitive resins for DLP 3D printing,” *Photochemistry and Photobiology*, vol. 95, no. 5, pp. 1219–1229, 2019. [Online]. Available: <https://doi.org/10.1111/php.13099> [Accessed: 06-07-2020].
- [415] G. Taormina *et al.*, “Special resins for stereolithography: In situ generation of silver nanoparticles,” *Polymers*, vol. 10, no. 2, p. 212, 2018. [Online]. Available: <https://doi.org/10.3390/polym10020212> [Accessed: 06-07-2020].
- [416] W. Wu *et al.*, “A therapeutic delivery system for chronic osteomyelitis via a multi-drug implant based on three-dimensional printing technology,” *Journal of Biomaterials Applications*, vol. 31, no. 2, pp. 250–260, 2016. [Online]. Available: <https://doi.org/10.1177/0885328216640660> [Accessed: 06-07-2020].
- [417] J. A. Inzana *et al.*, “3D printed bioceramics for dual antibiotic delivery to treat implant-associated bone infection,” *European cells & materials*, vol. 30, pp. 232–247, 2015. [Online]. Available: <https://doi.org/10.22203/eCM.v030a16> [Accessed: 06-07-2020].
- [418] S. C. Cox *et al.*, “Adding functionality with additive manufacturing: Fabrication of titanium-based antibiotic eluting implants,” *Materials Science and Engineering: C*, vol. 64, pp. 407–415, 2016. [Online]. Available: <https://doi.org/10.1016/j.msec.2016.04.006> [Accessed: 06-07-2020].
- [419] C. Han *et al.*, “Electrophoretic deposition of gentamicin-loaded silk fibroin coatings on 3D-printed porous cobalt–chromium–molybdenum bone substitutes to prevent orthopedic implant infections,” *Biomacromolecules*, vol. 18, no. 11, pp. 3776–3787, 2017. [Online]. Available: <https://doi.org/10.1021/acs.biomac.7b01091> [Accessed: 06-07-2020].

- [420] A. Maandi *et al.*, “OsteoFab technology,” Oxford Performance Materials, South Windsor, Connecticut, Whitepaper, 2020. [Online]. Available: <https://oxfordpm.com/osteofab-technology> [Accessed: 06-07-2020].
- [421] M. Wang *et al.*, “Antibacterial properties of PEKK for orthopedic applications,” *International journal of nanomedicine*, vol. 12, pp. 6471–6476, 2017. [Online]. Available: <http://doi.org/10.2147/IJN.S134983> [Accessed: 14-12-2017].
- [422] Y. Lin *et al.*, “Combination of polyetherketoneketone scaffold and human mesenchymal stem cells from temporomandibular joint synovial fluid enhances bone regeneration,” *Scientific reports*, vol. 9, no. 1, pp. 1–13, 2019. [Online]. Available: <https://doi.org/10.1038/s41598-018-36778-2> [Accessed: 06-07-2020].
- [423] C. Adamzyk *et al.*, “Bone tissue engineering using polyetherketoneketone scaffolds combined with autologous mesenchymal stem cells in a sheep calvarial defect model,” *Journal of Cranio-Maxillofacial Surgery*, vol. 44, no. 8, pp. 985–994, 2016. [Online]. Available: <https://doi.org/10.1016/j.jcms.2016.04.012> [Accessed: 06-07-2020].
- [424] M. G. Roskies *et al.*, “Three-dimensionally printed polyetherketoneketone scaffolds with mesenchymal stem cells for the reconstruction of critical-sized mandibular defects,” *The Laryngoscope*, vol. 127, no. 11, pp. E392–E398, 2017. [Online]. Available: <https://doi.org/10.1002/lary.26781> [Accessed: 06-07-2020].
- [425] S. Chernousova and M. Epple, “Silver as antibacterial agent: Ion, nanoparticle, and metal,” *Angewandte Chemie International Edition*, vol. 52, no. 6, pp. 1636–1653, 2013. [Online]. Available: <http://dx.doi.org/10.1002/anie.201205923> [Accessed: 27-10-2017].
- [426] H. Palza, “Antimicrobial polymers with metal nanoparticles,” *International Journal of Molecular Sciences*, vol. 16, no. 1, pp. 2099–2116, 2015. [Online]. Available: <https://doi.org/10.3390/ijms16012099> [Accessed: 19-10-2021].
- [427] J. S. Möhler *et al.*, “Silver bullets: A new lustre on an old antimicrobial agent,” *Biotechnology Advances*, vol. 36, no. 5, pp. 1391–1411, 2018. [Online]. Available: <https://doi.org/10.1016/j.biotechadv.2018.05.004> [Accessed: 06-07-2020].
- [428] M. Cloutier *et al.*, “Antibacterial coatings: Challenges, perspectives, and opportunities,” *Trends in Biotechnology*, vol. 33, no. 11, pp. 637–652, 2015. [Online]. Available: <https://doi.org/10.1016/j.tibtech.2015.09.002> [Accessed: 31-10-2017].
- [429] F. Paladini *et al.*, “Efficacy of silver treated catheters for haemodialysis in preventing bacterial adhesion,” *Journal of Materials Science: Materials in Medicine*, vol. 23, no. 8, pp. 1983–1990, 2012. [Online]. Available: <https://doi.org/10.1007/s10856-012-4674-7> [Accessed: 15-10-2018].
- [430] C. Rigo *et al.*, “Characterization and evaluation of silver release from four different dressings used in burns care,” *Burns*, vol. 38, no. 8, pp. 1131–1142, 2012. [Online]. Available: <https://doi.org/10.1016/j.burns.2012.06.013> [Accessed: 15-10-2018].
- [431] N. Gugala *et al.*, “Using a chemical genetic screen to enhance our understanding of the antibacterial properties of silver,” *Genes*, vol. 9, no. 7, 2018. [Online]. Available: <http://dx.doi.org/10.3390/genes9070344> [Accessed: 12-10-2018].
- [432] M. Salas-Orozco *et al.*, “Mechanisms of resistance to silver nanoparticles in endodontic bacteria: A literature review,” *Journal of Nanomaterials*, vol. 2019, 2019. [Online]. Available: <https://doi.org/10.1155/2019/7630316> [Accessed: 22-02-2019].
- [433] A. A. d. Lima e Silva *et al.*, “Heavy metal tolerance (cr, ag and hg) in bacteria isolated from sewage,” *Brazilian Journal of Microbiology*, vol. 43, no. 4, pp. 1620–1631, 2012. [Online]. Available: <http://dx.doi.org/10.1590/S1517-83822012000400047> [Accessed: 30-10-2018].
- [434] R. Kumar and H. Münstedt, “Silver ion release from antimicrobial polyamide/silver composites,” *Biomaterials*, vol. 26, no. 14, pp. 2081–2088, 2005. [Online]. Available: <https://doi.org/10.1016/j.biomaterials.2004.05.030> [Accessed: 31-10-2017].
- [435] R. Kumar and H. Münstedt, “Polyamide/silver antimicrobials: effect of crystallinity on the silver ion release,” *Polymer International*, vol. 54, no. 8, pp. 1180–1186, 2005. [Online]. Available: <http://dx.doi.org/10.1002/pi.1828> [Accessed: 31-10-2017].
- [436] R. Kumar *et al.*, “Polyamide/silver antimicrobials: Effect of filler types on the silver ion release,” *Journal of Biomedical Materials Research Part B: Applied Biomaterials*, vol. 75B, no. 2, pp. 311–319, 2005. [Online]. Available: <http://dx.doi.org/10.1002/jbm.b.30306> [Accessed: 31-10-2017].
- [437] C. Radheshkumar and H. Münstedt, “Morphology and mechanical properties of antimicrobial polyamide/silver composites,” *Materials Letters*, vol. 59, no. 14, pp. 1949–1953, 2005. [Online]. Available: <https://doi.org/10.1016/j.matlet.2005.02.033> [Accessed: 6-11-2017].
- [438] C. Damm *et al.*, “Long-term antimicrobial polyamide 6/silver-nanocomposites,” *Journal of Materials Science*, vol. 42, no. 15, pp. 6067–6073, 2007. [Online]. Available: <https://doi.org/10.1007/s10853-006-1158-5> [Accessed: 3-11-3017].
- [439] C. Damm and H. Münstedt, “Kinetic aspects of the silver ion release from antimicrobial polyamide/silver nanocomposites,” *Applied Physics A*, vol. 91, no. 3, pp. 479–486, 2008. [Online]. Available: <https://doi.org/10.1007/s00339-008-4434-1> [Accessed: 6-11-2017].

- [440] C. Damm *et al.*, “The antimicrobial efficacy of polyamide 6/silver-nano- and microcomposites,” *Materials Chemistry and Physics*, vol. 108, no. 1, pp. 61–66, 2008. [Online]. Available: <https://doi.org/10.1016/j.matchemphys.2007.09.002> [Accessed: 31-10-2017].
- [441] D. W. Van Krevelen and K. Te Nijenhuis, “Properties determining mass transfer in polymeric systems,” in *Properties of polymers: their correlation with chemical structure; their numerical estimation and prediction from additive group contributions*. Elsevier Science & Technology, 2009, ch. 18, pp. 655–663. [Online]. Available: <https://ebookcentral.proquest.com/lib/sheffield/detail.action?docID=428577> [Accessed: 14-10-2021].
- [442] W. Griehl and D. Ruestem, “Nylon-12-preparation, properties, and applications,” *Industrial & Engineering Chemistry*, vol. 62, no. 3, pp. 16–22, 1970. [Online]. Available: <https://pubs.acs.org/doi/pdf/10.1021/ie50723a005> [Accessed: 14-05-2018].
- [443] K. Pathmanathan *et al.*, “The dielectric properties of dry and water-saturated nylon-12,” *Journal of Polymer Science Part B: Polymer Physics*, vol. 30, no. 4, pp. 341–348, 1992. [Online]. Available: <https://doi.org/10.1002/polb.1992.090300404> [Accessed: 14-05-2018].
- [444] K. Yoshida *et al.*, “Characterization and inhibitory effect of antibacterial dental resin composites incorporating silver-supported materials,” *Journal of Biomedical Materials Research*, vol. 47, no. 4, pp. 516–522, 1999. [Online]. Available: [https://doi.org/10.1002/\(SICI\)1097-4636\(19991215\)47:4<516::AID-JBM7>3.0.CO;2-E](https://doi.org/10.1002/(SICI)1097-4636(19991215)47:4<516::AID-JBM7>3.0.CO;2-E) [Accessed: 14-12-2021].
- [445] J. R. Wingham *et al.*, “Tailored additives for incorporation of antibacterial functionality into laser sintered parts,” *Frontiers in Biomaterials Science*, vol. 1, p. 929006, 2022. [Online]. Available: <https://doi.org/10.3389/fbiom.2022.929006> [Accessed: 08-07-2022].
- [446] A. M. Mulligan *et al.*, “Effect of increasing silver content in phosphate-based glasses on biofilms of *Streptococcus sanguis*,” *Journal of Biomedical Materials Research Part A*, vol. 67A, no. 2, pp. 401–412, 2003. [Online]. Available: <https://doi.org/10.1002/jbm.a.10052> [Accessed: 11-10-2021].
- [447] H. L. Johnston *et al.*, “The solubility of silver oxide in water, in alkali and in alkaline salt solutions. the amphoteric character of silver hydroxide,” *Journal of the American Chemical Society*, vol. 55, no. 6, pp. 2311–2325, 1933. [Online]. Available: <https://pubs.acs.org/doi/pdf/10.1021/ja01333a016> [Accessed: 13-10-2021].
- [448] I. Ahmed *et al.*, “Antimicrobial effect of silver-doped phosphate-based glasses,” *Journal of Biomedical Materials Research Part A*, vol. 79A, no. 3, pp. 618–626, 2006. [Online]. Available: <https://doi.org/10.1002/jbm.a.30808> [Accessed: 09-07-2019].
- [449] I. Ahmed *et al.*, “The structure and properties of silver-doped phosphate-based glasses,” *Journal of Materials Science*, vol. 42, no. 23, pp. 9827–9835, 2007. [Online]. Available: <https://doi.org/10.1007/s10853-007-2008-9> [Accessed: 09-07-2019].
- [450] R. M. Moss *et al.*, “Structural characteristics of antibacterial bioresorbable phosphate glass,” *Advanced Functional Materials*, vol. 18, no. 4, pp. 634–639, 2008. [Online]. Available: <https://doi.org/10.1002/adfm.200700721> [Accessed: 11-10-2021].
- [451] R. D. Turner, J. R. Wingham *et al.*, “Use of silver-based additives for the development of antibacterial functionality in laser sintered polyamide 12 parts,” *Scientific Reports*, vol. 10, p. 892, 2020. [Online]. Available: <https://doi.org/10.1038/s41598-020-57686-4> [Accessed: 21-1-2020].
- [452] R. D. Turner, J. R. Wingham *et al.*, “Data relating to use of silver-based additives for the development of antibacterial functionality in laser sintered polyamide 12 parts,” 2020. [Online]. Available: <https://doi.org/10.15131/shef.data.11861430.v1> [Accessed: 23-2-2020].
- [453] J. Wingham *et al.*, “Data relating to micro-CT for analysis of laser sintered micro-composites,” 2020. [Online]. Available: <https://doi.org/10.15131/shef.data.11591283.v1> [Accessed: 28-1-2020].
- [454] *Standard Test Method for Tensile Properties of Plastics*, ASTM International Std. ASTM ISO/ASTM52 900-15, 2014. [Online]. Available: <https://doi.org/10.1520/D0638-14> [Accessed: 2-02-2018].
- [455] *ASTM E1570-11 Standard Practice for Computed Tomographic (CT) Examination*, ASTM International Std. ASTM E1570-11, 2011. [Online]. Available: <https://doi.org/10.1520/E1570-11> [Accessed: 25-10-2019].
- [456] M. Meyers and K. Chawla, “Fracture: Macroscopic aspects,” in *Mechanical behavior of materials*, 2nd ed. Cambridge; New York: Cambridge University Press, 2009, ch. 7, pp. 404–465.
- [457] T. Brugo *et al.*, “Fracture mechanics of laser sintered cracked polyamide for a new method to induce cracks by additive manufacturing,” *Polymer Testing*, vol. 50, pp. 301–308, 2016. [Online]. Available: <https://doi.org/10.1016/j.polymertesting.2016.01.024> [Accessed: 13-09-2018].
- [458] A. C. Jones *et al.*, “The correlation of pore morphology, interconnectivity and physical properties of 3D ceramic scaffolds with bone ingrowth,” *Biomaterials*, vol. 30, no. 7, pp. 1440–1451, 2009. [Online]. Available: <https://doi.org/10.1016/j.biomaterials.2008.10.056> [Accessed: 08-10-2019].
- [459] W. E. Lorensen and H. E. Cline, “Marching cubes: A high resolution 3D surface construction algorithm,” *SIGGRAPH Comput. Graph.*, vol. 21, no. 4, pp. 163–169, 1987. [Online]. Available: <http://doi.acm.org/10.1145/37402.37422> [Accessed: 05-09-2018].

- [460] Bruker. (2018) *Morphometric parameters measured by Skyscan CT-analyser software*. [Online]. Available: <http://bruker-microct.com/next/CTAn03.pdf> [Accessed: 20-09-2018].
- [461] A. J. Baddeley *et al.*, “Analysis of a three-dimensional point pattern with replication,” *Journal of the Royal Statistical Society. Series C (Applied Statistics)*, vol. 42, no. 4, pp. 641–668, 1993. [Online]. Available: <http://www.jstor.org/stable/2986181> [Accessed: 25-09-2018].
- [462] Formlabs, “Guide to selective laser sintering (SLS) 3D printing,” Formlabs, Whitepaper, 2022. [Online]. Available: <https://formlabs.com/uk/blog/what-is-selective-laser-sintering/> [Accessed: 17-06-2022].
- [463] Ricoh Europe. (2020) *PA12 selective laser sintering (SLS)*. [Online]. Available: <https://rapidfab.ricoh-europe.com/wp-content/uploads/2020/10/Ricoh-TDS-SLS-PA12-FInal-Web.pdf> [Accessed: 17-06-2022].
- [464] M. Omran, “3D printing polymer – ceramic composites for orbital floor reconstruction,” Ph.D. thesis, University of Sheffield, 2021. [Online]. Available: <https://etheses.whiterose.ac.uk/29201/> [Accessed: 04-11-2021].
- [465] F. Pfefferkorn and J. Weilhammer, “Open and flexible: Eos part property management provides both individualization and standardization,” EOS GmbH, Munich, Germany, Whitepaper, 2017. [Online]. Available: https://cdn0.scrvt.com/eos/7e99ba072eca9ad8/305801d70a4a/EOS-Whitepaper_EN_V2_Web.pdf [Accessed: 01-05-2020].
- [466] *Standard Test Method for Water Absorption of Plastics*, ASTM International Std. ASTM D570-98(2010)e1, 2010. [Online]. Available: <https://doi.org/10.1520/D0570-98R10E01> [Accessed: 18-04-2018].
- [467] *Plastics – Determination of water absorption*, The British Standards Institution Std. BS EN ISO 62:2008, 2008. [Online]. Available: <https://bsol.bsigroup.com/Bibliographic/BibliographicInfoData/00000000030172707> [Accessed: 15-05-2018].
- [468] J. Crank, “Diffusion in a sphere,” in *The Mathematics of Diffusion*, 2nd ed. Oxford: Clarendon Press, 1975, ch. 6, pp. 89–103.
- [469] A. P. Terzyk and P. A. Gauden, “The simple procedure of the calculation of diffusion coefficient for adsorption on spherical and cylindrical adsorbent particles,” *Separation Science and Technology*, vol. 36, no. 4, pp. 513–525, 2001. [Online]. Available: <https://doi.org/10.1081/SS-100102943> [Accessed: 18-05-2018].
- [470] Innovotech. (2019) *MBEC Assay Procedural Manual*. [Online]. Available: <https://www.innovotech.ca/wp-content/uploads/2020/01/MBEC-Procedural-Manual-v2.1-3.pdf> [Accessed: 18-06-2021].
- [471] O. Gordon *et al.*, “Silver coordination polymers for prevention of implant infection: Thiol interaction, impact on respiratory chain enzymes, and hydroxyl radical induction,” *Antimicrobial Agents and Chemotherapy*, vol. 54, no. 10, pp. 4208–4218, 2010. [Online]. Available: <https://doi.org/10.1128/AAC.01830-09> [Accessed: 15-10-2018].
- [472] A. A. Ahmed *et al.*, “Glass-forming compositions and physicochemical properties of degradable phosphate and silver-doped phosphate glasses in the P2O5-CaO-Na2O-Ag2O system,” *Journal of Materials Research and Technology*, vol. 8, no. 1, pp. 1003–1013, 2019, [Accessed: 17-06-2022].
- [473] I.-H. Lee *et al.*, “Effects of magnesium content on the physical, chemical and degradation properties in a MgO-CaO-Na2O-P2O5 glass system,” *Journal of Non-Crystalline Solids*, vol. 363, pp. 57–63, 2013. [Online]. Available: <https://doi.org/10.1016/j.jnoncrysol.2012.11.036> [Accessed: 24-1-2022].
- [474] H. Gao *et al.*, “Effect of composition on the release kinetics of phosphate controlled release glasses in aqueous medium,” *Journal of Controlled Release*, vol. 96, no. 1, pp. 21–28, 2004. [Online]. Available: <https://doi.org/10.1016/j.jconrel.2003.12.030> [Accessed: 24-1-2022].
- [475] N. Sharmin *et al.*, “Effect of boron oxide addition on fibre drawing, mechanical properties and dissolution behaviour of phosphate-based glass fibres with fixed 40, 45 and 50 mol% P2O5,” *Journal of Biomaterials Applications*, vol. 29, no. 5, pp. 639–653, 2014. [Online]. Available: <https://doi.org/10.1177/0885328214539824> [Accessed: 17-06-2022].
- [476] PubChem. (2020) *PubChem Periodic Table of Elements*. National Center for Biotechnology Information. [Online]. Available: <https://pubchem.ncbi.nlm.nih.gov/periodic-table/> [Accessed: 25-11-2020].
- [477] *Standard Test Method for Quantification of Pseudomonas aeruginosa Biofilm Grown Using Drip Flow Biofilm Reactor with Low Shear and Continuous Flow*, ASTM International Std. ASTM E2647-13, 2017. [Online]. Available: <https://doi.org/10.1520/E2647-13> [Accessed: 19-04-2018].
- [478] *Standard Test Method for Quantification of Pseudomonas aeruginosa Biofilm Grown with High Shear and Continuous Flow using CDC Biofilm Reactor*, ASTM International Std. ASTM E2562-17, 2017. [Online]. Available: <https://doi.org/10.1520/E2562-17> [Accessed: 19-04-2018].
- [479] The University of Sheffield. (2020, Jan. 21) *Sheffield scientists create 3D printed parts that can kill bacteria*. [Online]. Available: <https://www.sheffield.ac.uk/news/nr/3d-printed-parts-kill-bacteria-antibacterial-printing-manufacturing-research-1.879078> [Accessed: 29-06-2020].
- [480] TCT Magazine. (2020, Jan. 21) *University of Sheffield researchers 3D print antibacterial parts*. [Online]. Available: <https://www.tctmagazine.com/additive-manufacturing-3d-printing-news/university-of-sheffield-3d-print-antibacterial-parts/> [Accessed: 29-06-2020].

- [481] T. Vialva. (2020, Jan. 22) *Researchers develop 3D printed parts to fight infectious diseases*. 3D Printing Industry. [Online]. Available: <https://3dprintingindustry.com/news/researchers-develop-3d-printed-parts-to-fight-infectious-diseases-167571> [Accessed: 29-06-2020].
- [482] J. Chadwick. (2020, Jan. 21) *3D-printed anti-bacterial smartphone cases could help to stop the spread of superbugs like MRSA, scientists claim*. The Daily Mail. [Online]. Available: <https://www.dailymail.co.uk/sciencetech/article-7912565/3D-printed-anti-bacterial-smartphone-cases-help-stop-spread-superbugs-like-MRSA.html> [Accessed: 29-06-2020].

Appendix A

Laser Sintering Builds and Detailed Protocols

A.1 Laser Sintering Build Details

Descriptions of all builds carried out throughout this project can be found in Table A.1, with examples of some of the layouts used shown in Figures A.1 and A.2. Note that all of the tensile test specimens (Dogbones) were printed in the same orientation to ensure comparability between builds.

For all builds, the 3D CAD was first created using either Solidworks or Fusion 360. The .stl files were subsequently arranged and labelled (where necessary) using Magics 22.0. These were all built using an EOS Formiga P100, using the accompanying software to slice the arranged build files and transfer them to the machine.

| No. | Build Name | Material | Parameters | Description |
|-----|---------------|----------------------|------------|---|
| 1 | LS_2018_01_15 | 50/50 PA2200 | Standard | 150 Discs, 5 Dogbones |
| 2 | LS_2018_01_16 | Used PA2200 | Standard | 150 Discs, 5 Dogbones |
| 3 | LS_2018_01_17 | PA2200 | Standard | 150 Discs, 5 Dogbones |
| 4 | LS_2018_02_22 | Used PA2200 | Standard | 132 Pegs, Cage v2, 90 Pegs (48WP) |
| 5 | LS_2018_02_26 | PA2200 | Std. NC | 120 Discs, 132 Pegs, 5 Dogbones |
| 6 | LS_2018_02_27 | PA2200 – 0.3% B65003 | Std. NC | 120 Discs, 132 Pegs, 5 Dogbones |
| 7 | LS_2018_02_28 | PA2200 – 0.3% B45003 | Std. NC | 120 Discs, 132 Pegs, 5 Dogbones |
| 8 | LS_2018_03_01 | PA2200 – 0.5% B65003 | Std. NC | 120 Discs, 132 Pegs, 5 Dogbones |
| 9 | LS_2018_03_02 | PA2200 – 1% B65003 | Std. NC | 120 Discs, 132 Pegs <i>Note: Build failed during Dogbones (unrelated to material)</i> |
| 10 | LS_2018_04_30 | PA2200 | Std. NC | 280 Spheres, 72 Discs, 5 Dogbones, 156 Pegs, 24 Dry Test Slides, 12×1 cm ³ Cubes, 12×5 mm Cylinders |
| 11 | LS_2018_05_01 | PA2200 – 1% B65003 | Std. NC | 280 Spheres, 72 Discs, 5 Dogbones, 156 Pegs, 24 Dry Test Slides, 12×1 cm ³ Cubes, 12×5 mm Cylinders |
| 12 | LS_2018_05_02 | PA2200 – 1% B45003 | Std. NC | 280 Spheres, 72 Discs, 5 Dogbones, 156 Pegs, 24 Dry Test Slides, 12×1 cm ³ Cubes, 12×5 mm Cylinders |
| 13 | LS_2018_10_19 | 50/50 PA2200 | Standard | 12 Dogbones (as part of a bigger build) |
| 14 | LS_2018_11_09 | 50/50 PA2200 | Standard | 45 Dogbones (as part of a bigger build) |
| 15 | LS_2019_03_04 | PA2200 | Std. NC | Effect of geometry ellipsoids – 45× A , 40× B , 40× C , 40× D , 30× E , 30× F |
| 16 | LS_2019_03_06 | PA2200 – 1% B65003 | Std. NC | Effect of geometry ellipsoids – 45× A , 40× B , 40× C , 40× D , 30× E , 30× F |

Table A.1 *continued overleaf*

Table A.1 *continued*

| No. | Build Name | Material | Parameters | Description |
|-----|----------------|------------------|------------|--|
| 17 | LS_2020_09_03 | PA2200 – 1% PBG2 | Std. NC | 5 Dogbones, 21 Spheres, 24 Discs, 6 Cylinders, 6 Cubes. <i>Note: Build failed after Dogbones</i> |
| 18 | LS_2020_09_04 | PA2200 – 1% PBG2 | Std. NC | 5 Dogbones, 16 Spheres |
| 19 | LS_2020_09_08a | PA2200 – 1% PBG1 | Std. NC | 5 Dogbones, 16 Spheres. <i>Note: Build failed during Dogbones</i> |
| 20 | LS_2020_09_08b | PA2200 – 1% PBG1 | Std. NC | 5 Dogbones, 16 Spheres. <i>Note: Build failed during Dogbones</i> |
| 21 | LS_2020_11_30 | PA2200 | Std. NC | 5 Dogbones, 50 Spheres, 4 Tiles (for SEM/EDX) |
| 22 | LS_2020_12_01 | PA2200 – 1% P40 | Std. NC | 5 Dogbones, 50 Spheres, 4 Tiles (for SEM/EDX) |
| 23 | LS_2020_12_02 | PA2200 – 1% P45 | Std. NC | 5 Dogbones, 50 Spheres, 4 Tiles (for SEM/EDX) |
| 24 | LS_2020_12_03 | PA2200 – 1% P50 | Std. NC | 5 Dogbones, 50 Spheres, 4 Tiles (for SEM/EDX) |

Table A.1: List of all builds completed, all PA2200 is virgin unless otherwise stated.

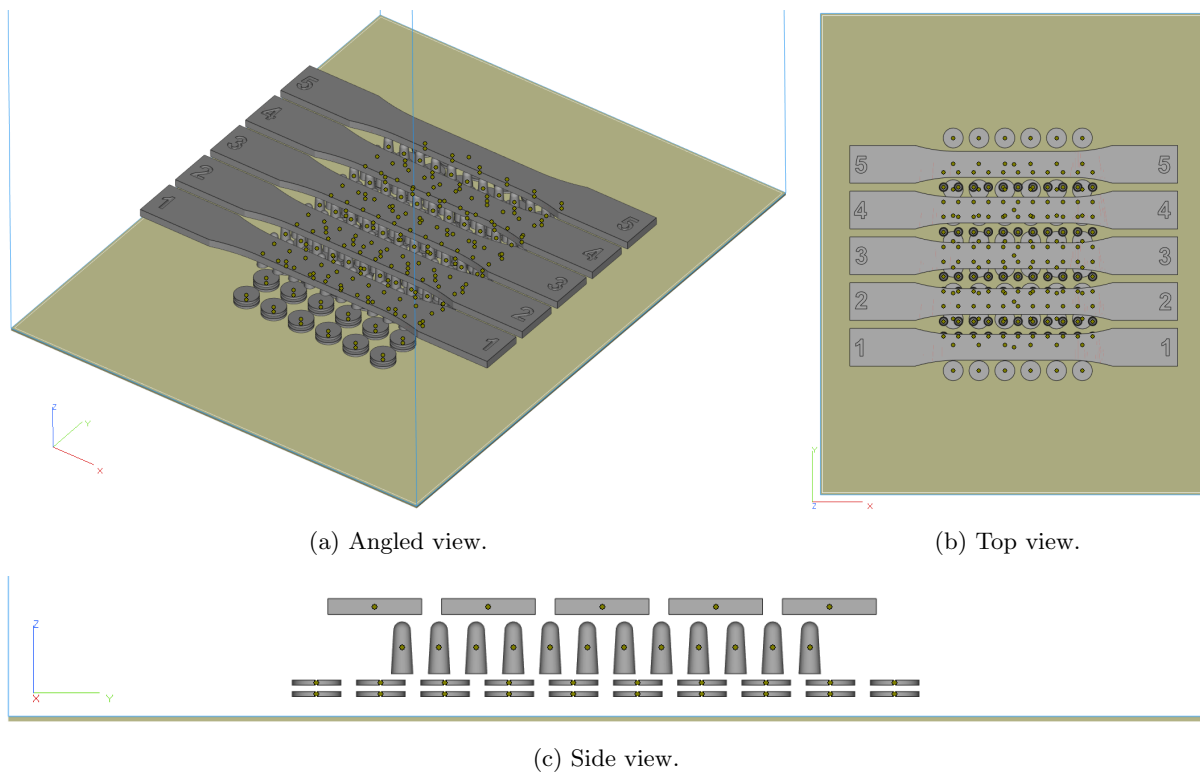
 Ω 

Figure A.1: Views of builds 5–8 created in Magics 22.0. This included 120 Discs, 132 Pegs, and 5 Dogbones.

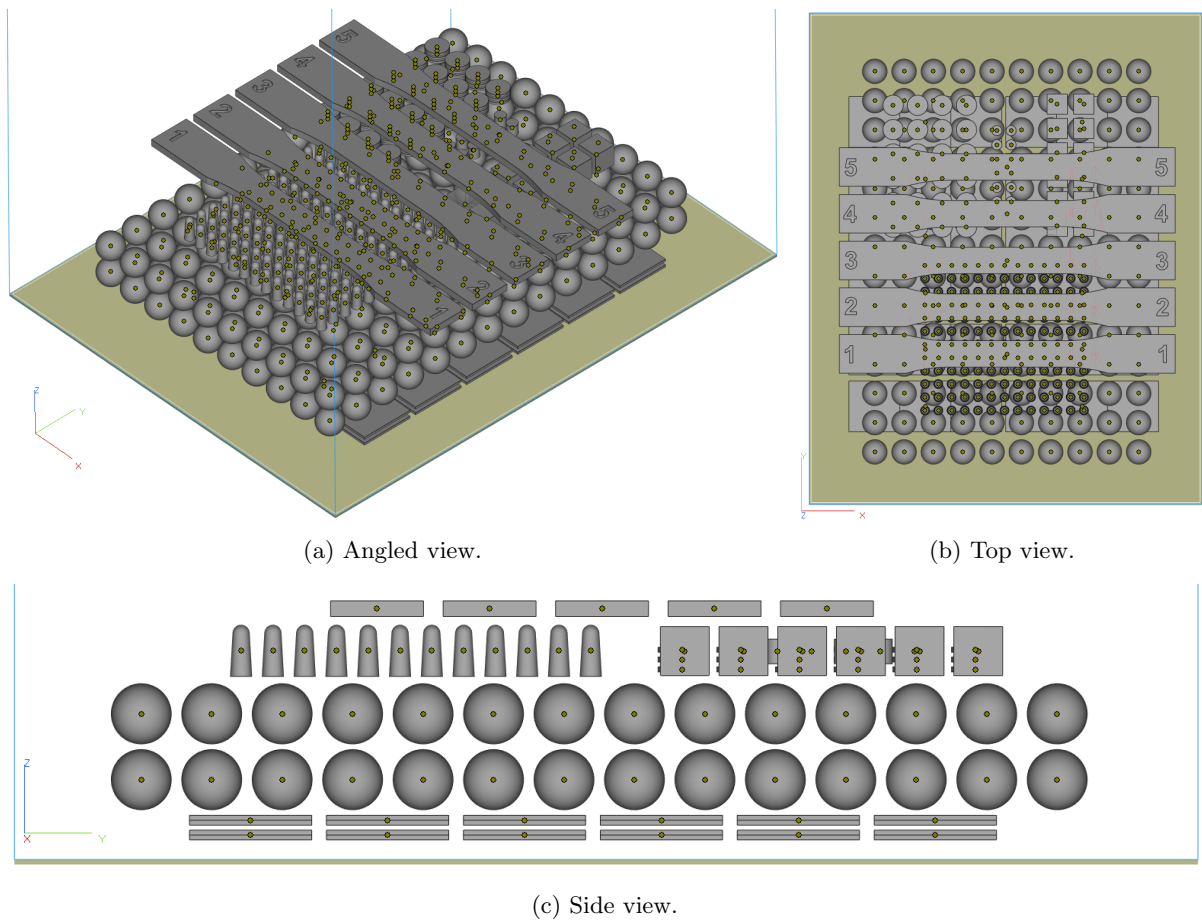


Figure A.2: Views of builds 10–12 created in Magics 22.0. This included 280 Spheres, 72 Discs, 5 Dogbones, 156 Pegs, 24 Dry Test Slides, $12 \times 1 \text{ cm}^3$ Cubes, and $12 \times 5 \text{ mm}$ Cylinders.

A.2 Part Dimensions

Dimensions of printed test specimens are shown in this section, with mean dimensions shown for each geometry per build.

| Build | Material | Width / mm | Thickness / mm | Area $\times 10^5$ / mm ² |
|-----------------|----------------------|------------------|-----------------|--------------------------------------|
| LS_2018_01_15 | 50/50 PA2200 | 12.95 \pm 0.02 | 3.29 \pm 0.02 | 4.26 \pm 0.02 |
| LS_2018_01_16 | Used PA2200 | 12.68 \pm 0.04 | 3.23 \pm 0.03 | 4.10 \pm 0.02 |
| LS_2018_01_17 | PA2200 | 13.05 \pm 0.05 | 3.30 \pm 0.01 | 4.31 \pm 0.02 |
| LS_2018_02_26 | PA2200 | 12.63 \pm 0.05 | 3.42 \pm 0.01 | 4.32 \pm 0.01 |
| LS_2018_02_27 | PA2200 + 0.3% B65003 | 12.64 \pm 0.04 | 3.41 \pm 0.02 | 4.32 \pm 0.03 |
| LS_2018_02_28 | PA2200 + 0.3% B45003 | 12.64 \pm 0.02 | 3.41 \pm 0.01 | 4.31 \pm 0.02 |
| LS_2018_03_01 | PA2200 + 0.5% B65003 | 12.59 \pm 0.07 | 3.31 \pm 0.08 | 4.18 \pm 0.12 |
| LS_2018_04_30 | PA2200 | 12.57 \pm 0.02 | 3.37 \pm 0.02 | 4.24 \pm 0.03 |
| LS_2018_05_01 | PA2200 + 1.0% B65003 | 12.59 \pm 0.03 | 3.36 \pm 0.01 | 4.23 \pm 0.02 |
| LS_2018_05_02 | PA2200 + 1.0% B45003 | 12.69 \pm 0.03 | 3.42 \pm 0.01 | 4.34 \pm 0.01 |
| LS_2018_10_19 | 50/50 PA2200 | 13.09 \pm 0.06 | 3.39 \pm 0.02 | 4.44 \pm 0.03 |
| LS_2018_11_09_A | 50/50 PA2200 | 12.95 \pm 0.02 | 3.25 \pm 0.01 | 4.20 \pm 0.02 |
| LS_2018_11_09_B | 50/50 PA2200 | 12.94 \pm 0.06 | 3.33 \pm 0.01 | 4.31 \pm 0.02 |
| LS_2018_11_09_C | 50/50 PA2200 | 12.91 \pm 0.03 | 3.23 \pm 0.01 | 4.18 \pm 0.02 |
| LS_2018_11_09_D | 50/50 PA2200 | 12.92 \pm 0.03 | 3.33 \pm 0.02 | 4.30 \pm 0.03 |
| LS_2018_11_09_E | 50/50 PA2200 | 12.94 \pm 0.02 | 3.33 \pm 0.01 | 4.31 \pm 0.01 |
| LS_2018_11_09_F | 50/50 PA2200 | 12.91 \pm 0.02 | 3.32 \pm 0.01 | 4.29 \pm 0.02 |
| LS_2018_11_09_G | 50/50 PA2200 | 12.92 \pm 0.03 | 3.23 \pm 0.01 | 4.18 \pm 0.03 |
| LS_2018_11_09_H | 50/50 PA2200 | 12.95 \pm 0.08 | 3.33 \pm 0.01 | 4.32 \pm 0.03 |
| LS_2018_11_09_J | 50/50 PA2200 | 12.94 \pm 0.07 | 3.32 \pm 0.01 | 4.30 \pm 0.03 |
| LS_2020_11_30 | PA2200 | 12.73 \pm 0.03 | 3.31 \pm 0.01 | 4.21 \pm 0.02 |
| LS_2020_12_01 | PA2200 + 1% P40 | 12.65 \pm 0.03 | 3.29 \pm 0.01 | 4.16 \pm 0.02 |
| LS_2020_12_02 | PA2200 + 1% P45 | 12.65 \pm 0.02 | 3.29 \pm 0.02 | 4.16 \pm 0.03 |
| LS_2020_12_03 | PA2200 + 1% P50 | 12.62 \pm 0.01 | 3.30 \pm 0.01 | 4.16 \pm 0.02 |

Table A.2: Dimensions of tensile test specimens (mean \pm standard deviation), all PA2200 is virgin unless otherwise stated. For each specimen, 3 width measurements and 3 thickness measurements were taken, with the mean values used.

| Build | Material | Length / mm | Base Diameter / mm |
|---------------|-------------|------------------|--------------------|
| LS_2018_02_26 | PA2200 | 10.54 \pm 0.01 | 3.92 \pm 0.01 |
| LS_2018_02_28 | 0.3% B45003 | 10.54 \pm 0.02 | 3.93 \pm 0.01 |
| LS_2018_02_27 | 0.3% B65003 | 10.56 \pm 0.02 | 3.92 \pm 0.01 |
| LS_2018_03_01 | 0.5% B65003 | 10.51 \pm 0.02 | 3.93 \pm 0.01 |
| LS_2018_03_02 | 1.0% B65003 | 10.55 \pm 0.03 | 3.96 \pm 0.01 |

Table A.3: Measured dimensions of the printed pegs (mean \pm standard deviation), all PA2200 is virgin unless otherwise stated. 15 pegs were chosen at random from each build, with 3 length and 3 diameter measurements taken for each peg, with the mean values used.

| Build | Material | d_S / mm | A_S / mm ² | V_S / mm ³ |
|---------------|--------------------|------------------|-------------------------|-------------------------|
| LS_2018_04_30 | PA2200 | 12.13 \pm 0.04 | 462.1 \pm 3.4 | 934.2 \pm 10.4 |
| LS_2018_05_01 | PA2200 + 1% B65003 | 12.13 \pm 0.04 | 462.3 \pm 2.7 | 934.6 \pm 8.1 |
| LS_2018_05_02 | PA2200 + 1% B45003 | 12.15 \pm 0.05 | 463.6 \pm 3.4 | 938.5 \pm 10.5 |
| LS_2020_12_01 | PA2200 + 1% P40 | 12.12 \pm 0.05 | 461.7 \pm 3.6 | 932.9 \pm 10.9 |
| LS_2020_12_02 | PA2200 + 1% P45 | 12.13 \pm 0.04 | 462.0 \pm 3.3 | 933.7 \pm 10.1 |
| LS_2020_12_03 | PA2200 + 1% P50 | 12.16 \pm 0.06 | 464.7 \pm 4.7 | 941.9 \pm 14.2 |

Table A.4: Measured dimensions of the printed spheres (mean \pm standard deviation), all PA2200 is virgin unless otherwise stated. For each build, 20 spheres were chosen at random to represent the build, with 5 measurements of d_S taken per sphere to account for any irregularities and the mean values used.

| Sample | | d_1 / mm | d_2 / mm | d_3 / mm | Surface Area / mm ² | Volume / mm ³ | Sphericity |
|-----------|---|------------|------------|------------|--------------------------------|--------------------------|------------|
| PA2200 | A | 12.09±0.04 | – | – | 459±3 | 926±10 | 1.00 |
| | B | 6.44±0.03 | 12.03±0.03 | 23.91±0.04 | 583±1 | 969±4 | 0.81 |
| | C | 4.93±0.02 | 12.03±0.02 | 31.49±0.06 | 703±2 | 978±7 | 0.68 |
| | D | 4.27±0.05 | 12.01±0.03 | 37.82±0.07 | 814±3 | 1017±12 | 0.60 |
| | E | 3.60±0.03 | 12.01±0.03 | 44.58±0.05 | 931±2 | 1009±10 | 0.52 |
| | F | 3.21±0.06 | 11.97±0.04 | 50.49±0.05 | 1034±3 | 1016±18 | 0.47 |
| 1% B65003 | A | 12.09±0.04 | – | – | 459±3 | 926±8 | 1.00 |
| | B | 6.43±0.03 | 12.02±0.06 | 23.90±0.04 | 583±3 | 967±7 | 0.81 |
| | C | 4.96±0.02 | 12.08±0.05 | 31.54±0.03 | 707±3 | 990±7 | 0.68 |
| | D | 4.25±0.03 | 12.04±0.03 | 37.86±0.06 | 816±2 | 1015±8 | 0.60 |
| | E | 3.58±0.02 | 12.01±0.04 | 44.58±0.04 | 930±3 | 1003±6 | 0.52 |
| | F | 3.14±0.07 | 12.01±0.04 | 50.53±0.06 | 1035±4 | 997±21 | 0.47 |

Table A.5: Measured dimensions of the height, width and length (d_1 , d_2 and d_3 respectively) of the printed ellipsoids, along with the calculated surface area, volume and sphericity. Results are shown as the mean \pm standard deviation, with 5 measurements of d_1 taken for each sphere (total 25 spheres), and 3 measurements per ellipsoid (d_1 , d_2 and d_3 ; total 20 ellipsoids).

A.3 Tensile Testing Protocol

Prepare the test specimens:

1. Manufacture the specimens according to ASTM D638 [454]. For each specimen, measure the thickness and width of the narrow section to ± 0.1 mm; take a minimum of three measurements and calculate the mean value.
2. Apply reflective tape at the gauge length (as in Figure A.3), use a guide to ensure repeatability.

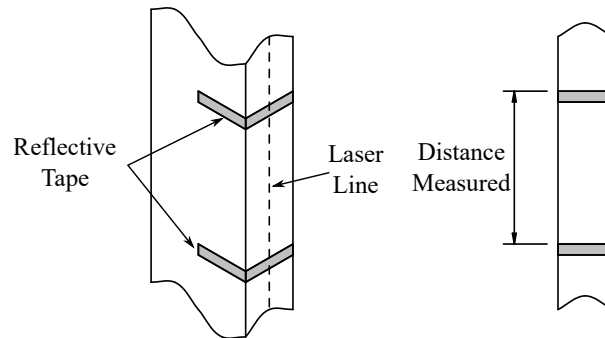


Figure A.3: Position of the reflective tape and the laser line on the specimen.

Tensile Testing:

1. Secure the specimen in the tensometer using the lower grip only.
2. Zero the force, then tighten the top grip. This was done so that the pre-load from tightening the grips is measured.
3. Zero the extension, then start the test. The relative speed of testing should be 10 mm/min.
4. When processing the data, a jump of ≥ 0.3 MPa in the stress measurements was interpreted as a fracture.

A.4 Water Uptake Protocol

Procedure based on ASTM D570 [466] and BS EN ISO 62 [467]:

1. Dry the specimens in an oven at $50 \pm 3^\circ\text{C}$ for 1-10 days, depending on the thickness of the specimens. A minimum of three specimens per material must be used, 1 cm^3 spheres were chosen for this.
2. Cool the specimens to room temperature in a desiccator, and immediately weigh to $\pm 0.001\text{ g}$.
3. Place the conditioned specimen in distilled water, at a temperature of $23 \pm 1^\circ\text{C}$. A minimum of 8 ml of distilled water should be used for every 1 cm^2 surface area, to ensure any extraction product does not become excessively concentrated in the water. Ensure that the specimens have minimal contact with other surfaces.
4. At the desired time points, remove the spheres from the water and remove the surface water with a dry cloth.
5. Weigh the specimens to $\pm 0.001\text{ g}$ and re-immerses in distilled water.

Note that for repeated measurements, the rate of water absorption could be decreased by the repeated removal from the water and drying of the surface.

6. For the total water uptake when substantially saturated; repeat the measurements at the end of the first week, and every two weeks thereafter.
7. Continue these measurements until the mean of the weight increase (from at least three measurements) is within 1%, or within 5 mg (whichever is greater).
8. Calculate the percent water uptake using Equation A.1.

$$\text{Increase in weight, \%} = \frac{\text{Wet weight} - \text{Conditioned weight}}{\text{Conditioned weight}} \times 100 \quad (\text{A.1})$$

9. To determine the diffusion constant of water in the material, plot a graph of increase in weight as a function of the square root of immersion time.
10. After immersion, the percentage of soluble matter lost can be found by reconditioning the specimens and using Equation A.2.

$$\text{Soluble matter lost, \%} = \frac{\text{Conditioned weight} - \text{Reconditioned weight}}{\text{Conditioned weight}} \times 100 \quad (\text{A.2})$$

A.5 Serial Dilution (Miles and Misra) Protocol

These methods are based on those described by Miles and Misra [363]. Note that for the tests in Section 5.4 this was modified to enable a higher throughput of samples, with $5\ \mu\text{l}$ dropped onto agar, rather than the $20\ \mu\text{l}$ described here.

To calculate the CFU/ml:

1. Ensure the agar plates are dry and allowed to rise to room temperature before use. This will allow for quicker absorption.
2. For unknown concentrations of bacteria, dilutions should be made to at least 10^{-8} . For this, prepare a 96 well plate by adding $90\ \mu\text{l}$ PBS to every column used for a dilution (for example, columns 2–9 for dilutions of 10^1 – 10^{-8}). If possible, include an extra column as a negative control.
3. Homogenise the bacterial suspension and add $100\ \mu\text{l}$ to column 1.
4. Carry out the first dilution by transferring $10\ \mu\text{l}$ from column 1 \rightarrow column 2, homogenise the suspension in column 2.
5. Repeat step 4 for the remaining dilutions (dilute 2 \rightarrow 3, 3 \rightarrow 4, and so on). The layout of the 96 well plate described here is shown in Figure A.4a.

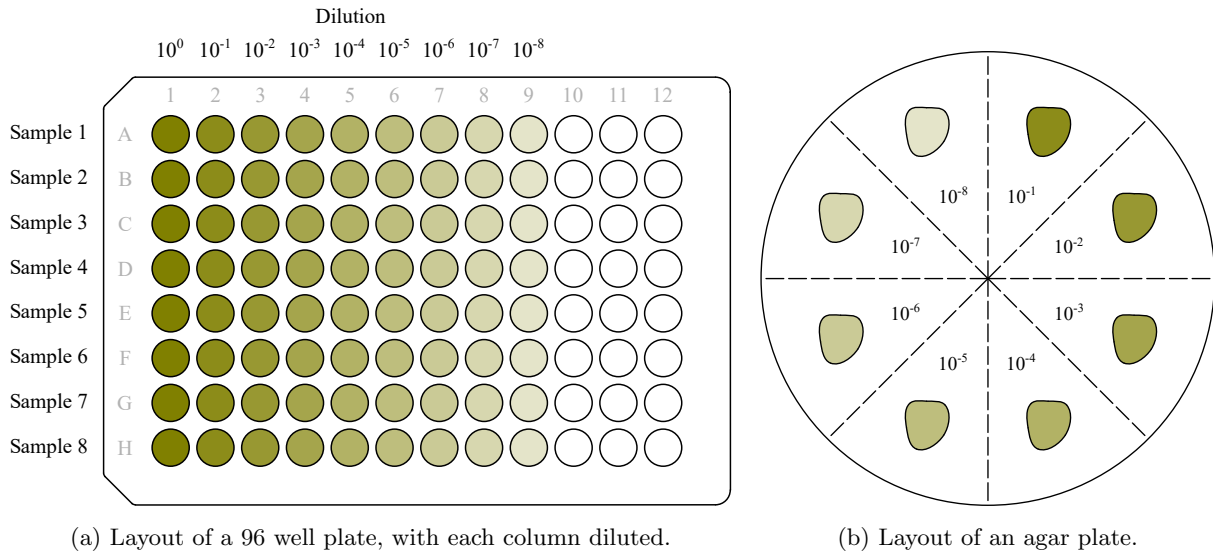


Figure A.4: Example experimental set-up for counting planktonic bacteria. The sample is diluted by factors of 10 in PBS using a 96 well plate, before being transferred to an agar plate and incubated.

6. Divide the agar plate into equal sectors (one per dilution, up to 8 per plate).
7. Drop $20\ \mu\text{l}$ of the dilution into its corresponding sector and allow to spread naturally over an area of 1.5–2 cm. Avoid touching the surface of the agar with the pipette tip for this. An example layout is shown in Figure A.4b.
8. Allow the plates to dry, before inverting and incubating at 37°C for 18–24 hours.
9. Observe each sector for growth. The sector chosen to count should be the one with the highest number of discrete colonies (usually 2–20).
10. Calculate the CFU/ml using Equation A.3.

$$\text{CFU per ml} = \text{Mean number of colonies per dilution} \times 50 \times \text{Dilution Factor} \quad (\text{A.3})$$

A.6 Static Peg Assay Protocol

Preparation of the 96 well plates:

1. Disinfect the pegs in 70% IMS for 15 minutes. Allow to air-dry for 30 minutes before use.
2. Dilute the overnight culture to $OD_{600} = 0.01$ in approximately 20 ml growth medium. The volume of overnight culture to add to the growth medium was calculated using Equation A.4.

$$\frac{\text{Target Optical Density}}{\text{Overnight Optical Density}} \times \text{Target Volume} = \text{Volume of Overnight to Add} \quad (\text{A.4})$$

3. Add 150 μl of growth medium to columns 2, 4, 6, 8 and 10; add 150 μl of the diluted culture to columns 1, 3, 5, 7 and 9.
4. Wrap in parafilm, then incubate for 24 hours in an orbital shaker at 37°C and 110 RPM. Reserve plate (“Planktonic”).
5. Rinse the pegs attached to the lid by filling the corresponding wells in a 96 well plate with 200 μl of PBS, then placing the lid on (submerge for approximately 10 seconds).
6. Incubate the lid for 15 minutes in 200 μl /well of PrestoBlue stain. Reserve plate (“Cell Viability”).
7. Rinse the pegs as in step 5.
8. Leave the lid in ambient conditions in 200 μl /well crystal violet.
9. Thoroughly rinse the lid with tap water until no more crystal violet stain is released.
10. Dry the lid by incubating (peg side up) overnight in an incubator at 37°C.
11. Immerse the pegs in 30% acetic acid (200 μl /well) for 30 minutes in ambient conditions to dissolve the cells. Reserve plate (“Crystal Violet”).

Reading 96 well plates (remove the lid prior to reading):

1. Read plate “Planktonic” – Absorbance at 600 nm.
2. Read plate “Cell Viability” – Excite at 550 nm, read absorbance at 590 nm.
3. Read plate “Crystal Violet” – Absorbance at 570 nm.

Appendix B

Additional Results

B.1 Particle Size Analysis

All of the key results acquired during the particle size analysis can be found in Table B.1, with the measured and processed size distributions shown graphically in Figures B.1 to B.6.

| Material | Run no. | D10 / μm | D50 / μm | D90 / μm | D[4,3] / μm | Weighted Residual / % |
|----------|---------|---------------------|---------------------|---------------------|------------------------|-----------------------|
| B65003 | 49 | 2.41 | 9.75 | 20.9 | 10.8 | 0.74 |
| | 50 | 2.45 | 9.78 | 20.8 | 10.8 | 0.81 |
| | 51 | 2.48 | 9.82 | 20.8 | 10.9 | 0.79 |
| | 52 | 2.46 | 9.76 | 20.6 | 10.8 | 0.84 |
| | 53 | 2.47 | 9.87 | 21.2 | 11.0 | 0.77 |
| | 54 | 2.46 | 9.81 | 20.9 | 10.9 | 0.83 |
| | 55 | 2.51 | 10.0 | 22.0 | 12.6 | 0.82 |
| | 56 | 2.52 | 9.85 | 21.1 | 11.0 | 0.80 |
| | 57 | 2.50 | 9.81 | 21.1 | 11.0 | 0.80 |
| | 58 | 2.53 | 9.88 | 21.2 | 11.1 | 0.88 |
| | Avg | 2.48 | 9.83 | 21.1 | 11.1 | 0.81 |
| | Std | 0.04 | 0.07 | 0.4 | 0.5 | 0.04 |
| B45003 | 71 | 0.518 | 3.28 | 6.54 | 3.50 | 0.86 |
| | 78 | 0.519 | 3.29 | 6.61 | 3.53 | 0.82 |
| | 82 | 0.524 | 3.31 | 6.65 | 3.55 | 0.78 |
| | 83 | 0.519 | 3.30 | 6.60 | 3.53 | 0.79 |
| | 84 | 0.512 | 3.30 | 6.59 | 3.52 | 0.80 |
| | 85 | 0.517 | 3.29 | 6.59 | 3.52 | 0.76 |
| | 90 | 0.515 | 3.30 | 6.66 | 3.54 | 0.66 |
| | 91 | 0.518 | 3.30 | 6.64 | 3.54 | 0.68 |
| | 72 | 0.571 | 3.34 | 6.57 | 3.56 | 0.35 |
| | 73 | 0.577 | 3.34 | 6.57 | 3.56 | 0.34 |
| | 74 | 0.517 | 3.30 | 6.66 | 3.54 | 0.37 |
| | 75 | 0.520 | 3.30 | 6.65 | 3.54 | 0.38 |
| | 76 | 0.520 | 3.29 | 6.64 | 3.53 | 0.33 |
| | 77 | 0.521 | 3.30 | 6.68 | 3.55 | 0.34 |
| | 79 | 0.587 | 3.36 | 6.64 | 3.59 | 0.37 |
| | 80 | 0.528 | 3.31 | 6.73 | 3.58 | 0.31 |
| | 86 | 0.518 | 3.29 | 6.69 | 3.55 | 0.33 |
| | 87 | 0.521 | 3.31 | 6.74 | 3.58 | 0.33 |
| | 88 | 0.515 | 3.30 | 6.74 | 3.57 | 0.35 |
| | 89 | 0.520 | 3.30 | 6.72 | 3.57 | 0.35 |
| Avg | 0.528 | 3.31 | 6.65 | 3.55 | 0.52 | |
| Std | 0.022 | 0.02 | 0.06 | 0.02 | 0.22 | |
| P40 | 141 | 1.68 | 15.1 | 41.9 | 18.8 | 0.62 |
| | 142 | 1.85 | 15.5 | 42.0 | 19.1 | 0.60 |
| | 143 | 1.93 | 15.8 | 42.3 | 19.3 | 0.61 |

Table B.1 *continued overleaf*

Table B.1 *continued*

| Material | Run no. | D10 / μm | D50 / μm | D90 / μm | D[4,3] / μm | Weighted Residual / % |
|----------|---------|---------------------|---------------------|---------------------|------------------------|-----------------------|
| | 144 | 1.94 | 15.7 | 42.1 | 19.2 | 0.60 |
| | 146 | 1.96 | 15.7 | 42.1 | 19.2 | 0.60 |
| | 147 | 1.98 | 15.8 | 42.2 | 19.3 | 0.65 |
| | 149 | 1.97 | 15.7 | 42.0 | 19.2 | 0.60 |
| | 150 | 1.98 | 15.7 | 42.1 | 19.2 | 0.50 |
| | 151 | 1.95 | 15.5 | 40.5 | 18.7 | 0.60 |
| | 152 | 1.94 | 15.4 | 40.4 | 18.6 | 0.58 |
| | 153 | 1.96 | 15.5 | 41.0 | 18.8 | 0.54 |
| | 154 | 1.96 | 15.4 | 40.6 | 18.7 | 0.52 |
| | 155 | 1.94 | 15.3 | 40.4 | 18.6 | 0.57 |
| | 156 | 1.94 | 15.4 | 40.4 | 18.6 | 0.55 |
| | 157 | 1.94 | 15.3 | 40.0 | 18.5 | 0.53 |
| | 158 | 1.96 | 15.4 | 40.1 | 18.5 | 0.56 |
| | Avg | 1.93 | 15.5 | 41.3 | 18.9 | 0.58 |
| | Std | 0.07 | 0.2 | 0.9 | 0.3 | 0.04 |
| P45 | 160 | 2.06 | 14.7 | 40.3 | 18.3 | 0.73 |
| | 161 | 2.12 | 14.8 | 40.3 | 18.4 | 0.72 |
| | 162 | 2.12 | 14.8 | 40.0 | 18.3 | 0.65 |
| | 163 | 2.10 | 14.7 | 40.0 | 18.3 | 0.70 |
| | 164 | 2.09 | 14.7 | 40.0 | 18.3 | 0.68 |
| | 165 | 2.09 | 14.7 | 39.9 | 18.2 | 0.68 |
| | 166 | 2.08 | 14.7 | 40.0 | 18.2 | 0.55 |
| | 167 | 2.09 | 14.7 | 40.2 | 18.3 | 0.51 |
| | 168 | 2.09 | 14.7 | 40.0 | 18.3 | 0.54 |
| | 169 | 2.11 | 14.9 | 40.4 | 18.4 | 0.53 |
| | 171 | 2.10 | 15.0 | 41.3 | 18.7 | 0.48 |
| | 172 | 2.12 | 14.9 | 41.3 | 18.7 | 0.48 |
| | 173 | 2.10 | 14.8 | 41.2 | 18.7 | 0.50 |
| | 174 | 2.06 | 14.7 | 41.0 | 18.5 | 0.49 |
| | 175 | 2.08 | 14.7 | 41.1 | 18.6 | 0.47 |
| | 176 | 2.10 | 14.8 | 41.2 | 18.6 | 0.48 |
| | 177 | 2.11 | 14.7 | 41.1 | 18.6 | 0.46 |
| | 178 | 2.09 | 14.6 | 40.9 | 18.5 | 0.56 |
| | 179 | 2.10 | 14.8 | 41.2 | 18.6 | 0.50 |
| | 180 | 2.11 | 14.8 | 41.3 | 18.7 | 0.51 |
| | Avg | 2.10 | 14.8 | 40.6 | 18.5 | 0.56 |
| | Std | 0.02 | 0.1 | 0.6 | 0.2 | 0.09 |
| P50 | 182 | 1.78 | 13.1 | 39.6 | 17.4 | 0.54 |
| | 183 | 1.72 | 12.9 | 39.6 | 17.3 | 0.49 |
| | 184 | 1.73 | 13.0 | 39.8 | 17.4 | 0.60 |
| | 185 | 1.74 | 13.0 | 39.9 | 17.4 | 0.69 |
| | 186 | 1.74 | 13.0 | 39.7 | 17.3 | 0.65 |
| | 187 | 1.73 | 13.0 | 39.6 | 17.3 | 0.71 |
| | 188 | 1.74 | 13.0 | 39.3 | 17.2 | 0.80 |
| | 189 | 1.73 | 13.0 | 40.0 | 17.5 | 0.90 |
| | 190 | 1.73 | 12.9 | 39.3 | 17.2 | 0.86 |
| | 191 | 1.74 | 13.0 | 39.4 | 17.2 | 0.85 |
| | 193 | 1.75 | 12.9 | 38.8 | 17.0 | 0.90 |
| | 194 | 1.73 | 12.9 | 38.6 | 17.0 | 0.86 |
| | 195 | 1.73 | 12.9 | 38.8 | 17.0 | 0.87 |
| | 196 | 1.73 | 12.9 | 39.3 | 17.2 | 0.98 |
| | 197 | 1.71 | 12.8 | 39.4 | 17.1 | 1.02 |
| | 198 | 1.74 | 12.9 | 39.5 | 17.2 | 1.03 |
| | 199 | 1.75 | 12.9 | 39.9 | 17.4 | 1.05 |
| | 200 | 1.76 | 12.9 | 39.6 | 17.3 | 1.05 |
| | 201 | 1.77 | 13.0 | 39.1 | 17.2 | 0.75 |
| | 202 | 1.79 | 13.1 | 39.2 | 17.2 | 0.90 |

Table B.1 *continued overleaf*

Table B.1 *continued*

| Material | Run no. | D10 / μm | D50 / μm | D90 / μm | D[4,3] / μm | Weighted Residual / % |
|----------|---------|---------------------|---------------------|---------------------|------------------------|-----------------------|
| | Avg | 1.74 | 13.0 | 39.4 | 17.2 | 0.83 |
| | Std | 0.02 | 0.1 | 0.4 | 0.1 | 0.17 |
| PA2200* | 12 | 36.2 | 56.7 | 85.9 | 58.8 | 0.52 |
| | 13 | 36.1 | 56.5 | 85.6 | 58.6 | 0.53 |
| | 14 | 35.9 | 56.0 | 84.3 | 57.9 | 0.55 |
| | 15 | 35.7 | 55.8 | 84.1 | 57.6 | 0.56 |
| | 16 | 35.8 | 56.0 | 84.3 | 57.8 | 0.57 |
| | 17 | 35.7 | 55.9 | 84.2 | 57.7 | 0.57 |
| | 18 | 35.5 | 55.9 | 84.8 | 57.9 | 0.57 |
| | 19 | 35.4 | 55.8 | 84.7 | 57.7 | 0.58 |
| | 20 | 35.4 | 55.8 | 84.7 | 57.7 | 0.58 |
| | 21 | 35.4 | 55.8 | 84.7 | 57.7 | 0.59 |
| | Avg | 35.7 | 56.0 | 84.7 | 57.9 | 0.56 |
| | Std | 0.3 | 0.3 | 0.6 | 0.4 | 0.02 |

Table B.1: Values of D10, D50, D90, D[4,3], and weighted residual for each particle size analysis run. These used a dry dispersion to avoid any dissolution of the phosphate glasses. *PA2200 used wet dispersion with additional ultrasonic agitation to avoid the particles agglomerating.

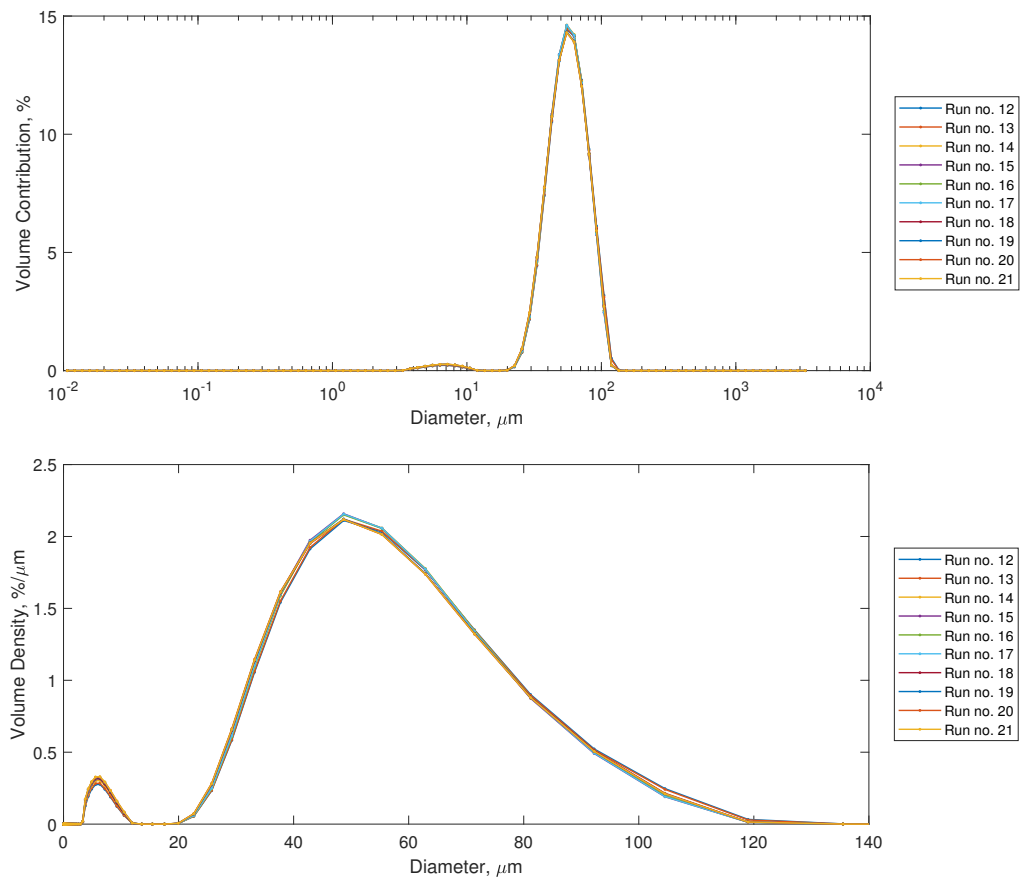


Figure B.1: PA2200. Showing Log scale (top) and Linear scale (bottom). 🚫

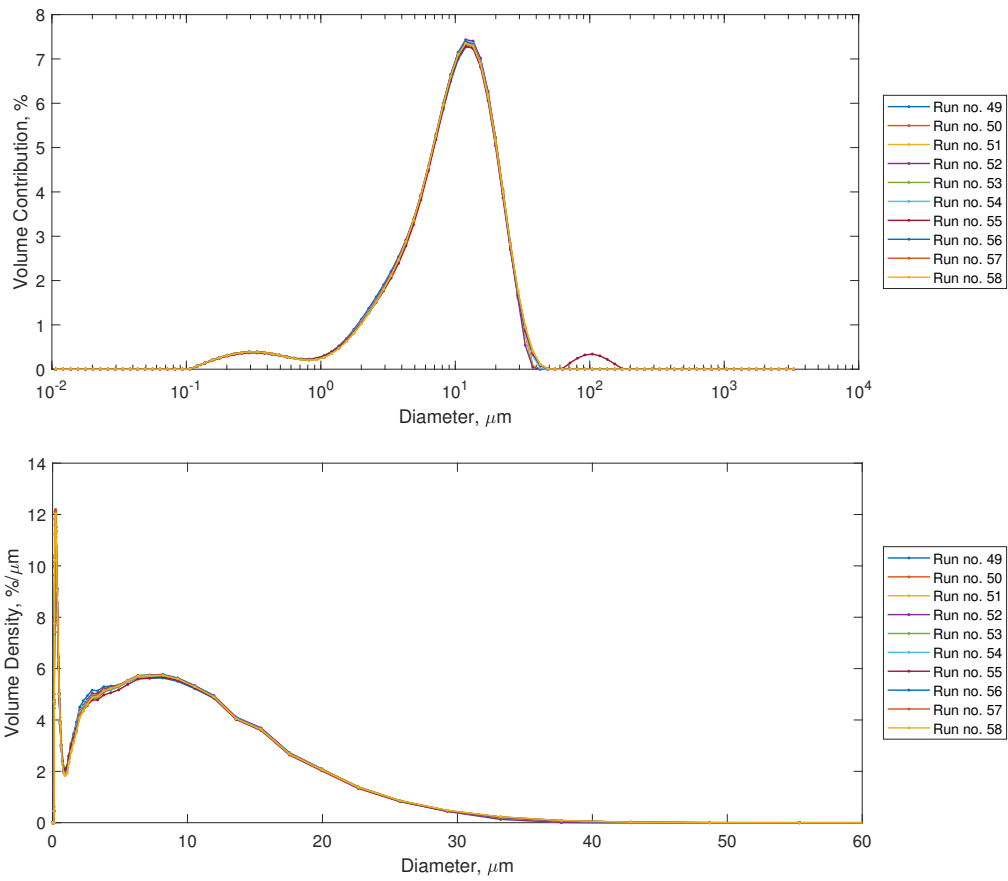


Figure B.2: B65003. Showing Log scale (top) and Linear scale (bottom).

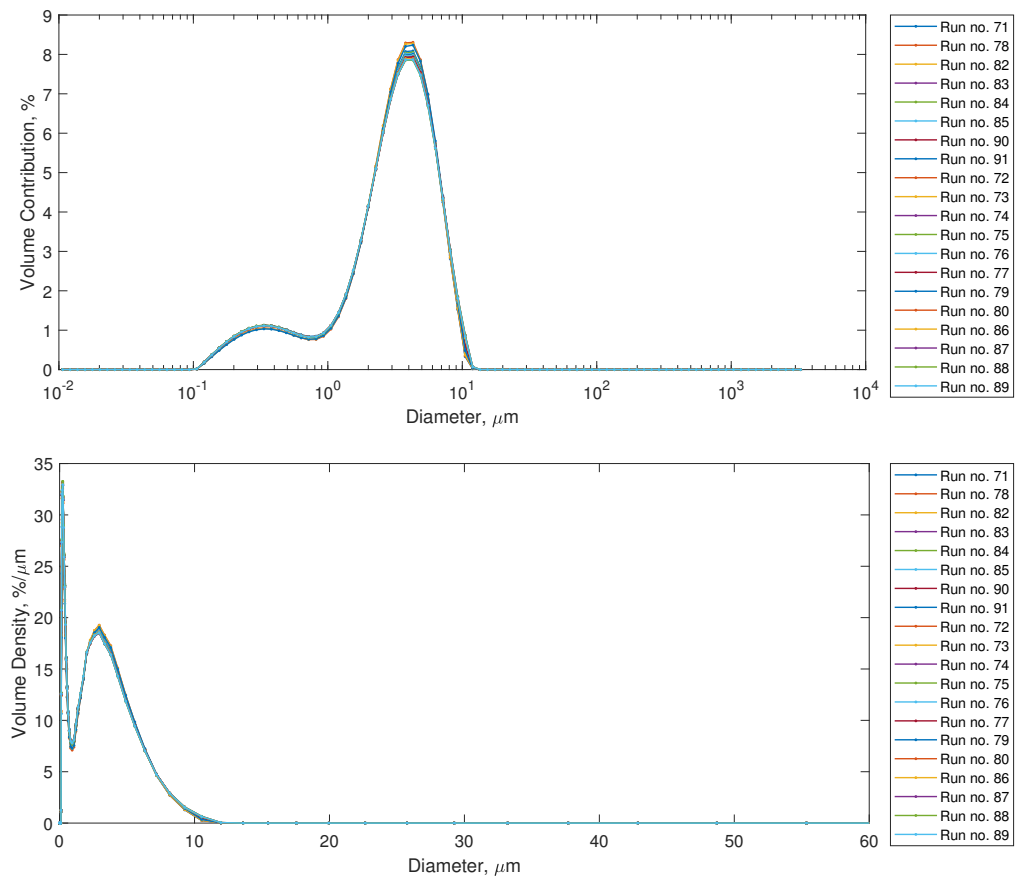


Figure B.3: B45003. Showing Log scale (top) and Linear scale (bottom).

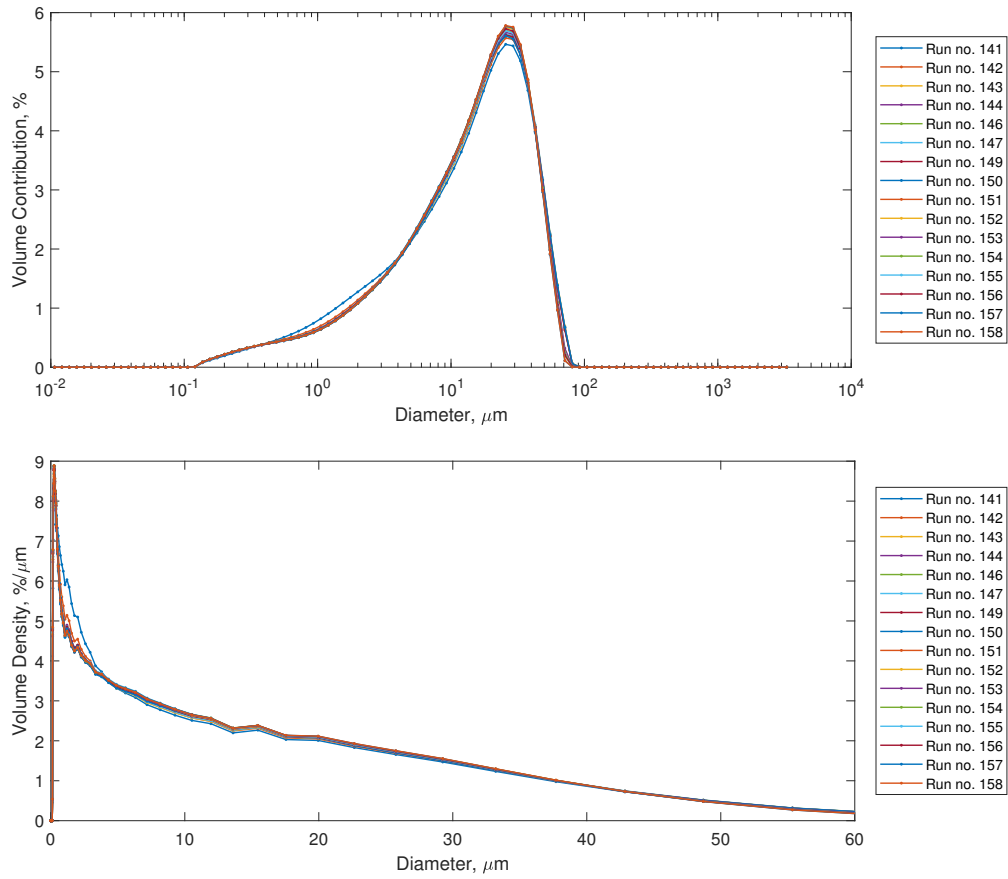


Figure B.4: P40. Showing Log scale (top) and Linear scale (bottom).

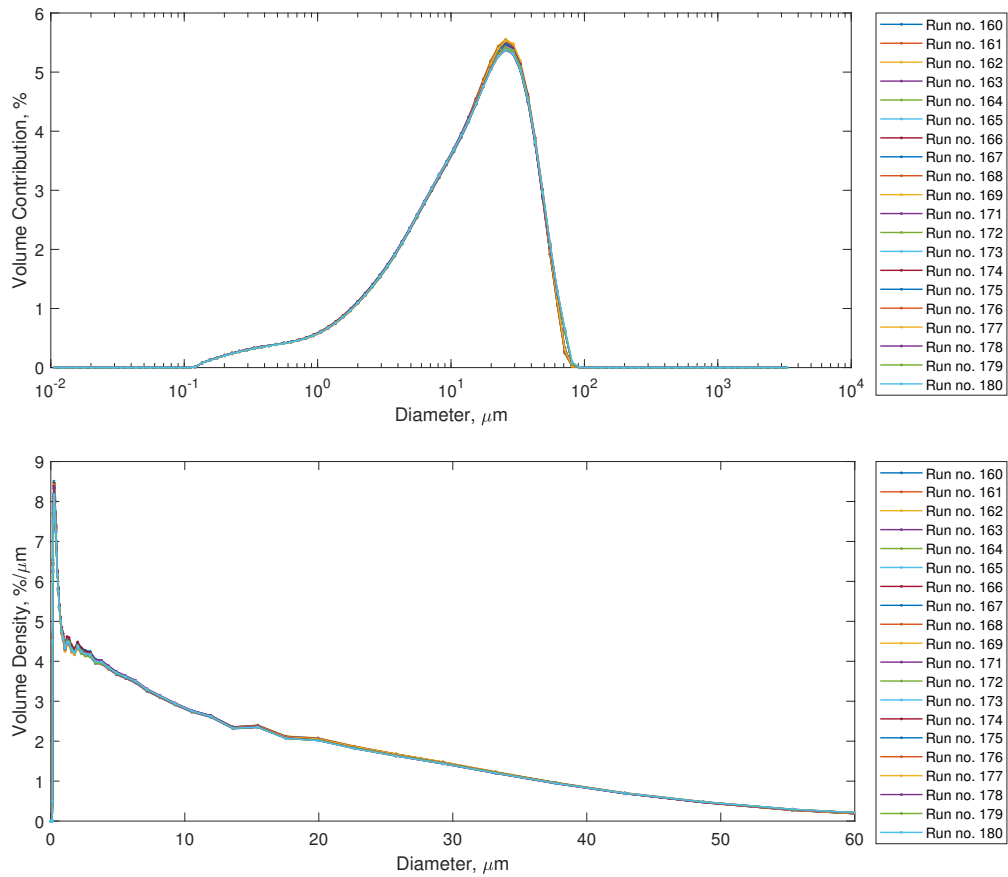


Figure B.5: P45. Showing Log scale (top) and Linear scale (bottom).

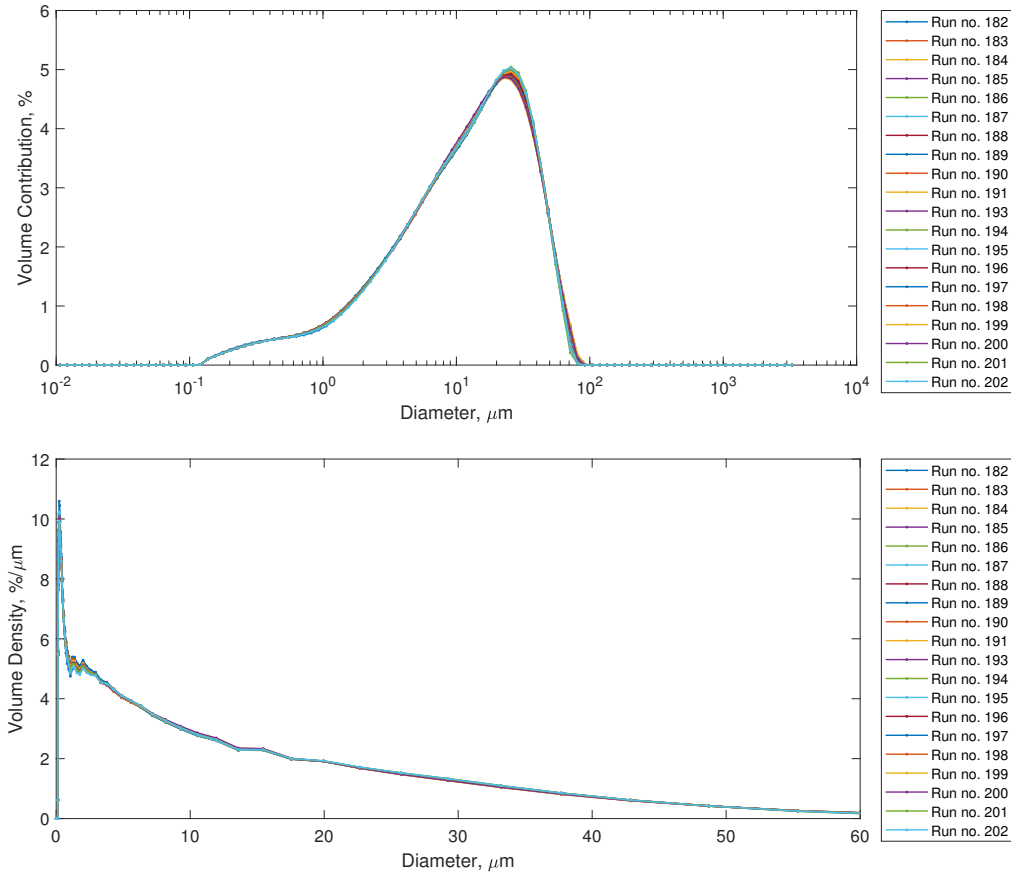


Figure B.6: P50. Showing Log scale (top) and Linear scale (bottom). 🇸🇬

B.2 Silver Additive Content

Individual results for the micro-composite composition (shown in Section 4.2.6), are shown in Table B.2.

| Material | Element, mg/kg | | | | | | | | | | | |
|-------------|----------------|------|-------|-----|-------|--------|------|-------|------|--------|-------|-----|
| | Ag | Al | B | Na | Ca | P | Cr | Si | Fe | Ti | Mg | Zr |
| | 129.0 | 40.6 | 176.0 | 4.2 | 597.0 | 4780.0 | 15.9 | 132.0 | 55.9 | 959.0 | 740.0 | 2.5 |
| 1.0% B65003 | 74.0 | 43.3 | 173.0 | 3.2 | 597.0 | 4830.0 | 12.6 | 153.0 | 76.7 | 1110.0 | 732.0 | 2.5 |
| | 137.0 | 50.5 | 177.0 | 1.9 | 604.0 | 4930.0 | 5.5 | 153.0 | 17.1 | 1110.0 | 757.0 | 2.6 |

Table B.2: Part composition from ICP, shown are 3 repeats of 1 cm³ spheres containing 1% B65003.

B.3 Effect of Autoclaving

B.3.1 Water Content

Directly from the Dried Mass

Where oven-drying of the specimens was possible, the value of m_{dried} was easily obtained by weighing the dried parts. Using Equation B.1, the value of w_t was then be calculated for time t , where m_t was the mass of the sample at time t [466,467].

$$w_t = \frac{m_t - m_{\text{dried}}}{m_{\text{dried}}} \times 100 \quad (\text{B.1})$$

As this process removed all moisture from the specimens, and had the potential to affect the mechanical properties (through the exposure to elevated temperatures), it could not be used before tensile testing. However, since the effect on the broken (post-test) specimens was of no concern, further oven-drying was carried out on these to measure m_{dried} for the broken specimens.

| Sample | Values of w_t to average for w_{test} | |
|--------|---|--|
| | Pre-Test | Post-Test |
| A | As printed (w_{int}) | ($m_{A,\text{pt}}$, $m_{A,\text{dried}}$) |
| B | After autoclaving (from $m_{B,\text{ac}}$, $m_{B,\text{int}}$, w_{int}) | ($m_{B,\text{pt}}$, $m_{B,\text{dried}}$) |
| C | As printed (w_{int}) | ($m_{C,\text{pt}}$, $m_{C,\text{dried}}$) |
| D | Air-dried (from $m_{D,\text{ad}}$, $m_{D,\text{int}}$, w_{int}) | ($m_{D,\text{pt}}$, $m_{D,\text{dried}}$) |
| E | Air-dried (from $m_{E,\text{ad}}$, $m_{E,\text{int}}$, w_{int}) | ($m_{E,\text{pt}}$, $m_{E,\text{dried}}$) |
| F | Air-dried (from $m_{F,\text{ad}}$, $m_{F,\text{int}}$, w_{int}) | ($m_{F,\text{pt}}$, $m_{F,\text{dried}}$) |
| G | Assumed 0 | – |
| H | Assumed 0 | – |
| J | Assumed 0 | – |

Table B.3: Values of w_t to average to obtain w_{test} . Shown are the conditions to calculate, and the values required (shown in brackets) for use with the either the direct or indirect method. The mass values (m), are initial (m_{int}), after autoclaving (m_{ac}), after air-drying (m_{ad}), after testing (m_{pt}), and after oven drying (m_{dried}).

Indirectly from the Initial Water Content

For the times where the direct method could not be used, the value of m_{dried} was calculated, rather than measured (denoted as m_{dried}^*), by using the initial water content of the build (w_{int}). Since sample sets G, H and J were oven-dried as whole specimens as part of the conditioning process, the value of m_{dried} (and their initial mass, m_{int}) were used to calculate w_{int} using Equation B.1. This initial water content (w_{int}) was assumed to be the same for all sample sets as all the specimens were manufactured in the same build.

With this value of w_{int} , the dried mass for any whole (pre-test) specimen could be determined by measuring their initial mass (m_{int}) and by rearranging Equation B.1 for m_{dried} (as shown in Equation B.2).

$$m_{\text{dried}}^* = m_{\text{int}} \left(\frac{100}{100 + w_{\text{int}}} \right) \quad (\text{B.2})$$

This value of m_{dried}^* was then used in place of m_{dried} in Equation B.1 to determine w_t .

Protocol Summary

The values of water content at the time of tensile testing w_{test} were an average of the pre- and post-test water content. The measurements required to calculate these for each sample set are shown in Table B.3.

Working backwards from these required measurements, and including the additional oven-drying steps necessitated by the direct method, the required protocol was developed.

B.3.2 Additional Results

The values of w_{test} for the samples are shown in Table B.4 (calculated from the mass values shown in Table B.5), where the pre- and post-test vales are shown alongside the mean. The negative values shown indicate that the mass increased after oven-drying, suggesting the water content increased during drying. However, the mass change for this was approximately 0.002 g, which could be attributed to a zeroing error, to a drift in the machine calibration or to human error when handling the samples. Since these values were small relative to the changes observed for the ‘‘Heat and Steam’’ samples, this was deemed acceptable and the values can be assumed to represent a 0% water content.

The values of the mechanical properties are shown in Table B.6, alongside the calculated values of w_{test} for each sample set.

| Sample Description | | Water Content / % | | |
|--------------------|----------------|-------------------|-----------|---------|
| | | Pre-Test | Post-Test | Average |
| As Built | A – No Drying | 0.13 | -0.02 | 0.05 |
| | D – Air-dried | 0.14 | 0.07 | 0.11 |
| | G – Oven-dried | 0 | – | 0 |
| Heat Only | C – No Drying | 0.13 | -0.03 | 0.05 |
| | F – Air-dried | 0.07 | 0.06 | 0.07 |
| | J – Oven-dried | 0 | – | 0 |
| Heat and Steam | B – No Drying | 1.01 | 0.68 | 0.84 |
| | E – Air-dried | 0.60 | 0.48 | 0.54 |
| | H – Oven-dried | 0 | – | 0 |

Table B.4: Calculated water content during testing, see Table B.3 for methodology. All values are ± 0.01 .

| Sample | Mass / g | | | | |
|--------|-------------|----------------|-------------|-------------|----------------|
| | Initial | Post-Autoclave | Pre-Test | Broken | Broken + Dried |
| A1 | – | – | – | 7.9768 | 7.9782 |
| A2 | – | – | – | 7.9861 | 7.9877 |
| A3 | – | – | – | 8.0155 | 8.0176 |
| A4 | – | – | – | 8.0175 | 8.0195 |
| A5 | – | – | – | 8.0220 | 8.0235 |
| Avg | – | – | – | 8.004±0.021 | 8.005±0.021 |
| B1 | 8.3802 | 8.5080 | 8.4510 | 8.4304 | 8.3731 |
| B2 | 8.3858 | 8.4895 | 8.4580 | 8.4425 | 8.3858 |
| B3 | 8.3962 | 8.5050 | 8.4710 | 8.4561 | 8.3999 |
| B4 | 8.4022 | 8.5151 | 8.4810 | 8.4672 | 8.4108 |
| B5 | 8.4219 | 8.5127 | 8.4940 | 8.4714 | 8.4145 |
| Avg | 8.397±0.016 | 8.506±0.010 | 8.471±0.017 | 8.454±0.017 | 8.397±0.017 |
| C1 | – | – | – | 8.0989 | 8.1005 |
| C2 | – | – | – | 8.1198 | 8.1218 |
| C3 | – | – | – | 8.1635 | 8.1656 |
| C4 | – | – | – | 8.1307 | 8.1331 |
| C5 | – | – | – | 8.0851 | 8.0872 |
| Avg | – | – | – | 8.120±0.030 | 8.122±0.030 |
| D1 | 8.4158 | – | 8.4169 | 8.4149 | 8.4085 |
| D2 | 8.4383 | – | 8.4433 | 8.3845 | 8.3782 |
| D3 | 8.4483 | – | 8.4404 | 8.3762 | 8.3705 |
| D4 | 8.4591 | – | 8.4651 | 8.4627 | 8.4569 |
| D5 | 8.4510 | – | 8.4512 | 8.4470 | 8.4411 |
| Avg | 8.443±0.017 | – | 8.443±0.018 | 8.417±0.038 | 8.411±0.038 |
| E1 | 8.4111 | 8.5204 | 8.4616 | 8.4236 | 8.3836 |
| E2 | 8.4325 | 8.5472 | 8.4801 | 8.4601 | 8.4204 |
| E3 | 8.4359 | 8.5310 | 8.4863 | 8.4493 | 8.4091 |
| E4 | 8.4940 | 8.5680 | 8.5051 | 8.5036 | 8.4631 |
| E5 | 8.4552 | 8.5680 | 8.4938 | 8.4905 | 8.4495 |
| Avg | 8.446±0.031 | 8.547±0.021 | 8.485±0.016 | 8.465±0.032 | 8.425±0.032 |
| F1 | 8.4340 | – | 8.4370 | 8.3748 | 8.3698 |
| F2 | 8.4783 | – | 8.4589 | 8.4511 | 8.4461 |
| F3 | 8.4714 | – | 8.4672 | 8.4144 | 8.4092 |
| F4 | 8.4862 | – | 8.4747 | 8.4718 | 8.4664 |
| F5 | 8.4318 | – | 8.4406 | 8.4370 | 8.4315 |
| Avg | 8.460±0.026 | – | 8.456±0.016 | 8.430±0.037 | 8.425±0.037 |
| G1 | 8.1733 | – | 8.1637 | – | – |
| G2 | 8.2275 | – | 8.1857 | – | – |
| G3 | 8.2055 | – | 8.1872 | – | – |
| G4 | 8.2226 | – | 8.1982 | – | – |
| G5 | 8.1501 | – | 8.1480 | – | – |
| Avg | 8.196±0.033 | – | 8.177±0.020 | – | – |
| H1 | 8.4510 | 8.5795 | 8.4614 | – | – |
| H2 | 8.4789 | 8.5840 | 8.4706 | – | – |
| H3 | 8.4622 | 8.5885 | 8.4742 | – | – |
| H4 | 8.4743 | 8.5727 | 8.4604 | – | – |
| H5 | 8.4066 | 8.5005 | 8.3990 | – | – |
| Avg | 8.455±0.029 | 8.565±0.037 | 8.453±0.031 | – | – |
| J1 | 8.4530 | – | 8.4432 | – | – |
| J2 | 8.4799 | – | 8.4580 | – | – |
| J3 | 8.4679 | – | 8.4534 | – | – |
| J4 | 8.4584 | – | 8.4469 | – | – |
| J5 | 8.4040 | – | 8.4023 | – | – |
| Avg | 8.453±0.029 | – | 8.441±0.022 | – | – |

Table B.5: Tensile specimen masses during the “effect of autoclaving” experiment. “Avg” values shown are mean ± standard deviation.

| Sample Conditioning | Elastic Modulus / MPa | | |
|-------------------------------|-----------------------|------------|----------|
| | As Built | Autoclaved | Oven |
| Immediate Testing (<24 hours) | 1744±87 | 1066±25 | 1630±55 |
| Air-dry (7 days) | 1792±52 | 1408±79 | 1870±171 |
| Oven-dry at 50°C (7 days) | 1746±134 | 1638±59 | 1746±89 |

(a) Elastic Modulus (E).

| Sample Conditioning | Ultimate Tensile Strength / MPa | | |
|-------------------------------|---------------------------------|------------|----------|
| | As Built | Autoclaved | Oven |
| Immediate Testing (<24 hours) | 48.9±0.2 | 42.7±0.3 | 49.3±0.2 |
| Air-dry (7 days) | 49.4±0.3 | 44.8±0.2 | 49.4±0.2 |
| Oven-dry at 50°C (7 days) | 50.2±0.2 | 48.9±0.3 | 50.2±0.3 |

(b) Ultimate Tensile Strength (σ_{uts}).

| Sample Conditioning | Elongation at Break / % | | |
|-------------------------------|-------------------------|------------|----------|
| | As Built | Autoclaved | Oven |
| Immediate Testing (<24 hours) | 24.8±1.7 | 46.5±5.1 | 25.6±4.0 |
| Air-dry (7 days) | 30.0±1.4 | 36.1±4.8 | 33.7±2.7 |
| Oven-dry at 50°C (7 days) | 26.1±2.7 | 24.5±3.2 | 25.5±2.0 |

(c) Elongation at Break (ε_{max}).

| Sample Conditioning | Water Content / % | | |
|-------------------------------|-------------------|------------|------------|
| | As Built | Autoclaved | Oven |
| Immediate Testing (<24 hours) | -0.02±0.00 | 0.84±0.00 | -0.03±0.00 |
| Air-dry (7 days) | 0.11±0.00 | 0.54±0.00 | 0.07±0.00 |
| Oven-dry at 50°C (7 days) | 0 | 0 | 0 |

(d) Water Content (w_t). Note oven-dried samples were assumed to have 0% water content.

Table B.6: Results of of the tensile testing for the effect of autoclave experiment.

B.4 Water Uptake

| Time, h | Mass, mg | | | | | | | | |
|---------|---------------|-------|-------|-------------|-------|-------|-------------|-------|-------|
| | Virgin PA2200 | | | 1.0% B65003 | | | 1.0% B45003 | | |
| 0 | 906.4 | 904.7 | 909.4 | 912.2 | 912.2 | 912.2 | 912.4 | 914.7 | 911.5 |
| 1 | 911.5 | 909.5 | 914.5 | 917.0 | 919.3 | 917.9 | 918.7 | 921.0 | 917.5 |
| 2 | 912.8 | 910.2 | 914.7 | 919.3 | 920.7 | 921.8 | 919.6 | 922.4 | 919.5 |
| 4 | 913.6 | 911.4 | 916.1 | 919.4 | 922.7 | 919.1 | 922.6 | 923.4 | 921.8 |
| 6 | 914.9 | 914.5 | 918.9 | 921.0 | 924.3 | 922.2 | 922.5 | 923.0 | 921.3 |
| 8 | 915.8 | 913.9 | 920.2 | 921.6 | 923.6 | 923.9 | 925.9 | 924.6 | 923.9 |
| 24 | 919.9 | 916.8 | 922.5 | 925.5 | 927.0 | 925.8 | 925.7 | 927.1 | 925.5 |
| 72 | 918.6 | 919.0 | 924.5 | 925.4 | 928.1 | 927.5 | 928.2 | 928.7 | 925.0 |
| 168 | 920.9 | 918.8 | 924.7 | 926.7 | 929.9 | 928.3 | 928.8 | 930.0 | 927.1 |
| 240 | 919.8 | 920.5 | 926.3 | 930.1 | 931.5 | 929.7 | 929.2 | 929.9 | 929.4 |
| 336 | 921.2 | 920.2 | 924.3 | 928.9 | 931.6 | 930.6 | 928.8 | 930.9 | 929.1 |
| 408 | 920.8 | 920.2 | 927.1 | 928.6 | 930.5 | 929.4 | 929.2 | 929.6 | 928.3 |
| 504 | 922.2 | 919.5 | 925.7 | 930.1 | 930.7 | 930.1 | 929.0 | 928.2 | 926.3 |
| 576 | 921.3 | 919.6 | 924.9 | 928.2 | 931.7 | 930.0 | 927.3 | 929.5 | 928.3 |
| 744 | 922.2 | 919.3 | 924.8 | 929.6 | 932.1 | 930.7 | 927.8 | 931.3 | 928.6 |
| 1152 | 922.9 | 921.4 | 927.0 | 930.2 | 932.9 | 932.3 | 930.0 | 929.8 | 928.6 |
| 1488 | 922.9 | 922.8 | 927.0 | 930.1 | 933.6 | 932.7 | 928.4 | 930.8 | 929.0 |
| 1824 | 924.3 | 923.6 | 929.0 | 930.6 | 933.4 | 932.8 | 930.9 | 932.8 | 930.8 |
| 2352 | 925.1 | 924.7 | 929.0 | 932.8 | 936.3 | 934.9 | 932.5 | 932.4 | 930.5 |
| 2760 | 924.9 | 922.5 | 932.3 | 935.1 | 934.7 | 933.0 | 931.8 | 931.7 | 929.8 |
| 3096 | 923.1 | 922.3 | 926.5 | 932.7 | 935.7 | 935.4 | 931.8 | 932.1 | 930.9 |

Table B.7: Measured mass of the spheres during water uptake testing in Section 4.3.2.

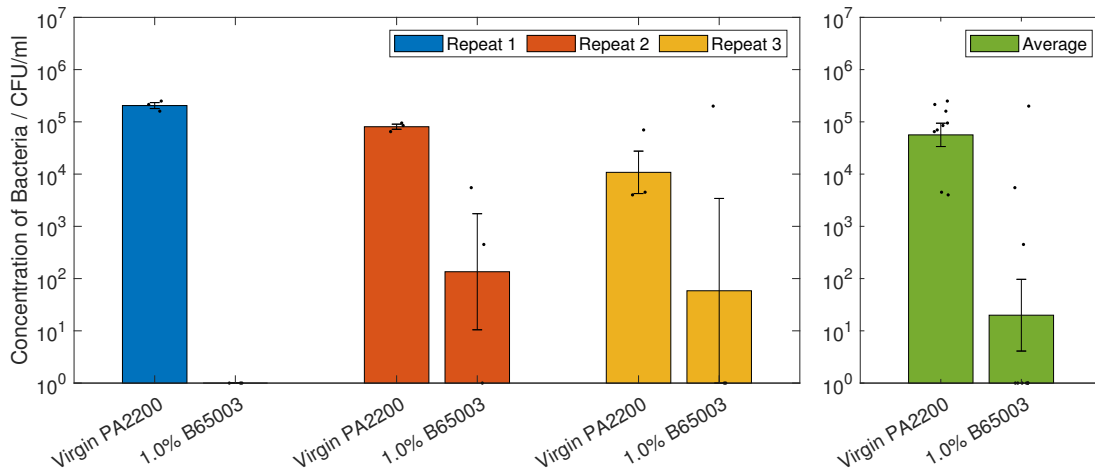
B.5 Silver Ion Release

| Sample time, h (extraction time) | Ag concentration, mg/l | | |
|-------------------------------------|------------------------|-------|-------|
| | 1.0% B65003 | | |
| 0 (0) | 0.000 | 0.000 | 0.000 |
| 1 (1) | 0.000 | 0.000 | 0.000 |
| 2 (1) | 0.000 | 0.000 | 0.000 |
| 3 (1) | 0.002 | 0.000 | 0.002 |
| 8 (5) | 0.005 | 0.004 | 0.004 |
| 24 (16) | 0.017 | 0.012 | 0.011 |
| 168 (144) | 0.092 | 0.083 | 0.134 |

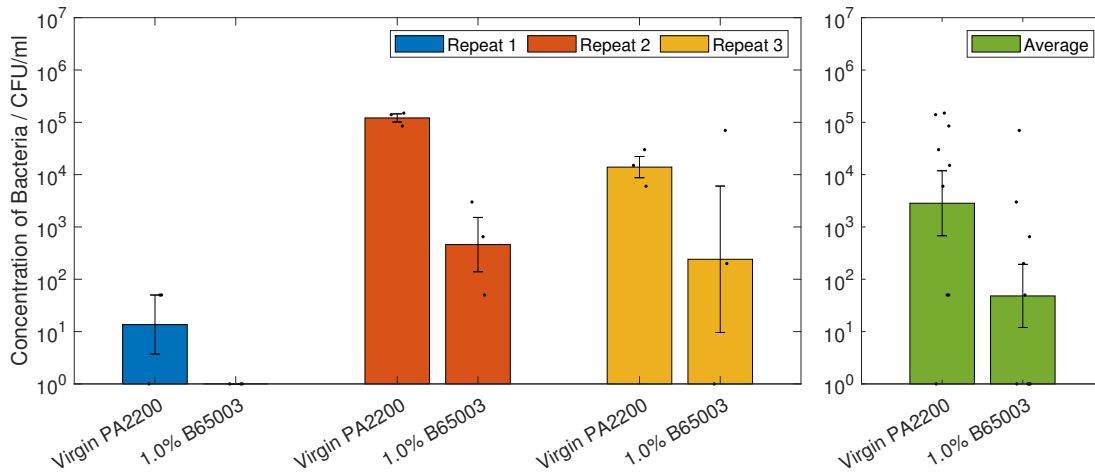
Table B.8: Ag⁺ release into 10 ml de-ionised water, measured using ICP.

B.6 Additional Microbial Testing (Carried out by R. Turner)

B.6.1 Nutrient-Poor Media

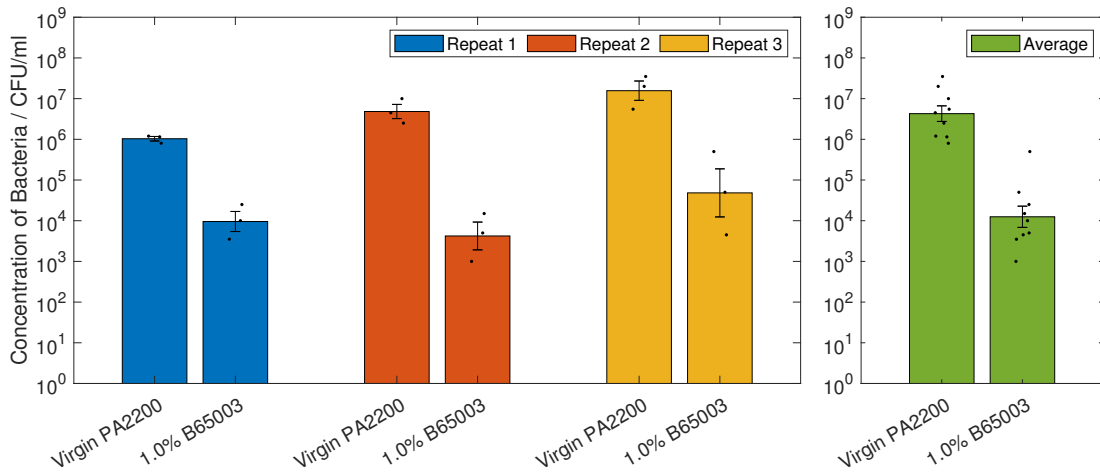


(a) Planktonic (*S. aureus* S235 in PBS).

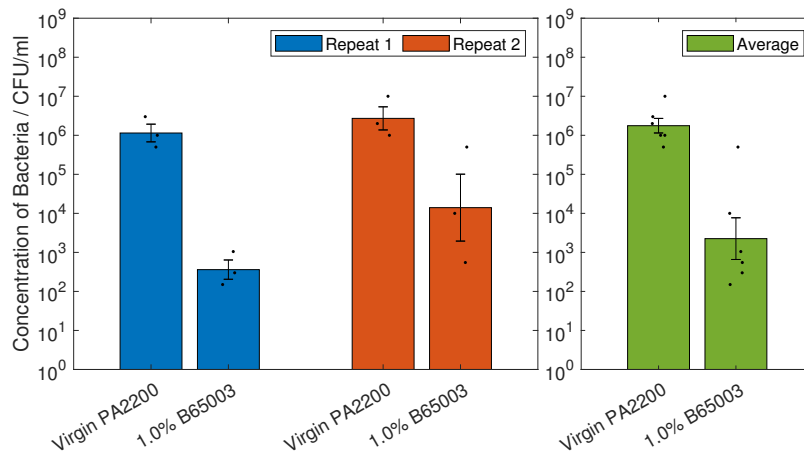


(b) Biofilm (*S. aureus* S235 in PBS).

Figure B.7: Contact efficacy against *S. aureus* of the parts in PBS, separated into repeats [452]. Results shown are geometric mean * geometric standard error. 🚫



(a) Planktonic (*P. aeruginosa* SOM1 in PBS).



(b) Biofilm (*P. aeruginosa* SOM1 in PBS).

Figure B.8: Contact efficacy against *P. aeruginosa* of the parts in PBS, separated into repeats [452]. Results shown are geometric mean * geometric standard error. 🦠

B.6.2 Nutrient-Rich Media

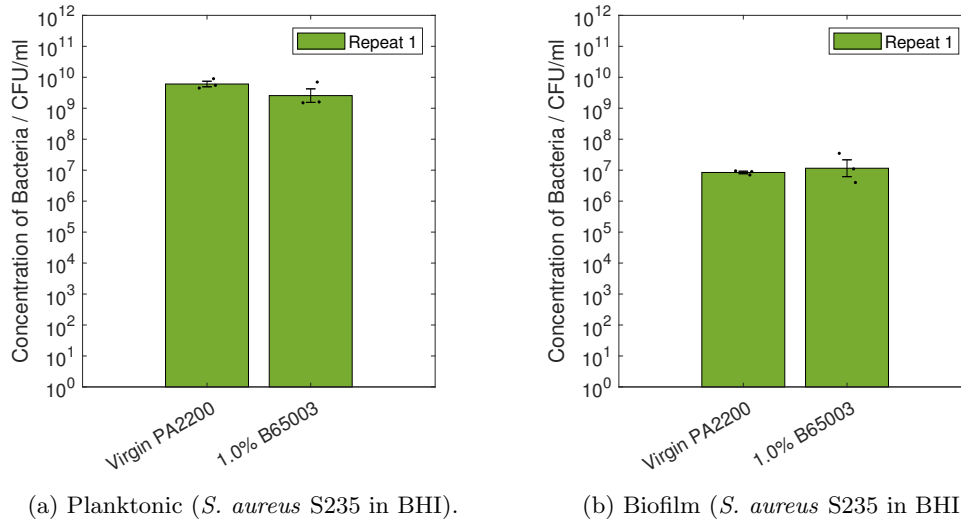


Figure B.9: Contact efficacy against *S. aureus* of the parts in BHI, only 1 repeat carried out [452]. Results shown are geometric mean \times geometric standard error. 🚫

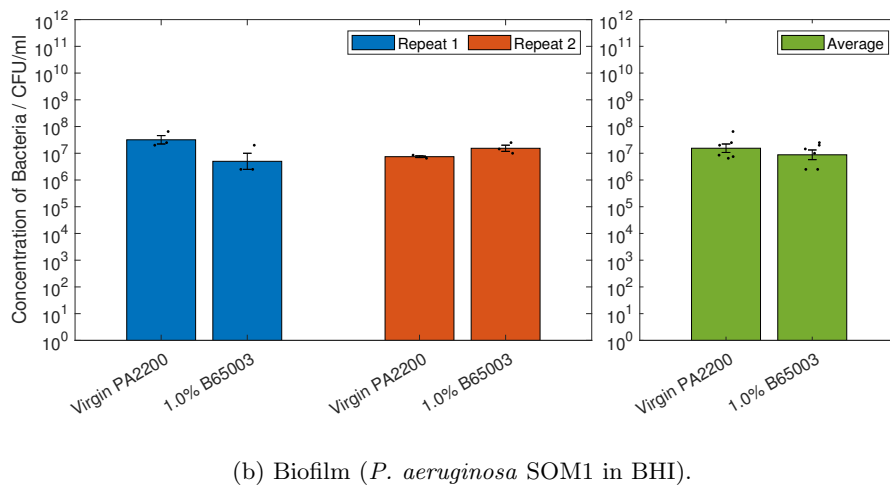
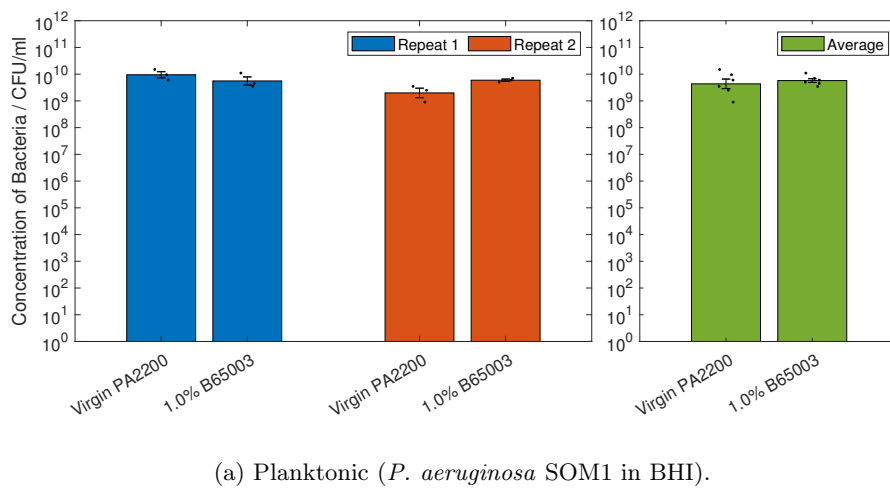
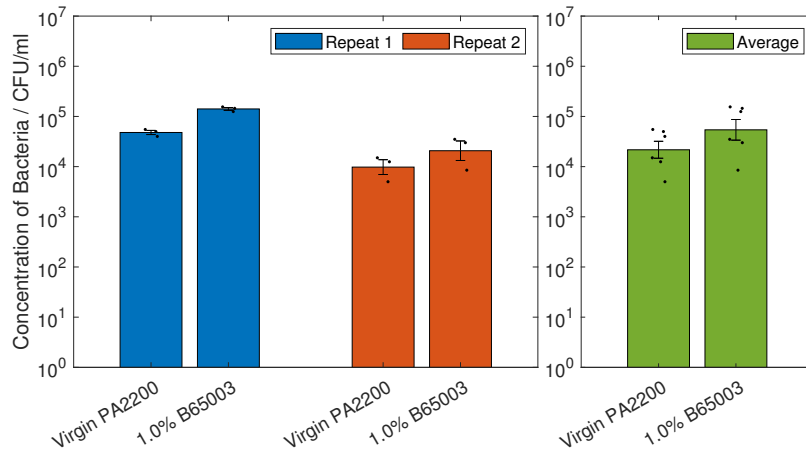
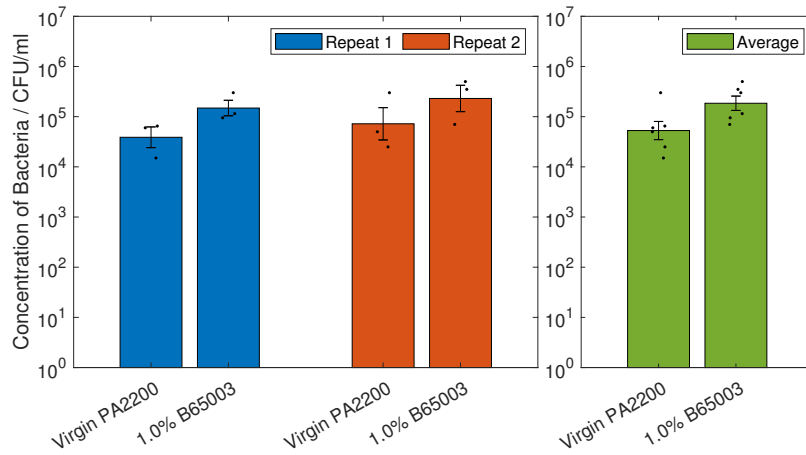


Figure B.10: Contact efficacy against *P. aeruginosa* of the parts in BHI, separated into repeats [452]. Results shown are geometric mean \times geometric standard error. 🚫

B.6.3 Nutrient-Poor Media with Glutathione



(a) Planktonic (*S. aureus* S235 in PBS with 1mM Glutathione).



(b) Biofilm (*S. aureus* S235 in PBS with 1mM Glutathione).

Figure B.11: Contact efficacy against *S. aureus* of the parts in PBS with 1mM Glutathione, separated into individual repeats [452]. Results shown are geometric mean * geometric standard error. 🦠

B.6.4 Non-Contact Efficacy

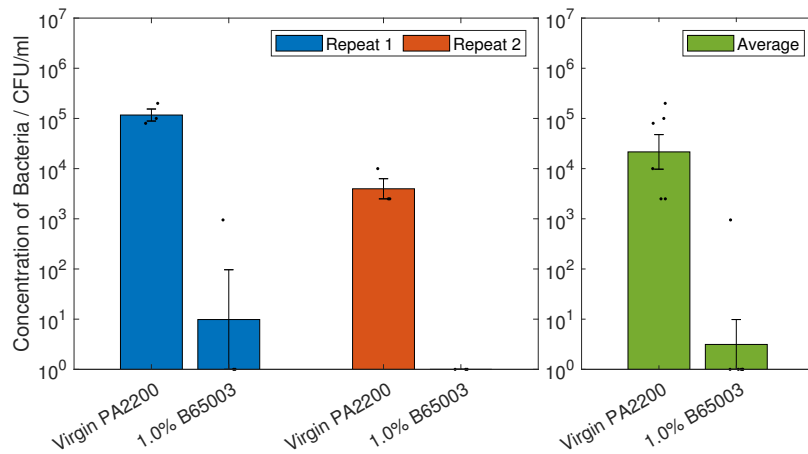


Figure B.12: Non-contact efficacy against *S. aureus* of the parts in PBS, separated into repeats [452]. Results shown are geometric mean \times geometric standard error. 🌐

B.6.5 Cytotoxicity

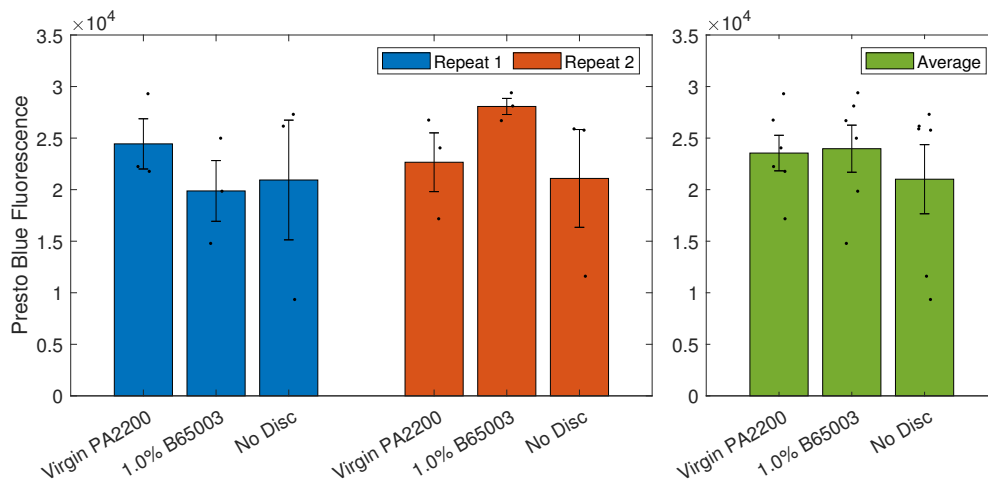


Figure B.13: Cytotoxicity measurements of the parts, separated into repeats. The cell metabolic activity was measured here using Presto Blue [452]. Results shown are the mean \pm standard error. 🌐

B.7 Colour Measurements

| Material | Card Sample Calibration | | | | Spectralon Calibration* | | | |
|----------|-------------------------|------|------|-----|-------------------------|-----|-----|-----|
| | Repeat | R | G | B | Repeat | R | G | B |
| PA2200 | 1 | 1023 | 1023 | 994 | 1 | 823 | 826 | 818 |
| | 2 | 1023 | 1023 | 995 | 2 | 825 | 827 | 819 |
| | 3 | 1023 | 1023 | 997 | 3 | 819 | 822 | 814 |
| | 4 | 1023 | 1023 | 980 | 4 | 823 | 825 | 817 |
| | 5 | 1023 | 1023 | 994 | 5 | 822 | 825 | 816 |
| | 6 | 1023 | 1023 | 998 | 6 | 801 | 803 | 792 |
| | 7 | 1023 | 1023 | 994 | 7 | 821 | 824 | 816 |
| | 8 | 1023 | 1023 | 998 | 8 | 805 | 811 | 798 |
| | 9 | 1023 | 1023 | 994 | 9 | 822 | 825 | 817 |
| | 10 | 1023 | 1023 | 995 | 10 | 825 | 828 | 821 |
| 1% P40 | 1 | 667 | 608 | 507 | 1 | 524 | 478 | 403 |
| | 2 | 682 | 619 | 515 | 2 | 525 | 478 | 403 |
| | 3 | 671 | 611 | 510 | 3 | 538 | 489 | 412 |
| | 4 | 638 | 576 | 464 | 4 | 521 | 476 | 400 |
| | 5 | 663 | 605 | 504 | 5 | 534 | 487 | 407 |
| | 6 | 660 | 602 | 500 | 6 | 522 | 476 | 399 |
| | 7 | 655 | 597 | 495 | 7 | 522 | 477 | 402 |
| | 8 | 649 | 589 | 476 | 8 | 515 | 470 | 387 |
| | 9 | 662 | 598 | 491 | 9 | 520 | 469 | 389 |
| | 10 | 657 | 596 | 491 | 10 | 529 | 480 | 398 |
| 1% P45 | 1 | 618 | 560 | 453 | 1 | 471 | 435 | 365 |
| | 2 | 609 | 550 | 436 | 2 | 492 | 445 | 367 |
| | 3 | 616 | 556 | 449 | 3 | 461 | 424 | 355 |
| | 4 | 632 | 575 | 465 | 4 | 479 | 439 | 362 |
| | 5 | 596 | 535 | 428 | 5 | 473 | 430 | 348 |
| | 6 | 619 | 561 | 455 | 6 | 467 | 452 | 373 |
| | 7 | 619 | 561 | 455 | 7 | 470 | 428 | 354 |
| | 8 | 615 | 556 | 450 | 8 | 472 | 432 | 354 |
| | 9 | 617 | 560 | 453 | 9 | 491 | 449 | 369 |
| | 10 | 622 | 564 | 457 | 10 | 476 | 435 | 358 |
| 1% P50 | 1 | 557 | 499 | 425 | 1 | 423 | 398 | 347 |
| | 2 | 571 | 513 | 435 | 2 | 416 | 381 | 329 |
| | 3 | 555 | 498 | 424 | 3 | 413 | 377 | 321 |
| | 4 | 548 | 490 | 414 | 4 | 424 | 389 | 336 |
| | 5 | 558 | 501 | 427 | 5 | 433 | 397 | 345 |
| | 6 | 552 | 494 | 419 | 6 | 434 | 399 | 348 |
| | 7 | 549 | 492 | 417 | 7 | 435 | 399 | 340 |
| | 8 | 574 | 516 | 438 | 8 | 433 | 399 | 348 |
| | 9 | 566 | 509 | 435 | 9 | 432 | 396 | 345 |
| | 10 | 556 | 499 | 425 | 10 | 446 | 408 | 352 |

Table B.9: Measured 10-bit RGB values ($/1023$) for virgin PA2200 parts, and the three custom additive microcomposite parts. *Spectralon calibration was carried out closer to the light source and sensor than the colour measurements.

Appendix C

Additional and Preliminary Experiments

C.1 Additional Tensile Testing

For all of the tensile testing shown here, the same methodology as Section 4.2.1 was used. For all of the values here, type I specimens were printed [454], and tested using a Tinius Olsen 5K with laser extensometer.

C.1.1 Effect of Powder Recycling

At the start of the project, it was thought that changes occurring in the powder due to reuse within the LS machine could affect the antimicrobial efficacy of the part. At that stage microbial testing was carried out solely with discs, with tensile specimens also printed to characterise the mechanical properties of the builds.

The results are shown in Figure C.1, with the statistical comparison shown in Table C.1.

| | 50/50 PA2200 | Used PA2200 | | 50/50 PA2200 | Used PA2200 |
|---------------|--------------|--------------|---------------|--------------|--------------|
| Virgin PA2200 | 0.958 | 0.009 | Virgin PA2200 | 0.401 | 0.000 |
| 50/50 PA2200 | – | 0.006 | 50/50 PA2200 | – | 0.000 |

(a) Young’s Modulus.

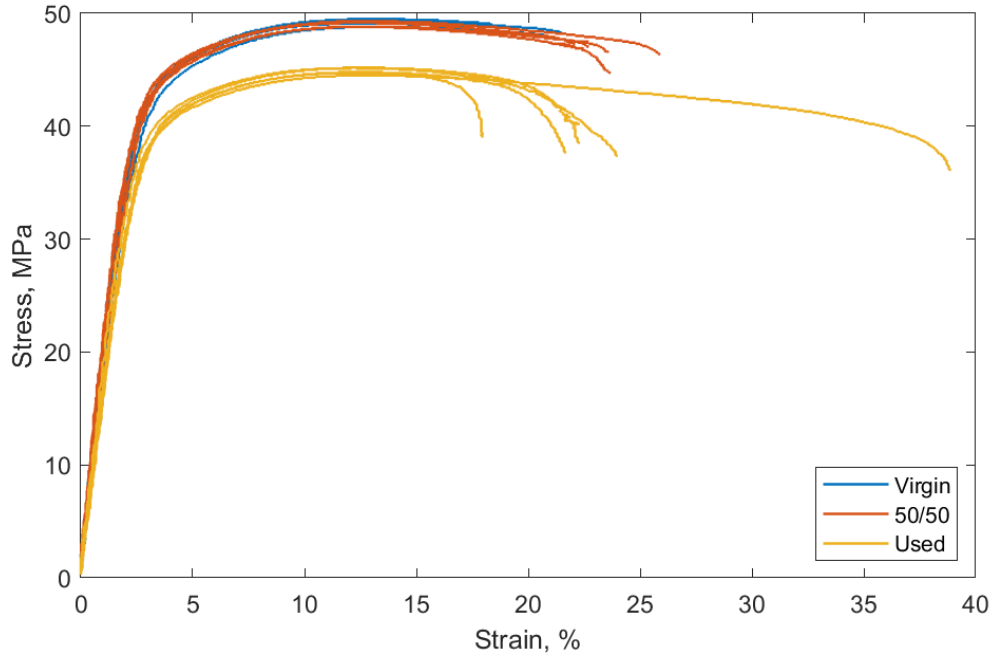
(b) Ultimate Tensile Strength.

| | 50/50 PA2200 | Used PA2200 |
|---------------|--------------|-------------|
| Virgin PA2200 | 0.008 | 0.181 |
| 50/50 PA2200 | – | 0.724 |

(c) Elongation at Break.

Table C.1: Statistical comparison of tensile test data. Shown are p values, where $p < 0.05$ (shown in bold) indicates a statistically significant difference.

Despite the large differences in mechanical properties found, the reduced reproducibility of printing with used or 50/50 powder, added to the potential for contamination, was deemed too significant an issue to continue testing the antimicrobial efficacy.



(a) Stress-strain curves from tensile testing.

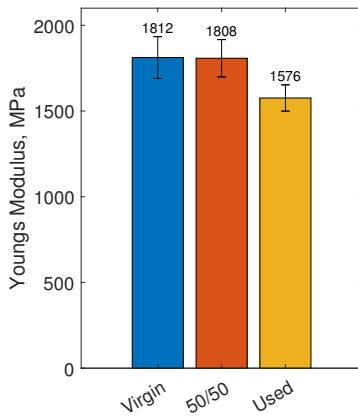
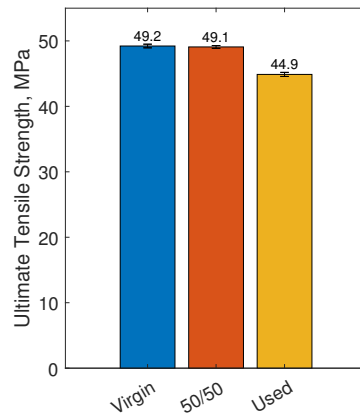
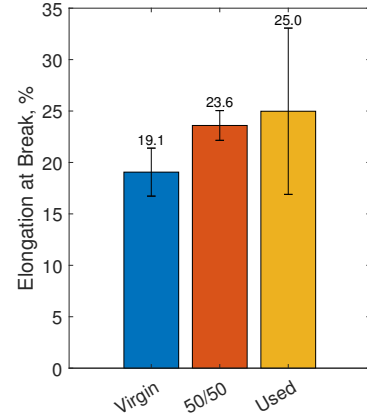
(b) Young's Modulus (E).(c) Ultimate Tensile Strength (σ_{uts}).(d) Elongation at Break (ε_{max}).

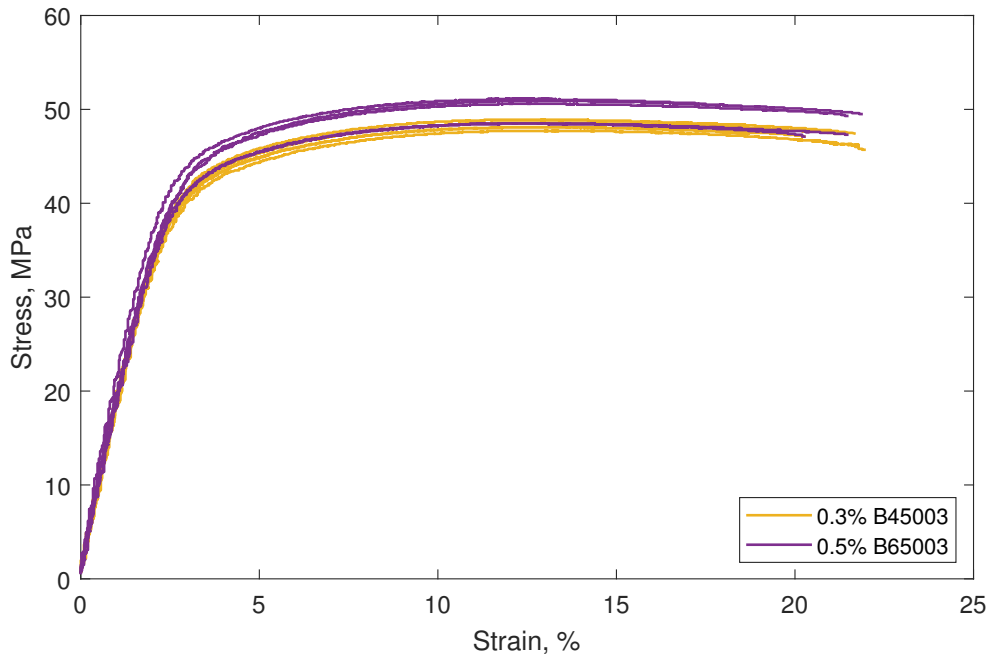
Figure C.1: Results of the tensile testing. 🚫

C.1.2 Effect of Additive Loading

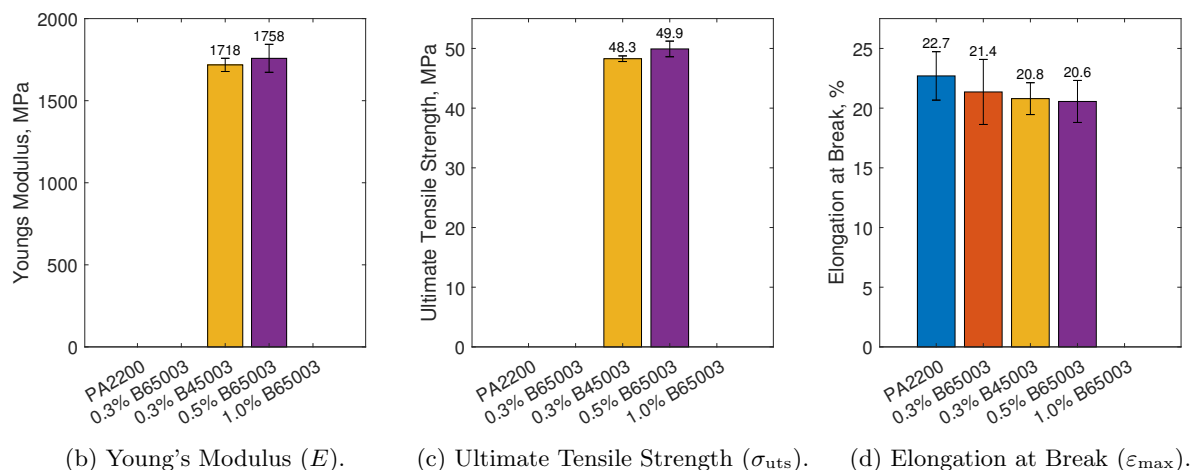
In the first trials for the commercially available silver phosphate glasses, different loadings of the additives were incorporated into the parts. These were based on BioCote's recommendation that only 0.3% of the additives would be necessary to see an antimicrobial effect; builds which were primarily used to create the pegs used in Section 4.4.3, with discs and tensile specimens also produced.

There were multiple issues while carrying out these experiments. Firstly, during the 1.0% B65003 print, the build failed in between the pegs and the tensile specimens (due to an unforeseeable machine error, unrelated to the material). Secondly, in the tensile testing there was an error with some of the force values measured by the load cell, meaning they could not be used for analysis.

Due to these, the results shown in Figure C.2 are significantly diminished compared to the original plan. As the results were incomplete, a statistical analysis was not carried out.



(a) Stress-strain curves from tensile testing.



(b) Young's Modulus (E).

(c) Ultimate Tensile Strength (σ_{uts}).

(d) Elongation at Break (ϵ_{max}).

Figure C.2: Results of the tensile testing, invalid or missing results have been omitted. 🚫

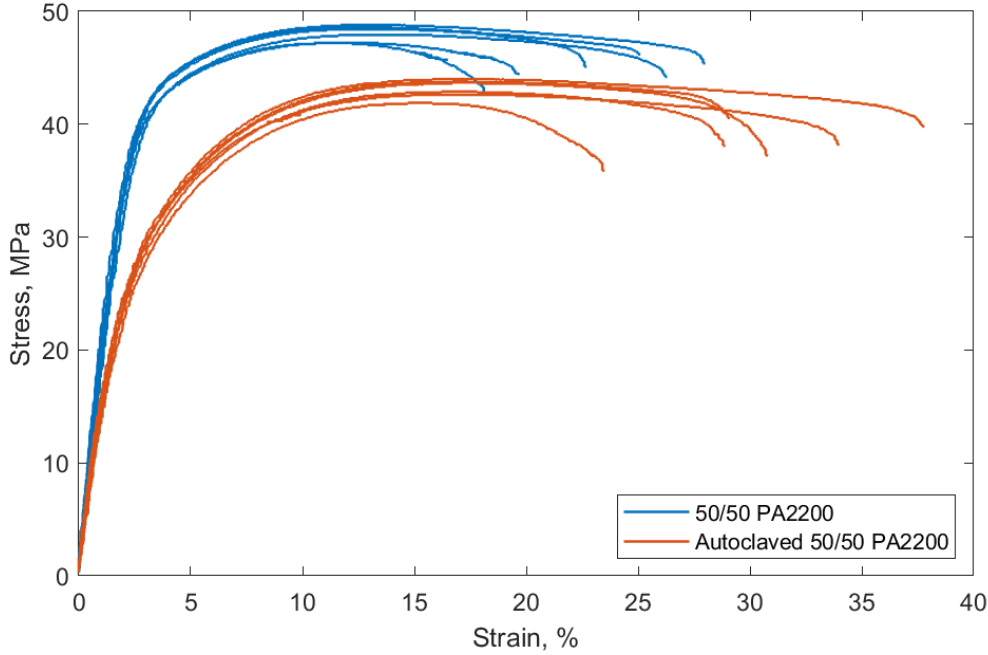
Although this could have shown some interesting results, it was becoming increasingly apparent how labour intensive any antimicrobial testing would be to carry out. For this reason, it was decided to focus on one loading per additive, with 1% chosen to maximise the chances of measuring an antimicrobial effect. Further work could be carried out to determine the minimum amount of additive needed to achieve the desired effect, or the maximum amount able to be processed in LS before disrupting the build.

C.1.3 Effect of Autoclaving – Preliminary Experiment

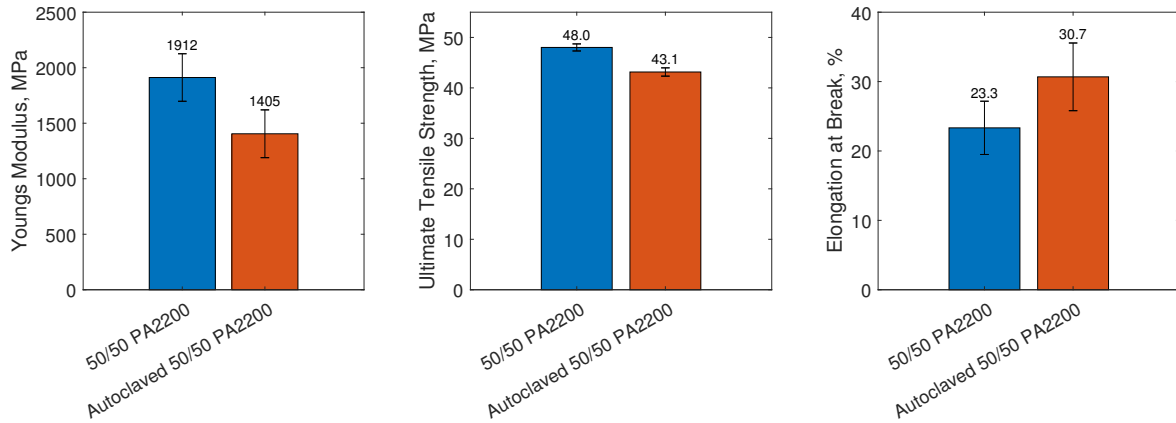
Before the more rigorous experiment in Section 4.3.1 was carried out, a preliminary experiment was performed to determine how large an effect autoclaving was likely to have. This was jointly carried out by the author and Maha Omran.

For this, two sets of 6 tensile specimens were produced. One set was autoclaved at 121°C and air dried for approx 24 hours, whereas the other was left in the “as built” condition. After testing, half of each tested specimen was dried in an oven at 50°C for 5 days to obtain the water content, with values of $0.06 \pm 0.00\%$ found for the as built samples and $0.55 \pm 0.02\%$ for the autoclaved samples.

The results of the tensile testing can be seen in Figure C.3, with the values of E , σ_{uts} and ε_{max} found to be significantly different (p -values of 0.010, 0.000, and 0.020 respectively).



(a) Stress-strain curves from tensile testing.



(b) Young's Modulus (E).

(c) Ultimate Tensile Strength (σ_{uts}).

(d) Elongation at Break (ε_{max}).

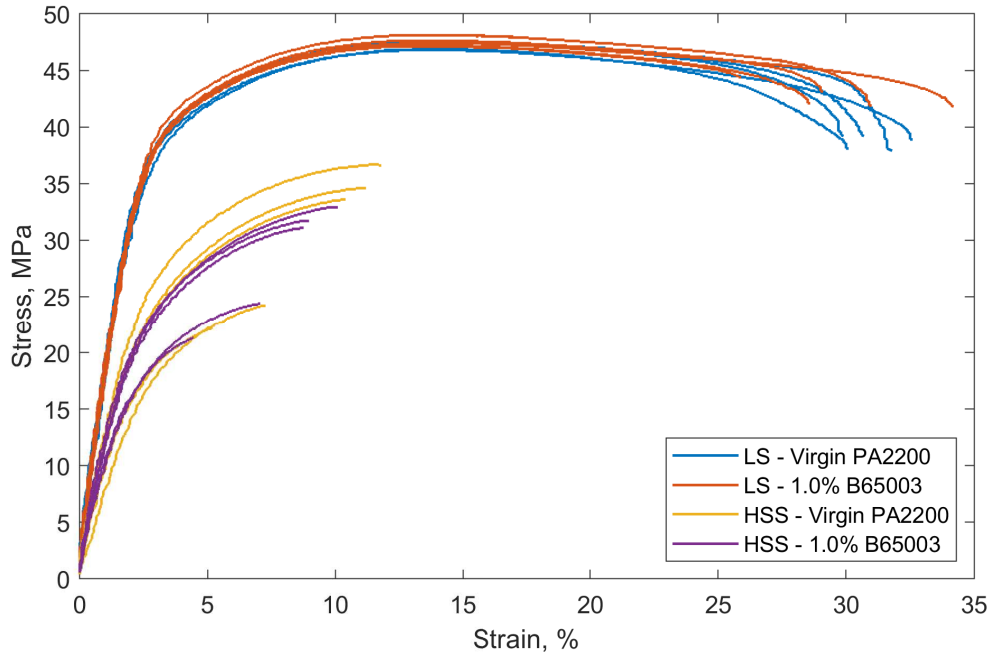
Figure C.3: Results of the preliminary tensile testing.

The differences found here were both significant, and unrecorded in the literature. It was therefore decided to investigate this further, leading to the results in Section 4.3.1 and the publication in [270].

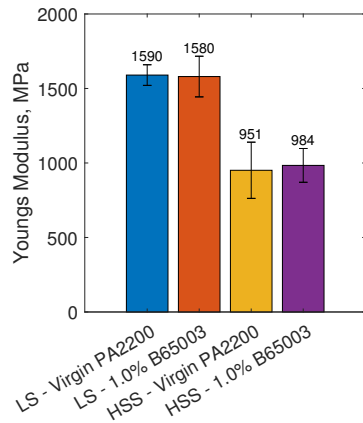
C.1.4 Comparison with High Speed Sintering

As well as being trialled in LS, the most thoroughly characterised microcomposite feedstock (1% B65003) was also briefly trialled in High Speed Sintering (HSS – see Section 1.4.4) by Robert (Bob) Turner.

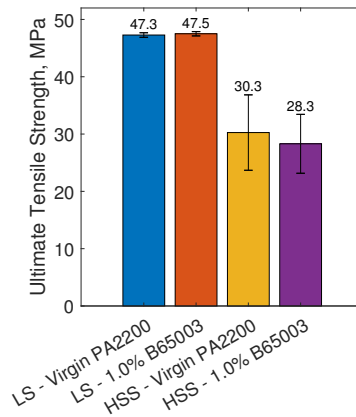
The microcomposite feedstock was successfully processed in HSS, with tensile specimens printed and jointly tested with the author. The results are shown in Figure C.4, with the corresponding values from the LS builds included for comparison. For all the measured properties, there were no significant differences in the materials within each process (LS or HSS), with a significant (and obvious) difference between the two processes.



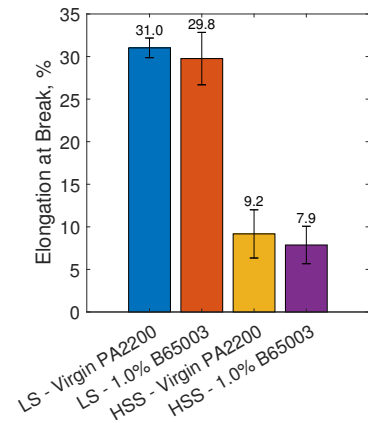
(a) Stress-strain curves.



(b) Elastic Modulus.



(c) Ultimate Tensile Strength.



(d) Elongation at Break

Figure C.4: Comparison of Laser Sintered (LS) and High Speed Sintered (HSS) parts. HSS parts were printed by R. Turner.

Although the material processed successfully in HSS, and some antibacterial testing was carried out HSS parts, the additional contamination of the CB ink was seen as a barrier at the time. For this reason, it was decided to focus solely on LS parts, with the potential for work on HSS in the future.

C.2 Preliminary Antimicrobial Testing

C.2.1 Sterilisation Testing

Methodology

To test the sterility of surfaces after printing, samples from each build were briefly placed on agar plates to transfer any surface bacteria. The plates were incubated for 72 hours at 37°C to encourage bacterial growth, with photos taken at 24 hour intervals. An example layout used to test the sterility is shown in Figure C.5. With this layout, four surfaces could be tested at once; with space for a positive control to ensure bacteria could grow, and a negative control to test for contamination of the plate.

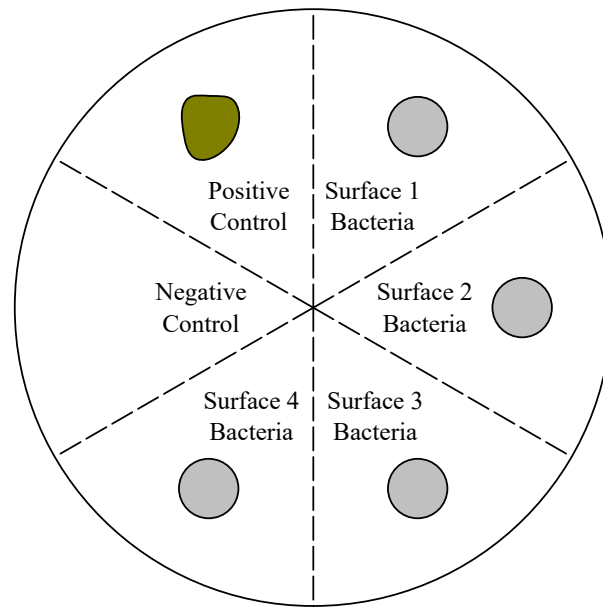


Figure C.5: Example layout of a Petri dish used for testing the sterility of disc surfaces.

To determine the level of sterilisation required, tests were first carried out using an intermediate-level disinfectant [365], namely 70% industrial methylated spirits (IMS), due to its relative simplicity. A chemical disinfectant was initially chosen over more effective sterilisation techniques due to the potential degradation of the printed parts when exposed to high temperatures or to UV light.

Results

The results of the Sterilisation tests are shown in Figures C.6 and C.7.

Discussion

The results shown in Figures C.6 and C.7 show that the immersion of the parts in 70% IMS for 15 minutes was sufficient to eliminate any CFUs on the surface of the discs. For this reason this was chosen as the initial method of sterilisation for the antimicrobial efficacy experiments.

However, this methodology only tests for CFUs on the surface. Further tests could involve submerging the discs in BHI and incubating for 24 hours, then reading either the OD_{600} or plating out to count the number of CFUs.

Another drawback of submerging the parts in 70% IMS is the potential for Ag^+ to leech out of the parts before the experiments start, thus reducing the measured antimicrobial efficacy. It is also possible that if the samples are not completely dried out prior to use, the absorbed IMS could provide a false reading and increase the antimicrobial efficacy measured.

Future experiments could test the effectiveness of other sterilisation techniques, such as the use of an autoclave or γ -radiation.



(a) 24 Hours.



(b) 48 Hours.



(c) 72 Hours.

Figure C.6: Photos of the plates at 24 hour intervals following the initial sterilisation test, with bacterial growth shown in red. V (Virgin), O (Used), SV (Sterilised Virgin in IMS), SO (Sterilised Used in IMS), C (Negative Control – no samples), +ve C (Positive Control – 10 ml of *S. aureus*).



(a) 24 Hours.



(b) 48 Hours.



(c) 72 Hours.

Figure C.7: Photos of the plates at 24 hour intervals following the initial sterilisation test, with bacterial growth shown in red. V (Virgin), O (Used), SV (Sterilised Virgin in IMS), SO (Sterilised Used in IMS), -ve (Negative Control – no samples), no positive control was available.

C.2.2 Contact Efficacy (Planktonic only)

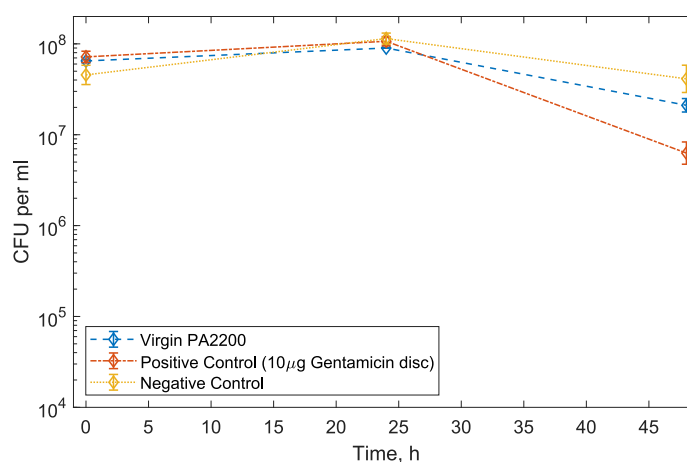
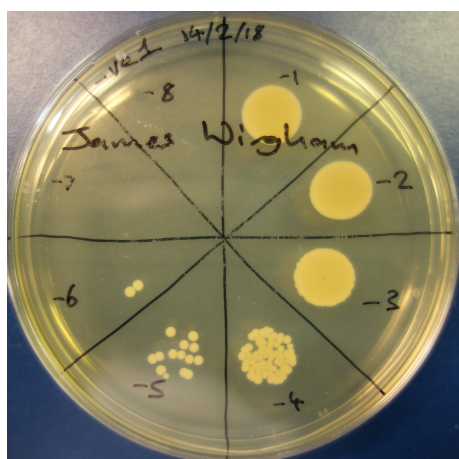
To determine the ability of the material to reduce the number of planktonic bacteria in a given volume, the following methodology was used.

Methodology

To prepare the samples:

1. Add 500 μl of the overnight bacteria of interest to 10 ml PBS.
2. Add the material of interest.
 - For the experiment, this was a 10 mm disc (as described in Section 4.4.3).
 - For a positive control, this was a 10 μg Gentamicin disc.
 - For a negative control, this was a 10 mm disc with no bacteria was added to the PBS.
3. Incubate in an orbital shaker for 24 hours at 37°C and 110 RPM.
4. Carry out a Miles and Misra serial dilution (Appendix A.5) to determine the CFU/ml.

Results



(a) Example of an incubated agar plate used to count bacteria.

(b) Colony forming units over a 48 hour time period using *S. aureus* S235. Results are geometric mean \times geometric standard error.

Figure C.8: Results of the preliminary bacteria reduction experiment with virgin PA2200 discs. 🍌

Discussion

The incubated agar plate shown in Figure C.8a was typical of the plates counted, with CFUs counted at a maximum dilution of 10^{-6} across all plates. This shows that the inclusion of dilutions up to 10^{-8} was sufficient to fully capture the data.

The CFU/ml count shown in Figure C.8b shows no significant difference for the PA2200 discs, as expected. The positive control shows a slight decrease in the number of CFUs; however, since this reduction was relatively small, changes to either the initial volume of the culture or the choice of positive control material should be made in future experiments.

C.3 Other Commercially Available Silver Phosphate Glasses

In addition to the two additives from BioCote, two other commercially available antimicrobial silver phosphate glasses were trialed in Laser Sintering from a different manufacturer. These two additives (which will remain unnamed here) used the same silver phosphate glass powder as each other, with the second including an additional taggant for easier identification of the additive. These are both shown in Figure C.9.



Figure C.9: Photos of the other commercially available additives used, shown is 20 g of each powder. 🚫

C.3.1 Particle Size Analysis

Before testing in LS, the only obvious difference with these powders compared to the other additives tested, was quoted datasheet particle sizes. The manufacturer's specification stated that the sizes was in the range of 2–4 μm , compared to the $<10 \mu\text{m}$ and $<40 \mu\text{m}$ for the BioCote powders. To more accurately quantify this, Laser Diffraction was used to measure the particle size distribution of the two powders.

Methodology and Results

The methodology used here was the same as in Sections 4.1.2 and 5.1.4, with the results shown in Table C.2 and Figure C.10. In these, all of the additives used throughout this thesis have been included for comparison.

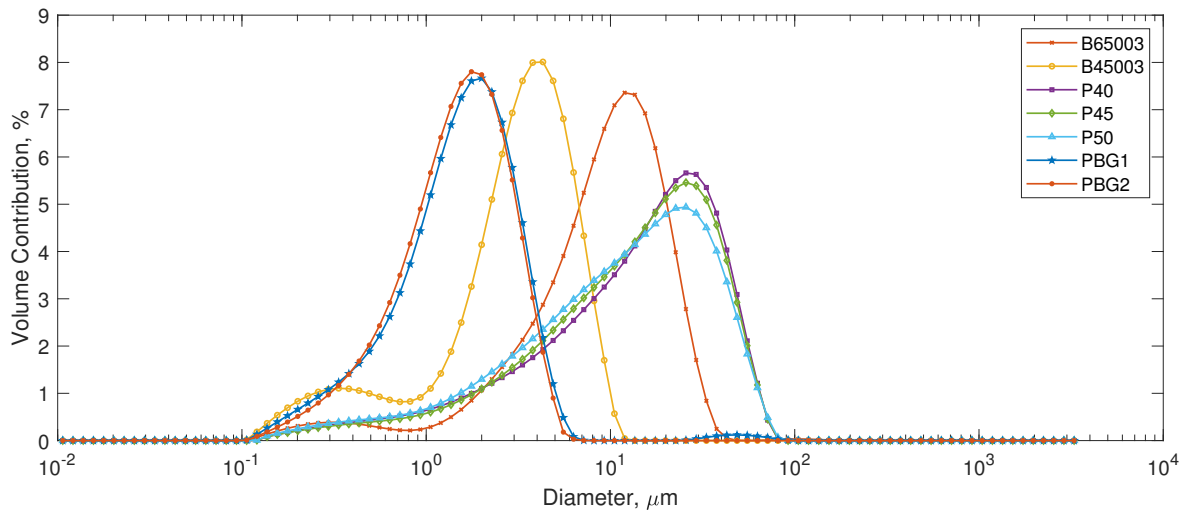
| Glass Additive | D10 / μm | D50 / μm | D90 / μm | D[4,3] / μm | Weighted Residual / % |
|----------------|---------------------|------------------------|---------------------|------------------------|-----------------------|
| PBG1 | 0.493 ± 0.029 | 1.59 ± 0.02 | 3.36 ± 0.09 | 2.13 ± 0.63 | 0.37 ± 0.07 |
| PBG2 | 0.519 ± 0.015 | 1.52 ± 0.02 | 3.15 ± 0.06 | 1.70 ± 0.03 | 0.45 ± 0.07 |
| B65003 | 2.48 ± 0.04 | 9.83 ± 0.07 (10.5) | 21.1 ± 0.4 | 11.1 ± 0.5 | 0.81 ± 0.04 |
| B45003 | 0.528 ± 0.022 | 3.31 ± 0.02 | 6.65 ± 0.06 | 3.55 ± 0.02 | 0.52 ± 0.22 |
| P40 | 1.93 ± 0.07 | 15.5 ± 0.2 | 41.3 ± 0.9 | 18.9 ± 0.3 | 0.58 ± 0.04 |
| P45 | 2.10 ± 0.02 | 14.8 ± 0.1 | 40.6 ± 0.6 | 18.5 ± 0.2 | 0.56 ± 0.09 |
| P50 | 1.74 ± 0.02 | 13.0 ± 0.1 | 39.4 ± 0.4 | 17.2 ± 0.1 | 0.83 ± 0.17 |

Table C.2: Results from particle size analysis. Values in brackets are those quoted by the manufacturer.

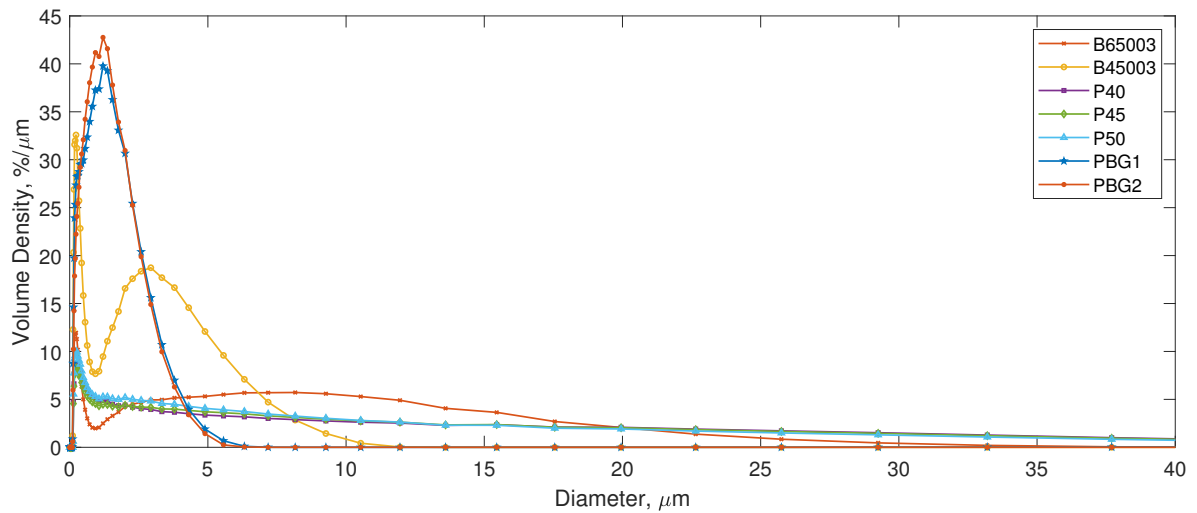
Discussion

As can be seen both from Table C.2 and Figure C.10, these other additives were both very similar in size and notably smaller than any of the other additives measured. The slight increase in D50 and D90 for PBG1 compared to PBG2 can be explained by the incorporation of an additional taggant into the powder, quoted as having a marginally larger particle size than the silver phosphate glass (mean 3–5 μm , max 10 μm).

When it comes to the likelihood of successfully incorporating additives into a Laser Sintering build, there is no set rule with what will and what will not print; with different approaches available for including additives of various sizes should one method prove unsuccessful (see Section 2.6.1). Anecdotally, it was observed that during the printing of the BioCote additives, the smaller additives appeared to create slightly more curl in the parts during printing. Ultimately, this did not affect the print overall, but could be an indicator that the smaller sizes here could prove problematic.



(a) Log scale – as measured from the Mastersizer 3000.



(b) Linear - normalised by bin width (area represents total volume)

Figure C.10: All glasses - average curves for each powder. The other commercial additives (B65003 and B45003), as well as the custom additives (P40, P45, and P50) have been included for comparison. 🚫

C.3.2 Laser Sintering

Before any other characterisation was carried out on the additives, they were trialed in LS to determine whether printing was even possible.

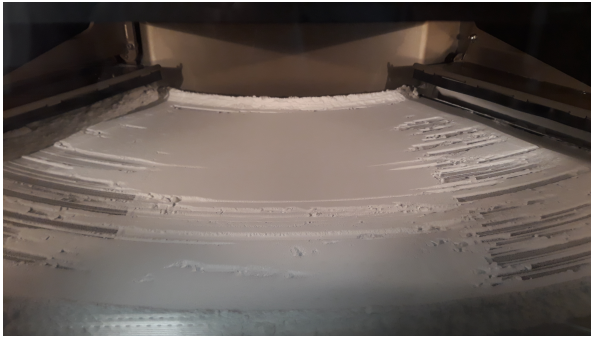
Methodology

The same methodology as Sections 4.1.4 and 5.1.5 was used for Laser Sintering. Both the PBG2 and PBG1 were incorporated at 1% by mass into virgin PA2200 using a rotary tumbler for 100 minutes. This was then processed in an EOS P100, with the standard setting for PA2200 used.

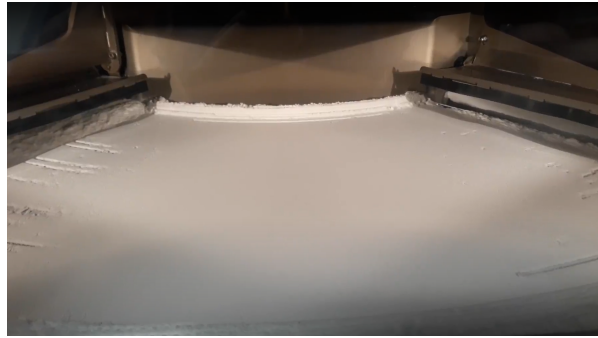
Part Printing

Photos of the build for 1% PBG2 can be seen in Figure C.11, where part way through the printing process, smaller parts curled and were swept up by the recoating blade causing the failure of the entire build. The parts produced in can be seen in Figure C.12. Here it can be seen that although the tensile specimens printed successfully, the subsequent dragging of parts across the bed exposed the surface of the tensile specimens, causing additional areas to be melted directly onto the parts.

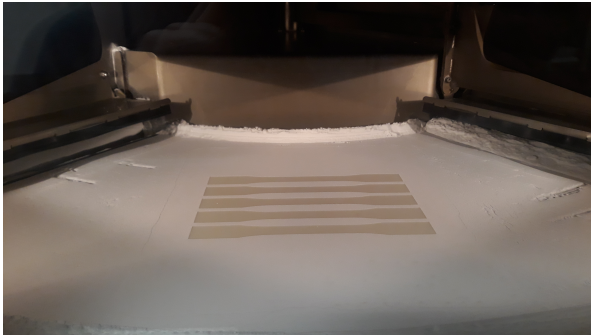
A second build was then made (excluding these smaller parts) which completed successfully, however some curl was present in the first layers of the tensile specimens. This can be seen in Figure C.13a,



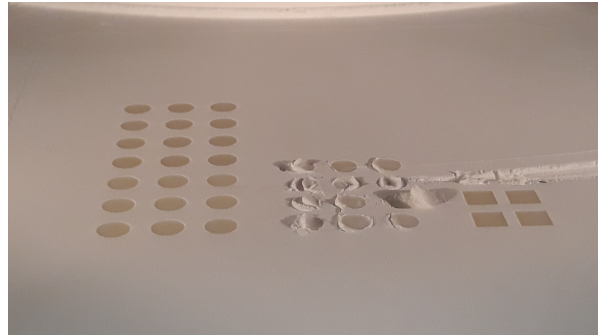
(a) Coating of the powder during the warm-up phase.



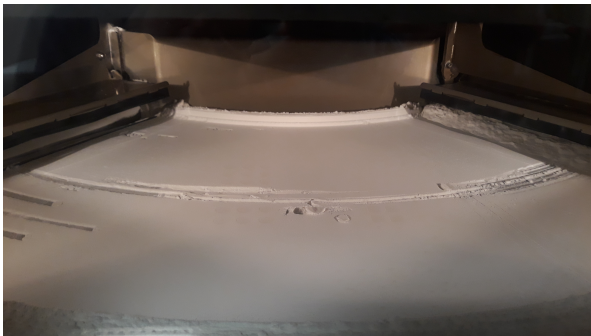
(b) The powder bed at the start of the build.



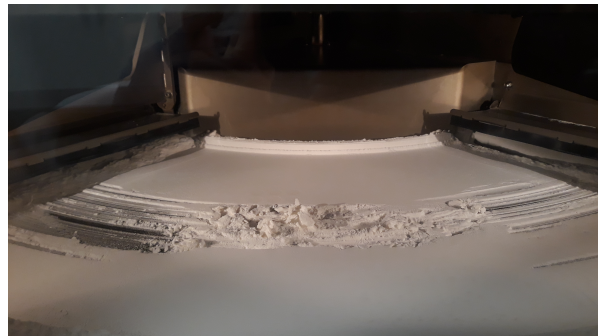
(c) Tensile specimens printed successfully.



(d) Discs curled and caught.



(e) Parts started to be moved by the recoating blade.



(f) This moved more and more parts.



(g) Complete failure of the build.

Figure C.11: Photos from the first build with 1% PBG2. 🚫

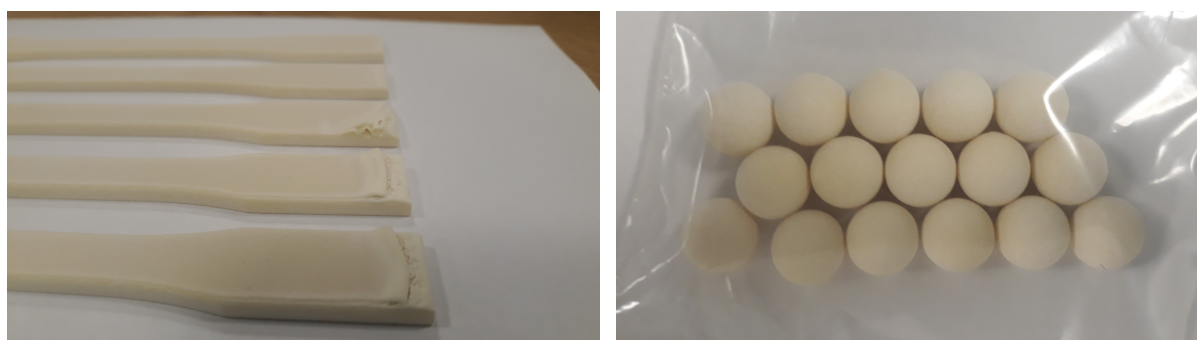


(a) Tensile specimens.

(b) Partially printed parts.

Figure C.12: Parts printed in the first build of 1% PBG2. 🚫

where the underside of the parts show the layers moved by the recoating blade; the rounded profile of the spheres (Figure C.13b) appeared to mitigate any effects of this curl and printed successfully.



(a) Underside of the tensile specimens.

(b) Spheres.

Figure C.13: Parts from the reduced build with 1% PBG2. 🚫

For PBG1, the reduced build (tensile specimens and spheres only) was again used. This was attempted twice, with the build failing while printing the tensile specimens both times.

During powder removal for both of the additives, the entire powder cake which had been exposed to the elevated temperatures in the build chamber appeared to be slightly more yellow in colour compared to the virgin powder. This raises the question of re-usability of the powder, an aspect which could lead to a large amount of waste if no powder recycling is possible.

Discussion

These trials show a variety of potential issues when processing a new material in Laser Sintering. Starting with the powder spreading (Figure C.11a), this initially displayed a large amount of agglomeration, resulting in an uneven layer of powder across the powder bed. As the temperature increased an even layer was eventually achieved (Figure C.11b), suggesting that moisture could potentially have been an issue in the feedstock; however, due to the careful storage of powders, this was thought to be unlikely.

During the printing the parts displayed an amount of curl (where a layer solidifies and shrinks slightly), causing the edges to rise above the powder bed. For a semi-crystalline polymer such as PA12, ideally each of the scanned areas should remain molten throughout the build, thus avoiding the curling of each layer (see Section 2.3.1 for details). This suggests that the parameters are not optimised for the powder.

If this optimisation of parameters was carried out, it was possible that the feedstock would be processable in its current form. However, in order to ensure a fair comparison with the other additives tested, these would also have to go through the same optimisation process. Since this can be a lengthy and involved process, and since both the BioCote and custom additives showed a negligible change in mechanical properties compared pure PA2200, it was decided not to progress any further with these additives.

Appendix D

Publications

Throughout the duration of this project, every effort has been taken to to disseminate the research more widely than in a PhD thesis¹. Journal articles published are briefly summarised below, with copies included at the end of this document (copyright permitting).

D.1 Overview

Use of silver-based additives for the development of antibacterial functionality in Laser Sintered polyamide 12 parts (2020)

This covers the main story of the thesis, focusing on the commercially available additives covered in Chapter 4. This joint first author publication in *Scientific Reports*, received a large amount of media coverage following a press release written with the University communications team [479]. This was released alongside the journal, with over 60 media outlets covering the story, including websites, newspapers, and radio. Outlets of note include, *TCT Magazine* [480], *3D Printing Industry* [481], and *The Daily Mail* [482].

- [451] R. D. Turner, **J. R. Wingham (Joint First Author)**, T. E. Paterson, J. Shepherd, and C. Majewski, “Use of silver-based additives for the development of antibacterial functionality in laser sintered polyamide 12 parts,” *Scientific Reports*, vol. 10, p. 892, 2020. [Online]. Available: <https://doi.org/10.1038/s41598-020-57686-4>.
- [452] R. D. Turner, **J. R. Wingham**, T. E. Paterson, J. Shepherd, and C. Majewski, “Data relating to use of silver-based additives for the development of antibacterial functionality in laser sintered polyamide 12 parts,” 2020. [Online]. Available: <https://doi.org/10.15131/shef.data.11861430.v1>.

Micro-CT for analysis of Laser Sintered micro-composites (2020)

This is a direct publication of Sections 4.2.4 and 4.2.5, with all work carried out and written up by the author (unless explicitly stated).

- [260] **J. R. Wingham**, R. Turner, J. Shepherd, and C. Majewski, “Micro-CT for analysis of laser sintered micro-composites,” *Rapid Prototyping Journal*, vol. 26, no. 4, pp. 649–657, 2020. [Online]. Available: <https://doi.org/10.1108/RPJ-08-2019-0211>.
- [453] **J. R. Wingham**, R. Turner, J. Shepherd, and C. Majewski, “Data relating to micro-CT for analysis of laser sintered micro-composites,” 2020. [Online]. Available: <https://doi.org/10.15131/shef.data.11591283.v1>.

Effect of Steam Autoclaving on Laser Sintered Polyamide 12 (2020)

This is a direct publication of Section 4.3.1, with all work carried out and written up by the author (unless explicitly stated).

- [270] **J. R. Wingham**, M. Omran, J. Shepherd, and C. Majewski, “Effect of steam autoclaving on laser sintered polyamide 12,” *Rapid Prototyping Journal*, vol. 27, no. 1, pp. 45–52, 2020. [Online]. Available: <https://doi.org/10.1108/RPJ-11-2019-0288>.

¹Well done for making it this far and thanks for reading to the very end of my Thesis! You are in a very small minority of people...

Tailored additives for incorporation of antibacterial functionality into laser sintered parts (2022)

This is a direct publication of Chapter 5, with all work carried out and written up by the author (unless explicitly stated).

- [445] **J. R. Wingham**, I. Ahmed, M. T. Islam, J. Shepherd, and C. Majewski, "Tailored additives for incorporation of antibacterial functionality into laser sintered parts," *Frontiers in Biomaterials Science*, vol. 1, p. 929006, 2022. [Online]. Available: <https://doi.org/10.3389/fbiom.2022.929006>.

Degradation of Laser Sintered polyamide 12 parts due to accelerated exposure to ultraviolet radiation (2021)

Although not part of this thesis, the experiments in this paper were carried out in part by the author and relate to the function and long-term use of LS parts. A copy of this is not included here as it is not relevant to the thesis, however this open access article is available at the link below.

- [287] A. S. D. Shackelford, R. J. Williams, R. Brown, **J. R. Wingham**, and C. Majewski, "Degradation of laser sintered nylon-12 parts due to accelerated exposure to ultraviolet radiation," *Additive Manufacturing*, vol. 46, p. 102132, 2021. [Online]. Available: <https://doi.org/10.1016/j.addma.2021.102132>.

OPEN

Use of silver-based additives for the development of antibacterial functionality in Laser Sintered polyamide 12 parts

Robert D. Turner^{1,2,3}, James R. Wingham^{1,3}, Thomas E. Paterson², Joanna Shepherd^{2*} & Candice Majewski^{1*}

Infectious diseases (exacerbated by antimicrobial resistance) cause death, loss of quality of life and economic burden globally. Materials with inherent antimicrobial properties offer the potential to reduce the spread of infection through transfer via surfaces or solutions, or to directly reduce microbial numbers in a host if used as implants. Additive Manufacturing (AM) techniques offer shorter supply chains, faster delivery, mass customisation and reduced unit costs, as well as highly complicated part geometries which are potentially harder to clean and sterilise. Here, we present a new approach to introducing antibacterial properties into AM, using Laser Sintering, by combining antimicrobial and base polymer powders prior to processing. We demonstrate that the mechanical properties of the resultant composite parts are similar to standard polymer parts and reveal the mode of the antibacterial activity. We show that antibacterial activity is modulated by the presence of obstructing compounds in different experimental media, which will inform appropriate use cases. We show that the material is not toxic to mammalian cells. This material could be quickly used for commercial products, and our approach could be adopted more generally to add new functionality to Laser Sintered parts.

The global Additive Manufacturing (AM) market has grown by an average of 26.9% annually for the last 30 years, with the overall revenue of the industry currently estimated at \$9.8 billion, and aerospace, automotive and healthcare being major sectors¹. Parts are produced in a layer-by-layer manner, directly from a Computer-Aided Design (CAD) file. This layer-by-layer approach provides key benefits through removing the need for tooling and increasing the ease with which complex geometries can be produced. However, despite their clear potential, the range of materials that can be used in AM processes is limited compared to more traditional manufacturing techniques, which in turn has restricted the range of applications in which they can be used.

Laser Sintering is an AM technology that produces parts by selectively scanning and melting consecutive cross-sections of polymer powder particles. Areas which have not been scanned remain as loose powder throughout the process, acting to support any overhanging areas, which in turn allows the economic production of highly complex part geometries. This geometric capability makes Laser Sintering highly suited to production of complex, optimised, products and devices, or to the production of products and devices personalised to individuals. However, particularly when considering hand-held and/or medical products, increasing geometric complexity can render them difficult and time-consuming to clean effectively, potentially providing increased chance of spread of bacteria. Incorporation of antibacterial properties into the parts themselves could reduce or eliminate this risk, and is the focus of this work.

Many antimicrobial products are currently available to purchase, with a growing global market for antimicrobial additives (materials that are added to base materials to yield antimicrobial properties). Antimicrobial products are used in the healthcare sector as well as in consumer goods - the demand for these is driven not only by a desire to improve health, but to develop opportunities to create added value. They have the potential to make a positive impact in healthcare in implants, prosthetics and splints², and surfaces and devices in clinical

¹Department of Mechanical Engineering, University of Sheffield, Royal Exchange Building, 64 Garden Street, Sheffield, S1 4BJ, UK. ²School of Clinical Dentistry, University of Sheffield, 19 Claremont Crescent, Sheffield, S10 2TA, UK. ³These authors contributed equally: Robert D. Turner and James R. Wingham. *email: j.shepherd@sheffield.ac.uk; c.majewski@sheffield.ac.uk

settings (e.g. sinks, instruments, keyboards). Adlhart and colleagues propose a helpful set of categories for antimicrobial surfaces: anti-adhesive surfaces (based on preventing microbial attachment³), contact-active surfaces (that kill microbes on contact) or biocide releasing surfaces (from which the active ingredient is eluted into the surroundings)⁴. If a material is not inherently antimicrobial, the different types are obtained either by mixing antimicrobial additives into the bulk material, or through direct physical modification (e.g. altered roughness) or chemical modification (e.g. attachment of a biocide) to the surface. The biocidal properties of copper, zinc and silver (amongst other metals) are exploited in commercial antimicrobial additives and in ongoing research⁵, with silver a well-established choice. We therefore chose to develop a composite material to be used in AM using silver-based additives.

Research into AM of antimicrobial materials is a small but rapidly growing field. Researchers have incorporated antimicrobials (or antibiotics) into polymer, metal and ceramic composites using a range of AM techniques. Fused Deposition Modelling (FDM) has been used to incorporate, for example, nitrofurantoin⁶ or silver nitrate⁷ for potential use in medicine and healthcare. Stereolithography (SLA) has been used to incorporate 4-aminosalicylic acid⁸ for customised drug-release kinetics, silver nanoparticles⁹ or quaternary ammonium compounds¹⁰. Binder Jetting has been employed, often exploiting the capacity to dissolve antibiotics in the liquid binder, to form polymer¹¹ or ceramic¹² composites, for potential bone implants amongst other applications. Robocasting has been used to incorporate a range of agents including levofloxacin¹³, quaternary ammonium compounds¹⁴ or silver nanoparticles¹⁵, in a field again largely aimed at developing bone implants. Selective Laser Melting (SLM) of titanium¹⁶ or cobalt-chromium-molybdenum¹⁷ has been employed by several groups to develop bone implants – adding antimicrobial functionality to these generally requires a post-processing step, likely due to the high temperatures involved in melting metal being deleterious to many antimicrobials. To the best of our knowledge, no antimicrobial materials made using Laser Sintering have been described to date in the academic literature.

The proposed antimicrobial effects of silver remain an active research topic and fall into two broad categories: direct reactions between silver ions and cellular components (proteins, membranes, DNA) or indirect damage caused by reactive oxygen species (e.g. hydrogen peroxide) generated by the silver^{18,19}. Xiu and coworkers showed that silver ions are equally toxic to *Escherichia coli* in aerobic and anaerobic conditions, contending on the basis of this that reactive oxygen has no role in the mechanism of action. However, an earlier study of *E. coli* and *Staphylococcus aureus*²⁰ contradicts this finding, arguing that there is a role for oxidative stress under aerobic conditions. It may be that this inconsistency can be explained by methodological differences. An important study highlights the protective effect of thiol groups in the experimental medium²¹. It seems reasonable on the basis of this to assume that silver can bind these thiols and as a result become unavailable to participate in any other reactions that might (directly or indirectly) harm microbes. It has also been established that increased levels of serum in growth medium for cultured human cells is protective against the toxic effects of silver²², perhaps by a similar thiol-binding mechanism. Whatever the mechanism of antimicrobial action, our concern as engineers is to develop an approach that can safely kill or inhibit microbes using silver ions, and all relevant previous research suggests that to do this silver ions must be available in proximity to the microbes. In this manuscript, we do not contribute to the debate on the mechanism of action of silver as an antimicrobial, but explain how our material delivers silver ions and under what circumstances it will be most useful.

Here, we have adopted a commercially available antimicrobial additive (Biocote B65003) and combined this with a widely used Laser Sintering powder (polyamide 12, EOS PA2200) to create an antimicrobial material suitable for a range of potential uses. We characterise the resulting composite parts, including their mechanical properties, antibacterial properties (using *S. aureus* as a model Gram positive organism and *Pseudomonas aeruginosa* as a model Gram negative), and demonstrate a lack of cytotoxic effects.

Results and Discussion

Processability of material. We printed polyamide 12 parts in a range of geometries using standard settings for this material on a commercial EOS Formiga P100 printer. We subsequently printed the same part geometries in polyamide 12 mixed with 1% B65003 silver phosphate glass. The parts were qualitatively near-identical (Fig. 1a). This straightforward experiment demonstrated the processability of a mix of sinterable and non-sinterable powders via a Laser Sintering 3D printer.

Mechanical properties of parts. Tensile testing was employed to ensure that there were no detrimental effects on the mechanical properties of the composite when compared with the standard polyamide 12 Laser Sintering material. We therefore printed “dogbones” for use in tensile testing, which involved measuring the force required to break the parts when subjected to a tensile load. This yielded measurements of Young’s Modulus (E – the stiffness of the material), Ultimate Tensile Strength (σ_{uts} – how much force per unit area is needed to break the material) and Elongation at Break (ϵ_{max} – how much the material ‘stretches’ before breaking) which were similar for both materials (Fig. 1b,c): The properties of the Laser Sintered parts were measured as; polyamide 12 ($E = 1590 \pm 69$ MPa, $\sigma_{\text{uts}} = 47.3 \pm 0.4$ MPa, $\epsilon_{\text{max}} = 31.0 \pm 1.2\%$) and 1.0% B65003 ($E = 1580 \pm 136$ MPa, $\sigma_{\text{uts}} = 47.5 \pm 0.4$ MPa, $\epsilon_{\text{max}} = 29.8 \pm 3.1\%$). A 2 sample Welch’s t-test was carried out to compare the materials to each other, with p values < 0.05 considered to be significantly different. The resulting p values were; 0.89 for E , 0.39 for σ_{uts} , and 0.43 for ϵ_{max} showing that there was no significant difference. These results indicate the materials can be used interchangeably, with no effect on the mechanical properties of printed parts.

Part structure and composition. Parts made of the base material and composite were imaged using SEM. This revealed the characteristic granular structure of the surface of the Laser Sintered polyamide (Fig. 2). Some differences in contrast were observed between the surface of the base material and the composite (compare Fig. 2a,b with Fig. 2c,d) due to the sensitivity to material of backscattered electrons.

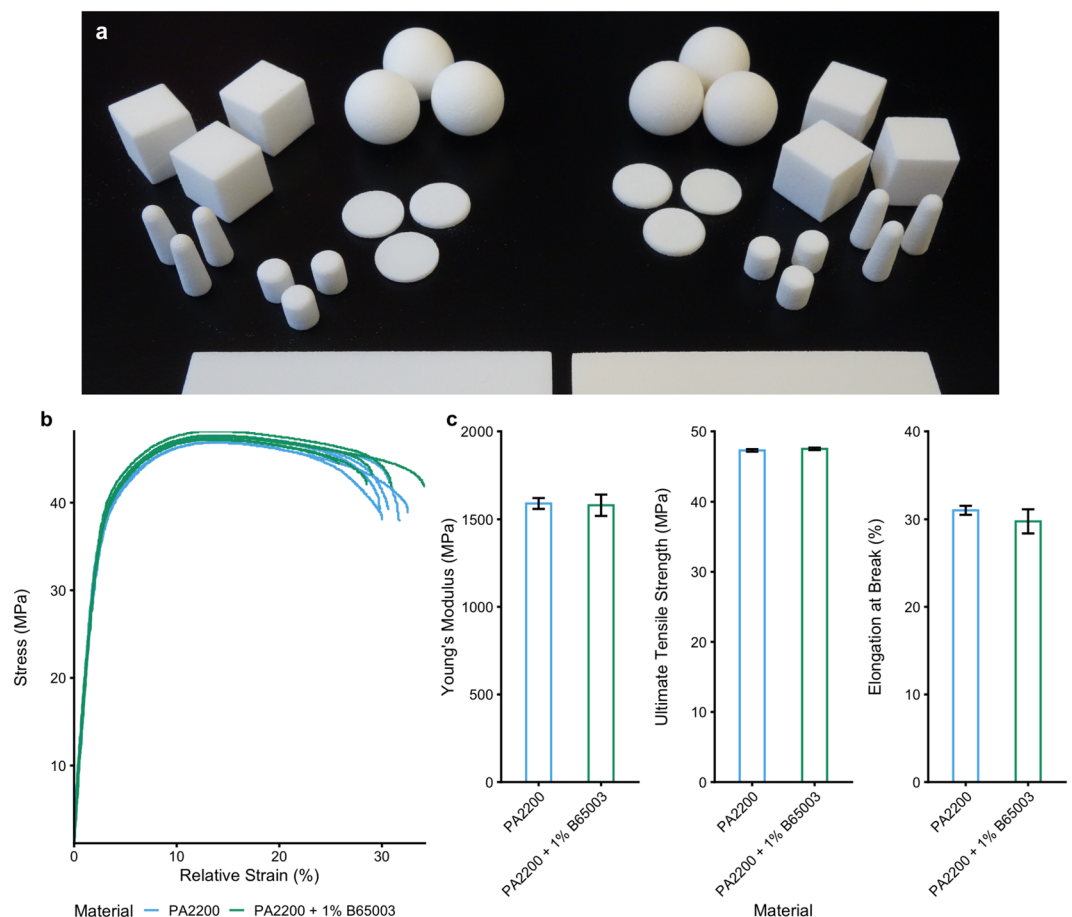


Figure 1. Engineering properties of parts (a) Photograph of a selection of parts made from PA2200 (left) alongside the 1% B65003 composite material (right). (b) Raw stress-strain curves from tensile testing. (c) A comparison of Young's modulus (E), ultimate tensile strength (σ_{UTS}) and elongation at break (ϵ_{max}) for both materials.

The silver phosphate glass was found to be distributed evenly throughout the parts on this basis of X-Ray micro tomography. The difference in electron density between this and the base polyamide 12 led to the silver phosphate glass appearing brighter, allowing analysis of its dispersion (Fig. 2e,f).

EDX elemental analysis was used to identify the distribution of the additive on the surface. A spectral analysis of both the B65003 additive and the composite part (Table 1), showed that although silver was present in the additive, the low concentration was such that it was below the detection limit when combined in the printed part. To map the location of the additive (Fig. 3), the elements phosphorus and oxygen were instead used as these were abundant in the additive but not in PA2200, as shown in Fig. 3c,d.

Composite parts release silver. Having validated the engineering properties of the parts, we next determined the extent to which the active antimicrobial, silver, was eluted. This was measured using Inductively Coupled Plasma-Optical Emission Spectroscopy (ICP-OES) which detects the concentration of silver ions in solution. In a preliminary test, silver phosphate glass was found to release far more silver ions than metallic silver powder, further validating this material as an antimicrobial additive (Table 2). We estimate our parts (containing 1.0% B65003) released a similar amount of silver per unit surface area over 24 hours ($\sim 0.012 \text{ mg/l/cm}^2$) as a previously reported compression moulded polyamide 12 composite containing 1.4% Nanosilver ($\sim 0.03 \text{ mg/l/cm}^2$)²³ released over 100 days. This indicates that our new AM approach yields a material that releases silver (loosely speaking) at least as well as existing (non-AM) materials. The surface area of our spheres (used in this calculation) was $4.62 \pm 0.01 \text{ cm}^2$ (standard error, $n = 100$ {20 parts, 5 measurements per part, pooled}).

Composite parts have an antibacterial effect against gram positive *Staphylococcus aureus* and gram negative *Pseudomonas aeruginosa*. Assured that our composite parts release silver, we then checked for antibacterial activity against two representative pathogens. Parts were incubated in Phosphate Buffered Saline (PBS) containing bacteria for 24 hours, after which the amount of bacteria in the medium (planktonic bacteria) and on the parts surface (biofilm) was measured. Bacteria survived for 24 hours in PBS with a normal polyamide 12 part. There were fewer planktonic *S. aureus* in PBS that had held a part made of the antibacterial composite than in the equivalent for polyamide 12, with some samples containing so few bacteria that they

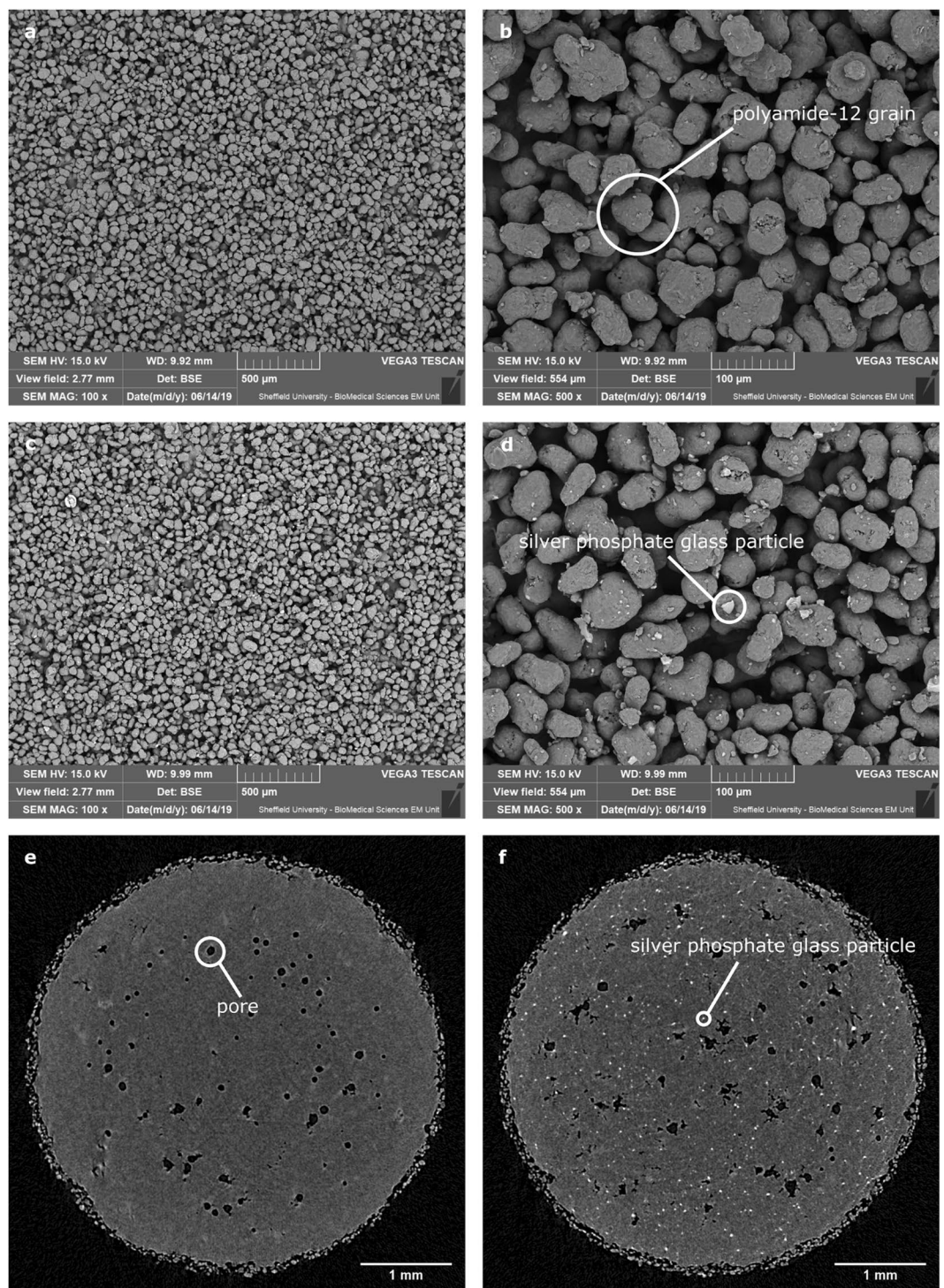


Figure 2. Images of parts – (a,b) SEM images of base material (sintered PA2200), (c,d) composite material. The lighter, more angular objects in d are likely silver phosphate glass. (e) X-Ray micro tomography section of base material (PA2200), showing pores. (f) X-Ray micro tomography section of the composite showing even distribution of silver phosphate glass particles.

were undetectable in our assay (Fig. 4a). This effect was mirrored for *S. aureus* biofilms (Fig. 4b). In the case of *P. aeruginosa* there was also a reduction in numbers of bacteria comparing antibacterial polyamide 12 (containing 1.0% B65003) to polyamide 12 for both planktonic organisms and those in biofilms on the surface of the parts (Fig. 4c,d).

Antibacterial effects do not require contact between parts and bacteria. To explore whether the anti-biofilm properties of our material were mediated by contact between bacteria and parts, we incubated parts

| Sample | Weight percentage \pm Standard Deviation (%) | | | | | | |
|----------------------|--|----------------|----------------|---------------|---------------|---------------|---------------|
| | O | C | P | Ti | Mg | Ca | Ag |
| B65003 | 63.6 \pm 0.4 | 16.5 \pm 0.4 | 12.6 \pm 0.1 | 0.0 \pm 0.0 | 3.5 \pm 0.0 | 2.9 \pm 0.0 | 0.9 \pm 0.1 |
| PA2200 + 1.0% B65003 | 72.5 \pm 0.1 | 27.1 \pm 0.1 | 0.2 \pm 0.0 | 0.1 \pm 0.0 | 0.0 \pm 0.0 | 0.0 \pm 0.0 | 0.0 \pm 0.0 |

Table 1. Composition of the silver phosphate glass additive (B65003) and the composite part (PA2200 + 1.0% B65003) obtained from EDX analysis.

| Sample | Mean Standard Error | n samples above 0.002 mg/l detection limit (/total) |
|--|-------------------------|---|
| Silver ion concentration after 24 hours incubation of silver or silver phosphate glass at 2 mg/ml in water | | |
| Control (Water) | NA | 0/4 |
| Silver Powder | 0.006 \pm 0.0016 mg/l | 3/4 |
| B65003 | 26 \pm 2.5 mg/l | 4/4 |
| Silver ion concentration after 24 hours incubation of polyamide 12 or antibacterial polyamide 12 (containing 1.0% B65003) spheres in 5 ml water | | |
| PA2200 | NA | 0/3 |
| PA2200 + 1.0% B65003 | 0.056 \pm 0.018 mg/l | 3/3 |

Table 2. ICP-OES measurements of silver concentration.

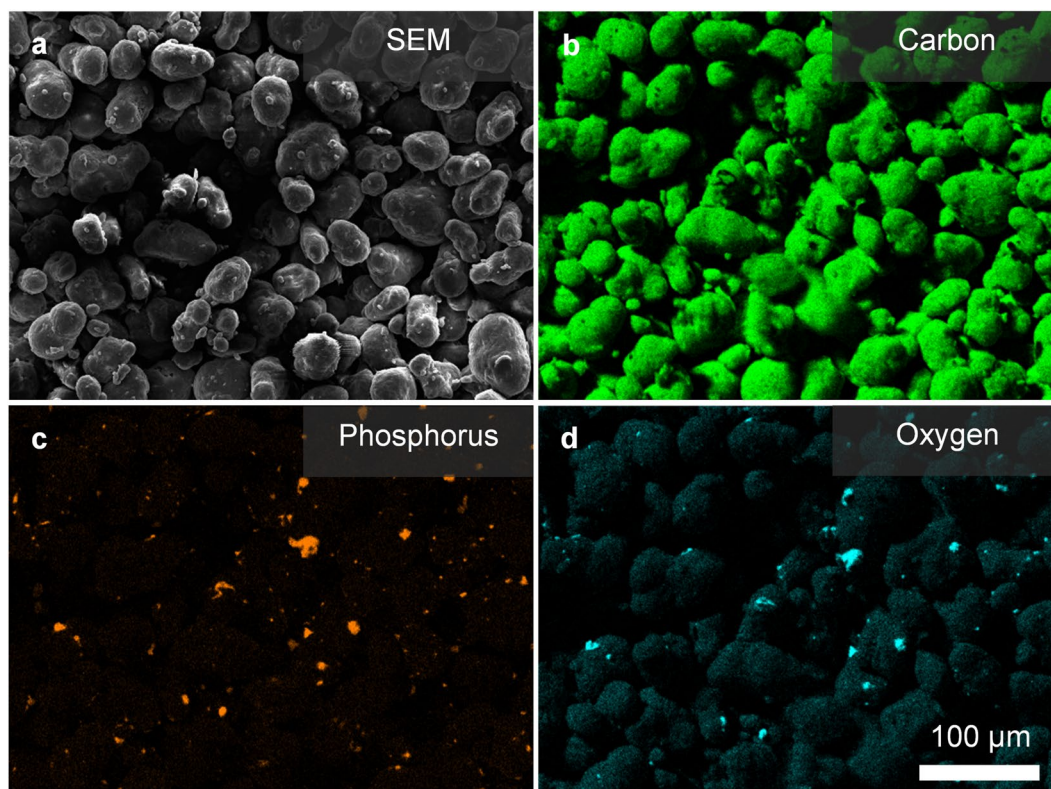


Figure 3. SEM and EDX map of composite PA2200 + B65003 surface. (a) SEM micrograph of the surface scanned with EDX. (b–d) Elemental map from EDX analysis of the surface with colour indicating detection of the corresponding element.

in PBS, removed them after 24 hours and then inoculated the PBS with bacteria. There were less bacteria in PBS that had contained antibacterial polyamide 12 (containing 1.0% B65003) than that which had held normal polyamide 12 (Fig. 4e). This proves that contact between parts and bacteria is not required for an antibacterial effect (it does not totally disprove that there may also be some contact mediated effects). We infer from this that silver ions are eluted from the antibacterial polyamide 12 (containing 1.0% B65003) in solution and diffuse to their targets. The anti-biofilm effect is therefore likely a consequence of bacterial mortality (likely prior to adhesion to the antibacterial polyamide 12 (containing 1.0% B65003)) rather than an anti-adhesion mechanism.

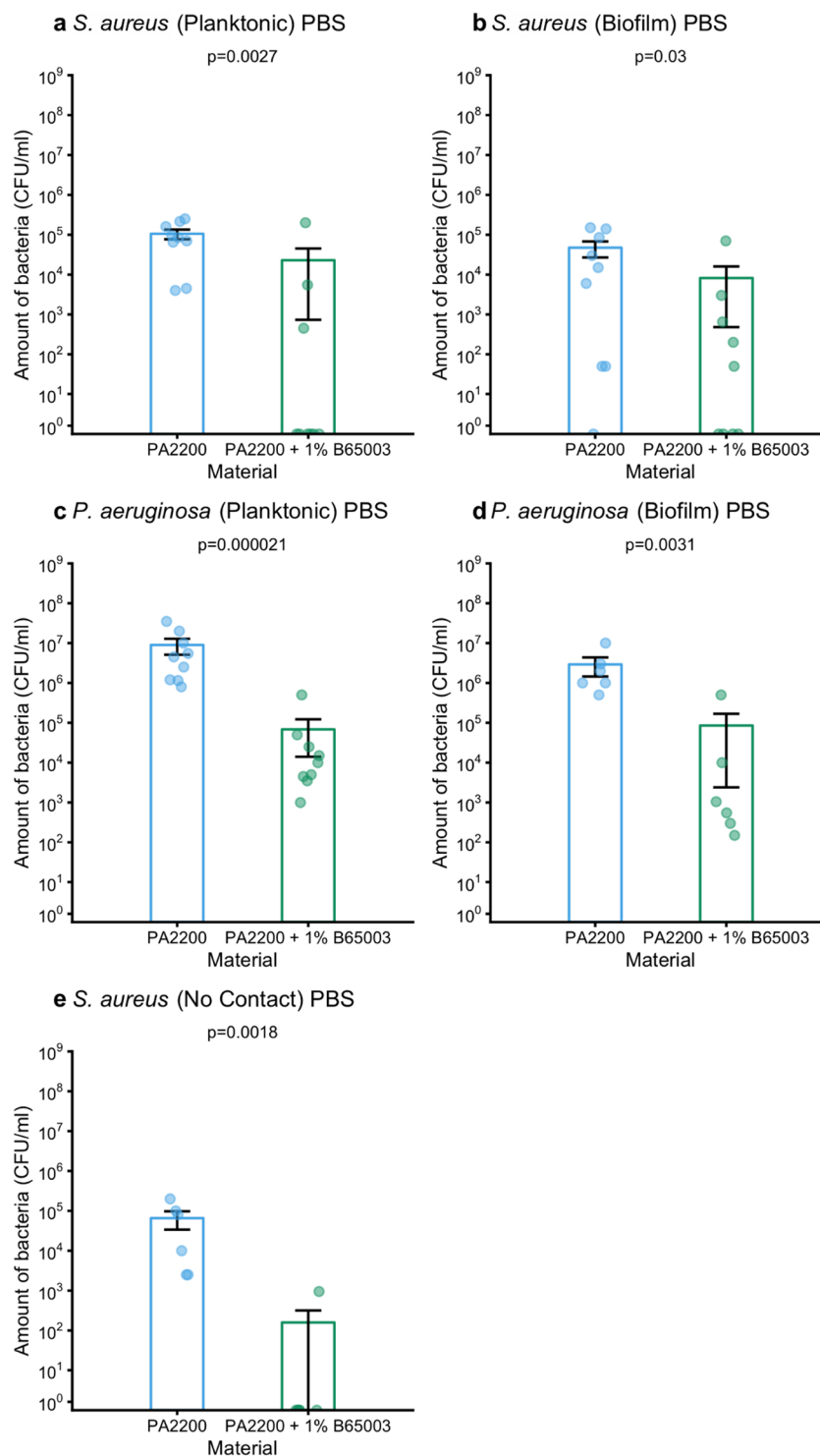


Figure 4. Comparison of amount of *S. aureus* (CFU/ml) in PBS surrounding (a), or attached to (b) polyamide 12 or antibacterial polyamide 12 (containing 1.0% B65003); and comparison of amount of *P. aeruginosa* (CFU/ml) in PBS surrounding (c), or attached to (d) polyamide 12 or antibacterial polyamide 12 (containing 1.0% B65003). Comparison of amount of *S. aureus* (CFU/ml) in PBS previously incubated with polyamide 12 or antibacterial polyamide 12 (containing 1.0% B65003) (e).

Antibacterial effects are diminished in rich media. PBS is reasonably representative of a very nutrient-poor (but osmotically stable and close to pH neutral) environment for bacteria, and is most relevant to partly hydrated fomite surfaces such as one might find in a kitchen or bathroom environment, or in some clinical or semi-clinical settings. However, we were also interested in the efficacy of our parts in a rich-media

environment; one containing a complex mix of biologically derived molecules in which bacteria had the nutrients needed to grow and divide. To investigate this we used Brain Heart Infusion (BHI), a commonly used rich medium for growing either *S. aureus* or *P. aeruginosa*. In this medium there was no difference between bacteria grown in media containing either polyamide 12 or antibacterial polyamide 12 (containing 1.0% B65003) for either species (Fig. 5a–d).

We hypothesised, informed by previous work^{21,22}, that the difference in performance between PBS and BHI was due to the presence of chemicals in BHI that react with silver ions, rendering them unable to perform their antibacterial function, particularly molecules with thiol (sulfhydryl) functional groups. To test this, we repeated our experiments in PBS containing 1 mM reduced glutathione (Fig. 5e,f). We saw no substantial difference in the efficacy of parts made of polyamide 12 or antibacterial polyamide 12 (containing 1.0% B65003) in this medium. This result, in the context of previous findings, strongly suggests that the presence of confounding chemicals explains the relative lack of efficacy in BHI as compared with PBS.

Composite parts do not have a cytotoxic effect. For any use case where parts are to come into contact with humans or animals, it is important to determine levels of toxicity. This was achieved by incubating parts with 2D monolayers of human fibroblast cells at the bottom of tissue culture wells. Such cells make up connective tissue, including dermal skin layers, and produce collagen. We found no difference in metabolic activity (measured using a Presto Blue assay) between any of the wells containing either no part, a part made from polyamide or antibacterial polyamide 12 (containing 1.0% B65003) (Fig. 6).

Conclusions

We have developed an approach for producing Additive Manufactured parts with antibacterial properties for use in the Laser Sintering process. The engineering properties of the new composite are indistinguishable from those of the standard polyamide 12 base material. The material is most effective in nutrient-poor hydrated environments (where reactions that interfere with the activity of the silver are less likely) and under these circumstances is able to reduce numbers of planktonic bacteria in its surroundings and numbers of biofilm bacteria attached to the surface. We have shown that there are no fundamental issues with cytotoxicity.

Efficacy against such diverse bacterial species as *S. aureus* and *P. aeruginosa*, in the context of the long history of silver as an antimicrobial agent, strongly suggests a spectrum of action against both Gram positive and Gram negative bacteria. Additional work would determine the breadth of antimicrobial activity of our material across other species, but given our evidence we would expect our material to be effective against further unwanted bacteria.

There are a range of potential uses for the material where favourable circumstances are present, including those that are intermittently hydrated, in kitchens, bathrooms and on hospital wards. However, a demonstrable lack of efficacy in rich BHI media and in PBS containing reduced glutathione should temper expectations of performance in nutrient-rich environments (e.g. *in vivo* or in the food industry). Future work will include field trials to validate laboratory results in real-world settings.

Methods

Materials. A polyamide 12 based powder was chosen as the base material (PA2200, EOS) for the antimicrobial composite. This was chosen as it is widely used in industry, meaning any added functionality could have a high impact in a relatively short timescale. A commercially available silver phosphate glass (B65003, BioCote) was chosen to create the antimicrobial effect. This material was provided in powder form, with particle size $<40\mu\text{m}$ and with an angular geometry as shown in Fig. 2d. Prior to printing, the powders were mixed for approximately 100 minutes in a rotary tumbler with 1.0% (by mass) of B65003 added to virgin (unused) PA2200.

Laser sintering. Parts were produced using an EOS Formiga P100 with the standard settings for PA2200. The key parameters used for both materials were, laser power 21 W, scan spacing 0.25 mm, and scan speed 2500 mm/s; as this was an experimental material no additional contour scan was used. Loose powder was removed from the parts using compressed air only, to limit the potential sources of contamination.

Mechanical properties. Tensile testing was carried out using a Tinius Olsen 5K with Laser Extensometer, in accordance with the methodology in ASTM D638. A type I specimen was used (Fig. 7), with a minimum of 5 specimens per material; the Young's Modulus (E), Ultimate Tensile Strength (σ_{uts}), and Elongation at Break (ϵ_{max}) were determined to characterise the mechanical properties.

Scanning electron microscopy. Samples were gold sputter-coated, then imaged using a TESCAN VEGA3 SEM using an accelerating voltage of 15 kV and detecting backscattered electrons.

Energy-dispersive x-ray spectroscopy. Samples were gold sputter-coated and a TESCAN VEGA3 SEM with attached Oxford EDX analysis was used. EDX whole area mapping using secondary electron at 15 kV with elements detected automatically chosen by the software (AZtec, Oxford instruments) based on all elements detectable within the sample.

Micro-CT. 5×5 mm cylinders were built and scanned using a Skyscan 1172 MicroCT Scanner using the following parameters: pixel size: $4.87\mu\text{m}$, voltage: 40 kV, intensity: $144\mu\text{A}$, total rotation: 180° , rotation step: 0.35° , time: 18 minutes, filter: none.

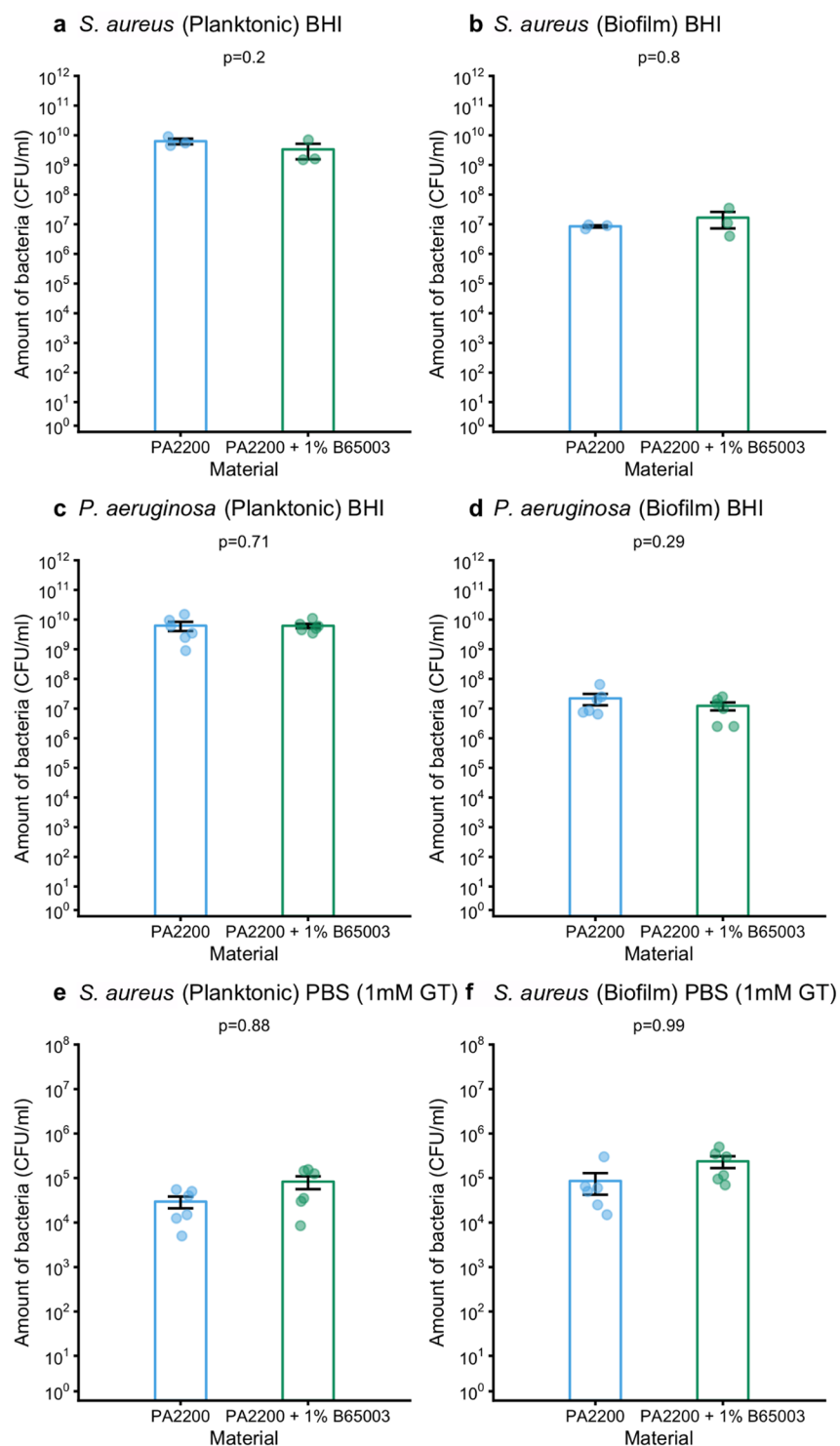


Figure 5. (a) comparison of the amount of *S. aureus* (CFU/ml) in BHI surrounding, or attached to polyamide 12 or antibacterial polyamide 12 (containing 1.0% B65003), (b) comparison of amount of *P. aeruginosa* (CFU/ml) in BHI surrounding, or attached to polyamide 12 or antibacterial polyamide 12 (containing 1.0% B65003), (c) comparison of the amount of *S. aureus* (CFU/ml) in PBS containing 1 mM reduced glutathione surrounding, or attached to polyamide 12 or antibacterial polyamide 12 (containing 1.0% B65003).

Inductively coupled plasma – optical emission spectroscopy. Powders or parts were incubated for 24 hours at 37 °C with agitation in distilled water. Supernatant was extracted and, for powder samples, was centrifuged (15 minutes at 2000 rpm) and filtered (0.2 μm filter) to remove suspended powder particles. ICP-OES was conducted using a Spectro-Ciros-Vision Optical Emission Spectrometer.

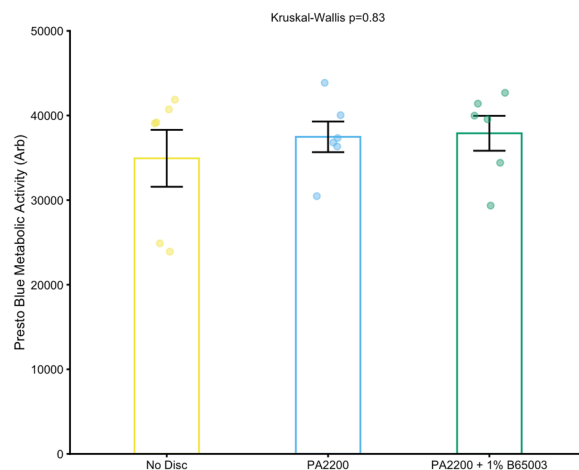


Figure 6. Comparison of metabolic activity between fibroblast monolayers containing parts, a disc made of polyamide 12 or one made of antibacterial polyamide 12 (containing 1.0% B65003). A Kruskal-Wallis test indicates no difference between groups.

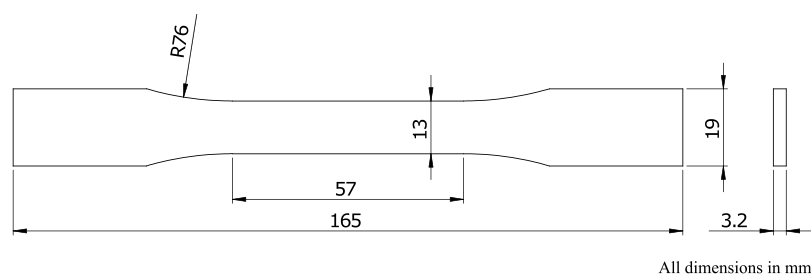


Figure 7. Dimensions of a type I tensile test specimen according to ASTM D638.

Bacterial strains and growth conditions. Bacterial strains used were clinical isolates of *Staphylococcus aureus* (S235) and *Pseudomonas aeruginosa* (SOM1) from the Charles Clifford Dental Hospital, Sheffield²⁴. These were maintained on Brain Heart Infusion (BHI) agar (Sigma-Aldrich) plates at 37 °C. Liquid cultures were in BHI broth (Oxoid). Species of bacteria come in a variety of “strains”. We chose to use “clinical isolates” (strains taken from infected patients) as opposed to strains sourced from a standard strain collection, as clinical isolates are more representative of the types of bacteria that are encountered in the real environment. BHI is a widely used medium derived from animal products it has all the nutrients that the bacteria need. As both *P. aeruginosa* and *S. aureus* are capable of living in a human host, we grew them at body temperature, 37 °C.

Incubation of parts with bacteria. Overnight cultures were diluted to $OD_{600} = 0.01$ (this is a proxy measurement for the number of bacteria in a liquid a – typical maximum is 10) in either PBS or BHI. This solution (5 ml) was then added to glass universals containing autoclaved test parts and incubated with agitation (so all of the test part was equally exposed) at 37 °C for 24 hours.

Release of biofilms. Parts were washed twice in PBS to release poorly attached bacteria before being vortexed for 30 s in 2 ml PBS to release the well attached biofilm.

Quantification of colony forming units. Bacterial suspensions were serially ten-fold diluted 10:90 μ l in PBS in 96-well microtitre plates. Each well in the plate then contained a number of bacteria that could be related back to the parent concentration. Subsequently, 20 μ l of each dilution was spotted onto BHI agar, such that at sufficiently high dilutions each individual bacterium could form a colony distinguishable from its neighbours, before overnight incubation and colony counting. Once bacteria had been counted at the dilution where the highest density of colonies could be distinguished, we were then able to calculate the number of bacteria in the parent culture using Eq. 1.

$$CFU/ml = \text{Count} \times 10^{\text{dilution}} \times 50 \quad (1)$$

The term Colony Forming Units (CFU) is used, as with this method we determine the number of colonies, not individual bacteria and in some cases more than one bacterium may be aggregated together in a single CFU.

Eukaryotic cell culture conditions. To obtain human dermal fibroblasts, human skin was obtained anonymously for medical research, with written informed consent, from individuals undergoing elective surgery for breast reduction or abdominoplasty. All methods were carried out in accordance with relevant guidelines and regulations and all experimental protocols were approved by the NHS Research Ethics Committee (REC), reference: 15/YH/017.

To isolate primary fibroblasts, dermis from donated skin was minced, then digested by 0.05% collagenase A in Dulbecco's Modified Eagle's Medium (DMEM) overnight at 37 °C with 5% CO₂. The cell suspension was centrifuged at 400 g and the pellet resuspended in medium (DMEM supplemented with 10% fetal calf serum (FCS), 0.25 mg.mL⁻¹ glutamine, 0.625 µg.mL⁻¹ amphotericin B, 100 I.U.mL⁻¹ penicillin, and 100 µg.mL⁻¹ streptomycin). Cells were cultured in fibroblast medium in T25 flasks and incubated at 37 °C with 5% CO₂. Medium was changed every 2 days, and cells were passaged as needed.

Quantification of metabolic activity in eukaryotic cells. Fibroblasts were seeded at 50,000 cells/ml in 12 well plates (1 ml/well) and cultured for 24 hours before parts were added. After a further 24 hours parts were removed and growth media was replaced with the same containing 10% Presto Blue (Invitrogen). This was allowed to develop for 40 minutes before readout on a Tecan Infinite 200 plate reader in fluorescence mode with excitation at 535 nm and emission at 590 nm. The fluorescence of the Presto Blue is proportional to the metabolic activity of the cells.

Data availability

The datasets generated during and/or analysed during the current study are available from the corresponding authors on reasonable request.

Received: 29 August 2019; Accepted: 21 December 2019;

Published online: 21 January 2020

References

1. Wohlers, T., Campbell, I., Diegel, O., Huff, R., Kowen, J. *Wohlers Report 2019: 3D Printing and Additive Manufacturing State of the Industry* (Wohlers Associates, 2019).
2. Paterson, A. M., Bibb, R., Campbell, R. I. & Bingham, G. Comparing additive manufacturing technologies for customised wrist splints. *Rapid Prototyping Journal* **21**, 230–243 (2015).
3. Katsikogianni, M. & Missirlis, Y. F. Concise review of mechanisms of bacterial adhesion to biomaterials and of techniques used in estimating bacteria-material interactions. *Eur. Cell. Mater.* **8**, 37–57 (2004).
4. Adlhart, C. *et al.* Surface modifications for antimicrobial effects in the healthcare setting: a critical overview. *J. Hosp. Infect.* **99**, 239–249 (2018).
5. Möhler, J. S., Sim, W., Blaskovich, M. A. T., Cooper, M. A. & Ziora, Z. M. Silver bullets: A new lustre on an old antimicrobial agent. *Biotechnol. Adv.* **36**, 1391–1411 (2018).
6. Sandler, N. *et al.* Towards fabrication of 3D printed medical devices to prevent biofilm formation. *Int. J. Pharm.* **459**, 62–64 (2014).
7. Tiimob, B. J. *et al.* Nanoengineered Eggshell-Silver tailored copolyester polymer blend film with antimicrobial properties. *J. Agric. Food Chem.* **65**, 1967–1976 (2017).
8. Wang, J., Goyanes, A., Gaisford, S. & Basit, A. W. Stereolithographic (SLA) 3D printing of oral modified-release dosage forms. *Int. J. Pharm.* **503**, 207–212 (2016).
9. Taormina, G., Sciancalepore, C., Bondioli, F. & Messori, M. Special resins for stereolithography: *In situ* generation of silver nanoparticles. *Polymers* **10** (2018).
10. Li, Z., Wang, C., Qiu, W. & Liu, R. Antimicrobial thiol-ene-acrylate photosensitive resins for DLP 3D printing. *Photochem. Photobiol.* **95**, 1219–1229 (2019).
11. Wu, W., Ye, C., Zheng, Q., Wu, G. & Cheng, Z. A therapeutic delivery system for chronic osteomyelitis via a multi-drug implant based on three-dimensional printing technology. *J. Biomater. Appl.* **31**, 250–260 (2016).
12. Inzana, J. A., Trombetta, R. P., Schwarz, E. M., Kates, S. L. & Awad, H. A. 3D printed bioceramics for dual antibiotic delivery to treat implant-associated bone infection. *Eur. Cell. Mater.* **30**, 232–247 (2015).
13. Puppi, D., Piras, A. M., Piroso, A., Sandreschi, S. & Chiellini, F. Levofloxacin-loaded star poly(ϵ -caprolactone) scaffolds by additive manufacturing. *J. Mater. Sci. Mater. Med.* **27**, 44 (2016).
14. Yang, Y. *et al.* Anti-infective efficacy, cytocompatibility and biocompatibility of a 3d-printed osteoconductive composite scaffold functionalized with quaternized chitosan. *Acta Biomater.* **46**, 112–128 (2016).
15. Zhang, Y. *et al.* 3d-printed bioceramic scaffolds with antibacterial and osteogenic activity. *Biofabrication* **9**, 025037 (2017).
16. Cox, S. C. *et al.* Adding functionality with additive manufacturing: Fabrication of titanium-based antibiotic eluting implants. *Mater. Sci. Eng. C Mater. Biol. Appl.* **64**, 407–415 (2016).
17. Han, C. *et al.* Electrophoretic deposition of Gentamicin-Loaded silk fibroin coatings on 3D-Printed porous Cobalt-Chromium-Molybdenum bone substitutes to prevent orthopedic implant infections. *Biomacromolecules* **18**, 3776–3787 (2017).
18. Xiu, Z.-M., Zhang, Q.-B., Puppala, H. L., Colvin, V. L. & Alvarez, P. J. J. Negligible particle-specific antibacterial activity of silver nanoparticles. *Nano Lett.* **12**, 4271–4275 (2012).
19. Xiu, Z.-M., Ma, J. & Alvarez, P. J. J. Differential effect of common ligands and molecular oxygen on antimicrobial activity of silver nanoparticles versus silver ions. *Environ. Sci. Technol.* **45**, 9003–9008 (2011).
20. Jung, W. K. *et al.* Antibacterial activity and mechanism of action of the silver ion in staphylococcus aureus and escherichia coli. *Appl. Environ. Microbiol.* **74**, 2171–2178 (2008).
21. Mulley, G., Jenkins, A. T. A. & Waterfield, N. R. Inactivation of the antibacterial and cytotoxic properties of silver ions by biologically relevant compounds. *PLoS One* **9**, e94409 (2014).
22. Hidalgo, E. & Domnguez, C. Study of cytotoxicity mechanisms of silver nitrate in human dermal fibroblasts. *Toxicol. Lett.* **98**, 169–179 (1998).
23. Kumar, R. & Münstedt, H. Silver ion release from antimicrobial polyamide/silver composites. *Biomaterials* **26**, 2081–2088 (2005).
24. Doroshenko, N. *et al.* Antibiotic functionalised polymers reduce bacterial biofilm and bioburden in a simulated infection of the cornea. *Biomater Sci* **6**, 2101–2109 (2018).

Acknowledgements

We are indebted to Kurt Bonser, Wendy Birtwistle and Jason Heath for technical advice and support. This work was funded by EPSRC grant EP/R036748/1 - 'When the drugs don't work. Manufacturing our pathogen defenses.' James R. Wingham is supported by an EPSRC DTP PhD studentship.

Author contributions

All authors planned experiments, analysed data and contributed to manuscript preparation. R.D. Turner, J.R. Wingham and T.E. Paterson carried out experiments.

Competing interests

The authors declare no competing interests.

Additional information

Correspondence and requests for materials should be addressed to J.S. or C.M.

Reprints and permissions information is available at www.nature.com/reprints.

Publisher's note Springer Nature remains neutral with regard to jurisdictional claims in published maps and institutional affiliations.



Open Access This article is licensed under a Creative Commons Attribution 4.0 International License, which permits use, sharing, adaptation, distribution and reproduction in any medium or format, as long as you give appropriate credit to the original author(s) and the source, provide a link to the Creative Commons license, and indicate if changes were made. The images or other third party material in this article are included in the article's Creative Commons license, unless indicated otherwise in a credit line to the material. If material is not included in the article's Creative Commons license and your intended use is not permitted by statutory regulation or exceeds the permitted use, you will need to obtain permission directly from the copyright holder. To view a copy of this license, visit <http://creativecommons.org/licenses/by/4.0/>.

© The Author(s) 2020



Tailored Additives for Incorporation of Antibacterial Functionality Into Laser Sintered Parts

James R. Wingham¹, Ifty Ahmed², Md Towhidul Islam³, Joanna Shepherd⁴ and Candice Majewski^{1*}

¹Department of Mechanical Engineering, The University of Sheffield, Sheffield, United Kingdom, ²Faculty of Engineering, Advanced Materials Research Group, University Nottingham, Nottingham, United Kingdom, ³School of Physical Sciences, University of Kent, Canterbury, United Kingdom, ⁴School of Clinical Dentistry, The University of Sheffield, Sheffield, United Kingdom

OPEN ACCESS

Edited by:

Cristina Scielzo,
San Raffaele Hospital (IRCCS), Italy

Reviewed by:

Dan Ioan Stoia,
Politehnica University of Timisoara,
Romania

Swee Leong Sing,

National University of Singapore,
Singapore

*Correspondence:

Candice Majewski
c.majewski@sheffield.ac.uk

Specialty section:

This article was submitted to
Bioinspired and Complex Materials,
a section of the journal
Frontiers in Biomaterials Science

Received: 26 April 2022

Accepted: 09 June 2022

Published: 08 July 2022

Citation:

Wingham JR, Ahmed I, Islam MT,
Shepherd J and Majewski C (2022)
Tailored Additives for Incorporation of
Antibacterial Functionality Into Laser
Sintered Parts.
Front. Front. Biomater. Sci. 1:929006.
doi: 10.3389/fbiom.2022.929006

Infectious disease is a major cause of death worldwide, and novel methods capable of controlling the spread of disease are in high demand. This research presents a method of producing antimicrobial microcomposites by exploiting the powder-based nature of the Laser Sintering Additive Manufacturing process, via the incorporation of silver-containing additives. Silver phosphate glass additives in different formulations were designed to determine the effect of dissolution rate on the antimicrobial efficacy. These were characterised and successfully incorporated into polyamide 12 parts, without affecting the mechanical properties. The printed microcomposite parts displayed both bactericidal and antibiofouling effects against Gram-positive and Gram-negative bacteria in nutrient-poor conditions, with the efficacy found to be more sensitive to silver content than degradation rate.

Keywords: polymer laser sintering, antibacterial material, phosphate glass, microcomposite, additive manufacturing

1 INTRODUCTION

Additive Manufacturing (AM) is increasingly being used for the production of functional, end-use parts; now constituting 33.7% of its applications, and with an estimated \$2.21 billion spent on these in 2021 (Wohlers et al., 2022). Covering a range of different processes, AM can be defined as the “process of joining materials to make parts from 3D model data, usually layer upon layer, as opposed to subtractive manufacturing and formative manufacturing technologies” (ISO/ASTM, 2021). First commercialised over 30 years ago, Laser Sintering (LS), a powder bed fusion process, is now well established as an AM technology; building parts by spreading thin layers of a powder feedstock, then selectively melting the material in each layer to form consecutive cross-sections of the printed part (Goodridge et al., 2012). With its ability to create complex geometries throughout the build volume without the need for support structures, LS is well suited to the manufacture of functional parts; ranging from one-off commissions and functional prototypes, to batch or mass production of end-use products. As a process LS is now relatively well understood, with substantial current research focusing on broadening the potential applications of LS by introducing new materials and adding new functionality into printed parts.

Polyamides (including PA12, PA11, and PA6) have long since dominated the market for polymer powder bed fusion (PBF) processes such as LS (Redwood et al., 2018), and have been reported to be the most profitable AM polymer (Wohlers et al., 2022). This is reflected in the availability of

materials, with 61% of currently available polymer powder feedstocks being polyamide-based, of which 46% contain additional additives (or fillers) to create a composite feedstock (Senvol, 2022). These additives can be used to alter the mechanical properties of the parts [e.g., carbon fibres for increased strength (Yan et al., 2011), or glass beads for increased stiffness (Seltzer et al., 2011)], increase the processability of the powder during printing [e.g., silica for enhancing powder flow (Verbelen et al., 2016), carbon black for increased laser energy absorption (Wagner et al., 2004)], or to add new functionality into printed parts [e.g., a brominated hydrocarbon to add flame resistance (Booth et al., 2012)]. The subject of much academic and industrial interest (Wang et al., 2017; Yuan et al., 2019), these composites allow the tailoring of material properties without many of the challenges associated with processing a new base polymer.

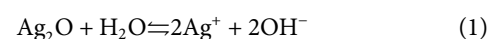
Alongside this, the spread of infectious disease is at the centre of global attention, and awareness of the need for new methods to control the spread of disease has never been higher. Exacerbated by the overuse of antibiotics, antimicrobial resistance (AMR) has become a major cause of death worldwide, responsible for 1.27 million deaths in 2019 and predicted to rise to 10 million a year by 2050 (Interagency Coordination Group on Antimicrobial Resistance, 2019; Antimicrobial Resistance Collaborators, 2022). To tackle this issue (and in addition to conserving antimicrobial efficacy by practising good antimicrobial stewardship only using antibiotics where appropriate), the largest impact can be made by controlling the spread of disease, thus reducing the initial level of infection and the subsequent need for treatment (O'Neill, 2016). Antimicrobial (antibacterial when dealing specifically with bacteria) materials could prove an effective tool for this, creating surfaces on which microbes are unable to survive, thereby reducing the potential routes of transmission for disease (Page et al., 2009). This can be especially effective for frequently used touchpoints, or equipment with complex or inaccessible parts which would otherwise be difficult to clean.

Antibacterial materials can be grouped into three main categories, based on how they react with bacteria. Anti-adhesive surfaces function by preventing the attachment of bacteria to the surface, avoiding or delaying the formation of biofilms¹ without harming the bacteria; contact-active surfaces cause cell death upon contact with the material, generally either through surface geometry or through anchoring antimicrobials to the surface; and biocide-releasing surfaces, which release antimicrobials into their surroundings to create a bactericidal effect, a category dominated by metal-containing surfaces releasing antimicrobial metal ions (Page et al., 2009; Campoccia et al., 2013; Adlhart et al., 2018). Antimicrobial metal-containing materials are starting to emerge in AM, with research into copper, zinc and silver-filled materials for material extrusion (Muwaffak et al., 2017; Tiimob et al., 2017; Zhang et al.,

2017) as well as commercially available filaments (Copper3D, 2022); with further research into silver-containing resins for vat photopolymerisation processes (such as stereolithography) (Taormina et al., 2018). In LS, the only commercial instance of an antimicrobial material is the proprietary PEKK material (OsteoFab technology) from Oxford Performance Materials (Maandi et al., 2020), primarily marketed for use in surgery to create bone scaffolds; with its surface geometry creating anti-adhesive and contact-active effects. Research has also been carried out into biocide-releasing LS PA12 parts (Turner et al., 2020), made by incorporating a commercially available phosphate-based silver-containing additive in the powder feedstock to create intrinsically antimicrobial parts.

Despite being used for thousands of years for its antimicrobial properties, the mechanisms by which silver acts against bacteria are not yet fully understood (Chernousova and Epple, 2013). Biologically inert in its metallic form (Möhler et al., 2018), its notoriety instead stems from the silver ions (Ag^+) which attack cells both directly (through disruption of the cell membrane, depletion of cellular thiols, ion mimicry, and destruction of Fe-S clusters) and indirectly (as the destroyed Fe-S clusters release Fe^{2+} and create cell damaging reactive oxygen species through the Fenton reaction) (Lemire et al., 2013; Palza, 2015). These ions are generally formed by reacting with water, a property that can be exploited by hygroscopic (able to absorb water) polymers such as polyamides to create antimicrobial materials. Silver-containing additives can be incorporated into the parts, with the absorbed water able to react with them and release Ag^+ ; this then diffuses throughout the part and into the surroundings, creating an intrinsically antimicrobial material (Palza, 2015). With the diffusion of water through polymers generally a slow process, the use of carrier materials for silver can be used to increase or further control the release of Ag^+ . Carriers such as zeolites can increase the Ag^+ release rate by aiding the water permeation into the composite part, through the generation of more free voids or by reducing the crystallinity of the polymer (Kumar et al., 2005). The speed of the reaction with the additives can also be increased (compared to with metallic silver) by including silver in a different form (such as silver oxide Ag_2O), to achieve equivalent or even faster rates of Ag^+ release, even with a lower total silver content (Palza, 2015; Mulligan et al., 2003; Kumar et al., 2005).

For silver oxide, the release of Ag^+ is governed by Eq. 1, in which the forward reaction (to create the silver ions) occurs in neutral or acidic solutions (Johnston et al., 1933).



To further tailor the release of Ag^+ , silver oxide can be combined with other oxides to create a glass. Phosphate (P_2O_5) based glasses are used in biomedical applications for their ability to dissolve completely in water, while controlling the release of antimicrobials such as silver (Ahmed et al., 2019). In its pure form phosphate dissolves quickly, however by adding other oxides (such as Na_2O , CaO , and MgO) in varying proportions, the release rate can be tailored to the desired application; creating an approximately linear dissolution rate

¹Biofilms are multilayered communities of bacteria which are usually heterogeneous in species composition, and are far less sensitive to antimicrobials than their free swimming (planktonic) counterparts.

TABLE 1 | Additive oxide compositions by molar percentage, with the designed formulation shown alongside the measured value from EDX (shown in brackets—raw data in supplementary information).

| Glass Name (abbreviation) | Designed Glass Formulation (Measured Value)/ molar% | | | | |
|------------------------------|---|---------|---------|-------------------|-------------------|
| | P ₂ O ₅ | MgO | CaO | Na ₂ O | Ag ₂ O |
| P40Mg24Ca16Na18Ag2 (P40) | 40 (42) | 24 (25) | 16 (14) | 18 (17) | 2 (2) |
| P45Mg19Ca16Na18Ag2 (P45) | 45 (48) | 19 (19) | 16 (15) | 18 (16) | 2 (2) |
| P50Mg14Ca16Na18Ag2 (P50) | 50 (52) | 14 (14) | 16 (15) | 18 (18) | 2 (2) |
| B65003 ^a | (48) | (34) | (17) | – | (1) |

^acommercial additive—calculated from the measurements in (Turner et al., 2020).

(and associated release of Ag⁺) over its lifetime (Mulligan et al., 2003; Ahmed et al., 2006).

This research aims to exploit the customisability of silver-doped phosphate-based glasses to create additives for Laser Sintering, and more deeply understand their effectiveness in manufacturing intrinsically antibacterial printed parts with LS. A method for producing the tailored additives is presented here, with the experiments designed to validate the method of production, and evaluate the antibacterial efficacy of the printed microcomposite parts. While there are obvious potential applications of this approach in healthcare settings (e.g., for complex invasive medical devices), there are likely to be additional applications throughout a wider range of industries (e.g., consumer goods).

2 MATERIALS AND METHODS

2.1 Overview

The research presented here builds on the work carried out by Turner et al. (2020), investigating the effects of altering the additive degradation rate on the antimicrobial efficacy of LS PA12 microcomposite parts. Here, three silver-doped phosphate-based glass formulations were developed based on the commercially available additive analysed by Turner et al. (2020). The proportions of P₂O₅ and MgO were altered to create glass compositions with different degradation rates; with decreased levels of P₂O₅ and increased levels of MgO both previously shown to reduce the degradation rate in water (Gao et al., 2004; Lee et al., 2013). The amounts of Ag₂O were designed to be kept constant, as increasing this has also been shown to affect the structure of phosphate-based glasses, increasing their strength and decreasing degradation rates (Ahmed et al., 2006, 2007; Moss et al., 2008).

The glasses were milled into powders and characterised, before being combined with PA12 powder to create composite feedstocks suitable for LS. All three feedstocks were successfully processed with LS, creating microcomposite parts with three different compositions. The mechanical properties of the microcomposites were determined and compared to pure PA12 parts, and the surface composition analysed. Finally the antimicrobial efficacy of the three microcomposites was investigated against both Gram-positive

and Gram-negative bacteria, with their bactericidal (ability to kill bacteria) and antibiofouling (ability to prevent or reduce biofilm formation) investigated in both contact and non-contact environments.

2.2 Powder Characterisation and 3D Printing

2.2.1 Production of Silver-Containing Additives

Three silver-doped phosphate-based glass formulations were developed to assess the effect of degradation rate on the antimicrobial efficacy of the printed parts; these were based on the measured composition of a commercial additive (B65003—BioCote (Turner et al., 2020)), the manufacturer's measurement of silver content in B65003 (1.9%), and personal experience. The chosen glasses were in the system of (50-*x*)P₂O₅-(14 + *x*)MgO-16CaO-18Na₂O-2Ag₂O (where *x* = 0, 5, 10), as shown in Table 1. The intended degradation rate was altered by varying the amount of phosphate in the glasses, with a higher phosphate content expected to lead to a faster degradation rate. This was used to denote the three formulations as P40, P45, and P50.

To manufacture the glasses, the precursors (NaH₂PO₄, MgHPO₄·3H₂O, CaHPO₄, P₂O₅—Sigma Aldrich, Ag₃PO₄—Alfa Aesar) were weighed and mixed to achieve the formulations in Table 1, before being transferred to a quartz crucible (VWR International) and placed in a furnace. Ordinarily, a platinum crucible would be used for glass production; however, to avoid any possibilities of the silver alloying with the platinum, quartz crucibles were instead used. The precursors were heated at a rate of 10°C/min, held at 350°C for 0.5 h to remove any H₂O, then heated further and held at 1,150°C for 1.5 h to achieve full melting. The resulting molten glass was then poured onto a steel plate and allowed to cool to room temperature. The glass was subsequently ground using a Retsch PM 100 ball mill, and sieved to obtain a < 45 μm particle size.

2.2.2 Characterisation of Silver-Containing Additives

In order to verify the composition of the additives produced, Energy-dispersive X-ray Spectroscopy (EDX) was used. For this, a small amount of each powder was attached to self-adhesive carbon pads, gold sputter-coated, and imaged using a TESCAN VEGA3 SEM, the attached Oxford EDX analysis and associated software (AZtec, Oxford instruments). An accelerating voltage of 15 kV was used, with back scattered electrons measured to

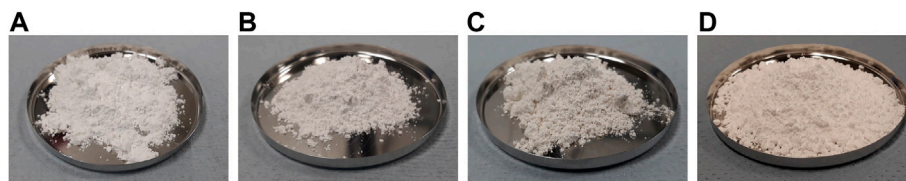


FIGURE 1 | Photos of the three custom silver phosphate glass additives produced, each amount shown is approximately 20 g. Showing **(A)** P40, **(B)** P45, **(C)** P50, **(D)** commercial additive B65003.

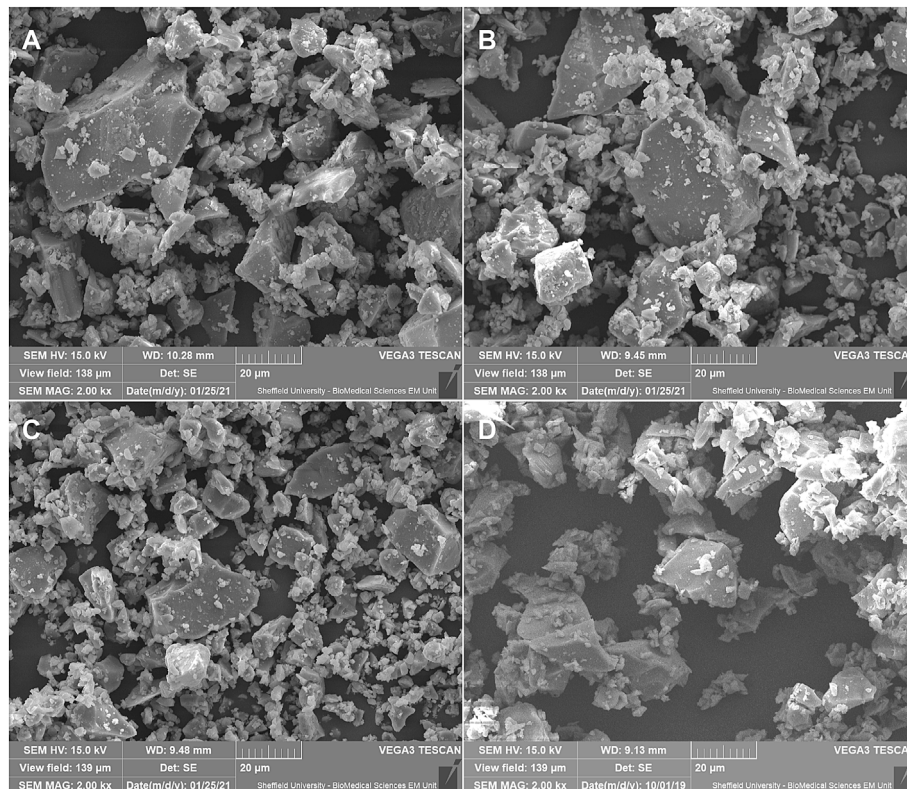


FIGURE 2 | SEM images of the phosphate-based glass additives at $\times 2,000$ magnification. Showing **(A)** P40 (custom-made) **(B)** P45 (custom-made) **(C)** P50 (custom-made), and **(D)** B65003 (commercial).

highlight differences in the material composition. The measured weight% compositions were converted to atomic% using their atomic mass (PubChem, 2020), with the molar% of the oxides calculated from the atomic% of each element (P, Mg, Ca, Na, Ag).

To characterise the morphology of the powders, Scanning Electron Microscopy (SEM) was carried out alongside the EDX analysis using the same samples and equipment. For this, a 15 kV accelerating voltage was again used, detecting scattered electrons to clearly view the particle shape.

To obtain a statistically significant size distribution, the powders were measured using a Mastersizer 3,000 laser diffraction particle size analyser. A dry dispersion unit was used to analyse the soluble phosphate glass powders, and a refractive index of 1.627 used. From this, the volume-based diameter metrics of D10, D50, and D90 (10,

50, and 90% along the cumulative distribution) were recorded, along with the average diameter weighted by volume (D [4,3]).

2.2.3 Laser Sintering

For each additive, a composite feedstock was created by adding 1% by weight to virgin polyamide 12 powder (PA2200—EOS). This was subsequently mixed in a rotary tumbler (EOS—mixing station P1) for approximately 100 min, with three acrylic blocks added to enhance mixing.

Test specimens were printed using an EOS Formiga P100 LS machine, with the default “performance” parameters for PA2200 used (Pfefferkorn and Weilhammer, 2017); these being laser power 21 W, scan spacing 0.25 mm, scan speed 2,500 mm/s, layer height 100 μm , bed temperature 170°C, with no contours

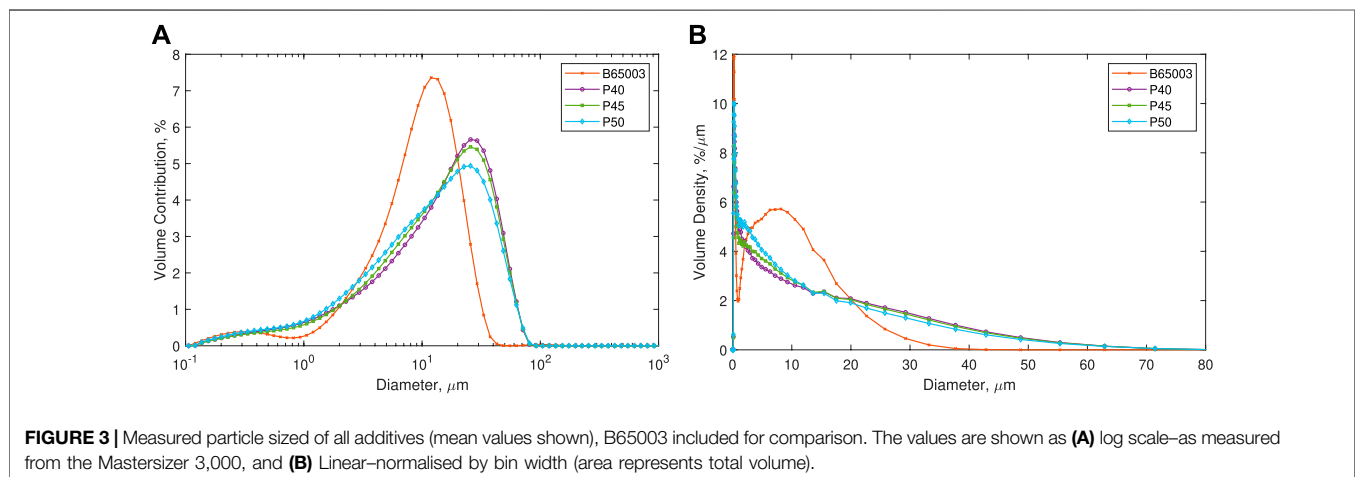


TABLE 2 | Results of the particle size analysis of the additives.

| Glass Additive | D10/ μm | D50/ μm | D90/ μm | D [4,3]/ μm | Weighted Residual/ % |
|----------------|--------------------|--------------------|--------------------|------------------------|----------------------|
| P40 | 1.93 ± 0.07 | 15.5 ± 0.2 | 41.3 ± 0.9 | 18.9 ± 0.3 | 0.58 ± 0.04 |
| P45 | 2.10 ± 0.02 | 14.8 ± 0.1 | 40.6 ± 0.6 | 18.5 ± 0.2 | 0.56 ± 0.09 |
| P50 | 1.74 ± 0.02 | 13.0 ± 0.1 | 39.4 ± 0.4 | 17.2 ± 0.1 | 0.83 ± 0.17 |
| B65003 | 2.48 ± 0.04 | 9.83 ± 0.07 | 21.1 ± 0.4 | 11.1 ± 0.5 | 0.81 ± 0.04 |

used. The same build layout and parameters were used for all four builds; tensile specimens were oriented in the x-direction (XYZ according to ISO/ASTM (2016)), with the laser alternately scanning layers at 0° and 90° to the direction of testing. Excess powder was removed from all parts using compressed air only to reduce any potential contamination.

2.3 Characterisation of Printed Microcomposites

Tensile testing was used to determine the mechanical properties of the printed parts; with the Young's modulus (E), ultimate tensile strength (σ_{uts}), and elongation at break (ϵ_{max}) used to characterise the parts. All testing was carried out in accordance with ASTM D638 (ASTM International, 2014), with $5 \times$ type I specimens tested per material. Testing was carried out on a Tinius Olsen 5K with Laser Extensometer, at a rate of 5 mm/min.

In order to qualitatively check the additive incorporation and dispersion on the part surface, SEM and EDX of the part surfaces were carried out. This utilised the same setup as for the additive analysis (see Section 2.2.2), with an accelerating voltage of 15 kV used and detecting back-scattered electrons. A whole area element map was obtained for the microcomposite parts, allowing for the identification of the additives and any other features on the part surface.

2.4 Antibacterial Testing

2.4.1 Bacterial Strains

The bacteria used were clinical isolate strains of the Gram-positive, methicillin-resistant *Staphylococcus aureus* S235

(MRSA—referred to as *S. aureus*), and Gram-negative *Pseudomonas aeruginosa* SOM1 (referred to as *P. aeruginosa*), provided by the Charles Clifford Dental Hospital, Sheffield. Both of these are examples of commonly found, biofilm forming bacteria, which can cause significant infection, especially in immunocompromised patients. Bacteria were maintained on stock Brain Heart Infusion (BHI) agar plates stored at 4°C . For experimental use, single colonies were picked from the plate, suspended in 15 ml BHI broth and incubated overnight at 37°C in a shaking incubator before use.

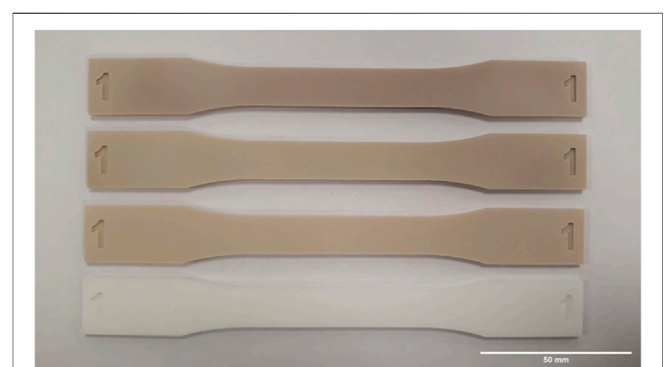
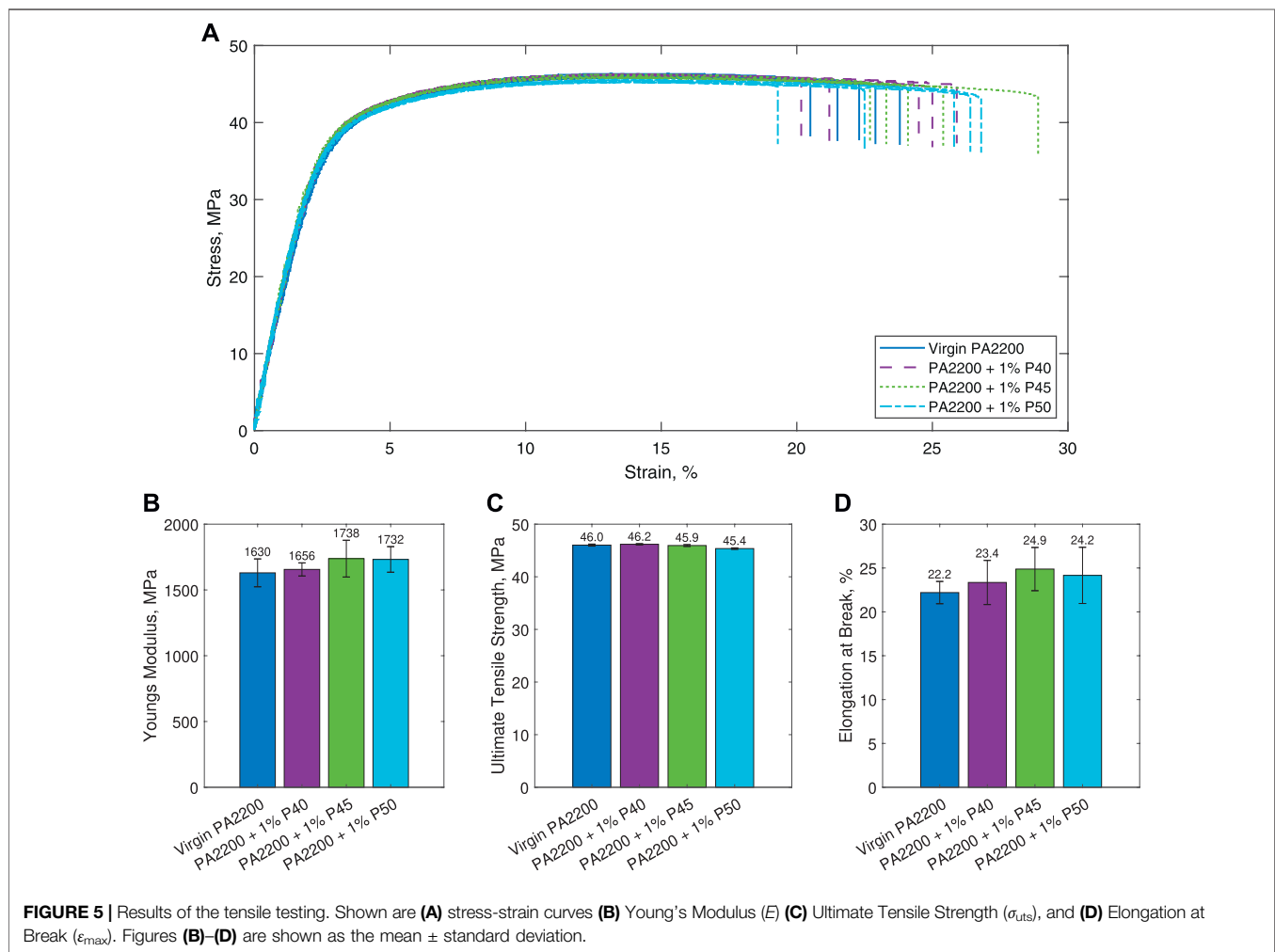


FIGURE 4 | Photo of the equivalent part from all three builds containing the custom additives and one without additives. Shown are (top to bottom), virgin PA2200 + 1% P50, virgin PA2200 + 1% P45, virgin PA2200 + 1% P40, virgin PA2200.



2.4.2 Powder Antibacterial Efficacy

Before testing the efficacy of the microcomposite parts, the additives were tested in isolation to determine the maximum possible effectiveness. In order to maintain a direct comparison with the part testing, conditions were identical to those used in part testing (see Section 2.4.3); with the mass of additive (approximately 10 mg) representative of the amount in a 1 cm³ part at 1% by weight.

The custom glasses were weighed out into glass universals to an accuracy of 10–12 μ g, before being sterilised (in a steam autoclave at 121°C); three samples were prepared per material per repeat. The chosen bacteria were grown in BHI, with the overnight cultures diluted to an OD₆₀₀ of 0.01 in Phosphate Buffered Saline (PBS); 5 ml of these were added to each sample and incubated in a shaking incubator (150 RPM at 37°C) for 24 h. Following this, 10 μ L of the powder/bacteria suspension was taken from each sample and a Miles and Misra serial dilution carried out to determine the number of CFUs, an indication of the number of viable bacteria present in the sample. This protocol is shown graphically in the **Supplementary Information**.

2.4.3 Contact Antibacterial Efficacy

The protocol described here was designed to replicate those used by Turner et al. (2020), with some changes included to increase reliability and allow for a higher throughput of samples. These included adding a negative control (no microcomposite part) and reducing the volume of the serial dilutions spotted onto agar (5 μ L compared to 20 μ L) to enable testing of a large number of samples simultaneously. Spherical 1 cm³ samples were printed from each material for these tests, including samples made from pure PA2200 for comparison.

Three spheres per material per repeat were used, with each one placed in a glass universal and sterilised (steam autoclave at 121°C) before use. Bacteria were grown overnight in BHI before being diluted to an OD₆₀₀ of 0.01 in PBS; 5 ml of which was added to each sample and incubated in a shaking incubator (either 150, 175 or 210 RPM depending on availability, at 37°C) for 24 h.

After incubation, 10 μ L of the surrounding media was taken from each sample to measure the unadhered planktonic bacteria, with a Miles and Misra serial dilution carried out to determine the number of CFUs. To isolate the biofilm attached to the part surface,

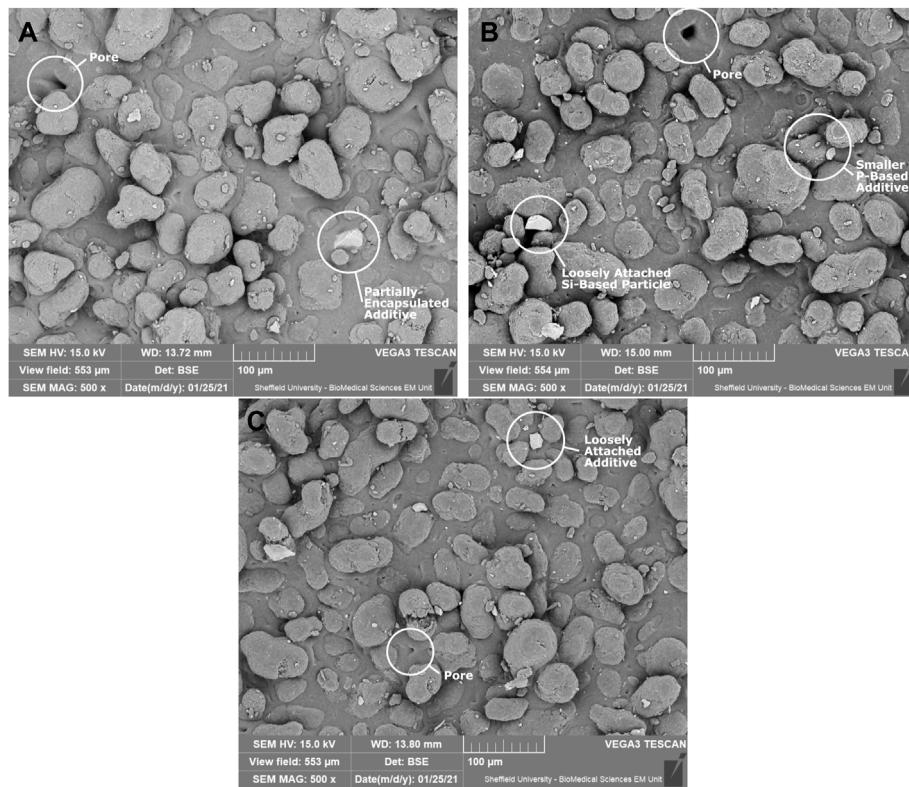


FIGURE 6 | SEM images of the microcomposite surfaces containing the custom additives. The brighter features are additives, with the majority of the smaller features over the entire surface found to be the custom-made phosphorus-based additives. All features identified were found on all three materials. Shown are **(A)** 1% P40 Part **(B)** 1% P45 Part, and **(C)** 1% P50 Part.

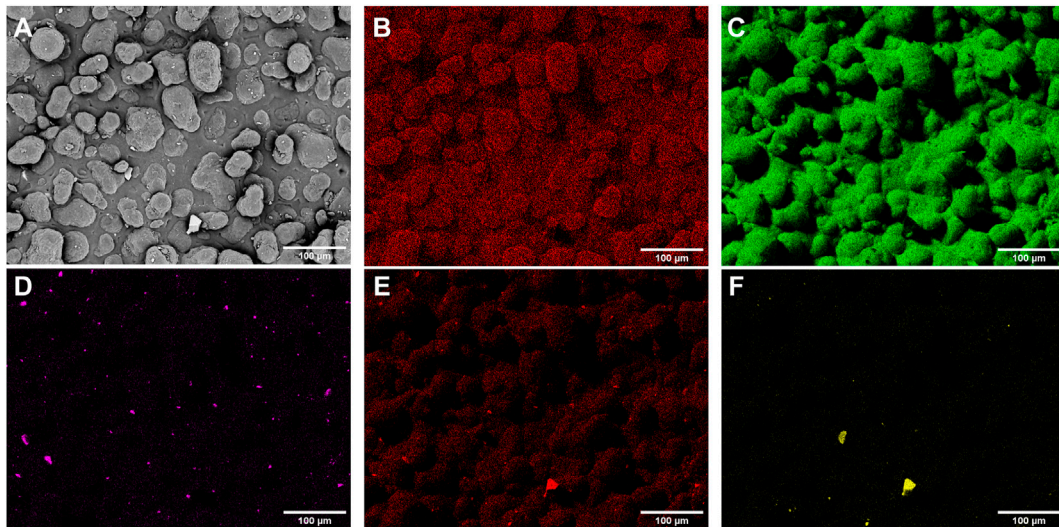
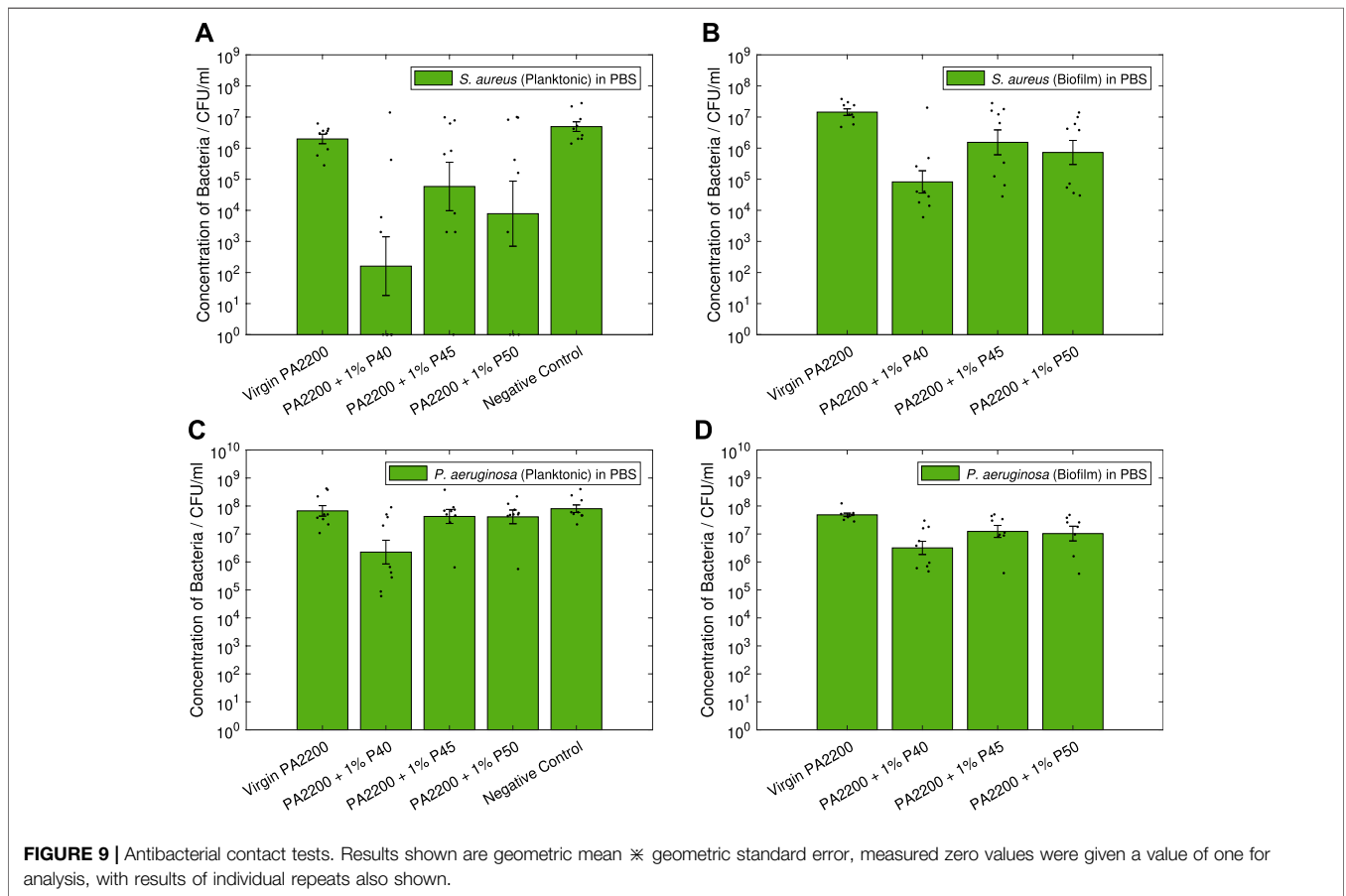
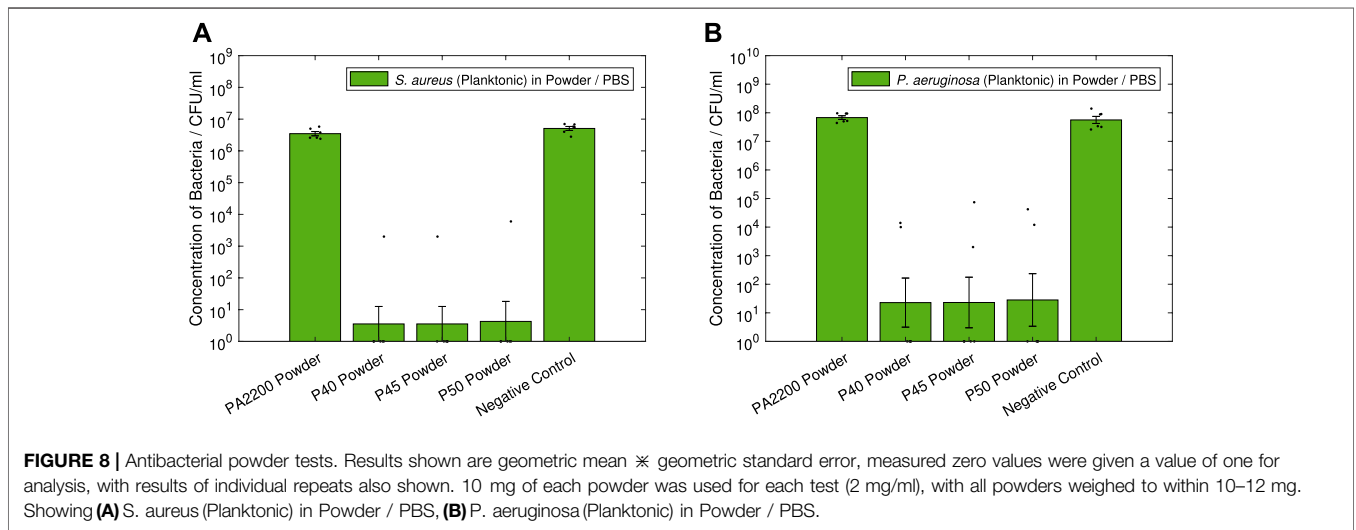


FIGURE 7 | SEM and elemental maps on the surface of a 1% P50 microcomposite part obtained with EDX, with phosphorus indicative of the additive location. Shown are **(A)** SEM image **(B)** Gold **(C)** Carbon **(D)** Phosphorus **(E)** Oxygen, and **(F)** Silicon. Additional maps for Calcium, Magnesium and Titanium are not shown, with the concentration of silver too low to be detected.

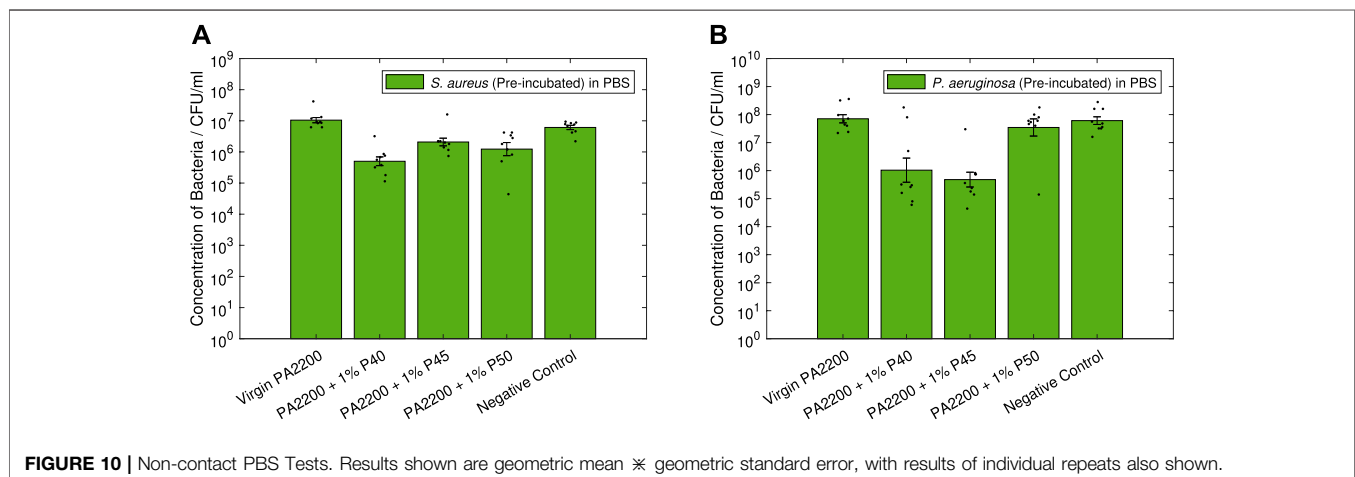


the remaining media was removed and each sphere rinsed twice with fresh PBS (5 ml each time) to remove loosely attached cells. 2 ml PBS was then added and each sphere was vortexed at the highest setting for 30 s to remove the attached biofilm. 10 μ L of the resulting suspension was removed, with a Miles and Misra serial dilution carried out to count the CFUs. This protocol is shown graphically in the **Supplementary Information**.

2.4.4 Non-Contact Antibacterial Efficacy

The non-contact protocols were again based on those used by Turner et al. (2020), with the same modification made as for the contact protocol (see **Section 2.4.3**).

Printed 1 cm³ spheres were used, with three spheres used per material per repeat; these were placed in glass universals and sterilised (steam autoclave at 121°C) before use. For the non-



contact testing, 5 ml PBS was added to each sample and incubated in a shaking incubator (150 RPM at 37°C) for 24 h, after which the spheres were removed. The bacteria (*P. aeruginosa* and *S. aureus*—grown overnight in BHI), were then added into each universal to an OD₆₀₀ of 0.01. These were incubated for a further 24 h in a shaking incubator (150 RPM at 37°C) for 24 h, after which 10 μ L of each suspension was removed, and a Miles and Misra dilution carried out to count the CFUs. This protocol is shown graphically in the **Supplementary Information**.

3 RESULTS

3.1 Powder Characterisation and 3D Printing

3.1.1 Additive Production

Photos of the three tailored additives produced are shown in **Figure 1**, where all the powders appear white in colour and similar to one another.

3.1.2 Additive Composition

The oxide molar% compositions of the additives are shown in **Table 1**, calculated from the weight% measured in EDX scanning (data available in the **Supplementary Information**). The data from Turner et al. (2020) has also been used here to calculate the composition of B65003 using the same method. Here it can be seen that the measured silver content (Ag₂O) was higher for P40 than anticipated, and slightly lower for both P45 and P50.

3.1.3 Powder Morphology

SEM images of the custom-made powdered glass additives can be seen in **Figure 2**, alongside a scan of the commercially available B65003 for comparison in **Figure 2D**. In these, all four powders can be seen to be similar in both size and shape.

3.1.4 Particle Size

The results of the particle size analysis are shown in **Figure 3**, with key values shown in **Table 2**; the values for B65003 have been included here for comparison. Here it can be seen that the three

tailored additives are very similar to one another, and broadly comparable to the commercial additive.

3.1.5 Laser Sintering

All the parts printed without any observable issues (such as curl or excessive smoking), validating the use of the standard PA2200 parameters. For the scanned areas of the build, there was a noticeable difference in colour for the additive-containing powders (see **Supplementary Information**), although this did not appear to affect the build. Photos of post-processed parts containing the custom additives can be seen in **Figure 4**.

3.2 Microcomposite Properties

3.2.1 Mechanical Properties

The results of the tensile testing can be seen in **Figure 5**, both as the raw stress-strain curves (**Figure 5A**) and comparing the measured values of E , σ_{uts} and ϵ_{max} (**Figures 5B–D**). No obvious decrease in the mechanical properties can be seen for any of the microcomposite parts compared to the pure PA12 parts.

A 2-sample Welch's t -test was used to determine whether there were any statistically significant differences in the measured values, where a p value of $p < 0.05$ indicates the means are significantly different. The only statistically significant difference identified from this was the σ_{uts} for 1% P50, which showed a 0.6 MPa decrease ($p < 0.001$) compared to PA2200.

3.2.2 Surface Composition

SEM images of parts containing the three custom additives are shown in **Figure 6**, with key features annotated. The elemental maps from EDX for a part containing 1% P50 are shown in **Figure 7**, with the maps of gold, carbon, phosphorus, oxygen, and silicon shown. In these, the gold is a result of the sputter-coating of the samples, the carbon is present in the polyamide 12 polymer matrix, the phosphorus and oxygen maps (in combination with calcium and magnesium—not shown) are indicative of the additive location, and the silicon and titanium maps are thought to be additional additives in the PA2200 powder from the manufacturer as well as post-printing contaminants.

3.3 Antibacterial Testing

3.3.1 Powder Antibacterial Efficacy

The results from the powder antibacterial testing can be seen in **Figure 8**, where all of the silver phosphate glass powders can be seen to be extremely effective against both *S. aureus* and *P. aeruginosa*. A Welch's *t*-test was used, with values of $p < 0.05$ deemed to be statistically significant.

In **Figure 8A**, all of the glass powders can be seen to have a significant antimicrobial effect on *S. aureus*; with large reductions in CFU/ml measured for P40 (6.0-log, $p < 0.001$), P45 (6.0-log, $p < 0.001$) and P50 (5.9-log, $p < 0.001$) compared to pure PA12. A similarly large effect can be seen in **Figure 8B** against *P. aeruginosa*, with 6.5-log ($p = 0.001$), 6.5-log ($p = 0.001$) and 6.4-log ($p = 0.001$) reductions measured for P40, P45 and P50 respectively. It is worth noting that for both strains of bacteria, the PA2200 powder showed no significant difference to the negative controls.

3.3.2 Contact Antibacterial Efficacy

Results of the contact testing for *S. aureus* are shown in **Figures 9A,B**, showing the planktonic and biofilm data respectively. In the planktonic data (**Figure 9A**), reductions compared to PA2200 can be seen for all the microcomposites, with 4.1-log, 1.5-log and 2.4-log reductions seen for 1% P40, 1% P45 and 1% P50 respectively. However with the variation measured, only 1% P40 showed a statistically significant reduction ($p = 0.002$), with 1% P50 only just above the 0.05 threshold ($p = 0.051$). All the microcomposites showed a significant reduction compared to the negative control. The *S. aureus* biofilm data (shown in **Figure 9B**), shows statistically significant reductions for all of the microcomposites compared to PA2200; showing a large decrease for 1% P40 (2.2-log, $p < 0.001$), and slightly smaller reductions for 1% P45 (1.0-log, $p = 0.043$) and 1% P50 (1.3-log, $p = 0.010$).

The results of the contact efficacy test for *P. aeruginosa* are shown in **Figures 9C,D**, for the planktonic and biofilm data respectively. In the planktonic data (**Figure 9C**), it can be seen that all the microcomposites display a small reduction in CFU compared to PA2200, with the only statistically significant reduction measured in 1% P40 (1.5-log, $p = 0.009$). Similarly for the biofilm data in **Figure 9D**, 1% P40 shows the largest reduction in CFU (1.2-log, $p = 0.001$), with smaller but still statistically significant differences measured in 1% P45 (0.6-log, $p = 0.025$) and 1% P50 (0.7-log, $p = 0.039$).

3.3.3 Non-Contact Antibacterial Efficacy

The results of the non-contact testing can be seen in **Figure 10** for both *S. aureus* and *P. aeruginosa*.

In **Figure 10A**, the microcomposites can all be seen to have statistically significant effect against *S. aureus*. Here it can be seen that 1% P40 shows the largest reduction in CFU (1.3-log, $p < 0.001$), followed by 1% P50 (0.9-log, $p = 0.002$) and 1% P45 (0.7-log, $p < 0.001$).

For *P. aeruginosa* (**Figure 10B**), only two of the microcomposites were seen to have a significant effect on the CFU. In this, 1% P45 can be seen to have the largest reduction (2.2-log, $p < 0.001$) followed by 1% P40 (1.8-log, $p = 0.002$), no significant difference can be seen for 1% P50.

4 DISCUSSION

4.1 Powder Characterisation and 3D Printing

4.1.1 Additive Composition

The measured compositions of the tailored additives (**Table 1**), show a slight deviation from the designed formulations. Of these, the phosphate (P_2O_5 —affecting the additive dissolution rate) and silver (Ag—affecting the total amount of Ag^+ which can be released) content were likely to be the most important in terms of the antimicrobial efficacy. For these reasons in the design of the glasses, the silver content was kept constant, with the compositions allowing for comparison of slow (P40), medium (P45), and fast (P50) degrading phosphate-based glass additives. The measured phosphate values for P40, P45 and P50 (42, 48, and 52%) were deemed sufficient to enable the comparison between different degradation rates.

The silver content of the three glasses also deviated from the expected values (expected to be 2%), with 5% by weight measured for P40, 4% for P45, and 3% for P50. This suggests that although P40 was expected to dissolve the slowest, the increased silver content could counteract this (as was the case in (Ahmed et al., 2007)), increasing the release rate of Ag^+ and its subsequent antimicrobial efficacy.

4.1.2 Powder Morphology

In the SEM images of the glass powders (shown in **Figure 2**), all three compositions can be seen to be very similar in both shape and size. The morphology is also very similar to that of the commercial B65003 additive (**Figure 2D**), with the distinctive jagged edges and irregularly sized particles.

In terms of the performance of these additives, this similarity was essential for comparing the chemical compositions, rather than the morphology or particle size. The SEM images shown here suggest that the manufacturing processes used to create the powders were consistent between the glasses, and reduces the likelihood of particle size or shape being the cause of any differences in the antimicrobial efficacy.

4.1.3 Particle Size

In the manufacture of the powders, a standard sieve size of 45 μm was used, which although slightly larger than the $< 40 \mu m$ specification of B65003, matched it as closely as possible. As expected, all three of the custom glasses were shown to be larger in size than the commercial additive (see **Table 2**), with the average particle sizes (D50) measured as 13.0–15.5 μm compared to 9.8 μm .

The shape of the distributions can also be seen to be different in **Figure 3**, with a longer tail off in the custom glasses and a greater proportion of smaller particles were measured compared to B65003. This difference was suspected to be due to additional sieving steps carried out commercially, removing smaller particles to be sold separately. In the production of the tailored additives here, the dramatic reduction in the yield this would bring, coupled with the increased production time and high cost of consumables, meant that this was impractical to replicate.

Comparing the custom glasses to each other, the shape of the distributions (**Figure 3**) can be seen to be very similar for all three,

with a subtly smaller size measured for P50. Although this slight difference could affect the efficacy of the powder, this would only act to increase the dissolution rate, which was already intended to be the highest in P50. Considering both this and the overwhelming similarities between the distributions, the results shown here suggest that the particle size is not likely to significantly affect the antimicrobial efficacy of the powders.

4.2 Microcomposite Properties

4.2.1 Mechanical Properties

The stress-strain plots (Figure 5A), show that all the materials follow a very similar profile with no major differences between any of the specimens tested. This is supported by the values of E , σ_{uts} , and ϵ_{max} (Figures 5B–D), which again show very similar values for all the materials. A Welch's t -test shows that the only statistically significant difference from the PA2200 specimens is the value of σ_{uts} for 1% P50 ($p < 0.001$). However, it is important to note that although statistically significant, this only represents a difference of 0.6 MPa. Practically, this would not be sufficient a decrease in properties to warrant changing the design in the majority of applications.

Although the tensile results presented here suggest the differences in the mechanical properties are small, it is worth noting that this only represents the specific LS parameters, sample orientation, additive loading, and surface finishing described in Section 2.2.3. It is known that altering individual parameters in the printing process (especially those affecting the Energy Density, including laser power, scan speed and scan spacing) will have significant effects on the tensile properties of the printed parts (Pilipović et al., 2018). Equally, the orientation and laser scanning strategy will also have a large effect on the tensile properties and fracture toughness of any parts produced (Stoia et al., 2019, 2020), which cannot be assumed to be similarly unaffected by the inclusion of the additives.

4.2.2 Surface Composition

The SEM images of the microcomposites (Figures 6A–C), show a number of key features one would expect to see on the surface of LS parts; these being a combination of partially melted powder particles, fully melted areas, and “open” pores in the fully melted areas. As expected for a microcomposite material, both partially encapsulated and loosely attached additive particles were seen in every material. This shows that the additives had been successfully incorporated into the parts, with no obvious effects on the microstructure at the surface. Due to the similarities with the commercial additive, the tailored additives were expected to be similarly randomly dispersed throughout the volume of the parts; with the dispersion previously extensively explored by Wingham et al. (2020) and Turner et al. (2020).

Combining these with EDX measurements (such as those in Figure 7), it was possible to further characterise the additives in the SEM images. For all the scans, phosphate-based particles were identified across the surface, suggesting that feedstock preparation was sufficient and the additives were relatively evenly dispersed. In some images, larger, loosely attached, silicon-based particles were also detected (see Figures 6B,C – compositions identified with EDX). Since none of these were

detected encapsulated in the parts, these were suspected to be contamination after printing, possibly during powder removal or in transport to SEM scanning; these were not thought to affect the performance of the parts.

In these experiments, the post-processing affecting the part surface comprised solely of powder removal using compressed air jets. This represents the default surface finish of LS parts, which is generally followed by additional post-processing (such as media blasting or vapour smoothing) to alter the finish and surface roughness of the parts (Tamburrino et al., 2021). With such a wide range of additional post-processing methods used in industry (each with the potential to affect the initial adhesion of bacteria to the surface, the release rate of Ag^+ from the part, and introduce other factors or contaminants), further testing should be carried out for any additional surface finishing to determine both the effects on the mechanical properties and the antimicrobial efficacy.

4.3 Antibacterial Testing

4.3.1 Powder Antibacterial Efficacy

For all three of the custom additives tested, the reduction in both *S. aureus* and *P. aeruginosa* measured (Figure 8) shows the powders are extremely antimicrobial, typically displaying a 6-log reduction or more in the measured CFUs. This quantifies the upper limit of the effectiveness expected from the microcomposite parts; however, since such a large difference was detected for all the powders, they were all predicted to have at least some antimicrobial effect.

During testing, the four powders could each be seen to react differently over the 24 h incubation. As expected, the PA2200 powder was not visibly affected. However for P40 and P45, these agglomerated together during autoclaving, with P40 turning a darker colour, likely due to the increased silver content and subsequent oxidation. P50 was not distinguishable as a powder after 24 h incubation, suggesting that (as per the additive design) this dissolved much more quickly. Although not quantifiable, this suggests that the designed differences in phosphate content for the three glass additives did result in significantly different dissolution rates.

4.3.2 Contact Antibacterial Efficacy

4.3.2.1 Antimicrobial Efficacy

For all the microcomposites, an antimicrobial effect against both *S. aureus* and *P. aeruginosa* was measured in the contact efficacy testing. In all tests (contact and non-contact), a general trend was observed of 1% P40 showing the largest antimicrobial efficacy, followed by 1% P50, and 1% P45 the least effective.

The only microcomposite to consistently show statistically significant reductions in CFU (planktonic and biofilm) was 1% P40, consistently outperforming the other glasses (Figure 9). This can be explained based on the measured composition of the glasses (Section 2.2.2), where P40 was found to contain a much higher amount of silver (5% by weight) compared to P45 and P50 (4 and 3%). Interestingly, this increase in performance was observed despite P40 being (theoretically, based on the measured phosphorus content) the slowest to dissolve of the three glasses. This suggests that the difference in silver content between the glasses was sufficient enough to negate the effects of a slower dissolution rate.

Whereas only 1% P40 showed significant reduction in CFU for the planktonic bacteria, all the microcomposites showed

statistically significant reductions in the biofilm formation on the parts (**Figures 9B,D**). As expected, the biofilm data for both *S. aureus* and *P. aeruginosa* show the same trends as the planktonic data, with a clear link between the two aspects. However the variability in the results for the biofilms was lower than the planktonic, particularly for PA2200, resulting in the lower *p*-values measured. In **Figure 9C**, 1% P45 and 1% P50 can be seen to have a negligible effect on planktonic *P. aeruginosa*; similarly for the biofilm data (**Figure 9D**), although statistically significant, the reductions here are small (0.6-log and 0.7-log), only showing a limited effect on the biofilms.

4.3.2.2 Sample Variation

In all of the tests (most notably in **Figure 9A**), a large spread in the measured CFU count can be seen for the microcomposite parts. As this variation was larger in the microcomposite samples than with PA2200 or the control, this was thought arise from differences in the antimicrobial efficacy of the individual spheres, rather than with the bacteria or the experimental method. The additive dispersion in the parts could be the cause of this, with the possibility that in some of the spheres there was a higher concentration of the glass near the surface. However, the mixing method and similarities to the commercial additives analysed by Wingham et al. (2020) strongly suggest the additives were dispersed throughout the bulk of the material. For this reason, any differences arising from this or the silver content of individual additive particles (which are potentially exacerbated by the short timescales) are expected to be mitigated as more of the part becomes saturated with water.

4.3.3 Non-Contact Antibacterial Efficacy

The non-contact tests shown in **Figure 10** clearly show that the microcomposite parts have an antimicrobial effect on the surrounding environment, even without contact with the surface. This supports the theory that the majority of this effect was due to the elution of Ag^+ into the surrounding media.

For *S. aureus*, the trend seen in **Figure 10A** is the same as the one seen with the contact tests, again with 1% P40 showing the largest reduction (1.3-log) in CFU. Despite all of the microcomposites showing statistically significant differences, the effect for 1% P45 and 1% P50 is lower (0.9-log and 0.7-log), again suggesting that the increased silver content of P40 outweighs the slower rate of dissolution.

Interestingly for *P. aeruginosa* (**Figure 10B**), the largest antimicrobial effect was observed with 1% P45 (2.2-log reduction), making it comparable to the efficacy of 1% P40 (1.8-log reduction). This stands in contrast to all the other antimicrobial testing carried out, suggesting that (although it is possible that other factors are in play), this could just be due to the random variation in the testing or the parts. As seen with the contact testing, 1% P50 showed no significant efficacy against *P. aeruginosa*.

5 CONCLUSION

This research presents a method of creating tailored microcomposites for use in Laser Sintering, to create

intrinsically antibacterial parts using Additive Manufacturing. The approach shows that though the use of silver-doped phosphate-based glasses, the properties of additives incorporated into the part can be tailored to an extent, with the silver content having the dominant effect on the part antibacterial efficacy. The printed microcomposite parts were found to be effective against representative strains of bacteria in nutrient-poor conditions, both against biofilm formation and planktonic cells. The incorporation of additives in the parts did not affect the mechanical properties, allowing for the addition of this functionality without the need for design alterations.

Future work should focus on the effect of additive loading, the effect of using different base polymers, and on determining the long-term effectiveness against a broad range of bacteria and other microbes.

DATA AVAILABILITY STATEMENT

The original contributions presented in the study are included in the article/**Supplementary Material**, further inquiries can be directed to the corresponding author.

AUTHOR CONTRIBUTIONS

JW, IA, and CM contributed to conception and design of the study. CM, JS, and IA provided resources and supervision. IA and MTI provided the phosphate-based glasses. JW and MTI carried out experimental work. JW wrote the first draft of the manuscript. All authors contributed to manuscript revision, read, and approved the submitted version.

FUNDING

Funded by The University of Sheffield Department of Mechanical Engineering Centenary Scholarship and the EPSRC Doctoral Training Partnership.

ACKNOWLEDGMENTS

This work is aligned with the EPSRC Future Manufacturing Hub in Manufacture using Advanced Powder Processes (EP/P006566/1). For the purpose of open access, the author has applied a Creative Commons Attribution (CC BY) licence to any Author Accepted Manuscript version arising.

SUPPLEMENTARY MATERIAL

The Supplementary Material for this article can be found online at: <https://www.frontiersin.org/articles/10.3389/fbiom.2022.929006/full#supplementary-material>

REFERENCES

- Adlhart, C., Verran, J., Azevedo, N. F., Olmez, H., Keinänen-Toivola, M. M., Gouveia, I., et al. (2018). Surface Modifications for Antimicrobial Effects in the Healthcare Setting: a Critical Overview. *J. Hosp. Infect.* 99, 239–249. doi:10.1016/j.jhin.2018.01.018
- Ahmed, A. A., Ali, A. A., and El-Fiqi, A. (2019). Glass-forming Compositions and Physicochemical Properties of Degradable Phosphate and Silver-Doped Phosphate Glasses in the P2O5-CaO-Na2O-Ag2O System. *J. Mater. Res. Technol.* 8, 1003–1013. doi:10.1016/j.jmrt.2018.07.012
- Ahmed, I., Abou Neel, E. A., Valappil, S. P., Nazhat, S. N., Pickup, D. M., Carta, D., et al. (2007). The Structure and Properties of Silver-Doped Phosphate-Based Glasses. *J. Mater. Sci.* 42, 9827–9835. doi:10.1007/s10853-007-2008-9
- Ahmed, I., Ready, D., Wilson, M., and Knowles, J. C. (2006). Antimicrobial Effect of Silver-Doped Phosphate-Based Glasses. *J. Biomed. Mat. Res.* 79A, 618–626. doi:10.1002/jbm.a.30808
- Antimicrobial Resistance Collaborators (2022). Global Burden of Bacterial Antimicrobial Resistance in 2019: a Systematic Analysis. *Lancet* 399, 629–655. doi:10.1016/S0140-6736(21)02724-0
- ASTM International (2014). *Standard Test Method for Tensile Properties of Plastics*. ASTM D638-14. doi:10.1520/D0638-14
- Booth, R. B., Thornton, B. C., Vanelli, D. L., and Gardiner, M. L. (2012). Methods and Systems for Fabricating Fire Retardant Materials. *U.S. Pat. No* 8236, 418.
- Campoccia, D., Montanaro, L., and Arciola, C. R. (2013). A Review of the Biomaterials Technologies for Infection-Resistant Surfaces. *Biomaterials* 34, 8533–8554. doi:10.1016/j.biomaterials.2013.07.089
- Chernousova, S., and Epple, M. (2013). Silver as Antibacterial Agent: Ion, Nanoparticle, and Metal. *Angew. Chem. Int. Ed.* 52, 1636–1653. doi:10.1002/anie.201205923
- Copper3D (2022). Antimicrobial Performance. Available at: <https://copper3d.com/pages/antimicrobial-performance> (Accessed 02 14, 2022).
- Gao, H., Tan, T., and Wang, D. (2004). Effect of Composition on the Release Kinetics of Phosphate Controlled Release Glasses in Aqueous Medium. *J. Control. Release* 96, 21–28. doi:10.1016/j.jconrel.2003.12.030
- Goodridge, R. D., Tuck, C. J., and Hague, R. J. M. (2012). Laser Sintering of Polyamides and Other Polymers. *Prog. Mater. Sci.* 57, 229–267. doi:10.1016/j.pmatsci.2011.04.001
- Interagency Coordination Group on Antimicrobial Resistance (2019). *No Time to Wait: Securing the Future from Drug-Resistant Infections. Report to the Secretary-General of the U. N. World Health Organization*.
- ISO/ASTM (2021). *Additive Manufacturing – General Principles – Fundamentals and Vocabulary*. West Conshohocken: ISO/ASTM 52900, 2021.
- ISO/ASTM (2016). *Standard Terminology for Additive Manufacturing – Coordinate Systems and Test Methodologies*. ISO/ASTM 52921:2016.
- Johnston, H. L., Cuta, F., and Garrett, A. B. (1933). The Solubility of Silver Oxide in Water, in Alkali and in Alkaline Salt Solutions. The Amphoteric Character of Silver Hydroxide. *J. Am. Chem. Soc.* 55, 2311–2325. doi:10.1021/ja01333a016
- Kumar, R., Howdle, S., and Münstedt, H. (2005). Polyamide/silver Antimicrobials: Effect of Filler Types on the Silver Ion Release. *J. Biomed. Mat. Res.* 75B, 311–319. doi:10.1002/jbm.b.30306
- Lee, I.-H., Shin, S.-H., Foroutan, F., Lakhkar, N. J., Gong, M.-S., and Knowles, J. C. (2013). Effects of Magnesium Content on the Physical, Chemical and Degradation Properties in a MgO–CaO–Na2O–P2O5 Glass System. *J. Non-Crystalline Solids* 363, 57–63. doi:10.1016/j.jnoncrysol.2012.11.036
- Lemire, J. A., Harrison, J. J., and Turner, R. J. (2013). Antimicrobial Activity of Metals: Mechanisms, Molecular Targets and Applications. *Nat. Rev. Microbiol.* 11, 371–384. doi:10.1038/nrmicro3028
- Maandi, A., Porteus, J., and Roberts, B. (2020). OsteoFab Technology. *Whitepaper, Oxford Performance Materials*. Connecticut: South Windsor.
- Möhler, J. S., Sim, W., Blaskovich, M. A. T., Cooper, M. A., and Ziara, Z. M. (2018). Silver Bullets: A New Lustre on an Old Antimicrobial Agent. *Biotechnol. Adv.* 36, 1391–1411. doi:10.1016/j.biotechadv.2018.05.004
- Moss, R. M., Pickup, D. M., Ahmed, I., Knowles, J. C., Smith, M. E., and Newport, R. J. (2008). Structural Characteristics of Antibacterial Bioresorbable Phosphate Glass. *Adv. Funct. Mat.* 18, 634–639. doi:10.1002/adfm.200700721
- Mulligan, A. M., Wilson, M., and Knowles, J. C. (2003). Effect of Increasing Silver Content in Phosphate-Based Glasses on Biofilms of *Streptococcus Sanguis*. *J. Biomed. Mat. Res.* 67A, 401–412. doi:10.1002/jbm.a.10052
- Muwaffak, Z., Goyanes, A., Clark, V., Basit, A. W., Hilton, S. T., and Gaisford, S. (2017). Patient-specific 3D Scanned and 3D Printed Antimicrobial Polycaprolactone Wound Dressings. *Int. J. Pharm.* 527, 161–170. doi:10.1016/j.ijpharm.2017.04.077
- O’Neill, J. (2016). *Tackling Drug-Resistant Infections Globally: Final Report and Recommendations*. Tech. rep. London: Review on Antimicrobial Resistance.
- Page, K., Wilson, M., and Parkin, I. P. (2009). Antimicrobial Surfaces and Their Potential in Reducing the Role of the Inanimate Environment in the Incidence of Hospital-Acquired Infections. *J. Mat. Chem.* 19, 3819–3831. doi:10.1039/B818698G
- Palza, H. (2015). Antimicrobial Polymers with Metal Nanoparticles. *Ijms* 16, 2099–2116. doi:10.3390/ijms16012099
- Pfefferkorn, F., and Weillhammer, J. (2017). *Open and Flexible: EOS Part Property Management Provides Both Individualization and Standardization*. Munich, Germany: Whitepaper, EOS GmbH.
- Pilipović, A., Brajlilić, T., and Drstvenšek, I. (2018). Influence of Processing Parameters on Tensile Properties of Sls Polymer Product. *Polymers* 10, 1208. doi:10.3390/polym10111208
- PubChem (2020). *Periodic Table of Elements*. Available at: <https://pubchem.ncbi.nlm.nih.gov/periodic-table/> (Accessed 11 25, 2020).
- Redwood, B., Schöffner, F., and Garret, B. (2018). “3D Printing Technologies and Materials,” in *The 3D Printing Handbook – Technologies, Design and Applications* (Arnhem: Coers & Roest), 1, 16–143.
- Seltzer, R., de la Escalera, F. M., and Segurado, J. (2011). Effect of Water Conditioning on the Fracture Behavior of PA12 Composites Processed by Selective Laser Sintering. *Mater. Sci. Eng. A* 528, 6927–6933. doi:10.1016/j.msea.2011.05.045
- Senvol (2022). Senvol Database: Industrial Additive Manufacturing Machines and Materials. Available at: <http://senvol.com/database/> (Accessed 01 31, 2022).
- Stoia, D. I., Marsavina, L., and Linul, E. (2019). Correlations between Process Parameters and Outcome Properties of Laser-Sintered Polyamide. *Polymers* 11, 1850. doi:10.3390/polym11111850
- Stoia, D. I., Marsavina, L., and Linul, E. (2020). Mode I Fracture Toughness of Polyamide and Alumide Samples Obtained by Selective Laser Sintering Additive Process. *Polymers* 12, 640. doi:10.3390/polym12030640
- Tamburrino, F., Barone, S., Paoli, A., and Razonale, A. V. (2021). Post-processing Treatments to Enhance Additively Manufactured Polymeric Parts: a Review. *Virtual Phys. Prototyp.* 16, 221–254. doi:10.1080/17452759.2021.1917039
- Taormina, G., Sciancalepore, C., Bondioli, F., and Messori, M. (2018). Special Resins for Stereolithography: *In Situ* Generation of Silver Nanoparticles. *Polymers* 10, 212. doi:10.3390/polym10020212
- Tiimob, B. J., Mwinyelle, G., Abdela, W., Samuel, T., Jeelani, S., and Rangari, V. K. (2017). Nanoengineered Eggshell-Silver Tailored Copolyester Polymer Blend Film with Antimicrobial Properties. *J. Agric. Food Chem.* 65, 1967–1976. doi:10.1021/acs.jafc.7b00133
- Turner, R. D., Wingham, J. R., Paterson, T. E., Shepherd, J., and Majewski, C. (2020). Use of Silver-Based Additives for the Development of Antibacterial Functionality in Laser Sintered Polyamide 12 Parts. *Sci. Rep.* 10, 892. doi:10.1038/s41598-020-57686-4
- Verbelen, L., Dadbakhsh, S., Van den Eynde, M., Kruth, J.-P., Goderis, B., and Van Puyvelde, P. (2016). Characterization of Polyamide Powders for Determination of Laser Sintering Processability. *Eur. Polym. J.* 75, 163–174. doi:10.1016/j.eurpolymj.2015.12.014
- Wagner, T., Höfer, T., Knies, S., and Eyerer, P. (2004). Laser Sintering of High Temperature Resistant Polymers with Carbon Black Additives. *Int. Polym. Process.* 19, 395–401. doi:10.3139/217.1846
- Wang, X., Jiang, M., Zhou, Z., Gou, J., and Hui, D. (2017). 3d Printing of Polymer Matrix Composites: A Review and Prospective. *Compos. Part B Eng.* 110, 442–458. doi:10.1016/j.compositesb.2016.11.034
- Wingham, J. R., Turner, R., Shepherd, J., and Majewski, C. (2020). Micro-CT for Analysis of Laser Sintered Micro-composites. *Rpj* 26, 649–657. doi:10.1108/RPJ-08-2019-0211
- Wohlers, T., Campbell, I., Diegel, O., Kowen, J., and Mostow, N. (2022). *Wohlers Report 2022: 3D Printing and Additive Manufacturing Global State of the Industry*. Washington, DC: ASTM International.

- Yan, C., Hao, L., Xu, L., and Shi, Y. (2011). Preparation, Characterisation and Processing of Carbon Fibre/polyamide-12 Composites for Selective Laser Sintering. *Compos. Sci. Technol.* 71, 1834–1841. doi:10.1016/j.compscitech.2011.08.013
- Yuan, S., Shen, F., Chua, C. K., and Zhou, K. (2019). Polymeric Composites for Powder-Based Additive Manufacturing: Materials and Applications. *Prog. Polym. Sci.* 91, 141–168. doi:10.1016/j.progpolymsci.2018.11.001
- Zhang, Y., Zhai, D., Xu, M., Yao, Q., Zhu, H., Chang, J., et al. (2017). 3D-printed Bioceramic Scaffolds with Antibacterial and Osteogenic Activity. *Biofabrication* 9, 025037. doi:10.1088/1758-5090/aa6ed6

Conflict of Interest: The authors declare that the research was conducted in the absence of any commercial or financial relationships that could be construed as a potential conflict of interest.

Publisher's Note: All claims expressed in this article are solely those of the authors and do not necessarily represent those of their affiliated organizations, or those of the publisher, the editors and the reviewers. Any product that may be evaluated in this article, or claim that may be made by its manufacturer, is not guaranteed or endorsed by the publisher.

Copyright © 2022 Wingham, Ahmed, Islam, Shepherd and Majewski. This is an open-access article distributed under the terms of the Creative Commons Attribution License (CC BY). The use, distribution or reproduction in other forums is permitted, provided the original author(s) and the copyright owner(s) are credited and that the original publication in this journal is cited, in accordance with accepted academic practice. No use, distribution or reproduction is permitted which does not comply with these terms.